Topological systems with strong electron-electron interactions

Inauguraldissertation

zur

Erlangung der Würde eines Doktors der Philosophie

vorgelegt der

Philosophisch-Naturwissenschaftlichen Fakultät

der Universität Basel

von

Katharina Laubscher

Basel, 2022

Genehmigt von der Philosophisch-Naturwissenschaftlichen Fakultät auf Antrag von

Prof. Dr. Jelena Klinovaja

Prof. Dr. Daniel Loss

Prof. Dr. Yuval Oreg

Basel, 21. Juni 2022

Prof. Dr. Marcel Mayor
Dekan

Summary

Over the last few decades, topological phases of matter have become an omnipresent topic in modern solid state physics. While conventional phases of matter and the phase transitions between them—like, for example, the transition from water to ice—can be fully understood from *local* properties of a system, topological phases of matter are characterized by *global* invariants that can be defined and described within the mathematical framework of topology. An early milestone in the field was the discovery of a peculiar class of materials—later termed topological insulators (TIs)—that exhibit a fully insulating bulk while their surfaces are conducting.[1] The so-called gapless surface states that are responsible for this effect allow for dissipationless transport of electrons along the surfaces of the system and exhibit a surprising robustness against perturbations. Indeed, it turns out that the existence of these surface states is guaranteed by topological—and therefore global—properties of the system, leaving them unaffected by any local imperfections of a particular sample.

Soon after the initial ideas had spread, it was realized that not only insulating but also superconducting systems can, at the mean-field level, be described within the framework of topology. One of the most striking features of topological superconductors (TSCs) is the fact that they can host so-called *Majorana bound states*.[2] These exotic quasiparticles are neither bosons nor fermions but so-called non-Abelian anyons. This means that, upon the spatial exchange of two Majorana bound states, the overall wave function of the system does not simply acquire a phase factor, but undergoes a more complicated rotation in a degenerate manifold of ground states. Apart from their fundamental interest, Majorana bound states—and non-Abelian anyons in general—are considered particularly interesting due to their potential use for quantum computation.[3] Indeed, it was predicted that Majorana bound states could in principle be used as a means to encode and process quantum information in a *non-local* way. This, in turn, would provide an intrinsic protection against quantum errors, which necessarily occur in any quantum computing device but can be expected to act *locally* in physically realistic scenarios.

Following the seminal works on topological insulators and superconductors, the field has been driven by the desire to access topological phases of matter with increasingly exotic properties. While the original theory of TIs and TSCs was built on single-particle band structure

[1] M. Z. Hasan and C. L. Kane, Rev. Mod. Phys. **82**, 4 (2010)
[2] S. R. Elliott and M. Franz, Rev. Mod. Phys. **87**, 137 (2015)
[3] C. Nayak, S. H. Simon, A. Stern, M. Freedman, and S. Das Sarma, Rev. Mod. Phys. **80**, 1083 (2008)

considerations, it has been found that the effects of strong electron-electron interactions can lead to even more exotic phases of matter, many properties of which remain elusive up to date. One of the most remarkable features of strongly interacting phases of matter is the *fractionalization* of quantum numbers: For example, when a two-dimensional electron gas is driven into the so-called fractional quantum Hall regime, quasiparticle excitations carrying only a *fraction* of the electronic charge e exist. Another intriguing consequence of strong interactions is the possible emergence of exotic bound states such as *parafermions*.[4] Indeed, to some extent, parafermions can be seen as the fractionalized cousins of Majorana bound states. With even richer non-Abelian exchange statistics than their conventional counterparts, parafermions are—at least theoretically—predicted to harbor significant potential as building blocks for future quantum computing devices.

Motivated both by potential technical applications as well as by fundamental theoretical interest, this Thesis is dedicated to studies of novel topological phases of matter with a particular focus on the effects of strong electron-electron interactions. To begin with, we give an introduction to Majorana bound states and topological superconductors in Chapter 1. While focusing mainly on non-interacting systems, this Chapter introduces some of the basic theoretical concepts that will frequently reappear throughout this Thesis. Next, in Chapters 2 and 3, we move on to strongly interacting phases of matter and study the emergence of parafermions in so-called *higher-order* TSCs. In particular, in Chapter 2, we construct a theoretical model for a fractional second-order TSC with parafermion corner states at two opposite corners of a rectangular sample. To treat the strong electron-electron interactions analytically, we make use of a *coupled-wires* construction. In this approach, a two- or three-dimensional system is built up from an array of weakly coupled one-dimensional wires, which makes it possible to incorporate interactions in the language of one-dimensional Abelian bosonization. Explicitly, our model consists of two tunnel-coupled layers of weakly coupled Rashba nanowires proximitized by a top and a bottom superconductor. We show that suitable interwire tunneling terms, together with sufficiently strong electron-electron interactions, can stabilize a helical TSC phase hosting Kramers pairs of parafermion edge states. Upon turning on a weak in-plane magnetic field, the system is then driven into a second-order TSC phase hosting zero-energy parafermion bound states localized at two opposite corners of a rectangular sample.

In Chapter 3, we propose an alternative model that can host Majorana and parafermion corner states. Instead of coupled Rashba nanowires, this model is based on coupled quasi-one-dimensional channels arising in bilayer graphene due to electrostatic gating. It is shown that suitable interchannel tunneling terms, combined with sufficiently strong electron-electron interactions, can drive the system into a fractional TI phase with fractionally charged helical edge states propagating along the edges of a finite sample. The interplay of weak proximity-induced superconductivity and a weak in-plane magnetic field can then drive a transition to a second-order TSC phase with parafermion corner states at all four corners of a rectangular sample. In the non-interacting case, these are reduced to Majorana corner states.

While the previously discussed models explicitly break time-reversal symmetry, it turns out that a magnetic field is not a necessary ingredient to obtain a second-order TSC. In Chapter 4, we present a theoretical construction of a time-reversal invariant second-order TSC with Kramers pairs of Majorana corner states. Our model is based on a layered struc-

[4] J. Alicea and P. Fendley, Annu. Rev. Condens. Matter Phys. **7**, 119 (2016)

ture consisting of two tunnel-coupled TI layers that are 'sandwiched' between two s-wave superconductors with a phase difference of π between them. The competition between interlayer tunneling and proximity-induced superconductivity can then bring the system into the second-order phase. In this Chapter, we restrict our attention to the non-interacting case for simplicity and brevity. However, we note that our model could also be extended to the fractional case by replacing the TI layers by *fractional* TI layers that could be described, e.g., via a model of coupled wires.

In Chapter 5, we move on to second-order phases in three dimensions and construct a coupled-wires model for a time-reversal invariant second-order topological insulator with helical hinge states. For suitably chosen interwire hoppings, we demonstrate that the system has a fully gapped bulk as well as fully gapped surfaces, but hosts two Kramers pairs of gapless helical hinge states that propagate along a path of hinges determined by the hierarchy of interwire hoppings and the boundary termination of the system. Furthermore, we show that sufficiently strong electron-electron interactions can drive the system into a *fractional* second-order TI phase with hinge states carrying only a fraction of the electronic charge e.

Via the coupled-wires approach, all our studies of strongly interacting phases of matter heavily relied on the one-dimensional bosonization formalism. However, many intricate details concerning technical aspects of the bosonization formalism are traditionally glossed over in such studies. For example, in bosonized language, Majorana and parafermion zero modes are usually derived from a semi-classical picture in the limit of infinitely strongly pinned bosonic fields in the bulk of the system, leaving the true spatial profile of the bound states unknown. This is why, in Chapter 6, we take one step back and study the bosonized formulation of the simplest possible toy model for a TSC—the Kitaev chain—in an abundance of technical detail. In particular, we derive the exact Majorana wave functions in a finite wire both in terms of the original fermions as well as in bosonized language using vertex algebra techniques. The two complementary viewpoints provided by the fermionic and bosonic formulations are then compared and reconciled, allowing us to provide a complete and exact account of how Majorana bound states manifest in a bosonized description of a one-dimensional TSC.

The previous Chapters have focused on the construction of theoretical toy models for exotic phases of matter and the necessary analytical tools to study them. In Chapters 7 and 8 of this Thesis, we take a slightly different perspective and focus on *signatures* of topological phases of matter, i.e., characteristic features that could be detected in experiments. In Chapter 7, we study an observable that we refer to as the *fractional boundary charge*. As suggested by the name, boundary charges are excess charges located at the boundary of a system with respect to some average background charge of the bulk. We use a coupled-wires construction to describe the fractional quantum Hall effect (FQHE) at odd filling factors $\nu = 1/(2l+1)$, where l is an integer, and calculate the fractional boundary charge arising in a Corbino disk geometry. If the hole of the disk is threaded by an external flux, we find that the fractional boundary charge depends linearly on the flux with a quantized slope that is determined by the filling factor. Furthermore, the FBC has $2l+1$ different branches that cannot be connected adiabatically, reflecting the $(2l+1)$-fold degeneracy of the ground state. We argue that these results allow for a promising way to probe FQHE samples via boundary charge measurements.

Subsequently, in Chapter 8, we shift our attention back to topological superconducting systems and study the effects of dilute classical magnetic impurities a two-dimensional time-reversal invariant TSC with helical Majorana edge states. First, we demonstrate that the

spin of a single magnetic impurity close to the edge of the TSC tends to align along the edge. The strong easy-axis spin anisotropy behind this effect originates from the interaction between the impurity and the Majorana edge states. We then compute the Ruderman-Kittel-Kasuya-Yosida (RKKY) interaction between two magnetic impurities placed close to the edge of the TSC. We find that, in the limit of large interimpurity distances, the RKKY interaction between the two impurities is mainly mediated by the Majorana edge states and leads to a ferromagnetic alignment of both spins along the edge. All of these effects are absent in trivial s-wave superconductors. As such, spectroscopy of dilute magnetic impurities could be a powerful tool to probe helical TSCs or topological materials with helical edge states in general.

Last but not least, in Chapter 9, we turn our attention to systems that exhibit one or more completely dispersionless—or so-called *flat*—bands. While such a peculiar band structure is interesting already in its own right, flat band systems have attracted particular attention since they can realize a variety of strongly correlated phases of matter. Indeed, since the kinetic energy is completely quenched in the flat band, even arbitrarily weak interactions can drastically modify the properties of the system. The same is true for disorder as well as for 'perturbations' due to, e.g., the presence of dilute impurities. This has motivated us to study the RKKY interaction between two classical magnetic impurities in two different one-dimensional lattice models that host flat bands. We start by obtaining exact results for the RKKY interaction in both models by numerical exact diagonalization and find that, in both cases, the RKKY interaction exhibits peculiar features that can directly be traced back to the presence of a flat band. Next, we compare our numerical data to results obtained via different analytical techniques. We discuss how the presence of a flat band can invalidate the conventional RKKY approximation based on non-degenerate second-order perturbation theory and highlight the need for degenerate perturbation theory or even non-perturbative approaches to accurately capture the effect of the flat band.

Contents

Chapter 1

Introduction

This introduction is adapted from:
K. Laubscher and J. Klinovaja
"Majorana bound states in semiconducting nanostructures,"
Journal of Applied Physics **130**, 081101 (2021)

1.1 Introduction

In 1937, the Italian physicist Ettore Majorana proposed the existence of an exotic type of fermion—later termed a Majorana fermion—which is its own antiparticle [1]. While the original idea of a Majorana fermion was brought forward in the context of high-energy physics [2], it later turned out that emergent excitations with related properties can also be constructed in condensed matter systems [3]. Of particular interest in this context are so-called *Majorana bound states* (MBSs) emerging at point-like defects in a special class of superconducting systems referred to as *topological superconductors* (TSCs) [4–6]. These MBSs are characterized by several intriguing properties: Firstly, similarly to their high-energy cousins, MBSs can be interpreted as being their own antiparticles in the sense that, in second-quantized language, the creation and annihilation operator associated with an MBS are equal to each other. This also immediately implies that an MBS carries both zero spin and zero charge. Secondly, MBSs appear at exactly zero energy and are separated from other, conventional quasiparticle excitations by a finite energy gap. For this reason, MBSs are also often referred to as Majorana zero modes (MZMs) and we will use the two terms interchangeably in the following. Thirdly—and probably most importantly—it was shown almost two decades ago that MBSs in a two-dimensional (2D) host material obey quantum exchange statistics that are neither fermionic nor bosonic [7–13]. Rather, MBSs are an example of so-called *non-Abelian anyons*. Loosely speaking, this means that exchanging two MBSs realizes a non-trivial rotation of the many-body ground state within a degenerate ground state subspace, with subsequent such rotations not necessarily commuting. This property makes non-Abelian anyons such as MBSs promising potential building blocks for topological quantum computers, where logical gates would then be performed by exchanging ('braiding') anyons [14, 15].

MBSs in condensed matter systems were first predicted to occur in the $\nu = 5/2$ fractional quantum Hall state [4] and in superconductors with an exotic spin-triplet pairing symmetry [8–13, 16]. Unfortunately, though, materials with intrinsic spin-triplet superconductivity

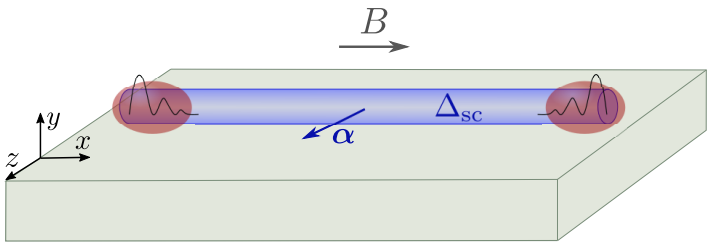

Figure 1.1: A nanowire (blue) placed on a superconducting substrate (green). The SOI vector $\boldsymbol{\alpha}$ is taken to lie along the z axis and determines the spin quantization axis. A magnetic field B is applied along the x axis such that it is oriented perpendicularly to the SOI vector. By proximity, the substrate induces a superconducting pairing of strength Δ_{sc} in the nanowire. In the topological phase [see Eq. (1.41)], MBSs (red) emerge at the wire ends.

turn out to be extremely rare. Crucially, it was later realized that an *effective* spin-triplet pairing component can be engineered from a conventional spin-singlet s-wave superconductor when combined with a material exhibiting *helical* bands, i.e., bands with spin-momentum locking [17]. With the realization of MBSs now suddenly seeming well within experimental reach, the field has witnessed a veritable explosion. Following the earliest proposals based on proximitized topological insulator (TI) edge or surface states [17,18], MBSs have subsequently been proposed to emerge in 2D semiconducting quantum wells [19–22] and one-dimensional (1D) semiconductor nanowires with strong Rashba spin-orbit interaction (SOI) [23–26], chains of magnetic adatoms deposited on a superconductor [27–32], TI nanowires [33–35], graphene-based structures such as carbon nanotubes and nanoribbons [36–42], planar Josephson junctions [43–47], and many more.

Due to its expected experimental feasibility, the Rashba nanowire model [23–26] is one of the most well-explored proposals among the above. Here, a semiconducting nanowire with strong Rashba SOI is placed in a magnetic field and proximitized by a conventional s-wave superconductor, see Fig. 1.1. The magnetic field, in combination with the strong SOI, leads to the emergence of a helical regime with two counterpropagating bulk modes carrying opposite spin projections. Since all of the required ingredients are in principle readily available in the laboratory, this proposal has triggered significant experimental activity, culminating in a series of works measuring zero-bias conductance peaks consistent with the signatures expected from MBSs [48–58]. However, it was soon realized that very similar zero-bias peaks can also appear due to alternative, non-topological mechanisms in the absence of MBSs [59–76]. As such, irrefutable experimental proof of the presence of MBSs has not been obtained up to date.

In spite of—or maybe exactly because of—these unresolved issues, the field of MBSs is a highly active and rapidly evolving research area. The goal of this Tutorial is to familiarize graduate students—both theorists and experimentalists—with some of the most well-known proposed realizations of MBSs in semiconducting nanostructures. We assume the reader to be familiar with elementary quantum mechanics and the formalism of second quantization. Furthermore, some basic knowledge of the Bogoliubov-de Gennes (BdG) formalism used to treat systems with superconducting order at the mean-field level is highly beneficial. Readers unfamiliar with this concept may for example consult Ref. [77] for a pedagogical introduction.

Throughout this Tutorial, we try to expose the relevant physical properties of the considered systems using only the simplest mathematical tools. In particular, we will not introduce the concept of topological invariants and the elaborate mathematical framework underlying the general theory of topological phases of matter. For this and other relevant aspects that are not covered in this Tutorial, we refer the reader to several excellent comprehensive reviews of the field [2–5, 78–87].

The Tutorial is organized as follows: In Sec. 1.2, we introduce some basic notions related to MBSs that will reappear frequently throughout the entire Tutorial. Using the Kitaev chain toy model [16], we demonstrate how isolated MBSs can emerge in a superconducting system and how their pinning to zero energy is guaranteed by particle-hole symmetry. We explain how an MBS can intuitively be pictured as 'half' a fermionic zero mode and how two spatially separated MBSs encode a non-local fermionic degree of freedom, leading to a two-fold ground state degeneracy of the system. After this introductory part focusing on a toy model, we turn our attention to more physical systems. First, in Sec. 1.3, we discuss the paradigmatic model of a Rashba nanowire proximitized by a conventional s-wave superconductor in the presence of a magnetic field. We identify the topological phase transition separating the trivial phase from the topological phase with a pair of MBSs at the wire ends, demonstrating how the exact MBS wave functions can be obtained in the limit of strong Rashba SOI. Furthermore, we also introduce the concept of synthetic SOI. In Sec. 1.4, we then turn our attention to proximitized TI edge states as an alternative platform for MBSs. We introduce the Jackiw-Rebbi mechanism [88, 89] leading to the emergence of bound states at mass domain walls and show how this mechanism can be exploited to construct MBSs. For completeness, we comment on a selection of other (quasi-)1D platforms hosting MBSs in Sec. 1.5. Finally, due to their recent interest, Sec. 1.6 is dedicated to 2D higher-order topological superconductors hosting so-called Majorana corner states. We conclude in Sec. 1.7.

1.2 Preliminaries

In this section, we introduce some basic notions needed to understand the emergence of Majorana zero modes in condensed matter systems. The simple ideas developed here will frequently reappear throughout the entire Tutorial.

Let us start by recalling that, within the formalism of second quantization, a single species of electrons is described by creation and annihilation operators $c^\dagger$, c satisfying the canonical anticommutation relations $\{c^\dagger, c^\dagger\} = \{c, c\} = 0$, $\{c, c^\dagger\} = 1$. If we now want to construct a quasiparticle excitation that behaves as its own antiparticle, $\gamma = \gamma^\dagger$, it is clear that it has to take the form of an equal-weight linear combination of electronic creation and annihilation operators, $\gamma = e^{i\phi}c + e^{-i\phi}c^\dagger$ for some phase ϕ. We can thus already guess that the most natural place to look for MBSs is in superconductors. Indeed, the quasiparticle excitations of a superconductor (also referred to as Bogoliubov quasiparticles) are linear combinations of electronic creation and annihilation operators [90]. However, it is not enough to just take a plain s-wave superconductor: In such a conventional superconductor, the Bogoliubov quasiparticles take the form $\gamma = uc_\sigma + vc^\dagger_{\bar{\sigma}}$ for some complex coefficients u and v and with spin $\sigma \in \{\uparrow, \downarrow\}$,[1] and where we have omitted any other degrees of freedom that might be present.

[1] Throughout this Tutorial, we use the shorthand notation $\bar{\uparrow} = \downarrow$, $\bar{\downarrow} = \uparrow$. A similar notation will be used for other quantum numbers as well.

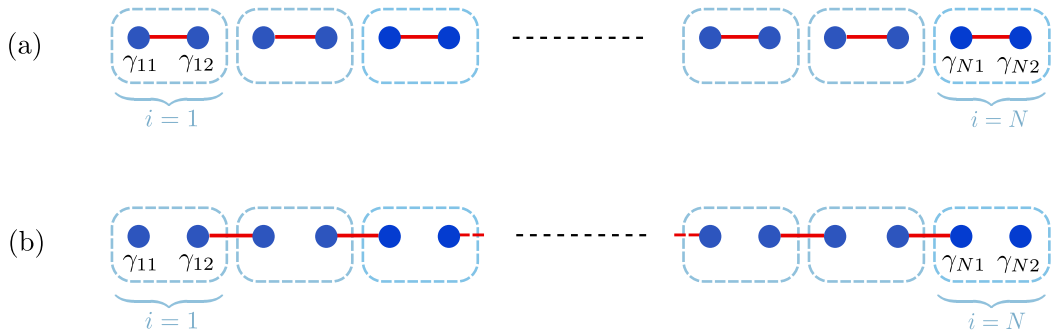

Figure 1.2: Pictorial representation of the Kitaev chain model [see Eq. (1.1)] in two limiting cases. For illustrative purposes, the physical fermion living on site i (light blue box) is split up into two Majorana operators γ_{i1}, γ_{i2} (blue dots) according to Eq. (1.2). (a) $\Delta = t = 0$. In this case, the chain is in the trivial phase, where Majorana operators belonging to the same site are coupled (red line). (b) $\Delta = t > 0$ and $\mu = 0$. In this case, the chain is in the topologically non-trivial phase, where Majorana operators belonging to neighboring sites are coupled (red line). This results in two Majorana operators γ_{11} and γ_{N2} at the ends of the chain not entering the Hamiltonian.

Clearly, such a particle can never be its own antiparticle due to the mismatching spin indices. Fortunately, there are ways to circumvent this problem: One can, for example, consider more exotic types of superconductors beyond the standard Bardeen-Cooper-Schrieffer (BCS) theory [90]. Indeed, it turns out that *spinless p-wave* superconductors are the simplest platforms capable of hosting MBSs. Even though this type of superconductivity is unlikely to occur naturally, we will see later that an effective spinless p-wave component can also be realized in heterostructures combining conventional s-wave superconductors with suitable other materials, such as, e.g., semiconductors with strong SOI. As such, studying of the simplest spinless p-wave superconductor can give important conceptual insights into the emergence of MBSs. We will therefore devote the remainder of this introductory section to a toy model based on spinless fermions with intrinsic p-wave pairing before moving to more physical models in the next sections.

Explicitly, we consider a 1D chain of spinless fermions described by the Hamiltonian [91]

$$H = \sum_{i=1}^{N-1} (-t c_i^\dagger c_{i+1} + \Delta c_i c_{i+1} + \text{H.c.}) - \mu \sum_{i=1}^{N} c_i^\dagger c_i. \tag{1.1}$$

Here, N is the number of sites, $t \geq 0$ is the nearest-neighbor hopping amplitude, $\Delta \geq 0$ is the superconducting pairing potential, which we have taken to be real for simplicity, and μ is the chemical potential. This Hamiltonian was popularized by Ref. [16] and is therefore often referred to as the *Kitaev chain*. Following the original work, we find it convenient to introduce new operators γ_{i1}, γ_{i2} for $i \in \{1, ..., N\}$ defined via

$$c_i = \frac{1}{2}(\gamma_{i1} + i\gamma_{i2}), \qquad c_i^\dagger = \frac{1}{2}(\gamma_{i1} - i\gamma_{i2}). \tag{1.2}$$

Loosely speaking, this can be thought of as separating the electron operator into its real and imaginary parts. The inverse relation of the above transformation reads

$$\gamma_{i1} = c_i^\dagger + c_i, \qquad \gamma_{i2} = i(c_i^\dagger - c_i), \tag{1.3}$$

and it can be checked that the new operators γ_{i1}, γ_{i2} satisfy the relations

$$\{\gamma_{i\alpha}, \gamma_{j\beta}\} = 2\delta_{ij}\delta_{\alpha\beta}, \qquad \gamma_{i\alpha}^\dagger = \gamma_{i\alpha}. \tag{1.4}$$

From the second relation, we thus see that the $\gamma_{i\alpha}$ correspond to Majorana operators in the sense discussed above.

Rewritten in terms of the Majorana operators, the Hamiltonian given in Eq. (1.1) takes the form

$$H = \frac{i}{2}\sum_{i=1}^{N-1}\left[(\Delta + t)\gamma_{i2}\gamma_{(i+1)1} + (\Delta - t)\gamma_{i1}\gamma_{(i+1)2}\right] - \frac{\mu}{2}\sum_{i=1}^{N}(i\gamma_{i1}\gamma_{i2} + 1). \tag{1.5}$$

While this Hamiltonian is rather complicated in its full form, a lot of insight can be gained by focusing on certain limiting cases. For future reference, let us start by briefly looking at the trivial case $\Delta = t = 0$, $\mu < 0$, where the chain simply consists of uncoupled sites. The Hamiltonian then takes the form

$$H = -\mu\sum_{i=1}^{N} c_i^\dagger c_i = -\frac{\mu}{2}\sum_{i=1}^{N}(i\gamma_{i1}\gamma_{i2} + 1). \tag{1.6}$$

We now see that this corresponds to the case where the two Majorana operators corresponding to a physical fermion are paired up, see Fig. 1.2(a). The system is fully gapped as adding a fermion costs a finite energy $-\mu$. This phase is called the (topologically) trivial phase and does not host any MBSs.

A more interesting situation arises for $\Delta = t$ and $\mu = 0$. In this case, the Hamiltonian reduces to

$$H = it\sum_{i=1}^{N-1}\gamma_{i2}\gamma_{(i+1)1}. \tag{1.7}$$

Pictorially, this now corresponds to the case where Majorana operators belonging to neighboring sites are paired up, see Fig. 1.2(b). It is therefore insightful to rewrite the Hamiltonian given in Eq. (1.7) in terms of new fermionic operators

$$d_i = \frac{1}{2}(\gamma_{i2} + i\gamma_{(i+1)1}), \quad d_i^\dagger = \frac{1}{2}(\gamma_{i2} - i\gamma_{(i+1)1}), \tag{1.8}$$

leading to

$$H = 2t\sum_{i=1}^{N-1}\left(d_i^\dagger d_i - \frac{1}{2}\right). \tag{1.9}$$

As such, we see that the bulk of the system is still gapped, i.e., adding a fermion of type d costs a finite energy $2t$. However, the two Majorana operators γ_{11} at the left end of the chain and γ_{N2} at the right end of the chain do not enter the Hamiltonian at all. This implies $[H, \gamma_{11}] = [H, \gamma_{N2}] = 0$, i.e., the two outermost sites of the chain now host two isolated zero-energy modes satisfying the Majorana property $\gamma_{11} = \gamma_{11}^\dagger$, $\gamma_{N2} = \gamma_{N2}^\dagger$. These are exactly the MBSs we were looking for, and we say that the system is now in the topologically nontrivial phase (topological phase) with one MBS at each end of the chain. As becomes clear from the pictorial representation in Fig. 1.2(b), we can think of each of the two MBSs as 'half' a

physical fermion. This also suggests that the two MBSs can be combined to form a single fermionic zero mode,

$$d_0 = \frac{1}{2}(\gamma_{11} + i\gamma_{N2}), \quad d_0^\dagger = \frac{1}{2}(\gamma_{11} - i\gamma_{N2}). \tag{1.10}$$

Since the constituent MBSs are localized far away from each other at opposite ends of the chain, this fermionic zero mode is highly delocalized. Furthermore, this non-local fermionic state can be filled or emptied at zero energy cost, leading to the presence of two degenerate ground states differing in their fermion number. This two-fold ground state degeneracy, together with the non-Abelian exchange statistics of MBSs, lies at the heart of the idea that MBSs can be used for topological quantum computation. While a detailed discussion of how MBSs can be used to perform topologically protected quantum gates is beyond the scope of this Tutorial, we refer the interested reader to several excellent reviews covering this topic [2, 3, 78, 79, 82, 83].

While the above discussion focused on two limiting cases corresponding to the fully dimerized situations shown in Fig. 1.2, the qualitative properties of the trivial and nontrivial phase persist also if one deviates from these fine-tuned points. Indeed, the number of MBSs at a given end of the chain is directly related to a *topological invariant*, meaning that it is robust under continuous changes of the system parameters as long as the bulk gap remains open and none of the protecting symmetries are broken. More generally, the theory of topological phases of matter states that topologically inequivalent phases are separated by closing points of the bulk gap and differ by the values of their topological invariant. In the case of the Kitaev chain, this invariant takes the values 0 (trivial phase) or 1 (topological phase) and gives the number of MBSs at one end of the chain.[2]

The above statement motivates us to look at the bulk spectrum of the Kitaev chain. Assuming periodic boundary conditions for the moment, we can rewrite the Hamiltonian given in Eq. (1.1) in momentum space. In order to account for the superconducting term, we resort to the standard BdG description employing the Nambu spinor $C_k^\dagger = (c_k^\dagger, c_{-k})$. The bulk Hamiltonian then takes the form $H = \frac{1}{2}\sum_k C_k^\dagger \mathcal{H}(k) C_k$ with

$$\mathcal{H}(k) = (-2t\cos k - \mu)\,\eta_z - 2\Delta \sin k\,\eta_y. \tag{1.11}$$

Here, η_i for $i \in \{x, y, z\}$ are Pauli matrices acting in particle-hole space. It is important to note that, as for any mean-field BdG Hamiltonian in the Nambu representation, the electron and hole components of $\mathcal{H}(k)$ are not independent [77]. More specifically, $\mathcal{H}(k)$ satisfies the so-called *particle-hole symmetry*

$$U_C \mathcal{H}(k) U_C^{-1} = -\mathcal{H}^*(-k) \tag{1.12}$$

with $U_C = \eta_x$ [92]. This symmetry guarantees that the spectrum of $\mathcal{H}(k)$ is symmetric around zero in the sense that for any eigenstate $\varphi_E(k)$ at energy $+E(k)$ there is also an eigenstate $U_C\varphi_E^*(-k)$ at energy $-E(-k)$. Explicitly, we find that the bulk energy spectrum is given by

$$E^2(k) = (2t\cos k + \mu)^2 + 4\Delta^2 \sin^2 k. \tag{1.13}$$

[2] More explicitly, when taking particle-hole symmetry as the only symmetry of the model, the Kitaev chain belongs to the class D in the symmetry classification of topological phases of matter [92, 93], which has a $\mathbb{Z}_2$ topological invariant in one dimension. Via the bulk-boundary correspondence, the value of this topological invariant is directly related to the number of MBSs at a given end of the chain.

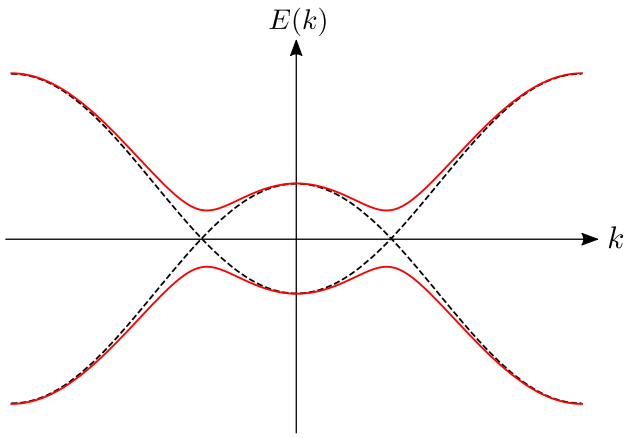

Figure 1.3: Bulk spectrum of the Kitaev chain, see Eq. (1.13). In the absence of superconductivity, i.e., for $\Delta = 0$, the spectrum is gapless (black dashed lines). Any finite Δ leads to a fully gapped spectrum (red solid lines) for any μ within the normal-state band. In this example, we have used $\mu/t = -1$ and $\Delta = 0$ for the black dashed line ($\Delta/t = 0.3$ for the red solid line).

We show an example plot of this energy spectrum in Fig. 1.3. It can easily be checked that, for any finite Δ, the bulk spectrum is fully gapped except for $\mu = \pm 2t$. Thus, these points mark the possible transition between topologically distinct phases. Starting from the fully dimerized case shown in Fig. 1.2(b), we can then infer that the Kitaev chain remains in the topologically nontrivial phase for any finite Δ and any chemical potential $|\mu| < 2t$, i.e., for any μ within the normal-state band. This also means that the two MBSs persist for any set of parameters within this range. However, the MBSs will generally cease to be perfectly localized to only the outermost sites of the chain. Instead, their spatial profile will decay exponentially into the bulk. This also means that in a chain of finite length, the two MBSs at opposite ends of the chain will acquire a finite overlap with each other, thereby lifting the exact two-fold ground state degeneracy discussed above. However, the energy splitting between the two ground states of opposite fermion parity is exponentially suppressed with the system length, meaning that our simplified picture introduced above remains valid in the limit of long chains.

An intuitive explanation for the stability of the MBSs can be given via a simple symmetry argument. This is easiest to understand when we first consider a semi-infinite system with a single end. In the topological phase, a single zero-energy MBS is located at this end [see, e.g., Fig. 1.2(b)]. Furthermore, the particle-hole symmetry discussed above can easily be recast to real space and also applies in the case of a finite system. This means that the spectrum of the BdG Hamiltonian is symmetric around zero energy, or, equivalently, the creation of a Bogoliubov quasiparticle at energy E is equivalent to the annihilation of a quasiparticle (i.e., the creation of a quasihole) at energy $-E$. It is now straightforward to see that a single isolated MBS at $E = 0$ cannot be removed from zero energy without violating particle-hole symmetry. This argument also remains valid for a long but finite chain: Since the overlap between the two MBSs is exponentially suppressed with the system size, it can become negligibly small for a sufficiently long chain. In this case, neither of the MBSs can be removed from zero energy by continuous changes of the system parameters or

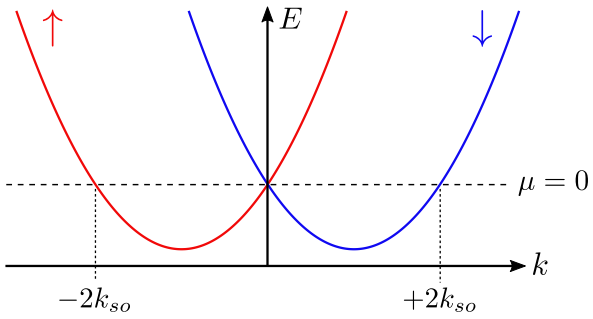

Figure 1.4: Bulk spectrum of a bare Rashba nanowire, see Eq. (1.17). The spectrum consists of two parabolas—one for spin up and one for spin down—shifted by $\pm k_{so}$. At $\mu = 0$, the Fermi momenta are given by $k = 0$ and $k = \pm 2k_{so}$.

arbitrary particle-hole symmetric local perturbations as long as the bulk gap remains open. The exponential suppression of the energy splitting between the two degenerate ground states is also referred to as the topological protection of the ground state degeneracy.

Last but not least, let us stress once again that the Kitaev chain should merely be viewed as a toy model. Firstly, electrons in solids naturally come with a spin degree of freedom, and secondly, intrinsic spin-triplet superconductors are very rare to almost non-existent in nature. It is therefore natural to ask whether there exist ways to enable topological superconducting phases in heterostructures based on conventional s-wave superconductors. Fortunately, this is indeed possible when so-called *helical* bands—i.e., bands with spin-momentum locking—are present. Indeed, when a conventional s-wave pairing term is projected onto a helical band, an effective spinless p-wave component emerges.[3]

In the remainder of this Tutorial, we will explore some of the most well-known realizations of MBSs based on conventional s-wave superconductors. Our main focus lies on proximitized Rashba nanowires in the presence of a magnetic field (Sec. 1.3) as well as proximitized topological insulator edge states (Sec. 1.4). In light of our previous discussion of the Kitaev chain, our main strategy will be to first identify the topologically inequivalent phases of the models under consideration by looking for closing points of the bulk gap. Subsequently, we will derive the conditions under which MBSs emerge by explicitly solving for localized zero-energy wave function solutions of the corresponding BdG equations.

1.3 Majorana bound states in nanowires

In this section, we study the paradigmatic example of MBSs arising in semiconducting Rashba nanowires in the presence of a magnetic field and proximity-induced s-wave superconductivity [23–26]. Due to its expected experimental feasibility, this setup is often considered one of the most promising proposals for the realization of MBSs. Indeed, over the last decade, significant progress has been reported in experiments based on InAs or InSb nanowires [48–50,54,55]. In the following, we present the theoretical arguments leading to the emergence of MBSs and demonstrate how the explicit MBS wave functions can be obtained in the limit of strong SOI. For this, we will closely follow the methods developed in Ref. [94].

[3] For an explicit demonstration of how this happens, see for example Ref. [78].

1.3.1 MBSs in Rashba nanowires: Minimal model

Our starting point is a 1D Rashba nanowire that is taken to be oriented along the x axis, see Fig. 1.1. The bare nanowire is described by the Hamiltonian $H_0 = H_{kin} + H_{SOI}$, where H_{kin} denotes the kinetic contribution to the Hamiltonian and H_{SOI} denotes the Rashba SOI. The SOI is characterized by the spin-orbit vector $\boldsymbol{\alpha}$, which is oriented perpendicular to the nanowire and defines our spin quantization axis. For concreteness, we assume that $\boldsymbol{\alpha}$ points along the z axis, see again Fig. 1.1. Explicitly, the kinetic term takes the form

$$H_{kin} = \sum_{\sigma} \int dx\, \Psi_{\sigma}^{\dagger}(x) \left(-\frac{\hbar^2 \partial_x^2}{2m} - \mu \right) \Psi_{\sigma}(x), \tag{1.14}$$

where $\Psi_{\sigma}(x)$ $[\Psi_{\sigma}^{\dagger}(x)]$ destroys (creates) an electron of spin $\sigma \in \{\uparrow, \downarrow\}$ at position x in the nanowire, m denotes the effective electron mass, and μ denotes the chemical potential. The SOI term is given by

$$H_{SOI} = -i\alpha \sum_{\sigma,\sigma'} \int dx\, \Psi_{\sigma}^{\dagger}(x) (\sigma_z)_{\sigma\sigma'} \partial_x \Psi_{\sigma'}(x), \tag{1.15}$$

where σ_i for $i \in \{x, y, z\}$ are Pauli matrices acting in spin space and $\alpha > 0$ denotes the strength of the SOI. Note that in this description, the chemical potential is measured relative to the SOI energy $E_{so} = m\alpha^2/(2\hbar^2)$. For a translationally invariant nanowire, H_0 can be written in momentum space as $H_0 = \sum_k \Psi_k^{\dagger} \mathcal{H}_0(k) \Psi_k$, where we have defined $\Psi_k^{\dagger} = (\psi_{k\uparrow}^{\dagger}, \psi_{k\downarrow}^{\dagger})$ and the Hamiltonian density $\mathcal{H}_0(k)$ is given by

$$\mathcal{H}_0(k) = \frac{\hbar^2 k^2}{2m} - \mu + \alpha k \sigma_z. \tag{1.16}$$

The bulk spectrum of H_0 is readily found to be

$$E_{0,\pm}(k) = \frac{\hbar^2 k^2}{2m} - \mu \pm \alpha k \tag{1.17}$$

and corresponds to two parabolas—one for each spin species—shifted relative to each other, see Fig. 1.4. In the special case $\mu = 0$, the Fermi points are given by $k = 0$ and $k = \pm 2k_{so}$, where the spin-orbit momentum k_{so} is given by $k_{so} = m\alpha/\hbar^2$. In general, for a small but possibly finite μ, we will call the branches close to $k = 0$ ($k = \pm 2k_{so}$) the interior (exterior) branches of the spectrum.

Let us now additionally consider the effect of a magnetic field of strength B oriented perpendicular to the SOI vector. For concreteness, we take the magnetic field to be oriented along the x axis in the following, see Fig. 1.1. The magnetic field gives rise to the Zeeman term

$$H_Z = \Delta_Z \sum_{\sigma,\sigma'} \int dx\, \Psi_{\sigma}^{\dagger}(x) (\sigma_x)_{\sigma\sigma'} \Psi_{\sigma'}(x) \tag{1.18}$$

with $\Delta_Z = g\mu_B B/2$, where g denotes the g-factor of the nanowire and μ_B the Bohr magneton. In the following, we will assume $\Delta_Z \geq 0$.

Finally, if the nanowire is brought in tunnel-contact with a bulk s-wave superconductor, we can account for the proximity-induced superconductivity via

$$H_{sc} = \frac{\Delta_{sc}}{2} \sum_{\sigma,\sigma'} \int dx\, \Psi_\sigma(x)(i\sigma_y)_{\sigma\sigma'}\Psi_{\sigma'}(x) + \text{H.c.}, \tag{1.19}$$

where we take Δ_{sc} to be real and non-negative for simplicity. The total Hamiltonian that we will be concerned with in the remainder of this section is then given by $H = H_0 + H_Z + H_{sc}$.

Assuming a translationally invariant system for the moment, we can rewrite H in momentum space. It then takes the form $H = \frac{1}{2}\sum_k \Psi_k^\dagger \mathcal{H}(k)\Psi_k$, where we have introduced the Nambu spinor $\Psi_k^\dagger = (\psi_{k\uparrow}^\dagger, \psi_{k\downarrow}^\dagger, \psi_{-k\uparrow}, \psi_{-k\downarrow})$ and the Hamiltonian density is given by

$$\mathcal{H}(k) = \left(\frac{\hbar^2 k^2}{2m} - \mu\right)\eta_z + \alpha k \sigma_z + \Delta_Z \eta_z \sigma_x + \Delta_{sc}\eta_y\sigma_y. \tag{1.20}$$

Here, η_i for $i \in \{x, y, z\}$ are Pauli matrices acting in particle-hole space. Like any BdG Hamiltonian, this Hamiltonian is particle-hole symmetric as expressed by Eq. (1.12). As discussed in Sec. 1.2, it is exactly this particle-hole symmetry that is responsible for pinning any isolated MBS—if present—to exactly zero energy. We will come back to this point when we explicitly solve for MBSs in Subsec. 1.3.2.[4]

Via a straightforward eigenvalue calculation, the spectrum of $\mathcal{H}(k)$ is found to be

$$E_\pm^2(k) = \left(\frac{\hbar^2 k^2}{2m} - \mu\right)^2 + \alpha^2 k^2 + \Delta_Z^2 + \Delta_{sc}^2 \pm 2\sqrt{\left(\frac{\hbar^2 k^2}{2m} - \mu\right)^2 (\Delta_Z^2 + \alpha^2 k^2) + \Delta_Z^2 \Delta_{sc}^2}. \tag{1.22}$$

By direct inspection, one can show that, for any finite Δ_{sc}, the above spectrum is always fully gapped except for a single gap closing point at $k = 0$ for[5]

$$\Delta_Z^2 = \mu^2 + \Delta_{sc}^2. \tag{1.23}$$

As we will see in the next subsection, this closing and reopening of the bulk gap corresponds to a topological phase transition between a trivial phase and a topologically nontrivial phase characterized by the emergence of an MBS at each wire end.

1.3.2 Majorana wave functions

In the following, we focus on the regime of strong SOI with $0 \leq \Delta_Z, \Delta_{sc} \ll E_{so}$. If we furthermore assume $|\mu| \ll E_{so}$, we can linearize the spectrum around the Fermi points for

[4] Furthermore, if and only if $\Delta_Z = 0$, the Hamiltonian also has time-reversal symmetry expressed by

$$U_T \mathcal{H}(k) U_T^{-1} = \mathcal{H}^*(-k) \tag{1.21}$$

with $U_T = i\sigma_y$ [92,93]. However, as we will see later, the existence of MBSs in this minimal model necessarily requires that time-reversal symmetry is broken.

[5] Recall that we are assuming $\alpha > 0$ throughout this entire section. In the absence of SOI, i.e., for $\alpha = 0$, the bulk gap can also close at points other than $k = 0$ and the arguments presented in the following do no longer hold.

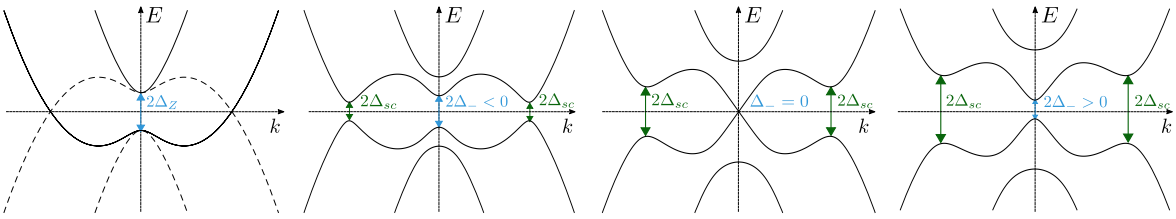

Figure 1.5: Bulk spectrum of a Rashba nanowire in the presence of a magnetic field and proximity-induced superconductivity, see Eq. (1.22). For simplicity, we depict the case $\mu = 0$. (a) In the absence of superconductivity, i.e., $\Delta_{sc} = 0$, a Zeeman gap of size $2\Delta_Z$ is opened around $k = 0$, while the exterior branches remain gapless. (b) If a small but finite $\Delta_{sc} > 0$ is turned on, the interior gap is modified to $2\Delta_-$ with $\Delta_- < 0$, while a gap of size $2\Delta_{sc}$ opens around $k = \pm 2k_{so}$. (c) As Δ_{sc} is increased, we eventually reach $\Delta_Z = \Delta_{sc}$, where the interior gap closes. (d) For $\Delta_{sc} > \Delta_Z$, the interior gap reopens with $\Delta_- > 0$. The closing and reopening of the bulk gap shown in panels (b)-(d) marks the phase transition between the topologically nontrivial phase with $\Delta_- < 0$ and the trivial phase with $\Delta_- > 0$.

$\mu = 0$, which are given by $k = 0$ and $k = \pm 2k_{so}$ (see again Fig. 1.4). The linearized fields take the form

$$\Psi_\uparrow(x) = e^{-2ik_{so}x} L_\uparrow(x) + R_\uparrow(x), \tag{1.24}$$

$$\Psi_\downarrow(x) = L_\downarrow(x) + e^{2ik_{so}x} R_\downarrow(x), \tag{1.25}$$

where $R_\sigma(x)$ $[L_\sigma(x)]$ is a slowly varying right-moving [left-moving] field and where we have explicitly taken out the rapidly oscillating factors $e^{\pm 2ik_{so}x}$. In the linearized model, the kinetic term takes the form

$$H_{kin} = -i\hbar v_F \sum_\sigma \int dx\, [R^\dagger_\sigma(x)\partial_x R_\sigma(x) - L^\dagger_\sigma(x)\partial_x L_\sigma(x)], \tag{1.26}$$

where the Fermi velocity is given by $v_F = \alpha/\hbar$ and where we have dropped all rapidly oscillating terms.[6] Similarly, the Zeeman term now reads

$$H_Z = \Delta_Z \int dx\, R^\dagger_\uparrow(x) L_\downarrow(x) + \text{H.c.}, \tag{1.27}$$

while the superconducting term takes the form

$$H_{sc} = \Delta_{sc} \int dx\, [R_\uparrow(x) L_\downarrow(x) + L_\uparrow(x) R_\downarrow(x)] + \text{H.c.} \tag{1.28}$$

As an additional simplification, we note that the interior and exterior branches are only coupled among themselves. This allows us to separate the total Hamiltonian into two decoupled subsystems H_i and H_e. For $l \in \{i, e\}$ we can write $H_l = \frac{1}{2}\int dx\, \Phi^\dagger_l(x)\mathcal{H}_l(x)\Phi_l(x)$ with $\Phi^\dagger_i = (R^\dagger_\uparrow, L^\dagger_\downarrow, R_\uparrow, L_\downarrow)$ and

$$\mathcal{H}_i(x) = -i\hbar v_F \partial_x \sigma_z - \mu\eta_z + \Delta_Z \eta_z \sigma_x + \Delta_{sc}\eta_y\sigma_y \tag{1.29}$$

[6] This is justified if the period of oscillation $\propto \pi/(2k_{so})$ is much smaller than all other relevant length scales in the problem, since the corresponding contributions average out in the spatial integral.

for the interior branches and similarly $\Phi_e^\dagger = (L_\uparrow^\dagger, R_\downarrow^\dagger, L_\uparrow, R_\downarrow)$ and

$$\mathcal{H}_e(x) = i\hbar v_F \partial_x \sigma_z - \mu\eta_z + \Delta_{sc}\eta_y\sigma_y \tag{1.30}$$

for the exterior branches. Passing to momentum space once again, the bulk energy spectra for the interior and exterior branches are readily found to be

$$E_{i,\pm}^2(k) = (\hbar v_F k)^2 + (\Delta_+^2 + \Delta_-^2)/2 \pm 2\sqrt{[(\Delta_+^2 - \Delta_-^2)/4]^2 + (\hbar v_F k)^2\mu^2}, \tag{1.31}$$

$$E_{e,\pm}^2(k) = (\hbar v_F k \pm \mu)^2 + \Delta_{sc}^2, \tag{1.32}$$

where the momentum k is now taken from the Fermi points and where we have defined $\Delta_\pm = \sqrt{\mu^2 + \Delta_{sc}^2} \pm \Delta_Z$. Consistent with Eq. (1.23), we find from Eq. (1.31) that the gap for the interior branches closes at $k = 0$ when $\Delta_- = 0$, while the exterior branches are always fully gapped for any finite Δ_{sc}.

Figure 1.5 illustrates this gap closing and reopening in more detail, where we chose to depict the case $\mu = 0$ for simplicity. In this case, we obtain the particularly simple expressions $\Delta_\pm = \Delta_{sc} \pm \Delta_Z$. Let us first consider the case $\Delta_{sc} = 0$, see Fig. 1.5(a). In this case, a gap of size $2\Delta_Z$ is opened for the interior branches, while the exterior branches stay gapless. We are thus in a so-called *helical* regime where there is only one gapless right-moving bulk mode with spin down and one left-moving bulk mode with spin up [95, 96]. If one now turns on a small but finite $\Delta_{sc} > 0$, the interior gap is modified to $2\Delta_-$ with $\Delta_- < 0$, while the exterior branches open a gap of size $2\Delta_{sc}$, see Fig. 1.5(b). As Δ_{sc} is increased, we eventually reach $\Delta_Z = \Delta_{sc}$, where the interior gap closes, see Fig. 1.5(c). Finally, for $\Delta_{sc} > \Delta_Z$, the interior gap reopens with $\Delta_- > 0$, see Fig. 1.5(d).

From our preliminary knowledge of the Kitaev chain, we can already guess that the above closing and reopening of the bulk gap could mark the phase transition between a topologically nontrivial phase with $\Delta_- < 0$ and a trivial phase with $\Delta_- > 0$. Indeed, since the phase with $\Delta_- < 0$ exhibits a single pair of helical (and, thus, effectively spinless) bulk modes gapped out by proximity-induced superconductivity, we find ourselves in a similar situation as in the Kitaev chain—with the difference that now we started from a spinful model and a conventional superconductor rather than just assuming spinless electrons with p-wave pairing. In the following, we will confirm that the phase with $\Delta_- < 0$ is indeed the topological phase by demonstrating that MBSs emerge at the wire ends if and only if $\Delta_- < 0$. This is done by explicitly solving the BdG equations corresponding to the linearized model for localized zero-energy bound states, where we again focus on the case $\mu = 0$ for simplicity.

As a first step, we determine zero-energy solutions of H_i and H_e independently. These are readily obtained by solving the BdG equation $\mathcal{H}_l\phi_l(x) = 0$ for $l \in \{i, e\}$. In the following, we focus on a semi-infinite system with a single edge at $x = 0$. In order to obtain normalizable eigenfunctions localized to this edge, we make an Ansatz for an exponentially decaying eigenfunction $\phi_l(x) = \phi_l(0)e^{-x/\xi_l}$, where $\xi_l > 0$ is a localization length that remains to be determined. Plugging in this Ansatz and imposing $\det[\mathcal{H}_l] = 0$, we find the possible values of ξ_l to be

$$\xi_i = \alpha/|\Delta_{sc} - \Delta_Z|, \tag{1.33}$$

$$\xi_i' = \alpha/(\Delta_{sc} + \Delta_Z) \tag{1.34}$$

for the interior branches and

$$\xi_e = \alpha/\Delta_{sc} \tag{1.35}$$

for the exterior branches. Note again that we assume $\Delta_Z, \Delta_{sc} \geq 0$ throughout this entire section, such that the above localization lengths are finite and positive whenever the system is fully gapped. Now solving for the corresponding eigenfunctions, we find two linearly independent, exponentially decaying solutions for the interior and exterior branches each. Up to normalization, these read

$$\phi_{i,1}(x) = \begin{pmatrix} -ip \\ 1 \\ ip \\ 1 \end{pmatrix} e^{-x/\xi_i}, \qquad \phi_{i,2}(x) = \begin{pmatrix} -i \\ -1 \\ -i \\ 1 \end{pmatrix} e^{-x/\xi_i'}, \tag{1.36}$$

$$\phi_{e,1}(x) = \begin{pmatrix} i \\ 1 \\ -i \\ 1 \end{pmatrix} e^{-x/\xi_e}, \qquad \phi_{e,2}(x) = \begin{pmatrix} i \\ -1 \\ i \\ 1 \end{pmatrix} e^{-x/\xi_e}, \tag{1.37}$$

where we have defined $p = \mathrm{sgn}(\Delta_{sc} - \Delta_Z)$. In second-quantized form, the full zero modes then read $\gamma_{l,s} = \int dx\, \phi_{l,s}^\dagger(x)\Phi_l(x)$ for $s \in \{1,2\}$. The oscillating phase factors $\pm e^{2ik_{so}x}$ can now be reincorporated by going back to the original basis $\Psi^\dagger = (\Psi_\uparrow^\dagger, \Psi_\downarrow^\dagger, \Psi_\uparrow, \Psi_\downarrow)$ and writing $\gamma_{l,s} = \int dx\, \psi_{l,s}^\dagger(x)\Psi(x)$, where we have defined $\psi_{i,1}(x) = \phi_{i,1}(x)$, $\psi_{i,2}(x) = \phi_{i,2}(x)$ and

$$\psi_{e,1}(x) = \begin{pmatrix} ie^{-2ik_{so}x} \\ e^{2ik_{so}x} \\ -ie^{2ik_{so}x} \\ e^{-2ik_{so}x} \end{pmatrix} e^{-x/\xi_e}, \tag{1.38}$$

$$\psi_{e,2}(x) = \begin{pmatrix} ie^{-2ik_{so}x} \\ -e^{2ik_{so}x} \\ ie^{2ik_{so}x} \\ e^{-2ik_{so}x} \end{pmatrix} e^{-x/\xi_e}, \tag{1.39}$$

and where we again neglect all rapidly oscillating terms.

As the next and final step, we now turn to the issue of boundary conditions. At the left edge of the system at $x = 0$, we demand that our zero-energy wave function $\psi_M(x) \propto \sum_{l,s} c_{l,s}\psi_{l,s}(x)$ satisfies vanishing boundary conditions $\psi_M(x = 0) = 0$. Here, there is an important difference between the two topologically nonequivalent regimes $\Delta_{sc} > \Delta_Z$ and $\Delta_{sc} < \Delta_Z$. In the first case, the four solutions $\psi_{l,s}$ are linearly independent at $x = 0$, showing that the boundary condition can never be fulfilled. This phase corresponds to the topologically trivial one with no zero-energy bound states at the wire ends. In the second case, however, we find that the linear combination $\psi_M(x) \propto \psi_{i,1}(x) - \psi_{e,1}(x)$ satisfies $\psi_M(0) = 0$. Explicitly, the total wave function is then given by

$$\psi_M(x) = \begin{pmatrix} i \\ 1 \\ -i \\ 1 \end{pmatrix} e^{-x/\xi_i} - \begin{pmatrix} ie^{-2ik_{so}x} \\ e^{2ik_{so}x} \\ -ie^{2ik_{so}x} \\ e^{-2ik_{so}x} \end{pmatrix} e^{-x/\xi_e}, \tag{1.40}$$

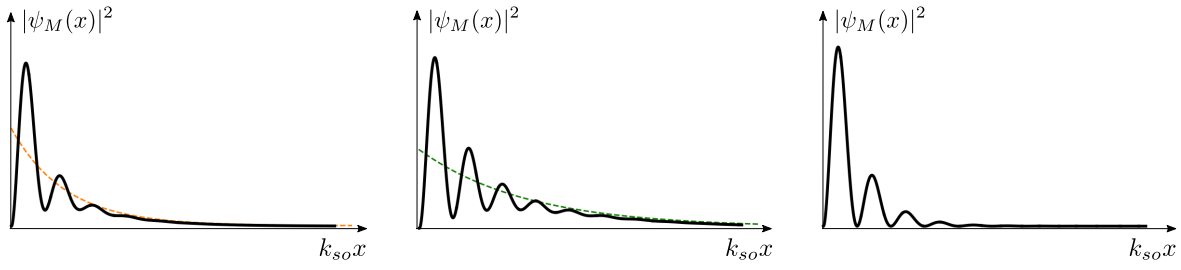

(a) (b) (c)

Figure 1.6: MBS probability density $|\psi_M(x)|^2$ obtained from Eq. (1.40) for different parameter values. In all cases, $|\psi_M(x)|^2$ exhibits characteristic oscillations with a period of π/k_{so} and decays exponentially into the bulk. (a) Deep in the topological phase, there are relatively few oscillations before a uniform exponential decay with decay length ξ_e (orange line) sets in. Here, we used $\Delta_Z/E_{so} = 0.5$, $\Delta_{sc}/E_{so} = 0.1$. (b) Close to the topological phase transition, the MBS probability density decays more slowly. At long distances, the decay length is given by ξ_i (green line). Here, we used $\Delta_Z/E_{so} = 0.3$, $\Delta_{sc}/E_{so} = 0.25$. (c) Intermediate regime with $\Delta_Z/E_{so} = 0.4$, $\Delta_{sc}/E_{so} = 0.2$, where the two decay lengths are equal.

where we have suppressed a normalization factor. Furthermore, we can also check that this solution indeed corresponds to a Majorana bound state: The operator $\gamma_M = \int dx\, \psi_M^\dagger(x)\Psi(x)$ satisfies the Majorana property $\gamma_M = \gamma_M^\dagger$ if and only if the wave function satisfies $\psi_M(x) = (f(x), g(x), f^*(x), g^*(x))^T$ for arbitrary functions f and g up to normalization. Our wave function $\psi_M(x)$ given in Eq. (1.40) can readily be brought into this form by defining $f(x) = ig^*(x) = i(e^{-x/\xi_i} - e^{-2ik_{so}x}e^{-x/\xi_e})$, which confirms that we are indeed looking at an MBS. Equivalently, we can also understand the Majorana property directly from the particle-hole symmetry operation defined in Eq. (1.12). Indeed, the above condition on $\psi_M(x)$ is nothing but $U_C\psi_M^*(x) = \psi_M(x)$. This once again reflects the fact that an isolated MBS is 'its own partner' under particle-hole symmetry and therefore has to stay pinned to zero energy.

Figure 1.6 shows example plots for the MBS probability density for different values of Δ_Z and Δ_{sc}. From Eq. (1.40) we note that there are two possibly different localization lengths ξ_i and ξ_e entering the Majorana wave function, where ξ_i (ξ_e) comes from the contribution of the interior (exterior) branches. The interplay between these two contributions causes oscillations in the MBS probability density with a period of π/k_{so}.

Note that while above we have focused on the case $\mu = 0$ for analytical simplicity, MBSs also exist in the more general case of finite μ as long as the bulk gap remains open. This stability can again be understood from the particle-hole symmetry of the BdG spectrum as discussed in Sec. 1.2. Alternatively, the presence of MBSs can also explicitly be verified by, e.g., numerical exact diagonalization of a corresponding tight-binding model. In conclusion, we identify the regime

$$|\Delta_Z| > \sqrt{\mu^2 + \Delta_{sc}^2} \tag{1.41}$$

as the topologically nontrivial phase of the Rashba nanowire model. We note that the same topological criterion could also be obtained directly from the exact bulk spectrum given in Eq. (22).

Let us close this subsection with a few remarks on the approximations that were made in order to arrive at Eqs. (1.40). Firstly, we were working in the limit of strong SOI such

that the superconducting and Zeeman terms can be treated as weak perturbations to the kinetic Hamiltonian. However, analytical solutions for the MBSs can also be obtained in the opposite limit of weak SOI, see Ref. [94]. Secondly, we have focused on a semi-infinite system with a single edge at $x = 0$. This corresponds to the ideal case where the MBS at $x = 0$ is completely independent of the second MBS at the other end of the system. In a nanowire of finite length, on the other hand, the two MBSs necessarily overlap and hybridize into a fermionic in-gap state with an energy that decreases exponentially with the length of the system. As such, the semi-infinite approximation is justified for large systems. For the explicit fermionic in-gap solutions and the 'quasi-MBS' wave functions in a system of arbitrary finite length, we refer the reader to Ref. [97]. Thirdly, we have also neglected orbital effects [98–101] caused by the magnetic field. If taken into account, in the limit of strong SOI, there are regimes in which the amplitude of the oscillating MBS splitting stays constant or even decays with increasing magnetic field, in stark contrast to the commonly studied case where orbital effects of the magnetic field are neglected [100]. Last but not least, electron-electron interactions were completely neglected in our considerations. As was shown in Refs. [102–107], MBSs can also survive in the presence of weak to moderate electron-electron interactions. Furthermore, also models with long-range hoppings and long-range pairing interactions have been studied [108, 109].

1.3.3 Rotating magnetic field and synthetic SOI

The setup described in the previous subsections requires SOI of Rashba type as a necessary ingredient. In addition, the chemical potential has to be fine-tuned to lie sufficiently close to the spin-orbit energy. These two requirements limit the experimental feasibility of the Rashba nanowire setup, in particular since the intrinsic SOI of the nanowire is a material-dependent property that cannot be fully controlled from the outset. A promising alternative is the so-called *synthetic* SOI induced by a rotating magnetic field generated by, e.g., suitably arranged nanomagnets [38,42,110–116]. Indeed, a local gauge transformation relates a Rashba nanowire subjected to a uniform magnetic field to a nanowire without SOI subjected to a helical magnetic field [117]. Therefore, both setups exhibit a topologically non-trivial phase with MBSs at the wire ends.

To make this statement explicit, let us consider the spin-dependent gauge transformation

$$\Psi_\sigma(x) = e^{-i\sigma k_{so} x}\tilde{\Psi}_\sigma(x), \tag{1.42}$$

where the fields $\tilde{\Psi}_\sigma(x)$ are now defined in a rotating frame. In the rotating frame, H_0 defined previously [see Eqs. (1.14) and (1.15)] takes the form

$$H_0 = \sum_\sigma \int dx\, \tilde{\Psi}^\dagger_\sigma(x) \left[-\frac{\hbar^2 \partial_x^2}{2m} - (\mu + E_{so}) \right] \tilde{\Psi}_\sigma(x). \tag{1.43}$$

This means that the SOI is now absent and the bulk spectrum is effectively given by two identical parabolas—one for spin up and one for spin down—centered around $k = 0$. While the superconducting term retains its form in terms of the new fields, the Zeeman term now reads

$$H_Z = \Delta_Z \int dx\, e^{2ik_{so}x} \tilde{\Psi}^\dagger_\uparrow(x) \tilde{\Psi}_\downarrow(x) + \text{H.c.}, \tag{1.44}$$

which takes the form of a Zeeman term induced by a helical magnetic field with a pitch of $2k_{so}$,

$$\tilde{B}(x) = B(\cos(2k_{so}x), -\sin(2k_{so}x), 0). \tag{1.45}$$

As before, MBSs can emerge from this setup if the chemical potential is tuned to lie in the gap opened by the helical magnetic field. Even more interestingly, however, it has been shown that in certain setups the need to fine-tune the chemical potential is eliminated. This can, for example, be realized in systems with Ruderman-Kittel-Kasuya-Yosida (RKKY) interaction [118–120]. Indeed, if magnetic impurities are placed on a superconducting substrate, a strong indirect exchange interaction of RKKY-type promotes a helical spin ordering with pitch $2k_F$ [27].

1.4 Majorana bound states in TI heterostructures

We have seen in the previous section that the presence of helical modes is crucial for the emergence of MBSs in 1D TSCs. While in Rashba nanowires the helical regime is realized due to strong SOI in combination with a magnetic field, a related approach—originally proposed in Refs. [17, 18] even before the nanowire setup—instead exploits the helical edge states of a 2D TI to engineer MBSs. As opposed to the nanowire case, where time-reversal symmetry needs to be explicitly broken in order to reach the helical regime, the helical regime in TIs emerges in the presence of time-reversal symmetry. Indeed, the key feature of a 2D TI is the existence of a pair of gapless helical edge states with an approximately linear dispersion [see also Fig. 1.8(a)] in addition to a fully gapped bulk. The two counterpropagating edge states carry opposite spin projections and are related to each other by time-reversal symmetry.

In the following, we will first review the general mechanism leading to the emergence of bound states at mass domain walls in a system with two counterpropagating linearly dispersing states [88, 89]. Subsequently, we will demonstrate how this can lead to the emergence of MBSs when the edge of a TI is proximitized by a conventional superconductor. As in the Rashba nanowire case, we identify the conditions under which MBSs can emerge in such a system and explicitly obtain their wave function solutions.

We note that we will not give a detailed review of the physics of TIs in this Tutorial. Instead, we work with a basic and rather generic edge-state picture that will be sufficient to understand the emergence of MBSs in such systems. We refer the reader to Refs. [6, 77, 121–123] for a pedagogical introduction to the field of TIs.

1.4.1 Primer: Mass domain walls and Jackiw-Rebbi bound states

Let us consider a massive 1D Dirac Hamiltonian $H = \int dx\, \Phi^\dagger(x)\mathcal{H}(x)\Phi(x)$ with $\Phi^\dagger = (R^\dagger, L^\dagger)$ and

$$\mathcal{H}(x) = -i\hbar v_F \sigma_z \partial_x - m\sigma_x, \tag{1.46}$$

where σ_i for $i \in \{x, y, z\}$ are Pauli matrices acting in right-/left-mover space. The bulk spectrum of this system is given by $E_\pm(k) = \pm\sqrt{(\hbar v_F k)^2 + m^2}$ and thus is gapped whenever $m \neq 0$. We will now allow the mass term to become position-dependent, i.e., $m = m(x)$. In particular, we consider the effect of a mass domain wall where $m(x \to -\infty) < 0$ and $m(x \to +\infty) > 0$. As was first shown by Jackiw and Rebbi in Ref. [88], such a domain wall binds a localized zero-energy state.

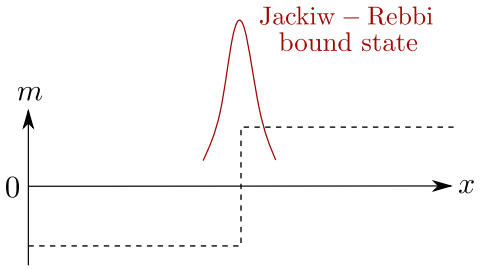

Figure 1.7: A Dirac Hamiltonian with a mass domain wall hosts a zero-energy bound state localized to the region where the mass changes its sign. As a particularly simple example, we depict the case of a step-function mass term $m(x) = m_0\,\mathrm{sgn}(x)$.

Let us illustrate this statement by considering the particularly simple case where the mass has a step-function profile $m(x) = m_0\,\mathrm{sgn}(x)$ with $m_0 > 0$, see Fig. 1.7. We can now readily solve for a normalizable zero-energy state by making the Ansatz

$$\phi(x) = \begin{cases} \phi_0^-\, e^{x/\xi_-} & x < 0, \\ \phi_0^+\, e^{-x/\xi_+} & x > 0, \end{cases} \tag{1.47}$$

with the respective localization lengths $\xi_\pm > 0$. By solving for zero-energy eigenstates in the intervals $(-\infty, 0)$ and $(0, +\infty)$ independently and then imposing continuity of the solution at $x = 0$ by requiring $\phi_0^+ = \phi_0^- =: \phi_0$, we find that there indeed exists a normalizable zero-energy solution with $\xi_\pm = \hbar v_F/m_0$ and $\phi_0 = (1, i)^T$ up to an overall normalization constant.

While we have presented a concrete example for illustrative purposes, it can be shown that the existence of the above solution does not depend on the exact form of the domain wall. Indeed, for a more general domain-wall profile with the asymptotic behavior $m(x \to -\infty) < 0$ and $m(x \to +\infty) > 0$, we find a zero-energy bound state of the form

$$\phi(x) \propto e^{-\int_0^x m(x')dx'/\hbar v_F} \begin{pmatrix} 1 \\ i \end{pmatrix}. \tag{1.48}$$

The fact that the above zero-energy solution exists independently of the exact mass profile function can be understood from the theory of symmetry-protected topological phases of matter. Indeed, the Hamiltonian given in Eq. (1.46) has a chiral symmetry [92,93] expressed by $\{\mathcal{H}(k), \sigma_y\} = 0$. The two phases with $m_0 \gtrless 0$ correspond to two topologically distinct phases that cannot smoothly be deformed into each other unless chiral symmetry is broken. A domain wall between these two distinct phases then hosts a bound state with an energy that is pinned to zero. This follows because chiral symmetry imposes that every state with energy $+E$ has a partner with energy $-E$. The single bound state at the domain wall can therefore not be removed from zero energy unless chiral symmetry is broken. Note that while this argument is superficially similar to the case of particle-hole symmetry discussed earlier, the zero-energy state found in the Jackiw-Rebbi model is an ordinary fermionic zero-mode and not an MBS. This can easily be seen from Eq. (48). Generally, since we are dealing with a usual single-particle Hamiltonian rather than a BdG Hamiltonian, there is no redundancy in the spectrum of excitations and each eigenstate of the Hamiltonian corresponds to a usual fermionic excitation.

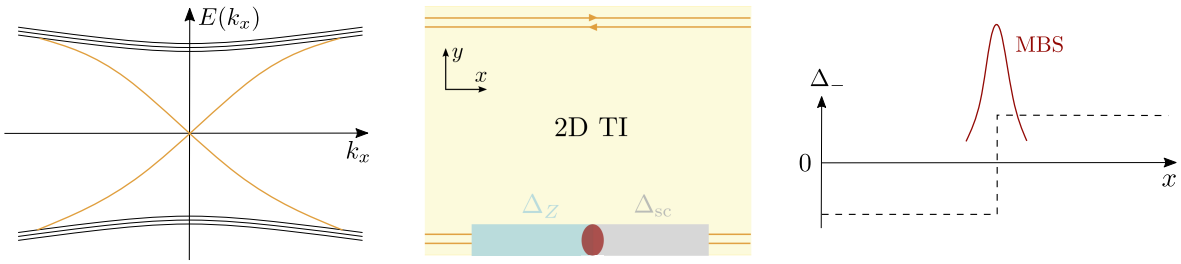

(a) (b) (c)

Figure 1.8: (a) Schematic spectrum of a 2D TI. We take the sample to be finite along the y axis and infinite along the x axis such that k_x remains a good quantum number. While the bulk exhibits an energy gap (black lines), there is a pair of gapless helical edge states (orange lines) propagating along the edges of the sample. (b) The gapless helical edge states of a 2D TI can be gapped out either by proximity-induced superconductivity (grey region) or by a magnetic term (light blue region). An interface between these two opposite gap-opening mechanisms hosts an MBS (shown in red). (c) The existence of a bound state can be understood from the fact that the Dirac mass $\Delta_- = \Delta_{sc} - \Delta_Z$ changes sign at the interface between the two regions. In that sense, the emerging MBS can be interpreted as a special variant of a Jackiw-Rebbi bound state (see Fig. 1.7) protected by particle-hole symmetry rather than chiral symmetry.

1.4.2 MBSs at domain walls in 2D TIs

With a basic understanding of the Jackiw-Rebbi model and the formation of bound states at mass domain walls, let us turn our attention to the construction of MBSs from the edge states of a 2D TI. For simplicity, we focus on the case where the spin component along one axis, say, the z axis, is conserved. Deep inside the bulk gap, we can linearize the edge state dispersion around the Dirac point $k = 0$, see Fig. 1.8(a). Therefore, the effective low-energy Hamiltonian describing the 1D edge states can be written in terms of a left-moving field $L(x)$ with spin up and a right-moving field $R(x)$ with spin down. The kinetic term then takes the form of a Dirac Hamiltonian

$$H_{kin} = -i\hbar v_F \int dx\, [R^\dagger(x)\partial_x R(x) - L^\dagger(x)\partial_x L(x)]. \tag{1.49}$$

We will now consider two different gap-opening mechanisms for the helical edge states: Firstly, an in-plane Zeeman term breaks time-reversal symmetry and couples the left- and the right-moving edge states due to the fact that they carry opposite spin projections. The corresponding term in the Hamiltonian can be written as

$$H_Z = \Delta_Z \int dx\, R^\dagger(x)L(x) + \text{H.c.}, \tag{1.50}$$

where Δ_Z is the strength of the Zeeman term. Secondly, placing the TI edge in proximity to a conventional s-wave superconductor gives rise to a proximity-induced superconducting term described by

$$H_{sc} = \Delta_{sc} \int dx\, R(x)L(x) + \text{H.c.}, \tag{1.51}$$

where the superconducting pairing potential Δ_{sc} is taken to be real. If we additionally allow for a small but possibly finite chemical potential (measured from the Dirac point), it is easy to check that the bulk spectrum of the total Hamiltonian $H = H_{kin} + H_Z + H_{sc}$ is once again given by Eq. (1.31). As such, we already know that the bulk will be fully gapped unless

$$\Delta_Z^2 = \Delta_{sc}^2 + \mu^2. \tag{1.52}$$

Motivated by our previous discussion of the Jackiw-Rebbi model, we would like to see what happens at a domain wall between the two topologically inequivalent phases separated by this gap closing point. If we assume for concreteness that $\Delta_Z \geq 0$, the two inequivalent gapped phases are characterized by $\Delta_- \gtrless 0$, where we have defined $\Delta_- = \sqrt{\Delta_{sc}^2 + \mu^2} - \Delta_Z$ in the exact same way as in Sec. 1.3. We will now confirm the existence of a domain wall bound state by an explicit calculation. Indeed, it will turn out that this domain wall bound state is an MBS protected by particle-hole symmetry. In the following, we set $\mu = 0$ for simplicity. Let us consider a TI edge separated into two segments, where one segment is in contact to a ferromagnet and the other one is proximitized by an s-wave superconductor, see Fig. 1.8(b). For simplicity, we will take the two segments to be semi-infinite and assume a step-function profile for $\Delta_Z, \Delta_{sc} > 0$. The total Hamiltonian incorporating the domain wall then reads $H = \frac{1}{2}\int dx\, \Phi^\dagger(x)\mathcal{H}(x)\Phi(x)$ with $\Phi^\dagger = (R^\dagger, L^\dagger, R, L)$ and

$$\mathcal{H}(x) = -i\hbar v_F \partial_x \sigma_z + \Theta(-x)\Delta_Z \eta_z \sigma_x + \Theta(x)\Delta_{sc}\eta_y\sigma_y, \tag{1.53}$$

where σ_i (η_i) for $i \in \{x, y, z\}$ are Pauli matrices acting in right-/left-mover (particle-hole) space and $\Theta(x)$ is the Heaviside step function. We can now adopt the strategy developed in the previous subsection to show that there is a single MBS localized at the interface, which we have taken to lie at $x = 0$ without loss of generality. This involves first solving for decaying eigenstates for $x > 0$ and $x < 0$ separately and then forming suitable linear combinations to satisfy the boundary condition at the interface. With the Ansatz $\phi_+(x) = \phi_+(0)e^{-x/\xi_+}$ for $x > 0$ [$\phi_-(x) = \phi_-(0)e^{x/\xi_-}$ for $x < 0$], we immediately obtain the localization lengths

$$\xi_- = \hbar v_F/\Delta_Z, \qquad x < 0, \tag{1.54}$$
$$\xi_+ = \hbar v_F/\Delta_{sc}, \qquad x > 0. \tag{1.55}$$

For each of the two segments, we find that the subspace of exponentially decaying zero-energy eigenfunctions is two-fold degenerate. Explicitly, this subspace is spanned by the linearly independent eigenfunctions

$$\phi_{-,1}(x) = \begin{pmatrix} -i \\ 1 \\ 0 \\ 0 \end{pmatrix} e^{x/\xi_-}, \qquad \phi_{-,2}(x) = \begin{pmatrix} 0 \\ 0 \\ i \\ 1 \end{pmatrix} e^{x/\xi_-}, \tag{1.56}$$

$$\phi_{+,1}(x) = \begin{pmatrix} -i \\ 0 \\ 0 \\ 1 \end{pmatrix} e^{-x/\xi_+}, \qquad \phi_{+,2}(x) = \begin{pmatrix} 0 \\ -i \\ 1 \\ 0 \end{pmatrix} e^{-x/\xi_+}, \tag{1.57}$$

where we suppress a normalization factor. Finally, demanding that the wave function is continuous at $x = 0$, we obtain a single bound state solution

$$\phi_M(x) = \begin{pmatrix} -i \\ 1 \\ i \\ 1 \end{pmatrix} \left[\Theta(-x) e^{x/\xi_-} + \Theta(x) e^{-x/\xi_+} \right], \tag{1.58}$$

where we have again suppressed a normalization factor. We can readily verify that this solution does indeed satisfy the Majorana property as it can be brought into the form $\phi_M(x) = (f(x), g(x), f^*(x), g^*(x))^T$ with

$$f(x) = -ig(x) = \begin{cases} -ie^{x/\xi_-}, & x < 0, \\ -ie^{-x/\xi_+}, & x > 0. \end{cases} \tag{1.59}$$

Again, the presence of the MBS does not depend on the exact profile of the domain wall. Indeed, any interface between a region dominated by magnetic field ($\Delta_- < 0$) and a region dominated by superconductivity ($\Delta_- > 0$) will host an MBS, see Fig. 1.8(c). This reflects the fact that the two phases with $\Delta_- \gtrless 0$ are topologically distinct and cannot be connected to each other without closing and reopening the bulk gap. Similarly, the MBS will also persist in the presence of a finite μ as long as the bulk gap remains open. Motivated by the basic mechanism discussed above, various realizations of MBSs in TI heterostructures have been proposed theoretically [124–131].

While the ideas discussed in this section are extremely appealing from a conceptual point of view, significant challenges are met in their experimental realization. This is mainly due to the fact that 2D TIs are highly nontrivial topological materials, the experimental detection and manipulation of which requires significant effort. Nevertheless, recent works report signatures of proximity-induced superconductivity on TI edge states [132,133]. Alternatively, the TI edge states could also be replaced by helical hinge states of a three-dimensional (3D) second-order TI.[7] In this latter case, zero-bias peaks consistent with MBSs were measured at domain walls between ferromagnetic and superconducting domains [139].

In variations of the above setup, MBSs could also be engineered from quantum Hall edge states in a suitable sample geometry [140–142]. As a side remark, we mention that proximitized quantum Hall systems have raised significant interest not only as potential hosts for MBSs, but also for *propagating* chiral Majorana edge states [143]. Signatures of proximity-induced superconductivity in quantum Hall edge states were studied in a series of recent works [140, 144–148].

Finally, it is worth noting that the above setups have also raised significant interest due to their possible generalization to the regime of strong electron-electron interactions, where even more exotic bound states are predicted to emerge. In particular, if the TI (quantum Hall) edge states are replaced by *fractional* TI (quantum Hall) edge states, domain walls between competing gap-opening mechanisms are theoretically predicted to host *parafermion* bound states [124–126, 141, 142, 148]. These exotic zero-energy modes can be seen as a formal

[7] As opposed to conventional 3D TIs with gapless surface states, 3D *second-order* TIs have gapped surfaces but host gapless chiral or helical 1D modes propagating along the hinges of the sample [134–137], see also Ref. [138] for a popular summary.

generalization of MBSs. In particular, while a pair of MBSs encodes a two-fold ground state degeneracy, a pair of $\mathbb{Z}_N$ parafermion zero modes is generally associated with an N-fold topologically protected ground state degeneracy. Braiding operations of parafermion zero modes then realize an even richer set of non-Abelian rotations on this ground state manifold. We refer the interested reader to Refs. [149–151] for pedagogical reviews of the topic.

On a related note, let us mention that systems of interacting MBSs provide an exciting playground to study novel phases of matter with even more exotic properties such as topological order, emergent supersymmetry, or chaotic behavior related to the Sachdev-Ye-Kitaev (SYK) model [152–157], see also Ref. [158] for a review.

1.5 Alternative realizations of Majorana bound states in 1D systems

The above ideas have inspired an ever-growing list of proposals aimed at the realization of MBSs in topologically non-trivial 1D systems. In the following, we will briefly highlight several directions that we consider to be of particularly high importance, referring the reader to the excellent reviews Refs. [2–5, 78–85] for a more exhaustive overview of the existing proposals.

Apart from nanowires, there are several alternative (quasi-)1D platforms that can host MBSs. In particular, extensive research has been carried out on graphene-based structures such as carbon nanoribbons and carbon nanotubes [36–41]. Since SOI effects in pristine graphene are generally weak, these setups often rely on synthetic SOI as discussed in Sec. 1.3.3. Furthermore, a topological superconducting phase with MBSs has also been predicted to occur in quasi-1D nanowires fabricated from three-dimensional TI materials. In particular, when the wire is proximitized by a conventional s-wave superconductor and a magnetic field is applied parallel to the wire, well-localized MBSs can emerge at the wire ends both in the presence [33, 34] or in the absence [35] of a vortex in the proximity-induced pairing potential. In this latter case, a non-uniform chemical potential in the wire cross-section is responsible for an exceptionally strong effective SOI.

Another family of promising proposals involves chains of magnetic impurities deposited on a superconducting substrate. Again, both a helical magnetic ordering of the impurities or—formally equivalent—a ferromagnetic ordering in combination with strong SOI may lead to the formation of MBSs. If the impurities are placed sufficiently close to each other, the chain can be described as an effective 1D nanowire and MBSs emerge in the same way as discussed in Sec. 1.3 [27–29]. For larger inter-impurity distances, on the other hand, a different mechanism becomes important. Indeed, if the exchange interaction between a magnetic atom and the quasiparticles in the superconductor is sufficiently strong, a localized sub-gap Yu-Shiba-Rusinov (YSR) state will emerge [159–161]. In the case of many magnetic impurities, the corresponding YSR states can overlap and form a chain. Such a YSR chain shows many similarities to the Kitaev chain [16] and, under specific assumptions, can be mapped onto the latter. As such, it becomes clear that a YSR chain can realize a topologically non-trivial phase with MBSs at its ends [30–32, 162–168]. Indeed, a series of experiments reported robust zero-bias peaks in chains of iron (Fe) or cobalt (Co) atoms placed on a superconductor [169–175]. For a detailed review of MBSs in magnetic chains we refer the reader to Refs. [85, 87]. We note that even more complicated non-collinear magnetic textures,

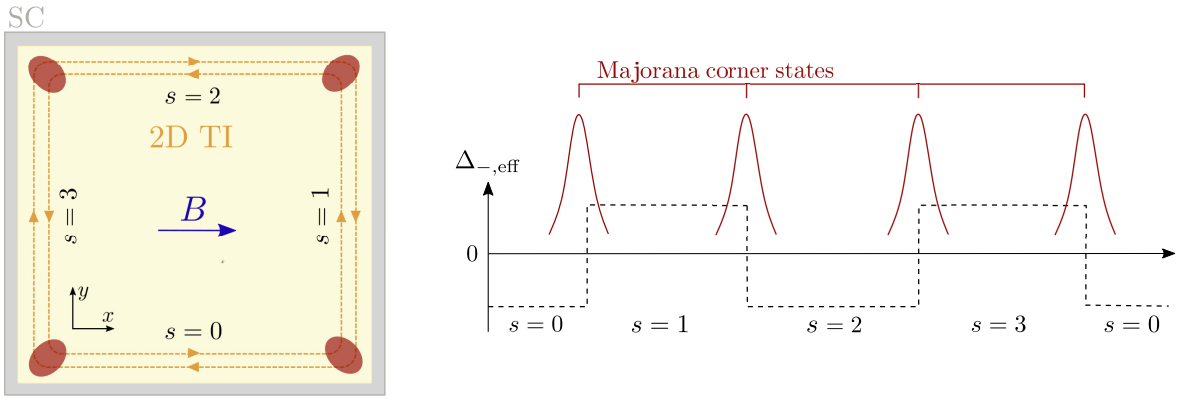

(a) (b)

Figure 1.9: (a) A 2D TI (yellow) described by the Hamiltonian given in Eq. (1.60) is placed on top of an s-wave superconductor (grey) and a Zeeman field is applied along the x direction (blue arrow). The Zeeman and superconducting terms gap out the helical edge states (orange) running along the edges of the sample. If the strength of the Zeeman term is larger than the proximity-induced superconductivity, we find one Majorana corner state (red) at each corner of the sample. (b) The existence of Majorana corner states can be explained by looking at the effective gap $\Delta_{-,\text{eff}} = \Delta_{sc,\text{eff}} - \Delta_{Z,\text{eff}}$, which is obtained by projecting the respective gap-opening terms onto the low-energy subspace spanned by the helical edge states propagating along the edges $s = 0, ..., 3$ of the sample. At each of the four corners, $\Delta_{-,\text{eff}}$ changes sign, giving rise to a Majorana corner state at each corner.

such as skyrmions or skyrmion chains, were proposed as an alternative route to generate topological superconducting phases [176–186].

Alternatively, we note that external driving provides a powerful tool to turn initially non-topological materials into topological ones [187, 188]. Indeed, it has been shown that a time-dependent magnetic or electric field can give rise to Floquet Majorana fermions [189–197]. Furthermore, one can also consider unconventional superconductors with p-wave and d-wave pairings [198–205]. Here, one should mention also odd-frequency superconductivity [206–210]. The odd-frequency pairing is hugely enhanced at the boundaries of the topological systems hosting MBSs [210–214].

Last but not least, it is worth mentioning that a magnetic field is not a necessary ingredient to generate MBSs. Indeed, there are many alternative ways in which competing gap-opening mechanisms can realize a phase transition between a trivial and a topological superconducting phase with MBSs. This is of particular importance since strong magnetic fields have a detrimental effect on superconductivity. Efforts to avoid this obstacle have resulted in an increased interest in time-reversal invariant systems. In particular, it has been found that a spinful time-reversal invariant 1D TSC hosts a *Kramers pair* of MBSs at each end in the topologically non-trivial phase [214–226]. Even though localized at the same position in real space, the two MBSs at a given end of the system are then protected from hybridizing by time-reversal symmetry.

1.6 Majorana corner states

In Sec. 1.4, a domain wall hosting an MBS was realized through couplings $\Delta_Z(x)$, $\Delta_{sc}(x)$ with an explicit spatial dependence. More recently, the concept of *higher-order* topological insulators and superconductors [134, 135, 137, 227–231] has opened up an alternative avenue towards the realization of MBSs in TI heterostructures. While conventional d-dimensional TIs and TSCs exhibit gapless edge states at their $(d-1)$-dimensional boundaries, nth-order d-dimensional TIs or TSCs exhibit gapless edge states at their $(d-n)$-dimensional boundaries. In particular, a 2D second-order topological superconductor (SOTSC) hosts MBSs at the corners of a rectangular sample [232–248].

One particular way to obtain such Majorana corner states is to start from a conventional (first-order) TI or TSC with helical edge states, which are then perturbatively gapped out by small additional terms. Depending on the symmetries of the model as well as the sample geometry, the gap acquired by the edge states is not necessarily of the same size or type for different edges. As such, domain walls between different gap-opening mechanisms emerge naturally even for spatially uniform gap-opening terms. In the following, we will illustrate this concept with two simple examples.

1.6.1 SOTSC with four corner states

Our first example is based on a model introduced in Ref. [232]. We start from a minimal model for a 2D TI, which can be interpreted as a simplified version of the Bernevig-Hughes-Zhang (BHZ) Hamiltonian originally brought forward in Ref. [249] to describe HgTe quantum wells. We consider a Hamiltonian of the form $H = \sum_{\mathbf{k}} \Psi_{\mathbf{k}}^\dagger \mathcal{H}(\mathbf{k}) \Psi_{\mathbf{k}}$ with $\Psi_{\mathbf{k}}^\dagger = (\psi_{\mathbf{k}\uparrow 1}^\dagger, \psi_{\mathbf{k}\uparrow \bar{1}}^\dagger, \psi_{\mathbf{k}\downarrow 1}^\dagger, \psi_{\mathbf{k}\downarrow \bar{1}}^\dagger)$, where $\psi_{\mathbf{k}\sigma\tau}^\dagger$ ($\psi_{\mathbf{k}\sigma\tau}$) creates (destroys) an electron with in-plane momentum $\mathbf{k} = (k_x, k_y)$, spin σ, and an additional local degree of freedom τ. The Hamiltonian density is taken to be

$$\mathcal{H}(\mathbf{k}) = \left(\frac{\hbar^2 k_x^2}{2m} + \frac{\hbar^2 k_y^2}{2m} + \epsilon \right) \tau_z + \lambda (k_x \sigma_z \tau_x - k_y \tau_y), \tag{1.60}$$

where σ_i and τ_i for $i \in \{x, y, z\}$ are Pauli matrices acting in spin space and on the local degree of freedom τ, respectively. The parameters m and λ are model-dependent constants, which we take to be strictly positive in the following. Furthermore, ϵ describes an energy shift between the two species $\tau \in \{1, \bar{1}\}$. The above Hamiltonian is time-reversal symmetric as defined in Eq. (1.21). Furthermore, the Hamiltonian has a four-fold rotational symmetry

$$\mathcal{H}(k_x, k_y) = U_{\pi/2} \mathcal{H}(-k_y, k_x) U_{\pi/2}^{-1} \tag{1.61}$$

with $U_{\pi/2} = e^{i\pi\sigma_z(2\tau_0 - \tau_z)/4}$.

For $\epsilon < 0$, it is well-known that the above Hamiltonian describes a TI [249]. An explicit calculation confirms that there is indeed a pair of gapless helical edge states propagating along the edges of a finite sample. Let us illustrate this in an example, where we will focus on the edge $s = 0$ shown in Fig. 1.9(a). Assuming a semi-infinite geometry such that the system is finite along the y axis and infinite along the x axis, k_x remains a good quantum number, whereas k_y has to be replaced by $-i\partial_y$. We now focus on the simple case $k_x = 0$, in

which case the Hamiltonian given in Eq. (1.60) reduces to

$$\mathcal{H}(0,-i\partial_y) = \left(\epsilon - \frac{\hbar^2\partial_y^2}{2m}\right)\tau_z + i\lambda\partial_y\tau_y. \tag{1.62}$$

Solving for normalizable zero-energy solutions $\Phi^0_\sigma(y)$ subject to the boundary condition $\Phi^0_\sigma(0) = 0$ now reduces to a standard problem of matching decaying eigenfunctions as discussed in several instances in the previous sections. We readily find

$$\Phi^0_\uparrow(y) = (1,1,0,0)^T(e^{-y/\xi_1} - e^{-y/\xi_2}), \tag{1.63}$$

$$\Phi^0_\downarrow(y) = (0,0,1,1)^T(e^{-y/\xi_1} - e^{-y/\xi_2}), \tag{1.64}$$

with $\xi_{1/2} = (-\lambda \pm \sqrt{\beta})/(2\epsilon)$ for $\beta = \lambda^2 + 2\hbar^2\epsilon/m$ and where we have suppressed a normalization factor. One can check that these solutions are indeed exponentially decaying for $y \to \infty$ if and only if $\epsilon < 0$.

Linear contributions in k_x can now in principle be included perturbatively in order to verify that the above solutions do indeed correspond to counterpropagating edge states with opposite velocities [232]. However, we will content ourselves with studying the solutions at $k_x = 0$ given above. This will allow us to determine the gap that is opened in the edge state spectrum under additional terms that we include perturbatively.

The first of these additional terms is a small in-plane Zeeman field that is taken along the x axis for concreteness, $\mathcal{H}_Z = \Delta_Z\sigma_x$, where we assume $\Delta_Z \geq 0$. Exploiting the rotational symmetry of the unperturbed Hamiltonian, we obtain the low-energy projection of the Zeeman term for the edge s via $\langle\Phi^s_\sigma|\mathcal{H}_Z|\Phi^s_{\sigma'}\rangle = \langle\Phi^0_\sigma|U^{-s}_{\pi/2}\mathcal{H}_Z U^s_{\pi/2}|\Phi^0_{\sigma'}\rangle$. Explicitly, this gives us

$$\langle\Phi^0_\sigma|\mathcal{H}_Z|\Phi^0_{\sigma'}\rangle = -\langle\Phi^2_\sigma|\mathcal{H}_Z|\Phi^2_{\sigma'}\rangle = \Delta_Z\delta_{\bar{\sigma}\sigma'}, \tag{1.65}$$

$$\langle\Phi^1_\sigma|\mathcal{H}_Z|\Phi^1_{\sigma'}\rangle = \langle\Phi^3_\sigma|\mathcal{H}_Z|\Phi^3_{\sigma'}\rangle = 0 \quad \forall\,\sigma,\sigma'. \tag{1.66}$$

As such, the Zeeman term fully gaps out the edge states along the x direction, while the edge states along the y direction are not affected. Furthermore, we consider a superconducting term induced by placing the TI in proximity to a bulk s-wave superconductor, see Fig. 1.9(a). The corresponding term in the Hamiltonian is given by $\mathcal{H}_{\text{sc}} = \Delta_{sc}\eta_y\sigma_y$, where η_y is an additional Pauli matrix acting in particle-hole space and we assume Δ_{sc} to be real and nonnegative for simplicity. It is clear that superconductivity opens a gap of equal size along all edges of the sample. Therefore, for $\Delta_Z > \Delta_{sc}$, a domain wall of the type discussed in Subsec. 1.4.2 is naturally realized at all four corners of a rectangular sample. We thus find one Majorana corner state per corner, see Fig. 1.9(b). Apart from the model presented here, other realizations of Majorana corner states via similar mechanisms were proposed in Refs. [233–242].

1.6.2 SOTSC with two corner states

Our second example is based on a model introduced in Ref. [243]. We start from a 2D time-reversal invariant topological superconductor with helical Majorana edge states propagating along the edges of a large but finite sample. While a detailed characterization of phases with

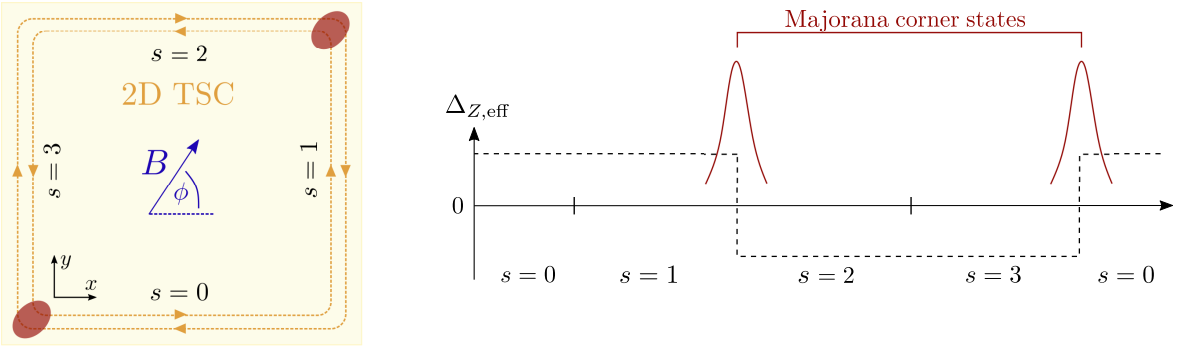

(a) (b)

Figure 1.10: (a) A 2D topological superconductor (yellow) with helical Majorana edge states (orange) described by the Hamiltonian given in Eq. (1.67) is subjected to an in-plane Zeeman field (blue) of an angle ϕ with respect to the x axis. The Zeeman field breaks time-reversal symmetry and gaps out the Majorana edge states. MBSs (red) appear at two opposite corners of the sample. (b) The existence of these Majorana corner states can be explained by looking at the effective gap $\Delta_{Z,\text{eff}}$ [see Eq. (1.71)], which is obtained by projecting the Zeeman term onto the low-energy subspace spanned by the helical edge states propagating along the edges $s = 0, ..., 3$ of the sample. At two opposite corners of the system, the effective gap changes sign, implying the presence of a bound state of Jackiw-Rebbi type. Since the edge states in the first-order phase correspond to helical Majorana edge states, these zero-energy corner states are MBSs protected by particle-hole symmetry.

propagating Majorana edge states is beyond the scope of this Tutorial, we will look at this example from a very simple point of view by just solving for edge state solutions in the usual way and giving an intuitive explanation why these edge states have Majorana character. For a more detailed discussion of phases with propagating Majorana edge states, we refer the reader to several reviews covering this topic [4, 5, 77–79].

Explicitly, we consider a Hamiltonian of the form $H = \frac{1}{2}\sum_{\mathbf{k}} \Psi_{\mathbf{k}}^\dagger \mathcal{H}(\mathbf{k}) \Psi_{\mathbf{k}}$ with

$$\mathcal{H}(\mathbf{k}) = \left(\frac{\hbar^2 k_x^2}{2m} + \frac{\hbar^2 k_y^2}{2m} \right) \eta_z + \lambda(k_y \sigma_x - k_x \eta_z \sigma_y)\tau_z + \Gamma \eta_z \tau_x + \Delta_{sc} \eta_y \tau_z \sigma_y \tag{1.67}$$

and $\Psi_{\mathbf{k}}^\dagger = (\psi_{\mathbf{k}\uparrow 1}^\dagger, \psi_{\mathbf{k}\downarrow 1}^\dagger, \psi_{\mathbf{k}\uparrow \bar{1}}^\dagger, \psi_{\mathbf{k}\downarrow \bar{1}}^\dagger, \psi_{-\mathbf{k}\uparrow 1}, \psi_{-\mathbf{k}\downarrow 1}, \psi_{-\mathbf{k}\uparrow \bar{1}}, \psi_{-\mathbf{k}\downarrow \bar{1}})$. The Pauli matrices σ_i, τ_i, and η_i for $i \in \{x, y, z\}$ have the same meaning as in the previous subsection. The parameters m, λ, and Γ depend on the microscopic realization of the model and are taken to be non-negative for simplicity. Furthermore, Δ_{sc} denotes the strength of the proximity-induced superconducting pairing, which is taken to be real and of opposite sign for the two species $\tau \in \{1, \bar{1}\}$. Originally, the above Hamiltonian was introduced in Ref. [250] to describe two tunnel-coupled layers of a 2D electron gas with strong Rashba SOI 'sandwiched' between a top and bottom superconductor with a phase difference of π. In this case, the local degree of freedom τ corresponds to the layer degree of freedom. The Hamiltonian is particle-hole symmetric and time-reversal symmetric as defined in Eqs. (1.12) and (1.21), respectively. Furthermore, we find a four-fold rotational symmetry

$$\mathcal{H}(k_x, k_y) = U_{\pi/2} \mathcal{H}(-k_y, k_x) U_{\pi/2}^{-1} \tag{1.68}$$

for $U_{\pi/2} = e^{i\pi\eta_z\sigma_z/4}$.

For $\Gamma > \Delta$, the system realizes a time-reversal invariant topological superconductor, as can be checked by a direct calculation of the edge state wave functions. For this, we focus again on the edge $s = 0$ as shown in Fig. 1.10(a). Assuming a semi-infinite geometry, k_x remains a good quantum number, and we restrict ourselves to the simplest case $k_x = 0$. After a short calculation outlined in Ref. [250], we find that the edge state wave functions are in this case given by

$$\Phi^0_+(y) = (f_1, g_1, f_2, g_2, f_1^*, g_1^*, f_2^*, g_2^*)^T, \tag{1.69}$$

$$\Phi^0_-(y) = (g_1^*, -f_1^*, g_2^*, -f_2^*, g_1, -f_1, g_2, -f_2)^T, \tag{1.70}$$

where $f_1 = g_2 = -if_2^* = -ig_1^* = e^{-y/\xi} - e^{2ik_{so}y}e^{-y/\xi'}$ with $\xi = \lambda/(\Gamma - \Delta_{sc})$ and $\xi' = \lambda/\Delta_{sc}$. We can now see why these edge states are referred to as propagating Majorana edge states: Indeed, the above solutions at $k_x = 0$ satisfy the Majorana property $U_C[\Phi^0_\pm(y)]^* = \Phi^0_\pm(y)$. Again, linear contributions in k_x could now be included perturbatively [243].

If an additional in-plane Zeeman field is added, time-reversal symmetry is broken and the helical edge states are gapped out. The corresponding term in the Hamiltonian can be written as $\mathcal{H}_Z = \Delta_Z[\cos(\phi)\eta_z\sigma_x + \sin(\phi)\sigma_y]$, where the angle ϕ describes the orientation of the Zeeman field. It is now straightforward to calculate the projection of the Zeeman term onto the low-energy subspace spanned by the helical edge states for a given edge. We find

$$\langle\Phi^s_+|\mathcal{H}_Z|\Phi^s_-\rangle = \langle\Phi^0_+|U^{-s}_{\pi/2}\mathcal{H}_Z U^s_{\pi/2}|\Phi^0_-\rangle = i\Delta_Z\cos(\phi - s\pi/2). \tag{1.71}$$

For the edge s, this leads to an effective mass term $-\Delta^s_{Z,\text{eff}}\rho_y$ with $\Delta^s_{Z,\text{eff}} = \Delta_Z\cos(\phi - s\pi/2)$ and where ρ_y is a Pauli matrix acting in the low-energy subspace spanned by the helical edge states. We therefore see that the effective mass changes sign at two opposite corners of the sample depending on the in-plane orientation ϕ of the magnetic field. Via the Jackiw-Rebbi mechanism discussed in Subsec. 1.4.1, these two corners host a zero-energy bound state. Since the helical edge states of the first-order phase already correspond to Majorana edge states, these zero-energy corner states are indeed MBSs protected by particle-hole symmetry. In Fig. 1.10, we illustrate the above mechanism for a generic angle $\phi \in (0, \pi/2)$. Other realizations of Majorana corner states involving similar arguments were proposed in Refs. [244–248].

1.7 Conclusions and Outlook

In this Tutorial, we have given a pedagogical introduction to the field of MBSs in semiconducting nanostructures. We have reviewed some of the currently most relevant platforms proposed to host MBSs, including proximitized Rashba nanowires in a magnetic field as well as proximitized edge states of topological insulators. In these examples, we have shown how MBSs emerge in the topologically nontrivial phase and how the explicit Majorana wave functions can be obtained by elementary methods. We have discussed the properties of the resulting MBSs and have presented some heuristic arguments about their stability.

Throughout this Tutorial, we chose to focus on a few selected topics that we believe to be of high relevance to experiments while at the same time readily accessible with elementary

mathematical tools. As an outlook, let us mention a few relevant aspects of MBSs that were not addressed in this Tutorial.

Firstly, we did not touch upon the characterization of topological superconductors via topological invariants. This important topic is already covered in various existing reviews, see for example Refs. [4, 5, 78, 81]. Secondly, we did not discuss the issues related to the experimental detection of MBSs. Among the standard signatures associated with MBSs is the presence of a robust zero-bias peak of the tunneling conductance as measured, e.g., in transport experiments [25, 26, 204, 251–256]. However, experiments based solely on zero-bias peaks are nowadays known to be insufficient to conclusively demonstrate the presence of MBSs. Instead, different non-topological states such as, e.g., Andreev bound states can give rise to almost identical zero-bias anomalies. For a detailed review of this problem, we refer to Ref. [59]. Although numerous works have reported signatures thought to be unambiguously associated with topological superconductivity, this issue is not yet settled and claims are being reconsidered [257]. While the basic theoretical ideas on which the existence of topological superconductors rests are sound and were never disproven, it is their implementation in real materials that poses substantial challenges. In particular, superconductivity in semiconducting structures is typically induced by the proximity effect [258–262]. However, if the proximity effect is weak—like in approaches based on sputtering—the superconducting gap is 'soft', which is usually attributed to disorder effects. On the other hand, if the hybridization with the bulk superconductor is too strong, the original properties of the underlying semiconductor may be lost. Typically, the superconductor 'metallizes' the semiconducting nanostructure, resulting in strongly reduced SOI and g-factors [263–267]. Moreover, due to screening, it is challenging to control the position of the chemical potential in order to tune it to the 'sweet spot'. Thus, future experiments need to find ways to avoid or reduce such metallization effects on the semiconductors. This can be achieved, e.g., by adding a thin insulating layer. Another Majorana signature worth mentioning is the fractional Josephson effect arising in a topological superconductor–normal metal–topological superconductor (TS–N–TS) junction, giving rise to an unconventional 4π-periodic Josephson current as opposed to the usual 2π-periodic Josephson current [16, 18, 23, 24, 268–274]. Alternatively, emerging exotic phases could be probed in cavities via photonic transport [275–278] characterized by the complex transmission coefficient that relates input and output photonic fields, allowing to probe the system in a global and non-invasive way. Moreover, this could also be used to manipulate states. Generally, these detection methods could be supplemented by additional signatures observable in the bulk such as, e.g., the closing of the topological bulk gap and the inversion of spin polarization in the energy bands [279–286]. For pedagogical reviews covering experimental Majorana signatures, we refer to Refs. [2, 3, 78, 79, 81].

Last but not least, we did not discuss the non-Abelian braiding statistics of MBSs in any detail. This choice was motivated by the fact that this Tutorial mainly focuses on 1D systems, where the process of spatially exchanging two MBSs is not as straightforward as in two dimensions. Nevertheless, braiding protocols for MBSs in strictly 1D systems have been brought forward [287, 288], which, however, typically rely on the presence of additional protecting symmetries or the ability to fine-tune certain system parameters. Alternatively, braiding schemes employing *networks* of topologically nontrivial 1D systems have been proposed [289–295], where the MBSs can either be moved physically or an effective braiding can be realized via tunable couplings between neighboring MBSs at fixed spatial positions. Similarly, also measurement-based braiding schemes allow one to mimic an effective braiding

of two MBSs without the need to physically move them [296–298]. For a review of Majorana braiding statistics and potential applications in topological quantum computation, we refer the interested reader to Refs. [2, 3, 78, 79, 82, 83].

Acknowledgments. We thank Daniel Loss for valuable discussions. This work was supported by the Swiss National Science Foundation and NCCR QSIT. This project received funding from the European Union's Horizon 2020 research and innovation program (ERC Starting Grant, grant agreement No 757725).

Bibliography

[1] E. Majorana, Il Nuovo Cimento **14**, 171 (1937).

[2] S. R. Elliott and M. Franz, Rev. Mod. Phys. **87**, 137 (2015).

[3] C. Beenakker, Annu. Rev. Condens. Matter Phys. **4**, 113 (2013).

[4] M. Sato and S. Fujimoto, J. Phys. Soc. Jpn. **85**, 072001 (2016).

[5] M. Sato and Y. Ando, Rep. Prog. Phys. **80**, 076501 (2017).

[6] M. Z. Hasan and C. L. Kane, Rev. Mod. Phys. **82**, 3045 (2010).

[7] G. Moore and N. Read, Nucl. Phys. B **360**, 362 (1991).

[8] G. E. Volovik, JETP Lett. **70**, 609 (1999).

[9] N. Read and D. Green, Phys. Rev. B **61**, 10267 (2000).

[10] T. Senthil and M. P. A. Fisher, Phys. Rev. B **61**, 9690 (2000).

[11] D. A. Ivanov, Phys. Rev. Lett. **86**, 268 (2001).

[12] G. E. Volovik, *The Universe in a Helium Droplet* (Oxford University Press, Oxford, 2003).

[13] G. E. Volovik, JETP Lett. **90**, 398 (2009).

[14] A. Y. Kitaev, Ann. Phys. **303**, 2 (2003).

[15] C. Nayak, S. H. Simon, A. Stern, M. Freedman, and S. Das Sarma, Rev. Mod. Phys. **80**, 1083 (2008).

[16] A. Y. Kitaev, Phys. Usp. **44**, 131 (2001).

[17] L. Fu and C. L. Kane, Phys. Rev. Lett. **100**, 096407 (2008).

[18] L. Fu and C. L. Kane, Phys. Rev. B **79**, 161408(R) (2009).

[19] J. D. Sau, R. M. Lutchyn, S. Tewari, and S. Das Sarma, Phys. Rev. Lett. **104**, 040502 (2010).

[20] J. Alicea, Phys. Rev. B **81**, 125318 (2010).

[21] M. Sato, Y. Takahashi, and S. Fujimoto, Phys. Rev. Lett. **103**, 020401 (2009).

[22] M. Sato, Y. Takahashi, and S. Fujimoto, Phys. Rev. B **82**, 134521 (2010).

[23] R. M. Lutchyn, J. D. Sau, and S. Das Sarma, Phys. Rev. Lett. **105**, 077001 (2010).

[24] Y. Oreg, G. Refael, and F. von Oppen, Phys. Rev. Lett. **105**, 177002 (2010).

[25] J. D. Sau, S. Tewari, R. M. Lutchyn, T. D. Stanescu, and S. Das Sarma, Phys. Rev. B **82**, 214509 (2010).

[26] T. D. Stanescu, R. M. Lutchyn, and S. Das Sarma, Phys. Rev. B **84**, 144522 (2011).

[27] J. Klinovaja, P. Stano, A. Yazdani, and D. Loss, Phys. Rev. Lett. **111**, 186805 (2013).

[28] M. M. Vazifeh and M. Franz, Phys. Rev. Lett. **111**, 206802 (2013).

[29] B. Braunecker and P. Simon, Phys. Rev. Lett. **111**, 147202 (2013).

[30] T.-P. Choy, J. M. Edge, A. R. Akhmerov, and C. W. J. Beenakker, Phys. Rev. B **84**, 195442 (2011).

[31] S. Nadj-Perge, I. K. Drozdov, B. A. Bernevig, and A. Yazdani, Phys. Rev. B **88**, 020407(R) (2013).

[32] F. Pientka, L. I. Glazman, and F. von Oppen, Phys. Rev. B **88**, 155420 (2013).

[33] A. Cook and M. Franz, Phys. Rev. B **84**, 201105(R) (2011).

[34] A. M. Cook, M. M. Vazifeh, and M. Franz, Phys. Rev. B **86**, 155431 (2012).

[35] H. F. Legg, D. Loss, and J. Klinovaja, arXiv:2103.13412.

[36] J. Klinovaja, S. Gangadharaiah, and D. Loss, Phys. Rev. Lett. **108**, 196804 (2012).

[37] R. Egger and K. Flensberg, Phys. Rev. B **85**, 235462 (2012).

[38] J. Klinovaja and D. Loss, Phys. Rev. X **3**, 011008 (2013).

[39] J. D. Sau and S. Tewari, Phys. Rev. B **88**, 054503 (2013).

[40] C. Dutreix, M. Guigou, D. Chevallier, and C. Bena, Eur. Phys. J. B **87**, 296 (2014).

[41] M. Marganska, L. Milz, W. Izumida, C. Strunk, and M. Grifoni, Phys. Rev. B **97**, 075141 (2018).

[42] M. M. Desjardins, L. C. Contamin, M. R. Delbecq, M. C. Dartiailh, L. E. Bruhat, T. Cubaynes, J. J. Viennot, F. Mallet, S. Rohart, A. Thiaville, A. Cottet, and T. Kontos, Nat. Mater. **18**, 1060 (2019).

[43] F. Pientka, A. Keselman, E. Berg, A. Yacoby, A. Stern, and B. I. Halperin, Phys. Rev. X **7**, 021032 (2017).

[44] M. Hell, M. Leijnse, and K. Flensberg, Phys. Rev. Lett. **118**, 107701 (2017).

[45] A. Fornieri, A. M. Whiticar, F. Setiawan, E. Portolés, A. C. C. Drachmann, A. Keselman, S. Gronin, C. Thomas, T. Wang, R. Kallaher, G. C. Gardner, E. Berg, M. J. Manfra, A. Stern, C. M. Marcus, and F. Nichele, Nature **569**, 89 (2019).

[46] H. Ren, F. Pientka, S. Hart, A. T. Pierce, M. Kosowsky, L. Lunczer, R. Schlereth, B. Scharf, E. M. Hankiewicz, L. W. Molenkamp, B. I. Halperin, and A. Yacoby, Nature **569**, 93 (2019).

[47] M. C. Dartiailh, W. Mayer, J. Yuan, K. S. Wickramasinghe, A. Matos-Abiague, I. Žutić, and J. Shabani, Phys. Rev. Lett. **126**, 036802 (2021).

[48] V. Mourik, K. Zuo, S. M. Frolov, S. R. Plissard, E. P. A. M. Bakkers, and L. P. Kouwenhoven, Science **336**, 1003 (2012).

[49] A. Das, Y. Ronen, Y. Most, Y. Oreg, M. Heiblum, and H. Shtrikman, Nat. Phys. **8**, 887 (2012).

[50] L. P. Rokhinson, X. Liu, and J. K. Furdyna, Nat. Phys. **8**, 795 (2012).

[51] M. T. Deng, C. L. Yu, G. Y. Huang, M. Larsson, P. Caroff, and H. Q. Xu, Nano Lett. **12**, 6414 (2012).

[52] J. R. Williams, A. J. Bestwick, P. Gallagher, S. S. Hong, Y. Cui, A. S. Bleich, J. G. Analytis, I. R. Fisher, and D. Goldhaber-Gordon, Phys. Rev. Lett. **109**, 056803 (2012).

[53] E. J. H. Lee, X. Jiang, R. Aguado, G. Katsaros, C. M. Lieber, and S. De Franceschi, Phys. Rev. Lett. **109**, 186802 (2012).

[54] H. O. H. Churchill, V. Fatemi, K. Grove-Rasmussen, M. T. Deng, P. Caroff, H. Q. Xu, and C. M. Marcus, Phys. Rev. B **87**, 241401(R) (2013).

[55] M. T. Deng, S. Vaitiekenas, E. B. Hansen, J. Danon, M. Leijnse, K. Flensberg, J. Nygård, P. Krogstrup, and C. M. Marcus, Science **354**, 1557 (2016).

[56] S. Vaitiekėnas, M.-T. Deng, J. Nygård, P. Krogstrup, and C. M. Marcus, Phys. Rev. Lett. **121**, 037703 (2018).

[57] M.-T. Deng, S. Vaitiekėnas, E. Prada, P. San-Jose, J. Nygård, P. Krogstrup, R. Aguado, and C. M. Marcus, Phys. Rev. B **98**, 085125 (2018).

[58] M. W. A. de Moor, J. D. S. Bommer, D. Xu, G. W. Winkler, A. E. Antipov, A. Bargerbos, G. Wang, N. van Loo, R. L. M. O. het Veld, S. Gazibegovic, D. Car, J. A. Logan, M. Pendharkar, J. S. Lee, E. P. A. M. Bakkers, C. J. Palmstrøm, R. M. Lutchyn, L. P. Kouwenhoven, and H. Zhang, New J. Phys. **20**, 103049 (2018).

[59] E. Prada, P. San-Jose, M. W. A. de Moor, A. Geresdi, E. J. H. Lee, J. Klinovaja, D. Loss, J. Nygård, R. Aguado, and L. P. Kouwenhoven, Nat. Rev. Phys. **2**, 575 (2020).

[60] G. Kells, D. Meidan, and P. W. Brouwer, Phys. Rev. B **86**, 100503(R) (2012).

[61] C. Fleckenstein, F. Dominguez, N. Traverso Ziani, and B. Trauzettel, Phys. Rev. B **97**, 155425 (2018).

[62] F. Peñaranda, R. Aguado, P. San-Jose, and E. Prada, Phys. Rev. B **98**, 235406 (2018).

[63] A. Ptok, A. Kobiałka, and T. Domański, Phys. Rev. B **96**, 195430 (2017).

[64] C. Moore, T. D. Stanescu, and S. Tewari, Phys. Rev. B **97**, 165302 (2018).

[65] C.-X. Liu, J. D. Sau, T. D. Stanescu, and S. Das Sarma, Phys. Rev. B **96**, 075161 (2017).

[66] D. J. Alspaugh, D. E. Sheehy, M. O. Goerbig, and P. Simon, Phys. Rev. Research **2**, 023146 (2020).

[67] C. Reeg, O. Dmytruk, D. Chevallier, D. Loss, and J. Klinovaja, Phys. Rev. B **98**, 245407 (2018).

[68] B. D. Woods, J. Chen, S. M. Frolov, and T. D. Stanescu, Phys. Rev. B **100**, 125407 (2019).

[69] C.-X. Liu, J. D. Sau, T. D. Stanescu, and S. Das Sarma, Phys. Rev. B **99**, 024510 (2019).

[70] J. Chen, B. D. Woods, P. Yu, M. Hocevar, D. Car, S. R. Plissard, E. P. A. M. Bakkers, T. D. Stanescu, and S. M. Frolov, Phys. Rev. Lett. **123**, 107703 (2019).

[71] E. J. H. Lee, X. Jiang, R. Aguado, G. Katsaros, C. M. Lieber, and S. De Franceschi, Phys. Rev. Lett. **109**, 186802 (2012).

[72] C. Jünger, R. Delagrange, D. Chevallier, S. Lehmann, K. A. Dick, C. Thelander, J. Klinovaja, D. Loss, A. Baumgartner, and C. Schönenberger, Phys. Rev. Lett. **125**, 017701 (2020).

[73] O. Dmytruk, D. Loss, and J. Klinovaja, Phys. Rev. B **102**, 245431 (2020).

[74] P. Yu, J. Chen, M. Gomanko, G. Badawy, E. P. A. M. Bakkers, K. Zuo, V. Mourik, and S. M. Frolov, arXiv:2004.08583.

[75] M. Kayyalha, D. Xiao, R. Zhang, J. Shin, J. Jiang, F. Wang, Y.-F. Zhao, R. Xiao, L. Zhang, K. M. Fijalkowski, P. Mandal, M. Winnerlein, C. Gould, Q. Li, L. W. Molenkamp, M. H. W. Chan, N. Samarth, and C.-Z. Chang, Science **367**, 64 (2020).

[76] M. Valentini, F. Peñaranda, A. Hofmann, M. Brauns, R. Hauschild, P. Krogstrup, P. San-Jose, E. Prada, R. Aguado, and G. Katsaros, arXiv:2008.02348.

[77] B. A. Bernevig and T. L. Hughes, *Topological Insulators and Topological Superconductors* (Princeton University Press, 2013).

[78] J. Alicea, Rep. Prog. Phys. **75**, 076501 (2012).

[79] R. Aguado, Riv. Nuovo Cim. **40**, 523 (2017).

[80] R. M. Lutchyn, E. P. A. M. Bakkers, L. P. Kouwenhoven, P. Krogstrup, C. M. Marcus, and Y. Oreg, Nat. Rev. Mater. **3**, 52 (2018).

[81] T. D. Stanescu and S. Tewari, J. Phys.: Condens. Matter **25**, 233201 (2013).

[82] S. Das Sarma, M. Freedman, and C. Nayak, npj Quantum Inf. **1**, 15001 (2015).

[83] M. Leijnse and K. Flensberg, Semicond. Sci. Technol. **27**, 124003 (2012).

[84] F. von Oppen, Y. Peng, and F. Pientka, in *Topological Aspects of Condensed Matter Physics: Lecture Notes of the Les Houches Summer School* (Oxford University Press, Oxford, 2017).

[85] R. Pawlak, S. Hoffman, J. Klinovaja, D. Loss, and E. Meyer, Progress in Particle and Nuclear Physics **107**, 1 (2019).

[86] N. P. de Leon, K. M. Itoh, D. Kim, K. K. Mehta, T. E. Northup, H. Paik, B. S. Palmer, N. Samarth, S. Sangtawesin, and D. W. Steuerman, Science **372**, eabb2823 (2021).

[87] B. Jäck, Y. Xie, and A. Yazdani, arXiv:2103.13210.

[88] R. Jackiw and C. Rebbi, Phys. Rev. D **13**, 3398 (1976).

[89] R. Jackiw and J. Schrieffer, Nucl. Phys. B **190**, 253 (1981).

[90] J. Bardeen, L. N. Cooper, and J. R. Schrieffer, Phys. Rev. **108**, 1175 (1957).

[91] E. Lieb, T. Schultz, and D. Mattis, Ann. Phys. **16**, 407 (1961).

[92] S. Ryu, A. P. Schnyder, A. Furusaki, and A. W. W. Ludwig, New J. Phys. **12**, 065010 (2010).

[93] C.-K. Chiu, J. C. Y. Teo, A. P. Schnyder, and S. Ryu, Rev. Mod. Phys. **88**, 035005 (2016).

[94] J. Klinovaja and D. Loss, Phys. Rev. B **86**, 085408 (2012).

[95] P. Středa and P. Šeba, Phys. Rev. Lett. **90**, 256601 (2003).

[96] J. Klinovaja, M. J. Schmidt, B. Braunecker, and D. Loss, Phys. Rev. Lett. **106**, 156809 (2011).

[97] V. Chua, K. Laubscher, J. Klinovaja, and D. Loss, Phys. Rev. B **102**, 155416 (2020).

[98] J. S. Lim, R. Lopez, and L. Serra, Europhys. Lett. **103**, 37004 (2013).

[99] B. Nijholt and A. R. Akhmerov, Phys. Rev. B **93**, 235434 (2016).

[100] O. Dmytruk and J. Klinovaja, Phys. Rev. B **97**, 155409 (2018).

[101] P. Wójcik and M. P. Nowak, Phys. Rev. B **97**, 235445 (2018).

[102] S. Gangadharaiah, B. Braunecker, P. Simon, and D. Loss, Phys. Rev. Lett. **107**, 036801 (2011).

[103] E. M. Stoudenmire, J. Alicea, O. A. Starykh, and M. P. A. Fisher, Phys. Rev. B **84**, 014503 (2011).

[104] H. Katsura, D. Schuricht, and M. Takahashi, Phys. Rev. B **92**, 115137 (2015).

[105] N. M. Gergs, L. Fritz, and D. Schuricht, Phys. Rev. B **93**, 075129 (2016).

[106] F. Domínguez, J. Cayao, P. San-Jose, R. Aguado, A. L. Yeyati, and E. Prada, npj Quant. Mater. **2**, 13 (2017).

[107] A. Wieckowski and A. Ptok, Phys. Rev. B **100**, 144510 (2019).

[108] O. Viyuela, D. Vodola, G. Pupillo, and M. A. Martin-Delgado, Phys. Rev. B **94**, 125121 (2016).

[109] P. Cats, A. Quelle, O. Viyuela, M. A. Martin-Delgado, and C. Morais Smith, Phys. Rev. B **97**, 121106(R) (2018).

[110] M. Kjaergaard, K. Wölms, and K. Flensberg, Phys. Rev. B **85**, 020503(R) (2012).

[111] J. Klinovaja, P. Stano, and D. Loss, Phys. Rev. Lett. **109**, 236801 (2012).

[112] J. Klinovaja and D. Loss, Phys. Rev. B **88**, 075404 (2013).

[113] A. Matos-Abiague, J. Shabani, A. D. Kent, G. L. Fatin, B. Scharf, and I. Žutić, Solid State Communications **262**, 1 (2017).

[114] G. L. Fatin, A. Matos-Abiague, B. Scharf, and I. Žutić, Phys. Rev. Lett. **117**, 077002 (2016).

[115] T. Zhou, N. Mohanta, J. E. Han, A. Matos-Abiague, and I. Žutić, Phys. Rev. B **99**, 134505 (2019).

[116] N. Mohanta, T. Zhou, J.-W. Xu, J. E. Han, A. D. Kent, J. Shabani, I. Žutić, and A. Matos-Abiague, Phys. Rev. Applied **12**, 034048 (2019).

[117] B. Braunecker, G. I. Japaridze, J. Klinovaja, and D. Loss, Phys. Rev. B **82**, 045127 (2010).

[118] M. A. Ruderman and C. Kittel, Phys. Rev. **96**, 99 (1954).

[119] T. Kasuya, Progr. Theoret. Phys. **16**, 45 (1956).

[120] K. Yosida, Phys. Rev. **106**, 893 (1957).

[121] X.-L. Qi and S.-C. Zhang, Rev. Mod. Phys. **83**, 1057 (2011).

[122] J. K. Asbóth, L. Oroszlány, and A. Pályi, *A Short Course on Topological Insulators*, Lecture Notes in Physics (Springer, 2016).

[123] Y. Ando, J. Phys. Soc. Jpn. **82**, 102001 (2013).

[124] M. Cheng, Phys. Rev. B **86**, 195126 (2012).

[125] J. Motruk, E. Berg, A. M. Turner, and F. Pollmann, Phys. Rev. B **88**, 085115 (2013).

[126] J. Klinovaja, A. Yacoby, and D. Loss, Phys. Rev. B **90**, 155447 (2014).

[127] J. Klinovaja and D. Loss, Phys. Rev. B **92**, 121410(R) (2015).

[128] C. Schrade, A. A. Zyuzin, J. Klinovaja, and D. Loss, Phys. Rev. Lett. **115**, 237001 (2015).

[129] J. Li, W. Pan, B. A. Bernevig, and R. M. Lutchyn, Phys. Rev. Lett. **117**, 046804 (2016).

[130] N. Traverso Ziani, C. Fleckenstein, L. Vigliotti, B. Trauzettel, and M. Sassetti, Phys. Rev. B **101**, 195303 (2020).

[131] C. Fleckenstein, N. Traverso Ziani, A. Calzona, M. Sassetti, and B. Trauzettel, Phys. Rev. B **103**, 125303 (2021).

[132] E. Bocquillon, R. S. Deacon, J. Wiedenmann, P. Leubner, T. M. Klapwijk, C. Brüne, K. Ishibashi, H. Buhmann, and L. W. Molenkamp, Nature Nanotech. **12**, 137 (2017).

[133] H.-H. Sun, M.-X. Wang, F. Zhu, G.-Y. Wang, H.-Y. Ma, Z.-A. Xu, Q. Liao, Y. Lu, C.-L. Gao, Y.-Y. Li, C. Liu, D. Qian, D. Guan, and J.-F. Jia, Nano Lett. **17**, 3035 (2017).

[134] W. A. Benalcazar, B. A. Bernevig, and T. L. Hughes, Phys. Rev. B **96**, 245115 (2017).

[135] Z. Song, Z. Fang, and C. Fang, Phys. Rev. Lett. **119**, 246402 (2017).

[136] J. Langbehn, Y. Peng, L. Trifunovic, F. von Oppen, and P. W. Brouwer, Phys. Rev. Lett. **119**, 246401 (2017).

[137] F. Schindler, A. M. Cook, M. G. Verginory, Z. Wang, S. S. P. Parking, B. A. Bernevig, and T. Neupert, Sci. Adv. **4**, eaat0346 (2018).

[138] S. A. Parameswaran and Y. Wan, Physics **10**, 132 (2017).

[139] B. Jäck, Y. Xie, J. Li, S. Jeon, B. A. Bernevig, and A. Yazdani, Science **364**, 1255 (2019).

[140] G.-H. Lee, K.-F. Huang, D. K. Efetov, D. S. Wei, S. Hart, T. Taniguchi, K. Watanabe, A.Yacoby, and P. Kim, Nature Phys. **13**, 693 (2017).

[141] D. J. Clarke, J. Alicea, and K. Shtengel, Nat. Commun. **4**, 1348 (2013).

[142] N. H. Lindner, E. Berg, G. Refael, and A. Stern, Phys. Rev. X **2**, 041002 (2012).

[143] X.-L. Qi, T. L. Hughes, and S.-C. Zhang, Phys. Rev. B **82**, 184516 (2010).

[144] S. Hart, H. Ren, T. Wagner, P. Leubner, M. Mühlbauer, C. Brüne, H. Buhmann, L. W. Molenkamp, and A. Yacoby, Nature Phys. **10**, 638 (2014).

[145] F. Amet, C. T. Ke, I. V. Borzenets, J. Wang, K. Watanabe, T. Taniguchi, R. S. Deacon, M. Yamamoto, Y. Bomze, S. Tarucha, and G. Finkelstein, Science **352**, 966 (2016).

[146] A. W. Draelos, M. T. Wei, A. Seredinski, C. T. Ke, Y. Mehta, R. Chamberlain, K. Watanabe, T. Taniguchi, M. Yamamoto, S. Tarucha, I. V. Borzenets, F. Amet, and G. Finkelstein, J. Low Temp. Phys. **191**, 288 (2018).

[147] L. Zhao, E. G. Arnault, A. Bondarev, A. Seredinski, T. F. Q. Larson, A. W. Draelos, H. Li, K. Watanabe, T. Taniguchi, F. Amet, H. U. Baranger, and G. Finkelstein, Nat. Phys. **16**, 862 (2020).

[148] Ö. Gül, Y. Ronen, S. Y. Lee, H. Shapourian, J. Zauberman, Y. H. Lee, K. Watanabe, T. Taniguchi, A. Vishwanath, A. Yacoby, and P. Kim, arXiv:2009.07836.

[149] J. Alicea and P. Fendley, Annu. Rev. Condens. Matter Phys. **7**, 119 (2016).

[150] J. Alicea and A. Stern, Phys. Scr. **2015**, 014006 (2015).

[151] T. L. Schmidt, Eur. Phys. J. Spec. Top. **229**, 621 (2020).

[152] F. Hassler and D. Schuricht, New J. Phys. **14**, 125018 (2012).

[153] B. M. Terhal, F. Hassler, and D. P. DiVincenzo, Phys. Rev. Lett. **108**, 260504 (2012).

[154] G. Kells, V. Lahtinen, and J. Vala, Phys. Rev. B **89**, 075122 (2014).

[155] A. Rahmani, X. Zhu, M. Franz, and I. Affleck, Phys. Rev. Lett. **115**, 166401 (2015).

[156] C.-K. Chiu, D. I. Pikulin, and M. Franz, Phys. Rev. B **91**, 165402 (2015).

[157] A. Chew, A. Essin, and J. Alicea, Phys. Rev. B **96**, 121119(R) (2017).

[158] A. Rahmani and M. Franz, Rep. Prog. Phys. **82**, 084501 (2019).

[159] L. Yu, Acta Phys. Sin. **21**, 75 (1965).

[160] H. Shiba, Prog. Theor. Phys. **40**, 435 (1968).

[161] A. I. Rusinov, Sov. Phys. JETP **29**, 1101 (1969).

[162] J. Li, H. Chen, I. K. Drozdov, A. Yazdani, B. A. Bernevig, and A. H. MacDonald, Phys. Rev. B **90**, 235433 (2014).

[163] F. Pientka, L. I. Glazman, and F. von Oppen, Phys. Rev. B **89**, 180505(R) (2014).

[164] A. Heimes, P. Kotetes, and G. Schön, Phys. Rev. B **90**, 060507(R) (2014).

[165] K. Pöyhönen, A. Westström, J. Röntynen, and T. Ojanen, Phys. Rev. B **89**, 115109 (2014).

[166] S. Hoffman, J. Klinovaja, and D. Loss, Phys. Rev. B **93**, 165418 (2016).

[167] G. M. Andolina and P. Simon, Phys. Rev. B **96**, 235411 (2017).

[168] A. Theiler, K. Björnson, and A. M. Black-Schaffer, Phys. Rev. B **100**, 214504 (2019).

[169] S. Nadj-Perge, I. K. Drozdov, J. Li, H. Chen, I. K. Jeon, J. Seo, A. H. MacDonald, B. A. Bernevig, and A. Yazdani, Science **346**, 602 (2014).

[170] M. Ruby, F. Pientka, Y. Peng, F. von Oppen, B. W. Heinrich, and K. J. Franke, Phys. Rev. Lett. **115**, 197204 (2015).

[171] R. Pawlak, M. Kisiel, J. Klinovaja, T. Meier, S. Kawai, T. Glatzel, D. Loss, and E. Meyer, npj Quantum Inf. **2**, 16035 (2016).

[172] B. E. Feldman, M. T. Randeria, J. Li, S. Jeon, Y. Xie, Z. Wang, I. K. Drozdov, B. A. Bernevig, and A. Yazdani, Nat. Phys. **13**, 286 (2016).

[173] M. Ruby, B. W. Heinrich, Y. Peng, F. von Oppen, and K. J. Franke, Nano Lett. **17**, 4473 (2017).

[174] S. Jeon, Y. Xie, J. Li, Z. Wang, B. A. Bernevig, and A. Yazdani, Science **358**, 772 (2017).

[175] H. Kim, A. Palacio-Morales, T. Posske, L. Rozsa, K. Palotas, L. Szunyogh, M. Thorwart, and R. Wiesendanger, Sci. Adv. **4**, eaar5251 (2018).

[176] S. Nakosai, Y. Tanaka, and N. Nagaosa, Phys. Rev. B **88**, 180503(R) (2013).

[177] K. Pöyhönen, A. Westström, S. S. Pershoguba, T. Ojanen, and A. V. Balatsky, Phys. Rev. B **94**, 214509 (2016).

[178] G. Yang, P. Stano, J. Klinovaja, and D. Loss, Phys. Rev. B **93**, 224505 (2016).

[179] U. Güngördü, S. Sandhoefner, and A. A. Kovalev, Phys. Rev. B **97**, 115136 (2018).

[180] M. Garnier, A. Mesaros, and P. Simon, Commun. Phys. **2**, 126 (2019).

[181] D. Steffensen, B. M. Andersen, and P. Kotetes, arXiv:2008.10626.

[182] S. Rex, I. V. Gornyi, and A. D. Mirlin, Phys. Rev. B **102**, 224501 (2020).

[183] A. Kubetzka, J. M. Bürger, R. Wiesendanger, and K. von Bergmann, Phys. Rev. Materials **4**, 081401(R) (2020).

[184] E. Mascot, J. Bedow, M. Graham, S. Rachel, and D. K. Morr, arXiv:2005.00027.

[185] N. Mohanta, S. Okamoto, and E. Dagotto, arXiv:2012.13502.

[186] S. A. Díaz, J. Klinovaja, D. Loss, and S. Hoffman, arXiv:2102.03423.

[187] F. Harper, R. Roy, M. S. Rudner, and S. L. Sondhi, Annu. Rev. Condens. Matter Phys. **11**, 345 (2020).

[188] M. S. Rudner and N. H. Lindner, Nat. Rev. Phys. **2**, 229 (2020).

[189] A. Kundu and B. Seradjeh, Phys. Rev. Lett. **111**, 136402 (2013).

[190] A. A. Reynoso and D. Frustaglia, Phys. Rev. B **87**, 115420 (2013).

[191] M. Thakurathi, A. A. Patel, D. Sen, and A. Dutta, Phys. Rev. B **88**, 155133 (2013).

[192] M. Thakurathi, K. Sengupta, and D. Sen, Phys. Rev. B **89**, 235434 (2014).

[193] M. Benito, A. Gómez-León, V. M. Bastidas, T. Brandes, and G. Platero, Phys. Rev. B **90**, 205127 (2014).

[194] V. Dal Lago, M. Atala, and L. E. F. Foa Torres, Phys. Rev. A **92**, 023624 (2015).

[195] M. Thakurathi, D. Loss, and J. Klinovaja, Phys. Rev. B **95**, 155407 (2017).

[196] D. T. Liu, J. Shabani, and A. Mitra, Phys. Rev. B **99**, 094303 (2019).

[197] K. Plekhanov, M. Thakurathi, D. Loss, and J. Klinovaja, Phys. Rev. Research **1**, 032013(R) (2019).

[198] T. O. Wehling, A. M. Black-Schaffer, and A. V. Balatsky, Adv. Phys. **63**, 1 (2014).

[199] Y. Ando and L. Fu, Annu. Rev. Condens. Matter Phys. **6**, 361 (2015).

[200] Y. Tanaka and S. Kashiwaya, Phys. Rev. Lett. **74**, 3451 (1995).

[201] S. Sasaki, M. Kriener, K. Segawa, K. Yada, Y. Tanaka, M. Sato, and Y. Ando, Phys. Rev. Lett. **107**, 217001 (2011).

[202] J. Linder, Y. Tanaka, T. Yokoyama, A. Sudbø, and N. Nagaosa, Phys. Rev. Lett. **104**, 067001 (2010).

[203] C.-R. Hu, Phys. Rev. Lett. **72**, 1526 (1994).

[204] K. Sengupta, I. Žutić, H.-J. Kwon, V. M. Yakovenko, and S. Das Sarma, Phys. Rev. B **63**, 144531 (2001).

[205] M. Alidoust, C. Shen, and I. Žutić, Phys. Rev. B **103**, L060503 (2021).

[206] J. Linder and A. V. Balatsky, Rev. Mod. Phys. **91**, 045005 (2019).

[207] Y. Tanaka, A. A. Golubov, S. Kashiwaya, and M. Ueda, Phys. Rev. Lett. **99**, 037005 (2007).

[208] Y. Tanaka and A. A. Golubov, Phys. Rev. Lett. **98**, 037003 (2007).

[209] C. Triola, J. Cayao, and A. M. Black-Schaffer, Ann. Phys. **532**, 1900298 (2020).

[210] Y. Tanaka, M. Sato, and N. Nagaosa, J. Phys. Soc. Jpn. **81**, 011013 (2012).

[211] J. Cayao and A. M. Black-Schaffer, Phys. Rev. B **98**, 075425 (2018).

[212] C. Fleckenstein, N. Traverso Ziani, and B. Trauzettel, Phys. Rev. B **97**, 134523 (2018).

[213] J. A. Krieger, A. Pertsova, S. R. Giblin, M. Döbeli, T. Prokscha, C. W. Schneider, A. Suter, T. Hesjedal, A. V. Balatsky, and Z. Salman, Phys. Rev. Lett. **125**, 026802 (2020).

[214] H. Ebisu, B. Lu, J. Klinovaja, and Y. Tanaka, Prog. Theor. Exp. Phys. **2016**, 083I01 (2016).

[215] C. L. M. Wong and K. T. Law, Phys. Rev. B **86**, 184516 (2012).

[216] F. Zhang, C. L. Kane, and E. J. Mele, Phys. Rev. Lett. **111**, 056402 (2013).

[217] S. Nakosai, J. C. Budich, Y. Tanaka, B. Trauzettel, and N. Nagaosa, Phys. Rev. Lett. **110**, 117002 (2013).

[218] A. Keselman, L. Fu, A. Stern, and E. Berg, Phys. Rev. Lett. **111**, 116402 (2013).

[219] J. Klinovaja and D. Loss, Phys. Rev. B **90**, 045118 (2014).

[220] A. Haim, A. Keselman, E. Berg, and Y. Oreg, Phys. Rev. B **89**, 220504(R) (2014).

[221] E. Gaidamauskas, J. Paaske, and K. Flensberg, Phys. Rev. Lett. **112**, 126402 (2014).

[222] E. Dumitrescu, J. D. Sau, and S. Tewari, Phys. Rev. B **90**, 245438 (2014).

[223] A. Haim, K. Wölms, E. Berg, Y. Oreg, and K. Flensberg, Phys. Rev. B **94**, 115124 (2016).

[224] C. Schrade, M. Thakurathi, C. Reeg, S. Hoffman, J. Klinovaja, and D. Loss, Phys. Rev. B **96**, 035306 (2017).

[225] M. Thakurathi, P. Simon, I. Mandal, J. Klinovaja, and D. Loss, Phys. Rev. B **97**, 045415 (2018).

[226] A. A. Aligia and L. Arrachea, Phys. Rev. B **98**, 174507 (2018).

[227] W. A. Benalcazar, B. A. Bernevig, and T. L. Hughes, Science **357**, 61 (2017).

[228] Y. Peng, Y. Bao, and F. von Oppen, Phys. Rev. B **95**, 235143 (2017).

[229] S. Imhof, C. Berger, F. Bayer, H. Brehm, L. Molenkamp, T. Kiessling, F. Schindler, C. H. Lee, M. Greiter, T. Neupert, and R. Thomale, Nat. Phys. **14**, 925 (2018).

[230] M. Geier, L. Trifunovic, M. Hoskam, and P. W. Brouwer, Phys. Rev. B **97**, 205135 (2018).

[231] F. Schindler, J. Appl. Phys. **128**, 221102 (2020).

[232] Y.-J. Wu, J. Hou, Y.-M. Li, X.-W. Luo, X. Shi, and C. Zhang, Phys. Rev. Lett. **124**, 227001 (2020).

[233] Y. Wang, M. Lin, and T. L. Hughes, Phys. Rev. B **98**, 165144 (2018).

[234] T. Liu, J. J. He, and F. Nori, Phys. Rev. B **98**, 245413 (2018).

[235] S. Franca, D. V. Efremov, and I. C. Fulga, Phys. Rev. B **100**, 075415 (2019).

[236] Z. Yan, Phys. Rev. B **100**, 205406 (2019).

[237] R.-X. Zhang, W. S. Cole, X. Wu, and S. Das Sarma, Phys. Rev. Lett. **123**, 167001 (2019).

[238] X. Zhu, Phys. Rev. Lett. **122**, 236401 (2019).

[239] K. Laubscher, D. Loss, and J. Klinovaja, Phys. Rev. Research **2**, 013330 (2020).

[240] X. Wu, X. Liu, R. Thomale, and C.-X. Liu, arXiv:1905.10648.

[241] S.-B. Zhang, A. Calzona, and B. Trauzettel, Phys. Rev. B **102**, 100503(R) (2020).

[242] K. Laubscher, D. Chughtai, D. Loss, and J. Klinovaja, Phys. Rev. B **102**, 195401 (2020).

[243] Y. Volpez, D. Loss, and J. Klinovaja, Phys. Rev. Lett. **122**, 126402 (2019).

[244] V. T. Phong, N. R. Walet, and F. Guinea, Phys. Rev. B **96**, 060505(R) (2017).

[245] E. Khalaf, Phys. Rev. B **97**, 205136 (2018).

[246] X. Zhu, Phys. Rev. B **97**, 205134 (2018).

[247] K. Laubscher, D. Loss, and J. Klinovaja, Phys. Rev. Research **1**, 032017(R) (2019).

[248] J. Ahn and B.-J. Yang, Phys. Rev. Research **2**, 012060(R) (2020).

[249] B. A. Bernevig, T. L. Hughes, and S.-C. Zhang, Science **314**, 1757 (2006).

[250] Y. Volpez, D. Loss, and J. Klinovaja, Phys. Rev. B **97**, 195421 (2018).

[251] C. J. Bolech and E. Demler, Phys. Rev. Lett. **98**, 237002 (2007).

[252] J. Nilsson, A. R. Akhmerov, and C. W. J. Beenakker, Phys. Rev. Lett. **101**, 120403 (2008).

[253] K. T. Law, P. A. Lee, and T. K. Ng, Phys. Rev. Lett. **103**, 237001 (2009).

[254] K. Flensberg, Phys. Rev. B **82**, 180516(R) (2010).

[255] M. Wimmer, A. R. Akhmerov, J. P. Dahlhaus, and C. W. J. Beenakker, New J. Phys. **13**, 053016 (2011).

[256] L. Fidkowski, J. Alicea, N. H. Lindner, R. M. Lutchyn, and M. P. A. Fisher, Phys. Rev. B **85**, 245121 (2012).

[257] S. Frolov, Nature **592**, 350 (2021).

[258] H. J. Suominen, M. Kjaergaard, A. R. Hamilton, J. Shabani, C. J. Palmstrøm, C. M. Marcus, and F. Nichele, Phys. Rev. Lett. **119**, 176805 (2017).

[259] N. W. Hendrickx, D. P. Franke, A. Sammak, M. Kouwenhoven, D. Sabbagh, L. Yeoh, R. Li, M. L. V. Tagliaferri, M. Virgilio, G. Capellini, G. Scappucci, and M. Veldhorst, Nat. Commun. **9**, 2835 (2018).

[260] E. Bakkers, MRS Bulletin **44**, 403 (2019).

[261] J. Ridderbos, M. Brauns, F. K. de Vries, J. Shen, A. Li, S. Kölling, M. A. Verheijen, A. Brinkman, W. G. van der Wiel, E. P. A. M. Bakkers, and F. A. Zwanenburg, Nano Lett. **20**, 122 (2020).

[262] K. Aggarwal, A. Hofmann, D. Jirovec, I. Prieto, A. Sammak, M. Botifoll, S. Martí-Sánchez, M. Veldhorst, J. Arbiol, G. Scappucci, J. Danon, and G. Katsaros, Phys. Rev. Research **3**, L022005 (2021).

[263] C. Reeg, D. Loss, and J. Klinovaja, Phys. Rev. B **96**, 125426 (2017).

[264] C. Reeg, D. Loss, and J. Klinovaja, Phys. Rev. B **97**, 165425 (2018).

[265] B. D. Woods, S. Das Sarma, and T. D. Stanescu, Phys. Rev. B **99**, 161118(R) (2019).

[266] G. W. Winkler, A. E. Antipov, B. van Heck, A. A. Soluyanov, L. I. Glazman, M. Wimmer, and R. M. Lutchyn, Phys. Rev. B **99**, 245408 (2019).

[267] T. Kiendl, F. von Oppen, and P. W. Brouwer, Phys. Rev. B **100**, 035426 (2019).

[268] K. T. Law and Patrick A. Lee, Phys. Rev. B **84**, 081304(R) (2011).

[269] L. Jiang, D. Pekker, J. Alicea, G. Refael, Y. Oreg, and F. von Oppen, Phys. Rev. Lett. **107**, 236401 (2011).

[270] P. San-Jose, E. Prada, and R. Aguado, Phys. Rev. Lett. **108**, 257001 (2012).

[271] P. A. Ioselevich and M. V. Feigel'man, Phys. Rev. Lett. **106**, 077003 (2011).

[272] D. M. Badiane, M. Houzet, and J. S. Meyer, Phys. Rev. Lett. **107**, 177002 (2011).

[273] F. Domínguez, F. Hassler, and G. Platero, Phys. Rev. B **86**, 140503(R) (2012).

[274] D. I. Pikulin and Y. V. Nazarov, Phys. Rev. B **86**, 140504(R) (2012).

[275] M. Trif and Y. Tserkovnyak, Phys. Rev. Lett. **109**, 257002 (2012).

[276] T. L. Schmidt, A. Nunnenkamp, and C. Bruder, Phys. Rev. Lett. **110**, 107006 (2013).

[277] O. Dmytruk, M. Trif, and P. Simon, Phys. Rev. B **92**, 245432 (2015).

[278] A. Cottet, M. C. Dartiailh, M. M. Desjardins, T. Cubaynes, L. C. Contamin, M. Delbecq, J. J. Viennot, L. E. Bruhat, B. Douçot, and T. Kontos, J. Phys.: Condens. Matter **29**, 433002 (2017).

[279] T. Gulden, M. Janas, Y. Wang, and A. Kamenev, Phys. Rev. Lett. **116**, 026402 (2016).

[280] P. Szumniak, D. Chevallier, D. Loss, and J. Klinovaja, Phys. Rev. B **96**, 041401(R) (2017).

[281] D. Chevallier, P. Szumniak, S. Hoffman, D. Loss, and J. Klinovaja, Phys. Rev. B **97**, 045404 (2018).

[282] M. Serina, D. Loss, and J. Klinovaja, Phys. Rev. B **98**, 035419 (2018).

[283] F. Yang, S.-J. Jiang, and F. Zhou, Phys. Rev. B **100**, 054508 (2019).

[284] S. Tamura, S. Hoshino, and Y. Tanaka, Phys. Rev. B **99**, 184512 (2019).

[285] D. Sticlet, C. P. Moca, and B. Dóra, Phys. Rev. B **102**, 075437 (2020).

[286] M. Mashkoori, S. Pradhan, K. Björnson, J. Fransson, and A. M. Black-Schaffer, Phys. Rev. B **102**, 104501 (2020).

[287] C.-K. Chiu, M. M. Vazifeh, and M. Franz, Europhys. Lett. **110**, 10001 (2015).

[288] P. San-Jose, J. Cayao, E. Prada, and R. Aguado, Sci. Rep. **6**, 21427 (2016).

[289] J. Alicea, Y. Oreg, G. Refael, F. von Oppen, and M. P. A. Fisher, Nature Phys. **7**, 412 (2011).

[290] J. D. Sau, S. Tewari, and S. Das Sarma, Phys. Rev. A **82**, 052322 (2010).

[291] D. J. Clarke, J. D. Sau, and S. Tewari, Phys. Rev. B **84**, 035120 (2011).

[292] T. Hyart, B. van Heck, I. C. Fulga, M. Burrello, A. R. Akhmerov, and C. W. J. Beenakker, Phys. Rev. B **88**, 035121 (2013).

[293] T. Karzig, Y. Oreg, G. Refael, and M. H. Freedman, Phys. Rev. X **6**, 031019 (2016).

[294] D. Aasen, M. Hell, R. V. Mishmash, A. Higginbotham, J. Danon, M. Leijnse, T. S. Jespersen, J. A. Folk, C. M. Marcus, K. Flensberg, and J. Alicea, Phys. Rev. X **6**, 031016 (2016).

[295] B. I. Halperin, Y. Oreg, A. Stern, G. Refael, J. Alicea, and F. von Oppen, Phys. Rev. B **85**, 144501 (2012).

[296] P. Bonderson, M. Freedman, and C. Nayak, Phys. Rev. Lett. **101**, 010501 (2008).

[297] P. Bonderson, M. Freedman, and C. Nayak, Ann. Phys. (NY) **324**, 787 (2009).

[298] T. Karzig, C. Knapp, R. M. Lutchyn, P. Bonderson, M. B. Hastings, C. Nayak, J. Alicea, K. Flensberg, S. Plugge, Y. Oreg, C. M. Marcus, and M. H. Freedman, Phys. Rev. B **95**, 235305 (2017).

Chapter 2

Fractional topological superconductivity and parafermion corner states

Adapted from:
K. Laubscher, D. Loss, and J. Klinovaja
"Fractional topological superconductivity and parafermion corner states,"
Phys. Rev. Research **1**, 032017 (2019)

We consider a system of weakly coupled Rashba nanowires in the strong spin-orbit interaction (SOI) regime. The nanowires are arranged into two tunnel-coupled layers proximitized by a top and bottom superconductor such that the superconducting phase difference between them is π. We show that in such a system strong electron-electron interactions can stabilize a helical topological superconducting phase hosting Kramers partners of $\mathbb{Z}_{2m}$ parafermion edge modes, where m is an odd integer determined by the position of the chemical potential. Furthermore, upon turning on a weak in-plane magnetic field, the system is driven into a second-order topological superconducting phase hosting zero-energy $\mathbb{Z}_{2m}$ parafermion bound states localized at two opposite corners of a rectangular sample. As a special case, zero-energy Majorana corner states emerge in the non-interacting limit $m = 1$, where the chemical potential is tuned to the SOI energy of the single nanowires.

2.1 Introduction

The search for topological phases of matter has generated an enormous amount of research. Motivated by the discovery and classification of topological insulators (TIs) and topological superconductors (TSCs), the field has been driven by the desire to access phases with increasingly exotic properties. In particular, it has been found that the effects of strong electron-electron interactions can lead to exotic fractionalized phases, which are considered particularly interesting due to their potential use for topological quantum computation. However, only one-dimensional (1D) systems allow for an analytically tractable description of such strong interactions via the bosonization formalism. In order to study strongly interacting systems in more than one dimension, one therefore resorts to the so-called *coupled-wire* approach, where two- or three-dimensional systems are built up from weakly coupled 1D channels, such as nanowires. This approach has proven to be exceptionally fruitful in accessing the fractional counterparts of several well-known topological phases such as fractional quantum Hall states [1–3], fractional TIs and TSCs [4–15], as well as fractional spin liquids [16–18].

Recently, a lot of interest has been raised by the generalization of conventional TIs/TSCs to so-called *higher-order* TIs/TSCs [19–39]. While a conventional d-dimensional TI/TSC exhibits $(d-1)$-dimensional gapless boundary modes, a d-dimensional nth-order TI/TSC hosts gapless modes at its $(d-n)$-dimensional boundaries. While electron-electron interactions have been taken into account in a few cases [40, 41], the main focus was on non-interacting systems, in particular neglecting the possible existence of exotic fractional phases supporting emergent parafermions. This raises the question whether a coupled-wire approach can be used to extend the class of higher-order topological phases to the *fractional* regime. In this work, we show that this is indeed possible and explicitly construct a two-dimensional (2D) fractional second-order TSC exhibiting exotic parafermion corner states.

Our model consists of two layers of coupled Rashba nanowires with proximity-induced superconductivity of a phase difference of π between the upper and lower layers, see Fig. 2.1. In a first step, we show that in the presence of strong electron-electron interactions, such a setup exhibits a helical topological superconducting phase with gapless helical $\mathbb{Z}_{2m}$ parafermion edge modes propagating along the edges. Here, m is an odd integer determined by the position of the chemical potential μ. In the special case $m = 1$, where μ is tuned to the SOI energy of the single nanowires, Majorana edge modes emerge even in the non-interacting regime. At lower densities, the fractional regime $m > 1$ emerges in the presence of strong electron-electron interactions as the SOI and Fermi wavevectors get commensurable.

In a second step, we include a small time-reversal breaking perturbation in the form of a weak in-plane magnetic field to gap out the helical edge modes. For a finite rectangular sample, we find $\mathbb{Z}_{2m}$ parafermions localized at two opposite corners of the system depending on the direction of the magnetic field, which places our model in the class of 2D fractional second-order TSCs. Unlike most examples of higher order topological phases, the stability of these corner states does not rely on spatial symmetries but is guaranteed by particle-hole symmetry alone. Also, the parafermion corner states found here emerge in a spatially uniform 2D system, while in previous studies parafermions have been constructed as bound states localized at interfaces of non-uniform 2D systems [42–49] or at ends of 1D wires [50–57].

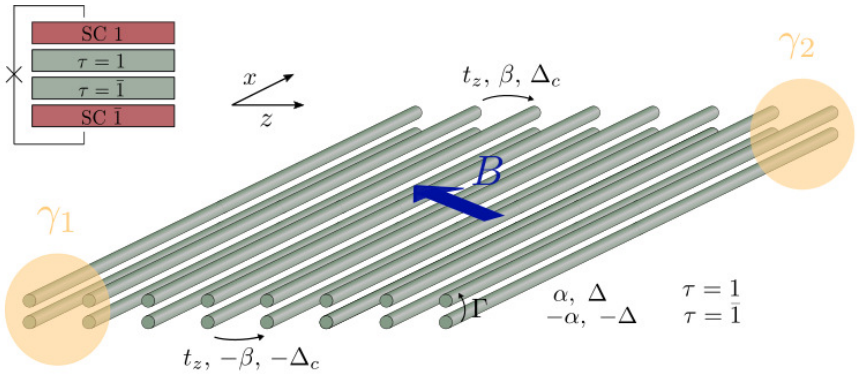

Figure 2.1: The setup consists of two layers of coupled Rashba nanowires where the index $\tau = 1$ ($\tau = \bar{1}$) denotes the upper (lower) layer. The strength of the Rashba SOI associated with propagation along the x direction is given by α ($-\alpha$) for the upper (lower) layer. Both layers are brought into proximity to an s-wave bulk superconductor such that there is a phase difference of π between them. In addition, the two layers are strongly coupled by interlayer tunneling of strength Γ. Neighboring nanowires of the same layer are weakly coupled via a spin-conserving hopping term of strength t_z, via a spin-flip hopping term of strength β ($-\beta$) associated with Rashba SOI along the z direction, and via a crossed-Andreev superconducting term of strength Δ_c ($-\Delta_c$), where the last two terms are again of opposite sign for the two layers. Finally, a weak in-plane magnetic field of strength B is applied. We show that in specific regions of parameter space, this system hosts two zero-energy corner states (here denoted by γ_1 and γ_2) at two opposite corners of a rectangular sample. In the non-interacting case, these states are Majorana zero modes, whereas strong electron-electron interactions lead to $\mathbb{Z}_{2m}$ parafermion corner states, where m is an odd integer depending on the position of the chemical potential.

2.2 Model

We consider two layers composed of coupled Rashba nanowires proximitized by bulk s-wave superconductors, see Fig. 2.1. Each nanowire of length L is modeled by a free-particle Hamiltonian

$$H_{0,n} = \sum_{\tau,\sigma} \int dx\ \psi^\dagger_{n\tau\sigma} \Big[-\frac{\hbar^2 \partial_x^2}{2m} - \mu + i\alpha\tau\sigma\partial_x \Big] \psi_{n\tau\sigma}. \tag{2.1}$$

Here, $\psi^\dagger_{n\tau\sigma}(x)$ [$\psi_{n\tau\sigma}(x)$] creates (destroys) an electron at position x in the n-th wire in the layer $\tau \in \{1, \bar{1}\}$ of spin $\sigma \in \{1, \bar{1}\}$, where we define the spin quantization axis along the SOI direction. The Rashba coefficient α is taken to be of equal magnitude for all nanowires, but of opposite sign for the two layers. The SOI energy associated with propagation along the nanowire is $E_{so} = \hbar^2 k_{so}^2/(2m)$ for $k_{so} = m\alpha/\hbar^2$, and the chemical potential μ is defined relative to E_{so}. The proximity-induced superconductivity is described by

$$H_{\Delta,n} = \Delta \sum_\tau \tau \int dx\, \psi_{n\tau 1}\psi_{n\tau\bar{1}} + \text{H.c.}, \tag{2.2}$$

where we have set the phase difference between the two superconductors to π. This can, for example, be realized by the Josephson-junction setup shown in the inset of Fig. 2.1,

where the phase difference between the two superconductors is adjusted by controlling the magnetic flux through the superconducting loop [58,59]. Alternatively, a thin insulating layer of randomly oriented magnetic impurities [60] could be placed between one of the layers and the corresponding superconductor such that the phase difference of π arises due to spin-flip tunneling via the impurities [61–64]. Furthermore, the two layers are coupled by interlayer tunneling of the form

$$H_{\Gamma,n} = \Gamma \sum_{\tau,\sigma} \int dx\, \psi^\dagger_{n\tau\sigma} \psi_{n\bar{\tau}\sigma}, \tag{2.3}$$

such that the total Hamiltonian describing an effective double nanowire (DNW) composed of two strongly coupled nanowires from different layers is given by $H_n = H_{0,n} + H_{\Delta,n} + H_{\Gamma,n}$. Finally, the DNWs are weakly coupled via a spin-conserving hopping term of strength t_z, via a spin-flip hopping term of strength β ($-\beta$) associated with Rashba SOI along the z direction as well as via a crossed-Andreev superconducting term of strength Δ_c ($-\Delta_c$), where the last two terms are again of opposite sign for the two layers. Here, $|t_z|, |\beta|, |\Delta_c| \ll |\Delta|, |\Gamma|$. The interwire Hamiltonian can then be written as

$$\begin{aligned} H_\perp = \sum_{n,\tau,\sigma,\sigma'} \int dx \{ & \Delta_c \tau\, \psi_{n\tau\sigma} (i\sigma_y)_{\sigma\sigma'} \psi_{(n+1)\tau\sigma'}/2 \\ & + \psi^\dagger_{n\tau\sigma} [-t_z \delta_{\sigma\sigma'} - i\beta\tau(\sigma_x)_{\sigma\sigma'}/2] \psi_{(n+1)\tau\sigma'} \} + \text{H.c.} \end{aligned} \tag{2.4}$$

The total Hamiltonian is now given by $H = \sum_n H_n + H_\perp$, which in momentum space takes the form $H = \frac{1}{2}\sum_{k_z} \int dk_x \Psi^\dagger_{\mathbf{k}} \mathcal{H}(\mathbf{k}) \Psi_{\mathbf{k}}$ in the basis $\Psi_{\mathbf{k}}$=($\psi_{\mathbf{k}1\uparrow}$, $\psi_{\mathbf{k}1\downarrow}$, $\psi^\dagger_{-\mathbf{k}1\uparrow}$, $\psi^\dagger_{-\mathbf{k}1\downarrow}$, $\psi_{\mathbf{k}\bar{1}\uparrow}$, $\psi_{\mathbf{k}\bar{1}\downarrow}$, $\psi^\dagger_{-\mathbf{k}\bar{1}\uparrow}$, $\psi^\dagger_{-\mathbf{k}\bar{1}\downarrow}$) with

$$\begin{aligned} \mathcal{H}(\mathbf{k}) = & \Big[\frac{\hbar^2 k_x^2}{2m} - 2t_z \cos(k_z a_z) - \mu \Big] \eta_z - \alpha k_x \tau_z \sigma_z \\ & + \beta \sin(k_z a_z) \tau_z \sigma_x + \Gamma \tau_x \eta_z + [\Delta + \Delta_c \cos(k_z a_z)] \tau_z \eta_y \sigma_y. \end{aligned} \tag{2.5}$$

Here, τ_i, η_i, and σ_i for $i \in \{x, y, z\}$ are Pauli matrices acting in layer, particle-hole, and spin space, respectively, and a_z is the spacing between neighboring nanowires. The system belongs to the symmetry class DIII [65] with time-reversal (particle-hole) symmetry given by $\mathcal{T} = i\sigma_y \mathcal{K}$ ($\mathcal{P} = \eta_x \mathcal{K}$).

2.3 Helical topological superconducting phase

We now demonstrate that the system can be brought into a helical topological superconducting phase hosting two counterpropagating $\mathbb{Z}_{2m}$ parafermion edge modes in the presence of strong electron-electron interactions. For this, we follow the method developed before for fractional TIs [4, 8]: First, we solve the DNW Hamiltonian H_n and demonstrate that, due to the interplay between Δ and Γ, the elementary excitations are given by gapless $\mathbb{Z}_{2m}$ parafermion modes. We note that, in contrast to Refs. [4, 8], there are two competing gap-opening mechanisms, such that when the system is brought close to the critical point $\Gamma \approx \Delta$, again half of the modes are left gapless. Second, we include weak hoppings between DNWs to gap out the parafermion modes in the bulk but leave Kramers pairs of gapless parafermion modes at the edges of the system. Again, if β and Δ_c counterbalance each other, the edge

modes propagating along the x axis are perfectly localized at the outermost DNWs. Importantly, the topological phase is robust against deviations from these fine-tuned points, which will, however, lead to increased localization lengths of the edge states.

For illustrative purposes, we first consider the non-interacting regime with $m = 1$ and set $\mu = 0$. To treat the DNW Hamiltonian H_n, we linearize the spectra of the single nanowires around the Fermi points [66] as $\psi_{n\tau\sigma}(x) = R_{n\tau\sigma}(x)e^{ik_F^{1\tau\sigma}x} + L_{n\tau\sigma}(x)e^{ik_F^{\bar{1}\tau\sigma}x}$, where $R_{n\tau\sigma}(x)$, $L_{n\tau\sigma}(x)$ vary slowly on the scale of k_{so}^{-1} and the Fermi momenta are given by $k_F^{r\tau\sigma} = (\sigma\tau + r)k_{so}$. [1] We note that upon a change of basis defined by $\bar{L}_{n\kappa\nu} = (L_{n\kappa\nu} - i\kappa\nu L_{n\bar{\kappa}\bar{\nu}})/\sqrt{2}$, $\bar{R}_{n\kappa\nu} = (R_{n\kappa\nu} - i\kappa\nu R_{n\bar{\kappa}\bar{\nu}})/\sqrt{2}$, H_n takes a block-diagonal form, while the structure of the Fermi momenta remains unchanged. For $\Delta \neq 0$, the exterior branches $\bar{R}_{n\kappa\kappa}$ and $\bar{L}_{n\kappa\bar{\kappa}}$ are fully gapped by superconductivity, whereas the interior branches $\bar{L}_{n\kappa\kappa}$ and $\bar{R}_{n\kappa\bar{\kappa}}$ have two competing gap-opening mechanisms given by interlayer tunneling and superconductivity. In the following, we thus focus on the interior branches only and tune the system to the critical point $\Delta = \Gamma$. In the new basis, the superconducting and tunneling term take the form $H_{\Gamma,n} = i\Gamma \sum_\kappa \int dx \bar{R}^\dagger_{n\kappa\bar{\kappa}} \bar{L}_{n\kappa\kappa}$ + H.c., $H_{\Delta,n} = \Delta \sum_\kappa \int dx \bar{R}^\dagger_{n\kappa\bar{\kappa}} \bar{L}^\dagger_{n\kappa\kappa}$ + H.c., where the two decoupled sectors labeled by κ are related by time-reversal symmetry. Focusing on the first sector (corresponding to $\kappa = 1$), we find two gapless counterpropagating Majorana modes per DNW that can be written as

$$\begin{aligned} \chi_{Ln1} &= (e^{-i\pi/4}\bar{L}_{n11} + e^{i\pi/4}\bar{L}^\dagger_{n11})/\sqrt{2}\,, \\ \chi_{Rn1} &= (e^{-i\pi/4}\bar{R}_{n1\bar{1}} + e^{i\pi/4}\bar{R}^\dagger_{n1\bar{1}})/\sqrt{2}\,. \end{aligned} \tag{2.6}$$

Next, we add small interwire hopping terms [see Eq. (2.4)], where we set $t_z = 0$ for simplicity. Focusing on the low-energy sector spanned by the states given in Eq. (2.6), $H_\perp$ takes a form similar to a Kitaev chain [67] of coupled 1D modes,

$$H_\perp = \frac{i}{2}\sum_{n=1}^{N-1}\int dx[(\beta - \Delta_c)\chi_{R(n+1)1}\chi_{Ln1} + (\beta + \Delta_c)\chi_{L(n+1)1}\chi_{Rn1}], \tag{2.7}$$

where N is the number of DNWs. At the special point $\Delta_c = \beta$, the modes χ_{L11} and χ_{RN1} do not enter $H_\perp$ and, thus, stay gapless in contrast to all other bulk modes. Obviously, the same is true for their time-reversal partners $\chi_{R1\bar{1}}$ and $\chi_{LN\bar{1}}$. Thus, the system is in a helical topological superconducting phase with Kramers partners of gapless Majorana modes propagating along the edges. Even though this result was derived using a considerable amount of fine-tuning, the topological properties of the system remain qualitatively identical for a broad range of parameters as long as the bulk gap does not close. In particular, our results do not change if a small t_z is included, see Fig. 2.2(a).

If, on the other hand, the system is infinite along the z axis and finite along the x axis, we apply the standard procedure of matching decaying eigenfunctions [68] to find a Kramers pair of gapless Majorana edge modes propagating perpendicular to the DNWs, see App. 2.B for details and again Fig. 2.2(a) for a numerical confirmation.

[1] The assumption of equal Fermi momenta for all nanowires can be relaxed to the requirement that the Fermi momenta of only the interior branches are approximately the same. While small deviations from this point do not alter our main conclusions, substantial differences suppress the interlayer tunneling due to momentum mismatch.

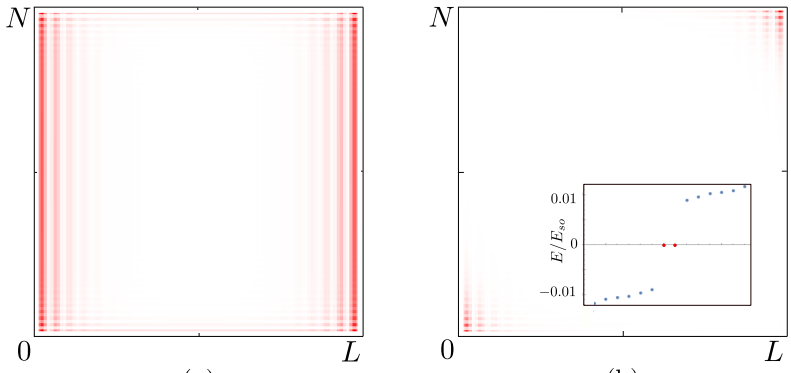

Figure 2.2: Probability density of low-energy states of H [see Eqs. (2.1)-(2.4)] obtained numerically. (a) For $\Delta_Z = 0$, the system is a helical TSC with Kramers partners of gapless Majorana modes propagating along the edges. (b) In the presence of a small in-plane magnetic field, $\Delta_Z > 0$, we find Majorana bound states localized at two opposite corners of the system. The inset shows the spectrum confirming that these two states (red dots) are indeed at zero energy. The numerical parameters are $N = 100$, $\mu = 0$, $k_{so}L = 85$, $\Gamma/E_{so} \approx 0.6$, $\Delta/E_{so} \approx 0.55$, $t_z/E_{so} \approx 0.01$, $\beta/E_{so} \approx 0.28$, $\Delta_c/E_{so} \approx 0.11$, and, in (b), $\Delta_Z/E_{so} \approx 0.07$ and $\phi = -\pi/16$. We note that the found topological phases are stable against disorder and do not rely on spatial symmetries.

2.4 Fractional helical topological superconducting phase

Now we focus on the fractional counterpart of the helical superconducting phase discussed above. We tune the chemical potential to a fractional value $\mu/E_{so} = -1 + 1/m^2$, where m is an odd integer. The new Fermi momenta are now given by $k_F^{r\tau\sigma} = (\tau\sigma + r/m)k_{so}$. For $m > 1$, the interlayer tunneling term given in Eq. (2.3) no longer conserves momentum and is therefore suppressed. However, for the special values of chemical potential introduced above, momentum-conserving terms can be constructed by including backscattering terms arising from electron-electron interactions [2, 69]. These terms are given by $\tilde{H}_{\Gamma,n} = i\tilde{\Gamma}\sum_\kappa \int dx (\bar{R}^\dagger_{n\kappa\bar{\kappa}}\bar{L}_{n\kappa\bar{\kappa}})^k (\bar{R}^\dagger_{n\kappa\bar{\kappa}}\bar{L}_{n\kappa\kappa})(\bar{R}^\dagger_{n\kappa\kappa}\bar{L}_{n\kappa\kappa})^k + \text{H.c.}$, where $k = (m-1)/2$. Similarly, we can write down a dressed superconducting term $\tilde{H}_{\Delta,n} = \tilde{\Delta}\sum_{\kappa,\nu}\kappa\nu\int dx (\bar{R}^\dagger_{n\kappa\bar{\nu}}\bar{L}_{n\kappa\bar{\nu}})^k (\bar{R}^\dagger_{n\kappa\bar{\nu}}\bar{L}^\dagger_{n\kappa\nu})(\bar{R}_{n\kappa\nu}\bar{L}^\dagger_{n\kappa\nu})^k + \text{H.c.}$ Here, the coupling constants $\tilde{\Gamma} \propto \Gamma g_B^{m-1}$ and $\tilde{\Delta} \propto \Delta g_B^{m-1}$, where g_B is the strength of a single backscattering process caused by electron-electron interactions, are assumed to be large [15, 50, 51, 70]. In order to treat the interacting Hamiltonian analytically, we adapt a bosonized language [54]: $\bar{R}_{n\kappa\nu}(x) = e^{i\phi_{1n\kappa\nu}(x)}$, $\bar{L}_{n\kappa\nu}(x) = e^{i\phi_{\bar{1}n\kappa\nu}(x)}$ for bosonic fields $\phi_{rn\kappa\nu}(x)$ satisfying standard non-local commutation relations. The dressed superconducting and tunneling terms can be simplified by introducing new bosonic operators $\eta_{rn\kappa\nu}(x) = \frac{m+1}{2}\phi_{rn\kappa\nu}(x) - \frac{m-1}{2}\phi_{\bar{r}n\kappa\nu}(x)$ obeying the commutation relations $[\eta_{rn\kappa\nu}(x), \eta_{r'n'\kappa'\nu'}(x')] = i\pi rm\delta_{rr'}\delta_{nn'}\delta_{\kappa\kappa'}\delta_{\nu\nu'}\text{sgn}(x-x')$. The DNW Hamiltonian takes the simple form

$$H_n = H_{0,n} + 2\sum_\kappa \int dx \left[\tilde{\Gamma}\sin(\eta_{1n\kappa\bar{\kappa}} - \eta_{\bar{1}n\kappa\kappa}) + \tilde{\Delta}\cos(\eta_{1n\kappa\bar{\kappa}} + \eta_{\bar{1}n\kappa\kappa}) + \tilde{\Delta}\cos(\eta_{1n\kappa\kappa} + \eta_{\bar{1}n\kappa\bar{\kappa}})\right] \quad (2.8)$$

with $H_{0,n} = \frac{v}{4\pi m}\sum_{r,\kappa,\nu}\int dx(\partial_x\eta_{rn\kappa\nu})^2$, where v is the Fermi velocity and we focus on the special values of Luttinger liquid (LL) parameters $K_{n\kappa\nu} = 1/m$. Again, half the modes are fully gapped by superconductivity, while for the other modes superconductivity and interlayer tunneling compete. Introducing conjugate fields $\varphi_{n\kappa} = (\eta_{1n\kappa\bar{\kappa}} - \eta_{\bar{1}n\kappa\kappa} - \pi/2)/(2\sqrt{m})$, $\theta_{n\kappa} = (\eta_{1n\kappa\bar{\kappa}} + \eta_{\bar{1}n\kappa\kappa})/(2\sqrt{m})$, the competing part of the above Hamiltonian can be rewritten as

$$H_n = \sum_{\kappa}\int dx\left\{\frac{v}{2\pi}[(\partial_x\varphi_{n\kappa})^2 + (\partial_x\theta_{n\kappa})^2] + 2\tilde{\Gamma}\cos(2\sqrt{m}\varphi_{n\kappa}) + 2\tilde{\Delta}\cos(2\sqrt{m}\theta_{n\kappa})\right\}. \quad (2.9)$$

For $\tilde{\Gamma} = \tilde{\Delta}$, this Hamiltonian corresponds to two time-reversed copies of a well-known self-dual sine-Gordon model [71,72]. For $m = 1$, we thus expect to find a single gapless Majorana mode per time-reversal sector, which is consistent with our analysis of the non-interacting regime in the previous section. To study the more general case, we start by noting that for our choice of LL parameters, the competing terms have the same scaling dimension, which allows us to explicitly study the properties of the system along the self-dual line. For $m > 1$, however, the superconducting and tunneling terms are irrelevant to first order in the renormalization group (RG) analysis, suggesting a flow to a trivial LL fixed point. To resolve this issue, Ref. [70] argued that upon including a third-order term in the RG equations, a multicritical fixed point is encountered, which in our case separates a gapless phase, a phase dominated by superconductivity, and a phase dominated by interlayer tunneling. Such a fixed point has been shown to be described by a $\mathbb{Z}_{2m}$ parafermion theory [72], which means in our case that there are two bulk $\mathbb{Z}_{2m}$ parafermion modes related by time-reversal symmetry residing within each DNW.

We now refermionize the above model in order to obtain an explicit expression for specific primary fields [72] of these parafermion theories. In particular, we define new composite chiral fermion operators $\bar{\psi}^{(m)}_{n\kappa\nu}(x) = \bar{R}^{(m)}_{n\kappa\nu}(x)e^{iq_F^{1\kappa\nu}x} + \bar{L}^{(m)}_{n\kappa\nu}(x)e^{iq_F^{\bar{1}\kappa\nu}x}$ with $\bar{R}^{(m)}_{n\kappa\nu} = e^{i\eta_{1n\kappa\nu}}$, $\bar{L}^{(m)}_{n\kappa\nu} = e^{i\eta_{\bar{1}n\kappa\nu}}$ and Fermi momenta $q_F^{r\kappa\nu} = \frac{m+1}{2}k_F^{r\kappa\nu} - \frac{m-1}{2}k_F^{\bar{r}\kappa\nu}$ [5]. The superconducting and tunneling term acting on the interior branches around $q_F = 0$ then take the form $H_{\Gamma,n} = i\tilde{\Gamma}\sum_\kappa\int dx\bar{R}^{(m)\dagger}_{n\kappa\bar{\kappa}}\bar{L}^{(m)}_{n\kappa\kappa} + \text{H.c.}$, $H_{\Delta,n} = \tilde{\Delta}\sum_\kappa\int dx\bar{R}^{(m)\dagger}_{n\kappa\bar{\kappa}}\bar{L}^{(m)\dagger}_{n\kappa\kappa} + \text{H.c.}$, from which we recover the non-interacting case by setting $m = 1$. Forgetting about the underlying model and thinking in terms of the new fermions only, one can perform the same steps as in the non-interacting case to show that the modes

$$\begin{aligned}\chi^{(m)}_{Ln1} &= (e^{-i\pi/4}\bar{L}^{(m)}_{n11} + e^{i\pi/4}\bar{L}^{(m)\dagger}_{n11})/\sqrt{2},\\ \chi^{(m)}_{Rn1} &= (e^{-i\pi/4}\bar{R}^{(m)}_{n1\bar{1}} + e^{i\pi/4}\bar{R}^{(m)\dagger}_{n1\bar{1}})/\sqrt{2}\end{aligned} \quad (2.10)$$

commute with the superconducting and tunneling term, and the same is true for their Kramers partners $\chi^{(m)}_{Ln\bar{1}}$, $\chi^{(m)}_{Rn\bar{1}}$. The above solutions satisfy $\chi^{(m)\dagger}_{rn\kappa} = \chi^{(m)}_{rn\kappa}$, which prompts us to identify them as the ψ_m primary fields of the $\mathbb{Z}_{2m}$ parafermion theories describing each DNW. Note that these fields are local in terms of electrons, which makes them particularly convenient to handle.

Similar to the non-interacting case, we introduce dressed interwire couplings for $m > 1$, which now couple the $\bar{R}^{(m)}_{n\kappa\nu}$, $\bar{L}^{(m)}_{n\kappa\nu}$ fields. Assuming that the interwire terms are relevant [see App. 2.A] and repeating the analysis of the integer case for the modes given in Eq. (2.10), we find that the bulk of the system is fully gapped, while there is a Kramers pair of gapless modes propagating along the edges of a finite sample. These modes correspond to ψ_m primary fields

of a $\mathbb{Z}_{2m}$ parafermion theory. However, it is expected [42] that there are indeed two full $\mathbb{Z}_{2m}$ parafermion theories residing at the edges of the system.

2.5 Majorana and parafermion corner states

We now show that in the presence of a weak in-plane magnetic field, the system enters a second-order topological superconducting phase. Let us start from the (non-interacting) Zeeman Hamiltonian

$$H_Z = \Delta_Z \sum_{n,\tau,\sigma,\sigma'} \int dx\, \psi^\dagger_{n\tau\sigma}[\cos(\phi)(\sigma_x)_{\sigma\sigma'} + \sin(\phi)(\sigma_z)_{\sigma\sigma'}]\psi_{n\tau\sigma'}. \tag{2.11}$$

For $m > 1$, momentum-conserving terms are once again constructed by including suitable backscattering processes, such that the dressed term then couples the $\bar{R}^{(m)}_{n\kappa\nu}$, $\bar{L}^{(m)}_{n\kappa\nu}$ fields. In the following, we focus on the regime where the magnetic field strength $\tilde{\Delta}_Z$ is small enough not to modify the bulk structure. However, as time-reversal symmetry is broken, the helical edge modes are gapped out. Assuming that the system size is large such that far away from the corners, all four edges can be treated independently, we calculate the projection of H_Z onto the edge states for all four edges, see App. 2.C. If we label the edges of a rectangular sample by an index $p = 0, ..., 3$ in counterclockwise order starting from the bottom edge, the projection of the Zeeman Hamiltonian onto the edge p is given by

$$\mathcal{H}^{\text{eff},p}_Z = -\tilde{\Delta}_Z \cos(\phi + \varphi_p)\gamma_y, \tag{2.12}$$

where we have defined $\varphi_p = p\pi/2$ and γ_y is a Pauli matrix acting on the low-energy subspace spanned, in this order, by the low-energy edge mode belonging to the time-reversal sector $\kappa = 1$ and its Kramers partner belonging to the sector $\kappa = \bar{1}$. This shows that the mass term changes sign at two corners of the system. Explicitly, the sign change occurs at two diagonally opposite corners of the sample depending on the direction of the magnetic field. For $\phi \in (0, \pi/2) \cup (\pi, 3\pi/2)$ [$\phi \in (\pi/2, \pi) \cup (3\pi/2, 2\pi)$] the sign change occurs at the top-left and bottom-right (top-right and bottom-left) corners. In the spirit of a Jackiw-Rebbi model [73], there are bound states at the corners where the mass term changes sign, which in our case inherit the exotic properties of the propagating modes and thus can be identified as zero-energy $\mathbb{Z}_{2m}$ parafermion corner states. Again, while this result was derived for the local ψ_m fields, we expect that our arguments generalize to the full set of $\mathbb{Z}_{2m}$ primary fields. In the non-interacting limit $m = 1$, we find zero-energy Majorana corner states, which is verified numerically in Fig. 2.2(b).

2.6 Conclusions

We have studied a system consisting of two layers of coupled Rashba nanowires in the presence of interlayer tunneling and proximity-induced superconductivity of a phase difference of π between the layers. We have shown that strong electron-electron interactions can stabilize a helical topological superconducting phase exhibiting Kramers partners of gapless $\mathbb{Z}_{2m}$ parafermion edge modes. Upon turning on a small in-plane magnetic field, the system enters a second-order topological superconducting phase hosting exotic zero-energy parafermion

bound states at two corners of a rectangular sample depending on the direction of the magnetic field.

Our analytical approach is limited to the perturbative regime. However, if the system parameters are increased resulting in non-perturbative gaps, the parafermions will still be present as long as the bulk gap is not closed. Such non-perturbative regimes could be accessed numerically. Thus, our model provides a proof of principle for the existence of helical fractional TSCs and second-order fractional TSCs and we envision it to be a representative of a more general class of systems exhibiting the same parafermionic features.

Acknowledgments. This work was supported by the Swiss National Science Foundation and NCCR QSIT. This project received funding from the European Union's Horizon 2020 research and innovation program (ERC Starting Grant, grant agreement No 757725). We acknowledge helpful discussions with Yanick Volpez.

2.A Dressed interwire terms

In this Appendix, we explicitly write down the dressed interwire terms coupling the gapless parafermion modes found to reside within each DNW (see the main text). Let us start from the non-interacting case $m = 1$. Focusing on the interior branches $\bar{L}_{n\kappa\kappa}$, $\bar{R}_{n\kappa\bar{\kappa}}$ defined in the main text, the interwire term for $t_z = 0$ reads

$$H_\perp = \frac{1}{2}\sum_{n,\kappa}[-i\beta\kappa(\bar{L}^\dagger_{n\kappa\kappa}\bar{R}_{(n+1)\kappa\bar{\kappa}} + \bar{R}^\dagger_{n\kappa\bar{\kappa}}\bar{L}_{(n+1)\kappa\kappa}) + \Delta_c(\bar{L}_{n\kappa\kappa}\bar{R}_{(n+1)\kappa\bar{\kappa}} - \bar{R}_{n\kappa\bar{\kappa}}\bar{L}_{(n+1)\kappa\kappa})] + \text{H.c.} \tag{2.13}$$

From the $m = 1$ case, momentum-conserving terms can be constructed for $m > 1$ by including backscattering processes in a similar way as was discussed for interlayer hopping and superconductivity in the main text. Explicitly, we define the dressed terms as

$$\begin{aligned} H_\perp = \frac{1}{2}\sum_{n,\kappa}[&- i\tilde{\beta}\kappa(\bar{L}^\dagger_{n\kappa\kappa}\bar{R}_{n\kappa\kappa})^k(\bar{L}^\dagger_{n\kappa\kappa}\bar{R}_{(n+1)\kappa\bar{\kappa}})(\bar{L}^\dagger_{(n+1)\kappa\bar{\kappa}}\bar{R}_{(n+1)\kappa\bar{\kappa}})^k \\ &- i\tilde{\beta}\kappa(\bar{R}^\dagger_{n\kappa\bar{\kappa}}\bar{L}_{n\kappa\bar{\kappa}})^k(\bar{R}^\dagger_{n\kappa\bar{\kappa}}\bar{L}_{(n+1)\kappa\kappa})(\bar{R}^\dagger_{(n+1)\kappa\kappa}\bar{L}_{(n+1)\kappa\kappa})^k \\ &+ \tilde{\Delta}_c(\bar{L}_{n\kappa\kappa}\bar{R}^\dagger_{n\kappa\kappa})^k(\bar{L}_{n\kappa\kappa}\bar{R}_{(n+1)\kappa\bar{\kappa}})(\bar{L}^\dagger_{(n+1)\kappa\bar{\kappa}}\bar{R}_{(n+1)\kappa\bar{\kappa}})^k \\ &- \tilde{\Delta}_c(\bar{R}_{n\kappa\bar{\kappa}}\bar{L}^\dagger_{n\kappa\bar{\kappa}})^k(\bar{R}_{n\kappa\bar{\kappa}}\bar{L}_{(n+1)\kappa\kappa})(\bar{R}^\dagger_{(n+1)\kappa\kappa}\bar{L}_{(n+1)\kappa\kappa})^k] + \text{H.c.}, \end{aligned} \tag{2.14}$$

where again $k = (m-1)/2$. As can easily be checked by changing to bosonic fields, the two competing terms in $H_\perp$ have the same structure as the two competing DNW terms introduced in the main text. Therefore, the arguments for the relevance of $H_\perp$ can be directly adapted from the corresponding arguments for H_n. In terms of the composite fermions defined in the main text, the interwire Hamiltonian reads

$$H_\perp = \frac{1}{2}\sum_{n,\kappa}[-i\tilde{\beta}\kappa(\bar{L}^{(m)\dagger}_{n\kappa\kappa}\bar{R}^{(m)}_{(n+1)\kappa\bar{\kappa}} + \bar{R}^{(m)\dagger}_{n\kappa\bar{\kappa}}\bar{L}^{(m)}_{(n+1)\kappa\kappa}) + \tilde{\Delta}_c(\bar{L}^{(m)}_{n\kappa\kappa}\bar{R}^{(m)}_{(n+1)\kappa\bar{\kappa}} - \bar{R}^{(m)}_{n\kappa\bar{\kappa}}\bar{L}^{(m)}_{(n+1)\kappa\kappa})] + \text{H.c.}, \tag{2.15}$$

from where we can repeat the analysis of the non-interacting case.

2.B Edge modes propagating along the z direction

To confirm the existence of helical edge modes propagating along the z direction, we assume that the system is finite along the x direction and infinite along the z direction and apply the standard procedure of matching decaying eigenfunctions. Once all terms in the Hamiltonian are dressed by suitable backscattering processes (see the main text as well as Appendix A), it is convenient to work directly in terms of the composite fermions $\bar{\psi}^{(m)}_{n\kappa\nu}$ for general m. Changing to momentum space along the z axis, we write the problem in terms of the Fourier-transformed fields $\bar{\psi}^{(m)}_{k_z\kappa\nu}$ and linearize the spectrum around the Fermi points [74],

$$\begin{aligned}
\bar{\psi}^{(m)}_{k_z 11}(x) &= \bar{R}^{(m)}_{k_z 11}(x)e^{2ik_{so}x} + \bar{L}^{(m)}_{k_z 11}(x),\\
\bar{\psi}^{(m)}_{k_z 1\bar{1}}(x) &= \bar{R}^{(m)}_{k_z 1\bar{1}}(x) + \bar{L}^{(m)}_{k_z 1\bar{1}}(x)e^{-2ik_{so}x},\\
\bar{\psi}^{(m)}_{k_z \bar{1}1}(x) &= \bar{R}^{(m)}_{k_z \bar{1}1}(x) + \bar{L}^{(m)}_{k_z \bar{1}1}(x)e^{-2ik_{so}x},\\
\bar{\psi}^{(m)}_{k_z \bar{1}\bar{1}}(x) &= \bar{R}^{(m)}_{k_z \bar{1}\bar{1}}(x)e^{2ik_{so}x} + \bar{L}^{(m)}_{k_z \bar{1}\bar{1}}(x).
\end{aligned} \tag{2.16}$$

Here, $\bar{R}^{(m)}_{k_z\kappa\nu}(x)$ $[\bar{L}^{(m)}_{k_z\kappa\nu}(x)]$ are again slowly varying right-moving (left-moving) fields. The total Hamiltonian separates into a part corresponding to the exterior branches and a part corresponding to the interior branches [75] given by

$$\mathcal{H}_{\text{int}} = i\hbar v\kappa_z\nu_z\partial_x + \tilde{\beta}\sin(k_z a_z)\kappa_z\nu_x + \tilde{\Gamma}\kappa_z\nu_y + [\tilde{\Delta} + \cos(k_z a_z)\tilde{\Delta}_c]\kappa_z\eta_y\nu_y \tag{2.17}$$

in the basis $\bar{\Psi}^{(m)}_{\text{int}} = (\bar{L}^{(m)}_{k_z 11}, \bar{R}^{(m)}_{k_z 1\bar{1}}, \bar{L}^{(m)\dagger}_{-k_z 11}, \bar{R}^{(m)\dagger}_{-k_z 1\bar{1}}, \bar{R}^{(m)}_{k_z \bar{1}1}, \bar{L}^{(m)}_{k_z \bar{1}\bar{1}}, \bar{R}^{(m)\dagger}_{-k_z \bar{1}1}, \bar{L}^{(m)\dagger}_{-k_z \bar{1}\bar{1}})$ for the interior branches and

$$\mathcal{H}_{\text{ext}} = -i\hbar v\kappa_z\nu_z\partial_x + [\tilde{\Delta} + \cos(k_z a_z)\tilde{\Delta}_c]\kappa_z\eta_y\nu_y \tag{2.18}$$

in the basis $\bar{\Psi}^{(m)}_{\text{ext}} = (\bar{R}^{(m)}_{k_z 11}, \bar{L}^{(m)}_{k_z 1\bar{1}}, \bar{R}^{(m)\dagger}_{-k_z 11}, \bar{L}^{(m)\dagger}_{-k_z 1\bar{1}}, \bar{L}^{(m)}_{k_z \bar{1}1}, \bar{R}^{(m)}_{k_z \bar{1}\bar{1}}, \bar{L}^{(m)\dagger}_{-k_z \bar{1}1}, \bar{R}^{(m)\dagger}_{-k_z \bar{1}\bar{1}})$ for the exterior branches. Here, κ_i and ν_i for $i \in \{x, y, z\}$ are Pauli matrices, and the two sectors labeled by κ are related by time-reversal symmetry. As in the main text, we focus on the regime $\tilde{\Gamma} \approx \tilde{\Delta}$ and $\tilde{\beta}, \tilde{\Delta}_c \ll \tilde{\Gamma}, \tilde{\Delta}$, and assume that all terms in the Hamiltonian are RG-relevant for all m. For $\tilde{\Delta}, \tilde{\Delta}_c > 0$, we then find Kramers pairs of zero-energy solutions at $k_z a_z = \pi$ which are exponentially localized to the system edges at $x = 0, L$. To demonstrate this, we consider the Hamiltonians

$$\mathcal{H}^{(a_z k_z=\pi)}_{\text{int}} = i\hbar v\kappa_z\nu_z\partial_x + \tilde{\Gamma}\kappa_z\nu_y + (\tilde{\Delta} - \tilde{\Delta}_c)\kappa_z\eta_y\nu_y, \tag{2.19}$$

$$\mathcal{H}^{(a_z k_z=\pi)}_{\text{ext}} = -i\hbar v\kappa_z\nu_z\partial_x + (\tilde{\Delta} - \tilde{\Delta}_c)\kappa_z\eta_y\nu_y, \tag{2.20}$$

and look for exponentially decaying zero-energy eigenfunctions. In particular, we find four solutions corresponding to interior modes,

$$\begin{aligned}
\phi^{\text{int}}_1(x) &= (-i, i, -1, 1, 0, 0, 0, 0)^T e^{-x/\xi_1},\\
\phi^{\text{int}}_2(x) &= (0, 0, 0, 0, -i, i, -1, 1)^T e^{-x/\xi_1},\\
\phi^{\text{int}}_3(x) &= (i, -i, -1, 1, 0, 0, 0, 0)^T e^{-x/\xi'_1},\\
\phi^{\text{int}}_4(x) &= (0, 0, 0, 0, i, -i, -1, 1)^T e^{-x/\xi'_1},
\end{aligned} \tag{2.21}$$

where $\xi_1 = \hbar v/(\tilde{\Gamma} - \tilde{\Delta} + \tilde{\Delta}_c)$ and $\xi_1' = \hbar v/(\tilde{\Gamma} + \tilde{\Delta} - \tilde{\Delta}_c)$. Similarly, we find four solutions corresponding to exterior modes,

$$\begin{aligned}
\phi_1^{\text{ext}}(x) &= (-i, 0, 0, 1, 0, 0, 0, 0)^T e^{-x/\xi_2}, \\
\phi_2^{\text{ext}}(x) &= (0, -i, 1, 0, 0, 0, 0, 0)^T e^{-x/\xi_2}, \\
\phi_3^{\text{ext}}(x) &= (0, 0, 0, 0, -i, 0, 0, 1)^T e^{-x/\xi_2}, \\
\phi_4^{\text{ext}}(x) &= (0, 0, 0, 0, 0, -i, 1, 0)^T e^{-x/\xi_2},
\end{aligned} \tag{2.22}$$

with $\xi_2 = \hbar v/(\tilde{\Delta} - \tilde{\Delta}_c)$. In the regime $\tilde{\Gamma}, \tilde{\Delta} > \tilde{\Delta}_c > 0$, $|\tilde{\Gamma} - \tilde{\Delta}| < \tilde{\Delta}_c$, the above solutions are exponentially localized to the left edge of the system at $x = 0$. By reinstating the oscillating factors $e^{\pm 2ik_{so}x}$ and imposing vanishing boundary conditions $\Phi_{\pm}^{(m)}(x = 0) = 0$, we find that one solution at the left edge of the system is given by

$$\Phi_+^{(m)}(x) = (e^{i\pi/4} f, -e^{i\pi/4} f^*, e^{-i\pi/4} f^*, -e^{-i\pi/4} f, 0, 0, 0, 0)^T, \tag{2.23}$$

where $f(x) = e^{-2ik_{so}x} e^{-x/\xi_2} - e^{-x/\xi_1}$ and where we omitted the normalization factor. Its Kramers partner can be obtained by time-reversal symmetry as $\Phi_-^{(m)} = -\bar{\mathcal{T}}\Phi_+^{(m)}$, and both solutions satisfy $\bar{\mathcal{P}}\Phi_{\pm}^{(m)} = \Phi_{\pm}^{(m)}$. Here, $\bar{\mathcal{T}}$ and $\bar{\mathcal{P}}$ are the representations of time-reversal and particle-hole symmetry in the new basis $\bar{\Psi}^{(m)}$, respectively, which are explicitly given by $\bar{\mathcal{T}} = \kappa_y \eta_z \mathcal{K}$ and $\bar{\mathcal{P}} = \eta_x \mathcal{K}$.

Together with the solutions along the x direction obtained in the main text, we can now combine the results for both semi-infinite geometries to conclude that there is a single pair of counterpropagating Majorana edge modes for a system which is large but finite both along the x and z direction.

2.C Effective edge Hamiltonian

In order to calculate the effective low-energy Hamiltonian describing the gap opened in the spectrum of edge states [see Eq. (11) in the main text], we start by expressing the Zeeman part of the Hamiltonian in terms of the new basis $\bar{\Psi}^{(1)}$ and include suitable backscattering processes for $m > 1$. We obtain the Hamiltonian

$$\mathcal{H}_Z = \tilde{\Delta}_Z[\cos(\phi)\kappa_y\nu_z - \sin(\phi)\kappa_y\nu_x] \tag{2.24}$$

in the basis $\bar{\Psi}^{(m)}$. Again, we assume that this term is relevant in the RG sense for all m. Let us first consider the edges aligned along the x direction. If the system is assumed to be infinite along the x direction, we find two Kramers partners of zero-energy wave functions at $k_x = 0$, which we label as $\Phi_{0,\pm}$ for the bottom edge ($p = 0$) and $\Phi_{2,\pm}$ for the top edge ($p = 2$) of the system in correspondence with the labeling of the edges used in the main text. We note that the DNW Hamiltonian exhibits an additional symmetry corresponding to the operator $\mathcal{O}_1 = \eta_y\nu_z$, which anticommutes with both interlayer tunneling as well as superconductivity. Furthermore, $\mathcal{O}_1$ commutes with the particle-hole symmetry operator $\bar{\mathcal{P}}$. For the edge states $\Phi_{0,+}^{(m)}$ and $\Phi_{0,-}^{(m)} = -\bar{\mathcal{T}}\Phi_{0,+}^{(m)}$, we find $\mathcal{O}_1\Phi_{0,\pm}^{(m)} = -\Phi_{0,\pm}^{(m)}$. We thus arrive at

$$\langle\Phi_{0,+}^{(m)}|\kappa_y\nu_x|\Phi_{0,-}^{(m)}\rangle = \langle\Phi_{0,+}^{(m)}|\mathcal{O}_1\kappa_y\nu_x\mathcal{O}_1|\Phi_{0,-}^{(m)}\rangle = -\langle\Phi_{0,+}^{(m)}|\kappa_y\nu_x|\Phi_{0,-}^{(m)}\rangle, \tag{2.25}$$

and therefore $\langle\Phi_{0,+}^{(m)}|\kappa_y\nu_x|\Phi_{0,-}^{(m)}\rangle = 0$. Here, we used that $\{\mathcal{O}_1, \kappa_y\nu_x\} = 0$. On the other hand, we have

$$\langle\Phi_{0,+}^{(m)}|\kappa_y\nu_z|\Phi_{0,-}^{(m)}\rangle = \langle\Phi_{0,+}^{(m)}|\kappa_y\nu_z(-\kappa_y\eta_z\mathcal{K})(\eta_x\mathcal{K})|\Phi_{0,+}^{(m)}\rangle = -i\langle\Phi_{0,+}^{(m)}|\mathcal{O}_1|\Phi_{0,+}^{(m)}\rangle = i. \tag{2.26}$$

Hence, we find

$$\mathcal{H}_Z^{\text{eff,p=0}} = -\tilde{\Delta}_Z\cos(\phi)\gamma_y, \tag{2.27}$$

where γ_y is a Pauli matrix acting on the low-energy subspace spanned by $\Phi_{0,\pm}^{(m)}$. In order to calculate the effective Hamiltonian for the top edge, we note that our system is invariant under rotation around the y axis by an angle π, which leads to

$$\mathcal{H}_Z^{\text{eff,p=2}} = -\mathcal{H}_Z^{\text{eff,p=0}} = \tilde{\Delta}_Z\cos(\phi)\gamma_y. \tag{2.28}$$

We now treat the edges along the z direction, where we use the properly normalized zero-energy wave functions found in Appendix B and label them as $\Phi_{1,\pm}^{(m)}$ for the right edge and $\Phi_{3,\pm}^{(m)}$ for the left edge. Again, we can use certain symmetries of the system to calculate the above matrix elements. In particular, the operator $\mathcal{O}_2 = \eta_y\nu_x$ anticommutes with the Hamiltonian at $k_z a_z = \pi$. At the same time, we have $[\mathcal{O}_2, \bar{\mathcal{P}}] = 0$. An explicit calculation yields $\mathcal{O}_2\Phi_{3,\pm}^{(m)}(x) = \Phi_{3,\pm}^{(m)}(x)$. Again, we can use the fact that $\{\mathcal{O}_2, \kappa_y\nu_z\} = 0$ to argue that $\langle\Phi_{3,+}^{(m)}|\kappa_y\nu_z|\Phi_{3,-}^{(m)}\rangle = 0$. On the other hand, we find

$$\langle\Phi_{3,+}^{(m)}|\kappa_y\nu_x|\Phi_{3,-}^{(m)}\rangle = \langle\Phi_{3,+}^{(m)}|\kappa_y\nu_x(-\kappa_y\eta_z\mathcal{K})(\eta_x\mathcal{K})|\Phi_{3,+}^{(m)}\rangle = -i\langle\Phi_{3,+}^{(m)}|\mathcal{O}_2|\Phi_{3,+}^{(m)}\rangle = -i. \tag{2.29}$$

Therefore, we arrive at

$$\mathcal{H}_Z^{\text{eff,p=3}} = -\tilde{\Delta}_Z\sin(\phi)\gamma_y. \tag{2.30}$$

Again, the effective Hamiltonian for the right edge can be obtained by exploiting the two-fold rotation symmetry of the system, which gives us

$$\mathcal{H}_Z^{\text{eff,p=1}} = -\mathcal{H}_Z^{\text{eff,p=3}} = \tilde{\Delta}_Z\sin(\phi)\gamma_y. \tag{2.31}$$

Combining the above results, we arrive at the effective Hamiltonian given in Eq. (11) of the main text. Following Ref. [73], we conclude that there exist zero-energy bound states at the corners where the mass term changes sign. Importantly, we note that this argument is independent of any gauge choice. If one would naively multiply an arbitrary phase factor to a solution on a particular edge, the time-reversal relation between the two Kramers partners at this edge changes, while the corresponding relations stay unmodified for all other edges, which would then contradict the idea of the solutions being connected to form a single set of counterpropagating edge modes.

Bibliography

[1] C. L. Kane, R. Mukhopadhyay, and T. C. Lubensky, Phys. Rev. Lett. **88**, 036401 (2002).

[2] J. C. Y. Teo and C. L. Kane, Phys. Rev. B **89**, 085101 (2014).

[3] J. Klinovaja and D. Loss, Eur. Phys. J. B **87**, 171 (2014).

[4] J. Klinovaja and Y. Tserkovnyak, Phys. Rev. B **90**, 115426 (2014).

[5] E. Sagi and Y. Oreg, Phys. Rev. B **90**, 201102(R) (2014).

[6] T. Meng and E. Sela, Phys. Rev. B **90**, 235425 (2014).

[7] T. Neupert, C. Chamon, C. Mudry, and R. Thomale, Phys. Rev. B **90**, 205101 (2014).

[8] J. Klinovaja, Y. Tserkovnyak, and D. Loss, Phys. Rev. B **91**, 085426 (2015).

[9] T. Meng, Phys. Rev. B **92**, 115152 (2015).

[10] E. Sagi and Y. Oreg, Phys. Rev. B **92**, 195137 (2015).

[11] R. A. Santos, C.-W. Huang, Y. Gefen, and D. B. Gutman, Phys. Rev. B **91**, 205141 (2015).

[12] J. Klinovaja, P. Stano, and D. Loss, Phys. Rev. Lett. **116**, 176401 (2016).

[13] S. Sahoo, Z. Zhang, and J. C. Y. Teo, Phys. Rev. B **94**, 165142 (2016).

[14] A. Vaezi, Phys. Rev. X **4**, 031009 (2014).

[15] E. Sagi, A. Haim, E. Berg, F. von Oppen, and Y. Oreg, Phys. Rev. B **96**, 235144 (2017).

[16] T. Meng, T. Neupert, M. Greiter, and R. Thomale, Phys. Rev. B **91**, 241106(R) (2015).

[17] G. Gorohovsky, R. G. Pereira, and E. Sela, Phys. Rev. B **91**, 245139 (2015).

[18] P.-H. Huang, J.-H. Chen, P. R. S. Gomes, T. Neupert, C. Chamon, and C. Mudry, Phys. Rev. B **93**, 205123 (2016).

[19] W. A. Benalcazar, J. C. Y. Teo, and T. L. Hughes, Phys. Rev. B **89**, 224503 (2014).

[20] W. A. Benalcazar, B. A. Bernevig, and T. L. Hughes, Science **357**, 61 (2017).

[21] W. A. Benalcazar, B. A. Bernevig, and T. L. Hughes, Phys. Rev. B **96**, 245115 (2017).

[22] Z. Song, Z. Fang, and C. Fang, Phys. Rev. Lett. **119**, 246402 (2017).

[23] Y. Peng, Y. Bao, and F. von Oppen, Phys. Rev. B **95**, 235143 (2017).

[24] S. Imhof, C. Berger, F. Bayer, H. Brehm, L. Molenkamp, T. Kiessling, F. Schindler, C. H. Lee, M. Greiter, T. Neupert, and R. Thomale, Nature Physics **14**, 925 (2018).

[25] M. Geier, L. Trifunovic, M. Hoskam, and P. W. Brouwer, Phys. Rev. B **97**, 205135 (2018).

[26] F. Schindler, A. M. Cook, M. G. Verginory, Z. Wang, S. S. P. Parking, B. A. Bernevig, and T. Neupert, Science Adv. **4**, 6 (2018).

[27] C.-H. Hsu, P. Stano, J. Klinovaja, and D. Loss, Phys. Rev. Lett. **121**, 196801 (2018).

[28] M. Ezawa, Scientific Reports **9**, 5286 (2019).

[29] M. Ezawa, Phys. Rev. Lett. **121**, 116801 (2018).

[30] X. Zhu, Phys. Rev. B **97**, 205134 (2018).

[31] Q. Wang, C.-C. Liu, Y.-M. Lu, and F. Zhang, Phys. Rev. Lett. **121**, 186801 (2018).

[32] Z. Yan, F. Song, and Z. Wang, Phys. Rev. Lett. **121**, 096803 (2018).

[33] T. Liu, J. J. He, and F. Nori, Phys. Rev. B **98**, 245413 (2018).

[34] X. Zhang, H.-X. Wang, Z.-K. Lin, Y. Tian, B. Xie, M.-H. Lu, Y.-F. Chen, and J.-H. Jiang, Nat. Phys. **15**, 582 (2019).

[35] Q. Wang, D. Wang, and Q.-H. Wang, EPL **124**, 50005 (2018).

[36] Y. Volpez, D. Loss, and J. Klinovaja, Phys. Rev. Lett. **122**, 126402 (2019).

[37] A. Agarwala, V. Juricic, and B. Roy, arXiv:1902.00507.

[38] D. Calugaru, V. Juricic, and B. Roy, Phys. Rev. B **99**, 041301(R) (2019).

[39] M. Kheirkhah, Y. Nagai, C. Chen, and F. Marsiglio, arXiv:1904.00990.

[40] Y. You, D. Litinski, and F. von Oppen, Phys. Rev. B **100**, 054513 (2019).

[41] Y. You, T. Devakul, F. J. Burnell, and T. Neupert, Phys. Rev. B **98**, 235102 (2018).

[42] R. S. K. Mong, D. J. Clarke, J. Alicea, N. H. Lindner, P. Fendley, C. Nayak, Y. Oreg, A. Stern, E. Berg, K. Shtengel, and M. P. A. Fisher, Phys. Rev. X **4**, 011036 (2014).

[43] N. H. Lindner, E. Berg, G. Refael, and A. Stern, Phys. Rev. X **2**, 041002 (2012).

[44] D. J. Clarke, J. Alicea, and K. Shtengel, Nat. Commun. **4**, 1348 (2013).

[45] M. Cheng, Phys. Rev. B **86**, 195126 (2012).

[46] J. Klinovaja, A. Yacoby, and D. Loss, Phys. Rev. B **90**, 155447 (2014).

[47] C. P. Orth, R. P. Tiwari, T. Meng, and T. L. Schmidt, Phys. Rev. B **91**, 081406(R) (2015).

[48] J. Klinovaja and D. Loss, Phys. Rev. B **92**, 121410(R) (2015).

[49] C. Fleckenstein, N. T. Ziani, and B. Trauzettel, Phys. Rev. Lett. **122**, 066801 (2019).

[50] Y. Oreg, E. Sela, and A. Stern, Phys. Rev. B **89**, 115402 (2014).

[51] J. Klinovaja and D. Loss, Phys. Rev. Lett. **112**, 246403 (2014).

[52] J. Klinovaja and D. Loss, Phys. Rev. B **90**, 045118 (2014).

[53] C. J. Pedder, T. Meng, R. P. Tiwari, and T. L. Schmidt, arXiv:1507.08881.

[54] M. Thakurathi, D. Loss, and J. Klinovaja, Phys. Rev. B **95**, 155407 (2017).

[55] F. Iemini, C. Mora, and L. Mazza, Phys. Rev. Lett. **118**, 170402 (2017).

[56] A. Calzona, T. Meng, M. Sassetti, and T. L. Schmidt, Phys. Rev. B **98**, 201110(R) (2018).

[57] L. Mazza, F. Iemini, M. Dalmonte, and C. Mora, Phys. Rev. B **98**, 201109(R) (2018).

[58] H. Ren, F. Pientka, S. Hart, A. T. Pierce, M. Kosowsky, L. Lunczer, R. Schlereth, B. Scharf, E. M. Hankiewicz, L. W. Molenkamp, B. I. Halperin, and A. Yacoby, Nature (London) **569**, 93 (2019).

[59] A. Fornieri, A. M. Whiticar, F. Setiawan, E. Portolés, A. C. C. Drachmann, A. Keselman, S. Gronin, C. Thomas, T. Wang, R. Kallaher, G. C. Gardner, E. Berg, M. J. Manfra, A. Stern, C. M. Marcus, and F. Nichele, Nature (London) **569**, 89 (2019).

[60] C. Schrade, A. A. Zyuzin, J. Klinovaja, and D. Loss, Phys. Rev. Lett. **115**, 237001 (2015).

[61] A. I. Buzdin, L. N. Bulaevskii, and S. V. Panyukov, Pis'ma Zh. Eksp. Teor. Fiz. **35**, 147 (1982) [JETP Lett. **35**, 178 (1982)].

[62] V. V. Ryazanov, V. A. Oboznov, A. Yu. Rusanov, A. V. Veretennikov, A. A. Golubov, and J. Aarts, Phys. Rev. Lett. **86**, 2427 (2001).

[63] B. I. Spivak and S. A. Kivelson, Phys. Rev. B **43**, 3740 (1991).

[64] J. A. van Dam, Y. V. Nazarov, E. P. A. M. Bakkers, and L. P. Kouwenhoven, Nature (London) **442**, 667 (2006).

[65] S. Ryu, A. P. Schnyder, A. Furusaki, and A. W. W. Ludwig, New J. Phys. **12**, 065010 (2010).

[66] J. Klinovaja and D. Loss, Phys. Rev. B **86**, 085408 (2012).

[67] A. Y. Kitaev, Phys.-Usp. **44**, 131 (2001).

[68] J. Klinovaja and D. Loss, Phys. Rev. Lett. **111**, 196401 (2013).

[69] T. Giamarchi, Quantum Physics in One Dimension (Oxford University Press, Oxford, 2004).

[70] D. Boyanovsky, J. Phys. A: Math. Gen. **22**, 2601 (1989).

[71] P. Lecheminant, A. O. Gogolin, and A. A. Nersesyan, Nucl. Phys. B **639**, 502 (2002).

[72] A. B. Zamolodchikov and V. A. Fateev, Zh. Eksp. Teor. Fiz. **89**, 380 (1985).

[73] R. Jackiw and C. Rebbi, Phys. Rev. D **13**, 3398 (1976).

[74] B. Braunecker, G. I. Japaridze, J. Klinovaja, and D. Loss, Phys. Rev. B **82**, 045127 (2010).

[75] J. Klinovaja, P. Stano, and D. Loss, Phys. Rev. Lett. **109**, 236801 (2012).

Chapter 3

Majorana and parafermion corner states from two coupled sheets of bilayer graphene

Adapted from:
K. Laubscher, D. Loss, and J. Klinovaja,
"Majorana and parafermion corner states from two coupled sheets of bilayer graphene",
Phys. Rev. Research **2**, 013330 (2020)

We consider a setup consisting of two coupled sheets of bilayer graphene in the regime of strong spin-orbit interaction, where electrostatic confinement is used to create an array of effective quantum wires. We show that for suitable interwire couplings the system supports a topological insulator phase exhibiting Kramers partners of gapless helical edge states, while the additional presence of a small in-plane magnetic field and weak proximity-induced superconductivity leads to the emergence of zero-energy Majorana corner states at all four corners of a rectangular sample, indicating the transition to a second-order topological superconducting phase. The presence of strong electron-electron interactions is shown to promote the above phases to their exotic fractional counterparts. In particular, we find that the system supports a fractional topological insulator phase exhibiting fractionally charged gapless edge states and a fractional second-order topological superconducting phase exhibiting zero-energy $\mathbb{Z}_{2m}$ parafermion corner states, where m is an odd integer determined by the position of the chemical potential.

3.1 Introduction

Over the last few decades, topological phases of quantum matter have been the subject of extensive studies, both in theory and in experiments. In particular, a lot of work has been dedicated to the description and classification of topological insulators (TIs) and topological superconductors (TSCs) in various spatial dimensions [1–3]. Recently, the generalization of conventional TIs and TSCs to *higher-order* TIs and TSCs has attracted strong interest [4–31]. While conventional d-dimensional TIs and TSCs exhibit gapless edge states at their $(d-1)$-dimensional boundaries, nth-order d-dimensional TIs or TSCs exhibit gapless edge states at their $(d-n)$-dimensional boundaries.

In the search for suitable platforms to realize topologically non-trivial physics, graphene and graphene-based systems [32, 33] such as carbon nanotubes and bilayer graphene (BLG) have attracted particular attention. While the unusual low-energy properties of these systems make them interesting in their own right, they also have been proposed to support topologically non-trivial phases of matter, hosting, e.g., gapless edge states or localized Majorana zero modes [34–43]. Unfortunately, most of these proposals require strong spin-orbit interaction (SOI) as a crucial ingredient, whereas SOI is weak in standard graphene [44]. In the last few years, however, considerable experimental progress in creating van der Waals heterostructures has made it possible to induce strong SOI in graphene by proximity to transition metal dichalcogenides (TMDs) [45–56], which has led to renewed interest in graphene-based systems as promising candidates to realize topologically non-trivial phases in the laboratory. These considerations, together with the recent interest in higher-order topological phases of matter, have prompted us to devise a graphene-based system realizing second-order topological superconducting phases. In particular, we consider an array of coupled quantum wires arising in bilayer graphene due to electrostatic confinement [57–61], see Fig. 3.1. The combined effects of competing interwire hopping terms, an in-plane magnetic field, and proximity-induced superconductivity lead to the formation of zero-energy corner states at all four corners of a rectangular sample. In the non-interacting case, these corner states are Majorana bound states. The major benefit of studying an array of coupled wires, however, is the additional possibility of including the effects of strong electron-electron interactions in an analytically tractable way [62–73]. Using bosonization techniques, we show that suitable interactions can drive the system into a fractional phase exhibiting zero-energy $\mathbb{Z}_{2m}$ parafermion corner states for an odd integer m, placing our model in the class of fractional second-order TSCs.

This paper is organized as follows. In Sec. 3.2, we describe a model for our setup, which consists of an array of coupled wires arising in bilayer graphene due to electrostatic confinement. In Sec. 3.3.1, we show that this system is a topological insulator for a certain range of parameters. Section 3.3.2 extends this result to the interacting case, showing that the system supports fractionally charged edge states for suitable values of chemical potential and sufficiently strong electron-electron interactions. In Sec. 3.4.1, we then include suitable superconducting and magnetic perturbations to gap out the helical edge states found previously and show that, in the non-interacting case, the system is driven into a second-order topological superconducting phase with Majorana corner states at all four corners of a rectangular sample. In Sec. 3.4.2, we again extend our analysis to the interacting case and show that the system can be driven into a phase hosting exotic $\mathbb{Z}_{2m}$ parafermion corner states, where m is an odd integer depending on the chemical potential. We summarize our results in Sec. 3.5.

3.2 Model

We consider a system consisting of two coupled sheets of AB-stacked bilayer graphene as shown in Fig. 3.1. Each layer of graphene is a honeycomb lattice consisting of two non-equivalent atoms A and B coupled by a hopping element t. Each sheet of bilayer graphene is then composed of two layers of graphene coupled by a hopping amplitude $t_\perp$ between the A atoms of the first layer and the B atoms of the second layer. The effective Hamiltonian for a single sheet of BLG in momentum space is then given by

$$\mathcal{H}_{\text{BLG}} = \hbar v_F(\lambda_z\gamma_x k_x + \gamma_y k_y) + \frac{t_\perp}{2}(\gamma_x\eta_x + \gamma_y\eta_y) - V\eta_z, \tag{3.1}$$

where λ_i, γ_i, and η_i for $i \in \{x, y, z\}$ are Pauli matrices acting in valley, sublattice, and layer space, respectively, v_F is the Fermi velocity for electrons in graphene, and the term

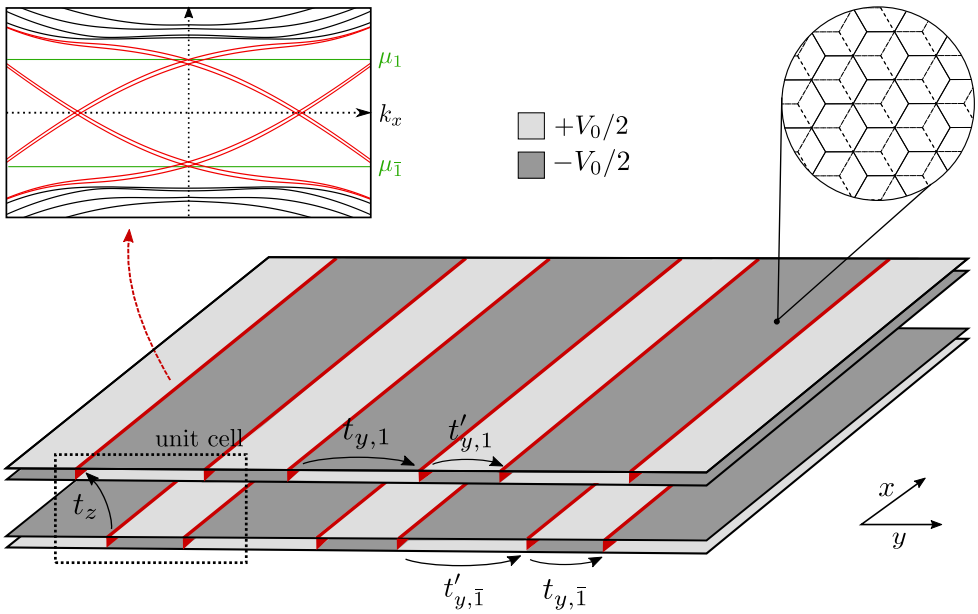

Figure 3.1: The model consists of two coupled sheets of AB-stacked bilayer graphene subject to electrostatic confinement, such that effective 1D wires arise at domain walls between gates set to opposite voltages $\pm V_0/2$. The upper left panel shows the spectrum of an effective wire localized at one of the domain walls with the in-gap states highlighted in red. Note that due to SOI each of the bands is split into two shifted copies. The light green lines labeled μ_1 and $\mu_{\bar{1}}$ indicate the values of chemical potential that will be of interest in the remainder of this paper. We now consider an array of such effective wires, where a unit cell is defined as consisting of four wires, see the dashed box. The wires are weakly coupled via a layer-conserving hopping term between neighboring wires within the same unit cell (between neighboring wires belonging to different unit cells) of strength $t_{y,\tau}$ ($t'_{y,\tau}$), as well as via an inter-bilayer hopping term of strength t_z. Note that in order to introduce a hierarchy of interwire terms, the wires are arranged in an armchair-like order. In particular, the setup shown here leads to $t_{y,1} \approx t'_{y,\bar{1}} < t_z < t'_{y,1} \approx t_{y,\bar{1}}$, as the strength of the hopping terms naturally decreases with the separation of the wires.

proportional to V describes a potential difference between the two graphene layers. Within each sheet of BLG, electrostatic confinement arising from a spatial modulation of V can then be used to form effective 1D wires. In particular, we consider creating one-dimensional domain walls between gates set to opposite voltages $\pm V_0/2$. This leads to propagating one-dimensional states localized around the region where the voltage changes sign [57]. In the following, consider an array of such effective wires, where the wires are arranged in an armchair-like order as shown in Fig. 3.1. For later convenience, we define a unit cell as consisting of four wires (two belonging to the upper layer, and two belonging to the lower layer). As such, each wire can be labeled by a unit cell index n as well as two indices (ν, τ), where $\nu \in \{1, \bar{1}\}$ denotes the position within the unit cell and $\tau \in \{1, \bar{1}\}$ denotes the layer.

The case of a single effective wire without SOI [57] as well as in the presence of curvature-induced SOI [61] has been thoroughly analyzed in previous works. However, even though the curvature-induced SOI is considerably larger than the intrinsic SOI of standard graphene, it is still relatively small [74–81]. In order to access a regime with stronger SOI and avoid the need for curvature, we consider a van der Waals heterostructure combining layers of graphene and a TMD [45–56]. In this case, the proximity-induced SOI is of the form $\mathcal{H}_{so} = \alpha\lambda_z\sigma_z + \alpha_R(\lambda_z\gamma_x\sigma_y - \gamma_y\sigma_x)$, where σ_i for $i \in \{x, y, z\}$ is a Pauli matrix acting in spin space [47,50]. While the predicted values for α and α_R vary across the literature and depend on the specific TMD that is used, we find that in our case, the Rashba-like term proportional to α_R is suppressed by strong interlayer tunneling $t_\perp$, which is why we focus on the term proportional to α.[1]

In the following, we consider a step function potential of strength $V_0/2$, where, without loss of generality, we assume $V_0 > 0$ and focus on the case where the direction of confinement is along the armchair direction of the graphene lattice. Adapting the results of Refs. [57, 61] to our setup to include the SOI, we find that the bulk gap of the spectrum is given by V_0, while there are eight in-gap modes per effective wire, see the spectrum shown in Fig. 3.1. Explicitly, the energies of the in-gap modes for wire ν in the layer τ are given by

$$E_{\lambda\kappa\nu\tau\sigma} = -\kappa\tau\left[\frac{\hbar v_F\lambda k_x}{2\sqrt{t_\perp}} - \kappa\nu\sqrt{\frac{(\hbar v_F k_x)^2}{4t_\perp} + \frac{V_0}{2\sqrt{2}}}\right]^2 + \kappa\tau\frac{V_0}{\sqrt{2}} + \alpha\lambda\tau\sigma - \mu_\tau. \tag{3.2}$$

Here, $\lambda \in \{1, \bar{1}\}$ is the valley index, $\sigma \in \{1, \bar{1}\}$ is the spin projection onto the z axis that is determined by the SOI of strength α (which we take to be of equal magnitude but of opposite sign for the two sheets of BLG), and $\kappa \in \{1, \bar{1}\}$ is an additional subband index. For now, we tune the chemical potential in layer τ to $\mu_\tau = \tau[V_0/(2\sqrt{2}) + \alpha]$, while an alternative choice is described in Appendix 3.A. Note that for these values of chemical potential, the sector $\kappa = 1$ ($\kappa = \bar{1}$) corresponds to modes with small Fermi momenta close to $k_x = 0$ (large Fermi momenta far away from $k_x = 0$). As an additional simplification, we note that for $\alpha \ll V_0$, the above energy spectrum is approximately linear for small k_x (i.e., in the sector $\kappa = 1$) such that

$$E_{\lambda 1\nu\tau\sigma} \approx \lambda\nu\tau\hbar v_F\sqrt{\frac{V_0}{2\sqrt{2}t_\perp}}\,k_x + \alpha\tau(\lambda\sigma - 1). \tag{3.3}$$

[1] Note that we did not include the intrinsic Kane-Mele SOI as well as a staggered sublattice potential term which is in principle allowed by symmetry, as those terms have been predicted to be orders of magnitude smaller than the SOI induced by proximity to the TMD layers [44, 48, 50].

To proceed, we work in the regime of strong spin-orbit interaction, which allows us to linearize the spectrum of each channel around the respective Fermi point. The electron operator for the nth unit cell can then be represented as $\Psi_n = \sum_{\kappa,\nu,\tau,\sigma}(R_{n\kappa\nu\tau\sigma}e^{ik_F^{(\nu\tau)\kappa\nu\tau\sigma}x} + L_{n\kappa\nu\tau\sigma}e^{ik_F^{(\bar{\nu}\tau)\kappa\nu\tau\sigma}x})$, where $R_{n\kappa\nu\tau\sigma}(x)$ [$L_{n\kappa\nu\tau\sigma}(x)$] are slowly right-moving [left-moving] fields and $k_F^{\lambda\kappa\nu\tau\sigma}$ are the respective Fermi momenta. Note that here and in the following we implicitly assume the presence of weak but finite intervalley scattering, which is why we do no longer consider the valley degree of freedom to be a good quantum number but treat modes differing only in their valley index as right and left moving modes of the same species. The effective Hamiltonian describing the uncoupled wires can be written as

$$H_0 = -i\hbar \sum_{n,\kappa,\nu,\tau,\sigma} \int dx\, v_\kappa (R^\dagger_{n\kappa\nu\tau\sigma}\partial_x R_{n\kappa\nu\tau\sigma} - L^\dagger_{n\kappa\nu\tau\sigma}\partial_x L_{n\kappa\nu\tau\sigma}), \tag{3.4}$$

where we have made use of the fact that the Fermi velocities of the different branches for a fixed κ are approximately the same given that $\alpha \ll V_0$. Explicitly, we note from Eq. (3.3) that, for the values of chemical potential of interest to us, we approximately have $v_1 = v_F\sqrt{V_0/(2\sqrt{2}t_\perp)}$.

We will now couple neighboring wires in various ways. Neglecting all fast oscillating terms, we consider the interwire Hamiltonian $H_\perp = H_y + H'_y + H_z$, where

$$H_y = \sum_{n,\nu,\tau} t_{y,\tau} \int dx\, R^\dagger_{n1\nu\tau(\nu\tau)} L_{n1\bar{\nu}\tau(\nu\tau)} + \text{H.c.}, \tag{3.5}$$

$$H'_y = \sum_{n,\tau} t'_{y,\tau} \int dx\, [R^\dagger_{(n+1)11\tau\tau} L_{n1\bar{1}\tau\tau} + L^\dagger_{(n+1)11\tau\bar{\tau}} R_{n1\bar{1}\tau\bar{\tau}}] + \text{H.c.}, \tag{3.6}$$

$$H_z = \sum_{n,\kappa,\nu,\tau,\sigma} t_z \int dx\, R^\dagger_{n\kappa\nu\tau\sigma} L_{n\kappa\nu\bar{\tau}\sigma} + \text{H.c.}, \tag{3.7}$$

with $0 \leq t_{y,\tau}, t'_{y,\tau}, t_z \ll \alpha$. Here, $t_{y,\tau}$ ($t'_{y,\tau}$) is a spin-conserving intralayer hopping element between neighboring wires within the same unit cell (between neighboring wires belonging to different unit cells) and t_z is a spin-conserving hopping element between neighboring wires belonging to different layers. The strength of these hopping amplitudes can be controlled by varying the interwire distance as well as the strength and the shape of the confinement potential.

Furthermore, if a superconducting TMD such as $NbSe_2$ is used, superconductivity will be induced in the graphene bilayers [53]. The corresponding effective Hamiltonian then reads

$$H_{sc} = \Delta_{sc} \sum_{n,\kappa,\nu,\tau,\sigma} \sigma \int dx\, R^\dagger_{n\kappa\nu\tau\sigma} L^\dagger_{n\kappa\nu\tau\bar{\sigma}} + \text{H.c.} \tag{3.8}$$

Additionally, we consider the effect of an in-plane Zeeman field along the x direction. Combined with intervalley scattering, which we assume to be present in the system with broken translational invariance, this term takes the form

$$H_Z = \Delta_Z \sum_{n,\nu,\tau} \int dx\, R^\dagger_{n1\nu\tau(\nu\tau)} L_{n1\nu\tau(\bar{\nu}\tau)} + \text{H.c.} \tag{3.9}$$

Finally, the total Hamiltonian is defined as $H = H_0 + H_\perp + H_Z + H_{sc}$. In the remainder of this paper, we will focus on the regime $\Delta_{sc}, \Delta_Z \ll t_{y,\tau}, t'_{y,\tau}, t_z$ such that the superconducting and Zeeman term can be treated as weak perturbations to the interwire terms. Numerically, however, our analysis can be extended to the non-perturbative regime, confirming that the found topological properties persist as long as the bulk gap is not closed.

3.3 Topological insulator phase

3.3.1 Non-interacting case

In this section, we demonstrate that our model supports a TI phase with Kramers partners of gapless edge states propagating along the edges of a large but finite sample. For this, we set $\Delta_Z = \Delta_{sc} = 0$. As can immediately be verified from Eqs. (3.5)-(3.7), the branches with $\kappa = \bar{1}$ are trivially gapped by interlayer hopping. As such, we focus on the sector $\kappa = 1$ in the following. For this sector, we find that the branches $R_{n1\nu\tau(\nu\bar{\tau})}$ and $L_{n1\nu\tau(\nu\tau)}$ are trivially gapped by interlayer hopping, whereas the different hopping processes compete for the branches $R_{n1\nu\tau(\nu\tau)}$ and $L_{n1\nu\tau(\nu\bar{\tau})}$, see Fig. 3.2. In the following, we are interested in the regime $t_{y,1} \approx t'_{y,\bar{1}} < t_z < t'_{y,1} \approx t_{y,\bar{1}}$. Such a hierarchy is natural for an armchair-like arrangement of the effective wires as shown in Fig. 3.1, as the strength of the hopping terms can be expected to decrease with the separation of the wires. For simplicity, let us assume that $t_{y,1} = t'_{y,\bar{1}} = 0$ and $t'_{y,1} = t_{y,\bar{1}}$. By direct inspection of Eqs. (3.5)-(3.7), we find that the bulk of the system is fully gapped.

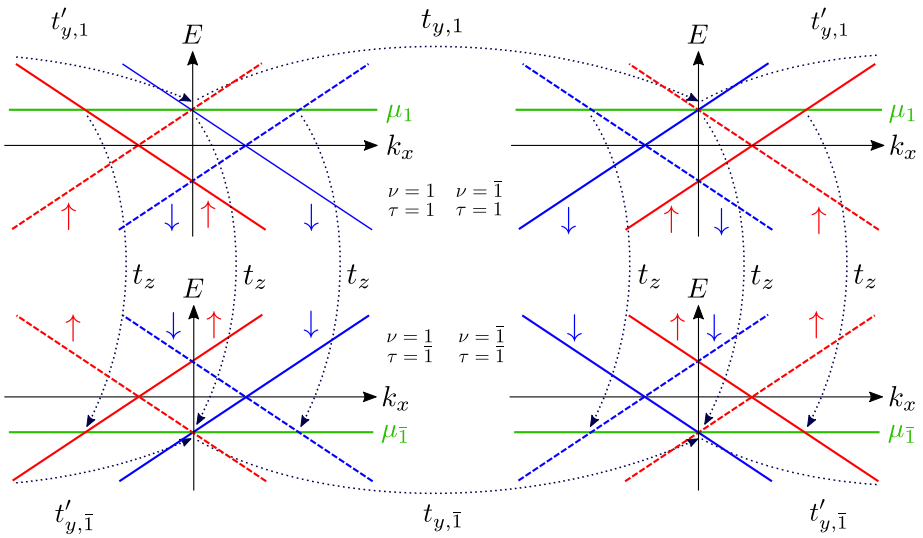

Figure 3.2: The spectrum of a single unit cell in the non-interacting case, where the chemical potential in layer τ is tuned to $\mu_\tau = \tau[V_0/(2\sqrt{2}) + \alpha]$. For simplicity, only the sector $\kappa = 1$ is shown. The branches $R_{n1\nu\tau(\nu\bar{\tau})}$ and $L_{n1\nu\tau(\nu\tau)}$ are trivially gapped by interlayer hopping of strength t_z. For the branches $R_{n1\nu\tau(\nu\tau)}$ and $L_{n1\nu\tau(\nu\bar{\tau})}$, on the other hand, the interlayer hopping term competes with intracell hopping of strength $t_{y,\tau}$ and intercell hopping of strength $t'_{y,\tau}$.

In order to find edge states in a system that is finite along the y direction and consists of N unit cells, we note that the parameter regime of our interest is in the same part of the topological phase diagram as the regime $t_z \ll t'_{y,1}$, see Appendix 3.B. In this limit, we find that the two modes R_{11111} and $L_{1111\bar{1}}$ ($R_{N1\bar{1}1\bar{1}}$ and $L_{N1\bar{1}11}$) at the left (right) edge of the system stay gapless. The presence of these helical edge states is not affected by deviations from the above fine-tuned point as long as the bulk gap does not close.

Let us now assume that the system is finite along the x direction and infinite along the y direction. We apply the standard procedure of matching decaying eigenfunctions to find edge states propagating along the y direction [82]. The projection of the Hamiltonian $H = H_0 + H_\perp$ onto the sector $\kappa = 1$ can then be written in momentum space as $H = \sum_{k_y} \int dx\, \Psi^\dagger_{k_y} \mathcal{H}(k_y) \Psi_{k_y}$, with the Hamiltonian density $\mathcal{H}(k_y)$ given by

$$\begin{aligned}\mathcal{H}(k_y) = &-i\hbar v_1 \partial_x \rho_z + t_z \tau_x \rho_x + \{[t_{y,1} + t'_{y,1}\cos(k_y a_y)](1+\tau_z) \\ &+ [t_{y,\bar{1}} + t'_{y,\bar{1}}\cos(k_y a_y)](1-\tau_z)\}(\nu_x \rho_x - \nu_y \tau_z \sigma_z \rho_y)/4 \\ &- [t'_{y,1}\sin(k_y a_y)(1+\tau_z) + t'_{y,\bar{1}}\sin(k_y a_y)(1-\tau_z)](\nu_y \rho_x + \nu_x \tau_z \sigma_z \rho_y)/4\end{aligned} \tag{3.10}$$

in the basis $\Psi_{k_y} = (R_{k_y 1111},\ L_{k_y 1111},\ R_{k_y 111\bar{1}},\ L_{k_y 111\bar{1}},\ R_{k_y 11\bar{1}1},\ L_{k_y 11\bar{1}1},\ R_{k_y 11\bar{1}\bar{1}},\ L_{k_y 11\bar{1}\bar{1}},\ R_{k_y 1\bar{1}11},\ L_{k_y 1\bar{1}11},\ R_{k_y 1\bar{1}1\bar{1}},\ L_{k_y 1\bar{1}1\bar{1}},\ R_{k_y 1\bar{1}\bar{1}1},\ L_{k_y 1\bar{1}\bar{1}1},\ R_{k_y 1\bar{1}\bar{1}\bar{1}},\ L_{k_y 1\bar{1}\bar{1}\bar{1}})$. Here, ν_i, τ_i, σ_i, and ρ_i for $i \in \{x, y, z\}$ are Pauli matrices acting in wire, layer, spin, and right/left mover space, respectively, and a_y is the size of a unit cell in the y direction. Next, we focus on $k_y = 0$ and a single edge of the system at $x = 0$. In order to satisfy vanishing boundary conditions, we require $R_{k_y 1\nu\tau\sigma}(0) = -L_{k_y 1\nu\tau\sigma}(0)$. From this condition, we find that, given $t_{y,\bar{1}} > t_z$, there are two exponentially decaying solutions localized to the edge of the system. These are given by

$$\begin{aligned}\Phi_+ &= (-a, b, 0, 0, ib, -ia, 0, 0, -ib, ia, 0, 0, a, -b, 0, 0)^T, \\ \Phi_- &= (0, 0, b, -a, 0, 0, ia, -ib, 0, 0, -ia, ib, 0, 0, -b, a)^T,\end{aligned} \tag{3.11}$$

in the basis of $\Psi_{k_y=0}$. Here we defined $a = e^{-x/\xi_1}$ and $b = e^{-x/\xi_2}$ with $\xi_1 = \hbar v_1/(t_{y,\bar{1}} - t_z)$ and $\xi_2 = \hbar v_1/t_z$. It is straightforward to verify that these edge states are Kramers partners and related by time-reversal via $\Phi_- = -i\sigma_y \rho_x \mathcal{K} \Phi_+$, where $\mathcal{K}$ denotes the complex conjugation.

Putting together all of the above results, we conclude that our system is in a topological insulator phase with a Kramers pair of gapless edge states running along the edges of a large but finite sample.

3.3.2 Interacting case

Let us now address the construction of the fractional counterpart of the above phase. For this, we tune the chemical potential in layer τ to $\mu_\tau = \tau[V_0/(2\sqrt{2}) + \alpha/m]$, where m is an odd integer and $m = 1$ reproduces the non-interacting case discussed above. Again, the interlayer hopping term given in Eq. (3.7) trivially gaps out the sector $\kappa = \bar{1}$ corresponding to large Fermi momenta. Therefore, we again focus on the sector $\kappa = 1$.

As a first step, we note that for $m > 1$ the hopping processes between neighboring wires belonging to the same layer [see Eqs. (3.5) and (3.6)] no longer conserve momentum. However, momentum-conserving terms can be constructed by including single-electron backscattering

processes arising from strong electron-electron interactions, see Fig. 3.3 for a graphical illustration in the case $m = 3$. Explicitly, the dressed interwire terms are given by

$$H_y^{(m)} = \sum_{n,\nu,\tau} t_{y,\tau}^{(m)} \int dx \, (R^\dagger_{n1\nu\tau(\nu\tau)} L_{n1\nu\tau(\nu\tau)})^k R^\dagger_{n1\nu\tau(\nu\tau)} L_{n1\bar{\nu}\tau(\nu\tau)} (R^\dagger_{n1\bar{\nu}\tau(\nu\tau)} L_{n1\bar{\nu}\tau(\nu\tau)})^k + \text{H.c.}, \tag{3.12}$$

$$H_y'^{(m)} = \sum_{n,\tau} t_{y,\tau}'^{(m)} \int dx \Big[(R^\dagger_{(n+1)11\tau\tau} L_{(n+1)11\tau\tau})^k R^\dagger_{(n+1)11\tau\tau} L_{n1\bar{1}\tau\tau} (R^\dagger_{n1\bar{1}\tau\tau} L_{n1\bar{1}\tau\tau})^k + (L^\dagger_{(n+1)11\tau\bar{\tau}} R_{(n+1)11\tau\bar{\tau}})^k L^\dagger_{(n+1)11\tau\bar{\tau}} R_{n1\bar{1}\tau\bar{\tau}} (L^\dagger_{n1\bar{1}\tau\bar{\tau}} R_{n1\bar{1}\tau\bar{\tau}})^k \Big] + \text{H.c.} \tag{3.13}$$

with $k = (m-1)/2$. Here, $t_{y,\tau}^{(m)} \propto t_{y,\tau} g_B^{m-1}$ and $t_{y,\tau}'^{(m)} \propto t'_{y,\tau} g_B^{m-1}$, where g_B is the amplitude of a single-electron backscattering process. In the following, let us assume that the above terms flow to strong coupling in a renormalization group (RG) sense. This can always be achieved if their bare coupling constants are sufficiently large or if their scaling dimensions are the lowest ones among all possible competing terms. The original interlayer hopping term given in Eq. (3.7) does not commute with the above terms and therefore cannot order simultaneously. Instead, the interlayer term that commutes with the above terms is, to lowest order, given by the dressed term

$$H_z^{(m)} = \sum_{n,\nu,\tau,\sigma} t_z^{(m)} \int dx \, (R^\dagger_{n1\nu\tau\sigma} L_{n1\nu\tau\sigma})^{\frac{m-1}{2}} R^\dagger_{n1\nu\tau\sigma} L_{n1\nu\bar{\tau}\sigma} (R^\dagger_{n1\nu\bar{\tau}\sigma} L_{n1\nu\bar{\tau}\sigma})^{\frac{m-1}{2}} + \text{H.c.}, \tag{3.14}$$

where again $t_z^{(m)} \propto t_z g_B^{m-1}$. Following the same arguments as above, we assume that this term flows to strong coupling. The total interwire Hamiltonian in the interacting case is now defined as $H_\perp^{(m)} = H_y^{(m)} + H_y'^{(m)} + H_z^{(m)}$.

In order to facilitate the analytical description of the interacting system, we introduce bosonic fields $\phi_{1n1\nu\tau\sigma}(x)$ and $\phi_{\bar{1}n1\nu\tau\sigma}(x)$ defined via $R_{n1\nu\tau\sigma}(x) = e^{i\phi_{1n1\nu\tau\sigma}(x)}$ and $L_{n1\nu\tau\sigma}(x) = e^{i\phi_{\bar{1}n1\nu\tau\sigma}(x)}$. The fields $\phi_{rn1\nu\tau\sigma}(x)$ satisfy the non-local commutation relation $[\phi_{rn1\nu\tau\sigma}(x), \phi_{r'n'1\nu'\tau'\sigma'}(x')] = ir\pi\delta_{rr'}\delta_{nn'}\delta_{\nu\nu'}\delta_{\tau\tau'}\delta_{\sigma\sigma'}\text{sgn}(x-x')$. With this choice, $R_{n1\nu\tau\sigma}$ and $L_{n1\nu\tau\sigma}$ satisfy the proper fermionic anticommutation relations among themselves, while the commutation relations between different species can be satisfied by an appropriate choice of Klein factors [83], which we will not explicitly include here. The dressed interwire terms given in Eqs. (3.12)-(3.14) can be simplified by introducing new bosonic operators $\eta_{rn1\nu\tau\sigma}(x) = \frac{m+1}{2}\phi_{rn1\nu\tau\sigma}(x) - \frac{m-1}{2}\phi_{\bar{r}n1\nu\tau\sigma}(x)$. The new fields obey the commutation relations $[\eta_{rn1\nu\tau\sigma}(x), \eta_{r'n'1\nu'\tau'\sigma'}(x')] = irm\pi\delta_{rr'}\delta_{nn'}\delta_{\nu\nu'}\delta_{\tau\tau'}\delta_{\sigma\sigma'}\text{sgn}(x-x')$ and, for $m > 1$, they carry fractional charge e/m [65]. In terms of these new fields, the dressed interwire terms take the form

$$H_y^{(m)} = 2\sum_{n,\nu,\tau} t_{y,\tau}^{(m)} \int dx \cos(\eta_{1n1\nu\tau(\nu\tau)} - \eta_{\bar{1}n1\bar{\nu}\tau(\nu\tau)}), \tag{3.15}$$

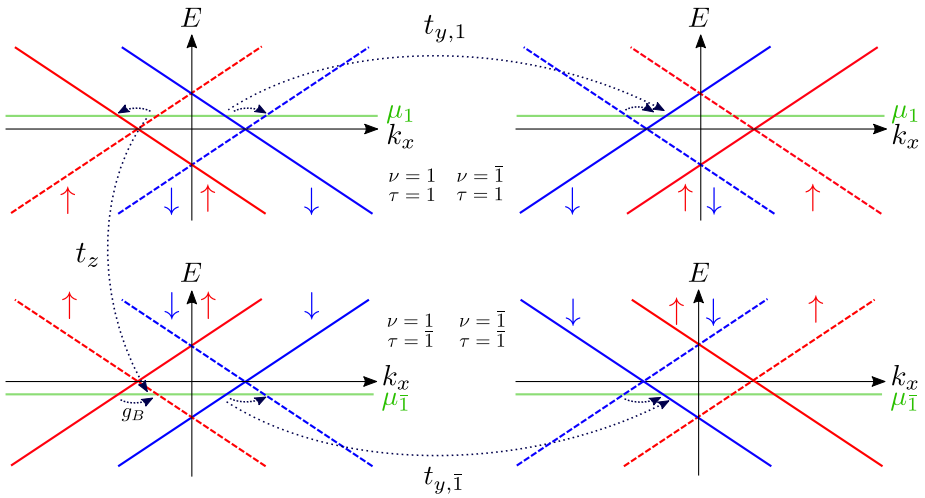

Figure 3.3: The spectrum of a single unit cell for $\mu_\tau = \tau[V_0/(2\sqrt{2}) + \alpha/3]$, corresponding to $m = 3$. Again, only the sector $\kappa = 1$ is shown. Both inter- and intracell hopping do not conserve momentum unless they are dressed by backscattering events of strength g_B arising from strong electron-electron interactions. In order to commute with the other interwire terms, the interlayer hopping term has to be dressed by electron-electron interactions as well. For clarity of the presentation, not all the terms of the interwire Hamiltonian $H_\perp$ [see Eqs. (3.12)-(3.14)] are shown.

$$H_y'^{(m)} = 2\sum_{n,\tau} t_{y,\tau}'^{(m)} \int dx\, [\cos(\eta_{1(n+1)11\tau\tau} - \eta_{\bar{1}n1\bar{1}\tau\tau}) + \cos(\eta_{\bar{1}(n+1)11\tau\bar{\tau}} - \eta_{1n1\bar{1}\tau\bar{\tau}})], \tag{3.16}$$

$$H_z^{(m)} = 2\sum_{n,\nu,\tau,\sigma} t_z^{(m)} \int dx \cos(\eta_{1n1\nu\tau\sigma} - \eta_{\bar{1}n1\nu\bar{\tau}\sigma}). \tag{3.17}$$

We note that the bulk of the system is now fully gapped, while for a system consisting of N unit cells the modes η_{111111} and $\eta_{\bar{1}11111}$ ($\eta_{1N1\bar{1}1\bar{1}}$ and $\eta_{\bar{1}N1\bar{1}11}$) at the left edge (right edge) of the system stay gapless. These edge states carry fractional charges e/m, as expected for a fractional TI.

In order to study the emerging fractional edge states further, let us define new composite chiral fermion operators $R^{(m)}_{n1\nu\tau\sigma} = e^{i\eta_{1n1\nu\tau\sigma}}$ and $L^{(m)}_{n1\nu\tau\sigma} = e^{i\eta_{\bar{1}n1\nu\tau\sigma}}$. In terms of these new composite fields, the dressed interwire terms simplify to

$$H_y^{(m)} = \sum_{n,\nu,\tau} t_{y,\tau}^{(m)} \int dx\, R^{(m)\dagger}_{n1\nu\tau(\nu\tau)} L^{(m)}_{n1\bar{\nu}\tau(\nu\tau)} + \text{H.c.}, \tag{3.18}$$

$$H_y'^{(m)} = \sum_{n,\tau} t_{y,\tau}'^{(m)} \int dx\, [R^{(m)\dagger}_{(n+1)11\tau\tau} L^{(m)}_{n1\bar{1}\tau\tau} + L^{(m)\dagger}_{(n+1)11\tau\bar{\tau}} R^{(m)}_{n1\bar{1}\tau\bar{\tau}}] + \text{H.c.}, \tag{3.19}$$

$$H_z^{(m)} = \sum_{n,\nu,\tau,\sigma} t_z^{(m)} \int dx\, R^{(m)\dagger}_{n1\nu\tau\sigma} L^{(m)}_{n1\nu\bar{\tau}\sigma} + \text{H.c.}, \tag{3.20}$$

from which we recover the non-interacting case for $m = 1$. Indeed, $H_{\perp}^{(m)}$ has the exact same form as in the non-interacting case, except that $R_{n1\nu\tau\sigma}$ ($L_{n1\nu\tau\sigma}$) is replaced by $R^{(m)}_{n1\nu\tau\sigma}$ ($L^{(m)}_{n1\nu\tau\sigma}$). We can now repeat the analysis from the non-interacting case for the new fields $R^{(m)}_{n1\nu\tau\sigma}$, $L^{(m)}_{n1\nu\tau\sigma}$ to find that the branches $R^{(m)}_{n1\nu\tau(\bar{\nu}\tau)}$ and $L^{(m)}_{n1\nu\tau(\nu\tau)}$ are again fully gapped, while the branches $R^{(m)}_{n1\nu\tau(\nu\tau)}$ and $L^{(m)}_{n1\nu\tau(\bar{\nu}\tau)}$ yield two gapless modes $R^{(m)}_{11111}$ and $L^{(m)}_{1111\bar{1}}$ ($R^{(m)}_{N1\bar{1}1\bar{1}}$ and $L^{(m)}_{N1\bar{1}11}$) at the left (right) edge of the system.

As in the non-interacting case, we also consider a semi-infinite geometry where the system is finite along the x direction and infinite along the y direction. By introducing the Fourier transforms $R^{(m)}_{k_y1\nu\tau\sigma}$ and $L^{(m)}_{k_y1\nu\tau\sigma}$ of the composite fields, one can repeat the procedure of matching decaying eigenfunctions employed in the non-interacting case and obtain analogous expressions for the gapless edge states propagating along the y direction, which are now given by

$$\begin{aligned}\Phi_+ &= \left(-\tilde{a}, \tilde{b}, 0, 0, i\tilde{b}, -i\tilde{a}, 0, 0, -i\tilde{b}, i\tilde{a}, 0, 0, \tilde{a}, -\tilde{b}, 0, 0\right)^T, \\ \Phi_- &= \left(0, 0, \tilde{b}, -\tilde{a}, 0, 0, i\tilde{a}, -i\tilde{b}, 0, 0, -i\tilde{a}, i\tilde{b}, 0, 0, -\tilde{b}, \tilde{a}\right)^T,\end{aligned} \tag{3.21}$$

in the basis $\Psi^{(m)}_{k_y=0}$, which corresponds to $\Psi_{k_y=0}$ but with $R_{n1\nu\tau\sigma}$ ($L_{n1\nu\tau\sigma}$) replaced by $R^{(m)}_{n1\nu\tau\sigma}$ ($L^{(m)}_{n1\nu\tau\sigma}$). Furthermore, we have defined $\tilde{a} = e^{-x/\xi_1^{(m)}}$ and $\tilde{b} = e^{-x/\xi_2^{(m)}}$ for $\xi_1^{(m)} = \hbar v_1^{(m)}/(t^{(m)}_{y,\bar{1}} - t_z^{(m)})$ and $\xi_2^{(m)} = \hbar v_1^{(m)}/t_z^{(m)}$, where $v_1^{(m)}$ is the velocity of the composite fields.

By continuity, we therefore find that our system hosts a Kramers pair of fractionally charged gapless edge states running along the edges of a large but finite sample, which allows us to identify our system as a fractional topological insulator. This means that we can write an effective edge theory in terms of two conjugate bosonic fields η_1 and $\eta_{\bar{1}}$ with $[\eta_r(l), \eta_{r'}(l')] = irm\pi\delta_{rr'}\mathrm{sgn}(l - l')$, where l is an edge coordinate which is defined mod $2[L + (N-1)a_y]$ and runs along the edge of the sample in the counterclockwise direction [17].

3.4 Majorana and parafermion corner states

3.4.1 Non-interacting case

In this section, we show that the terms H_{sc} and H_Z [see Eqs. (3.8) and (3.9)] can drive the system into a second-order topological superconducting phase. Again, we start by treating the non-interacting case. Importantly, we consider Δ_{sc} and Δ_Z to be small enough not to modify the bulk gap structure. However, they may modify the low-energy behavior of the system by gapping out the helical edge states found above. This statement is confirmed explicitly by considering the effective low-energy edge theory. We assume that the system size is sufficiently large such that far away from the corners all four edges can be treated independently. Crucially, we find that the Zeeman term $\mathcal{H}_Z = \Delta_Z(\sigma_x\rho_x - \nu_z\tau_z\sigma_y\rho_y)$ does not open a gap at $k_y = 0$ in the spectrum of the edges states propagating along the y direction. This can be verified explicitly by using the form of the edge state wave functions given in Eq. (3.11), for which we find $\langle\Phi_+|\mathcal{H}_Z|\Phi_-\rangle = \langle\Phi_+|\mathcal{H}_Z|\Phi_+\rangle = \langle\Phi_-|\mathcal{H}_Z|\Phi_-\rangle = 0$. Alternatively, one can arrive at the same conclusion in a more general way by exploiting the symmetries of the system. Indeed, at $k_y = 0$ the system has an additional symmetry represented by the operator $\mathcal{O} = \nu_z\tau_y\sigma_z\rho_x$, which anticommutes with the Hamiltonian $\mathcal{H}(k_y = 0)$ [see Eq. (3.10)]

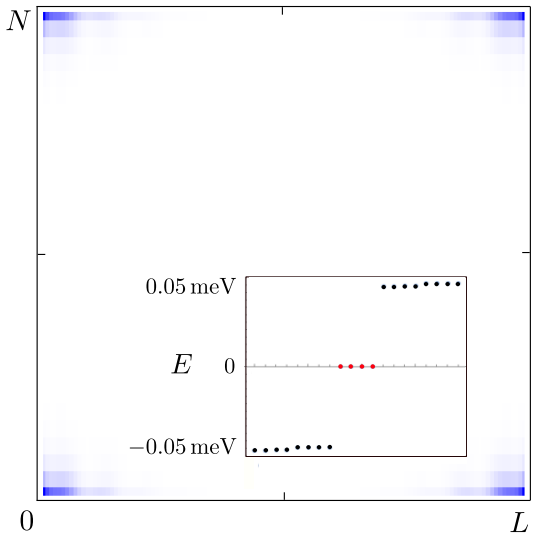

Figure 3.4: Probability density of low-energy states obtained numerically for a system of $N = 30$ unit cells consisting of four effective wires of length $L = 1.2\,\mu$m each. The single-wire spectrum is obtained by discretizing Eq. (3.3) and by setting $V_0 = 100\,\text{meV}$, $t = 2.7\,\text{eV}$, $t_\perp = 0.34\,\text{eV}$, and $\alpha = 1\,\text{meV}$. The other parameters [see Eqs. (3.5)-(3.9)] are chosen as $t_{y,1} = 0.01\,\text{meV}$, $t'_{y,1} = 0.79\,\text{meV}$, $t_{y,\bar{1}} = 0.81\,\text{meV}$, $t'_{y,\bar{1}} = 0.02\,\text{meV}$, $t_z = 0.4\,\text{meV}$, $\Delta_Z = 0.4\,\text{meV}$, and $\Delta_{sc} = 0.05\,\text{meV}$. One Majorana corner state is localized at each of the four corners of the system. The inset demonstrates that the energies of these states (red dots) are indeed at zero.

for $t_{y,1} + t'_{y,1} = t_{y,\bar{1}} + t'_{y,\bar{1}}$. In addition, $\Phi_\pm$ defined in Eq. (3.11) are eigenstates of $\mathcal{O}$: $\mathcal{O}\Phi_\pm = \Phi_\pm$. Furthermore, we find $\{\mathcal{H}_Z, \mathcal{O}\} = 0$, which then implies $\langle\Phi_+|\mathcal{H}_Z|\Phi_-\rangle = 0$. All other matrix elements are trivially zero as the edge states $\Phi_\pm$ are eigenstates of σ_z, showing that the magnetic term indeed does not open a gap in the spectrum of the edge states propagating along the y direction. Therefore, these edge states can only be gapped by superconductivity, whereas in the spectrum of the edge states propagating along the x direction both mechanisms can in principle open a gap. If we choose $|\Delta_Z| > |\Delta_{sc}|$, the magnetic term dominates over the superconducting one such that it is responsible for gapping the edge states propagating along the x direction. In analogy to previous works studying domain walls between competing gapping mechanisms in systems with helical edge states [84–86], we find localized Majorana zero modes at the domain walls between the regions where the superconducting/magnetic term dominates, which in this case means at all four corners of the system. However, in contrast to previous works, we apply both the superconducting as well as the magnetic term throughout the entire system. Figure 3.4 verifies our results numerically. Importantly, our numerical analysis confirms that the corner states are robust against small deviations from the fine-tuned point $t_{y,1} + t'_{y,1} = t_{y,\bar{1}} + t'_{y,\bar{1}}$. In addition, we confirmed numerically that the zero-energy corner states are robust against disorder that breaks all spatial symmetries but neither closes the bulk nor the edge state gaps. This confirms that the Majorana corner states are protected purely by the particle-hole symmetry enforced by superconductivity, while the spatial symmetry $\mathcal{O}$ is not playing a crucial role.

3.4.2 Interacting case

The above results can be extended rather straightforwardly to the interacting case. In order to gap out the edge states given in Eq. (3.21), the Zeeman term as well as the superconducting term need to be dressed by interactions in the standard way. To lowest order, the terms that can open a gap in the edge state spectrum are given by

$$H_{sc}^{(m)} = \Delta_{sc}^{(m)} \sum_{n,\nu,\tau,\sigma} \sigma \int dx\, R_{n1\nu\tau\sigma}^{(m)\dagger} L_{n1\nu\tau\bar{\sigma}}^{(m)\dagger} + \text{H.c.}, \tag{3.22}$$

$$H_{Z}^{(m)} = \Delta_{Z}^{(m)} \sum_{n,\nu,\tau} \int dx\, R_{n1\nu\tau(\nu\tau)}^{(m)\dagger} L_{n1\nu\tau(\bar{\nu\tau})}^{(m)} + \text{H.c.}, \tag{3.23}$$

with $\Delta_{sc}^{(m)} \propto \Delta_{sc} g_B^{m-1}$ and $\Delta_Z^{(m)} \propto \Delta_Z g_B^{m-1}$. Again, these terms have exactly the same form as in the non-interacting case, except that $R_{n1\nu\tau\sigma}$ ($L_{n1\nu\tau\sigma}$) is replaced by $R_{n1\nu\tau\sigma}^{(m)}$ ($L_{n1\nu\tau\sigma}^{(m)}$). In the following, we assume that the above terms are substantially smaller than the interwire terms and, therefore, will not modify the bulk gap structure but may open a gap in the spectrum of edge states. Starting from the fractional topological insulator phase established in Sec. 3.3.2, we note that the projection of the above terms onto the gapless edge states commutes with the interwire terms and therefore these terms can order simultaneously. In particular, the above terms can again always be made relevant if their bare coupling constants are of order unity or if their scaling dimensions are the lowest ones among all competing terms [64, 65].

We can now repeat the above symmetry argument to find that the magnetic term does not open a gap in the spectrum of the edge states propagating along the y direction; this gap is opened by superconductivity only. On the other hand, the edge states propagating along the x direction are gapped by the Zeeman term for $|\Delta_Z^{(m)}| > |\Delta_{sc}^{(m)}|$. We are thus effectively dealing with domain walls occurring naturally at the corners of a fractional 2D TI, despite the fact that the superconducting and magnetic terms are uniform and act both simultaneously on the entire system. Given this analogy to domain walls, we can follow Refs. [84–87] and show that every domain wall between a region gapped by superconductivity and a region gapped by a magnetic field hosts a zero-energy parafermion bound state that is spatially localized to the domain wall, i.e., to the corner of the sample. To make this statement explicit in terms of the fields considered here, we rewrite the left and right moving fields η_1 and $\eta_{\bar{1}}$ describing the low-energy edge theory in terms of conjugate fields $\varphi = (\eta_1 - \eta_{\bar{1}})/(2m)$ and $\theta = (\eta_1 + \eta_{\bar{1}})/(2m)$ with $[\varphi(l), \theta(l')] = \frac{i\pi}{2m}\text{sgn}(l - l')$. The dressed superconducting and magnetic terms given in Eqs. (3.22) and (3.23) projected onto the low-energy part of the spectrum now take the form $H_{sc}^{(m)} \propto \Delta_{sc}^{(m)} \int dl \cos(2m\theta)$ and $H_Z^{(m)} \propto \Delta_Z^{(m)} \int dl \cos(2m\varphi)$. Let us now label the edges of our system by $s \in \{0, ..., 3\}$ starting from the right edge of the sample and proceeding in counterclockwise order. In the strong-coupling regime, we find that along the x (y) edges we have $\varphi_i = \frac{\pi}{m}(p_i + 1/2)$ [$\theta_i = \frac{\pi}{m}(q_j + 1/2)$] for $p_i, q_j \in \mathbb{Z}$, where $i \in \{0, 2\}$, $j \in \{1, 3\}$ label the respective edge. These operators satisfy $[p_i(l), q_j(l')] = \frac{im}{2\pi}\text{sgn}(l - l')$. If we label the corners of a rectangular sample by $v \in \{0, ..., 3\}$ in counterclockwise order starting from the corner between edges 0 and 1, we can define operators acting locally on the corners as $\gamma_{2k} = e^{i\pi(p_{2k} - q_{2k+1})/m}$, $\gamma_{2k+1} = e^{i\pi(p_{2k+2} - q_{2k+1})/m}$ for $k \in \{0, 1\}$. These operators commute with the Hamiltonian as they act on domain walls between segments gapped by competing

mechanisms and satisfy $\mathbb{Z}_{2m}$ parafermionic commutation relations $\gamma_v \gamma_{v'} = \gamma_{v'} \gamma_v e^{-i\pi/m}$ for $v < v'$. As such, we find a single zero-energy $\mathbb{Z}_{2m}$ parafermion corner state per corner.

3.5 Conclusions

We have considered a model based on two coupled sheets of bilayer graphene in the strong SOI regime. Electrostatic confinement is used to create effective 1D quantum wires, which are then tunnel-coupled in various ways. For a certain range of parameters, this system can be brought into a topological insulator phase characterized by the presence of a Kramers pair of gapless helical edge states. Furthermore, a small in-plane magnetic field and weak proximity-induced superconductivity drive the system into a second-order topological superconducting phase with zero-energy Majorana corner states at all four corners of a rectangular sample. Even more interestingly, the fact that we are dealing with effective 1D systems allows us to take into account the effects of strong electron-electron interactions in an analytically tractable way. Using a bosonization approach, we have shown that for sufficiently strong electron-electron interactions and suitable values of chemical potential, the system can be brought into a fractional topological insulator phase with fractionally charged gapless helical edge states as well as into a fractional second-order topological superconducting phase hosting exotic $\mathbb{Z}_{2m}$ parafermion corner states, where m is an odd integer determined by the position of the chemical potential.

In particular, we envision the strong SOI in the graphene bilayers to be induced by proximity to a few layers of $NbSe_2$, which at the same time also induce superconductivity into the system. The recent progress in fabricating van der Waals heterostructures puts such a setup well into experimental reach. From a more general perspective, we therefore believe that our system demonstrates the potential use of electrostatically generated arrays of effective quantum wires in bilayer graphene as designer platforms to realize topologically non-trivial physics. On the other hand, we note that while gated bilayer graphene turns out to be a particularly convenient platform to realize the model proposed here, our results can readily be adapted to different realizations of coupled 1D wires with similar low-energy properties.

Acknowledgments. This work was supported by the Swiss National Science Foundation and NCCR QSIT. This project received funding from the European Union's Horizon 2020 research and innovation program (ERC Starting Grant, grant agreement No 757725).

3.A Alternative realization of the second-order phase

In this Appendix, we comment on an alternative realization of the second-order TSC phase. For this, we tune the chemical potential to $\mu_\tau = V_0/(2\sqrt{2}) + \tau\alpha$ instead of the values chosen in the main text. By replacing $\kappa\tau \to \tilde{\kappa}$, we note that the sector $\tilde{\kappa} = 1$ now once again corresponds to the modes with small Fermi momenta close to $k_x = 0$. Indeed, the spectrum for the sector $\tilde{\kappa} = 1$ is identical to the one shown in Fig. 3.2 and can be analyzed in the same way as in the main text. However, the sector $\tilde{\kappa} = \bar{1}$ has to be treated differently in this case. Indeed, the interlayer hopping term [see Eq. (3.7)] is not able to open a gap for the sector $\tilde{\kappa} = \bar{1}$ anymore, as it couples right-moving (left-moving) with right-moving (left-moving) modes. Therefore, the first-order topological insulator phase is not present in this case, as

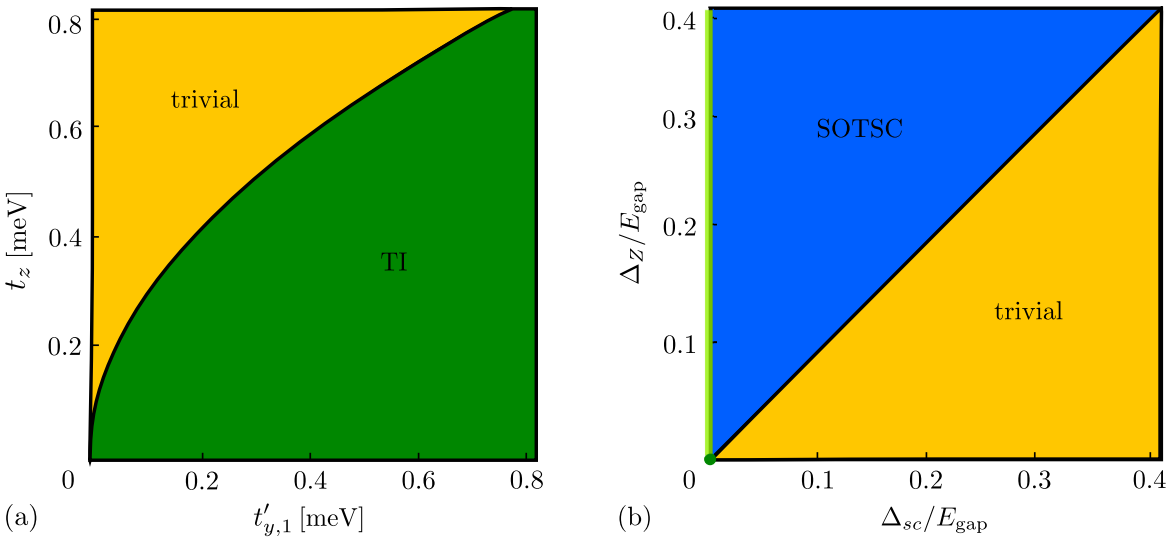

Figure 3.5: (a) Phase diagram of the first-order phase (i.e., $\Delta_Z = \Delta_{sc} = 0$) as a function of $t'_{y,1}$ and t_z. The bulk gap closing line at $t_z = \sqrt{(t_{y,1} + t'_{y,1})(t_{y,\bar{1}} + t'_{y,\bar{1}})}$ marks the transition from the topologically trivial phase to the TI phase with a Kramers pair of gapless edge states. (b) Phase diagram of the second-order phase as a function of Δ_Z and Δ_{sc}. Importantly, we consider both Δ_{sc} and Δ_Z to be smaller than the bulk gap E_{gap}, such that the bulk gap is never closed by these terms. However, the edge gap closes and reopens for $|\Delta_{sc}| = |\Delta_Z|$, corresponding to the phase transition between the topologically trivial phase and the second-order TSC (SOTSC) phase with one Majorana corner state per corner. The green dot at $\Delta_Z = \Delta_{sc} = 0$ corresponds to the first-order phase, while the light green line for $\Delta_{sc} = 0$ and $\Delta_Z > 0$ indicates the phase with partially gapped edge states (gapped along the x direction but gapless along the y direction). The other parameters are the same as in Fig. 3.4.

the bulk of the system is not fully gapped out. However, once superconductivity is taken into account, the gapless modes in the sector $\tilde{\kappa} = \bar{1}$ are trivially gapped out by superconductivity, while the sector $\tilde{\kappa} = 1$ can be treated in the exact same way as before. Therefore, we find a second-order TSC phase with the same properties as in the main text.

3.B Phase diagram in the non-interacting case

In the main text, we assumed $t_{y,1} = t'_{y,\bar{1}} = 0$ and $t'_{y,1} = t_{y,\bar{1}}$ for analytical simplicity. However, we argued that the topological properties of the system stay qualitatively the same in an extended region of parameter space. In this Appendix, we confirm this statement by calculating a condition for the closing of the bulk gap for a more general choice of hopping amplitudes. We start by considering the first-order phase with $\Delta_{sc} = \Delta_Z = 0$. To simplify matters, we focus on the case of $t_{y,\tau}, t'_{y,\tau}, t_z \geq 0$, but our analysis can easily be extended to account for negative values of the hopping amplitudes as well. The bulk Hamiltonian is obtained from Eq. (3.10) upon replacing $-i\partial_x \to k_x$, and has time-reversal symmetry expressed by $\mathcal{T} = i\sigma_y\rho_x\mathcal{K}$, where $\mathcal{K}$ denotes the complex conjugation. Therefore, our system belongs to the symmetry class AII [88]. As long as $t'_{y,1}, t_{y,\bar{1}} > t_{y,1}, t'_{y,\bar{1}}$, the bulk gap can only close at

$k_x = k_y = 0$, where the eigenenergies are explicitly given by

$$E_{1,\pm} = \pm t_z, \tag{3.24}$$

$$E_{2,\pm,\pm} = \pm\Big(t_{y,1} + t_{y,\bar{1}} + t'_{y,1} + t'_{y,\bar{1}} \pm \sqrt{(t_{y,1} - t_{y,\bar{1}} + t'_{y,1} - t'_{y,\bar{1}})^2 + 4t_z^2}\Big)/2. \tag{3.25}$$

Thus, we find that the bulk of the system is fully gapped except for the values $t_z = 0$ or $t_z^2 = (t_{y,1} + t'_{y,1})(t_{y,\bar{1}} + t'_{y,\bar{1}})$. These conditions define the potential boundaries between topologically non-equivalent phases. In our case, we can identify the region corresponding to the topologically non-trivial phase by checking for the existence of gapless edge states: In the main text, we argued that the system hosts a Kramers pair of gapless edge states for $t_{y,1} = t'_{y,\bar{1}} = 0$ and $t_{y,\bar{1}} = t'_{y,1} \gg t_z > 0$. Therefore, we identify the region of the phase diagram for which $0 < t_z^2 < (t_{y,1} + t'_{y,1})(t_{y,\bar{1}} + t'_{y,\bar{1}})$ as the topologically non-trivial one. This is visualized in Fig. 3.5(a).

Let us now turn to the second-order phase. In the presence of a magnetic field, $\Delta_Z \neq 0$, time-reversal symmetry is broken, while superconductivity, $\Delta_{sc} \neq 0$, enforces particle-hole symmetry. This places our system in the symmetry class D [88]. Assuming that Δ_{sc} and Δ_Z are much smaller than the bulk gap, these terms cannot result in a closing of the bulk gap. However, we find that the edge gap closes at the points $|\Delta_{sc}| = |\Delta_Z|$, which separates the topologically non-trivial second-order phase with one zero-energy Majorana corner state per corner from the trivial one with no corner states. The corresponding phase diagram is shown in Fig. 3.5(b).

Bibliography

[1] M. Z. Hasan and C. L. Kane, Rev. Mod. Phys. **82**, 3045 (2010).

[2] X.-L. Qi and S.-C. Zhang, Rev. Mod. Phys. **83**, 1057 (2011).

[3] M. Sato and Y. Ando, Rep. Prog. Phys. **80**, 076501 (2017).

[4] W. A. Benalcazar, J. C. Y. Teo, and T. L. Hughes, Phys. Rev. B **89**, 224503 (2014).

[5] W. A. Benalcazar, B. A. Bernevig, and T. L. Hughes, Science **357**, 61 (2017).

[6] W. A. Benalcazar, B. A. Bernevig, and T. L. Hughes, Phys. Rev. B **96**, 245115 (2017).

[7] Z. Song, Z. Fang, and C. Fang, Phys. Rev. Lett. **119**, 246402 (2017).

[8] Y. Peng, Y. Bao, and F. von Oppen, Phys. Rev. B **95**, 235143 (2017).

[9] S. Imhof, C. Berger, F. Bayer, H. Brehm, L. Molenkamp, T. Kiessling, F. Schindler, C. H. Lee, M. Greiter, T. Neupert, and R. Thomale, Nat. Phys. **14**, 925 (2018).

[10] M. Geier, L. Trifunovic, M. Hoskam, and P. W. Brouwer, Phys. Rev. B **97**, 205135 (2018).

[11] F. Schindler, A. M. Cook, M. G. Verginory, Z. Wang, S. S. P. Parking, B. A. Bernevig, and T. Neupert, Science Adv. **4**, 6 (2018).

[12] C.-H. Hsu, P. Stano, J. Klinovaja, and D. Loss, Phys. Rev. Lett. **121**, 196801 (2018).

[13] M. Ezawa, Sci. Rep. **9**, 5286 (2019).

[14] M. Ezawa, Phys. Rev. Lett. **121**, 116801 (2018).

[15] X. Zhu, Phys. Rev. B **97**, 205134 (2018).

[16] Q. Wang, C.-C. Liu, Y.-M. Lu, and F. Zhang, Phys. Rev. Lett. **121**, 186801 (2018).

[17] Z. Yan, F. Song, and Z. Wang, Phys. Rev. Lett. **121**, 096803 (2018).

[18] T. Liu, J. J. He, and F. Nori, Phys. Rev. B **98**, 245413 (2018).

[19] X. Zhang, H.-X. Wang, Z.-K. Lin, Y. Tian, B. Xie, M.-H. Lu, Y.-F. Chen, and J.-H. Jiang, Nat. Phys. **15**, 582 (2019).

[20] Q. Wang, D. Wang, and Q.-H. Wang, EPL **124**, 50005 (2018).

[21] Y. Volpez, D. Loss, and J. Klinovaja, Phys. Rev. Lett. **122**, 126402 (2019).

[22] K. Plekhanov, M. Thakurathi, D. Loss, and J. Klinovaja, Phys. Rev. Res. **1**, 032013(R) (2019).

[23] D. Calugaru, V. Juricic, and B. Roy, Phys. Rev. B **99**, 041301(R) (2019).

[24] A. Agarwala, V. Juricic, and B. Roy, arXiv:1902.00507.

[25] Z. Yan, Phys. Rev. Lett. **123**, 177001 (2019).

[26] S. Franca, D. V. Efremov, and I. C. Fulga, Phys. Rev. B **100**, 075415 (2019).

[27] R.-X. Zhang, W. S. Cole, and S. Das Sarma, Phys. Rev. Lett. **122**, 187001 (2019).

[28] S.-B. Zhang and B. Trauzettel, arXiv:1905.09308.

[29] Y. You, D. Litinski, and F. von Oppen, Phys. Rev. B **100**, 054513 (2019).

[30] Y. You, T. Devakul, F. J. Burnell, and T. Neupert, Phys. Rev. B **98**, 235102 (2018).

[31] K. Laubscher, D. Loss, and J. Klinovaja, Phys. Rev. Res. **1**, 032017(R) (2019).

[32] A. H. Castro Neto, F. Guinea, N. M. R. Peres, K. S. Novoselov, and A. K. Geim, Rev. Mod. Phys. **81**, 109 (2009).

[33] S. Das Sarma, S. Adam, E. H. Hwang, and E. Rossi, Rev. Mod. Phys. **83**, 407 (2011).

[34] C. L. Kane and E. J. Mele, Phys. Rev. Lett. **95**, 226801 (2005).

[35] M. L. Kiesel, C. Platt, W. Hanke, D. A. Abanin, and R. Thomale, Phys. Rev. B **86**, 020507(R) (2012).

[36] J. Klinovaja, S. Gangadharaiah, and D. Loss, Phys. Rev. Lett. **108**, 196804 (2012).

[37] J. D. Sau and S. Tewari, Phys. Rev. B **88**, 054503 (2013).

[38] R. Egger and K. Flensberg, Phys. Rev. B **85**, 235462 (2012).

[39] P. San-Jose, J. L. Lado, R. Aguado, F. Guinea, and J. Fernández-Rossier, Phys. Rev. X **5**, 041042 (2015).

[40] A. M. Black-Schaffer, Phys. Rev. Lett. **109**, 197001 (2012).

[41] C. Dutreix, M. Guigou, D. Chevallier, and C. Bena, Eur. Phys. J. B **87**, 296 (2014).

[42] J. Klinovaja and D. Loss, Phys. Rev. X **3**, 011008 (2013).

[43] M. Marganska, L. Milz, W. Izumida, C. Strunk, and M. Grifoni, Phys. Rev. B **97**, 075141 (2018).

[44] M. Gmitra, S. Konschuh, C. Ertler, C. Ambrosch-Draxl, and J. Fabian, Phys. Rev. B **80**, 235431 (2009).

[45] T. P. Kaloni, L. Kou, T. Frauenheim, and U. Schwingenschlögl, Appl. Phys. Lett. **105**, 233112 (2014).

[46] A. Avsar, J. Y. Tan, T. Taychatanapat, J. Balakrishnan, G. K. W. Koon, Y. Yeo, J. Lahiri, A. Carvalho, A. S. Rodin, E. C. T. O'Farrell, G. Eda, A. H. Castro Neto, and B. Özyilmaz, Nat. Commun. **5**, 4875 (2014).

[47] M. Gmitra and J. Fabian, Phys. Rev. B **92**, 155403 (2015).

[48] Z. Wang, D.-K. Ki, H. Chen, H. Berger, A. H. MacDonald, and A. F. Morpurgo, Nat. Commun. **6**, 8339 (2015).

[49] M. Gmitra, D. Kochan, P. Högl, and J. Fabian, Phys. Rev. B **93**, 155104 (2016).

[50] Z. Wang, D.-K. Ki, J. Y. Khoo, D. Mauro, H. Berger, L. S. Levitov, and A. F. Morpurgo, Phys. Rev. X **6**, 041020 (2016).

[51] A. M. Alsharari, M. M. Asmar, and S. E. Ulloa, Phys. Rev. B **94**, 241106(R) (2016).

[52] D. Kochan, S. Irmer, and J. Fabian, Phys. Rev. B **95**, 165415 (2017).

[53] Y. S. Gani, H. Steinberg, and E. Rossi, Phys. Rev. B **99**, 235404 (2019).

[54] M. Gmitra and J. Fabian, Phys. Rev. Lett. **119**, 146401 (2017).

[55] J. Y. Khoo, A. F. Morpurgo, and L. Levitov, Nano Lett. **17**, 7003 (2017).

[56] S. Zihlmann, A. W. Cummings, J. H. Garcia, M. Kedves, K. Watanabe, T. Taniguchi, C. Schönenberger, and P. Makk, Phys. Rev. B **97**, 075434 (2018).

[57] I. Martin, Y. M. Blanter, and A. F. Morpurgo, Phys. Rev. Lett. **100**, 036804 (2008).

[58] J. Li, K. Wang, K. J. McFaul, Z. Zern, Y. Ren, K. Watanabe, T. Taniguchi, Z. Qiao, and J. Zhu, Nat. Nanotechnol. **11**, 1060 (2016).

[59] L.-J. Yin, H. Jiang, J.-B. Qiao, and L. He, Nat. Commun. **7**, 11760 (2016).

[60] L. Ju, Z. Shi, N. Nair, Y. Lv, C. Jin, J. Velasco Jr, C. Ojeda-Aristizabal, H. A. Bechtel, M. C. Martin, A. Zettl, J. Analytis, and F. Wang, Nature (London) **520**, 650 (2015).

[61] J. Klinovaja, G. J. Ferreira, and D. Loss, Phys. Rev. B **86**, 235416 (2012).

[62] D. Poilblanc, G. Montambaux, M. Héritier, and P. Lederer, Phys. Rev. Lett. **58**, 270 (1987).

[63] L. P. Gorkov and A. G. Lebed, Phys. Rev. B **51**, 3285 (1995).

[64] C. L. Kane, R. Mukhopadhyay, and T. C. Lubensky, Phys. Rev. Lett. **88**, 036401 (2002).

[65] J. C. Y. Teo and C. L. Kane, Phys. Rev. B **89**, 085101 (2014).

[66] J. Klinovaja and Y. Tserkovnyak, Phys. Rev. B **90**, 115426 (2014).

[67] J. Klinovaja and D. Loss, Eur. Phys. J. B **87**, 171 (2014).

[68] E. Sagi and Y. Oreg, Phys. Rev. B **90**, 201102(R) (2014).

[69] T. Neupert, C. Chamon, C. Mudry, and R. Thomale, Phys. Rev. B **90**, 205101 (2014).

[70] J. Klinovaja, Y. Tserkovnyak, and D. Loss, Phys. Rev. B **91**, 085426 (2015).

[71] E. Sagi and Y. Oreg, Phys. Rev. B **92**, 195137 (2015).

[72] T. Meng, Phys. Rev. B **92**, 115152 (2015).

[73] S. Sahoo, Z. Zhang, and J. C. Y. Teo, Phys. Rev. B **94**, 165142 (2016).

[74] T. Ando, J. Phys. Soc. Jpn. **69**, 1757 (2000).

[75] D. Huertas-Hernando, F. Guinea, and A. Brataas, Phys. Rev. B **74**, 155426 (2006).

[76] F. Kuemmeth, S. Ilani, D. C. Ralph, and P. L. McEuen, Nature (London) **452**, 448 (2008).

[77] W. Izumida, K. Sato, and R. Saito, J. Phys. Soc. Jpn. **78**, 074707 (2009).

[78] L. Chico, M. P. López-Sancho, and M. C. Muñoz, Phys. Rev. B **79**, 235423 (2009).

[79] J. Klinovaja, M. J. Schmidt, B. Braunecker, and D. Loss, Phys. Rev. Lett. **106**, 156809 (2011).

[80] J. Klinovaja, M. J. Schmidt, B. Braunecker, and D. Loss, Phys. Rev. B **84**, 085452 (2011).

[81] G. A. Steele, F. Pei, E. A. Laird, J. M. Jol, H. B. Meerwaldt, and L. P. Kouwenhoven, Nat. Commun. **4**, 1573 (2013).

[82] J. Klinovaja and D. Loss, Phys. Rev. B **86**, 085408 (2012).

[83] T. Giamarchi, *Quantum Physics in One Dimension* (Oxford University Press, Oxford, 2004).

[84] M. Cheng, Phys. Rev. B **86**, 195126 (2012).

[85] D. J. Clarke, J. Alicea and K. Shtengel, Nat. Commun. **4**, 1348 (2013).

[86] J. Motruk, E. Berg, A. M. Turner, and F. Pollmann, Phys. Rev. B **88**, 085115 (2013).

[87] N. H. Lindner, E. Berg, G. Refael, and A. Stern, Phys. Rev. X **2**, 041002 (2012).

[88] S. Ryu, A. P. Schnyder, A. Furusaki, and A. W. W. Ludwig, New J. Phys. **12**, 065010 (2010).

Chapter 4

Kramers pairs of Majorana corner states in a topological insulator bilayer

Adapted from:
K. Laubscher, D. Chughtai, D. Loss, and J. Klinovaja,
"Kramers pairs of Majorana corner states in a topological insulator bilayer,"
Phys. Rev. B **102**, 195401 (2020)

We consider a system consisting of two tunnel-coupled two-dimensional topological insulators proximitized by a top and bottom superconductor with a phase difference of π between them. We show that this system exhibits a time-reversal invariant second-order topological superconducting phase characterized by the presence of a Kramers pair of Majorana corner states at all four corners of a rectangular sample. We furthermore investigate the effect of a weak time-reversal symmetry breaking perturbation and show that an in-plane Zeeman field leads to an even richer phase diagram exhibiting two nonequivalent phases with two Majorana corner states per corner as well as an intermediate phase with only one Majorana corner state per corner. We derive our results analytically from continuum models describing our system. In addition, we also provide independent numerical confirmation of the resulting phases using discretized lattice representations of the models, which allows us to demonstrate the robustness of the topological phases and the Majorana corner states against parameter variations and potential disorder.

4.1 Introduction

Motivated by the seminal work on one-dimensional (1D) p-wave superconductors [1], Majorana bound states have been predicted to occur in a variety of condensed matter systems as a signature of a topologically non-trivial superconducting phase. Apart from their fundamental interest, Majorana bound states are considered to be promising building blocks for topologically protected qubits due to their non-Abelian braiding statistics. Many well-known proposals for the experimental realization of Majorana bound states rely on the competition between a strong magnetic field and proximity-induced superconducting pairing [2, 3]. However, such setups suffer from the disadvantage that a strong magnetic field itself has a detrimental effect on superconductivity. To circumvent this issue, the concept of time-reversal invariant topological superconductivity has raised significant interest. In this case, Kramers pairs of Majorana bound states emerge in the absence of a magnetic field [4–23].

In the standard proposals, Majorana bound states are realized at the zero-dimensional edges of 1D topological superconductors (TSCs). More recently, the notion of topological insulators (TIs) and TSCs has been extended to capture also their *higher-order* generalizations [24–30]. While conventional d-dimensional TIs and TSCs exhibit gapless edge states at their $(d-1)$-dimensional boundaries, nth-order d-dimensional TIs or TSCs exhibit gapless edge states at their $(d-n)$-dimensional boundaries. In particular, a two-dimensional (2D) second-order topological superconductor (SOTSC) hosts Majorana bound states at the corners of a rectangular sample. By now, a large variety of platforms hosting such Majorana corner states (MCSs) has been proposed. While most of these proposals use an applied magnetic field to induce the second-order phase [31–42], the case of time-reversal invariant SOTSCs with Kramers pairs of MCSs has been studied less extensively. The few setups proposed so far rely on unconventional superconductivity as the relevant mechanism driving the transition to the second-order phase [43, 44]. This motivates us to look for an alternative model realizing a time-reversal invariant SOTSC based on conventional ingredients only. The setup we propose consists of two tunnel-coupled 2D TIs, each described by a Bernevig-Hughes-Zhang (BHZ) model, proximitized by a top and bottom superconductor of a phase difference of π, see Fig. 4.1. In the absence of interlayer tunneling and superconductivity, each TI layer hosts a pair of gapless helical edge states. Once interlayer tunneling and superconductivity are turned on, these edge states are gapped out. However, the resulting phase is not necessarily trivial. Indeed, we show that in a certain region of parameter space, the system is a SOTSC with a Kramers pair of MCSs at all four corners of a rectangular sample. These corner states are protected by particle-hole and time-reversal symmetry and cannot be removed unless one of the protecting symmetries is broken or the edge gap closes and reopens.

The paper is organized as follows. In Sec. 4.2 we describe our setup, which consists of two tunnel-coupled 2D TIs, each described by a BHZ model, in proximity to a top and a bottom superconductor of a phase difference of π, see Fig. 4.1. In Sec. 4.3, we obtain expressions for the gapless edge states appearing in the absence of superconductivity and interlayer tunneling. In this case, our model simply corresponds to two decoupled BHZ layers. In Sec. 4.4, we then perturbatively account for weak interlayer tunneling as well as weak proximity-induced superconductivity. As a consequence, the helical edge states found previously are gapped out. We show that there exists a regime of parameters for which the system is a time-reversal invariant SOTSC with a Kramers pair of MCSs at all four corners of a rectangular sample.

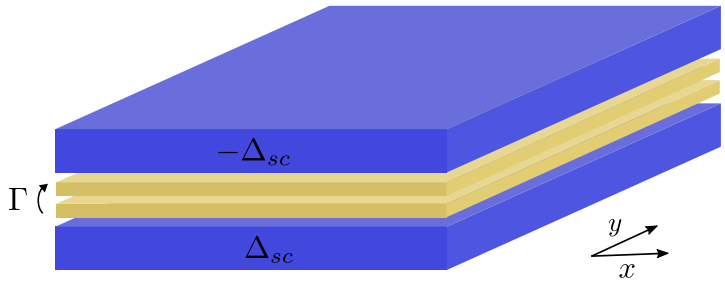

Figure 4.1: The setup consists of two 2D TI layers (yellow) coupled by an interlayer tunneling term of strength Γ. The two layers are proximitized by a top and bottom superconductor (blue) with a phase difference of π between them.

In order to account for a possible complication in some experimentally relevant setups, we additionally comment on the case of unequal interlayer tunneling amplitudes for particle-like and hole-like bands in Sec. 4.5. Finally, in Sec. 4.6, we discuss the case of broken time-reversal symmetry in the presence of a weak in-plane Zeeman field. We show that this enriches the phase diagram further, allowing us to access also a SOTSC phase with a single MCS per corner. We summarize our results in Sec. 4.7.

4.2 Model

We consider a 2D TI bilayer, where each of the two TI layers is described by a BHZ model [45]. In momentum space, the Hamiltonian of a single TI layer can then be written as $H_0 = \sum_{\mathbf{k}} \Psi_{\mathbf{k}}^\dagger \mathcal{H}_0(\mathbf{k}) \Psi_{\mathbf{k}}$ in the basis $\Psi_{\mathbf{k}} = (\psi_{\mathbf{k}1}, \psi_{\mathbf{k}\bar{1}}, \psi_{\mathbf{k}\bar{1}1}, \psi_{\mathbf{k}\bar{1}\bar{1}})$, where $\psi_{\mathbf{k}\sigma s}$ ($\psi_{\mathbf{k}\sigma s}^\dagger$) destroys (creates) an electron with in-plane momentum $\mathbf{k} = (k_x, k_y)$, orbital degree of freedom $\sigma \in \{1, \bar{1}\}$ and spin $s \in \{1, \bar{1}\}$. The Hamiltonian density is given by[1]

$$\mathcal{H}_0(\mathbf{k}) = \left(\frac{\hbar^2 k_x^2}{2m_x} + \frac{\hbar^2 k_y^2}{2m_y} + \epsilon \right) \sigma_z + \mu + \lambda_x k_x \sigma_x s_z + \lambda_y k_y \sigma_y, \tag{4.1}$$

where σ_i and s_i for $i \in \{x, y, z\}$ are Pauli matrices acting in orbital and spin space, respectively. The parameters m_x, m_y, λ_x, and λ_y are material-specific constants inherent to the BHZ model [45]. For simplicity, we assume $m_x, m_y, \lambda_x, \lambda_y > 0$ in the following. Furthermore, ϵ describes a relative energy shift between the particle-like ($\sigma = 1$) and hole-like ($\sigma = \bar{1}$) bands, and μ denotes the chemical potential.

We now proceed to describe the full TI bilayer as shown in Fig. 4.1. Relative to each other, the two TI layers are constructed such that edge states of the same spin polarization propagate in opposite directions for opposite layers. We furthermore account for tunneling between the two layers by a simple spin-conserving tunneling element. Finally, the two layers are proximitized by a top and a bottom s-wave superconductor such that the phase difference between them is π. This could, for example, be achieved by placing a layer of randomly

[1] We note that while Eq. (4.1) presents a rather simple toy model, the main conclusions of the following sections – in particular regarding the existence of the MCSs – remain unaltered if more elaborate corrections to the BHZ Hamiltonian are taken into account as long as these remain small enough compared to the other energy scales in the system.

oriented magnetic impurities between one of the layers and the neighboring superconductor [16, 46, 47]. Alternatively, a superconducting loop connecting the two superconductors allows one to tune the phase difference by varying the enclosed magnetic flux [48–50]. The total Hamiltonian can now be written as $H = \frac{1}{2}\sum_{\mathbf{k}} \Psi_{\mathbf{k}}^\dagger \mathcal{H}(\mathbf{k}) \Psi_{\mathbf{k}}$ in the basis $\Psi_{\mathbf{k}} = (\phi_{\mathbf{k}}, \phi_{-\mathbf{k}}^\dagger)$ with $\phi_{\mathbf{k}} = (\psi_{\mathbf{k}111}, \psi_{\mathbf{k}11\bar{1}}, \psi_{\mathbf{k}1\bar{1}1}, \psi_{\mathbf{k}1\bar{1}\bar{1}}, \psi_{\mathbf{k}\bar{1}11}, \psi_{\mathbf{k}\bar{1}1\bar{1}}, \psi_{\mathbf{k}\bar{1}\bar{1}1}, \psi_{\mathbf{k}\bar{1}\bar{1}\bar{1}})$, where the electron destruction (creation) operator $\psi_{\mathbf{k}\tau\sigma s}$ ($\psi_{\mathbf{k}\tau\sigma s}^\dagger$) now carries an additional subscript $\tau \in \{1, \bar{1}\}$ denoting the layer index. The Hamiltonian density is then given by

$$\begin{aligned}\mathcal{H}(\mathbf{k}) = &\left(\frac{\hbar^2 k_x^2}{2m_x} + \frac{\hbar^2 k_y^2}{2m_y} + \epsilon\right)\eta_z\sigma_z + \mu\eta_z \\ &+ \lambda_x k_x \tau_z \sigma_x s_z + \lambda_y k_y \eta_z \sigma_y + \Delta_{sc}\eta_y\tau_z s_y + \Gamma\eta_z\tau_x,\end{aligned} \tag{4.2}$$

where we have introduced additional Pauli matrices τ_i and η_i for $i \in \{x, y, z\}$ acting in layer and particle-hole space, respectively. The strength of the proximity-induced superconductivity is denoted by Δ_{sc}, while Γ denotes the strength of the interlayer tunneling.

The Hamiltonian given in Eq. (4.2) is time-reversal symmetric with $\mathcal{T} = is_y\mathcal{K}$ and particle-hole symmetric with $\mathcal{P} = \eta_x\mathcal{K}$, where $\mathcal{K}$ denotes the complex conjugation. As such, our model belongs to the symmetry class DIII [51]. Furthermore, our model has a twofold rotational symmetry around the z axis given by $U_\pi = e^{i\pi\eta_z s_z \sigma_z/2}$. Note that even in the isotropic case $m_x = m_y = m$ and $\lambda_x = \lambda_y = \lambda$, the presence of τ_z in the term proportional to λ_x breaks the usual fourfold rotational symmetry of the BHZ model given by $U_{\pi/2} = e^{i\pi\eta_z s_z(2\sigma_0 - \sigma_z)/4}$. This will turn out to be crucial to realize the second-order phase proposed in the following. However, for $\Gamma = 0$, we can define a generalized fourfold rotational symmetry $U'_{\pi/2} = e^{i\pi\eta_z\tau_z s_z(2\sigma_0 - \sigma_z)/4}$ such that $U'_{\pi/2}\mathcal{H}(k_x, k_y)[U'_{\pi/2}]^{-1} = \mathcal{H}(-k_y, k_x)$ in the isotropic case.

4.3 Edge states in the first-order phase

Let us first consider the case $\Delta_{sc} = \Gamma = 0$. In this case, our model simply corresponds to two decoupled copies of the BHZ model. Furthermore, we set $\mu = 0$ to simplify our analysis. The bulk spectrum is then given by

$$E_\pm(\mathbf{k}) = \pm\sqrt{\left(\frac{\hbar^2 k_x^2}{2m_x} + \frac{\hbar^2 k_y^2}{2m_y} + \epsilon\right)^2 + \lambda_x^2 k_x^2 + \lambda_y^2 k_y^2}. \tag{4.3}$$

We find that the bulk gap closes at $\mathbf{k} = 0$ for $\epsilon = 0$, separating a trivial phase for $\epsilon > 0$ from a topologically non-trivial TI phase for $\epsilon < 0$ [45]. In our case, the latter is characterized by the presence of one pair of counterpropagating helical edge states per layer.

The explicit form of these edge states is readily obtained by following the standard procedure of matching decaying eigenfunctions. Let us first focus on the edges along the x direction. For this, we consider a semi-infinite geometry such that the sample is finite along the y direction and infinite along the x direction. In this setting, k_x remains a good quantum number, while we replace k_y with $-i\partial_y$. For simplicity, we begin by solving for zero-energy eigenstates at $k_x = 0$ before perturbatively including linear contributions in k_x. Thus, we solve

$$\mathcal{H}(0, -i\partial_y) = \left(\epsilon - \frac{\hbar^2\partial_y^2}{2m_y}\right)\eta_z\sigma_z - i\lambda_y\partial_y\eta_z\sigma_y \tag{4.4}$$

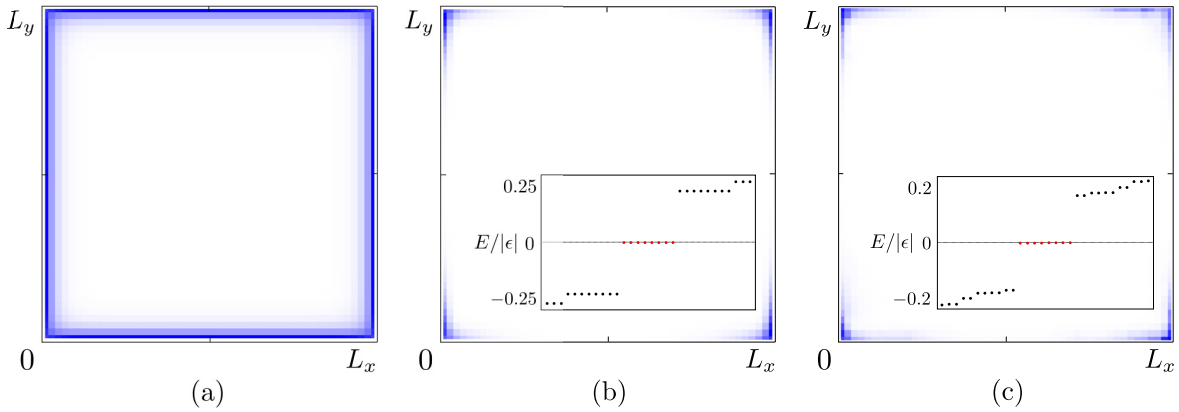

Figure 4.2: Probability density of low-energy states obtained numerically from a discretized version of Eq. (4.2), see Eq. (4.19). (a) For $\Delta_{sc} = \Gamma = 0$, we find gapless edge states running along the edges of a large but finite sample. In this case, our model simply corresponds to two decoupled 2D TIs with one Kramers pair of counterpropagating edge states per layer. (b) A Kramers pair of MCSs is localized at each of the four corners of the system for $|\Gamma| > |\Delta_{sc}|$. The inset demonstrates that the energies of these states (red dots) are indeed at zero. Here, we use $\Delta_{sc}/|\epsilon| \approx 0.31$ and $\Gamma/|\epsilon| \approx 0.63$. (c) The corner states are robust against potential disorder as long as the edge gap remains open. Here, we take the local fluctuations in the chemical potential to follow a normal distribution centered around the mean value $\mu = 0$ with standard deviation $\bar{\sigma}_\mu/|\epsilon| \approx 1.13$. The numerical lattice parameters are $t_x/|\epsilon| = t_y/|\epsilon| = 1.25$, $\alpha_x/|\epsilon| = \alpha_y/|\epsilon| = 1$, and $L_x = L_y = 50$ sites, with the definition of the discretized model and its parameters given in Appendix 4.A.

for exponentially decaying eigenfunctions $\Phi(y)$ with vanishing boundary conditions $\Phi(y = 0) = 0$. As both the layer index as well as the spin-projection along the z axis are good quantum numbers, we can express our solutions as eigenstates of τ_z and s_z. Furthermore, since $\{\mathcal{H}(0, -i\partial_y), \sigma_x\} = 0$ and we are looking for zero-energy eigenstates, the solutions are also eigenstates of σ_x. Therefore, we can write the solutions in terms of eigenstates $|\tau, s, a\rangle$ defined via $\tau_z s_z \sigma_x |\tau, s, a\rangle = \tau s a |\tau, s, a\rangle$, where $a \in \{1, \bar{1}\}$ is used to denote the eigenvalue of σ_x. Explicitly, we find that the solutions are given by

$$\Phi^x_{\tau s}(y) = |\tau, s, 1\rangle (e^{-y/\xi_1} - e^{-y/\xi_2}) \tag{4.5}$$

with $\xi_{1/2} = (-\lambda_y \pm \sqrt{\beta_y})/(2\epsilon)$ for $\beta_y = \lambda_y^2 + 2\hbar^2\epsilon/m_y$ and where we have suppressed a normalization factor. Note that since $\epsilon < 0$ in the topologically non-trivial phase, we have $\mathrm{Re}(\xi_{1/2}) > 0$, confirming that our solutions are indeed exponentially localized to the edge of the system. Furthermore, it is straightforward to see that the solutions are related by time-reversal symmetry as $\mathcal{T}\Phi^x_{\tau s}(y) = \bar{s}\Phi^x_{\tau \bar{s}}(y)$.

For the edges along the y direction, a similar consideration yields

$$\mathcal{H}(-i\partial_x, 0) = \left(\epsilon - \frac{\hbar^2\partial_x^2}{2m_x}\right)\eta_z\sigma_z - i\lambda_x\partial_x\tau_z s_z\sigma_x. \tag{4.6}$$

In this case, the solutions for the edge states turn out to be eigenstates of τ_z, s_z, and σ_y. Therefore, we will write them in terms of eigenstates $|\tau, s, b\rangle$ defined via $\tau_z s_z \sigma_y |\tau, s, b\rangle =$

$\tau s b|\tau, s, b\rangle$, where $b \in \{1, \bar{1}\}$ is used to denote the eigenvalue of σ_y. We arrive at

$$\Phi^y_{\tau s}(x) = |\tau, s, \tau s\rangle (e^{-x/\xi'_1} - e^{-x/\xi'_2}) \tag{4.7}$$

with $\xi'_{1/2} = (-\lambda_x \pm \sqrt{\beta_x})/(2\epsilon)$ for $\beta_x = \lambda_x^2 + 2\hbar^2\epsilon/m_x$ and where we have again omitted a normalization factor.

Finally, the kinetic term governing the low-energy spectrum can be found by taking into account the linear terms in k_x or k_y, respectively. Along the x direction, we find that

$$\lambda_x k_x \langle \Phi^x_{\tau s}|\tau_z\sigma_x s_z|\Phi^x_{\tau' s'}\rangle = \tau s \lambda_x k_x \delta_{\tau\tau'}\delta_{ss'}. \tag{4.8}$$

Indeed, the structure of the edge states given in Eq. (4.5) makes it immediately clear that states with $\tau s = +1$ ($\tau s = -1$) propagate in the positive (negative) x direction. Similarly, we find that

$$\lambda_y k_y \langle \Phi^y_{\tau s}|\sigma_y|\Phi^y_{\tau' s'}\rangle = \tau s \lambda_y k_y \delta_{\tau\tau'}\delta_{ss'} \tag{4.9}$$

along the y direction. Again, states with $\tau s = +1$ ($\tau s = -1$) propagate in the positive (negative) y direction. As expected, we therefore find a pair of counterpropagating gapless edge states per layer, see also Fig. 4.2(a) for a numerical verification. Within each layer, counterpropagating edge states carry opposite spin projections, while counterpropagating edge states in opposite layers carry the same spin projection.

4.4 Kramers pairs of Majorana corner states

In the following, we take into account the effects of superconductivity and interlayer tunneling in a perturbative way. For this, we assume Δ_{sc} and Γ to be small compared to the bulk gap of the first-order phase, such that their only effect will be to potentially gap out the edge states found above. In order to understand the emergence of corner states, we derive an effective Hamiltonian describing the low-energy edge physics for each edge.

Let us start by considering the tunneling term $\mathcal{H}_\Gamma = \Gamma\eta_z\tau_x$, while keeping $\Delta_{sc} = 0$ for the moment. For the edge states along the x direction, we obtain by direct calculation

$$\langle \Phi^x_{\tau s}|\mathcal{H}_\Gamma|\Phi^x_{\tau' s'}\rangle = \Gamma\delta_{\bar{\tau}\tau'}\delta_{ss'}. \tag{4.10}$$

As such, the tunneling term fully gaps out the edge states along the x direction.[2] Along the y direction, however, we obtain

$$\langle \Phi^y_{\tau s}|\mathcal{H}_\Gamma|\Phi^y_{\tau' s'}\rangle = 0 \tag{4.11}$$

for all τ, τ', s, and s', which may seem surprising at first. However, this is a direct consequence of the symmetries of the system. Indeed, we note that the system has an additional symmetry $\mathcal{O} = \tau_z\sigma_y$ that anticommutes with the Hamiltonian given in Eq. (4.6). Furthermore, we find $\mathcal{O}|\Phi^y_{\tau s}\rangle = s|\Phi^y_{\tau s}\rangle$. Together with $\{\mathcal{H}_{\text{tun}}, \mathcal{O}\} = 0$, we then find $\langle \Phi^y_{\tau s}|\mathcal{H}_\Gamma|\Phi^y_{\bar{\tau} s}\rangle = -\langle \Phi^y_{\tau s}|\mathcal{H}_\Gamma|\Phi^y_{\bar{\tau} s}\rangle = 0$. The other matrix elements are trivially zero by the definition of $\mathcal{H}_\Gamma$, which confirms Eq. (4.11).

[2] The twofold rotational symmetry of the model ensures that this is indeed the case for *both* edges along the x direction.

Let us now additionally consider the effect of superconductivity. Clearly, superconductivity will open a gap along all edges, leading to an effective edge Hamiltonian of the form

$$H^x_{\text{eff}}(k_x) = \lambda_x k_x \tau_z s_z + \Gamma \eta_z \tau_x + \Delta_{sc} \eta_y \tau_z s_y \tag{4.12}$$

for the edges along the x direction and

$$H^y_{\text{eff}}(k_y) = \lambda_y k_y \tau_z s_z + \Delta_{sc} \eta_y \tau_z s_y \tag{4.13}$$

for the edges along the y direction. From this it becomes clear that as long as $|\Delta_{sc}| > 0$, the edges along the y direction are trivially gapped by superconductivity. Along the x direction, on the other hand, the edge gap closes at $|\Delta_{sc}| = |\Gamma|$. Indeed, we recognize Eq. (4.12) to be the Hamiltonian of a time-reversal invariant 1D TSC as discussed in Ref. [9]. This system hosts a Kramers pair of Majorana bound states at domain walls separating a topological phase with $|\Gamma| > |\Delta_{sc}|$ from a trivial phase. In our model, these domain walls appear at the corners between x and y edges, leaving us with a Kramers pair of MCSs at all four corners of a rectangular sample. In Fig. 4.2(b), we have verified the existence of the corner states numerically. Furthermore, we have tested the stability of the corner states against potential disorder, see Fig. 4.2(c). In particular, we note that the symmetry $\mathcal{O}$ used to derive the corner states can be broken as long as the edge gap remains open. Indeed, the MCSs are protected solely by particle-hole and time-reversal symmetry and do not rely on any additional spatial symmetry.

4.5 Unequal tunneling amplitudes for particle-like and hole-like bands

In realistic setups we generally expect the interlayer tunneling amplitude for the particle-like and hole-like bands to be different in size. This constitutes an obstruction to the second-order topological phase presented here. In the following, we account for this by introducing a refined tunneling Hamiltonian

$$\mathcal{H}_\Gamma = \frac{\Gamma_e + \Gamma_h}{2} \eta_z \tau_x + \frac{\Gamma_e - \Gamma_h}{2} \eta_z \tau_x \sigma_z, \tag{4.14}$$

where Γ_e (Γ_h) is used to denote the tunneling amplitude for electrons (holes). Calculating the effective Hamiltonian along the x and y direction using the edge state solutions given in Eqs. (4.5) and (4.7), we find

$$H^x_{\text{eff}}(k_x) = \lambda_x k_x \tau_z s_z + \frac{\Gamma_e + \Gamma_h}{2} \eta_z \tau_x + \Delta_{sc} \eta_y \tau_z s_y \tag{4.15}$$

for the edges along the x direction and

$$H^y_{\text{eff}}(k_y) = \lambda_y k_y \tau_z s_z + \frac{\Gamma_e - \Gamma_h}{2} \eta_z \tau_x + \Delta_{sc} \eta_y \tau_z s_y \tag{4.16}$$

for the edges along the y direction. We therefore find that the SOTSC phase persists if $|\Gamma_e - \Gamma_h| < 2|\Delta_{sc}| < |\Gamma_e + \Gamma_h|$ or $|\Gamma_e + \Gamma_h| < 2|\Delta_{sc}| < |\Gamma_e - \Gamma_h|$.

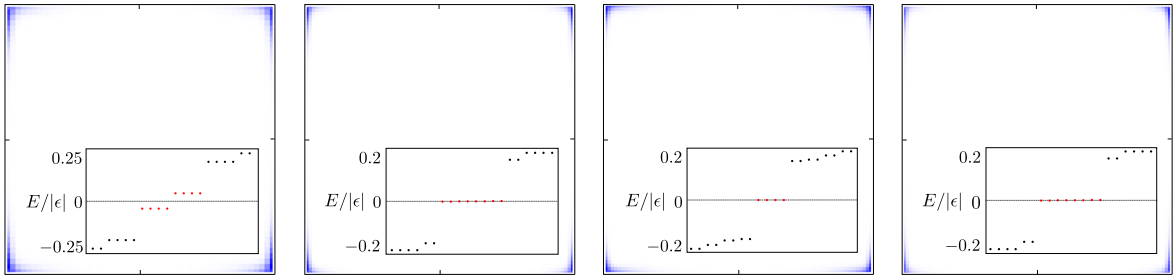

(a) (b) (c) (d)

Figure 4.3: (a) Probability density of low-energy states obtained numerically from a discretized version of Eq. (4.2) for a sample of 50×50 sites with $\Delta_{sc}/|\epsilon| \approx 0.31$ and $\Gamma/|\epsilon| \approx 0.63$ and in the additional presence of an out-of-plane Zeeman field of strength $\Delta_{Z,\perp}/|\epsilon| \approx 0.04$. We find that the two Kramers partners of MCSs at each corner hybridize and split away from zero energy, see the red dots in the inset. (b)-(d) Probability density of the lowest-energy state obtained numerically from a discretized version of Eq. (4.2) for a sample of $L_x = L_y = 80$ sites in the additional presence of an in-plane Zeeman field oriented along the x direction. (b) For a weak Zeeman field $0 \leq \Delta_{Z,||} < \Gamma - \Delta_{sc}$, there are two MCSs per corner. Here, we have used $\Delta_{sc}/|\epsilon| = 0.25$, $\Gamma/|\epsilon| = 0.5$ and $\Delta_{Z,||}/|\epsilon| \approx 0.13$. (c) In the intermediate regime $|\Gamma - \Delta_{sc}| < \Delta_{Z,||} < \Gamma + \Delta_{sc}$, we find one MCS per corner. Here, we have used $\Delta_{sc}/|\epsilon| = \Gamma/|\epsilon| \approx 0.38$ and $\Delta_{Z,||}/|\epsilon| \approx 0.19$. (d) For strong Zeeman fields $\Gamma + \Delta_{sc} < \Delta_{Z,||}$, we again find two MCSs per corner. Here, we have used $\Delta_{sc}/|\epsilon| = 0.25$, $\Gamma/|\epsilon| \approx 0.13$ and $\Delta_{Z,||}/|\epsilon| = 0.5$. The other numerical parameters are the same as in Fig. 4.2.

Studies of HgTe double quantum well structures have estimated Γ_h to be negligibly small compared to Γ_e in the experimentally accessible parameter range, i.e., $\Gamma_h \approx 0$ [52–54]. This excludes the double-well setup as a possible realization of the topological phase proposed here. However, other systems with similar low-energy properties may circumvent this issue. In particular, mono- and few-layer $Fe(Te_{1-x}Se_x)$ have recently been claimed to exhibit a low-energy band structure described by the BHZ Hamiltonian [55]. Similarly, the 2D transition metal dichalchogenides (TMDCs) MX_2 with $M \in \{W, Mo\}$ and $X \in \{S, Se, Te\}$ have been shown to exhibit the desired low-energy effective band structure [56]. It would therefore be interesting to investigate TI bilayers built from these materials as potential experimental realizations of the SOTSC proposed in this work.

4.6 Effect of Zeeman field and single-MCS phase

In this section, we additionally comment on the effects of a Zeeman field, which we again assume to be sufficiently weak compared to the bulk gap of the first-order phase. Since time-reversal symmetry is now broken, the fate of the MCSs is not a priori clear in this case. Indeed, we find that in the presence of an out-of-plane Zeeman term $\mathcal{H}_{Z,\perp} = \Delta_{Z,\perp}\eta_z s_z$, the Kramers pairs at each corner hybridize and split away from zero energy, see Fig. 4.3(a). Thus, the topological phase is destroyed in this case. On the other hand, however, we find that an in-plane Zeeman field does not completely destroy the topological properties of the system, but instead leads to a much richer phase diagram exhibiting two nonequivalent regions with

two MCSs per corner as well as an intermediate region with just one MCS per corner. For concreteness, let us consider the case when the in-plane field is oriented along the x direction, i.e., $\mathcal{H}_{Z,||} = \Delta_{Z,||}\eta_z s_x$. Other orientations of the in-plane Zeeman field lead to qualitatively identical results. Note that here we take the Zeeman field to be of equal strength for both the particle-like and the hole-like bands. Depending on the experimental realization, one may again need to generalize this in a way similar to the treatment of unequal tunneling amplitudes in Sec. 4.5. Calculating again the effective edge Hamiltonian, we find that

$$H^x_{\text{eff}}(k_x) = \lambda_x k_x \tau_z s_z + \Gamma \eta_z \tau_x + \Delta_{sc} \eta_y \tau_z s_y + \Delta_{Z,||} \eta_z s_x, \tag{4.17}$$

while the effective edge Hamiltonian along the y direction is still given by Eq. (4.13). Therefore, the edges along the y direction remain trivially gapped by superconductivity, whereas the edge gap along the x direction now closes at $\Delta_{Z,||} + \Gamma = \pm\Delta_{sc}$ and $\Delta_{Z,||} - \Gamma = \pm\Delta_{sc}$.

In the following, we comment on the different (second-order) topological phases separated by the above gap closing lines. For simplicity, we assume that $\Delta_{sc}, \Delta_{Z,||}, \Gamma \geq 0$. Firstly, we have checked numerically that for $0 < \Delta_{Z,||} < \Gamma - \Delta_{sc}$, the two MCSs per corner remain intact, see Fig. 4.3(b). However, they are now no longer protected by time-reversal symmetry and may split away from zero energy in the presence of magnetic disorder [57–60]. Secondly, we find that in the intermediate regime $|\Gamma - \Delta_{sc}| < \Delta_{Z,||} < \Gamma + \Delta_{sc}$, there is only one MCS per corner, see Fig. 4.3(c). Most interestingly, we find that for $\Gamma = \Delta_{sc}$ even an infinitesimal Zeeman field can drive the system into a SOTSC phase with one MCS per corner, as the competing tunneling and superconducting terms completely cancel each other. Finally, for $\Gamma + \Delta_{sc} < \Delta_{Z,||}$, we again find two MCSs per corner, see Fig. 4.3(d). Indeed, this regime is in the same region of the phase diagram as the limit $\Gamma = 0$ and $\Delta_{sc} < \Delta_{Z,||}$. In this case, we simply deal with two decoupled TI layers subjected to an in-plane Zeeman field. Indeed, a single TI layer in the presence of an in-plane Zeeman field has been shown to exhibit a SOTSC phase in Ref. [38]. To summarize, Fig. 4.4 displays the phase diagram of our system both in the absence [Fig. 4.4(a)] and presence [Fig. 4.4(b)] of an in-plane Zeeman field.

It is worth noting that another way to break time-reversal symmetry is by detuning the superconducting phase difference away from π. In this case, the superconducting term entering in Eq. (4.2) takes the more general form

$$\mathcal{H}_{sc} = \frac{\Delta_{sc}}{2}[(1+\tau_z)\eta_y s_y + (1-\tau_z)(\cos\phi\, \eta_y s_y - \sin\phi\, \eta_x s_y)], \tag{4.18}$$

where $\phi = \pi$ reproduces the time-reversal invariant case discussed above. For deviations from $\phi = \pi$, we find that the MCSs at each corner hybridize and split away from zero energy. However, similarly as in Ref. [9], we can exploit the interplay between a detuning of the superconducting phase difference and an out-of-plane Zeeman field to bring the corner states at a given corner back to zero energy. This is illustrated in Fig. 4.5. In particular, we note that this mechanism provides us with a way to go from a phase with zero-energy corner states at all four corner of the sample to a phase with zero-energy corner states only at two opposite corners of the sample.

Finally, let us mention that also the fermion parity pumping effect discussed in Ref. [9] can be observed in our system when the superconducting phase difference is adiabatically varied from 0 to 2π. This follows immediately from the fact that, in the low-energy limit, our system is nothing but two copies of the 1D system considered in Ref. [9] separated by two

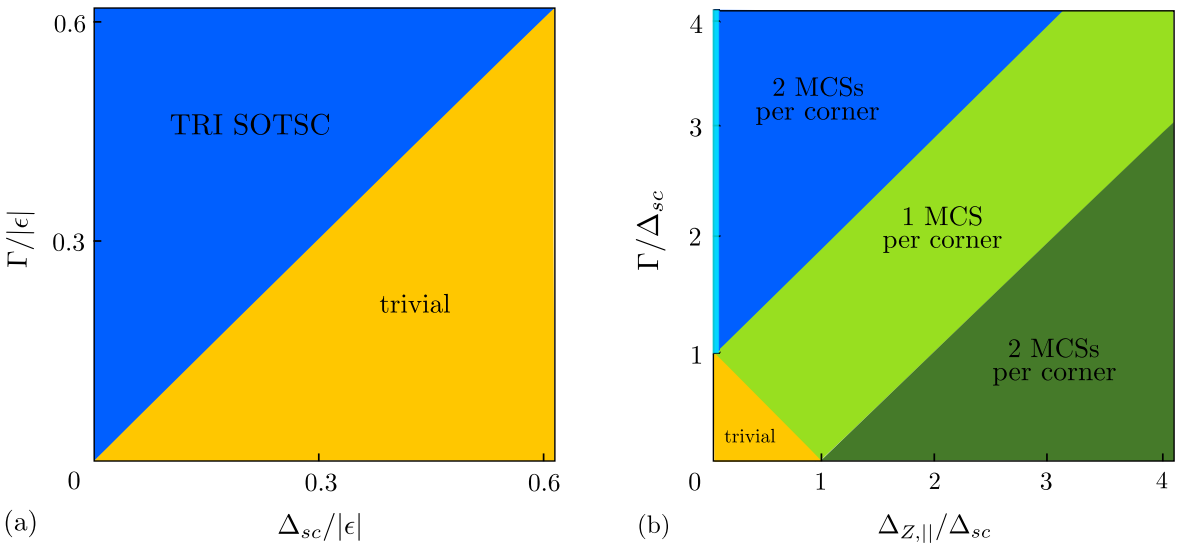

Figure 4.4: (a) Phase diagram of the time-reversal invariant system discussed in Sec. 4.4 as a function of Γ and Δ_{sc}. Note that we focus on the regime where both Γ and Δ_{sc} are sufficiently small compared to the bulk gap of the first-order phase such that our pertubative treatment of these terms is justified. We find that the edge gap closes and reopens for $\Gamma = \Delta_{sc}$, corresponding to the phase transition between the topologically trivial phase (shaded in yellow) and the SOTSC phase with a Kramers pair of MCSs per corner (shaded in dark blue). (b) In the presence of an in-plane Zeeman field, the phase diagram becomes even richer. For a weak Zeeman field $0 \leq \Delta_{Z,||} < \Gamma - \Delta_{sc}$, there are two MCSs per corner. The light blue line with $\Delta_{Z,||} = 0$ denotes the time-reversal invariant SOTSC phase discussed in Sec. 4.4, where the two MCSs at each corner are protected by time-reversal symmetry. For $0 < \Delta_{Z,||} < \Gamma - \Delta_{sc}$, see the region shaded in dark blue, the two MCSs per corner remain intact. However, they are now no longer protected by time-reversal symmetry and may split away from zero energy in the presence of disorder. In the intermediate regime $|\Gamma - \Delta_{sc}| < \Delta_{Z,||} < \Gamma + \Delta_{sc}$, see the region shaded in light green, we instead find that there is only one MCS per corner. Most interestingly, we find that for $\Gamma = \Delta_{sc}$ even an infinitesimal Zeeman field can drive the system into a SOTSC phase with one MCS per corner, as the competing tunneling and superconducting terms completely cancel each other. Finally, for $\Gamma + \Delta_{sc} < \Delta_{Z,||}$ (shaded in dark green), we again find two MCSs per corner. Indeed, this regime can be connected to the limit $\Gamma = 0$ and $\Delta_{sc} < \Delta_{Z,||}$. In this case, we simply deal with two independent copies of the system proposed in Ref. [38].

topologically trivial regions. For the single-MCS phase, on the other hand, we find that the MCSs persist for a finite range of phase detunings up to a critical value at which the edge gaps close.

4.7 Conclusions

We have proposed a versatile and experimentally feasible platform that realizes a 2D time-reversal invariant SOTSC phase hosting Kramers pairs of MCSs. Our setup consists of two

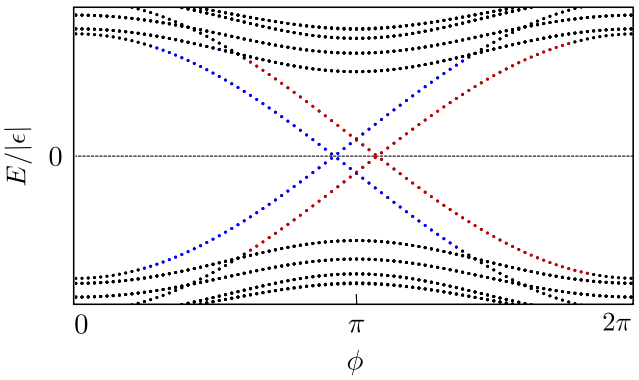

Figure 4.5: Energy spectrum obtained numerically from a discretized version of Eq. (4.2) for a sample of $L_x = L_y = 50$ sites in the presence of an out-of-plane Zeeman field of strength $\Delta_{Z,\perp}/|\epsilon| \approx 0.04$ and for a varying superconducting phase difference ϕ. The finite out-of-plane Zeeman field shifts the corner states away from zero energy at $\phi = \pi$, see also Fig. 4.3(a). However, by changing the superconducting phase away from $\phi = \pi$, the corner states at a given corner can be brought back to zero energy. The red (blue) lines are two-fold degenerate and correspond to the upper right and lower left (upper left and lower right) corners. The other numerical parameters are the same as in Fig. 4.2.

tunnel-coupled 2D TIs proximitized by a top and bottom s-wave superconductor with a phase difference of π between them. In the regime where the interlayer tunneling dominates over the proximity-induced superconductivity, we find a Kramers pair of MCSs at all four corners of a rectangular sample. Additionally, we have shown that a weak but finite in-plane Zeeman field further enriches the phase diagram. In particular, we find that there are now two nonequivalent SOTSC phases with two MCSs per corner as well as an intermediate phase with just one MCS per corner. Most interestingly, this single-MCS phase is accessible even for very weak Zeeman fields if the tunneling and superconducting term are of comparable strength. As the requirement of a strong magnetic field in combination with superconductivity is experimentally problematic, our proposal constitutes an interesting alternative route towards the realization of a single-MCS SOTSC phase that is accessible even for weak magnetic fields.

Acknowledgments. This work was supported by the Swiss National Science Foundation and NCCR QSIT. This project received funding from the European Union's Horizon 2020 research and innovation program (ERC Starting Grant, grant agreement No 757725).

4.A Lattice model for the BHZ Hamiltonian

In this Appendix, we present the discretized version of the Hamiltonian given in Eq. (4.2). In momentum space, the discretized Hamiltonian reads

$$\begin{aligned}\mathcal{H}(\mathbf{k}) = &[-2t_x\cos(k_x a_x) - 2t_y\cos(k_y a_y)]\eta_z\sigma_z + (\epsilon + 2t_x + 2t_y)\eta_z\sigma_z + \mu\eta_z \\ &+ 2\alpha_x\sin(k_x a_x)\tau_z\sigma_x s_z + 2\alpha_y\sin(k_y a_y)\eta_z\sigma_y + \Delta_{sc}\eta_y\tau_z s_y + \Gamma\eta_z\tau_x. \end{aligned} \tag{4.19}$$

Here, a_x (a_y) is the lattice spacing along the x (y) direction. The spin-conserving hopping amplitude t_x (t_y) defines the effective mass along the x (y) direction via $t_x = \hbar^2/(2m_x a_x^2)$ [$t_y = \hbar^2/(2m_y a_y^2)$]. Similarly, α_x (α_y) is related to λ_x (λ_y) via $\alpha_x = \lambda_x/(2a_x)$ [$\alpha_y = \lambda_y/(2a_y)$] [61].

Note that in the main part of our work, we focus on the isotropic case $t_x = t_y = t$ and $\alpha_x = \alpha_y = \alpha$. The strongly anisotropic case could, for example, be realized in the coupled-wire approach [62–73].

Bibliography

[1] A. Y. Kitaev, Phys. Usp. **44**, 131 (2001).

[2] R. M. Lutchyn, E. P. A. M. Bakkers, L. P. Kouwenhoven, P. Krogstrup, C. M. Marcus, and Y. Oreg, Nat. Rev. Mater. **3**, 52 (2018).

[3] E. Prada, P. San-Jose, M. W. A. de Moor, A. Geresdi, E. J. H. Lee, J. Klinovaja, D. Loss, J. Nygård, R. Aguado, and L. P. Kouwenhoven, Nat. Rev. Phys. **2**, 575 (2020).

[4] L. Fu and C. L. Kane, Phys. Rev. Lett. **100**, 096407 (2008).

[5] X. L. Qi, T. L. Hughes, S. Raghu, and S. C. Zhang, Phys. Rev. Lett. **102**, 187001 (2009).

[6] M. Sato and S. Fujimoto, Phys. Rev. B **79**, 094504 (2009).

[7] C. L. M. Wong and K. T. Law, Phys. Rev. B **86**, 184516 (2012).

[8] F. Zhang, C. L. Kane, and E. J. Mele, Phys. Rev. Lett. **111**, 056402 (2013).

[9] A. Keselman, L. Fu, A. Stern, and E. Berg, Phys. Rev. Lett. **111**, 116402 (2013).

[10] S. Nakosai, J. C. Budich, Y. Tanaka, B. Trauzettel, and N. Nagaosa, Phys. Rev. Lett. **110**, 117002 (2013).

[11] J. Klinovaja and D. Loss, Phys. Rev. B **90**, 045118 (2014).

[12] A. Haim, A. Keselman, E. Berg, and Y. Oreg, Phys. Rev. B **89**, 220504(R) (2014).

[13] E. Gaidamauskas, J. Paaske, and K. Flensberg, Phys. Rev. Lett. **112**, 126402 (2014).

[14] J. Klinovaja, A. Yacoby, and D. Loss, Phys. Rev. B **90**, 155447 (2014).

[15] E. Dumitrescu, J. D. Sau, and S. Tewari, Phys. Rev. B **90**, 245438 (2014).

[16] C. Schrade, A. A. Zyuzin, J. Klinovaja, and D. Loss, Phys. Rev. Lett. **115**, 237001 (2015).

[17] A. Haim, K. Wölms, E. Berg, Y. Oreg, and K. Flensberg, Phys. Rev. B **94**, 115124 (2016).

[18] H. Ebisu, B. Lu, J. Klinovaja, and Y. Tanaka, Prog. Theor. Exp. Phys. **2016**, 083I01 (2016).

[19] C. Schrade, M. Thakurathi, C. Reeg, S. Hoffman, J. Klinovaja, and D. Loss, Phys. Rev. B **96**, 035306 (2017).

[20] C.-H. Hsu, P. Stano, J. Klinovaja, and D. Loss, Phys. Rev. Lett. **121**, 196801 (2018).

[21] Y. Volpez, D. Loss, and J. Klinovaja, Phys. Rev. Res. **2**, 023415 (2020).

[22] M. Thakurathi, P. Simon, I. Mandal, J. Klinovaja, and D. Loss, Phys. Rev. B **97**, 045415 (2018).

[23] A. A. Aligia and L. Arrachea, Phys. Rev. B **98**, 174507 (2018).

[24] W. A. Benalcazar, B. A. Bernevig, and T. L. Hughes, Science **357**, 61 (2017).

[25] W. A. Benalcazar, B. A. Bernevig, and T. L. Hughes, Phys. Rev. B **96**, 245115 (2017).

[26] Z. Song, Z. Fang, and C. Fang, Phys. Rev. Lett. **119**, 246402 (2017).

[27] Y. Peng, Y. Bao, and F. von Oppen, Phys. Rev. B **95**, 235143 (2017).

[28] S. Imhof, C. Berger, F. Bayer, H. Brehm, L. Molenkamp, T. Kiessling, F. Schindler, C. H. Lee, M. Greiter, T. Neupert, and R. Thomale, Nat. Phys. **14**, 925 (2018).

[29] M. Geier, L. Trifunovic, M. Hoskam, and P. W. Brouwer, Phys. Rev. B **97**, 205135 (2018).

[30] F. Schindler, A. M. Cook, M. G. Verginory, Z. Wang, S. S. P. Parking, B. A. Bernevig, and T. Neupert, Science Adv. **4**, 6 (2018).

[31] T. Liu, J. J. He, and F. Nori, Phys. Rev. B **98**, 245413 (2018).

[32] Z. Yan, Phys. Rev. Lett. **123**, 177001 (2019).

[33] Y. Volpez, D. Loss, and J. Klinovaja, Phys. Rev. Lett. **122**, 126402 (2019).

[34] R.-X. Zhang, W. S. Cole, and S. Das Sarma, Phys. Rev. Lett. **122**, 187001 (2019).

[35] K. Laubscher, D. Loss, and J. Klinovaja, Phys. Rev. Res. **1**, 032017(R) (2019).

[36] S. Franca, D. V. Efremov, and I. C. Fulga, Phys. Rev. B **100**, 075415 (2019).

[37] K. Laubscher, D. Loss, and J. Klinovaja, Phys. Rev. Res. **2**, 013330 (2020).

[38] Y.-J. Wu, J. Hou, Y.-M. Li, X.-W. Luo, X. Shi, and C. Zhang, Phys. Rev. Lett. **124**, 227001 (2020).

[39] K. Plekhanov, M. Thakurathi, D. Loss, and J. Klinovaja, Phys. Rev. Res. **1**, 032013(R) (2019).

[40] S. A. A. Ghorashi, X. Hu, T. L. Hughes, and E. Rossi, Phys. Rev. B **100**, 020509(R) (2019).

[41] S. A. A. Ghorashi, T. L. Hughes, and E. Rossi, Phys. Rev. Lett. **125**, 037001 (2020).

[42] J. Ahn and B.-J. Yang, Phys. Rev. Research **2**, 012060(R) (2020).

[43] Q. Wang, C.-C. Liu, Y.-M. Lu, and F. Zhang, Phys. Rev. Lett. **121**, 186801 (2018).

[44] Z. Yan, F. Song, and Z. Wang, Phys. Rev. Lett. **121**, 096803 (2018).

[45] B. A. Bernevig, T. L. Hughes, and S.-C. Zhang, Science **314**, 1757 (2006).

[46] J. A. van Dam, Y. V. Nazarov, E. P. A. M. Bakkers, and L. P. Kouwenhoven, Nature (London) **442**, 667 (2006).

[47] O. Vavra, S. Gazi, D. S. Golubovic, I. Vavra, J. Derer, J. Verbeeck, G. Van Tendeloo, and V. V. Moshchalkov, Phys. Rev. B **74**, 020502(R) (2006).

[48] J. Shabani, M. Kjaergaard, H. J. Suominen, Y. Kim, F. Nichele, K. Pakrouski, T. Stankevic, R. M. Lutchyn, P. Krogstrup, R. Feidenhans'l, S. Kraemer, C. Nayak, M. Troyer, C. M. Marcus, and C. J. Palmstrøm, Phys. Rev. B **93**, 155402 (2016).

[49] H. Ren, F. Pientka, S. Hart, A. Pierce, M. Kosowsky, L. Lunczer, R. Schlereth, B. Scharf, E. M. Hankiewicz, L. W. Molenkamp, B. I. Halperin, and A. Yacoby, Nature **569**, 93 (2019).

[50] A. Fornieri, A. M. Whiticar, F. Setiawan, E. P. Martin, A. C. C. Drachmann, A. Keselman, S. Gronin, C. Thomas, T. Wang, R. Kallaher, G. C. Gardner, E. Berg, M. J. Manfra, A. Stern, C. M. Marcus, and F. Nichele, Nature **569**, 89 (2019).

[51] S. Ryu, A. P. Schnyder, A. Furusaki, and A. W. W. Ludwig, New J. Phys. **12**, 065010 (2010).

[52] S. S. Krishtopenko, W. Knap, and F. Teppe, Sci. Rep. **6**, 30755 (2016).

[53] P. Michetti, J. C. Budich, E. G. Novik, and P. Recher, Phys. Rev. B **85**, 125309 (2012).

[54] P. Michetti and B. Trauzettel, Appl. Phys. Lett. **102**, 063503 (2013).

[55] X. Wu, S. Qin, Y. Liang, H. Fan, and J. Hu, Phys. Rev. B **93**, 115129 (2016).

[56] X. Qian, J. Liu, L. Fu, and J. Li, Science **346**, 1344 (2014).

[57] C.-H. Hsu, P. Stano, J. Klinovaja, and D. Loss, Phys. Rev. B **92**, 235435 (2015).

[58] C. Reeg, C. Schrade, J. Klinovaja, and D. Loss, Phys. Rev. B **96**, 161407(R) (2017).

[59] S. Hoffman, J. Klinovaja, and D. Loss, Phys. Rev. B **93**, 165418 (2016).

[60] O. Dmytruk, M. Thakurathi, D. Loss, and J. Klinovaja, Phys. Rev. B **99**, 245416 (2019).

[61] Y. Volpez, D. Loss, and J. Klinovaja, Phys. Rev. B **97**, 195421 (2018).

[62] D. Poilblanc, G. Montambaux, M. Héritier, and P. Lederer, Phys. Rev. Lett. **58**, 270 (1987).

[63] L. P. Gorkov and A. G. Lebed, Phys. Rev. B **51**, 3285 (1995).

[64] T. Meng, T. Neupert, M. Greiter, R. Thomale, Phys. Rev. B **91**, 241106(R) (2015).

[65] J. C. Y. Teo and C. L. Kane, Phys. Rev. B **89**, 085101 (2014).

[66] J. Klinovaja and Y. Tserkovnyak, Phys. Rev. B **90**, 115426 (2014).

[67] J. Klinovaja and D. Loss, Eur. Phys. J. B **87**, 171 (2014).

[68] E. Sagi and Y. Oreg, Phys. Rev. B **90**, 201102(R) (2014).

[69] T. Neupert, C. Chamon, C. Mudry, and R. Thomale, Phys. Rev. B **90**, 205101 (2014).

[70] J. Klinovaja, Y. Tserkovnyak, and D. Loss, Phys. Rev. B **91**, 085426 (2015).

[71] E. Sagi and Y. Oreg, Phys. Rev. B **92**, 195137 (2015).

[72] T. Meng, Phys. Rev. B **92**, 115152 (2015).

[73] S. Sahoo, Z. Zhang, and J. C. Y. Teo, Phys. Rev. B **94**, 165142 (2016).

Chapter 5

Fractional second-order topological insulator from a three-dimensional coupled-wires construction

Adapted from:
K. Laubscher, P. Keizer, and J. Klinovaja,
"Fractional second-order topological insulator from a three-dimensional coupled-wires construction,"
arXiv preprint arXiv:2207.04026 (2022)

We construct a three-dimensional second-order topological insulator with gapless helical hinge states from an array of weakly tunnel-coupled Rashba nanowires. For suitably chosen interwire tunnelings, we demonstrate that the system has a fully gapped bulk as well as fully gapped surfaces, but hosts a Kramers pair of gapless helical hinge states propagating along a path of hinges that is determined by the hierarchy of interwire tunnelings and the boundary termination of the system. Furthermore, the coupled-wires approach allows us to incorporate electron-electron interactions into our description. At suitable filling factors of the individual wires, we show that sufficiently strong electron-electron interactions can drive the system into a fractional second-order topological insulator phase with hinge states carrying only a fraction e/p of the electronic charge e for an odd integer p.

5.1 Introduction

Recently, the concept of so-called higher-order topological insulators (HOTIs) has significantly enriched the existing classification of topological phases of matter [1–8]. While a conventional d-dimensional topological insulator (TI) exhibits gapless boundary states at its $(d-1)$-dimensional boundaries, a d-dimensional nth-order TI hosts gapless states at its $(d-n)$-dimensional boundaries. Of particular interest in this context are second-order TIs, which host topologically protected zero-energy corner states (gapless hinge states) in two (three) dimensions [9–30]. Experiments have reported signatures of second-order TI phases in a few materials [31–36] as well as in various artificial structures based on, e.g., mechanical, phononic, photonic, or electrical systems [37–44].

While the original theory of HOTIs builds on single-particle band structure considerations, it is interesting to ask whether there are exotic interaction-driven HOTI phases that do not fit into this conventional picture. While this question has by now been answered affirmatively [45–53], concrete toy models for strongly interacting HOTI phases are still extremely rare since analytical tools to study interacting systems in more than one dimension are scarce. One way forward is offered by the so-called coupled-wires approach [54, 55], where a two-dimensional (2D) or three-dimensional (3D) system is modeled as an array of weakly coupled one-dimensional (1D) wires. This then allows for an analytical treatment of strong electron-electron interactions via the standard 1D bosonization formalism [56]. Models of coupled wires have been used with high success to study a variety of exotic interacting first-order topological phases, including, for example, fractional quantum Hall states [54,55,57–62], fractional TIs [63–68], or interacting topological superconductors [68–70]. As for HOTI phases, models for strongly interacting second-order topological superconductors in two dimensions [47,48,52] and certain classes of 3D second-order TIs protected by subsystem symmetries [49] have been

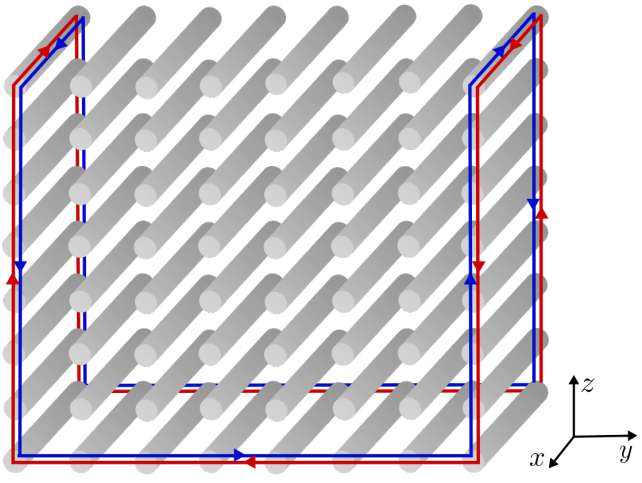

Figure 5.1: Cartoon of the coupled-wires model. The starting point is a 3D array of uncoupled Rashba nanowires (gray), which are taken to be aligned along the x axis. For suitable interwire couplings, the system is in a helical HOTI phase with a Kramers pair of gapless hinge states (shown in red and blue) propagating along a closed path of hinges.

brought forward. Nevertheless, a large variety of interacting HOTI phases do not yet have concrete realizations.

With this motivation, we construct a 3D coupled-wires model that is capable of realizing different second-order TI phases with gapless helical hinge states protected by time-reversal symmetry, see Fig. 5.1. For suitably chosen interwire couplings, the non-interacting system has a fully gapped bulk as well as fully gapped surfaces but hosts a Kramers pair of gapless helical hinge states propagating along a path of hinges that is determined by the hierarchy of interwire tunnelings and the boundary termination of the system. Furthermore, at fractional fillings and for sufficiently strong electron-electron interactions, the system can enter an exotic fractionalized phase with gapless helical hinge states that carry only a fraction of the electronic charge e. All of the HOTI phases constructed in this work should be seen as *extrinsic* HOTIs in the language of Ref. [7], meaning the helical hinge states are robust against local perturbations as long as both bulk and surface gaps remain open and time-reversal symmetry is maintained. As opposed to previous work in a similar direction [49], where even the non-fractionalized phase required the presence of interaction terms in order to maintain the protecting subsystem symmetry, we obtain conventional hinge states with charge e from only single-particle tunnelings between nearest-neighbor wires.

This paper is organized as follows. In Sec. 5.2, we introduce our model of weakly tunnel-coupled Rashba nanowires. In Sec. 5.3, we then show that this model exhibits a HOTI phase with gapless helical hinge states that propagate along a closed path of hinges of a finite 3D sample. We explain in detail how the path of the hinge states is determined by the hierarchy of interwire tunnelings and the boundary termination of the system, and provide some general insight into the construction of 3D HOTIs from lower-dimensional building blocks. In Sec. 5.4 we include electron-electron interactions into our description and show that, for sufficiently strong interactions, a fractional HOTI phase with fractionally charged hinge states can be realized. We conclude in Sec. 5.5.

5.2 Model

In this section, we construct a 3D model of coupled Rashba nanowires that exhibits a HOTI phase with gapless helical hinge states. The Rashba nanowires are taken to be aligned along the x direction, see Fig. 5.1. We now define a unit cell consisting of 8 wires, see Fig. 5.2. A given unit cell is labeled by two discrete indices (n, m) indicating its position along the y and z direction, respectively. Furthermore, the position of a wire within the unit cell is denoted by three indices (τ, η, ν), where $\tau \in \{1, \bar{1}\}$ denotes the left/right wire with respect to the y direction, $\eta \in \{1, \bar{1}\}$ the top/bottom two wires with respect to the z direction, and $\nu \in \{1, \bar{1}\}$ the top/bottom wire for a given η, see again Fig. 5.2. The electrons in wires with $\eta\nu = 1$ ($\eta\nu = \bar{1}$) are taken to have a positive (negative) effective mass $m^* > 0$ ($-m^* < 0$), such that the kinetic term describing the uncoupled wires takes the form

$$H_0 = \sum_{n,m} \sum_{\sigma,\tau,\eta,\nu} \int \mathrm{d}x \, \Psi^\dagger_{nm\sigma\tau\eta\nu}(x) \left[-\eta\nu \left(\frac{\hbar^2 \partial_x^2}{2m^*} + \mu \right) \right] \Psi_{nm\sigma\tau\eta\nu}(x), \tag{5.1}$$

where $\Psi^\dagger_{nm\sigma\tau\eta\nu}(x)$ [$\Psi_{nm\sigma\tau\eta\nu}(x)$] creates [destroys] an electron with spin $\sigma \in \{1, \bar{1}\}$ at the position x in the (τ, η, ν) wire of the unit cell (n, m) and μ denotes the chemical potential.

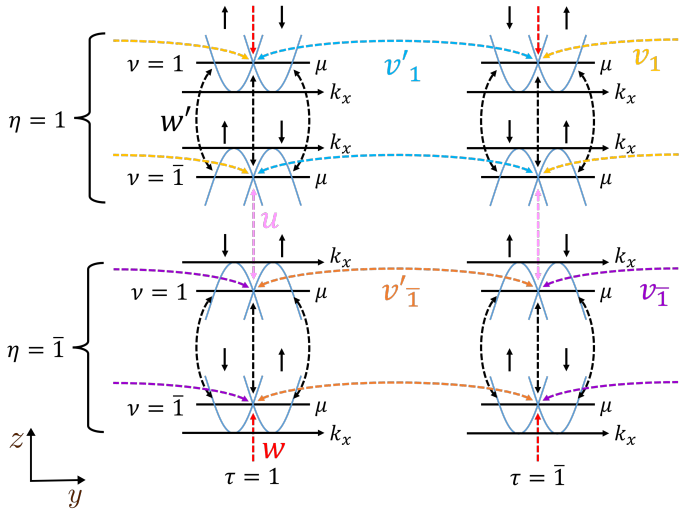

Figure 5.2: Schematic depiction of a single unit cell of the coupled-wires construction described in the main text. The spectrum of the uncoupled wires [see Eq. (5.3)] is represented by the blue parabolas. Wires with $\eta\nu = 1$ ($\eta\nu = \bar{1}$) have a positive (negative) effective mass and wires with $\tau\eta = 1$ ($\tau\eta = \bar{1}$) have positive (negative) SOI. The chemical potential μ is tuned to the crossing point between spin-up and spin-down branches at $k_x = 0$ and the dashed lines represent the different interwire tunnelings [see Eqs. (5.4)-(5.8)].

Additionally, we assume that the wires have strong spin-orbit interaction (SOI), which determines the spin quantization axis z. Wires with $\tau\eta = 1$ ($\tau\eta = \bar{1}$) are taken to have SOI of strength $\alpha > 0$ ($-\alpha < 0$), such that the corresponding term in the Hamiltonian reads

$$H_{\mathrm{SOI}} = -i\alpha \sum_{n,m} \sum_{\sigma,\tau,\eta,\nu} \sigma\tau\eta \int \mathrm{d}x\, \Psi^{\dagger}_{nm\sigma\tau\eta\nu} \partial_x \Psi_{nm\sigma\tau\eta\nu}. \tag{5.2}$$

Here and in the following, we suppress the position argument of the field operators for brevity. Combining Eqs. (5.1) and (5.2) and assuming infinitely long wires for now, we find the spectrum of a single unit cell to consist of 16 branches with energies given by

$$E_{\sigma\tau\eta\nu} = \eta\nu \left[\frac{\hbar^2 (k_x + \sigma\tau\eta k_{so})^2}{2m^*} - \tilde{\mu} \right]. \tag{5.3}$$

Here, we have introduced the spin-orbit momentum $k_{so} = m^*\alpha/\hbar^2$ and the shifted chemical potential $\tilde{\mu} = \mu + \hbar^2 k_{so}^2/2m^*$. As such, the original chemical potential μ now measures the shift away from the spin-orbit energy $E_{so} = \hbar^2 k_{so}^2/2m^*$.

We now proceed by coupling neighboring nanowires via different tunneling processes. In the following we set $\mu = 0$, such that the chemical potential lies at the crossing point between spin-up and spin-down branches at $k_x = 0$, see Fig. 5.2. This choice, together with the particular structure of the unit cell, allows for various momentum-conserving tunneling processes between nearest-neighbor wires.

Let us start by describing the tunneling processes along the z direction. Due to the spatial structure of the unit cell (see Fig. 5.2), all nearest-neighbor tunneling processes along the z

direction conserve the τ-index. First, we account for an intercell tunneling of strength w via

$$H_z = w \sum_{n,m} \sum_{\sigma,\tau} \tau \int \mathrm{d}x \, \Psi^\dagger_{n(m+1)\sigma\tau\bar{1}\bar{1}} \Psi_{nm\sigma\tau 11} + \mathrm{H.c.} \tag{5.4}$$

This term couples neighboring wires in adjacent unit cells and has a sign determined by τ. Furthermore, we introduce an intracell tunneling of strength w' (strength u) that couples neighboring wires with the same η (with opposite η) within the same unit cell. These terms read

$$H'_z = w' \sum_{n,m} \sum_{\sigma,\tau,\eta} \tau \int \mathrm{d}x \, \Psi^\dagger_{nm\sigma\tau\eta 1} \Psi_{nm\sigma\tau\eta\bar{1}} + \mathrm{H.c.}, \tag{5.5}$$

$$H''_z = u \sum_{n,m} \sum_{\sigma,\tau} \tau \int \mathrm{d}x \, \Psi^\dagger_{nm\sigma\tau 1\bar{1}} \Psi_{nm\sigma\tau\bar{1}1} + \mathrm{H.c.} \tag{5.6}$$

Again, the sign of these terms depends on the index τ. The reason behind this particular choice of signs will become clear in Sec. 5.3.

Next, we describe the tunneling processes along the y direction. By construction, tunneling terms coupling nearest-neighbor wires along the y direction conserve the η- and ν-index. First of all, we account for an intercell term with an η-dependent strength v_η via

$$H_y = \sum_{n,m} \sum_{\sigma,\eta,\nu} \int \mathrm{d}x \, v_\eta \, \Psi^\dagger_{(n+1)m\sigma 1\eta\nu} \Psi_{nm\sigma\bar{1}\eta\nu} + \mathrm{H.c.} \tag{5.7}$$

This term couples neighboring wires in adjacent unit cells. Similarly, we also introduce an η-dependent intracell tunneling of strength v'_η between neighboring wires of the same unit cell:

$$H'_y = \sum_{n,m} \sum_{\sigma,\eta,\nu} \int \mathrm{d}x \, v'_\eta \, \Psi^\dagger_{nm\sigma 1\eta\nu} \Psi_{nm\sigma\bar{1}\eta\nu} + \mathrm{H.c.} \tag{5.8}$$

All of the interwire terms given in Eqs. (5.4)-(5.8) are illustrated in Fig. 5.2. Finally, the total Hamiltonian H of our coupled-wires model is given by the sum

$$H = H_0 + H_{\mathrm{SOI}} + H_y + H'_y + H_z + H'_z + H''_z. \tag{5.9}$$

This Hamiltonian is time-reversal symmetric and conserves the z-component of the spin since only spin-conserving interwire tunnelings were included. However, once the system enters the HOTI phase (see Sec. 5.3 below), also processes in which the spin gets flipped will not change the topological properties of the system as long as the bulk and surface gaps remain open and time-reversal symmetry is maintained.

In the following, all of the interwire hopping amplitudes are considered to be small compared to the spin-orbit energy such that they can be treated as weak perturbations to Eq. (5.3). This allows us to linearize the spectrum of each wire around the respective Fermi points in order to simplify the description of our model. As such, we introduce slowly varying right- and left-moving fields $R_{nm\sigma\tau\eta\nu}(x)$ and $L_{nm\sigma\tau\eta\nu}(x)$ via

$$\Psi_{nm\sigma\tau\eta\nu} = R_{nm\sigma\tau\eta\nu} \, e^{ik_F^{1\sigma\tau\eta\nu} x} + L_{nm\sigma\tau\eta\nu} \, e^{ik_F^{\bar{1}\sigma\tau\eta\nu} x}, \tag{5.10}$$

where $k_F^{r\sigma\tau\eta\nu}$ are the Fermi momenta of the respective branches. Explicitly, these are given by $k_F^{(\eta\nu)(\bar{\tau}\eta)\tau\eta\nu} = 2k_{so}$, $k_F^{(\eta\nu)(\tau\eta)\tau\eta\nu} = k_F^{(\bar{\eta}\nu)(\bar{\tau}\eta)\tau\eta\nu} = 0$, and $k_F^{(\bar{\eta}\nu)(\tau\eta)\tau\eta\nu} = -2k_{so}$. From now on, to simplify our notation, we work in terms of the Hamiltonian density $\mathcal{H}$ defined via $H = \sum_{n,m} \int \mathrm{d}x\, \mathcal{H}(x)$ and give all individual contributions to the Hamiltonian in this form. In terms of right- and left-movers, the effective Hamiltonian of the uncoupled wires is then given by

$$\mathcal{H}_0 = -i\hbar \sum_{\sigma,\tau,\eta,\nu} v_F (R^\dagger_{nm\sigma\tau\eta\nu} \partial_x R_{nm\sigma\tau\eta\nu} - L^\dagger_{nm\sigma\tau\eta\nu} \partial_x L_{nm\sigma\tau\eta\nu}) \tag{5.11}$$

with the Fermi velocity $v_F = \alpha/\hbar$. In the same way, we can rewrite the tunneling terms in Eqs. (5.4)-(5.8) in terms of the new fields. Neglecting rapidly oscillating terms, we obtain

$$\mathcal{H}_z = \sum_\tau w\tau (R^\dagger_{n(m+1)\bar{\tau}\tau\bar{1}\bar{1}} L_{nm\bar{\tau}\tau 11} + L^\dagger_{n(m+1)\tau\tau\bar{1}\bar{1}} R_{nm\tau\tau 11}) + \text{H.c.}, \tag{5.12}$$

$$\mathcal{H}'_z = \sum_{\sigma,\tau,\eta,\nu} w'\tau R^\dagger_{nm\sigma\tau\eta\nu} L_{nm\sigma\tau\eta\bar{\nu}} + \text{H.c.}, \tag{5.13}$$

$$\mathcal{H}''_z = \sum_{\tau,\nu} u\tau R^\dagger_{nm(\tau\nu)\tau\bar{\nu}\nu} L_{nm(\tau\nu)\tau\nu\bar{\nu}} + \text{H.c.}, \tag{5.14}$$

$$\mathcal{H}_y = \sum_{\eta,\nu} v_\eta \left(R^\dagger_{(n+1)m\nu 1\eta\nu} L_{nm\nu\bar{1}\eta\nu} + L^\dagger_{(n+1)m\nu 1\eta\bar{\nu}} R_{nm\nu\bar{1}\eta\bar{\nu}}\right) + \text{H.c.}, \tag{5.15}$$

$$\mathcal{H}'_y = \sum_{\tau,\eta,\nu} v'_\eta R^\dagger_{nm(\tau\nu)\tau\eta\nu} L_{nm(\tau\nu)\bar{\tau}\eta\nu} + \text{H.c.} \tag{5.16}$$

5.3 Gapless hinge states

In the following, we focus on the parameter hierarchy $u, w \gg w' \gg v_1, v'_{\bar{1}} \gg v'_1, v_{\bar{1}} \geq 0$ and show that, in this regime, our system is a HOTI with a Kramers pair of gapless hinge states propagating along a closed path of hinges of a 3D sample. The required parameter hierarchy could, for example, be achieved by an appropriate spatial arrangement of the wires, as the interwire tunneling amplitudes are expected to decrease with increasing distance between the wires.

Let us start by considering a system of infinite extent along the x direction but a finite number of unit cells $N_y \times N_z$ along the y and z directions, respectively. We first discuss the tunneling terms along the z direction as these are assumed to be dominant. First of all, it is clear that the exterior modes with Fermi momenta at $\pm 2k_{so}$ are fully gapped by the w' term since this is the only term affecting these modes. For the interior modes with zero Fermi momentum, on the other hand, the u and w terms compete with the w' term. In the regime we consider, the u and w terms are dominant and couple the interior modes in a pairwise fashion, such that the bulk of the system is fully gapped. However, in a finite system, there are four modes per unit cell in the first ($m = 1$) and last ($m = N_z$) layer of wires with respect to the z direction that cannot be paired up, see Fig. 5.2. Explicitly, these modes are given by the Kramers pairs $R_{n1\bar{\tau}\tau\bar{1}\bar{1}}$, $L_{n1\tau\tau\bar{1}\bar{1}}$ and $R_{nN_z\tau\tau 11}$, $L_{nN_z\bar{\tau}\tau 11}$. As a next step, the tunneling terms along the y direction are added. Here, the hierarchy $v_1, v'_{\bar{1}} \gg v'_1, v_{\bar{1}}$ is chosen such that the intercell (intracell) tunneling dominates for $\eta = 1$ ($\eta = \bar{1}$). By inspection of Fig. 5.2, it becomes clear that these terms gap out all remaining modes except for the two Kramers

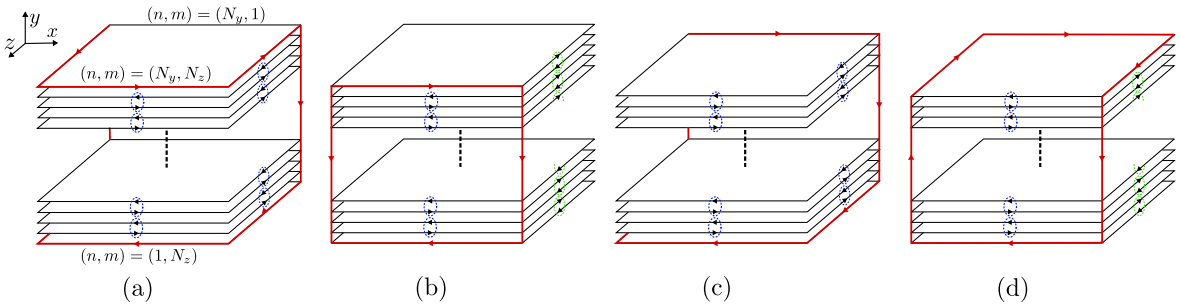

Figure 5.3: If the interwire tunneling amplitudes along the y direction are set to zero, the 3D coupled-wires model defined in Eq. (5.9) effectively realizes a stack of uncoupled 2D QSH layers (black rectangles). Small but non-zero v_η, v'_η then lead to the opening of gaps in the xy and yz surfaces by coupling counterpropagating QSH edge states in adjacent layers. Generally, gapless hinge states (red) will be found propagating along some edges of the first and last QSH layer of the stack as well as along hinges where two surfaces with incompatible dimerization patterns (shown pictorially in blue and green) meet. (a) For $v_1 > v'_{\bar{1}} \gg v_{\bar{1}}, v'_1$, the two yz surfaces are dimerized in a nontrivial way (blue ovals). This matches the pattern of the xy surface at $m = N_z$. (b) For $v'_{\bar{1}} > v_1 \gg v_{\bar{1}}, v'_1$, the two yz surfaces are dimerized in a trivial way (green ovals). This matches the pattern of the xy surface at $m = 1$. (c) If the last QSH layer of the stack is removed, one of the gapless hinge states is relocated from the $m = N_z$ plane to the $m = 1$ plane. Here, we depict the case $v_1 > v'_{\bar{1}} \gg v_{\bar{1}}, v'_1$. (d) Same as in (c), but with $v'_{\bar{1}} > v_1 \gg v_{\bar{1}}, v'_1$. For simplicity, only one spin sector is depicted in all panels.

pairs R_{1N_z1111}, $L_{1N_z\bar{1}111}$ and $R_{N_yN_z\bar{1}\bar{1}11}$, $L_{N_yN_z1\bar{1}11}$, which again cannot be paired up. These remaining gapless states are tightly localized to two hinges of our sample at $(n,m) = (1, N_z)$ and $(n,m) = (N_y, N_z)$ and therefore correspond to the hinge states we are looking for.

Up to now, we have assumed a system that is infinite along the x direction. However, the question remains as to what happens in a finite 3D sample. We start by noting that, in the limit where there is no coupling along the y direction, the system with $u, w \gg w'$ is nothing but a stack of 2D quantum spin Hall (QSH) insulators [67] stacked along the y direction, see Fig. 5.3. Note that due to the sign choice in Eqs. (5.4)-(5.6), QSH edge states with the same spin projection propagate in opposite directions for layers with opposite τ indices. By construction, our 3D stack of QSH layers has fully gapped xz surfaces (with the surface gap equal to the QSH gap of the individual layers), while the other surfaces are gapless. To see what happens to these surfaces once the layers are coupled, it is instructive to project the tunneling terms along the y direction onto the gapless edge states of the 2D QSH layers. From Fig. 5.2, we can read off that the two xy surfaces are gapped in opposite dimerization patterns: the surface at $m = 1$ is gapped out trivially by the $v'_{\bar{1}}$ process, while the surface at $m = N_z$ is gapped nontrivially by the v_1 process and hosts two gapless hinge states as discussed above. For the yz surfaces, on the other hand, we find that the v_1 and $v'_{\bar{1}}$ processes compete. For simplicity, we focus on the case $u = w$ in the following. In this case, we find that the yz surfaces are gapless if $v_1 = v'_{\bar{1}}$ and fully gapped otherwise, see App. 5.A. The dimerization pattern according to which the yz surfaces are gapped out depends on whether v_1 or $v'_{\bar{1}}$ dominates, see Figs. 5.3(a) and (b). Generally, gapless hinge states will be found along some edges of the first and last QSH layer of the stack as well as along hinges where two

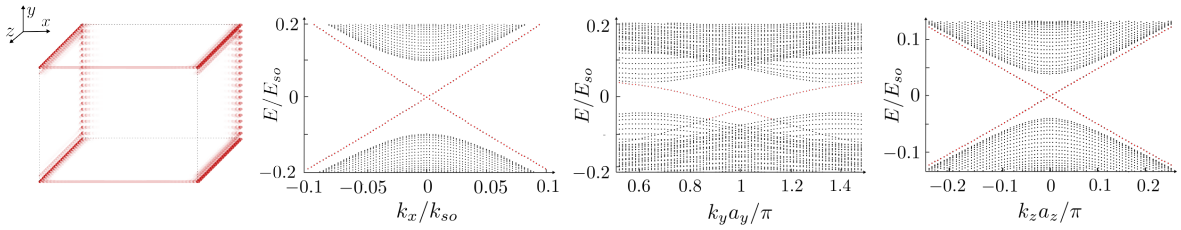

(a) (b) (c) (d)

Figure 5.4: (a) Numerically calculated probability density of the lowest-energy state of a discretized version of Eq. (5.9) in a finite sample with $N_y \times N_z = 20 \times 30$ unit cells and wires of length $\ell = 160/k_{so}$. Here, we have chosen $v_1 > v_{\bar{1}}' \gg v_{\bar{1}}, v_1'$, such that we find ourselves in the situation illustrated in Fig. 5.3(a). Indeed, the hinge state follows the expected path around the sample. (b)-(d) Zoom around the Dirac point of the edge state spectrum in dependence on k_x, k_y, and k_z for a system that is taken to be infinite along the x, y, or z direction, respectively. In all three cases, the energies of the helical edge states (red dots) are clearly visible inside the gap. Each branch of the edge-state spectrum is twofold (fourfold) degenerate for edge states propagating along the x and y (z) direction in agreement with the results shown in the panel (a). The numerical parameters are $u = w \approx 0.78E_{so}$, $w' \approx 0.31E_{so}$, $v_1 \approx 0.34E_{so}$, $v_{\bar{1}}' \approx 0.19E_{so}$, and $v_{\bar{1}} = v_1' = 0$ for all panels.

topologically inequivalent surfaces—i.e., in our case, surfaces with incompatible dimerization patterns—meet, see again Fig. 5.3.

Furthermore, we note that also the boundary termination of the sample can influence the path of the hinge states [27, 71]. Indeed, for the construction presented so far, both pairs of gapless hinge states propagating along the x direction lie in the plane at $m = N_z$. This can be changed if the surface termination of the sample is adjusted. If, for example, the last QSH layer of the stack (i.e., the $\tau = \bar{1}$ part of all unit cells in the plane $n = N_y$) is removed from the sample, one pair of hinge states is relocated from the $m = N_z$ plane to the $m = 1$ plane, see Figs. 5.3(c) and (d).

All of these findings can be checked numerically by exact diagonalization. In the following, we focus on the situation shown in Fig. 5.3(a), but the other cases can be treated in a similar way. The probability density of the lowest-energy state in a finite 3D sample reveals the presence of tightly localized hinge states following the expected path of hinges, see Fig. 5.4(a). In Figs. 5.4(b)–(d), a zoom around the Dirac point of the edge state spectrum in dependence on k_x, k_y, and k_z for a system taken to be infinite along the x, y, or z direction, respectively, confirms the presence of helical edge states with in-gap energies. Note that the energy gaps in the three semi-infinite geometries generally differ in size since different surfaces are gapped by different mechanisms. This also explains the different localization lengths for hinge states propagating along the x, y, or z direction. We also note that while our analytical arguments were based on the strictly perturbative regime $u, w \gg w' \gg v_1, v_{\bar{1}}' \gg v_1', v_{\bar{1}} \geq 0$, the topological phase is actually found for a broader range of parameters. In particular, the requirement of $w' \gg v_1, v_{\bar{1}}'$ can be relaxed, see also App. 5.A. Furthermore, we have checked numerically that the hinge states are robust against potential disorder as long as the bulk and surface gaps remain open, see App. 5.B.

5.4 Fractional second-order topological insulator

In this section, we show how the HOTI found in Sec. 5.3 can be promoted to a more exotic, *fractional* HOTI with gapless helical hinge states that carry only a fraction of the electronic charge e. For this, we start by shifting the chemical potential to a fractional value

$$\mu = (-1 + 1/p^2)E_{so} \tag{5.17}$$

for an odd integer p. The new Fermi momenta of the uncoupled wires are now given by $k_F^{(\eta\nu)(\bar{\tau}\eta)\tau\eta\nu} = k_{so}(1 + 1/p)$, $k_F^{(\bar{\eta}\nu)(\tau\eta)\tau\eta\nu} = -k_{so}(1 + 1/p)$, $k_F^{(\bar{\eta}\nu)(\bar{\tau}\eta)\tau\eta\nu} = k_{so}(1 - 1/p)$, and $k_F^{(\eta\nu)(\tau\eta)\tau\eta\nu} = -k_{so}(1 - 1/p)$. For $p = 1$, we retrieve the case discussed in Sec. 5.3. For $p > 1$, on the other hand, the interwire tunneling terms given in Eqs. (5.4) and (5.6)-(5.8) do no longer conserve momentum and can therefore not lead to the opening of gaps. However, new momentum-conserving processes can be constructed by taking into account single-electron backscattering processes originating from electron-electron interactions. For the interwire tunneling terms along the z direction given in Eqs. (5.4) and (5.6), these new momentum-conserving multi-electron processes read

$$\begin{aligned}\tilde{\mathcal{H}}_z = \tilde{w} \sum_{\tau} \tau \big[&(R^{\dagger}_{n(m+1)\bar{\tau}\tau\bar{1}\bar{1}} L_{n(m+1)\bar{\tau}\tau\bar{1}\bar{1}})^q (R^{\dagger}_{n(m+1)\bar{\tau}\tau\bar{1}\bar{1}} L_{nm\bar{\tau}\tau 11})(R^{\dagger}_{nm\bar{\tau}\tau 11} L_{nm\bar{\tau}\tau 11})^q \\ &+ (L^{\dagger}_{n(m+1)\tau\tau\bar{1}\bar{1}} R_{n(m+1)\tau\tau\bar{1}\bar{1}})^q (L^{\dagger}_{n(m+1)\tau\tau\bar{1}\bar{1}} R_{nm\tau\tau 11})(L^{\dagger}_{nm\tau\tau 11} R_{nm\tau\tau 11})^q \big] + \text{H.c.},\end{aligned} \tag{5.18}$$

$$\tilde{\mathcal{H}}''_z = \tilde{u} \sum_{\tau,\nu} \tau \, (R^{\dagger}_{nm(\tau\nu)\tau\bar{\nu}\nu} L_{nm(\tau\nu)\tau\bar{\nu}\nu})^q (R^{\dagger}_{nm(\tau\nu)\tau\bar{\nu}\nu} L_{nm(\tau\nu)\tau\nu\bar{\nu}})(R^{\dagger}_{nm(\tau\nu)\tau\nu\bar{\nu}} L_{nm(\tau\nu)\tau\nu\bar{\nu}})^q + \text{H.c.}, \tag{5.19}$$

where we have defined $q = (p - 1)/2$. The amplitudes of the above terms are given by $\tilde{w} \propto w\, g_B^{p-1}$ and $\tilde{u} \propto u\, g_B^{p-1}$, where g_B denotes the strength of a single-electron backscattering process. In Fig. 5.5, we pictorially represent the process corresponding to Eq. (5.18) for the case $p = 3$. In the following, let us assume that the above terms are relevant in the renormalization group (RG) sense and that they are the dominant interwire tunneling terms in our model. This can always be achieved if their bare coupling constants are sufficiently large or if their scaling dimensions are the lowest ones among all possible competing terms. Next, we consider the w' term given in Eq. (5.5). While this term conserves momentum for all p, it does not commute with the terms given in Eqs. (5.18) and (5.19) and can therefore not order simultaneously. To lowest order in the interaction, the term that commutes with Eqs. (5.18) and (5.19) is again given by the 'dressed' term

$$\tilde{\mathcal{H}}'_z = \tilde{w}' \sum_{\sigma,\tau,\eta,\nu} \tau \, (R^{\dagger}_{nm\sigma\tau\eta\nu} L_{nm\sigma\tau\eta\nu})^q (R^{\dagger}_{nm\sigma\tau\eta\nu} L_{nm\sigma\tau\eta\bar{\nu}})(R^{\dagger}_{nm\sigma\tau\eta\bar{\nu}} L_{nm\sigma\tau\eta\bar{\nu}})^q + \text{H.c.}, \tag{5.20}$$

where again $\tilde{w}' \propto w'\, g_B^{p-1}$. We assume that this term is relevant in the RG sense but weak compared to the u and w terms discussed above, such that we have $\tilde{u}, \tilde{w} \gg \tilde{w}'$.

To gain further insight into the interacting model, we now switch to a bosonized language [56] by writing

$$\begin{aligned} R_{nm\sigma\tau\eta\nu}(x) &\propto e^{i\phi_{1nm\sigma\tau\eta\nu}(x)}, \\ L_{nm\sigma\tau\eta\nu}(x) &\propto e^{i\phi_{\bar{1}nm\sigma\tau\eta\nu}(x)}, \end{aligned} \tag{5.21}$$

where the bosonic fields $\phi_{rnm\sigma\tau\eta\nu}$ with $r \in \{1, \bar{1}\}$ satisfy the standard non-local commutation relations

$$[\phi_{rnm\sigma\tau\eta\nu}(x), \phi_{r'n'm'\sigma'\tau'\eta'\nu'}(x')] = ir\pi\delta_{nn'}\delta_{mm'}\delta_{rr'}\delta_{\sigma\sigma'}\delta_{\tau\tau'}\delta_{\eta\eta'}\delta_{\nu\nu'}\,\mathrm{sgn}(x-x'). \tag{5.22}$$

This relation guarantees that fermionic fields of the same species satisfy the correct anticommutation relations. For fermionic fields of different species, the anticommutation relations need to be enforced by a proper choice of Klein factors, which we will not include here explicitly [55]. To proceed, it will be useful to introduce a new set of bosonic fields defined as

$$\chi_{rnm\sigma\tau\eta\nu} = \frac{p+1}{2}\phi_{rnm\sigma\tau\eta\nu} - \frac{p-1}{2}\phi_{\bar{r}nm\sigma\tau\eta\nu}. \tag{5.23}$$

The new fields obey the commutation relations

$$[\chi_{rnm\sigma\tau\eta\nu}(x), \chi_{r'n'm'\sigma'\tau'\eta'\nu'}(x')] = ir\pi p\delta_{nn'}\delta_{mm'}\delta_{rr'}\delta_{\sigma\sigma'}\delta_{\tau\tau'}\delta_{\eta\eta'}\delta_{\nu\nu'}\,\mathrm{sgn}(x-x'). \tag{5.24}$$

In terms of these new fields, the interwire tunneling terms along the z direction then take the relatively simple form

$$\tilde{\mathcal{H}}_z \propto \tilde{w}\sum_{\tau}\tau\big[\cos\left(\chi_{\bar{1}n(m+1)\tau\tau\bar{1}\bar{1}} - \chi_{1nm\tau\tau11}\right) + \cos\left(\chi_{1n(m+1)\bar{\tau}\tau\bar{1}\bar{1}} - \chi_{\bar{1}nm\bar{\tau}\tau11}\right)\big], \tag{5.25}$$

$$\tilde{\mathcal{H}}'_z \propto \tilde{w}'\sum_{\sigma,\tau,\eta,\nu}\tau\cos\left(\chi_{1nm\sigma\tau\eta\nu} - \chi_{\bar{1}nm\sigma\tau\eta\bar{\nu}}\right), \tag{5.26}$$

$$\tilde{\mathcal{H}}''_z \propto \tilde{u}\sum_{\nu,\tau}\tau\cos\left(\chi_{1nm(\tau\nu)\tau\bar{\nu}\nu} - \chi_{\bar{1}nm(\tau\nu)\tau\nu\bar{\nu}}\right). \tag{5.27}$$

Terms of this form frequently appear in the context of coupled-wires models and have been thoroughly studied in previous works [54, 55, 57–59, 62–67]. In the regime of strong coupling, which is the regime of interest here, the arguments of the cosines get 'pinned' to constant values in order to minimize the corresponding terms in the Hamiltonian. It then becomes clear that Eqs. (5.25)-(5.27) lead to a fully gapped bulk since all fields are pinned pairwise. In a finite sample, however, the fields $\chi_{1n1\bar{\tau}\tau\bar{1}\bar{1}}$, $\chi_{\bar{1}n1\tau\tau\bar{1}\bar{1}}$ and $\chi_{1nN_z\tau\tau11}$, $\chi_{\bar{1}nN_z\bar{\tau}\tau11}$ remain gapless.

Similarly to the non-interacting case, we now include interwire tunneling processes along the y direction to gap out all remaining fields except a single pair of helical hinge states. Again, the terms given in Eqs. (5.7) and (5.8) have to be combined with backscattering processes to ensure momentum conservation. For the sake of brevity, we directly write the resulting multi-electron processes in terms of bosonic fields and defer their fermionic expressions to App. 5.C. To lowest order in the interaction, the momentum-conserving tunneling terms are given by

$$\tilde{\mathcal{H}}_y \propto \sum_{\eta,\nu}\tilde{v}_\eta\big[\cos\left(\chi_{1(n+1)m\nu1\eta\nu} - \chi_{\bar{1}nm\nu\bar{1}\eta\nu}\right) + \cos\left(\chi_{\bar{1}(n+1)m\nu1\eta\bar{\nu}} - \chi_{1nm\nu\bar{1}\eta\bar{\nu}}\right)\big], \tag{5.28}$$

$$\tilde{\mathcal{H}}'_y \propto \sum_{\tau,\eta,\nu}\tilde{v}'_\eta\cos\left(\chi_{1nm(\tau\nu)\tau\eta\nu} - \chi_{\bar{1}nm(\tau\nu)\bar{\tau}\eta\nu}\right), \tag{5.29}$$

where again $\tilde{v}_\eta \propto v_\eta\, g_B^{p-1}$ and $\tilde{v}'_\eta \propto v'_\eta\, g_B^{p-1}$. If these terms are relevant but weaker than the tunneling terms along the z direction discussed previously, we find that the bulk of the system is fully gapped, while for a finite system of $N_y \times N_z$ unit cells the fields χ_{11N_z1111}, $\chi_{\bar{1}1N_z\bar{1}111}$, $\chi_{1N_yN_z\bar{1}\bar{1}11}$, and $\chi_{\bar{1}N_yN_z1\bar{1}11}$ stay gapless. These are again our two Kramers pairs of gapless hinge states propagating along the x direction. Importantly, these modes now carry a fractional charge e/p [59].

Indeed, we can understand the emergence of the fractional HOTI phase in the same way as is shown in Fig. 5.3, with the only difference that the QSH layers are now replaced by *fractional* QSH layers [67]. In the same way as before, gapless hinge states propagate along certain edges of the first and last layer of the stack as well as along hinges where surfaces with incompatible dimerization patterns meet. As such, the path of the fractional hinge states can again be controlled by adjusting the interwire tunneling amplitudes as well as the surface termination of the sample.

5.5 Conclusions

We have constructed a 3D model of coupled Rashba nanowires that can realize a HOTI phase with a Kramers pair of gapless helical hinge states propagating along a closed path of hinges of a finite sample. The specific choice of interwire tunneling amplitudes and surface termination allow for control over the path that the gapless hinge states take. Moreover, the coupled-wires approach allows us to incorporate strong electron-electron interactions into our description. For sufficiently strong interactions, we have shown that the system can enter a fractional HOTI phase with gapless hinge states that carry only a fraction of the electronic charge e.

The emergence of hinge states can be intuitively understood by viewing our model as a stack of (fractional) QSH layers that are coupled in a nontrivial way such that different

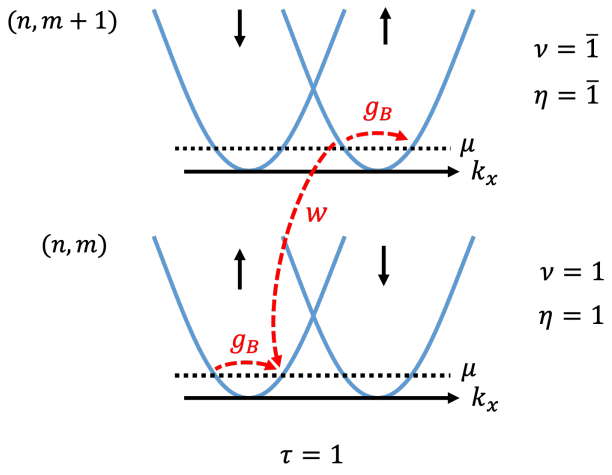

Figure 5.5: Pictorial representation of the interwire tunneling term defined in Eq. (5.18) for $p = 3$. The chemical potential is tuned to $\mu = -8E_{so}/9$, such that the momentum mismatch of the interwire tunneling can be exactly compensated by two backscattering terms of strength g_B.

surfaces are gapped out in different, incompatible dimerization patterns. We note that while we have focused on the time-reversal invariant case, we can straightforwardly obtain a formal description the time-reversal broken case with a (fractional) chiral hinge mode by focusing on just one spin sector of our model. More physically, one could also think of modeling a (fractional) chiral HOTI by starting from a coupled-wires description of a stack of (fractional) quantum Hall layers and then coupling adjacent layers in suitable dimerization patterns in a similar way as in this work.

Finally, while coupled-wires models are mainly a theoretical tool to analytically construct and describe exotic, strongly interacting phases, we note that some aspects of our construction—in particular the picture of coupled QSH layers—are closely related to recent experimental work on 3D HOTIs in layered systems [33, 34].

Acknowledgments. K. L. and P. K. contributed equally to this work. This work was supported by the Swiss National Science Foundation and NCCR QSIT. This project received funding from the European Union's Horizon 2020 research and innovation program (ERC Starting Grant, grant agreement No 757725).

5.A Gap-opening terms in the yz plane

In this Appendix, we discuss the details of how the interwire tunneling terms along the y direction lead to the HOTI phase discussed in the main text. When only the interwire tunneling terms along the z direction are taken into account, the system corresponds to a stack of uncoupled 2D QSH layers stacked along the y direction. By construction, it is clear that the xy surfaces are fully gapped by the hopping terms along the y direction, see Fig. 5.2. The question remains what happens to the yz surfaces. To see this, we can look at the explicit expressions for the uncoupled QSH edge states in a system that is assumed to be infinite along the z direction, such that k_z is a good quantum number. For simplicity, we focus on the case $u = w$. At $k_z = 0$, the gapless QSH edge states in the nth layer can be labeled by a fixed spin σ and a fixed τ, while their η- and ν-components are given by four-component wave functions $\phi_{n\tau\sigma}(x)$. For $\tau = 1$, these are found to be

$$\phi_{n11}(x) = \frac{1}{\sqrt{\mathcal{N}}}\left[\begin{pmatrix}-i\\-1\\i\\1\end{pmatrix}e^{-x/\xi_1} + \begin{pmatrix}ie^{-2ik_{so}x}\\e^{-2ik_{so}x}\\-ie^{2ik_{so}x}\\-e^{2ik_{so}x}\end{pmatrix}e^{-x/\xi_2}\right], \tag{5.30}$$

$$\phi_{n1\bar{1}}(x) = \frac{1}{\sqrt{\mathcal{N}}}\left[\begin{pmatrix}i\\-1\\-i\\1\end{pmatrix}e^{-x/\xi_1} + \begin{pmatrix}-ie^{2ik_{so}x}\\e^{2ik_{so}x}\\ie^{-2ik_{so}x}\\-e^{-2ik_{so}x}\end{pmatrix}e^{-x/\xi_2}\right], \tag{5.31}$$

where $\mathcal{N}$ is a normalization constant. Here, we have defined $\xi_1 = \alpha/(u - w')$ and $\xi_2 = \alpha/w'$. The wave functions for $\tau = \bar{1}$ can be obtained from the above by reversing the role of spin up and spin down. We can now calculate the projection of the v_1 and $v_{\bar{1}}'$ terms onto these edge states. The v_1 term couples edge states in adjacent unit cells via the matrix element

$$v_1 \left\langle \phi_{(n+1)1\sigma}(x)\right| \frac{\mathbb{1} + \eta_z}{2} \left|\phi_{n\bar{1}\sigma}(x)\right\rangle = \frac{v_1}{2}, \tag{5.32}$$

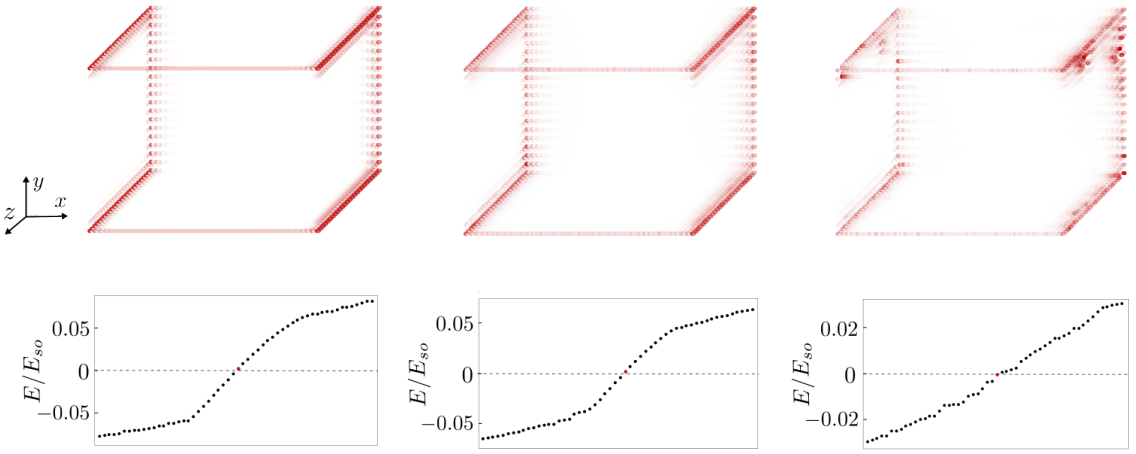

(a) (b) (c)

Figure 5.6: Numerically calculated probability density of the lowest-energy state (top row) and low-energy spectrum (bottom row) of a discretized version of Eq. (5.9) with additional potential disorder drawn from a normal distribution with zero mean value and standard deviation σ_μ. (a) $\sigma_\mu = 0$. (b) $\sigma_\mu \approx 0.31E_{so}$. (c) $\sigma_\mu \approx 0.55E_{so}$. We find that the hinge modes are robust against potential disorder even if σ_μ exceeds the minimum surface gap $\Delta \approx 0.13E_{so}$, see panel (b). However, if σ_μ gets too large, the surface gap closes and the hinge modes tend to get localized, see panel (c). The parameters are the same as in Fig. 5.4.

where η_z is a Pauli matrix acting on the η subspace (see Fig. 5.2 for an illustration). The $v'_{\bar{1}}$ term, on the other hand, couples edge states in the same unit cell via the matrix element

$$v'_{\bar{1}} \left\langle \phi_{n1\sigma}(x) \middle| \frac{\mathbb{1} - \eta_z}{2} \middle| \phi_{n\bar{1}\sigma}(x) \right\rangle = \frac{v'_{\bar{1}}}{2}. \tag{5.33}$$

We now see that, at $v_1 = v'_{\bar{1}}$, the gaps induced by the two terms are equal and the yz surfaces are thus gapless. Otherwise, the yz surfaces will be fully gapped and the corresponding dimerization pattern will be set by whichever one of the two terms dominates. Additionally, we see that, due to the spatial structure of the unit cell, the gaps opened by the tunneling terms along the y direction are suppressed by an additional factor of $1/2$. Generally, the strict requirement $u, w \gg w' \gg v_1, v'_{\bar{1}}$ can be relaxed as long as the 2D bulk gap of the individual QSH layers [given by $E_{\text{gap}} = \min(u - w', w')$] is not closed by the tunneling terms along the y direction.

5.B Stability against potential disorder

In Fig. 5.6, we present numerical data demonstrating that the hinge modes found in the main text are robust against potential disorder. To model the disorder, we allow for random fluctuations of the chemical potential following a normal distribution with zero mean value and a standard deviation of σ_μ. Figure 5.6(b) shows that the hinge modes are robust against potential disorder even if σ_μ significantly exceeds the minimum surface gap Δ [$\Delta \approx 0.13E_{so}$

for the parameters used in Fig. 5.4]. However, if σ_μ gets even larger, the surface gap closes and the hinge modes tend to get localized, see Fig. 5.6(c).

5.C Dressed interwire tunneling terms along the y direction

For completeness, this Appendix gives the full fermionic form of the dressed interwire tunneling terms along the y direction. These read:

$$\tilde{\mathcal{H}}_y = \sum_{\eta,\nu} \tilde{v}_\eta \left[(R^\dagger_{(n+1)m\nu 1\eta\nu} L_{(n+1)m\nu 1\eta\nu})^q (R^\dagger_{(n+1)m\nu 1\eta\nu} L_{nm\nu\bar{1}\eta\nu})(R^\dagger_{nm\nu\bar{1}\eta\nu} L_{nm\nu\bar{1}\eta\nu})^q \right.$$
$$\left. + (L^\dagger_{(n+1)m\nu 1\eta\bar{\nu}} R_{(n+1)m\nu 1\eta\bar{\nu}})^q (L^\dagger_{(n+1)m\nu 1\eta\bar{\nu}} R_{nm\nu\bar{1}\eta\bar{\nu}})(L^\dagger_{nm\nu\bar{1}\eta\bar{\nu}} R_{nm\nu\bar{1}\eta\bar{\nu}})^q \right] + \text{H.c.}, \tag{5.34}$$

$$\tilde{\mathcal{H}}'_y = \sum_{\tau,\eta,\nu} \tilde{v}'_\eta \, (R^\dagger_{nm(\tau\nu)\tau\eta\nu} L_{nm(\tau\nu)\tau\eta\nu})^q (R^\dagger_{nm(\tau\nu)\tau\eta\nu} L_{nm(\tau\nu)\bar{\tau}\eta\nu})(R^\dagger_{nm(\tau\nu)\bar{\tau}\eta\nu} L_{nm(\tau\nu)\bar{\tau}\eta\nu})^q + \text{H.c.} \tag{5.35}$$

Bibliography

[1] W. A. Benalcazar, B. A. Bernevig, and T. L. Hughes, Science **357**, 61 (2017).

[2] W. A. Benalcazar, B. A. Bernevig, and T. L. Hughes, Phys. Rev. B **96**, 245115 (2017).

[3] Z. Song, Z. Fang, and C. Fang, Phys. Rev. Lett. **119**, 246402 (2017).

[4] Y. Peng, Y. Bao, and F. von Oppen, Phys. Rev. B **95**, 235143 (2017).

[5] J. Langbehn, Y. Peng, L. Trifunovic, F. von Oppen, and P. W. Brouwer, Phys. Rev. Lett. **119**, 246401 (2017).

[6] S. Imhof, C. Berger, F. Bayer, H. Brehm, L. Molenkamp, T. Kiessling, F. Schindler, C. H. Lee, M. Greiter, T. Neupert, and R. Thomale, Nature Physics **14**, 925 (2018).

[7] M. Geier, L. Trifunovic, M. Hoskam, and P. W. Brouwer, Phys. Rev. B **97**, 205135 (2018).

[8] F. Schindler, A. M. Cook, M. G. Verginory, Z. Wang, S. S. P. Parking, B. A. Bernevig, and T. Neupert, Science Adv. **4**, 6 (2018).

[9] G. van Miert and C. Ortix, Phys. Rev. B **98**, 081110(R) (2018).

[10] M. Ezawa, Phys. Rev. B **97**, 155305 (2018).

[11] M. Ezawa, Phys. Rev. Lett. **121**, 116801 (2018).

[12] E. Khalaf, Phys. Rev. B **97**, 205136 (2018).

[13] C.-H. Hsu, P. Stano, J. Klinovaja, and D. Loss, Phys. Rev. Lett. **121**, 196801 (2018).

[14] R. Okugawa, S. Hayashi, and T. Nakanishi, Phys. Rev. B **100**, 235302 (2019).

[15] D. Călugăru, V. Juričić, and B. Roy, Phys. Rev. B **99**, 041301(R) (2019).

[16] S. Franca, D. V. Efremov, and I. C. Fulga, Phys. Rev. B **100**, 075415 (2019).

[17] Y. Volpez, D. Loss, and J. Klinovaja, Phys. Rev. Lett. **122**, 126402 (2019).

[18] R.-X. Zhang, W. S. Cole, X. Wu, and S. Das Sarma, Phys. Rev. Lett. **123**, 167001 (2019).

[19] T. Nag, V. Juričić, and B. Roy, Phys. Rev. Research **1**, 032045(R) (2019).

[20] X.-L. Sheng, C. Chen, H. Liu, Z. Chen, Z.-M. Yu, Y. X. Zhao, and S. A. Yang, Phys. Rev. Lett. **123**, 256402 (2019).

[21] W. A. Benalcazar, T. Li, and T. L. Hughes, Phys. Rev. B **99**, 245151 (2019).

[22] B. Roy, Phys. Rev. Research **1**, 032048(R) (2019).

[23] K. Plekhanov, M. Thakurathi, D. Loss, and J. Klinovaja, Phys. Rev. Research **1**, 032013(R) (2019).

[24] K. Plekhanov, F. Ronetti, D. Loss, and J. Klinovaja, Phys. Rev. Research **2**, 013083 (2020).

[25] K. Laubscher, D. Chughtai, D. Loss, and J. Klinovaja, Phys. Rev. B **102**, 195401 (2020).

[26] S.-B. Zhang, A. Calzona, and B. Trauzettel, Phys. Rev. B **102**, 100503(R) (2020).

[27] C. Yoon, C.-C. Liu, H. Min, F. Zhang, arXiv:2005.14710.

[28] A. Tiwari, M.-H. Li, B. A. Bernevig, T. Neupert, and S. A. Parameswaran, Phys. Rev. Lett. **124**, 046801 (2020).

[29] C.-A. Li, S.-B. Zhang, J. C. Budich, and B. Trauzettel, arXiv:2108.08630.

[30] A. K. Ghosh, T. Nag, and A. Saha, Phys. Rev. B **103**, 045424 (2021).

[31] F. Schindler, Z. Wang, M. G. Vergniory, A. M. Cook, A. Murani, S. Sengupta, A. Y. Kasumov, R. Deblock, S. Jeon, I. Drozdov, H. Bouchiat, S. Guéron, A. Yazdani, B. A. Bernevig, and T. Neupert, Nature Physics **14**, 918 (2018).

[32] L. Aggarwal, P. Zhu, T. L. Hughes, and V. Madhavan, Nat. Commun. **12**, 4420 (2021).

[33] R. Noguchi, M. Kobayashi, Z. Jiang, K. Kuroda, T. Takahashi, Z. Xu, D. Lee, M. Hirayama, M. Ochi, T. Shirasawa, P. Zhang, C. Lin, C. Bareille, S. Sakuragi, H. Tanaka, S. Kunisada, K. Kurokawa, K. Yaji, A. Harasawa, V. Kandyba, A. Giampietri, A. Barinov, T. K. Kim, C. Cacho, M. Hashimoto, D. Lu, S. Shin, R. Arita, K. Lai, T. Sasagawa, and T. Kondo, Nat. Mater. **20**, 473 (2021).

[34] N. Shumiya, M. S. Hossain, J.-X. Yin, Z. Wang, M. Litskevich, C. Yoon, Y. Li, Y. Yang, Y.-X. Jiang, G. Cheng, Y.-C. Lin, Q. Zhang, Z.-J. Cheng, T. A. Cochran, D. Multer, X. P. Yang, B. Casas, T.-R. Chang, T. Neupert, Z. Yuan, S. Jia, H. Lin, N. Yao, L. Balicas, F. Zhang, Y. Yao, and M. Z. Hasan, arXiv:2110.05718.

[35] Y.-B. Choi, Y. Xie, C.-Z. Chen, J. Park, S.-B. Song, J. Yoon, B. J. Kim, T. Taniguchi, K. Watanabe, J. Kim, K. C. Fong, M. N. Ali, K. T. Law, and G.-H. Lee, Nat. Mater. **19**, 974 (2020).

[36] A. Kononov, G. Abulizi, K. Qu, J. Yan, D. Mandrus, K. Watanabe, T. Taniguchi, and C. Schönenberger, Nano Lett. **20**, 4228 (2020).

[37] M. Serra-Garcia, V. Peri, R. Süsstrunk, O. R. Bilal, T. Larsen, L. G. Villanueva, and S. D. Huber, Nature **555**, 342 (2018).

[38] J. Noh, W. A. Benalcazar, S. Huang, M. J. Collins, K. P. Chen, T. L. Hughes, and M. C. Rechtsman, Nature Photon. **12**, 408 (2018).

[39] H. Xue, Y. Yang, F. Gao, Y. Chong, and B. Zhang, Nature Mater. **18**, 108 (2019).

[40] X. Ni, M. Weiner, A. Alu, and A. B. Khanikaev, Nature Mater. **18**, 113 (2019).

[41] S. Mittal, V. V. Orre, G. Zhu, M. A. Gorlach, A. Poddubny, and M. Hafezi, Nat. Photon. **13**, 692 (2019).

[42] A. E. Hassan, F. K. Kunst, A. Moritz, G. Andler, E. J. Bergholtz, and M. Bourennane, Nat. Photon. **13**, 697 (2019).

[43] B.-Y. Xie, G.-X. Su, H.-F. Wang, H. Su, X.-P. Shen, P. Zhan, M.-H. Lu, Z.-L. Wang, and Y.-F. Chen, Phys. Rev. Lett. **122**, 233903 (2019).

[44] X. Zhang, Z.-K. Lin, H.-X. Wang, Z. Xiong, Y. Tian, M.-H. Lu, Y.-F. Chen, and J.-H. Jiang, Nat. Commun. **11**, 65 (2020).

[45] Y. You, D. Litinski, and F. von Oppen, Phys. Rev. B **100**, 054513 (2019).

[46] Y. You, T. Devakul, F. J. Burnell, and T. Neupert, Phys. Rev. B **98**, 235102 (2018).

[47] K. Laubscher, D. Loss, and J. Klinovaja, Phys. Rev. Research **1**, 032017(R) (2019).

[48] K. Laubscher, D. Loss, and J. Klinovaja, Phys. Rev. Research **2**, 013330 (2020).

[49] J. May-Mann, Y. You, T. L. Hughes, and Z. Bi, arXiv:2202.01231.

[50] A. Hackenbroich, A. Hudomal, N. Schuch, B. A. Bernevig, and N. Regnault, Phys. Rev. B **103**, L161110 (2021).

[51] J.-H. Zhang, Y. Qi, and Z.-C. Gu, arXiv:2204.13558.

[52] J.-H. Zhang, arXiv:2201.07023.

[53] H. Li, H.-Y. Kee, and Y. B. Kim, arXiv:2206.0071.

[54] C. L. Kane, R. Mukhopadhyay, and T. C. Lubensky, Phys. Rev. Lett. **88**, 036401 (2002).

[55] J. C. Y. Teo and C. L. Kane, Phys. Rev. B **89**, 085101 (2014).

[56] T. Giamarchi, *Quantum Physics in One Dimension* (Oxford University Press, Oxford, 2004).

[57] J. Klinovaja and D. Loss, Eur. Phys. J. B **87**, 171 (2014).

[58] E. Sagi, Y. Oreg, A. Stern, and B. I. Halperin, Phys. Rev. B **91**, 245144 (2015).

[59] J. Klinovaja, Y. Tserkovnyak, and D. Loss, Phys. Rev. B **91**, 085426 (2015).

[60] P. M. Tam and C. L. Kane, Phys. Rev. B **103**, 035142 (2021).

[61] K. Laubscher, C. S. Weber, D. M. Kennes, M. Pletyukhov, H. Schoeller, D. Loss, and J. Klinovaja, Phys. Rev. B **104**, 035432 (2021).

[62] J. Klinovaja and D. Loss, Phys. Rev. Lett. **111**, 196401 (2013),

[63] J. Klinovaja and Y. Tserkovnyak, Phys. Rev. B **90**, 115426 (2014).

[64] E. Sagi and Y. Oreg, Phys. Rev. B **90**, 201102(R) (2014).

[65] T. Meng, Phys. Rev. B **92**, 115152 (2015).

[66] R. A. Santos, C.-W. Huang, Y. Gefen, and D. B. Gutman, Phys. Rev. B **91**, 205141 (2015).

[67] E. Sagi and Y. Oreg, Phys. Rev. B **92**, 195137 (2015).

[68] T. Neupert, C. Chamon, C. Mudry, and R. Thomale, Phys. Rev. B **90**, 205101 (2014).

[69] E. Sagi, A. Haim, E. Berg, F. von Oppen, and Y. Oreg, Phys. Rev. B **96**, 235144 (2017).

[70] C. Li, H. Ebisu, S. Sahoo, Y. Oreg, and M. Franz, Phys. Rev. B **102**, 165123 (2020).

[71] A. Mook, S. A. Díaz, J. Klinovaja, and D. Loss, Phys. Rev. B **104**, 024406 (2021).

Chapter 6

Majorana zero modes and their bosonization

Adapted from:
V. Chua, K. Laubscher, J. Klinovaja, and D. Loss
"Majorana zero modes and their bosonization,"
Phys. Rev. B **102**, 155416 (2020)

The simplest continuum model of a one-dimensional non-interacting superconducting fermionic symmetry-protected topological (SPT) phase is studied in great detail using analytical methods. In a first step, we present a full exact diagonalization of the fermionic Bogoliubov-de Gennes Hamiltonian for a system of finite length and with open boundaries. In particular, we derive exact analytical expressions for the Majorana zero modes emerging in the topologically non-trivial phase, revealing their spatial localization, their transformation properties under symmetry operations, and the exact finite-size energy splitting of the associated quasi-degenerate ground states. We then proceed to analyze the model via exact operator bosonization in both open and closed geometries. In the closed wire geometry, we demonstrate fermion parity switching from twisting boundary conditions in the topologically non-trivial phase. For the open wire, on the other hand, we first take a semiclassical approach employing the Mathieu equation to study the two quasi-degenerate ground states as well as their energy splitting at finite system sizes. We then finally derive the exact forms of the Majorana zero modes in the bosonic language using vertex-algebra techniques. These modes are verified to be in exact agreement with the results obtained from the fermionic description. The complementary viewpoints provided by the fermionic and bosonic formulations of the superconducting SPT phase are reconciled, allowing us to provide a complete and exact account of how Majorana zero modes manifest in a bosonized description of an SPT phase.

6.1 Introduction

Majorana zero modes (MZMs) may be conceptualized as "half electrons" with the distinguishing feature that they cost practically no additional energy to excite from the ground state. Hence their presence leads to effectively degenerate ground states which must differ by the parity (even vs. odd) of their fermion number [1]. Majorana zero modes naturally emerge as a symptom of non-trivial topology in fermionic symmetry-protected topological (SPT) phases [2] of the right symmetries. For some time now, academic interest and excitement in MZMs has been driven by the fact that they represent the simplest possible setup for the implementation of topological quantum computation, a powerful but technologically challenging paradigm for quantum computation exploiting the non-Abelian braiding properties of anyonic quasiparticles [3].

In this work, we revisit the simplest possible continuum model of a fermionic SPT phase in one dimension, namely that of a time-reversal symmetric topological superconductor without Kramers degeneracy. This continuum model is the low-energy linearized limit of the celebrated Kitaev Majorana chain [1]. The main results of this work are: (1) the exact analytic forms of the MZM operators, (2) their energy splitting in a system of finite length, (3) the correct bosonized Hamiltonian incorporating open boundary conditions, and (4) the exact MZM operators from constructive bosonization and vertex algebra methods. We find that with *open boundaries* and *finite system lengths*, the exact bosonized Hamiltonian will acquire an inhomogeneous topological superconducting mass term that vanishes at the boundaries. This insight elegantly illustrates the reason behind the MZMs behaving as approximate zero modes in a finite system. More importantly, our novel derivation of exact analytical MZM operators in both the fermionic and bosonic language not only confirms their quasi-degeneracy, but also their spatial localization and their transformation properties under time-reversal symmetry. These last two points are absolutely crucial for the demonstration of symmetry fractionalization [4–6], which is a defining property of fermionic SPT phases.

Thus far, there have been several actively pursued experimental proposals [7] to synthesize and manipulate MZMs, the most popular of which is based on nanowires [8, 9] and a combination of strong Rashba spin-orbit coupling, proximity-induced superconductivity as well as weak magnetic fields [10–15]. An alternative setup is based on chains of magnetic adatoms on superconducting substrates [16–25]. It was predicted theoretically that under the right conditions, these setups could result in a topologically non-trivial superconducting wire with the tell-tale signs of localized MZMs at its ends. At the level of a 'gedanken experiment' [26], topological braiding was then proposed between networks of topological nanowires that are created and manipulated by electrostatic gating.

Extensions involving more exotic quasiparticles known as mphparafermions have been recognized for some time to possess even greater potential as building blocks for topological quantum computation [3]. However, such claims are also accompanied by more challenging experimental configurations [27–40]. Although these appear to be more exciting and cutting edge, they are nevertheless extremely daunting. The motivation for this work is partly driven by basic questions regarding the bosonization of this and related models such as the symmetry-enriched topological parafermionic models [32, 41–45].

The paper is organized as follows. In Sec. 6.2 the model is briefly introduced and our main results are summarized. This is followed by a detailed discussion of the continuum fermionic model in Sec. 6.3. Topics that are touched upon are the model's symmetries, its

formulation in terms of Majorana fields, the topological and trivial phases, and the treatment of open boundary conditions through unfolding. Then, in Sec. 6.4, an exact diagonalization of the topological Bogoliubov-de Gennes Hamiltonian with open boundaries and finite lengths is presented. In Sec. 6.5 bosonization is first applied to the model with closed but twisted boundary conditions. At the semi-classical level, we demonstrate how the topological and trivial phases are distinguished by the response of the ground state(s) to twisted boundary conditions. Thereafter, in Sec. 6.6, bosonization is finally applied to the model with open boundaries and finite lengths through unfolding. Here the topological and trivial phases can be distinguished at the semi-classical level by the quasi-degeneracy of the ground states. The Majorana zero modes are derived within bosonization and the resulting expressions are shown to agree with the ones obtained in Sec. 6.4. Finally, in Sec. 6.7, we discuss and summarize the overall results of this work. For the sake of completeness, additional material is included in the Appendices 6.A, 6.B, 6.C, and 6.D.

6.2 Model and summary of main results

In the interest of readability, we present a short summary of our main results without going into the minutiae of our methods.

Fermionic formulation: We specialize to the model Hamiltonian

$$H = \int_0^{\mathrm{L}} \mathcal{H}\, \mathrm{d}x, \tag{6.1a}$$

$$\mathcal{H} = -iv_F \left(R^\dagger \partial_x R - L^\dagger \partial_x L \right) + i\Delta(R^\dagger L^\dagger - LR), \tag{6.1b}$$

where $R(x)$ and $L(x)$ are relativistic right- and left-moving chiral fermionic fields, respectively. Here, $\Delta > 0$ is a constant mean-field superconducting (SC) pairing potential, v_F is the Fermi velocity and we work in units of $\hbar = 1$. In a system of size L with open boundary conditions, there arise two MZM operators. The enforcement of open boundary conditions is executed by the unfolding method [46–48] which relates $R(x)$ and $L(x)$ according to

$$L(x) \equiv -R(-x) \tag{6.2}$$

in the extended domain $-\mathrm{L} \leqslant x \leqslant \mathrm{L}$ and with *antiperiodic* boundary conditions $R(x+2\mathrm{L}) = -R(x)$. The MZM operators are explicitly given as

$$\gamma_0 := \int_{-\mathrm{L}}^{\mathrm{L}} \mathrm{d}x\; a(x)[R(x) + R^\dagger(x)] \equiv \gamma_0^\dagger, \tag{6.3a}$$

$$\gamma_{\mathrm{L}} := \int_{-\mathrm{L}}^{\mathrm{L}} \mathrm{d}x\; b(x)[R(x) + R^\dagger(x)] \equiv \gamma_{\mathrm{L}}^\dagger, \tag{6.3b}$$

where the real-valued wavefunctions $a(x), b(x)$ are

$$a(x) := \mathcal{N}_\kappa \sinh(\kappa(\mathrm{L} - |x|)), \tag{6.4a}$$

$$b(x) := \mathcal{N}_\kappa \sinh(\kappa x), \tag{6.4b}$$

with constants κ and $\mathcal{N}_\kappa$ defined implicitly and explicitly by

$$\kappa = \frac{\Delta}{v_F}\tanh(\kappa \mathrm{L}), \quad \mathcal{N}_\kappa := \mathrm{L}^{-\frac{1}{2}}\sqrt{\frac{\sinh(2\kappa \mathrm{L})}{2\kappa \mathrm{L}} - 1}. \tag{6.5}$$

Here, $\mathcal{N}_\kappa$ is the normalization prefactor and the parameter κ is determined by imposing boundary conditions on the decaying eigenmodes. We note that these expressions remain valid as long as the localization length v_F/Δ is smaller than the system length L. At exactly $\mathrm{L} = v_F/\Delta$ a finite-length topological transition occurs where these modes become extended [49], as is detailed in Appendix 6.D. The asymptotic behavior of

$$a(x) \sim \mathrm{L}^{-\frac{1}{2}}\mathrm{e}^{-\kappa|x|}, \qquad b(x) \sim \mathrm{L}^{-\frac{1}{2}}\mathrm{sgn}(x)\mathrm{e}^{\kappa(\mathrm{L}-|x|)} \tag{6.6}$$

in the limit of large $\mathrm{L} \gg v_F/\Delta$ exemplifies the spatial locality of these operators. Moreover, the exact fermionic quasiparticle excitation operator is given by

$$\psi_{E_{i\kappa}} := \frac{\gamma_0 - i\gamma_\mathrm{L}}{2} \tag{6.7}$$

and satisfies $[H, \psi^\dagger_{E_{i\kappa}}] = E_{i\kappa}\psi^\dagger_{E_{i\kappa}}$ with the energy splitting

$$E_{i\kappa} = \sqrt{\Delta^2 - v_F^2\kappa^2} \sim 2\Delta \mathrm{e}^{-\frac{\Delta \mathrm{L}}{v_F}}. \tag{6.8}$$

Equivalently, the MZMs obey the commutation relations

$$[H, \gamma_0] = iE_{i\kappa}\gamma_\mathrm{L}, \qquad [H, \gamma_\mathrm{L}] = -iE_{i\kappa}\gamma_0. \tag{6.9}$$

One of the most crucial properties of γ_0 and γ_L are their transformations under spinless time-reversal $\mathcal{T}$,

$$\mathcal{T}\gamma_0\mathcal{T}^{-1} = +\gamma_0, \qquad \mathcal{T}\gamma_\mathrm{L}\mathcal{T}^{-1} = -\gamma_\mathrm{L}, \tag{6.10}$$

since $\mathcal{T}R(x)\mathcal{T}^{-1} = R(-x)$. Here, $\mathcal{T}$ is anti-linear and satisfies $\mathcal{T}^2 = +1$. The fact that γ_0 and γ_L transform oppositely in sign under $\mathcal{T}$ is a clear demonstration of symmetry fractionalization [4, 50], since the two MZMs are spatially localized on different boundaries.

The exact MZM solutions given above can be verified by direct substitution as is done in Appendix 6.C. The main bulk of Sec. 6.4 is dedicated to the intuition and derivation of these solutions, as well as a full exact diagonalization of H. Using these eigenmode solutions, the Bardeen-Cooper-Schrieffer (BCS) quasi-degenerate ground states are constructed.

Bosonization: We proceed to carry out finite-size bosonization on H with closed and open boundary conditions. The case of open boundaries is analyzed using the unfolding procedure. Since unfolding reduces the number of chiral fields to just $R(x)$ in a domain of size 2L, we need to bosonize only a *single* chiral field with 2L-antiperiodic boundary conditions

$$R(x) = \frac{1}{\sqrt{2\mathrm{L}}} : \mathrm{e}^{i\phi^R(x)} : \mathrm{e}^{-i\frac{\pi x}{2\mathrm{L}}}, \tag{6.11}$$

where $\phi^R(x) \sim \phi^R(x)+2\pi$ is a non-local compact bosonic chiral field. Here : : denotes bosonic normal ordering. The bosonized Hamiltonian is then given by

$$H = \int_0^{\mathrm{L}} \mathrm{d}x \, \left(\frac{v_F}{2\pi} \left([\partial_x \varphi(x)]^2 + [\partial_x \vartheta(x)]^2 \right) - \frac{2\Delta}{\mathrm{L}} \sin\left[\frac{\pi x}{\mathrm{L}}\right] : \cos[2\vartheta(x)] : \right), \tag{6.12}$$

where the local conjugate fields are

$$\vartheta(x) = +\frac{\phi^R(x) + \phi^R(-x)}{2}, \tag{6.13a}$$

$$\varphi(x) = -\frac{\phi^R(x) - \phi^R(-x)}{2}. \tag{6.13b}$$

Importantly, we note that the SC pairing potential now has a $\sin(\pi x/\mathrm{L})$ modulation – vanishing at $x = 0, \pm\mathrm{L}$ – stemming from the fact that $R(x)$ and $L(x)$ are no longer independent due to unfolding. This is further reflected in the expressions of $\varphi(x)$ and $\vartheta(x)$ above, which show that they are *non-local* superpositions of $\phi^R(x)$ in the extended domain $[-\mathrm{L}, \mathrm{L}]$. At a more technical level, the compactification radii of the bosonic fields ϑ and φ are doubled from π to 2π as when compared to the closed wire geometry. This is absolutely crucial for the semi-classical understanding of the topological degeneracy in terms of degenerate minima.

Next, we exactly bosonize the explicit MZM operators γ_0 and γ_{L}, yielding

$$\gamma_0 = \frac{1}{\sqrt{2\mathrm{L}}} \int_{-\mathrm{L}}^{\mathrm{L}} \mathrm{d}x \; a(x) [: \mathrm{e}^{i\phi^R(x)} : + : \mathrm{e}^{-i\phi^R(x)} :] \mathrm{e}^{-i\frac{\pi x}{2\mathrm{L}}}, \tag{6.14a}$$

$$\gamma_{\mathrm{L}} = \frac{1}{\sqrt{2\mathrm{L}}} \int_{-\mathrm{L}}^{\mathrm{L}} \mathrm{d}x \; b(x) [: \mathrm{e}^{i\phi^R(x)} : + : \mathrm{e}^{-i\phi^R(x)} :] \mathrm{e}^{-i\frac{\pi x}{2\mathrm{L}}}. \tag{6.14b}$$

Using these expressions one can again verify the validity of Eq. (6.9) within the bosonized formulation. This entails using vertex algebra methods based around the exact operator identity between normal-ordered vertex operators [51]

$$: \mathrm{e}^{i\alpha\phi^R(x)} : : \mathrm{e}^{i\beta\phi^R(y)} := \left[\mathrm{e}^{-i\frac{\pi x}{\mathrm{L}}} - \mathrm{e}^{-i\frac{\pi y}{\mathrm{L}}} \right]^{\alpha\beta} : \mathrm{e}^{i[\alpha\phi^R(x) + \beta\phi^R(y)]} : \tag{6.15}$$

for $\alpha, \beta \in \mathbb{Z}$. In the extremely degenerate (flat band) limit when $v_F = 0$ these bosonized MZM operators take the exactly localized forms

$$\gamma_0 = \mathcal{N} \left(: \mathrm{e}^{i\phi^R(0)} : + : \mathrm{e}^{-i\phi^R(0)} : \right) \propto R(0) + R^\dagger(0), \tag{6.16a}$$

$$\gamma_{\mathrm{L}} = -i\mathcal{N} \left(: \mathrm{e}^{i\phi^R(\mathrm{L})} : + : \mathrm{e}^{-i\phi^R(\mathrm{L})} : \right) \propto i[R(\mathrm{L}) - R^\dagger(\mathrm{L})], \tag{6.16b}$$

where $\mathcal{N}$ is an infinite normalization constant. In this special limit, H reduces to just the modulated cosine potential that goes as $\sin\left[\frac{\pi x}{\mathrm{L}}\right] \cos[2\vartheta(x)]$. The fact that the SC pairing potential explicitly vanishes at the boundaries makes it abundantly clear that the above expressions for γ_0 and γ_{L} are indeed zero-energy modes. Their particular Majorana form has to do with an inversion symmetry (present even when $v_F > 0$) that we shall discuss later. Let us just mention that the corresponding superpositions are sensitive to the sign of Δ, which we have so far taken to be positive. Lastly, in terms of the mode expansion of $\phi^R(x)$,

$$\phi^R(x) = \vartheta_0 + \frac{\pi Q x}{\mathrm{L}} + \sum_{n>0} \frac{1}{\sqrt{n}} \left(a_n \mathrm{e}^{i\frac{n\pi x}{\mathrm{L}}} + a_n^\dagger \mathrm{e}^{-i\frac{n\pi x}{\mathrm{L}}} \right), \tag{6.17}$$

the MZMs in the extreme limit $v_F = 0$ have the simplified forms

$$\gamma_0 \propto \mathrm{e}^{i\vartheta_0}, \qquad \gamma_\mathrm{L} \propto -i\mathrm{e}^{i\vartheta_0}(-1)^Q, \tag{6.18}$$

where ϑ_0 is the zero mode for the current density phase operator and Q is the total charge operator conjugate to it. Even though these appear to be non-local expressions [35], they are in fact limits of the local expansions given in Eq. (6.14). This just highlights the point that non-local bosonic expressions for topological quasiparticle operators – Majoranas in this case – are often entirely local in terms of fermionic fields.

The derivation of the above results and claims are the contents of Secs. 6.5 and 6.6. Along the way, we shall also cover and contrast the case of closed boundary conditions while demonstrating the fermion parity switching effect [52, 53] under magnetic flux threading. Also, in Sec. 6.6.4, we introduce and employ vertex algebra methods from the conformal field theory of current algebras. Finally, we should mention that although a large body of our bosonization results are exact – and in complete agreement with the fermionic approach – we have also utilized semi-classical methods, a point of novelty being that we use the phase-space formulation [54] of the classical action for the zero modes and the physical observables of charge and current.

6.3 Continuum fermionic model and open boundaries

The physical setting is that of one-dimensional spinless fermions $\Psi(x)$ with a low-energy linearized expansion

$$\Psi(x) \approx R(x)\mathrm{e}^{ik_F x} + L(x)\mathrm{e}^{-ik_F x}, \tag{6.19}$$

where k_F is a Fermi momentum and $R(x)$, $L(x)$ are independent slow-moving right and left chiral fields respectively. They satisfy the usual canonical anticommutation relations $\{R(x), R^\dagger(y)\} = \delta(x-y)$ and similarly for $L(x)$.

For additional insight into the effects of competing gapping terms, we initially consider a Hamiltonian that is slightly more general than the one given in Eq. (6.1). Here, an additional k_F-dependent backscattering term is present. Such a term naturally competes with the SC pairing that would otherwise favor the topological MZM phase [55,56]. Explicitly, we consider a (1+1)-dimensional continuum model with Lagrangian and Hamiltonian

$$\mathcal{L} := iR^\dagger\partial_t R + iL^\dagger\partial_t L - \mathcal{H}, \tag{6.20a}$$

$$\mathcal{H} := -iv_F\left(R^\dagger\partial_x R - L^\dagger\partial_x L\right) + \Delta\mathrm{e}^{i\chi}R^\dagger L^\dagger - \mathrm{M}\mathrm{e}^{-i2k_F x}R^\dagger L + \mathrm{h.c.}, \tag{6.20b}$$

where $\mathrm{M} \geq 0$ is a single-particle backscattering term and $\chi \in \mathbb{R}$ is a constant SC phase parameter. The $\mathrm{e}^{\pm i2k_F x}$ phases in the backscattering term are necessary to ensure momentum conservation. Such a model arises effectively in nanowires with strong spin-orbit coupling (usually Rashba-type), Zeeman coupling to a magnetic field and proximity-induced SC pairing of the s-wave form [7–9]. This model has been studied many times in the literature from the point of view of bosonization [52, 57–59]. More directly, it may also appear in the low-energy limit of Kitaev's Majorana lattice model [1]

$$H = \sum_{j\in\mathbb{Z}}\left[-tc_{j+1}^\dagger c_j - \tfrac{\Delta}{2}\mathrm{e}^{i\chi}c_{j+1}^\dagger c_j^\dagger + \mathrm{M}c_{2j+1}^\dagger c_{2j} + \mathrm{h.c.}\right] - \mu\sum_{j\in\mathbb{Z}}c_j^\dagger c_j. \tag{6.21}$$

Near half-filling $\mu = 0$, this model can be linearized with $k_F = \mu/(2t)$ and $v_F \approx 2t$, where the Fermi momenta are now calculated from their values at half-filling given by $\pm\pi/2$. It should be noted that the M process represents dimerization on the lattice and at $\Delta = \mu = 0$ we have the famed Su-Schrieffer-Heeger [60] (SSH) model. The fact that the SSH and Kitaev models share *almost* the same low-energy effective description has to do with a duality transformation relating the two [61]. However, key differences lie in the implementation of symmetry transformations and open boundary conditions [62].

Interest in Eqs. (6.20) has to do with the emergence of a non-trivial superconducting topological phase yielding boundary Majorana zero modes whenever $0 \leq \mathrm{M} < \Delta$. Intuitively speaking, large Δ favors a gapped topological phase, while large M favors a topologically trivial charge-density wave phase with period $1/2k_F$ [63–68].

It should be noted that the Kitaev chain has a predecessor in the exactly solvable Lieb-Schultz-Mattis (LSM) anti-ferromagnetic chain [69], where boundary-localized quasi-degenerate bound states akin to MZMs were first derived exactly. At granularity of the lattice, the fermion-spin duality is supplied by the Jordan-Wigner transform. By contrast, bosonization, which will be discussed at length in Secs. 6.5 and 6.6, is a fermion-boson duality that emerges in the continuum limit.

6.3.1 Symmetries

For clarity, we shall assume first that the system is closed and neglect complications arising from boundaries. Without mass terms ($\Delta = \mathrm{M} = 0$), there is full $\widehat{U(1)}_L \times \widehat{U(1)}_R$ conformal symmetry with central charges $c = 1$ in each chirality. Thus, as Heisenberg fields, R and L propagate freely as $R(x,t) = R(x - v_F t)$, $L(x,t) = L(x + v_F t)$. There are two global symmetries, total $U(1)_{R+L}$ symmetry and chiral $U(1)_{R-L}$ symmetry, defined respectively by

$$(R, L) \mapsto (R\mathrm{e}^{i\theta_1}, L\mathrm{e}^{i\theta_1}), \tag{6.22}$$

$$(R, L) \mapsto (R\mathrm{e}^{i\theta_2}, L\mathrm{e}^{-i\theta_2}) \tag{6.23}$$

for $\theta_{1,2} \in \mathbb{R}$. They are infinitesimally generated by the total charge (number) operator

$$Q := \int \mathrm{d}x \ : [R^\dagger(x)R(x) + L^\dagger(x)L(x)] : \tag{6.24}$$

and the total chiral charge (current) operator

$$J := \int \mathrm{d}x \ : [R^\dagger(x)R(x) - L^\dagger(x)L(x)] :, \tag{6.25}$$

respectively. Here, : : denotes fermion normal ordering with respect to the filled Fermi sea of negative-energy states. Non-zero values of M and Δ will not only break the conformal symmetries but also the global $U(1)_{R+L}$ and $U(1)_{R-L}$ symmetries. We consider these broken symmetries next on a case by case basis.

<u>M $\neq 0$ and $\Delta \neq 0$:</u> In this case, only *fermion parity* (F) and *spinless time-reversal* ($\mathcal{T}$) are symmetries with actions

$$FRF^{-1} = -R, \qquad FLF^{-1} = -L, \tag{6.26}$$

$$\mathcal{T}\, R\, \mathcal{T}^{-1} = -i\mathrm{e}^{i\chi}L, \qquad \mathcal{T}\, L\, \mathcal{T}^{-1} = -i\mathrm{e}^{i\chi}R. \tag{6.27}$$

Fermion parity is a *linear* symmetry ($Fi = iF$), but time-reversal is *anti-linear* ($\mathcal{T}i = -i\mathcal{T}$) and χ-dependent in order to compensate for the SC phase. Both are representations of $\mathbb{Z}_2$ because $F^2 = \mathcal{T}^2 = 1$. However, F satisfies the additional identity

$$F \equiv (-1)^Q \equiv (-1)^J. \tag{6.28}$$

It is convenient to perform a $U(1)$ phase rotation[1]

$$R \to R\,\mathrm{e}^{i\chi/2+i\pi/4}, \qquad L \to L\,\mathrm{e}^{i\chi/2+i\pi/4}, \tag{6.29}$$

which effectively sets $\chi = \pi/2$. At this special point, the Hamiltonian density takes the simpler form

$$\mathcal{H} = -iv_F\left(R^\dagger\partial_x R - L^\dagger\partial_x L\right) + i\Delta R^\dagger L^\dagger - \mathrm{M}\mathrm{e}^{-i2k_F x}R^\dagger L + \mathrm{h.c.} \tag{6.30}$$

Because F and $\mathcal{T}$ are the only symmetries, the model falls under the BDI-class of free fermion models [70]. This is made more apparent in the Bogoliubov-de Gennes (BdG) form of the Hamiltonian with the Nambu 4-spinor $\Psi(x) := [R(x), L^\dagger(x), L(x), R^\dagger(x)]^T$,

$$H = \frac{1}{2}\int \mathrm{d}x\, \Psi^\dagger(x)\,\mathcal{H}_{\mathrm{BdG}}\,\Psi(x) + \mathrm{const.}, \tag{6.31a}$$

$$\mathcal{H}_{\mathrm{BdG}} = \begin{pmatrix} -iv_F\sigma^z\partial_x - \Delta\sigma^y & -\mathrm{M}\mathrm{e}^{-i2k_F x}\sigma^z \\ -\mathrm{M}\mathrm{e}^{i2k_F x}\sigma^z & iv_F\sigma^z\partial_x + \Delta\sigma^y \end{pmatrix}. \tag{6.31b}$$

Here $\mathcal{H}_{\mathrm{BdG}}$ is traceless (particle-hole symmetric) and anticommutes with $\mathbb{1}\otimes\sigma^x$. Time-reversal is expressed by $\mathrm{T} = (\sigma^z\otimes\sigma^x)K$ with K denoting complex conjugation, giving $[\mathcal{H}_{\mathrm{BdG}}, \mathrm{T}] = 0$. As with all BDI-class BdG Hamiltonians, there is an anti-linear symmetry corresponding to charge conjugation, $\mathrm{C} := \mathrm{T}(\mathbb{1}\otimes\sigma^x) \equiv K(\sigma^z\otimes\mathbb{1})$, such that $\{\mathrm{C}, \mathcal{H}_{\mathrm{BdG}}\} = 0$.

<u>$\mathrm{M} \neq 0$ but $\Delta = 0$:</u> Now there is Q conservation but no J conservation with F and $\mathcal{T}$ still remaining as symmetries. Essentially, the $U(1)_{R-L}$ group has been broken down to $\mathbb{Z}_2$ while $U(1)_{R+L}$ remains unbroken. Nevertheless, there exists a linear charge-conserving spatial inversion symmetry $\mathcal{I}$ acting as

$$\mathcal{I}\,R(x)\,\mathcal{I} = \mathrm{e}^{i\theta_x}L(-x), \tag{6.32a}$$

$$\mathcal{I}\,L(x)\,\mathcal{I} = \mathrm{e}^{-i\theta_x}R(-x). \tag{6.32b}$$

The constant phase $\theta_x \in [0, 2\pi)$ is not set a priori because the action of $\mathcal{I}$ and chiral rotations generated by J do not commute. Rather, because J is odd under $\mathcal{I}$, conjugation by chiral rotations generated by J changes the value of θ_x. One can set $\theta_x = 0$ as a choice of 'chiral gauge'. However, imposing open boundary conditions will result in singling out a specific value of θ_x, which effectively breaks the chiral symmetry at the open boundaries.

<u>$\Delta \neq 0$ but $\mathrm{M} = 0$:</u> Conversely, there is now J conservation at the expense of Q conservation and $\mathcal{I}$ symmetry. More interestingly, there exists an additional linear $\mathbb{Z}_2$ symmetry that may

[1] This phase rotation is not a $U(1)$ electromagnetic gauge transformation because the superconducting order parameter $\Delta\,\mathrm{e}^{i\chi}$ is unchanged. For a detailed discussion we recommend Ref. [103].

be thought of as a *unitary* charge conjugation transformation because it exchanges particles and holes in the manner of a unitary Bogoliubov transformation. This symmetry, which we denote by I_x—to distinguish it from the true spatial inversion $\mathcal{I}$—is defined by

$$\mathrm{I}_x R(x)\mathrm{I}_x = -R^\dagger(x), \qquad \mathrm{I}_x L(x)\mathrm{I}_x = -L^\dagger(x), \tag{6.33a}$$

$$\mathrm{I}_x R^\dagger(x)\mathrm{I}_x = -R(x), \qquad \mathrm{I}_x L^\dagger(x)\mathrm{I}_x = -L(x), \tag{6.33b}$$

where the -1 signs are for later convenience. In terms of the Nambu spinor field $\Psi(x)$ we have

$$\mathrm{I}_x \Psi(x)\mathrm{I}_x = -(\sigma^x \otimes \sigma^x)\Psi(x), \tag{6.34}$$

which gives another symmetry of Eq. (6.31). This symmetry will allow us to attach ± 1 quantum numbers to quasiparticle eigenstates of H and will be exploited to exactly diagonalize the Hamiltonian with open boundaries.

6.3.2 In terms of Majoranas

The Lagrangian can also be expressed in a relativistic form that will make the relativistic symmetries of the theory more apparent. A Majorana representation is obtained by defining

$$\lambda := \frac{1}{2}\begin{pmatrix} R + R^\dagger \\ L + L^\dagger \end{pmatrix}, \qquad \lambda' := \frac{1}{2i}\begin{pmatrix} R - R^\dagger \\ L - L^\dagger \end{pmatrix}. \tag{6.35}$$

This implies the reality conditions $\lambda^\dagger = \lambda^T$, $(\lambda')^\dagger = (\lambda')^T$, and the canonical anticommutation relations $\{\lambda_\alpha(x), \lambda_\beta(y)\} = \{\lambda'_\alpha(x), \lambda'_\beta(y)\} = \frac{1}{2}\delta(x-y)\delta_{\alpha\beta}$. Under time reversal the Majorana fields transform oppositely as

$$\mathcal{T}\lambda\mathcal{T}^{-1} = \sigma^x\lambda, \qquad \mathcal{T}\lambda'\mathcal{T}^{-1} = -\sigma^x\lambda', \tag{6.36}$$

whereas under spatial inversion, they transform identically as

$$\mathcal{I}\,\lambda\,\mathcal{I} = \sigma^x\lambda, \qquad \mathcal{I}\,\lambda'\,\mathcal{I} = \sigma^x\lambda'. \tag{6.37}$$

Direct substitution leads to the Lagrangian

$$\begin{aligned}\mathcal{L} = {} & i\lambda^T(\partial_t + \sigma^z v_F \partial_x)\lambda + i(\lambda')^T(\partial_t + \sigma^z v_F \partial_x)\lambda' + \mathrm{M}\sin(2k_F x)[\lambda^T\sigma^y\lambda + (\lambda')^T\sigma^y\lambda'] \\ & + i\mathrm{M}\cos(2k_F x)\lambda^T\sigma^x\lambda' + \Delta[\lambda^T\sigma^y\lambda - (\lambda')^T\sigma^y\lambda'].\end{aligned} \tag{6.38}$$

Next, we define the Dirac matrices

$$\gamma^0 = \sigma^x, \qquad \gamma^1 = -i\sigma^y, \qquad \gamma_5 = \gamma^0\gamma^1 = \sigma^z, \tag{6.39}$$

such that $\{\gamma^\mu, \gamma^\nu\} = 2g^{\mu\nu}$ in the (+1,−1) metric signature. Then, defining $\overline{\lambda} := \lambda^\dagger\gamma^0$, $\overline{\lambda}' := (\lambda')^\dagger\gamma^0$ gives

$$\begin{aligned}\mathcal{L} = {} & i\overline{\lambda}(\gamma^0\partial_t + v_F\gamma^1\partial_x)\lambda + i\overline{\lambda}'(\gamma^0\partial_t + v_F\gamma^1\partial_x)\lambda' + i\mathrm{M}\cos(2k_F x)\overline{\lambda}\lambda' \\ & + i\mathrm{M}\sin(2k_F x)\left[\overline{\lambda}\gamma_5\lambda - \overline{\lambda}'\gamma_5\lambda'\right] + i\,\Delta[\overline{\lambda}\gamma_5\lambda - \overline{\lambda}'\gamma_5\lambda'].\end{aligned} \tag{6.40}$$

Thus, only when $k_F = 0$ the Lagrangian is actually relativistically invariant. We remind the reader that in the case of Kitaev's Majorana chain, we calculate the Fermi momenta from their half-filling value, see Eq. (6.21). Thus, $k_F = 0$ corresponds to half-filling. At that point we have a theory of *two* continuum relativistic Majorana chains [50] λ and λ' with competing masses: one *scalar* with strength M, and another *pseudo-scalar* with strength Δ.

The two types of massive phases that are possible with the Lagrangian in Eq. (6.40) are separated by a critical point at $\Delta = \mathrm{M}$. The topologically trivial phase is the one with $\mathrm{M} > \Delta \geq 0$ and vice versa. However confirming either type of phase is not so straightforward. The simplest method involves introducing open boundaries as will be discussed in Sec. 6.4.2. Alternatively, one could introduce a lattice model whose low-energy continuum limit is described by either the Hamiltonian of Eq. (6.31) or the Lagrangian of Eq. (6.40). This is carried out explicitly in Appendix 6.D. With a lattice model, one then computes a chiral winding number defined over the first Brillouin zone.

Another more intrinsic approach that avoids open boundaries and lattice models proceeds by computing the Pauli-Villars regularized partition function in the limit $\mathrm{M} = 0$ when the Majorana Lagrangians have decoupled. Then, as was argued in Ref. [71], the topological phase exists whenever the pseudo-scalar mass (Δ) has a sign opposite to that of the regulator mass. However, since pseudo-scalar mass terms appear with both signs in the Lagrangian Eq. (6.40), either λ or λ' will always be topologically non-trivial while the other is trivial. Thus, the system as a whole will always remain topologically non-trivial irrespective of the sign of Δ in the decoupled chain limit where $\mathrm{M} = 0$.

6.3.3 Open boundaries and unfolding

We start by revisiting the analysis of Refs. [47, 72] and note that similar concepts appeared earlier in the bosonization of open spin-1/2 chains [46, 73]. The basic idea is to impose Dirichlet boundary conditions on the fast moving fermionic field

$$\Psi(x) = R(x)\mathrm{e}^{ik_F x} + L(x)\mathrm{e}^{-ik_F x}. \tag{6.41}$$

The boundary conditions that can be imposed take the general form

$$R(0) + \mathrm{e}^{i\delta_0} L(0) = 0, \tag{6.42a}$$

$$R(\mathrm{L}) + \mathrm{e}^{i(\delta_L - 2k_F \mathrm{L})} L(\mathrm{L}) = 0, \tag{6.42b}$$

where L is the system length, δ_0 and δ_L are reflection phase shifts, and the additional $2k_F\mathrm{L}$ phase is for later convenience. More generally, we can also impose boundary conditions that mix R and $L^\dagger$ and vice-versa. These are Andreev-type boundary conditions [74], which do not conserve electric charge and require superconducting reservoirs at the boundaries.

We then proceed by an operation known as *unfolding*, which entails relabeling the $L(x)$ field by $R(-x)$ defined on an extended space $[-\mathrm{L}, \mathrm{L}]$ that is topologically equivalent to S^1. Specifically, the relabeling is

$$L(x) \equiv -\mathrm{e}^{-i\delta_0} R(-x), \qquad 0 \leqslant x \leqslant \mathrm{L}\,, \tag{6.43}$$

in accordance to the boundary condition at $x = 0$. Identification of the points at $x = \mathrm{L}$ and $x = -\mathrm{L}$ requires that the unfolded $R(x)$ field satisfies quasiperiodic boundary conditions

$$R(\mathrm{L}) = R(-\mathrm{L})\, \mathrm{e}^{i(\delta_\mathrm{L} - \delta_0 - 2k_F \mathrm{L})}, \tag{6.44}$$

where the quasiperiodic phase depends on $k_F\mathrm{L}$ and the phases $\delta_0, \delta_\mathrm{L}$.

It is illuminating to consider this unfolding operation from the point of view of inversion symmetry. For open boundaries it is more natural to take the center of inversion to lie at $x = \mathrm{L}/2$ as opposed to $x = 0$. Then, the inversion transformation is redefined by

$$\mathcal{I}\, R(x)\, \mathcal{I} = \mathrm{e}^{i\theta_x} L(\mathrm{L} - x), \tag{6.45}$$

$$\mathcal{I}\, L(x)\, \mathcal{I} = \mathrm{e}^{-i\theta_x} R(\mathrm{L} - x). \tag{6.46}$$

Applying this inversion operation to the boundary conditions (6.42) yields the condition

$$2\theta_x = \delta_\mathrm{L} + \delta_0 - 2k_F\mathrm{L}. \tag{6.47}$$

Thus, the inversion phase θ_x, which was formerly arbitrary because of J conservation, has now been fixed (symmetry-broken) by the phases set by the boundary conditions. Incidentally, this also implies that the imposition of open boundary conditions necessarily breaks J conservation, i.e., $U(1)_{R-L}$ symmetry.

Next, the 2-spinor field $[R(x), L(x)]^T$ can be decomposed into inversion eigenstates with parities $\sigma = \pm 1$ such that

$$L(\mathrm{L} - x) = \sigma \mathrm{e}^{-i\theta_x} R(x), \qquad R(\mathrm{L} - x) = \sigma \mathrm{e}^{i\theta_x} L(x). \tag{6.48}$$

Applying these to the boundary conditions at $x = 0, \mathrm{L}$ gives

$$R(\mathrm{L}) = -\sigma \mathrm{e}^{+i[\frac{\delta_\mathrm{L} - \delta_0}{2} - k_F\mathrm{L}]}\, R(0), \tag{6.49}$$

$$L(\mathrm{L}) = -\sigma \mathrm{e}^{-i[\frac{\delta_\mathrm{L} - \delta_0}{2} - k_F\mathrm{L}]}\, L(0). \tag{6.50}$$

This shows that for even parity states with $\sigma = +1$, the R, L fields obey antiperiodic boundary conditions between $x = 0$ and $x = \mathrm{L}$ up to constant phases $\mathrm{e}^{\pm i[\frac{\delta_\mathrm{L} - \delta_0}{2} - k_F\mathrm{L}]}$. Conversely, when the inversion parity is odd, $\sigma = -1$, the R, L fields will obey periodic boundary conditions up to constant phases $\mathrm{e}^{\pm i[\frac{\delta_\mathrm{L} - \delta_0}{2} - k_F\mathrm{L}]}$. We use this information to write the R field as an equal superposition of periodic (Ramond) and antiperiodic (Neveu-Schwarz) right-moving fermionic fields. The names Ramond (R) and Neveu-Schwarz (NS) is the nomenclature used in conformal field theory[2] to describe periodic and antiperiodic fermions on the string sheet. Expanding the chiral field $R(x)$ yields

$$\begin{aligned} R(x) &:= R^{(\mathrm{R})}(x)\mathrm{e}^{-ik'_F x} + R^{(\mathrm{NS})}(x)\mathrm{e}^{-ik'_F x} \\ &= \frac{1}{\sqrt{2\mathrm{L}}} \sum_{n=-\infty}^{\infty} \left(R_n \mathrm{e}^{i\frac{2\pi}{\mathrm{L}} n x} + R_{n+\frac{1}{2}} \mathrm{e}^{i\frac{2\pi}{\mathrm{L}}(n+\frac{1}{2})x} \right) \mathrm{e}^{-ik'_F x}, \end{aligned} \tag{6.51}$$

where $k'_F := k_F + (\delta_0 - \delta_\mathrm{L})/(2\mathrm{L})$. Note that in the limit of large L, the difference between k_F and k'_F diminishes. The normalization constant above has been selected such that

$$\{R(x), R^\dagger(y)\} = \sum_{m=-\infty}^{\infty} \delta(x - y + 2m\mathrm{L}) \left(\mathrm{e}^{-i2k'_F \mathrm{L}} \right)^m. \tag{6.52}$$

[2]Here we use the cylindrical coordinates $x - iv_F\tau = \frac{i\mathrm{L}}{\pi} \ln z$ so that the case of Ramond (R) fermions really does correspond to a periodic fermion. Transforming between planar (z) and cylindrical (x, τ) holomorphic coordinates results in an extra $z^{-1/2}$ Jacobian which exchanges periodic and antiperiodic boundary conditions.

This anticommutation relation suggests that the $R(x)$ field is quasiperiodic in the extended domain with period 2L and twisting $\mathrm{e}^{-i2k'_F\mathrm{L}}$. This is nothing more than the unfolding operation that was just described. Finally, because of the requirements of inversion symmetry, we define the left-moving fields by

$$L^{(\mathrm{R})}(x) := -R^{(\mathrm{R})}(\mathrm{L}-x) = -R^{(\mathrm{R})}(-x), \tag{6.53a}$$

$$L^{(\mathrm{NS})}(x) := +R^{(\mathrm{NS})}(\mathrm{L}-x) = -R^{(\mathrm{NS})}(-x). \tag{6.53b}$$

This implies

$$L(x) := L^{(\mathrm{R})}(x)\mathrm{e}^{ik'_F x} + L^{(\mathrm{NS})}(x)\mathrm{e}^{ik'_F x} = -R(-x), \tag{6.53c}$$

where we have analytically continued the fields into $x < 0$. These new unfolded chiral fields are 2L-quasiperiodic such that

$$R(x+2\mathrm{L}) = \mathrm{e}^{-i2k'_F\mathrm{L}}R(x), \tag{6.54a}$$

$$L(x+2\mathrm{L}) = \mathrm{e}^{i2k'_F\mathrm{L}}L(x). \tag{6.54b}$$

In this manner, a non-zero k_F and reflection phases acquired at the open boundaries can influence the continuum model through a quasiperiodic twisting after unfolding.

The above quasiperiodic boundary conditions for the unfolded chiral fields differ from the ones stated in the standard literature such as Refs. [47, 48, 75]. They only agree when $\mathrm{e}^{i2k'_F\mathrm{L}} = 1$, which corresponds to an implicit assumption that k'_F is exactly quantized in units of π/L such that $R(x) \equiv -L(-x)$ is periodic with periodicity 2L. Nevertheless, the chiral field may also be analytically continued to an antiperiodic field with $R(x+2\mathrm{L}) = -R(x)$. In this case, k'_F is a half-integer multiple of π/L such that $\mathrm{e}^{i2k'_F\mathrm{L}} = -1$ and the boundary condition at $x = \mathrm{L}$ in Eq. (6.42) remains satisfied. Often, these differences become less important – in regard to bulk properties – in the limit of large L.

One important point to appreciate is that the Dirichlet boundary condition Eqs. (6.42) selects inversion-symmetric solutions from the periodic and antiperiodic modes for the closed version of the wire. Half are from the NS and the other half from the R types, and this depends on their properties under inversion. In fact, the exact eigenstates of an open system will alternate between even and odd inversion parity states. This observation is also suggestive of the connection between the fermion parity switching effect and twisted boundary conditions in an open wire with quasi-zero modes.

6.4 Exact fermionic eigenstates with open boundaries

We shall now carry out a full diagonalization of the continuum fermionic Hamiltonian of Eq. (6.30) in the limit $\mathrm{M} = 0$ such that

$$H = \int_0^{\mathrm{L}} \mathrm{d}x\big[-iv_F R^\dagger \partial_x R + iv_F L^\dagger \partial_x L + i\Delta(R^\dagger L^\dagger - LR)\big] \tag{6.55}$$

at finite L and with open boundaries through unfolding. Our approach significantly extends the analyses of Refs. [47, 57] as it does not make an approximation for large system lengths

L. As was noted in Sec. 6.3.1, there is an enhanced linear $\mathbb{Z}_2$ symmetry I_x whenever $\mathrm{M} = 0$, and this will serve as a guide for us in carrying out an exact analytic diagonalization.

First, we define a two-component Nambu spinor field

$$\psi(x) := \begin{pmatrix} R(x) \\ L^\dagger(x) \end{pmatrix}, \tag{6.56}$$

which is an effective linearized representation of the microscopic field $\Psi(x) \approx R(x)\mathrm{e}^{ik_F x} + L(x)\mathrm{e}^{-ik_F x}$. For reasons that will become clearer later, we will demand now that $\mathrm{e}^{2ik'_F L} = -1$, which leads to an antiperiodic (NS) unfolded $R(x)$ fermion. The simplest way to satisfy this condition as well as $\Psi(0) = \Psi(\mathrm{L}) = 0$ is to have

$$\delta_0 = \delta_\mathrm{L} = 0, \qquad k_F = \left(n + \frac{1}{2}\right)\frac{\pi}{\mathrm{L}} \tag{6.57}$$

for $n \in \mathbb{Z}$. This leads to $L(x) \equiv -R(-x)$, implying

$$R(0) + L(0) = 0, \qquad R(\mathrm{L}) - L(\mathrm{L}) = 0. \tag{6.58}$$

Therefore, we find $R(x + 2\mathrm{L}) = -R(x)$ and $\psi(x + 2\mathrm{L}) = -\psi(-x)$. Moreover, we must also have that

$$\psi(x) \equiv -\sigma^x[\psi^\dagger(-x)]^T, \tag{6.59}$$

which is a reality condition that translates to a condition on the Majorana fields λ, λ' as

$$\lambda(x) = -\sigma^x\lambda(-x), \qquad \lambda'(x) = -\sigma^x\lambda'(-x). \tag{6.60}$$

The Hamiltonian in terms of $\psi(x)$ is

$$H = \int_0^\mathrm{L} \mathrm{d}x\, \psi^\dagger(x)\left[-iv_F\sigma^z\partial_x - \Delta\sigma^y\right]\psi(x), \tag{6.61}$$

which after unfolding corresponds to

$$H = \frac{1}{2}\int_{-\mathrm{L}}^\mathrm{L} \mathrm{d}x\, \psi^\dagger(x)\left[-iv_F\sigma^z\partial_x - \Delta\, s(x)\sigma^y\right]\psi(x). \tag{6.62}$$

Here, we have introduced the 2L-periodic square wave form

$$s(x) := \mathrm{sgn}\left[\sin(\tfrac{\pi x}{\mathrm{L}})\right] = 2\sum_{n\ \mathrm{odd}} \frac{\mathrm{e}^{i\frac{n\pi x}{\mathrm{L}}}}{in\pi}, \tag{6.63}$$

which serves as a profile function for a mass domain wall. Hence we have the BdG mode Hamiltonian [47, 57]

$$\mathcal{H}_\mathrm{BdG} = -iv_F\sigma^z\partial_x - \Delta\, s(x)\,\sigma^y, \tag{6.64}$$

which contains in it a mass domain wall at $x = 0, \pm\mathrm{L}$.

To diagonalize H, one needs to find operators

$$\psi_E^\dagger := \int_{-\mathrm{L}}^{\mathrm{L}} \mathrm{d}x\ \psi^\dagger(x) \cdot \phi_E(x) \tag{6.65}$$

that satisfy

$$[H, \psi_E^\dagger] = E\psi_E^\dagger, \qquad \mathcal{H}_{\mathrm{BdG}}\, \phi_E(x) = E\phi_E(x) \tag{6.66}$$

such that ϕ_E is a normalized BdG eigenmode. Due to fermionic Nambu doubling, the negative-energy eigenmodes are redundant because it can be shown that $\psi_{-E} \propto \psi_E^\dagger$. Tentatively, this yields the diagonalization

$$H = \sum_{E \geqslant 0} E\, \psi_E^\dagger \psi_E \quad + E_0 \mathbb{1}, \tag{6.67}$$

where E_0 is the formally infinite ground state energy.

Although superficially similar to Eq. (6.31), $\mathcal{H}_{\mathrm{BdG}}$ in Eq. (6.64) has its symmetries expressed differently. Specifically, time reversal T and unitary charge conjugation I_x have the following actions on 2-spinor wavefunctions $\chi(x)$ defined over $[-\mathrm{L}, \mathrm{L}]$:

$$\mathrm{T} : \chi(x) \mapsto [\chi(-x)]^*, \tag{6.68a}$$

$$\mathrm{I}_x : \chi(x) \mapsto \sigma^x \chi(-x). \tag{6.68b}$$

In this sense, I_x now plays the role of an inversion symmetry in the unfolded domain. This is because $R(-x) = -L(x)$ such that coordinate inversion in the unfolded domain $x \mapsto -x$ automatically exchanges left and right movers. For this reason, we will from now on refer to I_x as an inversion symmetry.

Linear momentum is not conserved because $\mathcal{H}_{\mathrm{BdG}}$ is *not* invariant under arbitrary finite amounts of spatial translations. Nevertheless, $\mathcal{H}_{\mathrm{BdG}}$ is *locally* translationally invariant in the sense that $\mathcal{H}_{\mathrm{BdG}}$ commutes with the infinitesimal generator $-i\partial_x$ everywhere except where $s(x)$ is discontinuous. This suggests diagonalizing the BdG Hamiltonian in $(0, \mathrm{L})$ and $(-\mathrm{L}, 0)$ separately at first and then forming superpositions. The relevant BdG equations are

$$\begin{pmatrix} -iv_F\partial_x & i\Delta \\ -i\Delta & iv_F\partial_x \end{pmatrix} w_>(x) = E w_>(x), \quad x \in (0, \mathrm{L}), \tag{6.69}$$

$$\begin{pmatrix} -iv_F\partial_x & -i\Delta \\ i\Delta & iv_F\partial_x \end{pmatrix} w_<(x) = E w_<(x), \quad x \in (-\mathrm{L}, 0). \tag{6.70}$$

6.4.1 Extended states

We focus first on states above the SC gap ($E^2 \geqslant \Delta^2$) in $0 < x < \mathrm{L}$. The obvious eigenfunction candidates are plane waves of the form

$$w_>(x) = \begin{pmatrix} u_k \\ v_k \end{pmatrix} \mathrm{e}^{ikx}, \quad k > 0. \tag{6.71}$$

Direct substitution then leads to

$$\begin{pmatrix} \xi_k & i\Delta \\ -i\Delta & -\xi_k \end{pmatrix} \begin{pmatrix} u_k \\ v_k \end{pmatrix} = E \begin{pmatrix} u_k \\ v_k \end{pmatrix}, \tag{6.72}$$

where $\xi_k := v_F k$ is the normal state dispersion. The resulting BdG mean-field eigenvalue equation is readily diagonalized with solutions

$$w^{(+)}_{>,k}(x) = \begin{pmatrix} \cos\theta_k \\ -i\sin\theta_k \end{pmatrix} \mathrm{e}^{ikx}, \qquad E = +E_k, \tag{6.73}$$

$$w^{(-)}_{>,k}(x) = \begin{pmatrix} \sin\theta_k \\ i\cos\theta_k \end{pmatrix} \mathrm{e}^{ikx}, \qquad E = -E_k, \tag{6.74}$$

where the BdG dispersion is given by

$$E_k := \sqrt{\Delta^2 + \xi_k^2} \tag{6.75}$$

and the angle $\theta_k \in [0, \pi/4)$ is defined by

$$\tan 2\theta_k = \frac{\Delta}{\xi_k}. \tag{6.76}$$

This also implies the 'reflection' property

$$\cos\theta_k = \sin\theta_{-k}. \tag{6.77}$$

The eigenmodes in the negative domain $-\mathrm{L} < x < 0$ can be obtained by replacing $\Delta \to -\Delta$, which simply corresponds to multiplying the eigenmodes given in Eqs. (6.73) and (6.74) by σ^z. This yields

$$w^{(+)}_{<,k}(x) = \begin{pmatrix} \cos\theta_k \\ i\sin\theta_k \end{pmatrix} \mathrm{e}^{ikx}, \qquad E = +E_k, \tag{6.78}$$

$$w^{(-)}_{<,k}(x) = \begin{pmatrix} \sin\theta_k \\ -i\cos\theta_k \end{pmatrix} \mathrm{e}^{ikx}, \qquad E = -E_k. \tag{6.79}$$

However, $w^{(\pm)}_{>,k}(x)$ and $w^{(\pm)}_{<,k}(x)$ do not agree at the boundary points $x = 0, \pm\mathrm{L}$. Nonetheless, we can exploit the fact that $E_k = E_{-k}$ and consider *superpositions* of degenerate energy eigenstates with opposite k wavenumbers.

Because $\mathcal{H}_{\mathrm{BdG}}$ is invariant under inversion as defined by I_x, we can attempt to determine continuous eigenfunctions from I_x-symmetric eigenstates, i.e., from eigenstates with even (+1) and odd (-1) I_x parities. The superpositions that achieve this for $E = +E_{\pm k}$ are exactly

$$\begin{aligned} \phi^{(+)}_{>,k}(x) &= \frac{1}{\sqrt{4\mathrm{L}\mathrm{N}_k}} \left[\mathrm{e}^{i\theta_k} w^{(+)}_{>,k}(x) - i\mathrm{e}^{-i\theta_k} w^{(+)}_{>,(-k)}(x) \right] \\ &= \frac{1}{\sqrt{4\mathrm{L}\mathrm{N}_k}} \begin{pmatrix} \cos(kx + 2\theta_k) + i\sin(kx) \\ -\cos(kx + 2\theta_k) + i\sin(kx) \end{pmatrix}, \end{aligned} \tag{6.80a}$$

$$\begin{aligned} \varphi^{(+)}_{>,k}(x) &= \frac{1}{\sqrt{4\mathrm{L}\mathrm{N}_k}} \left[\mathrm{e}^{-i\theta_k} w^{(+)}_{>,k}(x) + i\mathrm{e}^{i\theta_k} w^{(+)}_{>,(-k)}(x) \right] \\ &= \frac{1}{\sqrt{4\mathrm{L}\mathrm{N}_k}} \begin{pmatrix} \cos(kx - 2\theta_k) + i\sin(kx) \\ \cos(kx - 2\theta_k) - i\sin(kx) \end{pmatrix}, \end{aligned} \tag{6.80b}$$

and their analytic continuations through

$$\phi^{(+)}_{<,k}(x) = \phi^{(+)}_{>,k}(-x)^*, \qquad \varphi^{(+)}_{<,k}(x) = \varphi^{(+)}_{>,k}(-x)^* \tag{6.81}$$

as required by time-reversal symmetry. The k-dependent $O(1)$ constant N_k is chosen such that the eigenfunctions are properly normalized over $[-\mathrm{L}, \mathrm{L}]$. Finally, we arrive at the normalized entire eigenfunctions

$$\phi_k^{(+)}(x) = \frac{1}{\sqrt{2\mathrm{L}\mathrm{N}_k}} \begin{pmatrix} \cos(k|x| + 2\theta_k) + i\sin(kx) \\ -\cos(k|x| + 2\theta_k) + i\sin(kx) \end{pmatrix}, \tag{6.82}$$

$$\varphi_k^{(+)}(x) = \frac{1}{\sqrt{2\mathrm{L}\mathrm{N}_k}} \begin{pmatrix} \cos(k|x| - 2\theta_k) + i\sin(kx) \\ \cos(k|x| - 2\theta_k) - i\sin(kx) \end{pmatrix}, \tag{6.83}$$

valid for $-\mathrm{L} \leqslant x \leqslant \mathrm{L}$ and a $k > 0$ which is yet undetermined. Note that $\phi_0^{(+)}(x) \equiv 0$ and $\varphi_0^{(+)}(x) \equiv 0$, which excludes the $k = 0$ solution entirely. Moreover, the negative k values are excluded since they have already been used in forming the superpositions.

It is easy to verify that these states are I_x eigenstates with

$$\mathrm{I}_x \phi_k^{(+)} = -\phi_k^{(+)}, \qquad \mathrm{I}_x \varphi_k^{(+)} = +\varphi_k^{(+)}. \tag{6.84}$$

More importantly, they are continuous at $x = 0$. However, at $x = \pm\mathrm{L}$, enforcing the antiperiodic boundary condition leads to quantization of k through the conditions

$$\cos(k\mathrm{L} + 2\theta_k) = 0 \quad \text{for} \quad \phi_k^{(+)}, \tag{6.85}$$

$$\cos(k\mathrm{L} - 2\theta_k) = 0 \quad \text{for} \quad \varphi_k^{(+)}, \tag{6.86}$$

which give the self-consistent equations

$$k_{n,1} = \left(n + \frac{1}{2}\right)\frac{\pi}{\mathrm{L}} - \frac{2\theta_{k_{n,1}}}{\mathrm{L}} \quad \text{for} \quad \phi_{k_{n,1}}^{(+)}, \quad n \in \mathbb{N}, \tag{6.87a}$$

$$k_{n,2} = \left(n + \frac{1}{2}\right)\frac{\pi}{\mathrm{L}} + \frac{2\theta_{k_{n,2}}}{\mathrm{L}} \quad \text{for} \quad \varphi_{k_{n,2}}^{(+)}, \quad n \in \mathbb{N} \cup \{0\}. \tag{6.87b}$$

In general, these have to be solved numerically for each n. However, in the limit of large n either $k_{n,1}$ or $k_{n,2}$ approaches a half-integer multiple of π/L because $\theta_k \to 0$ in the limit of large k. One should also note that while $\varphi_{k_{0,2}}^{(+)}$ is a viable solution irrespective of Δ, its counterpart $\phi_{k_{0,1}}^{(+)}$ is not whenever $v_F/\Delta < \mathrm{L}$. Nevertheless, solutions to $k_{0,1}$ in Eq. (6.87) will exist when $v_F/\Delta \geqslant \mathrm{L}$, which is the regime where the coherence length is longer than or equal to the system length. In fact, the mode $\phi_{k_{0,1}}^{(+)}$ is continuously connected to the topological MZM eigenfunction that we will describe in the next subsection.

Finally, the solutions for the quantized values of $k = k_{n,1}, k_{n,2}$ lead to the fermionic Bogoliubon operators

$$\phi_n := \int_{-\mathrm{L}}^{\mathrm{L}} \mathrm{d}x \, [\phi_{k_{n,1}}^{(+)}(x)]^\dagger \psi(x), \tag{6.88}$$

$$\varphi_n := \int_{-\mathrm{L}}^{\mathrm{L}} \mathrm{d}x \, [\varphi_{k_{n,2}}^{(+)}(x)]^\dagger \psi(x), \tag{6.89}$$

that diagonalize the part of H above the SC gap. It is convenient to define the functions

$$u_k(x) := \frac{1}{\sqrt{\mathrm{L}\mathrm{N}_k}} \left[\cos(k|x| + 2\theta_k) + i\sin(kx)\right], \tag{6.90}$$

$$v_k(x) := \frac{1}{\sqrt{\mathrm{L}\mathrm{N}_k}} \left[\cos(k|x| - 2\theta_k) + i\sin(kx)\right], \tag{6.91}$$

which allows us to express our eigenfunction solutions more neatly as

$$\phi^{(+)}_{k_{n,1}}(x) = \frac{1}{\sqrt{2}} \begin{pmatrix} u_{k_{n,1}}(x) \\ -[u_{k_{n,1}}(x)]^* \end{pmatrix}, \tag{6.92}$$

$$\varphi^{(+)}_{k_{n,2}}(x) = \frac{1}{\sqrt{2}} \begin{pmatrix} v_{k_{n,2}}(x) \\ [v_{k_{n,2}}(x)]^* \end{pmatrix}. \tag{6.93}$$

In addition, these functions satisfy $[u_k(-x)]^* = u_k(x)$ and $[v_k(-x)]^* = v_k(x)$ as is required by time-reversal symmetry T and inversion symmetry I_x. This then yields the following equivalent expressions for the Bogoliubon operators:

$$\phi_n = \int_{-\mathrm{L}}^{\mathrm{L}} \mathrm{d}x \, \frac{[u_{k_{n,1}}(x)]^*}{\sqrt{2}} \Big[R(x) + R^\dagger(x) \Big], \tag{6.94}$$

$$\varphi_n = \int_{-\mathrm{L}}^{\mathrm{L}} \mathrm{d}x \, \frac{[v_{k_{n,2}}(x)]^*}{\sqrt{2}} \Big[R(x) - R^\dagger(x) \Big]. \tag{6.95}$$

When expressed in terms of the Majorana field operators $\lambda(x)$, $\lambda'(x)$ defined in Eqs. (6.35), these expressions translate to

$$\phi_n = 2 \int_0^{\mathrm{L}} \mathrm{d}x \, [\phi^{(+)}_{k_{n,1}}(x)]^\dagger \lambda(x), \tag{6.96}$$

$$\varphi_n = 2i \int_0^{\mathrm{L}} \mathrm{d}x \, [\varphi^{(+)}_{k_{n,2}}(x)]^\dagger \sigma^z \lambda'(x). \tag{6.97}$$

This just reflects the fact that the theory is comprised of two decoupled Majorana field theories with opposite pseudo-scalar masses as described by the Lagrangian in Eq. (6.40) in the limit $\mathrm{M} = 0$. One may also interpret each Majorana model as being an independent Kitaev Majorana chain as is explicitly discussed in Appendix 6.D.

6.4.2 In-gap states and Majorana zero modes

We now move on to the localized states that have their energies in the SC gap ($E^2 < \Delta^2$). It is best to work directly in the unfolded $[-\mathrm{L}, \mathrm{L}]$ domain. Recall the BdG Hamiltonian

$$\mathcal{H}_{\mathrm{BdG}} = -iv_F \sigma^z \partial_x - \Delta \, \mathrm{sgn}[\sin(\tfrac{\pi x}{\mathrm{L}})] \sigma^y, \tag{6.98}$$

the eigenvalue equation of which we can rearrange as

$$\left[\partial_x - l \, \mathrm{sgn}[\sin(\tfrac{\pi x}{\mathrm{L}})] \, \sigma^x - i\sigma^z \epsilon \right] w(x) = 0 \tag{6.99}$$

with $l := \frac{\Delta}{v_F}$ and $\epsilon := \frac{E}{v_F}$. For the moment, we will not fix the I_x parity of the spinor-valued function $w(x)$.

Now applying the linear differential operator on the LHS of Eq. (6.99) twice to $w(x)$ yields

$$\left[-\partial_x^2 + 2l \sum_{m=-\infty}^{\infty} (-1)^m \delta(x - m\mathrm{L}) \sigma^x \right] w(x) = -(l^2 - \epsilon^2) w(x) \tag{6.100}$$

after using

$$\partial_x \left[\mathrm{sgn}(\sin(\tfrac{\pi x}{\mathrm{L}}))\right] = 2 \sum_{m=-\infty}^{\infty} (-1)^m \delta(x - m\mathrm{L}). \tag{6.101}$$

This then suggests that we expand $w(x)$ in the eigenbasis of σ^x as

$$w(x) = a(x) \begin{pmatrix} 1 \\ -1 \end{pmatrix} + ib(x) \begin{pmatrix} 1 \\ 1 \end{pmatrix}, \tag{6.102}$$

which yields the following decoupled Kronig-Penney like time-independent Schrödinger equations with delta-function potentials

$$\left[-\partial_x^2 - 2l \sum_{m=-\infty}^{\infty} (-1)^m \delta(x - m\mathrm{L})\right] a(x) = -(l^2 - \epsilon^2) a(x), \tag{6.103a}$$

$$\left[-\partial_x^2 + 2l \sum_{m=-\infty}^{\infty} (-1)^m \delta(x - m\mathrm{L})\right] b(x) = -(l^2 - \epsilon^2) b(x). \tag{6.103b}$$

This is a somewhat unusual Kronig-Penney model because of the alternating sign of the delta-function potential. However, because $a(x)$ and $b(x)$ are required to be antiperiodic as opposed to being generally quasiperiodic, the 'crystal-momentum' is located at the boundary of the first Brillouin zone. Moreover, because the 'Hamiltonian' operator is purely real – as opposed to just being Hermitian – the functions $a(x)$ and $b(x)$ can be chosen to be purely real. It is then easy to appreciate that $a(x)$ and $b(x)$ must vanish where the singular potential is positive in order to be 2L-antiperiodic. Thus we have the nodal conditions

$$a(\mathrm{L}) = a(-\mathrm{L}) = 0, \qquad b(0) = 0, \tag{6.104}$$

which accompany the kinks at $a'(0)$ and $b'(\mathrm{L})$. In the domain $-\mathrm{L} < x < \mathrm{L}$, the normalized functions with these properties are

$$a(x) = \mathcal{N}_\kappa \sinh(\kappa(\mathrm{L} - |x|)), \tag{6.105}$$

$$b(x) = \mathcal{N}_\kappa \sinh(\kappa x), \tag{6.106}$$

with inverse decay length $\kappa := +\sqrt{l^2 - \epsilon^2}$ and

$$\mathcal{N}_\kappa = \frac{1}{\sqrt{\mathrm{L}}} \left(\frac{\sinh(2\kappa\mathrm{L})}{2\kappa\mathrm{L}} - 1\right)^{-\frac{1}{2}} \tag{6.107}$$

as a normalization constant. Here $a(x)$ is allowed to be even because it vanishes at the boundaries $x = \pm\mathrm{L}$, whilst $b(\pm\mathrm{L})$ is allowed to take non-zero values because it is an odd function. Because $a(x)$ and $b(x)$ are really required to be 2L-antiperiodic, these functions can be described as Fourier series:

$$a(x) = \mathcal{N}_\kappa \sum_{n \text{ odd}} \frac{4\kappa\mathrm{L}\cosh(\kappa\mathrm{L})}{(n\pi)^2 + (2\kappa\mathrm{L})^2} \, \mathrm{e}^{i\frac{n\pi x}{2\mathrm{L}}}, \tag{6.108}$$

$$b(x) = \mathcal{N}_\kappa \sum_{n \text{ odd}} \frac{4\kappa\mathrm{L}\cosh(\kappa\mathrm{L})}{(n\pi)^2 + (2\kappa\mathrm{L})^2} \, i^{-n} \, \mathrm{e}^{i\frac{n\pi x}{2\mathrm{L}}}. \tag{6.109}$$

In fact, it is easy to see from the Fourier series representations that $b(x) = a(x - \mathrm{L})$.

Finally, we can derive the exact 'gap equation' from the kink conditions at $x = 0, \mathrm{L}$ which read as

$$-a'(0^+) + a'(0^-) = 2la(0), \tag{6.110}$$
$$-b'(-\mathrm{L} + 0^+) + b'(\mathrm{L}^-) = 2lb(\mathrm{L}). \tag{6.111}$$

These are identical conditions which translate to[3]

$$\kappa = l \tanh(\kappa \mathrm{L}) \quad \Longleftrightarrow \quad \frac{iv_F\kappa}{\Delta} = \tan(i\kappa \mathrm{L}), \tag{6.112}$$

or, in terms of the original parameters,

$$\sqrt{1 - \left(\tfrac{E}{\Delta}\right)^2} = \tanh\left(\frac{\Delta \mathrm{L}}{v_F}\sqrt{1 - \left(\tfrac{E}{\Delta}\right)^2}\right). \tag{6.113}$$

By identifying v_F/Δ with the SC coherence length, we see that as $|E| \to \Delta$ we have $\mathrm{L} \to v_F/\Delta$. Likewise, as $\mathrm{L} \to \infty$ with v_F/Δ finite, then $|E| \to 0$. Thus we have the correct limits describing the extremely small and infinite L limits, respectively, as compared to the SC coherence length. Moreover it is easy to see from Eqs. (6.105) and (6.106) that as $\mathrm{L} \to \infty$, $a(x)$ and $b(x)$ approach the expected exponentially localized forms. By contrast, as $\Delta \to v_F/\mathrm{L}$ from above (while all other parameters remain finite) we have $\kappa \to 0$, meaning that these solutions cease to be normalized eigenfunctions at points beyond $\Delta < v_F/\mathrm{L}$.

To arrive at an estimate of $|E|$ in the large L limit, we use the asymptotic expansion

$$\tanh x = 1 - 2\mathrm{e}^{-2x} + O(\mathrm{e}^{-4x}) \tag{6.114}$$

to arrive at

$$\kappa \approx l(1 - 2\mathrm{e}^{-2\kappa \mathrm{L}}) \quad \Rightarrow \quad |E| \sim 2\Delta \mathrm{e}^{-\frac{\Delta \mathrm{L}}{v_F}}. \tag{6.115}$$

We note that here the usual oscillating prefactor to the finite-size energy splitting is absent (equal to one) due to our choice that k_F is a half-integer multiple of π/L. With this choice of k_F, we find a constraint from above on the value of the finite-size energy splitting. Shown in Fig. 6.1 is a comparison between this asymptotic estimate, Eq. (6.113) and the numerically computed gaps for a Kitaev lattice model realization. As is discussed in Appendix 6.D, the continuum SC wire model may be realized as two Kitaev Majorana chains of opposite SC "mass terms" in accordance with the discussion in Sec. 6.3.2.

We can now write down the exact finite L eigenstates of the original BdG equation. These are not surprisingly given by the equal superpositions

$$\Phi^{(\pm)}(x) := \frac{a(x)}{2}\begin{pmatrix}1\\-1\end{pmatrix} \pm \frac{ib(x)}{2}\begin{pmatrix}1\\1\end{pmatrix} \equiv \frac{\mathcal{N}_\kappa}{2}\begin{pmatrix}\sinh(\kappa(\mathrm{L} - |x|)) \pm i\sinh(\kappa x)\\ -\sinh(\kappa(\mathrm{L} - |x|)) \pm i\sinh(\kappa x)\end{pmatrix} \tag{6.116}$$

[3]It is amusing to point out that this gap equation relating κ and l is identical to the self-consistent Weiss mean-field equation with κ as the order parameter and L^{-1} as the temperature.

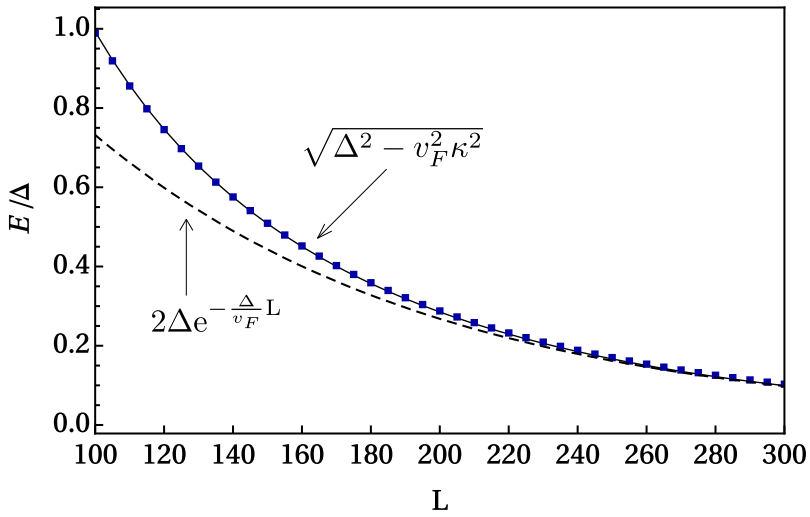

Figure 6.1: Comparison of the in-gap energy E using Eq. (6.113) [solid line] and numerically computed eigenvalues of the lattice model given in Eq. (6.440) [square points]. The numerical parameters are $t' = 0.99$ and $t = 1.0$, where $v_F = (t + t')a/2$ and $\Delta = t - t'$. The coherence length is given by $v_F/\Delta = 99.5$ in units of a. The dashed line is the asymptotic form given in Eq. (6.115), which underestimates the energy gap for short lengths.

with energies $\pm E_{i\kappa} = \pm\sqrt{\Delta^2 - v_F^2\kappa^2}$. This specific linear combination respects time-reversal symmetry $[\Phi^{(\pm)}(-x)]^* = \Phi^{(\pm)}(x)$. To check that these are indeed eigenfunctions of Eq. (6.98), one can first verify that for $0 < x < \mathrm{L}$ we have

$$\partial_x a(x) + l a(x) = -\sqrt{l^2 - \kappa^2}\, b(x), \tag{6.117a}$$
$$\partial_x b(x) - l b(x) = +\sqrt{l^2 - \kappa^2} a(x), \tag{6.117b}$$

using the gap equation Eq. (6.113) and hyperbolic trigonometric identities. Even more generally, we can derive similar equations for $-\mathrm{L} < x < 0$ and taken together produce

$$[v_F\partial_x + \Delta s(x)]a(x) = -E_{i\kappa} b(x), \tag{6.118a}$$
$$[v_F\partial_x - \Delta s(x)]b(x) = +E_{i\kappa} a(x) \tag{6.118b}$$

in $-\mathrm{L} < x < \mathrm{L}$. Using these one readily obtains

$$[-iv_F\sigma^z\partial_x - \Delta s(x)\sigma^y]\begin{pmatrix} a(x) \\ -a(x)\end{pmatrix} = iE_{i\kappa}\begin{pmatrix} b(x) \\ b(x)\end{pmatrix}, \tag{6.119a}$$
$$[-iv_F\sigma^z\partial_x - \Delta s(x)\sigma^y]\begin{pmatrix} ib(x) \\ ib(x)\end{pmatrix} = E_{i\kappa}\begin{pmatrix} a(x) \\ -a(x)\end{pmatrix}. \tag{6.119b}$$

Together, these relations can be used to show that

$$[-iv_F\sigma^z\partial_x - \Delta s(x)\sigma^y]\Phi^{(\pm)}(x) = \pm E_{i\kappa}\Phi^{(\pm)}(x). \tag{6.120}$$

Defining the fermionic eigenmode operator

$$\psi^\dagger_{E_{i\kappa}} := \int_{-\mathrm{L}}^{\mathrm{L}} \mathrm{d}x\ \psi^\dagger(x)\,\Phi^{(+)}(x) \tag{6.121}$$

then implies that $[H, \psi^\dagger_{E_{i\kappa}}] = E_{i\kappa}\psi^\dagger_{E_{i\kappa}}$.

It will furthermore prove useful to define the Majorana operators

$$\gamma_0 := \int_{-\mathrm{L}}^{\mathrm{L}} \mathrm{d}x\ a(x)[R(x) + R^\dagger(x)], \tag{6.122a}$$

$$\gamma_{\mathrm{L}} := \int_{-\mathrm{L}}^{\mathrm{L}} \mathrm{d}x\ b(x)[R(x) + R^\dagger(x)], \tag{6.122b}$$

which are localized at $x = 0$ and $x = \pm\mathrm{L}$ respectively. This leads to

$$\psi_{E_{i\kappa}} = \int_{-\mathrm{L}}^{\mathrm{L}} \mathrm{d}x\ [\Phi^{(+)}(x)]^\dagger\,\psi(x) \equiv \frac{\gamma_0 - i\gamma_{\mathrm{L}}}{2} \tag{6.123}$$

and

$$[H, \gamma_0] = iE_{i\kappa}\gamma_{\mathrm{L}}, \qquad [H, \gamma_{\mathrm{L}}] = -iE_{i\kappa}\gamma_0. \tag{6.124}$$

The first of these commutation relations is explicitly verified in Appendix 6.C.

6.4.3 Full diagonalization and symmetry fractionalization

The extended and localized eigenmodes lead to the final diagonalization of H as

$$H = -\frac{i}{2}E_{i\kappa}\gamma_0\gamma_{\mathrm{L}} + E_{k_{0,2}}\varphi_0^\dagger\varphi_0 + \sum_{n>0}\Big[E_{k_{n,1}}\phi_n^\dagger\phi_n + E_{k_{n,2}}\varphi_n^\dagger\varphi_n\Big] + \text{const.} \tag{6.125}$$

In second-quantized form, time-reversal $\mathcal{T}$ corresponds to the anti-linear transformation[4]

$$\mathcal{T}R(x)\mathcal{T}^{-1} = R(-x), \qquad \mathcal{T}R^\dagger(x)\mathcal{T}^{-1} = R^\dagger(-x) \tag{6.126}$$

because of unfolding. Thus, while the excitation operators φ_n, ϕ_n are time-reversal invariant, we have that

$$\mathcal{T}\gamma_0\mathcal{T}^{-1} = +\gamma_0, \qquad \mathcal{T}\gamma_{\mathrm{L}}\mathcal{T}^{-1} = -\gamma_{\mathrm{L}}, \tag{6.127}$$

as required for time-reversal symmetry of H. Since the overlap $\int_0^{\mathrm{L}} a(x)b(x)\,\mathrm{d}x \sim \mathrm{e}^{-\kappa\mathrm{L}}$ is exponentially suppressed, we have the delocalization of symmetry properties. This is the hallmark of fractionalization of symmetry transformations [4,6,50] that is a defining property of SPT phases.

In the short length limit where $\mathrm{L} < v_F/\Delta \leqslant \infty$, the solution $\Phi^{(+)}(x)$ is no longer a valid eigenfunction. Rather, the extended state solution $\phi^{(+)}_{k_{0,1}}(x)$ replaces it as the lowest positive-energy eigenfunction. Physically speaking, in the short L limit, the quantization scale of

[4] This differs by an irrelevant sign from our previous definition of $\mathcal{T}$.

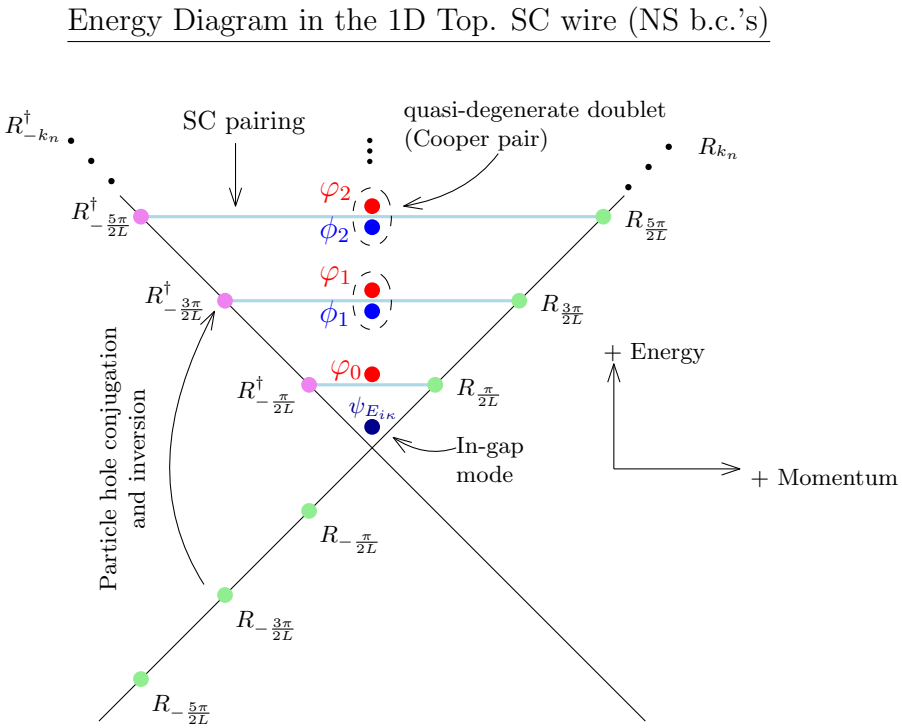

Figure 6.2: Schematic energy diagram of the diagonalized linearized model for an open wire of length L obeying 2L-antiperiodic (NS) boundary conditions after unfolding. Note that with the SC pairing interaction turned on, energy levels are pushed up (pushed down if we are counting states into the filled Fermi sea), which is not shown to scale here for the sake of clarity. Also, the SC pairing function having the square-wave profile $\Delta s(x)$ couples all momentum eigenstates amongst themselves. The solid light blue line only denotes the most dominant channel which couples a particle-hole pair with opposite momenta.

the kinetic energy exceeds the SC gap Δ such that only extended state solutions exist. The change from localized to extended state occurs at exactly $\mathrm{L} = v_F/\Delta$, where the functions $a(x)$ and $b(x)$ become piecewise linear functions with $\kappa = 0$.

It is interesting to note that under the change of sign $\Delta \to -\Delta$, the roles of $k_{n,1}$ and $k_{n,2}$ in Eq. (6.87) are exchanged because the relation $2\theta_k = \tan^{-1}(\frac{\Delta}{v_F k})$ is odd in Δ. In this instance, $\varphi^{(+)}_{k_{0,2}}(x)$ is no longer a viable eigenfunction but instead turns into a topological localized boundary mode with $\mathrm{I}_x = +1$. At the same time, $\Phi^{(+)}(x)$ as defined above gets replaced by $\phi^{(+)}_{k_{0,1}}(x)$ with $\mathrm{I}_x = -1$. In this way, we always have a single topological boundary mode irrespective of the sign of Δ. This is one of the biggest differences with the SSH model, where the sign of the 'mass' plus a choice of open boundary conditions dictates whether or not topological boundary modes will be present in the open wire energy spectrum.

6.4.4 BCS wavefunction

With the explicit 1-body eigensolutions to the BdG Hamiltonian at hand, we can express the exact many-body BCS wavefunction for a finite system of length L with open boundaries.

This is surprisingly not as straightforward as it seems. Typically, the ground state BCS wavefunction $|\mathrm{BCS}\rangle$ should be defined such that

$$\varphi_n|\mathrm{BCS}\rangle = \phi_n|\mathrm{BCS}\rangle = 0 \qquad \forall\ n \in \mathbb{N}, \tag{6.128}$$

$$\varphi_0|\mathrm{BCS}\rangle = \psi_{E_{i\kappa}}|\mathrm{BCS}\rangle = 0, \qquad v_F\kappa = \Delta\tanh(\kappa \mathrm{L}). \tag{6.129}$$

Naively, one would then take

$$|\mathrm{BCS}\rangle = \psi_{E_{i\kappa}}\varphi_0 \prod_{n>0} \phi_n\varphi_n|\mathrm{vac}\rangle, \tag{6.130}$$

where $|\mathrm{vac}\rangle$ is the particle-number vacuum which is annihilated by all $R(x)$. There are, however, problems with this definition: In the limit $\Delta = 0$ we have that

$$\phi_n\varphi_n = R^\dagger_{-k_n}R_{k_n}, \qquad k_n = \left(n + \frac{1}{2}\right)\frac{\pi}{\mathrm{L}}, \tag{6.131}$$

which then annihilates the vacuum state $|\mathrm{vac}\rangle$. Nevertheless, in the limit $\Delta = 0$, we expect that the state $|\mathrm{BCS}\rangle$ will become $|0\rangle$, i.e., the filled Fermi sea. It turns out that the relevant state to act on is the 'anti-Fermi sea' $|\bar{0}\rangle$ defined by

$$|\bar{0}\rangle := \prod_{n\geqslant 0} R^\dagger_{k_n}|\mathrm{vac}\rangle. \tag{6.132}$$

This is chosen such that

$$\prod_{n\geqslant 0}(R^\dagger_{-k_n}R_{k_n})|\bar{0}\rangle = \prod_{n\geqslant 0} R^\dagger_{-k_n}|\mathrm{vac}\rangle = |0\rangle.$$

Hence we define the BCS ground state to be

$$|\mathrm{BCS}\rangle := \psi_{E_{i\kappa}}\varphi_0 \prod_{n>0} \phi_n\varphi_n|\bar{0}\rangle. \tag{6.133}$$

By analogy with the usual s-wave BCS wavefunctions, we see that the (hard-core) bosonic operators $b_n := \phi_n\varphi_n$ are the "Cooper pair" annihilation operators for an open wire. However, the Bogoliubons ϕ_n and φ_n are only approximately degenerate because $k_{n,1} \neq k_{n,2}$. Also implicit is the recognition that in the small Δ limit, where $v_F/\Delta \geqslant \mathrm{L}$, the mode $\psi_{E_{i\kappa}}$ is replaced continuously by the extended mode ϕ_0. Hence, we see that the boundary fermionic mode $\psi_{E_{i\kappa}}$ was once part of a Cooper pair $b_0 = \phi_0\varphi_0$ that was 'broken off' and localized when the system length L exceeded the SC coherence length v_F/Δ. Moreover, by changing the sign of Δ, we can make φ_0 evolve into the topological boundary mode when $|\Delta| > v_F/\mathrm{L}$. A schematic energy diagram of the diagonalized open wire is shown in Fig. 6.2.

Relative to $|\mathrm{BCS}\rangle$, we can define two quasi-degenerate ground states

$$|\Omega_0\rangle := |\mathrm{BCS}\rangle, \qquad |\Omega_1\rangle := \psi^\dagger_{E_{i\kappa}}|\mathrm{BCS}\rangle. \tag{6.134}$$

This gives $\gamma_0 = \sigma^x$ and $\gamma_\mathrm{L} = \sigma^y$ when projected onto the quasi-degenerate ground state manifold. Moreover, $|\Omega_0\rangle$ and $|\Omega_1\rangle$ only differ in their correlation functions due to the different occupations of the boundary mode $\psi_{E_{i\kappa}}$. Otherwise, contributions to correlation functions from the bulk extended modes ϕ_n and φ_n are always identical. In Appendix 6.A, we will discuss in detail the "topological" contribution to the correlation functions due to $\psi_{E_{i\kappa}}$.

6.4.5 Extreme superconducting limit

It is clear that the topological boundary mode $\psi_{E_{i\kappa}}$ cannot appear in the normal metal phase when $\Delta = 0$. In fact, the localized in-gap states already cease to exist whenever $v_F/\Delta \geqslant \mathrm{L}$. Let us now consider the other extreme limit when the SC interaction is infinitely strong with $v_F/\Delta = 0$ and $\kappa \to \infty$. For the in-gap state wavefunctions this gives

$$a(x)^2 \to \sum_{m=-\infty}^{\infty} \delta(x - 2m\mathrm{L}), \tag{6.135}$$

$$b(x)^2 \to \sum_{m=-\infty}^{\infty} \delta(\mathrm{L} - x - 2m\mathrm{L}). \tag{6.136}$$

Taking the square root, we formally arrive at

$$a(x) \to \sum_{m=-\infty}^{\infty} (-1)^m \sqrt{\delta(x - 2m\mathrm{L})}, \tag{6.137}$$

$$b(x) \to \sum_{m=-\infty}^{\infty} (-1)^m \sqrt{\delta(\mathrm{L} - x - 2m\mathrm{L})}. \tag{6.138}$$

The notion of a square root to the Dirac delta function needs some clarification because these are not generalized functions in the conventional Schwartz theory of distributions.[5] Rather they require a construction known as non-linear generalized functions in order to have a rigorous definition [76, 77]. With this caveat in mind, we recognize that in this artificial limit there exist perfectly localized exact Majorana zero modes at the boundary points $x = 0, \mathrm{L}$. Moreover, these infinitely localized Majorana operators commute exactly with the Hamiltonian H in Eq. (6.62) in the limit $v_F = 0$. This is easy to appreciate since the SC pairing potential exactly vanishes at $x = 0, \mathrm{L}$ but is constant and non-zero everywhere else.

We should point out that this extreme limit is not technically accessible in a lattice model. This is because the zero correlation length is smaller than the finite lattice spacing, which invalidates the continuum approximation. Nonetheless, there are similarities with the flat band limit of a lattice model, namely that the dispersion is exactly zero and if the model possesses topological boundary modes, these are also exactly lattice-localized zero-energy modes.

From the point of view of the bulk eigenmodes, one has in this limit $\theta_{k_{n,1}} = \theta_{k_{n,2}} = \pi/4$ for all n. This means that

$$k_{n,1} = \left(n + \frac{1}{2}\right)\frac{\pi}{\mathrm{L}} - \frac{\pi}{2\mathrm{L}} = \frac{n\pi}{\mathrm{L}}, \quad n = 1, 2, \ldots$$

$$k_{n,2} = \left(n + \frac{1}{2}\right)\frac{\pi}{\mathrm{L}} + \frac{\pi}{2\mathrm{L}} = \frac{(n+1)\pi}{\mathrm{L}}, \quad n = 0, 1, \ldots$$

so that $k_{n,1} = k_{n-1,2} = n\pi/\mathrm{L}$ for $n \in \mathbb{N}$. One can think of this as a rearrangement of modes such that there is a preference to form a Cooper pair out of $\phi_n \varphi_{n-1}$.

[5] Naively one could try taking the definition of $\sqrt{\delta(x)}$ to be the square root of the limit of appropriately normalized Gaussian functions. However, one would find that the normalization of such functions diminishes too rapidly in the limit such that they (weakly) converge to the zero function within the space of Schwartz generalized functions.

6.5 Bosonization with closed boundaries

In this section, we bosonize the continuum model with closed periodic and antiperiodic boundary conditions. Contrasting periodic vs. antiperiodic boundary conditions is important because of the intimate relationship between 1D topological superconducting phases and fermion parity switches [52, 53]: Namely, the number of fermion number parity switches (modulo 2) induced by adiabatic flux threading – which twists boundary conditions – is the very definition of a $\mathbb{Z}_2$ SPT topological index. Such a fermion parity switching property is also responsible for the 4π Josephson junction period in the topological phase.

6.5.1 Bosonization preliminaries

We consider two sources of twisted boundary conditions. The first one is a threaded magnetic flux through the closed wire of length L, which acts *equally* on left- and right-moving fields, while the second one is a chiral magnetic flux with *opposite* action on left and right movers. We write our bosonized fermionic fields in normal-ordered form as [78]

$$R(x) = \frac{\eta^R}{\sqrt{\mathrm{L}}} :\mathrm{e}^{i\phi^R(x)}: \mathrm{e}^{i\frac{\pi x}{\mathrm{L}}(\delta_J+\delta_Q-1)} = \frac{\eta^R}{\sqrt{\mathrm{L}}} :\mathrm{e}^{i[\vartheta(x)-\varphi(x)]}: \mathrm{e}^{i\frac{\pi x}{\mathrm{L}}(\delta_J+\delta_Q-1)}, \tag{6.139a}$$

$$L(x) = \frac{\eta^L}{\sqrt{\mathrm{L}}} :\mathrm{e}^{i\phi^L(x)}: \mathrm{e}^{i\frac{\pi x}{\mathrm{L}}(\delta_J-\delta_Q+1)} = \frac{\eta^L}{\sqrt{\mathrm{L}}} :\mathrm{e}^{i[\vartheta(x)+\varphi(x)]}: \mathrm{e}^{i\frac{\pi x}{\mathrm{L}}(\delta_J-\delta_Q+1)}, \tag{6.139b}$$

where $\phi^{R,L}(x)$ are non-local bosonic chiral fields and $\vartheta(x), \varphi(x)$ are their corresponding local conjugate fields. The $\eta^{R,L}$ are the Klein factors, which we take here to be Hermitian Majorana operators, and δ_Q, δ_J represent the effect of twisted boundary conditions. As Klein factors, $\eta^L = (\eta^L)^\dagger$ and $\eta^R = (\eta^R)^\dagger$ must satisfy

$$\{\eta^R, \eta^L\} = 0, \qquad (\eta^R)^2 = (\eta^L)^2 = 1. \tag{6.140}$$

Their role is to ensure the correct anticommutation statistics between R and L operators. Normal ordering : : is taken with respect to the reference non-interacting Fermi sea (vacuum) $|0\rangle$ that is annihilated by the topological number operators Q, J and positive-frequency bosonic excitation operators defined in the free limit. For reference, the unnormal-ordered forms are

$$R(x) = \frac{\eta^R}{\sqrt{2\pi\epsilon}}\mathrm{e}^{i\phi^R(x)}\mathrm{e}^{i\frac{\pi x}{\mathrm{L}}(\delta_J+\delta_Q)} = \frac{\eta^R}{\sqrt{2\pi\epsilon}}\mathrm{e}^{i[\vartheta(x)-\varphi(x)]}\mathrm{e}^{i\frac{\pi x}{\mathrm{L}}(\delta_J+\delta_Q)}, \tag{6.141a}$$

$$L(x) = \frac{\eta^L}{\sqrt{2\pi\epsilon}}\mathrm{e}^{i\phi^L(x)}\mathrm{e}^{i\frac{\pi x}{\mathrm{L}}(\delta_J-\delta_Q)} = \frac{\eta^L}{\sqrt{2\pi\epsilon}}\mathrm{e}^{i[\vartheta(x)+\varphi(x)]}\mathrm{e}^{i\frac{\pi x}{\mathrm{L}}(\delta_J-\delta_Q)}, \tag{6.141b}$$

where $\epsilon > 0$ is the UV cutoff taken to zero at the end of the calculation. It is important to point out that normal ordering yields additional $\mathrm{e}^{\pm i\frac{\pi x}{\mathrm{L}}}$ phase factors, and that neglecting these phase factors often leads to the wrong identification of boundary condition type.

In both normal- and unnormal-ordered forms, periodic (R) boundary conditions correspond to

$$\delta_Q + \delta_J = 1 \mod 2, \tag{6.142}$$

whereas antiperiodic (NS) boundary conditions correspond to

$$\delta_Q + \delta_J = 0 \mod 2. \tag{6.143}$$

For convenience, we limit δ_Q and δ_J to integral values, but this is not a physical requirement. [6] Hence we have

$$R(x+\mathrm{L}) = R(x)\mathrm{e}^{i\pi(\delta_J+\delta_Q-1)}, \tag{6.144}$$

$$L(x+\mathrm{L}) = L(x)\mathrm{e}^{i\pi(\delta_J-\delta_Q+1)}. \tag{6.145}$$

Note that δ_Q has an alternative interpretation as a quantized shift in the Fermi momentum k_F in units of π/L. Absorbing the boundary condition shifts $\delta_{Q,J}$ into Q and J is a convention often used by many authors [72, 79]. However, because δ_Q and δ_J commute with the zero modes of $\varphi(x)$ and $\vartheta(x)$, they do not fluctuate quantum-mechanically, nor do they contain data about actual particle occupation numbers. For this reason, we prefer to keep them separate from Q and J.

The conjugate bosonic fields $\varphi(x)$ and $\vartheta(x)$ satisfy the equal-time commutator

$$[\varphi(x), \vartheta(y)] = -i\pi\varepsilon_1(x-y) \tag{6.146}$$

with

$$\varepsilon_1(x-y) := \frac{1}{\mathrm{L}}(x-y) + \frac{i}{2\pi}\ln\left(\frac{1-\mathrm{e}^{+\frac{i2\pi}{\mathrm{L}}(x-y)}}{1-\mathrm{e}^{-\frac{i2\pi}{\mathrm{L}}(x-y)}}\right) = \left\lceil\frac{x-y}{\mathrm{L}}\right\rceil - \frac{1}{2}, \tag{6.147}$$

where $\lceil * \rceil$ denotes the integer ceiling. The function $\varepsilon_1(x)$ is L-periodic in x, possesses a branch cut at $x = 0$ and is a Green's function with respect to ∂_x,

$$\varepsilon_1'(x-y) = \sum_{m\in\mathbb{Z}} \delta(x-y-m\mathrm{L}). \tag{6.148}$$

Thus, Eq. (6.146) is the finite-length version of the often-quoted bosonized commutation relation [48, 75]

$$[\varphi(x), \vartheta(y)] = -\frac{i\pi}{2}\mathrm{sgn}(x-y) \tag{6.149}$$

for $|x-y| < \mathrm{L}$. The conjugate fields $\vartheta(x), \varphi(x)$ have the mode expansion

$$\varphi(x) = \varphi_0 - \frac{\pi Q}{\mathrm{L}}x - \sum_{q\neq 0}\sqrt{\frac{\pi}{2|q|\mathrm{L}}}(a_q + a_{-q}^\dagger)\mathrm{e}^{iqx}, \tag{6.150a}$$

$$\vartheta(x) = \vartheta_0 + \frac{\pi J}{\mathrm{L}}x + \sum_{q\neq 0}\sqrt{\frac{\pi}{2|q|\mathrm{L}}}\,\mathrm{sgn}(q)\,(a_q - a_{-q}^\dagger)\mathrm{e}^{iqx}, \tag{6.150b}$$

[6] At special integral values of δ_Q and δ_J [e.g., $\delta_Q = 1$ and $\delta_J = 2$], the spectrum of momentum states is shifted by quantized integral amounts. One can then singularly 'gauge' away the effect of the twisted boundary conditions, essentially by relabeling momentum states. However, because the bosonized Hamiltonian is normal-ordered with respect to a reference vacuum $|0\rangle$ that remains fixed, the Hamiltonian will not appear to be invariant under the singular gauge transformation.

where the sums run over $q \in (2\pi/\mathrm{L})\mathbb{Z}$ and $[a_q, a_{q'}^\dagger] = \delta_{qq'}$. Here, ϑ_0 and φ_0 are zero modes such that

$$[\varphi_0, \vartheta_0] = 0, \qquad [\varphi_0, J] = -[\vartheta_0, Q] = i, \tag{6.151a}$$

$$[Q, J] = 0, \qquad [\varphi_0, Q] = [\vartheta_0, J] = 0. \tag{6.151b}$$

It is important to emphasize that the integer-quantized operators Q and J are not completely independent and must satisfy the parity selection rule

$$F := (-1)^Q \equiv (-1)^J \quad \Longleftrightarrow \quad Q = J \bmod 2, \tag{6.152}$$

where F is the fermion number parity operator. This is a necessary constraint given the fermionic field representations of Q and J introduced in Eqs. (6.24) and (6.25).

More importantly, the angular bosonic fields φ and ϑ have to be compactified [80] with radius π,

$$\varphi(x) \sim \varphi(x) + \pi, \qquad \vartheta(x) \sim \vartheta(x) + \pi, \tag{6.153}$$

in line with the mode expansion in Eqs. (6.150).

Before bosonizing the Hamiltonian in Eq. (6.30), we introduce the following equivalent expressions of the bosonic fields

$$\varphi(x) = \varphi_0 - \frac{\pi Q}{\mathrm{L}} x - \pi \int_{-\mathrm{L}/2}^{\mathrm{L}/2} \zeta_1(x-y)\rho(y)\,\mathrm{d}y, \tag{6.154a}$$

$$\vartheta(x) = \vartheta_0 + \frac{\pi J}{\mathrm{L}} x + \pi \int_{-\mathrm{L}/2}^{\mathrm{L}/2} \zeta_1(x-y)j(y)\,\mathrm{d}y, \tag{6.154b}$$

where ζ_1 defined as

$$\zeta_1(x-y) := \varepsilon_1(x-y) - \frac{x-y}{\mathrm{L}} \equiv \sum_{n>0} \frac{\sin\left(\frac{2\pi n}{\mathrm{L}}(x-y)\right)}{n\pi} \tag{6.155}$$

is the descending saw-tooth function of period L such that

$$\zeta_1'(x) = -\frac{1}{\mathrm{L}} + \sum_{m\in\mathbb{Z}} \delta(x + m\mathrm{L}). \tag{6.156}$$

The physical charge and current densities are given by

$$\rho_{\mathrm{tot}}(x) = -\tfrac{1}{\pi}\partial_x\varphi(x) = \tfrac{Q}{\mathrm{L}} + \rho(x), \tag{6.157a}$$

$$j_{\mathrm{tot}}(x) = +\tfrac{1}{\pi}\partial_x\vartheta(x) = \tfrac{J}{\mathrm{L}} + j(x). \tag{6.157b}$$

The derivation of these uncommon but useful bosonization expressions is extensively described in Appendix 6.B. There, it is also shown that the fields $\rho(x)$ and $j(x)$ satisfy the finite-length current algebra commutation relation

$$[\rho(x), j(y)] = -\frac{i}{\pi} \sum_{m\in\mathbb{Z}} \delta'(x - y - m\mathrm{L}) = -\frac{i}{\pi}\varepsilon''(x-y). \tag{6.158}$$

Finally, we must emphasize a redundant $\mathbb{Z}_2$ 'gauge symmetry' that is always present with this type of bosonization convention. Indeed, in the bosonization expressions of Eqs. (6.139), the Klein factors and zero modes always appear in the combinations[7]

$$\eta^R \mathrm{e}^{i(\vartheta_0+\varphi_0)}, \qquad \eta^L \mathrm{e}^{i(\vartheta_0-\varphi_0)}. \tag{6.159}$$

These combinations are *invariant* under the discrete transformation

$$\eta^R \to -\eta^R, \qquad \eta^L \to -\eta^L, \tag{6.160}$$

$$\varphi_0 \to \varphi_0, \qquad \vartheta_0 \to \vartheta_0 + \pi. \tag{6.161}$$

Roughly speaking, the combinations of operators in Eq. (6.159) are $\mathbb{Z}_2$ slave-particle fractionalizations [81,82] of the fermionic operators that raise or lower the fermion number. This internal $\mathbb{Z}_2$ gauge symmetry is generated by the $\mathbb{Z}_2$ charge operator

$$\xi := i\eta^L\eta^R(-1)^Q, \qquad \xi^2 = 1. \tag{6.162}$$

Hence, the nominal Hilbert space is always twice as big as compared to the physical Hilbert space of the underlying chiral fermions. Fortunately, we can project onto the physical Hilbert space by selecting a gauge fixing choice. In this instance, a convenient choice is just to fix the gauge to $\xi = 1$ such that

$$F \equiv (-1)^Q = i\eta^L\eta^R. \tag{6.163}$$

6.5.2 Bosonized Hamiltonian and action

Applying this bosonization dictionary to the fermionic Hamiltonian given in Eq. (6.30) in the case of coincident Fermi points $k_F = 0$ gives

$$H = \int_{-\mathrm{L}/2}^{\mathrm{L}/2} (\mathcal{H}_0 + \mathcal{H}_1)\,\mathrm{d}x, \tag{6.164a}$$

$$\mathcal{H}_0 = \frac{v_F}{2\pi} : \left\{[\partial_x\varphi(x)]^2 + [\partial_x\vartheta(x)]^2\right\} : + \frac{\pi v_F}{\mathrm{L}^2}[Q\,(\delta_Q - 1) + J\,\delta_J], \tag{6.164b}$$

$$\mathcal{H}_1 = \left(\frac{2\mathrm{M}}{\mathrm{L}}\right) F : \sin\left(2\varphi(x) - \left(\tfrac{2\pi}{\mathrm{L}}x\right)\delta_Q\right) : - \left(\frac{2\Delta}{\mathrm{L}}\right) F : \cos\left(2\vartheta(x) + \left(\tfrac{2\pi}{\mathrm{L}}x\right)\delta_J\right) : . \tag{6.164c}$$

We have chosen to focus on the $k_F = 0$ case since the competition between backscattering and superconducting interactions is most intense at half-filling. However, this comment only applies to the Kitaev wire interpretation of the model which remains the most convenient for our purpose. By contrast, the realization in Rashba nanowires is more complicated and involves charge/spin density order set by k_F [55,56].

Very often, authors [48,75] neglect the effect of Klein factors by setting $F \equiv i\eta^L\eta^R = 1$. However, this can lead to mistakes because of the parity switching effect. In fact, one can already appreciate [52] from Eq. (6.164c) the role that twisted boundary conditions (δ_Q, δ_J) and F will play in deciding the pinned values of the fields φ and ϑ. Thus we must allow F to be a degree of freedom even though it is an integral of motion.

[7] To add confusion to matters, these products of operators are sometimes also referred to as Klein factors (see, e.g., Ref. [79])

Although exactly solvable in the fermionic representation, the bosonized Hamiltonian in Eq. (6.164) cannot be so transparently dealt with. Nevertheless, one can still gain a great deal of intuition from the effective low-energy approach. This is best carried out with an action/functional approach. As is derived in Appendix 6.B, the real-time classical action associated to the model for fixed fermion parity $F = \pm 1$ can be expressed as $S_{\text{tot}}[\varphi, \vartheta] := S_c[\rho, j] + S_0[\varphi, \vartheta] + S_1[\varphi, \vartheta]$, where

$$\begin{aligned} S_c[\rho, j] := &-\pi \int \mathrm{d}t \int_{-\mathrm{L}/2}^{\mathrm{L}/2} \mathrm{d}x \int_{-\mathrm{L}/2}^{\mathrm{L}/2} \mathrm{d}y \; \zeta_1(x-y)\, j(x)\, \partial_t \rho(y) \\ &- \int \mathrm{d}t \int_{-\mathrm{L}/2}^{\mathrm{L}/2} \mathrm{d}x \; \frac{\pi v_F}{2} [\rho(x)^2 + j(x)^2], \end{aligned} \tag{6.165a}$$

$$S_0[\varphi, \vartheta] := \int \mathrm{d}t \left(J\, \partial_t \varphi_0 - Q\, \partial_t \vartheta_0 - \frac{\pi v_F}{2\mathrm{L}} (J^2 + Q^2) - \frac{\pi v_F}{\mathrm{L}} [Q(\delta_Q - 1) + J\, \delta_J] \right), \tag{6.165b}$$

$$\begin{aligned} S_1[\varphi, \vartheta] := \int \mathrm{d}t \int_{-\mathrm{L}/2}^{\mathrm{L}/2} \mathrm{d}x \Big\{ &\left(\tfrac{2\Delta}{\mathrm{L}}\right) F \cos\left[2\vartheta(x) + \left(\tfrac{2\pi}{\mathrm{L}} x\right) \delta_J\right] \\ &- \left(\frac{2\mathrm{M}}{\mathrm{L}}\right) F \sin\left[2\varphi(x) - \left(\tfrac{2\pi}{\mathrm{L}} x\right) \delta_Q\right] \Big\}, \end{aligned} \tag{6.165c}$$

and the local conjugate fields $\varphi(x)$ and $\vartheta(x)$ are related to ρ, j, φ_0, ϑ_0, Q, and J by Eqs. (6.154). Compared to Eq. (6.330a), we have now included additional cosine potentials that arise from the fermionic mass terms. Note that in order to derive the correct classical action from the quantum Hamiltonian and the canonical commutation relations, one must first decide on an operator ordering convention. As detailed in Appendix 6.B, we choose to work in the convention that the non-zero bosonic modes $a_q^{(\dagger)}$ are Wick normal-ordered, while the zero modes ϑ_0, φ_0 and their charges J, Q are qp-ordered, where the angular operators act as the q's and the charges as the p's. This yields cosine potentials that are independent of the UV cutoff.

We now proceed by semi-classically examining the action S_{tot} when either one of the cosine terms dominates. By seeking homogeneous saddle points of the action, we set $\rho = 0$ and $j = 0$, which gives the simplified effective Lagrangian

$$\begin{aligned} L_{\text{eff}} = &J\, \partial_t \varphi_0 - Q\, \partial_t \vartheta_0 - \tfrac{\pi v_F}{2\mathrm{L}} [J(J + 2\delta_J) + Q(Q + 2\delta_Q - 2)] \\ &- F \left\{ 2\mathrm{M} \left(\frac{\sin[\pi(Q + \delta_Q)]}{\pi(Q + \delta_Q)} \right) \sin(2\varphi_0) - 2\Delta \left(\frac{\sin[\pi(J + \delta_J)]}{\pi(J + \delta_J)} \right) \cos(2\vartheta_0) \right\}, \end{aligned} \tag{6.166}$$

where we have performed the finite integrals in the cosine terms. In general, for simultaneously non-zero couplings, both potentials will compete and we can expect tunneling between saddle-point minima of the two potentials. In principle, once the saddle points have been determined, one could reincorporate fluctuations by expanding about the saddle-point solution in ρ and j perturbatively [81, 83].

Next, we would like to define the fermion parity quantum eigenstates which will correspond to possible saddle points of pinned states. These are conventionally defined as

$$|\vartheta_0 = \theta\rangle_+ := \sum_{m \text{ even}} \mathrm{e}^{im\theta}|Q = m\rangle, \tag{6.167a}$$

$$|\vartheta_0 = \theta\rangle_- := \sum_{m \text{ odd}} \mathrm{e}^{im\theta}|Q = m\rangle, \tag{6.167b}$$

$$|\varphi_0 = \phi\rangle_+ := \sum_{m \text{ even}} \mathrm{e}^{-im\phi}|J = m\rangle, \tag{6.167c}$$

$$|\varphi_0 = \phi\rangle_- := \sum_{m \text{ odd}} \mathrm{e}^{-im\phi}|J = m\rangle, \tag{6.167d}$$

and satisfy

$$|\vartheta_0 = (\theta + \pi)\rangle_\pm = \pm|\vartheta_0 = \theta\rangle_\pm, \tag{6.168}$$

$$|\varphi_0 = (\phi + \pi)\rangle_\pm = \pm|\varphi_0 = \phi\rangle_\pm. \tag{6.169}$$

Hence these quantum states obey the compactification radius conditions of Eq. (6.153). Moreover,

$$\mathrm{e}^{i\vartheta_0}|\vartheta_0 = \theta\rangle_\pm = \mathrm{e}^{i\theta}|\vartheta_0 = \theta\rangle_\mp, \tag{6.170}$$

$$\mathrm{e}^{-i\varphi_0}|\varphi_0 = \phi\rangle_\pm = \mathrm{e}^{-i\phi}|\varphi_0 = \phi\rangle_\mp, \tag{6.171}$$

since raising and lowering obviously changes fermion parity. More importantly, this means that it is *possible* to pin both φ_0 and ϑ_0 simultaneously [since they commute from Eqs. (6.151)] but only in the specific tensor product combinations

$$|\vartheta_0 = \theta\rangle_+ \otimes |\varphi_0 = \phi\rangle_+, \qquad |\vartheta_0 = \theta\rangle_- \otimes |\varphi_0 = \phi\rangle_-, \tag{6.172}$$

in accordance to the fermion parity rule. We should emphasize that these ϑ_0, φ_0 'vacuum states' are meant to represent variational ground states in the limit of infinitely strong pinning.

In the following subsections, we shall examine the topologically trivial and non-trivial phases separately. We do so by considering the cases where $\mathrm{M} \neq 0$, $\Delta = 0$ and $\Delta \neq 0$, $\mathrm{M} = 0$ in turn.

Trivial phase

The saddle point of the trivial phase can be characterized by an effective theory when $\Delta = 0$, leaving the potential derived from fermionic backscattering as the only interaction term in Eq. (6.166). In this limit, Q itself becomes an integral of motion and hence a conserved quantum number in the effective quantum description. Hence in minimizing the potential energy we can set $Q = -\delta_Q$ with $\delta_Q = 0, 1$, which also implies $F = (-1)^{\delta_Q}$. This yields the effective Hamiltonian

$$H_{\text{eff}} = \frac{\pi v_F}{2\mathrm{L}}\left[J(J + 2\delta_J) + \delta_Q(2 - \delta_Q)\right] + 2\mathrm{M}(-1)^{\delta_Q}\sin(2\varphi_0). \tag{6.173}$$

Varying δ_Q can be seen to be equivalent to varying the chemical potential (Fermi momentum) by non-quantized values. For this reason, we shall set $\delta_Q = 1$ and let the twisted boundary

conditions merely specify changes in δ_J. Explicitly, we have periodic (antiperiodic) boundary conditions for $\delta_J = 0$ ($\delta_J = 1$). Note that this automatically determines the fermion parity as $F = (-1)^{\delta_Q} = -1$ and the charge as $Q = -1$. Nevertheless, it is important to remember that the fermion parity has not actually been fixed. Rather, the low-energy sector just prefers to have an even parity in the absence of twisting by a chiral magnetic field.

Periodic boundary conditions: In the Ramond (R) case we have $\delta_J = 0$, leading to the effective Hamiltonian

$$H_{\text{eff}}^{(R)} = \frac{\pi v_F}{2\text{L}} \left(J^2 + 1\right) - 2\text{M}\sin(2\varphi_0), \tag{6.174}$$

which resembles the Hamiltonian of a Josephson junction. It is minimized by $J = 0$ and $\varphi_0 = \pi/4 \bmod \pi$. From the effective Lagrangian, we still have the Poisson bracket $\{\varphi_0, J\} = 1$ and hence in the quantum theory we must have that $[\varphi_0, J] = i$. In the limit of strong pinning, where $\text{M} \gg v_F/\text{L}$, the variationally optimized non-degenerate pinned ground state is then

$$|\Psi_{\text{M}}^{(R)}\rangle = |Q = -1\rangle \otimes |\varphi_0 = \tfrac{\pi}{4}\rangle_-. \tag{6.175}$$

Antiperiodic boundary conditions: Turning to the Neveu-Schwarz (NS) case, we now have the condition $\delta_J = 1$. This then results in the effective Hamiltonian

$$H_{\text{eff}}^{(NS)} = \frac{\pi v_F}{2\text{L}} \left[J(J+2) + 1\right] - 2\text{M}\sin(2\varphi_0) \tag{6.176}$$

with the same variational ground state in the strongly pinned limit,

$$|\Psi_{\text{M}}^{(NS)}\rangle = |Q = -1\rangle \otimes |\varphi_0 = \tfrac{\pi}{4}\rangle_-, \tag{6.177}$$

and the same fermion parity $F = -1$. In short, we do not see a switch in fermion number parity of the variational ground state whenever the quasiperiodic boundary conditions are twisted by a magnetic field threaded through the closed 1D system.

Topological phase

The saddle point of the topologically non-trivial phase can be characterized by an effective theory at $\text{M} = 0$. In this limit, J becomes an integral of motion and hence a conserved quantum number in the effective quantum description. From minimizing the potential energy, we set $J = -\delta_J$, where $\delta_J = 0, 1$. In contrast to the trivial phase, taking $\delta_Q = 1$ does not fix the fermion parity. In fact, the fermion parity of the effective low-energy sector is now explicitly set by the choice of twisted boundary condition with $F = (-1)^{\delta_J}$. The effective Hamiltonian that results is

$$H_{\text{eff}} = \frac{\pi v_F}{2\text{L}} \left(\delta_J^2 + Q^2\right) - 2\Delta(-1)^{\delta_J}\cos(2\vartheta_0). \tag{6.178}$$

Periodic boundary conditions: Setting $J = \delta_J = 0$ and hence $F = 1$, we arrive at another Josephson-junction type Hamiltonian

$$H_{\text{eff}}^{(R)} = \frac{\pi v_F}{2\text{L}} Q^2 - 2\Delta\cos(2\vartheta_0), \tag{6.179}$$

minimized by $Q = 0$ and $\vartheta_0 = 0 \bmod \pi$. Again, in the strong pinning limit, we have the variational ground state

$$|\Psi_\Delta^{(R)}\rangle = |\vartheta_0 = 0\rangle_+ \otimes |J = 0\rangle. \tag{6.180}$$

Antiperiodic boundary conditions: Now instead setting $\delta_J = 1$ and hence $F = -1$, we arrive at a different Josephson-junction type Hamiltonian

$$H_{\text{eff}}^{(NS)} = \frac{\pi v_F}{2\mathrm{L}}(Q^2 + 1) + 2\Delta\cos(2\vartheta_0), \tag{6.181}$$

minimized by $Q = 0$ and $\vartheta_0 = \pi/2 \bmod \pi$. In the strongly pinned limit, the variational ground state is

$$|\Psi_\Delta^{(NS)}\rangle = |\vartheta_0 = \frac{\pi}{2}\rangle_- \otimes |J = -1\rangle. \tag{6.182}$$

Physically, the non-zero J is a result of attempting to 'screen' the applied magnetic flux, much like in the Luttinger-liquid problem [72]. Hence, there is now fermion number parity switching which is indicative of a topologically non-trivial phase.

6.5.3 Mathieu function solutions to the effective Hamiltonians

In principle, we should include the effects of fluctuations from the "kinetic terms" that are proportional to Q^2 and J^2. This could be carried out to lowest order by using the harmonic approximation on $\sin(2\varphi_0)$ and $\cos(2\vartheta_0)$ about their pinning values. In the lowest non-trivial order, one then obtains a simple harmonic oscillator ground state eigenfunction as the variational ground state. More accurately, we can use solutions of the Mathieu equation to obtain exact normalizable eigenstates [84] to the Josephson-junction like Hamiltonians of Eqs. (6.174), (6.176), (6.179) and (6.181). The Mathieu equation is [85]

$$\frac{\mathrm{d}^2 y(z)}{\mathrm{d}z} + [a - 2q\cos(2z)]y(z) = 0, \tag{6.183}$$

where a and q are constants. It can be seen that all of the Eqs. (6.174), (6.179) and (6.181) may be brought into this form, where $z = \varphi_0$ or $z = \vartheta_0$, a is proportional to the energy, and q is proportional to M or Δ. Equation (6.176) can also be treated this way but requires a Floquet-type solution to the Mathieu equation which we will not discuss here. For our purposes we require the periodic solutions $y(u+\pi) = +y(u)$ (even fermion parity) and the doubly-periodic solutions $y(u+\pi) = -y(u)$ (odd fermion parity). These are real eigensolutions for real q and depend smoothly on q. They are denoted by $ce_r(z,q)$, $se_{r+1}(z,q)$ where $r = 0, 1, 2, \ldots$. Their eigenvalues (characteristics) are conventionally denoted by $a_r(q)$ and $b_r(q)$ such that

$$\partial_z^2 ce_r(z,q) + [a_r(q) - 2q\cos(2z)]ce_r(z,q) = 0, \tag{6.184}$$

$$\partial_z^2 se_r(z,q) + [b_r(q) - 2q\cos(2z)]se_r(z,q) = 0. \tag{6.185}$$

Now specializing to the topologically non-trivial phase, the low-energy effective (unnormalized) ground state wavefunction and energy for the periodic (R) case is

$$|\Psi_\Delta^{(R)}\rangle = \sqrt{\frac{2}{\pi}}\int_0^\pi \mathrm{d}\vartheta\; ce_0(\vartheta - \tfrac{\pi}{2}, \tfrac{2\Delta\mathrm{L}}{\pi v_F})\; |\vartheta\rangle_+ \otimes |J = 0\rangle, \tag{6.186}$$

$$E_\Delta^{(R)} = \frac{\pi v_F}{2\mathrm{L}} a_0(\tfrac{2\Delta\mathrm{L}}{\pi v_F}). \tag{6.187}$$

For the antiperiodic (NS) case we instead have

$$|\Psi_\Delta^{(NS)}\rangle = \sqrt{\frac{2}{\pi}} \int_0^\pi \mathrm{d}\vartheta \; se_1(\vartheta, \tfrac{2\Delta \mathrm{L}}{\pi v_F}) \; |\vartheta\rangle_- \otimes |J=-1\rangle, \tag{6.188}$$

$$E_\Delta^{(NS)} = \frac{\pi v_F}{2\mathrm{L}} + \frac{\pi v_F}{2\mathrm{L}} b_1(\tfrac{2\Delta \mathrm{L}}{\pi v_F}). \tag{6.189}$$

Their difference is

$$\begin{aligned} \delta E_\Delta = E_\Delta^{(NS)} - E_\Delta^{(R)} &= \frac{\pi v_F}{2\mathrm{L}} \left(1 + b_1(\tfrac{2\Delta \mathrm{L}}{\pi v_F}) - a_0(\tfrac{2\Delta \mathrm{L}}{\pi v_F})\right) \\ &\sim \frac{\pi v_F}{2\mathrm{L}} \left(1 + 2^5 \sqrt{\frac{2}{\pi}} \left(\frac{2\Delta \mathrm{L}}{\pi v_F}\right)^{3/4} \mathrm{e}^{-4\sqrt{\frac{2\Delta \mathrm{L}}{\pi v_F}}}\right) \end{aligned} \tag{6.190}$$

as $\mathrm{L} \to \infty$, where we have used the asymptotic relation [85]

$$b_{r+1}(q) - a_r(q) \sim \frac{2^{4r+5}}{r!} \sqrt{\frac{2}{\pi}} \, q^{\frac{r}{2}+\frac{3}{4}} \mathrm{e}^{-4\sqrt{q}}. \tag{6.191}$$

This demonstrates the fermion parity switching effect between NS and R variational solutions to the topologically non-trivial phase, with an energy splitting of $\pi v_F/(2\mathrm{L})$ to leading order. Furthermore, it is interesting to note that as $\mathrm{L} \to \infty$, the eigenfunctions $|\Psi_\Delta^{(NS)}\rangle$ and $|\Psi_\Delta^{(R)}\rangle$ turn into square-root Dirac delta functions localized at their respective pinning values, meaning that their respective squared amplitudes – in angle space – approach that of a Dirac delta function in the infinitely pinned limit.

6.6 Bosonization with open boundaries

In this section, we bosonize the fermionic model with open boundaries using the unfolding procedure of Sec. 6.3.3.

6.6.1 Bosonization preliminaries

Recall the linearization

$$\Psi(x) = R(x)\mathrm{e}^{ik_F x} + L(x)\mathrm{e}^{-ik_F x} \tag{6.192}$$

and the number-conserving boundary conditions

$$R(0) + \mathrm{e}^{i\delta_0} L(0) = 0, \tag{6.193}$$

$$R(\mathrm{L}) + \mathrm{e}^{i(\delta_\mathrm{L} - 2k_F \mathrm{L})} L(\mathrm{L}) = 0. \tag{6.194}$$

We take $\delta_0 = \delta_\mathrm{L} = 0$ and $k_F \in \frac{\pi}{2\mathrm{L}} + \frac{\pi}{\mathrm{L}}\mathbb{N}$, which gives us Dirichlet boundary conditions $\Psi(0) = \Psi(\mathrm{L}) = 0$ and an antiperiodic (NS) $R(x)$ field in $[-\mathrm{L}, \mathrm{L}]$,

$$R(x + 2\mathrm{L}) = -R(x), \qquad L(x) \equiv -R(-x). \tag{6.195}$$

Then we bosonize the *single* chiral fermionic field $R(x)$, such that

$$R(x) = \frac{\eta^R}{\sqrt{2\mathrm{L}}} : \mathrm{e}^{i\phi^R(x)} : \mathrm{e}^{-i\frac{\pi x}{2\mathrm{L}}}, \tag{6.196a}$$

$$R^\dagger(x) = \frac{\eta^R}{\sqrt{2\mathrm{L}}} : \mathrm{e}^{-i\phi^R(x)} : \mathrm{e}^{-i\frac{\pi x}{2\mathrm{L}}}. \tag{6.196b}$$

The additional phase twisting of $\mathrm{e}^{-i\frac{\pi x}{2\mathrm{L}}}$ that is equal for both $R(x)$ and $R^\dagger(x)$ is a result of normal ordering the zero mode. The chiral field $\phi^R(x)$ has the mode expansion [47, 86]

$$\phi^R(x) := \vartheta_0 + \frac{\pi Q x}{\mathrm{L}} + \sum_{n>0} \frac{1}{\sqrt{n}} \left(a_n \mathrm{e}^{i\frac{n\pi x}{\mathrm{L}}} + a_n^\dagger \mathrm{e}^{-i\frac{n\pi x}{\mathrm{L}}} \right) \tag{6.197}$$

with $[\vartheta_0, Q] = -i$ and $[a_n, a_{n'}^\dagger] = \delta_{nn'}$. The compactification radius of ϕ^R remains to be 2π,

$$\phi^R(x) \sim \phi^R(x) + 2\pi, \tag{6.198}$$

which leads to the quantization of the eigenvalues of Q in $\mathbb{Z}$. The mode expansion yields the usual non-local commutation relation for a system of length 2L, i.e.

$$\begin{aligned} [\phi^R(x), \phi^R(y)] &= i2\pi\, \varepsilon_2(x-y) \\ &\equiv i2\pi \left\lceil \frac{x-y}{2\mathrm{L}} \right\rceil - i\pi \\ &= i\pi\, \mathrm{sgn}(x-y) \quad \text{for } |x-y| < 2\mathrm{L}. \end{aligned} \tag{6.199}$$

The kernel function $\varepsilon_2(x-y)$ is defined analogously to $\varepsilon_1(x-y)$, except that it has a period of 2L instead of L.

A crucial exact operator identity is the product of vertex functions

$$: \mathrm{e}^{i\alpha\phi^R(x)} : : \mathrm{e}^{i\beta\phi^R(y)} := \left[\mathrm{e}^{-i\frac{\pi x}{\mathrm{L}}} - \mathrm{e}^{-i\frac{\pi y}{\mathrm{L}}} \right]^{\alpha\beta} : \mathrm{e}^{i[\alpha\phi^R(x) + \beta\phi^R(y)]} : \tag{6.200}$$

for $\alpha, \beta \in \mathbb{Z}$. This is just the conformal field theory operator product expansion (OPE) for normal-ordered vertex functions of a chiral field $\phi^R(x)$ in a system of length 2L. It can be used to verify many other bosonization identities like the canonical anticommutation relations for an antiperiodic $R(x)$,

$$\{R(x), R^\dagger(y)\} = \sum_{m=-\infty}^{\infty} (-1)^m \delta(x - y - 2m\mathrm{L}). \tag{6.201}$$

Furthermore, the unfolding relation between $R(x)$ and $L(x)$ gives

$$L(x) = -\frac{\eta^R}{\sqrt{2\mathrm{L}}} : \mathrm{e}^{i\phi^R(-x)} : \mathrm{e}^{i\frac{\pi x}{2\mathrm{L}}}, \tag{6.202a}$$

$$L^\dagger(x) = -\frac{\eta^R}{\sqrt{2\mathrm{L}}} : \mathrm{e}^{-i\phi^R(-x)} : \mathrm{e}^{i\frac{\pi x}{2\mathrm{L}}}. \tag{6.202b}$$

It is crucial to realize that both R and L are the *same* field such that $\eta^L \equiv -\eta^R$.

Next, we define the angular bosonic fields

$$\vartheta(x) := \frac{\phi^R(x) + \phi^R(-x)}{2}, \qquad \varphi(x) := -\frac{\phi^R(x) - \phi^R(-x)}{2}, \tag{6.203}$$

which are local, $[\varphi(x), \varphi(y)] = [\vartheta(x), \vartheta(y)] = 0$, since ε_2 is an odd function. However, they remain mutually non-local because

$$\begin{aligned}[\varphi(x), \vartheta(y)] &= -i\pi \left[\varepsilon_2(x-y) + \varepsilon_2(x+y)\right] \\ &= -i\pi\, \Theta(x-y) \quad \text{for } \; 0 < x, y < \mathrm{L}.\end{aligned} \tag{6.204}$$

Their mode expansions take the form

$$\vartheta(x) = \vartheta_0 + \sum_{n>0} \frac{1}{\sqrt{n}} \left(a_n + a_n^\dagger\right) \cos\left(\frac{n\pi x}{\mathrm{L}}\right), \tag{6.205a}$$

$$\varphi(x) = -\frac{\pi Q}{\mathrm{L}} x + i \sum_{n>0} \frac{1}{\sqrt{n}} \left(a_n - a_n^\dagger\right) \sin\left(\frac{n\pi x}{\mathrm{L}}\right). \tag{6.205b}$$

Hence, ϑ (φ) satisfies homogeneous Neumann (Dirichlet) boundary conditions at $x = 0, \mathrm{L}$. Both fields remain periodic in $x \in [-\mathrm{L}, \mathrm{L}]$ modulo 2π such that their compactification radius is 2π and not π:

$$\varphi(x) \sim \varphi(x) + 2\pi, \qquad \vartheta(x) \sim \vartheta(x) + 2\pi. \tag{6.206}$$

The Neumann condition on $\vartheta(x)$ means that the current density

$$j(x) := \frac{1}{\pi} \partial_x \vartheta(x) \tag{6.207}$$

vanishes at the boundaries, $j(0) = j(\mathrm{L}) = 0$. Likewise the fluctuating charge density defined by

$$\rho(x) := -\frac{1}{\pi} \partial_x \varphi(x) - \frac{Q}{\mathrm{L}} \tag{6.208}$$

obeys the integral sum rule $\int_0^{\mathrm{L}} \rho(x)\, \mathrm{d}x = 0$. It is clear that there cannot be any topological windings in $\vartheta(x)$ leading to the conclusion that $J = 0$ always. This is entirely consistent with our earlier assertions in Sec. 6.3.3 regarding the incompatibility of $U(1)_{R-L}$ symmetry and open boundary conditions.

Next, we have the mode expansions

$$\rho(x) = -\frac{i}{\mathrm{L}} \sum_{n>0} \sqrt{n} (a_n - a_n^\dagger) \cos\left(\frac{n\pi x}{\mathrm{L}}\right), \tag{6.209}$$

$$j(x) = -\frac{1}{\mathrm{L}} \sum_{n>0} \sqrt{n} (a_n + a_n^\dagger) \sin\left(\frac{n\pi x}{\mathrm{L}}\right), \tag{6.210}$$

from which we can directly verify that they satisfy the modified current algebra

$$[\rho(x), j(y)] = -\frac{i}{\pi} \sum_{m=-\infty}^{\infty} \left[\delta'(x - y + 2m\mathrm{L}) + \delta'(x + y + 2m\mathrm{L})\right], \tag{6.211}$$

which now has *two* Schwinger terms. Alternatively, we can express ϕ^R in terms of ρ and j:

$$\frac{1}{\pi}\partial_x\phi^R(x) = j(x) + \rho(x) + \frac{Q}{\mathrm{L}}, \tag{6.212a}$$

$$\frac{1}{\pi}[\partial_x\phi^R](-x) = -j(x) + \rho(x) + \frac{Q}{\mathrm{L}}. \tag{6.212b}$$

Accompanying this is the functional relation

$$\phi^R(x) = \vartheta_0 + \frac{\pi Q}{\mathrm{L}}x + \pi\int_{-\mathrm{L}}^{\mathrm{L}} \zeta_2(x-y)[j(y)+\rho(y)]\mathrm{d}y, \tag{6.213}$$

where

$$\zeta_2(x-y) := \varepsilon_2(x-y) - \frac{x-y}{2\mathrm{L}} \equiv \sum_{n>0}\frac{\sin\left[\frac{n\pi}{\mathrm{L}}(x-y)\right]}{\pi n} \tag{6.214}$$

is the descending saw-tooth function of period 2L. These expressions also lead to the following equivalent expressions for the angular fields:

$$\vartheta(x) = \vartheta_0 + \pi\int_{-\mathrm{L}}^{\mathrm{L}} \zeta_2(x-y)j(y)\,\mathrm{d}y, \tag{6.215a}$$

$$\varphi(x) = -\frac{\pi Q}{\mathrm{L}}x - \pi\int_{-\mathrm{L}}^{\mathrm{L}} \zeta_2(x-y)\rho(y)\,\mathrm{d}y. \tag{6.215b}$$

The convolutions with the saw-tooth function ζ_2 effectively implement anti-derivatives. In short, three things to note are:

(1) J and φ_0 are now absent,

(2) the parity rule $(-1)^Q = (-1)^J$ is no longer relevant,

(3) the compactification radii of the ϑ, φ fields are now doubled to 2π from π as previously in Sec. 6.5.

These new aspects make the open system drastically different from the closed one from the point of view of bosonization.

6.6.2 Bosonized Hamiltonian and action

Now we apply the open boundary bosonization dictionary to the fermionic Hamiltonian in Eq. (6.30). The normal-ordered kinetic term is given by

$$\begin{aligned} H_0 &= \frac{v_F}{4\pi}\int_0^{\mathrm{L}} \mathrm{d}x : \left([\partial_x\phi^R(x)]^2 + [\partial_x\phi^R(-x)]^2\right) : \\ &= \frac{\pi v_F}{2}\int_0^{\mathrm{L}} \mathrm{d}x : \left(j(x)^2 + \rho(x)^2\right) : + \frac{\pi v_F}{2\mathrm{L}}Q^2, \end{aligned} \tag{6.216}$$

and is missing the inductive J^2 term.

Next, we consider the backscattering terms like $R^\dagger L$. An application of the product formula Eq. (6.200) yields

$$R^\dagger(x)L(x) = -\frac{i}{4\mathrm{L}}\left[\frac{:\mathrm{e}^{i2\varphi(x)}:}{\sin(\frac{\pi x}{\mathrm{L}})}\right]. \tag{6.217}$$

Taking the limits $x \to 0, \mathrm{L}$ produces divergences and suggests the need to fermion normal order [cf. Eq. (6.349)]. Doing so gives

$$:R^\dagger(x)L(x): := \lim_{\epsilon\to 0}\Big[R^\dagger(x+\epsilon)L(x) - \langle 0|R^\dagger(x+\epsilon)L(x)|0\rangle\Big] = -\frac{i}{4\mathrm{L}}\left[\frac{:\mathrm{e}^{i2\varphi(x)}:-1}{\sin(\frac{\pi x}{\mathrm{L}})}\right] \tag{6.218}$$

and an analogous expression for its Hermitian conjugate. Note that for $x \to 0^+$, we have

$$:R^\dagger(0^+)L(0^+): = \frac{1}{2\pi}\partial_x\varphi(0), \tag{6.219}$$

as can be checked by applying L'Hôpital's rule. Further manipulation with trigonometric identities then gives the final normal-ordered bosonized form for the backscattering term

$$:\mathrm{e}^{-i2k_Fx}R^\dagger(x)L(x) + \mathrm{e}^{i2k_Fx}L^\dagger(x)R(x): := \frac{1}{2\mathrm{L}}\left(\frac{:\sin[2\varphi(x)-2k_Fx]:}{\sin(\frac{\pi x}{\mathrm{L}})} + \frac{\sin[2k_Fx]}{\sin(\frac{\pi x}{\mathrm{L}})}\right). \tag{6.220}$$

Importantly, we notice that:

(a) there is an additional 'form factor' that is sensitive to how near x is to either boundary,

(b) the $2k_Fx$ shift in the sine potential promotes charge-density order in the phase field $\varphi(x)$.

This result comes from the fact that $R(x)$ and $L(x)$ are no longer independent because $\phi^R(x)$ and $\phi^L(y) \equiv \phi^R(-y)$ no longer commute. This leads to additional factors when fusing the vertex operators in $R^\dagger(x)L(y)$. Nevertheless, deep in the bulk when $x \approx \mathrm{L}/2$ and $\sin[\frac{\pi x}{\mathrm{L}}] \approx 1$, one recovers the translationally invariant form of this term. Lastly, the second term in the parentheses is not an operator but a pure function and integrates to a constant,

$$\frac{1}{2\mathrm{L}}\int_0^{\mathrm{L}} \mathrm{d}x\, \frac{\sin(k_Fx)}{\sin(\frac{\pi x}{\mathrm{L}})} = \frac{1}{2}, \tag{6.221}$$

because $k_F \in \frac{\pi}{2\mathrm{L}} + (\frac{\pi}{\mathrm{L}})\mathbb{Z}$. Hence we may replace the above expression by

$$:\mathrm{e}^{-i2k_Fx}R^\dagger(x)L(x) + \mathrm{e}^{i2k_Fx}L^\dagger(x)R(x): := \frac{1}{2\mathrm{L}}\left(\frac{:\sin[2\varphi(x)-2k_Fx]:}{\sin(\frac{\pi x}{\mathrm{L}})} + 1\right) \tag{6.222}$$

without loss of accuracy.

By contrast, bosonizing the SC pairing potential gives

$$R^\dagger(x)L^\dagger(x) - L(x)R(x) = \frac{2i}{\mathrm{L}}\sin\left(\frac{\pi x}{\mathrm{L}}\right):\cos[2\vartheta(x)]:. \tag{6.223}$$

The remarkable thing about this expression is that it vanishes at the boundary, consistent with $R^\dagger(0)L^\dagger(0) = -R^\dagger(0)R^\dagger(0) = 0$. Nevertheless, deep in the bulk where $x \approx \mathrm{L}/2$ we recover the translationally invariant form of Sec. 6.5.

Finally, the total bosonized Hamiltonian is then given by

$$\begin{aligned} H = \int_0^{\mathrm{L}} \mathrm{d}x \Big\{ \frac{\pi v_F}{2} :\big(j(x)^2 + \rho(x)^2\big): + \frac{\pi v_F}{2\mathrm{L}^2} Q^2 \\ - \left(\frac{\mathrm{M}}{\mathrm{L}}\right) \left(\frac{:\sin[2\varphi(x) - 2k_F x]:}{2\sin[\frac{\pi x}{\mathrm{L}}]} + \frac{1}{2} \right) - \left(\frac{2\Delta}{\mathrm{L}}\right) \sin[\tfrac{\pi x}{\mathrm{L}}] :\cos[2\vartheta(x)]: \Big\}. \end{aligned} \tag{6.224}$$

This bosonized Hamiltonian corresponds to the following real-time classical action that is obtained by the same methods as in Appendix 6.B,

$$S = \int \mathrm{d}t (L_0 + L_1) \tag{6.225a}$$

$$\begin{aligned} L_0 = -\pi \int_0^{\mathrm{L}} \int_0^{\mathrm{L}} j(x)[\zeta_2(x-y) + \zeta_2(x+y)]\partial_t \rho(y)\, \mathrm{d}x\, \mathrm{d}y - Q\partial_t \vartheta_0 \\ - \int_0^{\mathrm{L}} \frac{\pi v_F}{2} (j(x)^2 + \rho(x)^2)\, \mathrm{d}x - \frac{\pi v_F}{2\mathrm{L}} Q^2, \end{aligned} \tag{6.225b}$$

$$L_1 = \int_0^{\mathrm{L}} \mathrm{d}x \left\{ \left(\frac{\mathrm{M}}{\mathrm{L}}\right) \left(\frac{\sin[2\varphi(x) - 2k_F x]}{2\sin[\frac{\pi x}{\mathrm{L}}]} + \frac{1}{2} \right) + \left(\frac{2\Delta}{\mathrm{L}}\right) \sin[\tfrac{\pi x}{\mathrm{L}}] \cos[2\vartheta(x)] \right\}, \tag{6.225c}$$

subject to the constraints that $\vartheta(x)$ and $\varphi(x)$ are related to $j(x), \rho(x)$, ϑ_0, and Q by Eqs. (6.215). From this action, we will perform a saddle-point analysis in the trivial and topological phases just like in Sec. 6.5.

Trivial phase

Setting $\Delta = 0$, we may integrate out the field $\vartheta(x)$ in favor of $\varphi(x)$. Since the degrees of freedom contained in $\vartheta(x)$ – namely ϑ_0 and $j(x)$ – appear in Gaussian form, we can do this exactly. This performs a Legendre transformation from a phase-space action to a configuration-space action in terms of $\varphi(x)$. By standard arguments we arrive at the total Lagrangian density

$$\mathcal{L}_{\mathrm{M}} = \frac{1}{2\pi} \left(\frac{1}{v_F} [\partial_t \varphi(x)]^2 - v_F [\partial_x \varphi(x)]^2 \right) + \left(\frac{\mathrm{M}}{2\mathrm{L}}\right) \frac{\sin[2\varphi(x) - 2k_F x]}{\sin(\frac{\pi x}{\mathrm{L}})}, \tag{6.226}$$

where for convenience we have dropped the constant term which arises from fermion normal ordering. The influence of Q now manifests as a topological winding condition

$$\varphi(0) - \varphi(\mathrm{L}) = \pi Q \in \pi\mathbb{Z}. \tag{6.227}$$

Seeking saddle-point solutions, the Euler-Lagrange equation of motion is

$$[\partial_x^2 - v_F^{-2}\partial_t^2]\, \varphi(x,t) + \left(\frac{\pi \mathrm{M}}{v_F \mathrm{L}}\right) \frac{\cos[2\varphi(x,t) - 2k_F x]}{\sin(\frac{\pi x}{\mathrm{L}})} = 0. \tag{6.228}$$

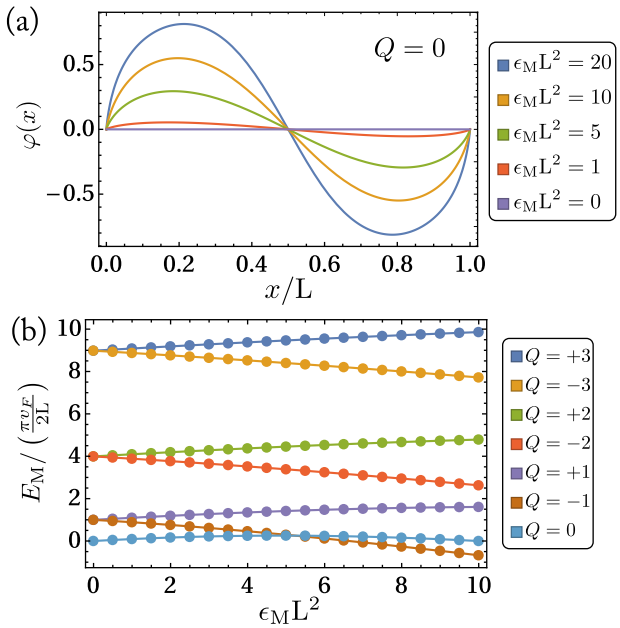

Figure 6.3: Numerical solutions to the non-linear saddle-point ODE of Eq. (6.229), where we have set $k_F = \pi/(2\mathrm{L})$. (a) Solutions in the $Q = 0$ sector at varying pinning potential strength ϵ_M. (b) Saddle-point energies at varying pinning potential strength ϵ_M for different Q sectors. The sectors corresponding to $Q = 0$ and $Q = -1$ happen to cross at large interaction strengths.

Focusing first on static solutions, we set $\partial_t\varphi = 0$ and note that the homogeneous solutions $\varphi(x) = 0, \pi$ are no longer viable solutions. This is in stark contrast to the closed wire and can directly be attributed to the presence of open boundaries.

Nevertheless we can obtain numerical solutions (see Fig. 6.3) to the Euler-Lagrange equations, which may be re-expressed as the non-linear ODE

$$\varphi_{xx}(x) + \epsilon_\mathrm{M}\frac{\cos[2\varphi(x) - 2k_F x]}{\sin(\frac{\pi x}{\mathrm{L}})} = 0 \tag{6.229}$$

such that $\varphi(0) = 0$, $\varphi(\mathrm{L}) = -\pi Q$ and the newly introduced non-linearity parameter $\epsilon_\mathrm{M} := \pi\mathrm{M}/(v_F\mathrm{L})$ has dimensions of $(\text{length})^{-2}$. Hence, at this level of approximation, the variational energies in the different Q sectors are generically split and the saddle-point ground state is *non-degenerate*.

Topological phase

Next we will focus on the topologically non-trivial phase and set $\mathrm{M} = 0$ in Eq. (6.225c). Since $[\vartheta_0, Q] = -i$, Q is no longer an integral of motion. We integrate out ρ and Q in favor of j and ϑ_0. Again because ρ and Q appear only in Gaussian contributions in the action, their functional integration amounts to a Legendre transformation. Consequently, this gives the simplified Lagrangian density in terms of $\vartheta(x)$

$$\mathcal{L} = \frac{1}{2\pi}\left\{\frac{1}{v_F}[\partial_t\vartheta(x)]^2 - v_F[\partial_x\vartheta(x)]^2\right\} + \left(\frac{2\Delta}{\mathrm{L}}\right)\sin\left[\frac{\pi x}{\mathrm{L}}\right]\cos[2\vartheta(x)]. \tag{6.230}$$

In this situation, the field $\vartheta(x)$ is constrained not to have any topological windings ($J \equiv 0$) and must satisfy homogeneous Neumann boundary conditions $\vartheta'(0) = \vartheta'(\mathrm{L}) = 0$. We are then led to the equation of motion

$$[\partial_x^2 - v_F^{-2}\partial_t^2]\vartheta(x,t) - \left(\frac{4\pi\Delta}{v_F\mathrm{L}}\right)\sin\left[\frac{\pi x}{\mathrm{L}}\right]\sin[2\vartheta(x,t)] = 0, \tag{6.231}$$

and focusing on static saddle-point solutions yields

$$\vartheta_{xx}(x) - \epsilon_\Delta \sin\left[\frac{\pi x}{\mathrm{L}}\right]\sin(2\vartheta(x)) = 0. \tag{6.232}$$

Here, $\epsilon_\Delta := 4\pi\Delta/(v_F\mathrm{L}) > 0$ is a non-linearity parameter with dimensions of $(\text{length})^{-2}$. In contrast to the trivial case, homogeneous saddle-point solutions are now permissible and the ones with minimum energy correspond to

$$\vartheta(x) = \vartheta_0 = 0, \pi \mod 2\pi. \tag{6.233}$$

The situation is similar to the variational solutions to the topological phase in the closed wire, with the exception that there are no parity constraints and ϑ_0 is unique mod 2π instead of π.

Nonetheless, to obtain finite variational energies we need to include kinetic fluctuations to ϑ_0. Again, this is easily achieved by the semi-classical approximation $\rho = 0$ and $j = 0$, which we know is consistent with saddle-point solutions. This yields the effective Lagrangian

$$L_{\text{eff}} = -Q\partial_t\vartheta_0 - \frac{\pi v_F}{2\mathrm{L}}Q^2 + \left(\frac{4\Delta}{\pi}\right)\cos 2\vartheta_0, \tag{6.234}$$

where we have performed the spatial integral over the finite interval. This then yields the effective quantum Hamiltonian

$$H_{\text{eff}} = \frac{\pi v_F}{2\mathrm{L}}Q^2 - \left(\frac{4\Delta}{\pi}\right)\cos(2\vartheta_0), \tag{6.235}$$

where $[\vartheta_0, Q] = -i$. The kinetic term now splits the degeneracy between even and odd fermion parity states. As a basis of fermion parity eigenstates, we can define the zero-mode kets

$$|\vartheta_0 = \theta\rangle := \sum_{m\in\mathbb{Z}} \mathrm{e}^{im\theta}|Q = m\rangle, \tag{6.236}$$

$$|\vartheta_0 = \theta\rangle_+ := \sum_{m \text{ even}} \mathrm{e}^{im\theta}|Q = m\rangle, \tag{6.237}$$

$$|\vartheta_0 = \theta\rangle_- := \sum_{m \text{ odd}} \mathrm{e}^{im\theta}|Q = m\rangle, \tag{6.238}$$

and express the two lowest eigensolutions to H_{eff} as Mathieu functions [see Sec. 6.5.3]:

$$|\Psi_\Delta^{(0)}\rangle = \sqrt{\frac{1}{\pi}}\int_{-\pi}^{\pi} \mathrm{d}\theta\, ce_0(\theta - \tfrac{\pi}{2}, \tfrac{4\Delta\mathrm{L}}{\pi^2 v_F})|\vartheta_0 = \theta\rangle_+, \tag{6.239}$$

$$|\Psi_\Delta^{(1)}\rangle = \sqrt{\frac{1}{\pi}}\int_{-\pi}^{\pi} \mathrm{d}\theta\, se_1(\theta - \tfrac{\pi}{2}, \tfrac{4\Delta\mathrm{L}}{\pi^2 v_F})|\vartheta_0 = \theta\rangle_-. \tag{6.240}$$

These have the respective energies

$$E_{\Delta}^{(0)} = \frac{\pi v_F}{2\mathrm{L}} a_0(\tfrac{4\Delta \mathrm{L}}{\pi^2 v_F}), \qquad E_{\Delta}^{(1)} = \frac{\pi v_F}{2\mathrm{L}} b_1(\tfrac{4\Delta \mathrm{L}}{\pi^2 v_F}). \tag{6.241}$$

In the strongly pinned regime where $\Delta \gg v_F/\mathrm{L}$, these wavefunctions are strongly localized about $|\vartheta_0 = 0\rangle$ and $|\vartheta_0 = \pi\rangle$ in equal measure. The splitting in energy between these states is [85]

$$\begin{aligned} \delta E_{\Delta} &= \frac{\pi v_F}{\mathrm{L}} \left[b_1(\tfrac{4\Delta \mathrm{L}}{\pi^2 v_F}) - a_0(\tfrac{4\Delta \mathrm{L}}{\pi^2 v_F}) \right] \\ &\sim 2^5 \sqrt{\frac{2}{\pi}} \left(\frac{\pi v_F}{\mathrm{L}} \right) \left(\frac{4\Delta \mathrm{L}}{\pi^2 v_F} \right)^{3/4} \mathrm{e}^{-4\sqrt{\frac{4\Delta \mathrm{L}}{\pi^2 v_F}}}, \end{aligned} \tag{6.242}$$

demonstrating the asymptotically exact degeneracy in the limit of large L. However, this estimate for the energy splitting is not quite right because the decay appears to take the form $\sim \mathrm{L}^{-\frac{1}{4}} \mathrm{e}^{-\beta\sqrt{\mathrm{L}}}$, where $\beta > 0$ is a constant. This asymptotic is much slower than the exponential form $\sim \mathrm{e}^{-\alpha \mathrm{L}}$ ($\alpha > 0$) obtained from solving the free fermionic model [see Sec. 6.4.2]. This implies that spatially homogeneous tunneling events whose kinetic energetics are captured solely by the capacitive term $\frac{v_F Q^2}{2\mathrm{L}}$ are insufficient to arrive at the correct asymptotic estimate for the quasi-degenerate energy splitting. To do so, we argue that *localized* instanton kinks between the quasi-degenerate 'vacua' $|\Psi_{\Delta}^{(0)}\rangle \pm |\Psi_{\Delta}^{(1)}\rangle$ are necessary at the semi-classical level. These kinks are tunneling events due to the transversal of localized π-kinks in the $\vartheta(x)$ field through the bulk. Physically, they are localized superconducting phase slips connecting degenerate semi-classical ground states. From the Lagrangian Eq. (6.230), we see that at low energy, these kinks are predisposed to nucleate near the open boundaries where the potential energy barrier is low due to the $\sin[\pi x/\mathrm{L}]$-modulated cosine potential. Although their effective semi-classical equations of motion in the bulk should be affected by the changing strength of the cosine potential, we can expect on purely qualitative grounds that these π-kinks should have a rest mass that scales, to lowest order, like $m_{\mathrm{kink}} \sim v_F/\xi_{\Delta}$ with $\xi_{\Delta} = \frac{v_F}{\Delta}$. Here ξ_{Δ} is just the superconducting correlation length of the system.

This is in contrast to the analyses of Refs. [52, 87], where the correct exponential law for the quasi-degenerate energy splitting was also derived. However, those studies are based on a homogeneous cosine potential and spatially uniform instanton kinks to the lowest order in the semi-classical approximation. In principle, the exact eigenstates of the Mathieu equation incorporate all higher-order spatially uniform instanton kink fluctuations. Yet, the resulting degeneracy splitting does not diminish quickly enough with L to reflect the local energy gap of the system. That is, one that is characterized by a correlation length scale and localized semi-classical fluctuations. In Sec. 6.6.3, we will discuss the relationship between these boundary-localized kinks and local Majorana zero mode operators.

6.6.3 Majorana zero modes in the extreme SC limit

The semi-classical analysis of the previous subsection yielded quasi-degenerate ground states of opposite fermion number parity that are present only in the topologically non-trivial phase. Unfortunately, the bosonic semi-classical approach was still unable to verify that this quasi-degeneracy is associated with boundary-localized MZMs. However, in the extreme superconducting limit $v_F = 0$, we can indeed derive the MZM operators analytically. In this case, the

total Hamiltonian is just the SC pairing potential in an open wire. Despite being a singular Hamiltonian, it remains possible to capture many of the qualitative properties that are protected by the SC excitation gap.

First, we have to consider the effects of a charge-conjugation symmetry that is present in the model. Recall that the Lagrangian in the topological phase with $\mathrm{M} = 0$ is

$$\mathcal{L} = \frac{1}{2\pi}\left[\frac{1}{v_F}(\partial_t\vartheta)^2 - v_F(\partial_x\vartheta)^2\right] + \left(\frac{2\Delta}{\mathrm{L}}\right)\sin\left(\frac{\pi x}{\mathrm{L}}\right)\cos(2\vartheta). \tag{6.243}$$

Recall also that the $\mathbb{Z}_2$ inversion symmetry I_x which was defined in Sec. 6.4 acts *linearly* by

$$\mathrm{I}_x : R(x) \mapsto -R^\dagger(x), \qquad \mathrm{I}_x : R^\dagger(x) \mapsto -R(x), \tag{6.244}$$

because it acts on $\psi(x) = [R(x), -R^\dagger(-x)]^T$ by

$$\mathrm{I}_x : \psi(x) \mapsto \sigma^x\psi(-x). \tag{6.245}$$

When translated to the bosonic fields, this transformation acts linearly as

$$\mathrm{I}_x : \phi^R(x) \mapsto \pi - \phi^R(x), \qquad \mathrm{I}_x : \eta^R \mapsto \eta^R. \tag{6.246}$$

This means that

$$\mathrm{I}_x : \vartheta(x) \mapsto \pi - \vartheta(x), \qquad \mathrm{I}_x : \varphi(x) \mapsto -\varphi(x), \tag{6.247}$$

such that the density and current are odd under this transformation, i.e.,

$$j(x) \mapsto -j(x), \qquad \rho(x) \mapsto -\rho(x), \qquad Q \mapsto -Q. \tag{6.248}$$

Likewise, the zero mode transforms as

$$\vartheta_0 \mapsto \pi - \vartheta_0. \tag{6.249}$$

These properties prompt us to identify I_x as a *unitary* charge conjugation operation.

The crucial point to note is that the cosine in the Lagrangian is invariant under this transformation because

$$\cos(2\vartheta(x)) \mapsto \cos(2\pi - 2\vartheta(x)) \equiv \cos(2\vartheta(x)). \tag{6.250}$$

The kinetic term is trivially invariant because it depends only on the square of gradient terms. Next, it is also important to note that this symmetry respects the required boundary conditions and constraints that are

$$\begin{aligned} &j(0) = j(\mathrm{L}) = 0, && \int_0^{\mathrm{L}} \rho(x)\,\mathrm{d}x = 0, \\ &\varphi(0) = 0, && \varphi(\mathrm{L}) = -\pi Q. \end{aligned}$$

Furthermore, spinless time-reversal symmetry $\mathcal{T}$ acts on fermions by

$$i \mapsto -i, \qquad R^{(\dagger)}(x) \mapsto L^{(\dagger)}(x) \equiv -R^{(\dagger)}(-x). \tag{6.251}$$

This translates to the chiral bosons as the anti-linear transformations

$$\phi^R(x) \mapsto \pi - \phi^R(-x), \qquad \eta^R \mapsto \eta^R, \tag{6.252}$$

$$\vartheta(x) \mapsto \pi - \vartheta(x), \qquad \varphi(x) \mapsto \varphi(x), \tag{6.253}$$

and gives

$$\rho(x) \mapsto \rho(x), \qquad j(x) \mapsto -j(x), \tag{6.254a}$$
$$\vartheta_0 \mapsto \pi - \vartheta_0, \qquad Q \mapsto Q. \tag{6.254b}$$

It is straightforward to verify that the Lagrangian, the Hamiltonian, and the constraints/boundary conditions on $\rho(x)$ and $j(x)$ are invariant under $\mathcal{T}$. Because $\mathcal{T}^2 = 1$ there are no degenerate Kramers pairs and we can always choose a basis of energy eigenstates that are Kramers singlets. In particular, if an eigenstate is non-degenerate, then it must be a Kramers singlet.

Now we specialize to the $v_F = 0$ limit in the Hamiltonian formulation. Notice that the local vertex operators $:\mathrm{e}^{\pm i\phi^R(0)}:$ and $:\mathrm{e}^{\pm i\phi^R(\mathrm{L})}:$ exactly commute with the Hamiltonian

$$H = H_1 = -\left(\frac{2\Delta}{\mathrm{L}}\right)\int_0^{\mathrm{L}} \mathrm{d}x\ \sin[\tfrac{\pi x}{\mathrm{L}}] :\cos[2\vartheta(x)]: \tag{6.255}$$

precisely because the Hamiltonian density is exactly zero at the boundaries. Moreover, for $\Delta > 0$ the cosine potential is exactly minimized by

$$\vartheta(x) = \theta_{\min}, \qquad \theta_{\min} = 0, \pi \mod 2\pi. \tag{6.256}$$

Furthermore, under I_x, we have that $\theta_{\min} \to \pi - \theta_{\min}$ such that the degenerate 'vacua' transform non-trivially under I_x. This suggests that we should express the Hermitian Majorana zero mode operators in the combinations of vertex operators

$$\tilde{\gamma}_0 = \mathcal{N}\left(:\mathrm{e}^{i\phi^R(0)}: + :\mathrm{e}^{-i\phi^R(0)}:\right), \tag{6.257a}$$
$$\tilde{\gamma}_{\mathrm{L}} = -i\mathcal{N}\left(:\mathrm{e}^{i\phi^R(\mathrm{L})}: + :\mathrm{e}^{-i\phi^R(\mathrm{L})}:\right), \tag{6.257b}$$

where $\mathcal{N}$ is a formal normalization constant that is fixed by the conditions $\tilde{\gamma}_0^2 = \tilde{\gamma}_{\mathrm{L}}^2 = 1$. The phase factor $-i$ in $\tilde{\gamma}_{\mathrm{L}}$ is necessary to make it Hermitian. The particular equal superposition of $:\mathrm{e}^{\pm i\phi^R(x)}:$ is crucial such that both $\tilde{\gamma}_0$ and $\tilde{\gamma}_{\mathrm{L}}$ transform non-trivially under I_x,

$$\tilde{\gamma}_0 \mapsto -\tilde{\gamma}_0, \qquad \tilde{\gamma}_{\mathrm{L}} \mapsto -\tilde{\gamma}_{\mathrm{L}}. \tag{6.258}$$

However, the complementary case where $\Delta < 0$ would have led to $\theta_{\min} = -\frac{\pi}{2}, \frac{\pi}{2}$, which is invariant under I_x. In this instance we would have chosen the other linear combination of boundary vertex operators that would have made $\tilde{\gamma}_0$ and $\tilde{\gamma}_{\mathrm{L}}$ invariant under I_x. In this sense the sign of Δ dictates the specific I_x sector of the ground state, which is in complete agreement with our prior analysis in Sec. 6.4.2. Furthermore, the expressions for $\tilde{\gamma}_0$ and $\tilde{\gamma}_{\mathrm{L}}$ agree with those of our exact treatment of the same extreme limit in Sec. 6.4.5. Finally, under time-reversal $\mathcal{T}$ we have

$$\widetilde{\gamma}_0 \mapsto +\widetilde{\gamma}_0, \qquad \widetilde{\gamma}_{\mathrm{L}} \mapsto -\widetilde{\gamma}_{\mathrm{L}}, \tag{6.259}$$

consistent with symmetry fractionalization.

It is important to appreciate that the Majorana zero mode operators in Eqs. (6.257) are purely local fermionic operators, though singular in their normalization. An alternative but non-local expression that has been suggested by Cheng [35] and Mazza et al. [88] is

$$\tilde{\gamma}_0 = \mathrm{e}^{i\vartheta_0}, \qquad \tilde{\gamma}_\mathrm{L} = -i\mathrm{e}^{i\vartheta_0}(-1)^Q. \tag{6.260}$$

However these operators are only Hermitian and square to 1 in the low-energy subspace where $\vartheta_0 = \theta_\mathrm{min}$. They are clearly non-local because neither Q nor ϑ_0 are local operators. The non-locality of these Majorana zero modes derives from the application of a low-energy projection onto the subspace of degenerate ground states. Moreover, we will next demonstrate that the expressions in Eqs. (6.257) reduce to the above forms under the appropriately defined low-energy projection. We should remark that the main interest of Refs. [35, 88] lies with parafermionic zero modes derived from a generalization of the Hamiltonian in Eq. (6.224) where M = 0 but $\cos[2\vartheta(x)]$ is replaced by $\cos[2M\vartheta(x)]$ with $M \in \mathbb{N}$. The case of $M = 1$ directly corresponds to SC Majorana zero modes.

Next, recall that the phase field $\vartheta(x)$ has the operator expansion

$$\vartheta(x) = \vartheta_0 + \pi \int_{-\mathrm{L}}^{\mathrm{L}} \zeta_2(x-y) j(y)\, \mathrm{d}y. \tag{6.261}$$

Thus, demanding that $\vartheta(x)$ is uniform is tantamount to requiring that $j(x) = 0$. From the mode expansion of $j(x)$ in Eq. (6.210), this is equivalent to the condition that $a_n = -a_n^\dagger$ for all positive integers n. Hence, we define a variational ground state manifold spanned by the tensor product of states

$$|\vartheta_0 = \theta\rangle \otimes |\widetilde{\Omega}\rangle \tag{6.262}$$

with

$$\mathrm{e}^{i\vartheta_0}|\vartheta_0 = \theta\rangle = \mathrm{e}^{i\theta}|\vartheta_0 = \theta\rangle, \tag{6.263}$$

$$\langle\vartheta_0 = \theta'|\vartheta_0 = \theta\rangle = 2\pi \sum_{m\in\mathbb{Z}} \delta(\theta' - \theta - 2m\pi) \tag{6.264}$$

for $\theta, \theta' \in (-\pi, \pi]$. Note that as opposed to the zero-mode kets in Eqs. (6.237) and (6.238), the ket $|\vartheta_0 = \theta\rangle$ does not have a definite fermion parity. The state $|\widetilde{\Omega}\rangle$ is characterized by the condition

$$a_n|\widetilde{\Omega}\rangle = -a_n^\dagger|\widetilde{\Omega}\rangle. \tag{6.265}$$

This makes $|\widetilde{\Omega}\rangle$ quite different from the filled Fermi sea $|0\rangle$ which is annihilated by all such a_n. Finally, the choice of sign of $\Delta > 0$ leads to $|\vartheta_0 = 0\rangle$ and $|\vartheta_0 = \pi\rangle$ as being the only two possible pinning minima. Projecting onto the subspace spanned by the states

$$|\vartheta_0 = 0\rangle \otimes |\widetilde{\Omega}\rangle, \qquad |\vartheta_0 = \pi\rangle \otimes |\widetilde{\Omega}\rangle \tag{6.266}$$

yields the effective non-local Hamiltonian

$$H_\mathrm{eff} = -\left(\frac{4\Delta}{\pi}\right)\cos(2\vartheta_0), \tag{6.267}$$

which is the previously considered effective Hamiltonian without the fluctuation or charge capacitive term $\propto v_F Q^2$.

More importantly, the vertex operators acting on this subspace simplify to

$$: \mathrm{e}^{i\alpha\phi^R(x)} : |\widetilde{\Omega}\rangle = \mathrm{e}^{i\alpha\vartheta_0}\mathrm{e}^{i\alpha\frac{\pi Q x}{\mathrm{L}}} \exp\left(2\alpha \sum_{n>0} \frac{a_n^\dagger}{\sqrt{n}} \sin\left(\frac{n\pi x}{\mathrm{L}}\right)\right) |\widetilde{\Omega}\rangle, \tag{6.268}$$

which is derived using Eq. (6.265). These relations can then be used to derive the correlation function

$$\langle R(-x)R^\dagger(y)\rangle = \left(\langle\vartheta_0=\theta|\otimes\langle\widetilde{\Omega}|\right) R(-x)R^\dagger(y) \left(|\vartheta_0=\theta\rangle\otimes|\widetilde{\Omega}\rangle\right) \tag{6.269}$$

$$= \frac{1}{2\mathrm{L}}\mathrm{e}^{\frac{i\pi}{2}(x-y)}\mathrm{e}^{i\frac{\pi}{\mathrm{L}}x}\langle\vartheta_0=\theta|\mathrm{e}^{i2\vartheta_0}\mathrm{e}^{-\frac{i\pi Q}{\mathrm{L}}(x-y)}|\vartheta_0=\theta\rangle \tag{6.270}$$

$$\times \langle\widetilde{\Omega}| \exp\left(2\sum_{n>0}\frac{a_n}{\sqrt{n}}[\sin(\tfrac{n\pi x}{\mathrm{L}}) - \sin(\tfrac{n\pi y}{\mathrm{L}})]\right)|\widetilde{\Omega}\rangle \tag{6.271}$$

for $\theta = 0, \pi$. It is only non-zero whenever $x = y$ because of the delta-function normalization of the $|\vartheta_0 = \theta\rangle$ kets. Thus, we are led to

$$\langle R(-x)R^\dagger(y)\rangle = \mathrm{e}^{i\frac{\pi x}{\mathrm{L}}}\delta(x-y). \tag{6.272}$$

Lastly, we have that

$$: \mathrm{e}^{\pm i\phi^R(0)} : |\widetilde{\Omega}\rangle = \mathrm{e}^{\pm i\vartheta_0}|\widetilde{\Omega}\rangle, \tag{6.273}$$

$$: \mathrm{e}^{\pm i\phi^R(\mathrm{L})} : |\widetilde{\Omega}\rangle = \mathrm{e}^{\pm i\vartheta_0}(-1)^Q|\widetilde{\Omega}\rangle. \tag{6.274}$$

This means that for $|\vartheta_0 = \theta_{\min}\rangle\otimes|\widetilde{\Omega}\rangle$ with $\theta_{\min} = 0, \pi$, we have the eigenvalue equations

$$\tilde{\gamma}_0 \left(|\vartheta_0=\theta_{\min}\rangle\otimes|\widetilde{\Omega}\rangle\right) = +2\mathcal{N}\cos\theta_{\min}\left(|\vartheta_0=\theta_{\min}\rangle\otimes|\widetilde{\Omega}\rangle\right), \tag{6.275}$$

$$i\tilde{\gamma}_{\mathrm{L}} \left(|\vartheta_0=\theta_{\min}\rangle\otimes|\widetilde{\Omega}\rangle\right) = -2\mathcal{N}\cos\theta_{\min}\left(|\vartheta_0=\theta_{\min}\rangle\otimes|\widetilde{\Omega}\rangle\right). \tag{6.276}$$

Thus we recover the non-local forms of Eq. (6.260) since $\pi = -\pi \bmod 2\pi$. The singular normalization of $\tilde{\gamma}_0$ and $\tilde{\gamma}_{\mathrm{L}}$ derives from the fact that the eigenkets of ϑ_0 are delta-function normalized.

It should be emphasized that by neglecting the kinetic contributions entirely, we have an artificial degeneracy of the model with singularly localized Majorana zero mode operators. The previous analysis of Sec. 6.6.2 in fact does a better job of lifting this degeneracy by providing some fluctuations about the pinned minima. However, as was already mentioned, the exact energy splitting derived from that effective Hamiltonian is not sufficiently suppressed with increasing L because the fluctuations in ϑ_0 and Q are non-local by nature. To remedy this situation we really do need to diagonalize the model in local bosonic degrees of freedom. This is the topic of the next subsection. In a sense, we intend to smear the operators $\tilde{\gamma}_0, \tilde{\gamma}_{\mathrm{L}}$ in Eq. (6.257) into the bulk and thereby produce Majorana 'wavefunctions'. This smearing is essentially driven by the non-zero kinetic term.

6.6.4 Majorana zero modes from the vertex algebra

While Secs. 6.6.2 and 6.6.3 provided complementary results on MZMs and the quasi-degenerate ground states, we shall now explicitly derive the exact bosonized MZMs. The approach taken here uses the machinery of vertex algebras [89].

First, recall the bosonization identity for the open wire given in Eqs. (6.196),

$$R(x) = \frac{1}{\sqrt{2\mathrm{L}}} : \mathrm{e}^{i\phi^R(x)} : \mathrm{e}^{-i\frac{\pi x}{2\mathrm{L}}}, \tag{6.277}$$

where we can safely drop the Klein factor η^R since it does not play a role after unfolding. The normal-ordered Hamiltonian Eq. (6.224) then bosonizes to

$$H = H_0 + H_1, \tag{6.278a}$$

$$H_0 = \frac{v_F}{4\pi} \int_{-\mathrm{L}}^{\mathrm{L}} \mathrm{d}x \ : [\partial_x \phi^R(x)]^2 :, \tag{6.278b}$$

$$H_1 = \frac{i\Delta}{4\mathrm{L}} \int_{-\mathrm{L}}^{\mathrm{L}} \mathrm{d}x \ s(x) \left[: \mathrm{e}^{i\phi^R(-x)} :: \mathrm{e}^{i\phi^R(x)} : - : \mathrm{e}^{-i\phi^R(x)} :: \mathrm{e}^{-i\phi^R(-x)} : \right], \tag{6.278c}$$

where we have set $\mathrm{M} = 0$ to focus only on the topological phase, and $s(x) := \mathrm{sgn}(\sin[\frac{\pi x}{\mathrm{L}}])$ is the square wave form. The goal is to determine a fermionic operator $\widetilde{\psi}_E$ that has the expansion

$$\widetilde{\psi}_E = \int_{-\mathrm{L}}^{\mathrm{L}} \frac{\mathrm{d}x}{2\mathrm{L}} \ \widetilde{\psi}(x) [: e^{i\phi^R(x)} : + : e^{-i\phi^R(x)} :] \mathrm{e}^{-i\frac{\pi x}{2\mathrm{L}}} \tag{6.279}$$

such that it is an exact quasiparticle excitation satisfying

$$[H_0 + H_1, \widetilde{\psi}_E] = -E\widetilde{\psi}_E \tag{6.280}$$

with energy $0 < E < \Delta$. Note that the superposition of vertex operators in Eq. (6.279) was chosen such that $\mathrm{I}_x = -1$ for this operator. This is based on the previous subsection's analysis regarding the consequences of $\Delta > 0$ when choosing the I_x symmetry of the ground state. The additional phase factor $\mathrm{e}^{-i\frac{\pi x}{2\mathrm{L}}}$ is to ensure that antiperiodic boundary conditions are satisfied, i.e., $\widetilde{\psi}(x + 2\mathrm{L}) = -\widetilde{\psi}(x)$, while maintaining a single-valued integrand. Also, being non-degenerate, $\widetilde{\psi}_E$ must be a Kramers singlet under time-reversal symmetry $\mathcal{T}$. This leads to the symmetry condition on the wavefunction

$$\widetilde{\psi}(x) = [\widetilde{\psi}(-x)]^*. \tag{6.281}$$

One should think of the expansion Eq. (6.279) as a superposition of Mandelstam kinks [51] in the chiral field ϕ^R. For $\frac{v_F}{\mathrm{L}} < \Delta$, we expect to find two Majorana zero modes of the form

$$\tilde{\gamma}_0 = \frac{\widetilde{\psi}_E + \widetilde{\psi}_E^\dagger}{2}, \qquad \tilde{\gamma}_{\mathrm{L}} = i\frac{\widetilde{\psi}_E - \widetilde{\psi}_E^\dagger}{2}. \tag{6.282}$$

However, the spatial localization profiles of $\tilde{\gamma}_0$ and $\tilde{\gamma}_{\mathrm{L}}$ remain to be determined.

The solution to this problem in terms of fermionic operators, as we have seen in Sec. 6.4, is fairly straightforward and entails working with Nambu space and the Bogoliubov-de Gennes Hamiltonian. However, in this subsection, we choose to work entirely in the bosonic language.

First, we require expressions for commutators of vertex operators with H_0 and H_1. The computation of such commutators is most naturally done using operator product expansions (OPEs) of the conformal field theory defined by H_0 alone. Although the total Hamiltonian does not describe a conformally invariant theory, the computation of *equal-time* commutation relations using OPEs remains valid. Note that this involves analytically continuing $x \to x + iv_F\tau$ for short times τ in order to evaluate equal-time commutators using the well-known relationship between radially ordered products and equal-time commutators [90–92].

We begin by defining the holomorphic coordinate in radial quantization in the $\mathbb{C}$ plane

$$z = \mathrm{e}^{-i\frac{\pi}{\mathrm{L}}(x+iv_F\tau)} \in \mathbb{C}, \qquad \tau \in [-\infty, \infty]. \tag{6.283}$$

The chiral fields then take the holomorphic form[8]

$$\phi^R(z) = \vartheta_0 + iQ\ln z + \sum_{n>0} \frac{1}{\sqrt{n}} \left(a_n z^{-n} + a_n^\dagger z^n \right), \tag{6.284}$$

which can be regarded as the H_0-evolved Heisenberg operator

$$\phi^R(z(x,\tau)) \equiv \phi^R(z(x+iv_F\tau, 0)) \equiv \mathrm{e}^{H_0\tau}\phi^R(z(x,0))\mathrm{e}^{-H_0\tau}. \tag{6.285}$$

As such, x has been holomorphically continued to complex values. In the new coordinates, the vertex operator takes the elegant form [93]

$$: e^{i\alpha\phi^R(z)} : = \ \mathrm{e}^{i\alpha\vartheta_0} z^{-\alpha Q} \mathrm{e}^{i\alpha\phi_+^R(z)} \mathrm{e}^{i\alpha\phi_-^R(z)}, \tag{6.286}$$

where

$$\phi_+^R(z) := \sum_{n>0} \frac{a_n^\dagger z^n}{\sqrt{n}}, \qquad \phi_-^R(z) := \sum_{n>0} \frac{a_n z^{-n}}{\sqrt{n}}. \tag{6.287}$$

The set of vertex operators themselves satisfy the fundamental product identities

$$: e^{i\alpha\phi^R(z)} :: e^{i\beta\phi^R(w)} : = (z-w)^{\alpha\beta} : e^{i[\alpha\phi^R(z) + \beta\phi^R(w)]} : \tag{6.288a}$$

$$= (-1)^{\alpha\beta} : e^{i\beta\phi^R(w)} :: e^{i\alpha\phi^R(z)} : \tag{6.288b}$$

for $|z| > |w|$.

Changing coordinate system from (x,τ) to z at zero time $\tau = 0$ gives $\bar{z}z = 1$ with

$$\mathrm{d}x = \frac{i\mathrm{L}}{\pi}\frac{\mathrm{d}z}{z}, \qquad \partial_x = -\frac{i\pi}{\mathrm{L}}\, z\partial_z. \tag{6.289}$$

Thus the kinetic Hamiltonian H_0 in holomorphic coordinates is

$$H_0 = -\frac{\pi v_F}{2\mathrm{L}} \oint_{|z|=1} \frac{\mathrm{d}z}{i2\pi}\, z\, : [\partial_z\phi^R(z)]^2 := \frac{\pi v_F}{\mathrm{L}} \oint_{|z|=1} \frac{\mathrm{d}z}{i2\pi}\, z\, T(z), \tag{6.290}$$

[8] In some more common conventions of the holomorphic expansion of the chiral field (see, e.g., Refs. [75,81]) z is replaced by $1/z$ below. This has to do with our convention for the Fourier series expansion such that a_n is accompanied by the phase $\mathrm{e}^{+i\frac{\pi x}{\mathrm{L}}}$.

where $T(z)$ is the stress-energy tensor of a free chiral boson,

$$T(z) = -\frac{1}{2} : \partial_z \phi^R(z) \partial_z \phi^R(z) : = \sum_{n=-\infty}^{\infty} \frac{L_n}{z^{n+2}}, \tag{6.291}$$

with L_n for $n \in \mathbb{Z}$ being the Virasoro generators. Applying the residue theorem yields

$$H_0 = \frac{\pi v_F}{\mathrm{L}} \oint_{|z|=1} \frac{\mathrm{d}z}{i2\pi} \sum_{n=-\infty}^{\infty} \frac{L_n}{z^{n+1}} = \frac{\pi v_F}{\mathrm{L}} L_0, \tag{6.292}$$

which just means that H_0 implements radial dilations, i.e., time translations. Implementing the same transformation steps to H_1 gives

$$H_1 = \frac{i\Delta}{2} \oint_{|z|=1} \frac{\mathrm{d}z}{i2\pi} \frac{s(z)}{z} \left[: \mathrm{e}^{i\phi^R(z^{-1})} : : \mathrm{e}^{i\phi^R(z)} : - : \mathrm{e}^{-i\phi^R(z)} : : \mathrm{e}^{-i\phi^R(z^{-1})} : \right], \tag{6.293}$$

with the square wave form in terms of z given by

$$s(z) := 2 \sum_{n \text{ odd}} \frac{z^{-n}}{in\pi}. \tag{6.294}$$

Note that on the equal-time circle $|z| = 1$, $s(z)$ is discontinuous and so the expression above has to be interpreted as a formal distribution [89]. Finally, the fermionic quasiparticle operator Eq. (6.279) becomes

$$\widetilde{\psi}_E = \oint_{|z|=1} \frac{\mathrm{d}z}{i2\pi z} \, \widetilde{\psi}(z) \sqrt{z} \left[: e^{i\phi^R(z)} : + : e^{-i\phi^R(z)} : \right]. \tag{6.295}$$

Also, $\sqrt{z}$ is not single-valued on $\mathbb{C}$ because of a branch cut which is taken here to lie on the negative real line. Hence, to maintain single-valuedness of the integrand, $\widetilde{\psi}(z)$ must also contain the same branch cut with $\widetilde{\psi}(\mathrm{e}^{i2\pi} z) = -\widetilde{\psi}(z)$. This is nothing more than a restatement of antiperiodic NS boundary conditions.

Now we need to define the operation of radial ordering, which is the equivalent of time ordering in radial quantization. We denote this ordering operation by $\mathcal{R}$ and for any two field operators $A(z)$ and $B(w)$ depending holomorphically on the complex variables z, w, we define

$$\mathcal{R}\{A(z)B(w)\} = \begin{cases} A(z)B(w) & |z| > |w|, \\ (-1)^{\pi(A,B)} B(w)A(z) & |w| > |z|. \end{cases} \tag{6.296}$$

Here, the exchange sign $(-1)^{\pi(A,B)}$ is set by the mutual braiding relation of A and B. Since we are only dealing with fermions in the present situation, this phase is determined by the $\mathbb{Z}_2$ grading of operators into bosonic (even) and fermionic (odd) grades. Thus $(-1)^{\pi(A,B)} = (-1)^{|A||B|}$, such that we have a negative sign if and only if both A and B are fermionic. The $\mathbb{Z}_2$ grade $|A| \in \{0, 1\}$ of any graded operator A is determined by its commutation relation with the fermion parity operator as

$$(-1)^Q A (-1)^Q = (-1)^{|A|} A. \tag{6.297}$$

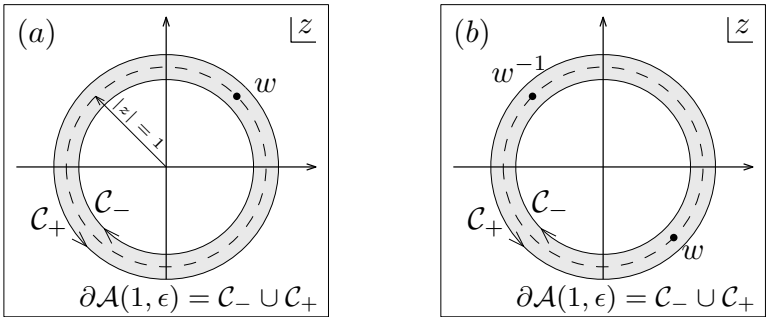

Figure 6.4: Contour plots used to compute commutators via OPEs in the radial quantization scheme. The shaded region denotes the annulus $\mathcal{A}(1,\epsilon)$ centered at $z=0$ with radii $(1-\epsilon, 1+\epsilon)$. Its boundary $\partial\mathcal{A}(1,\epsilon)$ is composed of the two counterwinding contours $\mathcal{C}_-$ and $\mathcal{C}_+$. As ϵ tends to zero, the Cauchy residue theorem produces contributions only from singularities on the zero-time circle $|z|=1$. (a) The contour used to compute general commutators when there is only one pole at $z=w$. (b) The contour used to compute $[H_1, :\mathrm{e}^{\pm i\phi^R(w)}:]$, which now includes an extra singularity at $z=w^{-1}$.

More generally, for any two vertex operators $A(z) = :\mathrm{e}^{i\alpha\phi^R(z)}:$ and $B(w) = :\mathrm{e}^{i\beta\phi^R(w)}:$ we have

$$(-1)^{\pi(A,B)} = (-1)^{\alpha\beta} \tag{6.298}$$

due to the fundamental braiding relation in Eq. (6.288).

Consider next the following equal-time operator

$$\mathcal{O}_A := \oint_{|z|=1} \frac{\mathrm{d}z}{i2\pi}\, A(z). \tag{6.299}$$

Computing its *generalized* commutator with another local operator $B(w)$ at the same zero time ($|w|=1$) yields

$$[\mathcal{O}_A, B(w)]_\pi = \oint_{|z|=1} \frac{\mathrm{d}z}{i2\pi}\, [A(z), B(w)]_\pi = \oint_{\partial\mathcal{A}(1,\epsilon)} \frac{\mathrm{d}z}{i2\pi} \mathcal{R}\{A(z)B(w)\}. \tag{6.300}$$

Here, ϵ is a positive infinitesimal number to be taken to zero, and $\mathcal{A}(1,\epsilon)$ is an annulus centered at 0 with radius 1 and thickness 2ϵ. The contour $\partial\mathcal{A}(1,\epsilon)$ denotes its oriented boundary with the outer boundary running anti-clockwise [see Fig. 6.4(a)]. Hence, to compute a commutator we need to evaluate a contour integral of a radially ordered product in the limit $\epsilon \to 0$. This then involves the use of the OPE between $A(z)$ and $B(w)$, the poles of which will yield the desired result.

To see this method in action we consider the commutator $[H_0, :\mathrm{e}^{\pm i\phi^R(z)}:]$. Recall the well celebrated OPE between $T(z)$ and $:\mathrm{e}^{i\alpha\phi^R(z)}:$,

$$T(z) :\mathrm{e}^{i\alpha\phi^R(z)}: \;=\; \frac{\alpha^2}{2(z-w)^2} :\mathrm{e}^{i\alpha\phi^R(w)}: + \frac{1}{z-w}\partial_w \left(:\mathrm{e}^{i\alpha\phi^R(w)}:\right) + \text{regular}, \tag{6.301}$$

which remains valid irrespective of whether $|w| < |z|$ or $|w| > |z|$. Plugging this expansion into (6.300) gives

$$\begin{aligned}[H_0, :\mathrm{e}^{\pm i\phi^R(w)}:] &= \frac{\pi v_F}{\mathrm{L}} \oint_{\partial\mathcal{A}} \frac{\mathrm{d}z}{i2\pi}\, z\, \mathcal{R}\{T(z) : \mathrm{e}^{\pm i\phi^R(w)} :\} \\ &= \frac{\pi v_F}{\mathrm{L}} \left[w\partial_w(:\mathrm{e}^{\pm i\phi^R(w)}:) + \tfrac{1}{2} : \mathrm{e}^{\pm i\phi^R(w)} : \right]. \end{aligned} \tag{6.302}$$

Notice that the final expression on the RHS is really just a special case of the following general commutation relation [91] between the Virasoro generators and a primary field ϕ with scaling dimension Δ_ϕ

$$[L_m, \phi(z)] = z^{m+1}\partial_z\phi(z) + \Delta_\phi(m+1)z^m\phi(z), \tag{6.303}$$

where the scaling dimension of $:\mathrm{e}^{i\alpha\phi^R(w)}:$ is $\alpha^2/2$. Moreover, we can express Eq. (6.302) in a more compact form by multiplying with $\sqrt{w}$ such that

$$[H_0, (\sqrt{w} : \mathrm{e}^{\pm i\phi^R(w)} :)] = \frac{\pi v_F}{\mathrm{L}} w\partial_w(\sqrt{w} : \mathrm{e}^{\pm i\phi^R(w)} :). \tag{6.304}$$

The factor $\sqrt{w}$ essentially neutralizes the scaling dimension of the vertex operator. From the bosonization identity

$$R^{(\dagger)}(x) = \sqrt{\frac{w}{2\mathrm{L}}} : \mathrm{e}^{\pm i\phi^R(w)} : \tag{6.305}$$

with $w = \mathrm{e}^{-i\frac{\pi x}{\mathrm{L}}}$, we then recover the Heisenberg equation of motion for the chiral fermionic field under time evolution by H_0,

$$[H_0, R^{(\dagger)}(x)] = iv_F\partial_x R^{(\dagger)}(x). \tag{6.306}$$

Finally, using the result Eq. (6.304) leads to the commutator

$$[H_0, \widetilde{\psi}_E] = -\frac{\pi v_F}{\mathrm{L}} \oint_{|z|=1} \frac{\mathrm{d}z}{i2\pi z}\, z\partial_z\widetilde{\psi}(z) \left[\sqrt{z}(:\mathrm{e}^{i\phi^R(z)}: + :\mathrm{e}^{-i\phi^R(z)}:) \right] \tag{6.307}$$

after an integration by parts.

For the H_1 term, things are more complicated because there is now more than one singularity and we need to apply Wick's theorem when using the OPEs. First, the following OPEs can be derived from the fundamental product Eq. (6.288):

$$:\mathrm{e}^{\pm i\phi^R(z)}::\mathrm{e}^{\mp i\phi^R(w)}: = \begin{cases} +\frac{1}{z-w} + \text{reg.} & |z| > |w|, \\ -\frac{1}{z-w} + \text{reg.} & |w| > |z|, \end{cases} \tag{6.308}$$

$$:\mathrm{e}^{\pm i\phi^R(z^{-1})}::\mathrm{e}^{\mp i\phi^R(w)}: = \begin{cases} +\frac{(z/w)}{z-w^{-1}} + \text{reg.} & |z| > |w|, \\ -\frac{(z/w)}{z-w^{-1}} + \text{reg.} & |w| > |z|. \end{cases} \tag{6.309}$$

Applying these OPEs to the calculation of the commutator then yields[9]

$$[H_1, (\sqrt{w} : \mathrm{e}^{i\phi^R(w)} :)] = i\Delta s(w)\sqrt{w^{-1}} : \mathrm{e}^{-i\phi^R(w^{-1})} : \tag{6.310}$$

[9]We only keep OPEs that yield singularities, whereas we can neglect products like $:\mathrm{e}^{i\phi^R(z)}::\mathrm{e}^{i\phi^R(w)}:$ that are regular.

for $w = \mathrm{e}^{-i\frac{\pi x}{\mathrm{L}}}$. Firstly, when applying Wick's theorem, we have to include an exchange sign when permuting vertex operators. Since these vertex operators have mutual fermionic statistics, this introduces a negative sign. Secondly, there are now singularities at $z = w$ and $z = w^{-1}$ and so we have the situation depicted in Fig. 6.4(b). The same type of calculation then gives

$$[H_1, (\sqrt{w} : \mathrm{e}^{-i\phi^R(w)} :)] = i\Delta s(w)\sqrt{w^{-1}} : \mathrm{e}^{i\phi^R(w^{-1})} : . \tag{6.311}$$

Together these commutators produce

$$\begin{aligned}[H_1, \widetilde{\psi}_E] &= i\Delta \oint_{|z|=1} \frac{\mathrm{d}z}{i2\pi z}\, \widetilde{\psi}(z)\, s(z)\sqrt{z^{-1}} \left[: \mathrm{e}^{-i\phi^R(z^{-1})} : + : \mathrm{e}^{i\phi^R(z^{-1})} :\right] \\ &= -i\Delta \oint_{|z|=1} \frac{\mathrm{d}z}{i2\pi z}\, s(z)\widetilde{\psi}(z^{-1})\sqrt{z} \left[: \mathrm{e}^{i\phi^R(z)} : + : \mathrm{e}^{-i\phi^R(z)} :\right] \end{aligned} \tag{6.312}$$

after making the change of dummy variable $z \to 1/z$.

Putting the pieces together and comparison with Eq. (6.280) then requires the eigenvalue equation

$$\left(\frac{\pi v_F}{\mathrm{L}}\right) z\frac{\partial\widetilde{\psi}(z)}{\partial z} + i\Delta s(z)\widetilde{\psi}(z^{-1}) = E\widetilde{\psi}(z) \tag{6.313}$$

to hold on the zero-time line $|z| = 1$. Transforming back to the spatial coordinate x and taking the real and imaginary parts of $\widetilde{\psi}(x) \equiv \widetilde{\psi}(-x)^*$ then gives the BdG eigenvalue equations Eq. (6.118). Hence, although we have managed to avoid Nambu space, ultimately we still need to solve a single-particle BdG equation which describes the spatial profile of the Majorana modes. Fortunately, this has already been done in great detail in Sec. 6.4.2. Nevertheless, this entire exercise was a good check to see if one can derive the same eigenvalue equation from purely bosonic methods. Finally, for the sake of completeness, the desired wavefunction $\widetilde{\psi}(x)$ from Sec. 6.4.2 is given by

$$\widetilde{\psi}(x) = \sqrt{\frac{\mathrm{L}}{2}}[a(x) + ib(x)], \tag{6.314}$$

$$a(x) = \mathcal{N}_\kappa \sinh(\kappa(L - |x|)), \quad b(x) = \mathcal{N}_\kappa \sinh(\kappa x), \tag{6.315}$$

where the quantities $\mathcal{N}_\kappa$ and κ are as defined in Sec. 6.4.2. The Majorana operators are themselves given by

$$\widetilde{\gamma}_0 := \int_{-\mathrm{L}}^{\mathrm{L}} \mathrm{d}x\, \frac{a(x)}{\sqrt{2\mathrm{L}}}[: \mathrm{e}^{i\phi^R(x)} : + : \mathrm{e}^{-i\phi^R(x)} :]\mathrm{e}^{-i\frac{\pi x}{2\mathrm{L}}}, \tag{6.316}$$

$$\widetilde{\gamma}_{\mathrm{L}} := \int_{-\mathrm{L}}^{\mathrm{L}} \mathrm{d}x\, \frac{b(x)}{\sqrt{2\mathrm{L}}}[: \mathrm{e}^{i\phi^R(x)} : + : \mathrm{e}^{-i\phi^R(x)} :]\mathrm{e}^{-i\frac{\pi x}{2\mathrm{L}}}, \tag{6.317}$$

which is nothing more than the bosonization of Eqs. (6.122).

6.7 Summary and discussion

In this work, a very simple continuum model of a one-dimensional fermionic SPT phase [2] was analyzed in great detail using analytic methods. The topological non-trivialness of the

phase is evidenced by the appearance of isolated Majorana zero modes (MZMs) localized on open boundaries. These MZMs are protected from weak disorder and interactions by fermion parity and spinless time-reversal symmetries. As was first established by Fidkowski and Kitaev [50], this topological class of fermionic SPT phases (BDI-class) possesses a $\mathbb{Z}_8$ classification. Consequently, we can regard the model studied here as a generator of this $\mathbb{Z}_8$ "group of SPT phases" by stacking multiple copies of it. In addition, the continuum model is realized effectively in the low-energy limit of Kitaev's Majorana chain model.

What distinguishes this work from the previous studies is the exact analytic diagonalization of the Bogoliubov-de Gennes (BdG) mean-field Hamiltonian at finite lengths and open boundaries. The resulting free-fermion eigenmodes and their energies were then used to write down the exact quasi-degenerate ground states and their Bogoliubon quasiparticle excitations. In particular, at finite lengths, we uncover the exact MZM operators with boundary-localized wavefunctions and the associated exact Bogoliubon quasiparticle excitation energy. This energy eigenvalue becomes suppressed by large bulk lengths and is a symptom of the many-body quasi-degenerate energy splitting between opposite fermion number parity ground state sectors. Additionally, the symmetry fractionalization of the SPT phase can be confirmed from the transformation of the exact MZM operators under spinless time-reversal.

With an in-depth characterization of the model in the language of free fermions, we then proceeded to perform finite-length bosonization analyses using normal-ordered vertex operators. We have also been careful to include zero modes, their associated conjugate momenta (topological windings), and Klein factors in the form of anticommuting Majorana operators (Clifford algebra generators). Bosonization was carried out in both open and closed wire geometries at finite lengths. This allowed for comparisons between the two geometry types, which we found to be qualitatively and quantitatively very different. Also, for both geometries we employed a novel rewriting of the bosonized Hamiltonian and classical Lagrangian that is explicit in zero modes, currents and charges. In $1+1$ dimensions, the quantum current and charge density fields satisfy an $U(1)$ current algebra which is reflected in our finite-length action.

In a closed wire geometry, our bosonization approach was able to demonstrate, at a semiclassical level, fermion parity switching from twisting boundary conditions by a threaded magnetic flux. This effect, which may be taken to be another operational definition of an SPT phase, is limited to only the topological phase. We also clarified a subtle mathematical point which relates to the $\mathbb{Z}_2$ gauge fixing of products of Klein factors $i\eta^R\eta^L$ and total fermion number parity. Technically speaking, there is an often overlooked internal $\mathbb{Z}_2$ gauge symmetry which appears whenever the fermionic charge-raising/lowering operator (sometimes also called the Klein factor) is factored into a zero-mode exponential and a Majorana operator. Fixing the gauge of this internal symmetry then leads to a direct relationship between fermion parity and the products of Klein factors $i\eta^R\eta^L$.

With open boundary conditions, the situation is drastically different and much of it relates to the presence of topological MZMs. For one, unfolding consolidates left- and right-moving bosonic fields into a single chiral field in the extended domain. As a consequence, there is now only one zero mode ϑ_0, and the compactification radii of the conjugate fields $\varphi(x), \vartheta(x)$ are doubled. This latter fact produces (quasi-)degenerate ground states in the relevant pinned phases of the sine-Gordon model. Such a spontaneous symmetry breaking by ordering in bosonic fields actually corresponds to a global symmetry breaking of fermion parity, which is forbidden by the boson-fermion superselection rule [94]. Restoration of this symmetry then

requires a finite amount of virtual tunneling between bosonic ground state sectors that can produce an exponentially suppressed energy splitting due to gapped bulk excitations.

Secondly, consistent use of normal-ordered vertex operators leads to bosonic sine-Gordon potentials that are spatially modulated by the envelope function $\sin(\pi x/\mathrm{L})$. This is quite surprising and is another significant difference from the closed geometry case where such potentials are translationally invariant. We note that past studies, as far as we are aware, have overlooked this feature by misapplying the bosonization dictionary, and in particular often using unnormal-ordered vertex operators. In particular, bosonizing the superconducting pairing potential results in a modulated cosine potential that vanishes at the boundaries. Considered in isolation, this cosine mass term will produce the topological phase with exact fermionic zero modes singularly localized at the boundary points. We then showed that kinetic energy fluctuations lift this exact degeneracy at finite lengths. We first demonstrate this at an effective semi-classical level. Our semi-classical analysis utilizes exact solutions to the Mathieu equation, which yield a finite-size quasi-degenerate energy splitting that scales as $\sim \mathrm{e}^{-a\sqrt{L}}$. This is in contrast to the $\sim \mathrm{e}^{-bL}$ behavior seen in the exact fermionic treatment and indicates that zero mode fluctuations, which are non-local in nature, are insufficient to qualitatively capture the restoration of fermion parity symmetry. Nevertheless, one can view this semi-classical result as an upper bound.

Thirdly, the non-local semi-classical treatment points to the necessity of local bosonic fluctuations in order to properly capture the low-energy physics. Guided by our exact fermionic solutions, we then presented a full understanding of how this occurs entirely in the bosonic language. Our method uses vertex algebras and their operator product expansions in order to determine the bosonic analog of the BdG eigenvalue equation satisfied by the exact Majorana zero mode operators. We are then able to verify that the MZM operators in terms of bosons are identical to their fermionic counterparts. In particular, in the extreme SC limit, where kinetic fluctuations are quenched ($v_F = 0$), we recover local but singular forms of the MZM operators. Our analysis therefore provides a rigorous derivation of the results previously suggested by Refs. [35, 88].

The totality of results – especially the exact ones – in this work reinforces our understanding of MZMs in one-dimensional SPT phases, whilst also demonstrating the many subtleties that can arise when applying bosonization. The fermionic and bosonic formulations are equivalent but complementary formulations of the same physics. As such, they naturally emphasize different aspects. The bosonic point of view of this SPT phase with open boundaries is essentially that of a spontaneously broken discrete symmetry, in this case Ising symmetry. Hence it more naturally describes the quasi-degenerate ground states of opposite fermion parity which are already accessible at the semi-classical level. However, it is at the expense of understanding the boundary MZMs which are truly quantum-mechanical objects. This aspect becomes more intuitive and natural in the fermionic picture. That complete equivalency is ever present between these dual points of view and the manner in which it occurs is probably one of the main takeaways of this work.

There are two extensions of this work which naturally suggest themselves. First, it will be interesting to study the effects of local density-density interactions to the exact free MZM operators. Previous studies including interactions have either been limited to closed wires [57] using renormalization group arguments or operate at the level of the lattice with the Jordan-Wigner transform [95]. As is well known, bosonization is an indispensable tool to

expose the integrability of the interacting Tomonaga-Luttinger liquid, which is obscured in the fermionic formulation. Therefore, a more detailed understanding of how the free fermion picture of boundary MZMs is changed by interactions at the level of quantum operators using bosonization is an attractive proposition. An approach based on the Schrieffer-Wolff transformation [96, 97] could serve this purpose.

The second extension would be to parafermionic theories, whereby the $\mathbb{Z}_2$ Ising symmetry as expressed in the bosonized theory is generalized to a $\mathbb{Z}_N$ group. The simplest theoretical setup which purportedly hosts topologically protected parafermionic boundary operators and the associated quasi-degenerate ground states involves proximity-induced SC on fractional quantum Hall edge states [27–29] and fractional topological insulators [32]. Thus far these models are best understood within a bosonized language, but a quantitatively detailed and rigorous description of the quasi-degenerate energy splitting between ground states and the topological parafermionic zero mode (PZM) operators remains lacking. The most common realization of PZMs in this context is that of interface quasiparticle operators that straddle domains of oppositely pinned bosonic order.

Acknowledgments. This work was supported by the Swiss National Science Foundation and NCCR QSIT. We also would like to thank C. Reeg, M. Thakurathi, P. Aseev, S. Hoffman, D. Chevallier and S. Díaz for useful discussions. VC would like to thank especially E. Fradkin for teaching him about (higher-dimensional) bosonization, Schwinger terms and how to read off commutators from classical actions.

6.A The topological contribution to correlation functions

In this Appendix, we calculate the contribution to all single-particle correlation functions due to either the occupation or vacancy of the quasi-zero mode $\psi_{E_{i\kappa}}$ relative to the ground state $|\Omega_0\rangle$. The non time-ordered single particle Green's functions are defined by

$$G^<(x,y;t) := \langle \mathrm{e}^{iHt}\Psi^\dagger(x)\mathrm{e}^{-iHt}\Psi(y)\rangle, \tag{6.318a}$$

$$G^>(x,y;t) := \langle \mathrm{e}^{iHt}\Psi(x)\mathrm{e}^{-iHt}\Psi^\dagger(y)\rangle, \tag{6.318b}$$

$$F(x,y;t) := \langle \mathrm{e}^{iHt}\Psi(x)\mathrm{e}^{-iHt}\Psi(y)\rangle, \tag{6.318c}$$

where H is the many-body mean-field Hamiltonian. Retarded, advanced and time-ordered Green's functions may then be obtained from those above. Expansion of $\Psi^{(\dagger)}$ in terms of exact BdG quasi-particle creation and annihilation operators gives

$$\begin{aligned} G^<(x,y;t) = \sum_E \Big[&\{\Psi^\dagger(x),\psi_E^\dagger\}\{\psi_E,\Psi(y)\}\langle\psi_E\psi_E^\dagger\rangle \mathrm{e}^{-iEt} \\ &+\{\Psi^\dagger(x),\psi_E\}\{\psi_E^\dagger,\Psi(y)\}\langle\psi_E^\dagger\psi_E\rangle \mathrm{e}^{+iEt}\Big], \end{aligned} \tag{6.319a}$$

$$\begin{aligned} F(x,y;t) = \sum_E \Big[&\{\Psi(x),\psi_E^\dagger\}\{\psi_E,\Psi(y)\}\langle\psi_E\psi_E^\dagger\rangle \mathrm{e}^{-iEt} \\ &+\{\Psi(x),\psi_E\}\{\psi_E^\dagger,\Psi(y)\}\langle\psi_E^\dagger\psi_E\rangle \mathrm{e}^{+iEt}\Big], \end{aligned} \tag{6.319b}$$

with $G^>(x,y;t)$ obtained by the replacement $\Psi^\dagger \leftrightarrow \Psi$ in $G^<(x,y;t)$.

As was stated, the difference between correlation functions in the quasi-degenerate ground states $|\Omega_0\rangle$ and $|\Omega_1\rangle$ is the occupation configuration of the boundary-localized quasi-zero mode

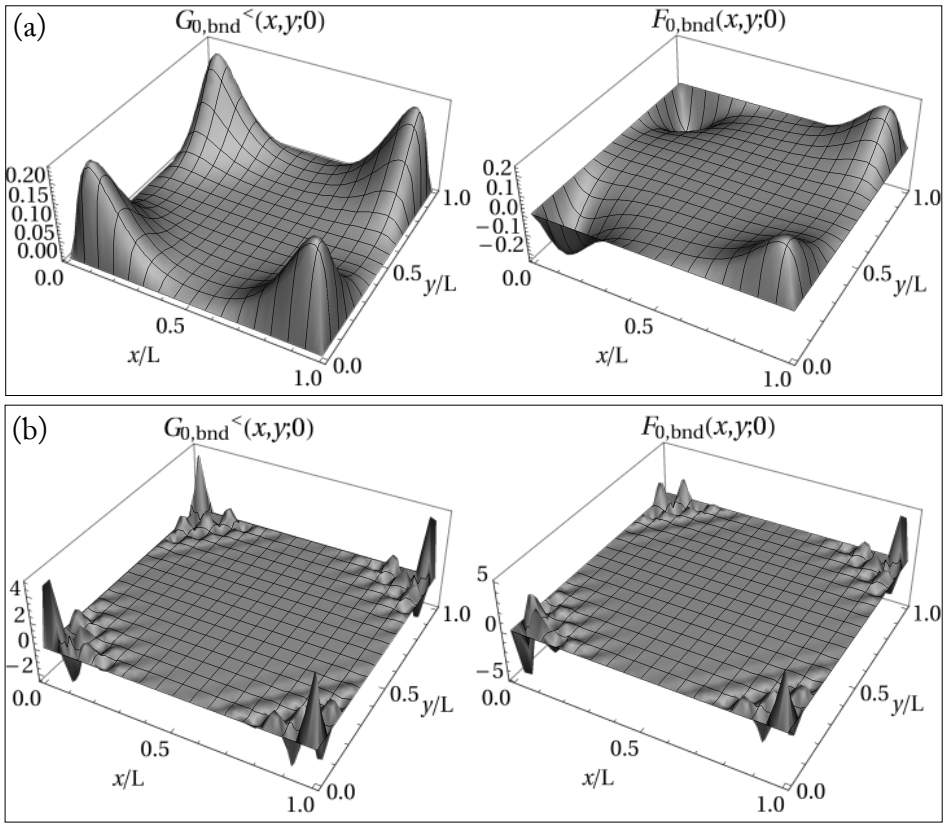

Figure 6.5: Plots of the ground state static correlation functions $G^{<}_{0,\mathrm{bnd}}(x,y;0)$ and $F_{0,\mathrm{bnd}}(x,y;0)$ as defined in the main text. These are the topological boundary mode contributions to the $\langle\Psi^\dagger(x)\Psi(y)\rangle$ and $\langle\Psi(x)\Psi(y)\rangle$ correlation functions, respectively. The data shown is with $\kappa = 12\mathrm{L}^{-1}$ and Fermi momentum (a) $k_F = 1.5\pi/\mathrm{L}$, (b) $k_F = 15.5\pi/\mathrm{L}$.

$\psi_{E_{i\kappa}} = (\gamma_0 - i\gamma_\mathrm{L})/2$ composed of the localized Majoranas. Hence, we define the topological contributions to the Green's functions by

$$G^{<}_{0,\mathrm{bnd}}(x,y;t) = \{\Psi^\dagger(x),\psi^\dagger_{E_{i\kappa}}\}\{\psi_{E_{i\kappa}},\Psi(y)\}\langle\Omega_0|\psi_{E_{i\kappa}}\psi^\dagger_{E_{i\kappa}}|\Omega_0\rangle \mathrm{e}^{-iE_{i\kappa}t}, \tag{6.320}$$

$$G^{<}_{1,\mathrm{bnd}}(x,y;t) = \{\Psi^\dagger(x),\psi_{E_{i\kappa}}\}\{\psi^\dagger_{E_{i\kappa}},\Psi(y)\}\langle\Omega_1|\psi^\dagger_{E_{i\kappa}}\psi_{E_{i\kappa}}|\Omega_1\rangle \mathrm{e}^{+iE_{i\kappa}t}, \tag{6.321}$$

with $G^{>}_{(0,1),\mathrm{bnd}}(x,y;t)$ defined analogously with $\Psi^\dagger \leftrightarrow \Psi$, and

$$F_{0,\mathrm{bnd}}(x,y;t) = \{\Psi(x),\psi^\dagger_{E_{i\kappa}}\}\{\psi_{E_{i\kappa}},\Psi(y)\}\langle\Omega_0|\psi_{E_{i\kappa}}\psi^\dagger_{E_{i\kappa}}|\Omega_0\rangle \mathrm{e}^{-iE_{i\kappa}t}, \tag{6.322}$$

$$F_{1,\mathrm{bnd}}(x,y;t) = \{\Psi(x),\psi_{E_{i\kappa}}\}\{\psi^\dagger_{E_{i\kappa}},\Psi(y)\}\langle\Omega_1|\psi^\dagger_{E_{i\kappa}}\psi_{E_{i\kappa}}|\Omega_1\rangle \mathrm{e}^{+iE_{i\kappa}t}. \tag{6.323}$$

Next, we define the auxiliary functions

$$\begin{aligned} A^{(\pm)}_\kappa(x,y) := \mathcal{N}^2_\kappa \big[&\sin(k_F x)\sin(k_F y)\sinh(\kappa[\mathrm{L}-|x|])\sinh(\kappa[\mathrm{L}-|y|]) \\ &\pm\cos(k_F x)\cos(k_F y)\sinh(\kappa x)\sinh(\kappa y)\big], \end{aligned} \tag{6.324}$$

$$\begin{aligned} B^{(\pm)}_\kappa(x,y) := \mathcal{N}^2_\kappa \big[&\sin(k_F x)\cos(k_F y)\sinh(\kappa[\mathrm{L}-|x|])\sinh(\kappa y) \\ &\pm\cos(k_F x)\sin(k_F y)\sinh(\kappa x)\sinh(\kappa[\mathrm{L}-|y|])\big]. \end{aligned} \tag{6.325}$$

The topological contributions then take the form

$$G^{<(>)}_{0,\mathrm{bnd}}(x,y;t) = \Big[A^{(+)}_\kappa(x,y) \mp B^{(+)}_\kappa(x,y)\Big]\, \mathrm{e}^{-iE_{i\kappa}t}, \tag{6.326}$$

$$G^{<(>)}_{1,\mathrm{bnd}}(x,y;t) = \Big[A^{(+)}_\kappa(x,y) \pm B^{(+)}_\kappa(x,y)\Big]\, \mathrm{e}^{+iE_{i\kappa}t}, \tag{6.327}$$

$$F_{0,\mathrm{bnd}}(x,y;t) = -\Big[A^{(-)}_\kappa(x,y) - B^{(-)}_\kappa(x,y)\Big]\, \mathrm{e}^{-iE_{i\kappa}t}, \tag{6.328}$$

$$F_{1,\mathrm{bnd}}(x,y;t) = -\Big[A^{(-)}_\kappa(x,y) + B^{(-)}_\kappa(x,y)\Big]\, \mathrm{e}^{+iE_{i\kappa}t}. \tag{6.329}$$

Notice that the $B^{(\pm)}_\kappa(x,y)$ pieces represent non-local correlations involving bulk-separated boundaries. Nevertheless, the relative signs between $A^{(\pm)}_\kappa$ and $B^{(\pm)}_\kappa$ in the superpositions ensure that locality is restored in the limit that $E_{i\kappa} = 0$ as $\mathrm{L}\to\infty$.

Shown in Fig. 6.5 are example plots of the functions $G^{<}_{0,\mathrm{bnd}}(x,y;t)$ and $F_{0,\mathrm{bnd}}(x,y;t)$ in the equal-time limit $t = 0$. They decay into the central bulk region (at a rate κ) and exhibit k_F oscillations. Analogous plots for the first excited state $|\Omega_1\rangle$ show similar behavior but with opposite signs for correlation functions between boundary points. In principle, these non-local topological contributions to the correlation functions could be measured by scanning tunneling microscopy in short topological wires.

6.B Current algebra and the bosonic action

In this lengthy Appendix, we present a careful derivation of the classical action for the bosonized continuum fermionic model in Eq. (6.20). Specifically, the following equivalent forms of the action S_{tot} will be derived,

$$\begin{aligned}
S_{\mathrm{tot}} \equiv{}& -\pi\int \mathrm{d}t \int_{-\mathrm{L}/2}^{\mathrm{L}/2}\mathrm{d}x\int_{-\mathrm{L}/2}^{\mathrm{L}/2}\mathrm{d}y\; \zeta_1(x-y)\; j(x)\partial_t\rho(y) - \int \mathrm{d}t\int_{-\mathrm{L}/2}^{\mathrm{L}/2}\mathrm{d}x\,\frac{\pi v_F}{2}\left(j(x)^2+\rho(x)^2\right)\\
&+\int \mathrm{d}t\left(J\,\partial_t\varphi_0 - Q\,\partial_t\vartheta_0 - \frac{\pi v_F}{2\mathrm{L}}(J^2+Q^2) - \frac{\pi v_F}{\mathrm{L}}(Q[\delta_Q-1]+J\delta_J)\right)\\
\equiv{}& \int\mathrm{d}t\int_{-\mathrm{L}/2}^{\mathrm{L}/2}\mathrm{d}x\left\{\frac{1}{\pi}\partial_x\vartheta\partial_t\varphi - \frac{v_F}{2\pi}(\partial_x\vartheta^2+\partial_x\varphi^2)\right\} - \int\mathrm{d}t\Big[Q\partial_t\vartheta_0 + \frac{\pi v_F}{\mathrm{L}}(Q[\delta_Q-1]+J\delta_J)\Big]\\
\equiv{}& \int\mathrm{d}t\int_{-\mathrm{L}/2}^{\mathrm{L}/2}\mathrm{d}x\left\{\frac{1}{\pi}\partial_x\varphi\partial_t\vartheta - \frac{v_F}{2\pi}(\partial_x\vartheta^2+\partial_x\varphi^2)\right\} + \int\mathrm{d}t\left[J\partial_t\varphi_0 - \frac{\pi v_F}{\mathrm{L}}(Q[\delta_Q-1]+J\delta_J)\right],
\end{aligned} \tag{6.330a}$$

valid in the massless limit ($\mathrm{M}=\Delta=0$) with twisted boundary conditions (parametrized by δ_Q, δ_J) and finite length L. This derivation will involve the discussion of Schwinger terms in current algebras (ρ, j), zero momentum modes (ϑ_0,φ_0), topological windings (Q,J), and the strict adherence to a finite length.

There are many reasons for desiring a classical action of the bosonized theory, some of the most important ones being the application of perturbative renormalization group techniques and the development of semi-classical approximations at strong pinning. We will be mainly interested in the latter as we discuss fermion parity switching and the bosonized MZMs in the infinitely pinned limit. However, in this appendix we shall consider only the case of closed

boundaries in the massless limit because the case of open boundaries with cosine mass terms is specially treated in the main text.

The bosonic action is often taken for granted and is by now established textbook material. In spite of that, most standard references [48, 75, 81, 98] on the subject remain unclear about the fate of zero modes and twisted boundary conditions. In fact, the action is often quoted in its sine-Gordon form which follows from the integration of either one of the fields ϑ, φ at the expense of the other. However, the actions quoted above represent 'phase-space' actions where the quantum commutation relations between conjugate pairs (ϑ, φ) and (ρ, j) can be easily read off. This form of the action is particularly suited for the discussion of competing pinning potentials in ϑ and φ, which is awkward to do with the sine-Gordon formulation. Furthermore, there are additional terms on the right-hand sides of S_{tot} above that are typically absent in most standard treatments. Yet they explicitly involve the zero modes, topological windings and twisted boundary conditions.

6.B.1 Bosonization convention

The existence of several competing bosonization conventions in the literature often leads to confusion and misunderstandings, [10] see for example the comments by von Delft and Schoeller [79] and the tower of babel appendix by Giamarchi [48]. To make matters worse, the form of the action S_{tot} can depend on these details. For example, if one chooses to use non-commuting zero modes instead of Klein factors, then there should be an additional $i\vartheta_0\partial_t\varphi_0$ term in the Lagrangian. In another case, if one decides not to normal-order then the final bosonized action can acquire an explicit dependence on a UV cutoff scale. It is for reasons like these that we are compelled to restate our bosonization convention here. For the experts, we will just mention that our convention is closer to the one used by string theorists [90, 92, 93] and is a form of constructive or operator bosonization [78, 79].

First, we recall the following bosonization identities [Eq. (6.139)] for the right- and left-moving Fermi fields in a system of finite length L,

$$R(x) \equiv \frac{\eta^R}{\sqrt{\mathrm{L}}} : \mathrm{e}^{i\phi^R(x)} : \mathrm{e}^{i\frac{\pi x}{\mathrm{L}}(\delta_J+\delta_Q-1)}, \tag{6.331a}$$

$$L(x) \equiv \frac{\eta^L}{\sqrt{\mathrm{L}}} : \mathrm{e}^{i\phi^L(x)} : \mathrm{e}^{i\frac{\pi x}{\mathrm{L}}(\delta_J-\delta_Q+1)}, \tag{6.331b}$$

expressed in normal-ordered form. The chiral bosonic fields are compact bosons with the compactification radii

$$\phi^R \sim \phi^R + 2\pi, \qquad \phi^L \sim \phi^L + 2\pi. \tag{6.332}$$

They have the mode expansions

$$\phi^R(x) = \phi_0^R + \frac{2\pi Q^R x}{\mathrm{L}} + \sum_{q\neq 0}\left(\frac{2\pi}{|q|\mathrm{L}}\right)^{\frac{1}{2}}\left(\Theta(q)a_q + \Theta(-q)a_{-q}^\dagger\right)\mathrm{e}^{iqx}, \tag{6.333}$$

$$\phi^L(x) = \phi_0^L - \frac{2\pi Q^L x}{\mathrm{L}} - \sum_{q\neq 0}\left(\frac{2\pi}{|q|\mathrm{L}}\right)^{\frac{1}{2}}\left(\Theta(-q)a_q + \Theta(q)a_{-q}^\dagger\right)\mathrm{e}^{iqx}, \tag{6.334}$$

[10] This is acutely frustrating for graduate students learning bosonization for the first time. Ordinarily, specialists adhere to a single convention over time and lose the ability to translate between conventions.

where $q \in \frac{2\pi}{\mathrm{L}}\mathbb{Z}$ and $\Theta(x)$ is the Heaviside step function. The only non-zero commutation relations amongst the operators are

$$[\phi_0^R, Q^R] = -i, \qquad [\phi_0^L, Q^L] = -i, \qquad [a_q, a_{q'}^\dagger] = \delta_{qq'}. \tag{6.335}$$

Due to the compactification radii of $\phi^{R,L}$, the operators Q^R, Q^L are integer-quantized and represent occupation numbers of the R and L fermions. The operators $\phi_0^{R,L}$ are known as the zero-momentum ($q = 0$) modes. The bosonic normal ordering : : is defined such that all annihilation operators a_q are ordered to the right of the creation operators $a_q^\dagger$ and the charges $Q^{R,L}$ are ordered to the right of the zero modes $\phi_0^{R,L}$. This entails Wick-ordering for the annihilation and creation operators and qp-ordering for the zero mode and number operators. For example, this means that

$$: \mathrm{e}^{i\phi^R(x)} : \equiv \mathrm{e}^{i\phi_0^R} \mathrm{e}^{i\frac{2\pi}{\mathrm{L}}Q^R x}\, \mathrm{e}^{i\phi_+^R(x)} \mathrm{e}^{i\phi_-^R(x)}, \tag{6.336}$$

where

$$\phi_+^R(x) = \sum_{q>0} \left(\frac{2\pi}{q\mathrm{L}}\right)^{\frac{1}{2}} a_q^\dagger \mathrm{e}^{-iqx}, \qquad \phi_-^R(x) = [\phi_+^R(x)]^\dagger, \tag{6.337}$$

and analogously for $\phi_\pm^L(x)$. With these relations, one can explicitly verify the commutation relations

$$[\phi^R(x), \phi^R(y)] = +i2\pi\, \varepsilon_1(x-y), \tag{6.338}$$
$$[\phi^L(x), \phi^L(y)] = -i2\pi\, \varepsilon_1(x-y), \tag{6.339}$$
$$[\phi^L(x), \phi^R(y)] = 0, \tag{6.340}$$

and

$$[\phi_-^R(x+i0^+), \phi_+^R(y)] = -\ln\left(1 - \mathrm{e}^{i\frac{2\pi}{\mathrm{L}}(x-y+i0^+)}\right), \tag{6.341}$$
$$[\phi_-^L(x+i0^+), \phi_+^L(y)] = -\ln\left(1 - \mathrm{e}^{-i\frac{2\pi}{\mathrm{L}}(x-y-i0^+)}\right), \tag{6.342}$$

where the $i0^+$ convergence factors are remnants of the Wick normal-ordering prescription. The function ε_1 is defined as

$$\varepsilon_1(x-y) := \frac{1}{\mathrm{L}}(x-y) + \frac{i}{2\pi}\ln\left(\frac{1 - \mathrm{e}^{+\frac{i2\pi}{\mathrm{L}}(x-y+i0^+)}}{1 - \mathrm{e}^{-\frac{i2\pi}{\mathrm{L}}(x-y-i0^-)}}\right) = \left\lceil \frac{x-y}{\mathrm{L}} \right\rceil - \frac{1}{2}, \tag{6.343}$$

where $\lceil * \rceil$ denotes the integer ceiling. Because ε_1 is a function that depends on the difference of two logarithmic functions which are holomorphic on mutually exclusive regions of the complex plane, ε_1 should be understood to be a hyperfunction [99]. It is also implied here that principal branches are used when evaluating the arg and ln multi-functions. More importantly, ε_1 is a Green's function [100] in the sense that

$$\varepsilon_1'(x-y) = \sum_{m\in\mathbb{Z}} \delta(x - y + m\mathrm{L}), \tag{6.344}$$

where the RHS is the L-periodic Dirac delta function. One can also see from plotting $\varepsilon_1(x)$ that it has discontinuities at intervals of L, in accordance to its derivative being a Dirac delta comb. Finally, for $|x-y| < \mathrm{L}$, we have

$$\varepsilon_1(x-y) = \frac{1}{2}\mathrm{sgn}(x-y), \tag{6.345}$$

which gives the usual non-local commutator for $\phi^{R,L}$ in the infinite L limit.

Using these bosonic commutators, all of the canonical anticommutation relations for $R(x), L(x)$ can be reproduced; with the effects of twisted boundary conditions included. Verifying this may be done using the vertex operator product identities [51, 92]

$$:\mathrm{e}^{i\alpha\phi^R(x)}::\mathrm{e}^{i\beta\phi^R(y)}: = \left[\mathrm{e}^{-i\frac{2\pi x}{\mathrm{L}}} - \mathrm{e}^{-i\frac{2\pi y}{\mathrm{L}}}\right]^{\alpha\beta} :\mathrm{e}^{i[\alpha\phi^R(x)+\beta\phi^R(y)]}:, \tag{6.346a}$$

$$:\mathrm{e}^{i\alpha\phi^L(x)}::\mathrm{e}^{i\beta\phi^L(y)}: = \left[\mathrm{e}^{i\frac{2\pi x}{\mathrm{L}}} - \mathrm{e}^{i\frac{2\pi y}{\mathrm{L}}}\right]^{\alpha\beta} :\mathrm{e}^{i[\alpha\phi^L(x)+\beta\phi^L(y)]}: \tag{6.346b}$$

for $\alpha, \beta \in \mathbb{Z}$. These are derived by adhering to the normal-ordered product convention and using the Baker-Campbell-Hausdorff identity.

The bosonization and operator product identities may then be used to bosonize the fermion densities giving

$$:R^\dagger(x)R(x): =: \rho^R(x) := +\frac{1}{2\pi}\partial_x\phi^R(x), \tag{6.347}$$

$$:L^\dagger(x)L(x): =: \rho^L(x) := -\frac{1}{2\pi}\partial_x\phi^L(x), \tag{6.348}$$

where fermionic normal ordering is defined using point-splitting

$$:\mathcal{A}(x)\mathcal{B}(x): = \lim_{\epsilon\to 0}\left[\mathcal{A}(x+\epsilon)\mathcal{B}(x) - \langle 0|\mathcal{A}(x+\epsilon)\mathcal{B}(x)|0\rangle\right] \tag{6.349}$$

with $|0\rangle$ being the filled Fermi sea. Next, the local conjugate fields are defined by

$$\vartheta(x) = \frac{\phi^L(x)+\phi^R(x)}{2}, \qquad \varphi(x) = \frac{\phi^L(x)-\phi^R(x)}{2}, \tag{6.350}$$

and have the commutators

$$[\varphi(x), \vartheta(y)] = -i\pi\varepsilon_1(x-y), \tag{6.351a}$$

$$[\varphi(x), \varphi(y)] = [\vartheta(x), \vartheta(y)] = 0. \tag{6.351b}$$

These fields are related to the charge density and current by

$$\rho_{\mathrm{tot}}(x) =: \rho^R(x) + \rho^L(x) : = -\frac{1}{\pi}\partial_x\varphi(x), \tag{6.352}$$

$$j_{\mathrm{tot}}(x) =: \rho^R(x) - \rho^L(x) : = +\frac{1}{\pi}\partial_x\vartheta(x). \tag{6.353}$$

They have the mode expansions

$$\varphi(x) = \varphi_0 - \frac{\pi Q x}{\mathrm{L}} - \sum_{q\neq 0}\left(\frac{\pi}{2|q|\mathrm{L}}\right)^{\frac{1}{2}}(a_q + a_{-q}^\dagger)\mathrm{e}^{iqx}, \tag{6.354}$$

$$\vartheta(x) = \vartheta_0 + \frac{\pi J x}{\mathrm{L}} + \sum_{q\neq 0}\left(\frac{\pi}{2|q|\mathrm{L}}\right)^{\frac{1}{2}}\mathrm{sgn}(q)\,(a_q - a_{-q}^\dagger)\mathrm{e}^{iqx}, \tag{6.355}$$

accompanied by the non-zero commutation relations

$$[\vartheta_0, Q] = -i, \qquad [\varphi_0, J] = i. \tag{6.356}$$

The bosonic fields φ, ϑ are also compact bosons with compactification radii

$$\varphi \sim \varphi + \pi, \qquad \vartheta \sim \vartheta + \pi. \tag{6.357}$$

Their respective topological windings Q, J are integer-quantized and subject to the parity condition

$$(-1)^Q = (-1)^J = 1 \quad \Leftrightarrow \quad Q = J \bmod 2. \tag{6.358}$$

Employing the presented fermion-boson dictionary then translates the free-fermion Hamiltonian

$$H_0 = \int_0^{\mathrm{L}} \left\{ -iv_F R^\dagger \partial_x R + iv_F L^\dagger \partial_x L \right\} \mathrm{d}x \tag{6.359}$$

into the bosonized Hamiltonian

$$H_0 = \int_0^{\mathrm{L}} \frac{v_F}{2\pi} : \left([\partial_x \vartheta]^2 + [\partial_x \varphi]^2 \right) : \mathrm{d}x + \frac{\pi v_F}{\mathrm{L}} \left(Q[\delta_Q - 1] + J\delta_J \right). \tag{6.360}$$

The additional $J\delta_J$ term arises from the diamagnetic response to the applied magnetic flux, while the $Q(\delta_Q - 1)$ term may be interpreted as a Fermi pressure term.

The next goal is now to determine a classical action which, when quantized, does not only give the correct bosonized Hamiltonian but also the correct commutators between the bosonic fields φ and ϑ as described above. This will be extremely useful when performing semi-classical approximations based on saddle points.

6.B.2 Current algebra and Schwinger terms

An unconventional way to dequantize the bosonic theory is to work directly with the non-zero-mode ($q \neq 0$) contributions to the current and density. These are defined to be

$$\rho(x) := \rho_{\mathrm{tot}}(x) - \frac{Q}{\mathrm{L}}, \quad j(x) := j_{\mathrm{tot}}(x) - \frac{J}{\mathrm{L}}, \tag{6.361}$$

and constitute non-zero contributions to the current and density obeying

$$\int_0^{\mathrm{L}} \rho(x) \mathrm{d}x = \int_0^{\mathrm{L}} j(x) \mathrm{d}x = 0. \tag{6.362}$$

Their mode expansions are

$$\rho(x) = \frac{i}{\mathrm{L}} \sum_{q \neq 0} \left(\frac{|q|\mathrm{L}}{2\pi} \right)^{\frac{1}{2}} \mathrm{sgn}(q) \left[a_q + a_{-q}^\dagger \right] \mathrm{e}^{iqx}, \tag{6.363a}$$

$$j(x) = \frac{i}{\mathrm{L}} \sum_{q \neq 0} \left(\frac{|q|\mathrm{L}}{2\pi} \right)^{\frac{1}{2}} \left[a_q - a_{-q}^\dagger \right] \mathrm{e}^{iqx}. \tag{6.363b}$$

These expressions are independent of Q and J since

$$[\rho, Q] = [\rho, J] = 0, \qquad [j, Q] = [j, J] = 0. \tag{6.364}$$

Thus, Q and J are the constant background charge and current. However, although Q and J commute with each other, the non-zero-mode counterparts ρ and j do not. Instead they satisfy a special commutation relation known as *current algebra*

$$[\rho(x), j(y)] = -\frac{i}{\pi} \sum_{m\in\mathbb{Z}} \delta'(x - y - m\mathrm{L}) = -\frac{i}{\pi}\varepsilon_1''(x - y). \tag{6.365}$$

The right-hand side of the above equation is understood in the sense of distributions, such that

$$\int_0^{\mathrm{L}} \mathrm{d}x \int_0^{\mathrm{L}} \mathrm{d}y\; g(x)\, \delta'(x - y)\, f(y) = \int_0^{\mathrm{L}} \mathrm{d}x\; g(x)\, \partial_x f(x). \tag{6.366}$$

The δ' term in Eq. (6.365) is known as a *Schwinger term* and is an ultra-local term because it depends on the derivative of the Dirac delta function.

Now, reversing the Dirac quantization scheme yields the classical bracket

$$\{\rho(x), j(y)\} = -\frac{1}{\pi} \sum_{m\in\mathbb{Z}} \delta'(x - y + m\mathrm{L}). \tag{6.367}$$

More generally, the Poisson bracket for functionals $F[\rho, j], G[\rho, j]$ is implied to be

$$\begin{aligned} \{F, G\} &:= \int \mathrm{d}x \int \mathrm{d}y\; \kappa(x, y) \left(\tfrac{\delta F}{\delta\rho(x)} \tfrac{\delta G}{\delta j(y)} - \tfrac{\delta G}{\delta\rho(x)} \tfrac{\delta F}{\delta j(y)} \right) \\ &= -\tfrac{1}{\pi} \int \mathrm{d}x \left[\tfrac{\delta F}{\delta\rho(x)} \partial_x \left(\tfrac{\delta G}{\delta j(x)} \right) - \tfrac{\delta G}{\delta\rho(x)} \partial_x \left(\tfrac{\delta F}{\delta j(x)} \right) \right], \end{aligned} \tag{6.368a}$$

where

$$\kappa(x, y) := -\tfrac{1}{\pi} \sum_{m\in\mathbb{Z}} \delta'(x - y + m\mathrm{L}). \tag{6.368b}$$

One can check that all the properties of a Poisson bracket are satisfied: skew symmetry, associativity (Leibniz rule) and Jacobi identity.

Generally, the classical Poisson bracket and the quantum (Dirac) commutator do not necessarily agree. The situations when they do not agree require the methods of Deformation Quantization [101]. Fortunately, within the context of one-dimensional bosonization, the underlying commutator algebra is that of the simple harmonic oscillator – i.e., the Heisenberg algebra – such that the Dirac prescription remains exact.

Since the Schwinger term δ' is ultra-local, the (functional) symplectic form that is taken from the inverse of the Poisson bracket kernel function is expected to be non-local. Let X, Y be functional vector fields

$$\begin{aligned} X &= \int \mathrm{d}x \left(X_\rho(x) \frac{\delta}{\delta\rho(x)} + X_j(x) \frac{\delta}{\delta j(x)} \right), \\ Y &= \int \mathrm{d}x \left(Y_\rho(x) \frac{\delta}{\delta\rho(x)} + Y_j(x) \frac{\delta}{\delta j(x)} \right). \end{aligned}$$

Expressing the symplectic 2-form Ω as

$$\Omega[X,Y] := \int \mathrm{d}x \int \mathrm{d}y\, \lambda(x,y)\,[X_j(x)Y_\rho(y) - Y_j(x)X_\rho(y)] \tag{6.369}$$

then requires that

$$\int \mathrm{d}z\, \kappa(x,z)\lambda(z,y) = -\tfrac{1}{\pi}\partial_x \lambda(x,y) = \sum_{m\in\mathbb{Z}} \delta(x-y+m\mathrm{L}). \tag{6.370}$$

Thus, λ is a Green's function to the derivative operator ∂_x, and using Eq. (6.344) it must have the form

$$\lambda(x,y) = -\pi\,[\varepsilon_1(x-y) + C(y)]\,, \tag{6.371}$$

where $C(y)$ is only a function of y. Typically this is resolved by selecting boundary conditions. The most natural choice happens to be

$$C(y) \equiv 0, \tag{6.372}$$

which ensures that $\lambda(x,y) = -\lambda(y,x)$. Taking this on faith for the moment, we then have the symplectic 2-form

$$\Omega[X,Y] = -\pi \int_0^{\mathrm{L}} \mathrm{d}x \int_0^{\mathrm{L}} \mathrm{d}y\, \varepsilon_1(x-y)\,[X_j(x)Y_\rho(y) - Y_j(x)X_\rho(y)]\,. \tag{6.373}$$

This leads to the real-time finite L phase-space classical Lagrangian for ρ and j

$$\mathcal{L}[\rho,j] = -\pi \int_0^{\mathrm{L}} \mathrm{d}x \int_0^{\mathrm{L}} \mathrm{d}y\, \varepsilon_1(x-y)\; j(x)\partial_t\rho(y) - H[\rho,j], \tag{6.374a}$$

$$H[\rho,j] := \int_0^{\mathrm{L}} \mathrm{d}x\, \frac{\pi v_F}{2}\left(j(x)^2 + \rho(x)^2\right), \tag{6.374b}$$

where the Hamiltonian is inferred from Eq. (6.360). Here ρ is taken to be the "position" coordinate and j the "momentum", although they are clearly interchangeable by an integration by parts in time. Variation of the action leads to the equations of motion

$$\rho(x,t) = -\frac{1}{v_F}\int \mathrm{d}y\, \varepsilon_1(x-y)\,\partial_t j(y,t), \tag{6.375a}$$

$$j(x,t) = -\frac{1}{v_F}\int \mathrm{d}y\, \varepsilon_1(x-y)\,\partial_t \rho(y,t). \tag{6.375b}$$

Comparing these equations of motion with the mode expansions Eq. (6.363) and the known time-dependencies $a_q \mathrm{e}^{-i|q|t}$, $a_{-q}^\dagger \mathrm{e}^{i|q|t}$ demonstrates that they are *incorrect*. However, this gives us hints towards the correct form of the RHS. We note that we require a function $\zeta_1(x-y)$ with the properties that

$$\zeta_1(x-y) = -\zeta_1(y-x) \tag{6.376}$$

and

$$\int_0^{\mathrm{L}} \mathrm{d}y\, \zeta_1(x-y)\, \partial_y(\mathrm{e}^{iqy}) = \mathrm{e}^{iqx} \tag{6.377}$$

whenever $q \in \frac{2\pi}{\mathrm{L}}\mathbb{Z}$ and $q \neq 0$. This then leads to the unique solution

$$\begin{aligned}
\zeta_1(x-y) &:= \varepsilon_1(x-y) - \frac{x-y}{\mathrm{L}} \\
&= -\frac{1}{\pi}\arg(1 - \mathrm{e}^{+\frac{i2\pi}{\mathrm{L}}(x-y+i0^+)}) \\
&= -\frac{i}{2\pi}\sum_{n\neq 0} \frac{\left(\mathrm{e}^{\frac{i2\pi}{\mathrm{L}}(x-y)}\right)^n}{n} \\
&= \sum_{n>0} \frac{\sin\left[\frac{2\pi n}{\mathrm{L}}(x-y)\right]}{\pi n},
\end{aligned} \tag{6.378}$$

which is just the descending saw-tooth function of period L. This function is not quite a Green's function because

$$\partial_x \zeta_1(x-y) = \sum_{m\in\mathbb{Z}} \delta(x-y+m\mathrm{L}) - \frac{1}{\mathrm{L}}. \tag{6.379}$$

However, when limiting ourselves to functions which integrate to zero over the interval $[0, \mathrm{L}]$, the above expression still shows the behavior expected of a Green's function. Incorporating this subtle issue, we arrive at the correct final L-periodic Lagrangian

$$\mathcal{L}[\rho, j] \;= -\pi \int_{-\mathrm{L}/2}^{\mathrm{L}/2} \mathrm{d}x \int_{-\mathrm{L}/2}^{\mathrm{L}/2} \mathrm{d}y\; \zeta_1(x-y)\; j(x)\partial_t\rho(y) - H[\rho, j], \tag{6.380a}$$

$$H[\rho, j] := \int_0^{\mathrm{L}} \mathrm{d}x\, \frac{\pi v_F}{2}\left(j(x)^2 + \rho(x)^2\right), \tag{6.380b}$$

which yields the equations of motion

$$\rho(x,t) = -\frac{1}{v_F}\int \mathrm{d}y\, \zeta_1(x-y)\, \partial_t j(y,t), \tag{6.381a}$$

$$j(x,t) = -\frac{1}{v_F}\int \mathrm{d}y\, \zeta_1(x-y)\, \partial_t \rho(y,t). \tag{6.381b}$$

The correctness of these equations can be verified from the mode expansions of ρ and j. These give the conservation laws

$$\partial_t\rho + v_F\partial_x j = 0, \qquad \partial_t j + v_F\partial_x\rho = 0, \tag{6.382}$$

where the first equation is the continuity equation and the second equation comes from the duality $\rho \leftrightarrow j$ that is only valid for (1+1)-dimensional massless relativistic fluids. Both lead to the more conventional massless Klein-Gordon equations of motion

$$(\partial_t^2 - v_F^2\partial_x^2)\rho = 0, \qquad (\partial_t^2 - v_F^2\partial_x^2)j = 0. \tag{6.383}$$

As a final technical remark, we note that in determining the classical action, we have made use of the fact that the quantum Hamiltonian Eq. (6.360) is boson normal-ordered according to our earlier described prescription. Implicitly, this means that the construction of the partition function/time-evolution operator in terms of a functional integral unambiguously employs the Wick-ordering of the $a_q, a_q^\dagger$ operators. It should be stressed that different operator ordering conventions will in general yield different functional integral actions [83, 102].

6.B.3 Full action for the bosonic fields

The non-local action in Eq. (6.380) was originally written down in a related form for the chiral boson by Floreanini and Jackiw [54] in the case of infinite L. However, this formulation is rarely encountered in the literature. To connect it to Eq. (6.330) we recall that

$$\rho(x) = -\frac{1}{\pi}\partial_x\varphi(x) - \frac{Q}{\mathrm{L}}, \qquad j(x) = \frac{1}{\pi}\partial_x\vartheta(x) - \frac{J}{\mathrm{L}}. \tag{6.384}$$

This leads to the following relationship between the angular fields ϑ, φ and ρ,j:

$$\varphi(x) = \varphi_0 - \frac{\pi Q}{\mathrm{L}}x - \pi\int_{-\mathrm{L}/2}^{\mathrm{L}/2}\zeta(x-y)\rho(y)\,\mathrm{d}y, \tag{6.385}$$

$$\vartheta(x) = \vartheta_0 + \frac{\pi J}{\mathrm{L}}x + \pi\int_{-\mathrm{L}/2}^{\mathrm{L}/2}\zeta(x-y)j(y)\,\mathrm{d}y. \tag{6.386}$$

In fact, these expressions can be verified by substituting the mode expansions Eqs. (6.363) and performing a spatial integration by parts. Thus we have succeeded in simply expressing the angular fields ϑ, φ as a *functional* of the zero modes ϑ_0, φ_0, the constant background charges Q, J and the current/density fields j, ρ. The advantage of these expressions is that they allow us to appreciate the non-local dependence between the ϑ, φ fields and the normally measurable observables Q, J and ρ, j.

An important point to notice is that the zero modes φ_0, ϑ_0 represent spatial averages of $\varphi(x), \vartheta(x)$ and may be extracted according to

$$\varphi_0 = \frac{1}{\mathrm{L}}\int_{-\mathrm{L}/2}^{\mathrm{L}/2}\varphi(x)\,\mathrm{d}x, \qquad \vartheta_0 = \frac{1}{\mathrm{L}}\int_{-\mathrm{L}/2}^{\mathrm{L}/2}\vartheta(x)\,\mathrm{d}x. \tag{6.387}$$

However, these relations are very much dependent on the limits of integration despite the L-periodicity. Moreover, it may be sometimes desirable to use different limits of integration such as

$$\varphi_0 = \frac{1}{\mathrm{L}}\int_0^{\mathrm{L}}\tilde{\varphi}(x)\,\mathrm{d}x, \qquad \vartheta_0 = \frac{1}{\mathrm{L}}\int_0^{\mathrm{L}}\tilde{\vartheta}(x)\,\mathrm{d}x, \tag{6.388}$$

which requires using a different set of fields defined by

$$\tilde{\varphi}(x) = \varphi_0 - \frac{\pi Q}{\mathrm{L}}\left(x - \frac{\mathrm{L}}{2}\right) - \pi\int_0^{\mathrm{L}}\zeta(x-y)\rho(y)\,\mathrm{d}y, \tag{6.389}$$

$$\tilde{\vartheta}(x) = \vartheta_0 + \frac{\pi J}{\mathrm{L}}\left(x - \frac{\mathrm{L}}{2}\right) + \pi\int_0^{\mathrm{L}}\zeta(x-y)j(y)\,\mathrm{d}y. \tag{6.390}$$

These fields differ from $\varphi(x), \vartheta(x)$ by multiples of $\pi Q, \pi J$. Equivalently, the zero modes of $\tilde{\varphi}(x), \tilde{\vartheta}(x)$ and $\varphi(x), \vartheta(x)$ differ by multiples of $\pi Q, \pi J$. In fact, the commutation relations

$$[\vartheta_0, Q] = -i, \qquad [\varphi_0, J] = i, \qquad [\vartheta_0, \varphi_0] = 0 \tag{6.391}$$

remain unchanged under the 'gauge' transformation

$$\vartheta_0 \to \vartheta_0 + cJ, \qquad \varphi_0 \to \varphi_0 - cQ \tag{6.392}$$

for any $c \in \mathbb{R}$. Thus, fixing a spatial averaging convention implicitly fixes this gauge choice in the zero modes. Counterintuitively, this also means that the zero modes are not coordinate invariant.

Finally, we can add the action capturing the physics of Q, J and φ_0, ϑ_0 to the current-algebra Lagrangian $\mathcal{L}[\rho, j]$ in Eq. (6.380), which yields the total action

$$\begin{aligned} S_{\text{tot}}[\varphi, \vartheta] = &-\pi \int \mathrm{d}t \int_{-\mathrm{L}/2}^{\mathrm{L}/2} \mathrm{d}x \int_{-\mathrm{L}/2}^{\mathrm{L}/2} \mathrm{d}y \; \zeta_1(x-y)\; j(x) \partial_t \rho(y) \\ &- \int \mathrm{d}t \int_{-\mathrm{L}/2}^{\mathrm{L}/2} \mathrm{d}x \, \frac{\pi v_F}{2} \left(j(x)^2 + \rho(x)^2 \right) \\ &+ \int \mathrm{d}t \left(J\, \partial_t \varphi_0 - Q\, \partial_t \vartheta_0 - \frac{\pi v_F}{2\mathrm{L}} (J^2 + Q^2) - \frac{\pi v_F}{\mathrm{L}} (Q[\delta_Q - 1] + J\delta_J) \right). \end{aligned} \tag{6.393}$$

After some manipulation, this gives us the other two equivalent forms in Eqs. (6.330). However, the form given in Eq. (6.394) reveals the separation between the zero and non-zero modes. In fact, one can already read off the correct commutation relations amongst the zero modes and the topological charge/current from the action above. The other more common forms of the action in Eqs. (6.330) obscure this separation between zero and non-zero modes, but highlight the need to include the zero-mode contributions $Q\partial_t\varphi_0$ and $J\partial_t\vartheta_0$, which are often wrongly neglected in the infinite L limit. It is furthermore worth emphasizing that the limits of integration play an important role here. To illustrate this, let us outline one of the necessary derivations connecting Eq. (6.394) and the rest of Eqs. (6.330). The temporal term for ρ, j can be seen to be

$$\begin{aligned} &- \pi \int_{-\mathrm{L}/2}^{\mathrm{L}/2} \mathrm{d}x \int_{-\mathrm{L}/2}^{\mathrm{L}/2} \mathrm{d}y \; j(x) \partial_t [\zeta(x-y)\rho(y)] \\ &= \frac{1}{\pi} \int_{-\mathrm{L}/2}^{\mathrm{L}/2} \mathrm{d}x \left[\partial_x \vartheta(x) + \frac{\pi J}{\mathrm{L}} \right] \partial_t \left[\varphi(x) - \varphi_0 + \frac{\pi Q}{\mathrm{L}} x \right] \\ &= \frac{1}{\pi} \int_{-\mathrm{L}/2}^{\mathrm{L}/2} \mathrm{d}x \, \partial_x \vartheta(x) \partial_t \varphi(x) - J \partial_t \varphi_0 + \partial_t Q \int_{-\mathrm{L}/2}^{\mathrm{L}/2} \mathrm{d}x \left(\frac{x}{\mathrm{L}} \right) \partial_x \vartheta(x). \end{aligned}$$

The last term on the RHS can be integrated by parts to give zero due to boundary conditions. Thus we have that

$$-\pi \int_{-\mathrm{L}/2}^{\mathrm{L}/2} \mathrm{d}x \int_{-\mathrm{L}/2}^{\mathrm{L}/2} \mathrm{d}y \; j(x) \partial_t [\zeta(x-y)\rho(y)] + J\partial_t\varphi_0 = \frac{1}{\pi} \int_{-\mathrm{L}/2}^{\mathrm{L}/2} \mathrm{d}x \, \partial_x \vartheta(x) \partial_t \varphi(x)$$

as desired. If we had instead chosen the less symmetric limits $\int_0^{\mathrm{L}} \mathrm{d}x$, then the action for $\tilde{\varphi}$ and $\tilde{\vartheta}$ would have been obtained.

Finally, we may also express the action in terms of the chiral fields $\phi^R(x), \phi^L(x)$. By the change of variables

$$\phi^R(x) = \vartheta(x) - \varphi(x), \tag{6.394}$$

$$\phi^L(x) = \vartheta(x) + \varphi(x), \tag{6.395}$$

one obtains

$$S_{\mathrm{tot}}[\phi^R, \phi^L] = \int \mathrm{d}t \left(L_R[\phi^R] + L_L[\phi^L] \right) \tag{6.396}$$

with the Lagrangians

$$\begin{aligned} L_R[\phi^R] &= -\frac{1}{4\pi} \int_{-\mathrm{L}/2}^{\mathrm{L}/2} \left(\partial_t \phi^R + v_F \partial_x \phi^R \right) \partial_x \phi^R \, \mathrm{d}x \\ &= -Q^R \partial_t \phi_0^R - \pi \int_{-\mathrm{L}/2}^{\mathrm{L}/2} \mathrm{d}x \int_{-\mathrm{L}/2}^{\mathrm{L}/2} \mathrm{d}y \; \rho^R(x) \zeta(x-y) \partial_t \rho^R(y) \\ &\quad - \frac{\pi v_F}{\mathrm{L}} (Q^R)^2 - \pi v_F \int_{-\mathrm{L}/2}^{\mathrm{L}/2} [\rho^R(x)]^2 \mathrm{d}x \end{aligned} \tag{6.397}$$

and

$$\begin{aligned} L_L[\phi^L] &= +\frac{1}{4\pi} \int_{-\mathrm{L}/2}^{\mathrm{L}/2} \left(\partial_t \phi^L - v_F \partial_x \phi^L \right) \partial_x \phi^L \, \mathrm{d}x \\ &= -Q^L \partial_t \phi_0^L + \pi \int_{-\mathrm{L}/2}^{\mathrm{L}/2} \mathrm{d}x \int_{-\mathrm{L}/2}^{\mathrm{L}/2} \mathrm{d}y \; \rho^L(x) \zeta(x-y) \partial_t \rho^L(y) \\ &\quad - \frac{\pi v_F}{\mathrm{L}} (Q^L)^2 - \pi v_F \int_{-\mathrm{L}/2}^{\mathrm{L}/2} [\rho^L(x)]^2 \mathrm{d}x, \end{aligned} \tag{6.398}$$

where we also have the mode expansion

$$\phi^R(x) = \phi_0^R + \frac{2\pi Q^R}{\mathrm{L}} x + 2\pi \int_{-\mathrm{L}/2}^{\mathrm{L}/2} \zeta(x-y) \rho^R(y) \, \mathrm{d}y, \tag{6.399}$$

$$\phi^L(x) = \phi_0^L + \frac{2\pi Q^L}{\mathrm{L}} x + 2\pi \int_{-\mathrm{L}/2}^{\mathrm{L}/2} \zeta(x-y) \rho^L(y) \, \mathrm{d}y. \tag{6.400}$$

6.C Direct verification of the diagonalized Hamiltonian

This appendix presents an explicit verification of the Hamiltonian diagonalization in Eq. (6.125). Recall first that the Hamiltonian is

$$H = \int_0^{\mathrm{L}} \mathrm{d}x \left[-i v_F (R^\dagger \partial_x R - L^\dagger \partial_x L) + i\Delta (R^\dagger L^\dagger - LR) \right], \tag{6.401}$$

which upon unfolding into the extended domain $[-\mathrm{L}, \mathrm{L}]$ via

$$L(x) \equiv -R(-x), \qquad R(x + 2\mathrm{L}) = -R(x)$$

leads to

$$H := H_0 + H_1, \tag{6.402a}$$

$$H_0 := \int_{-\mathrm{L}}^{\mathrm{L}} \mathrm{d}x \left(-iv_F R^\dagger \partial_x R \right), \tag{6.402b}$$

$$H_1 := \int_{-\mathrm{L}}^{\mathrm{L}} \mathrm{d}x \left(-\tfrac{i\Delta}{2} s(x)[R^\dagger(x)R^\dagger(-x) - R(-x)R(x)] \right), \tag{6.402c}$$

where $s(x) := \mathrm{sgn}(\sin(\frac{\pi x}{\mathrm{L}}))$ is the periodic square wave form. The presence of $s(x)$ introduces two domain walls in the SC pairing potential at $x = 0, \pm\mathrm{L}$, where we expect to find localized Majorana modes.

6.C.1 Majorana zero mode operators

The Majorana operator localized around $x = 0$ is claimed to be

$$\gamma_0 = \int_{-\mathrm{L}}^{\mathrm{L}} \mathrm{d}x \; a(x)[R(x) + R^\dagger(x)] = \gamma_0^\dagger, \tag{6.403}$$

where

$$a(x) = \mathcal{N}_\kappa \sinh(\kappa[\mathrm{L} - |x|]) \qquad \text{for } x \in [-\mathrm{L}, \mathrm{L}], \tag{6.404}$$

$$\mathcal{N}_\kappa = \frac{1}{\sqrt{\mathrm{L}}} \left(\frac{\sinh(2\kappa\mathrm{L})}{2\kappa\mathrm{L}} - 1 \right)^{-1/2}. \tag{6.405}$$

The normalization $\int_{-\mathrm{L}}^{\mathrm{L}} a(x)^2 \mathrm{d}x = 1$ implies $\gamma_0^2 = 1$. The inverse decay length $\kappa > 0$ satisfies the gap equation

$$\frac{v_F \kappa}{\Delta} = \tanh(\kappa\mathrm{L}), \tag{6.406}$$

which implies the relations

$$v_F \kappa = E_{i\kappa} \sinh(\kappa\mathrm{L}), \tag{6.407a}$$

$$\Delta = E_{i\kappa} \cosh(\kappa\mathrm{L}), \tag{6.407b}$$

where

$$E_{i\kappa} = \sqrt{\Delta^2 + v_F^2 (i\kappa)^2} = \sqrt{\Delta^2 - v_F^2 \kappa^2} \tag{6.408}$$

is the quasi-degenerate energy splitting. Note that $a(x)$ is continuous throughout $[-\mathrm{L}, \mathrm{L}]$ and is an even function, $a(-x) = a(x)$.

The goal is then to verify that

$$H = -\tfrac{i}{2} E_{i\kappa} \gamma_0 \gamma_\mathrm{L} + \ldots, \tag{6.409}$$

where γ_{L} is the other Majorana operator localized around $x = \pm\mathrm{L}$. This is achieved by checking that

$$[H, \gamma_0] = iE_{i\kappa}\gamma_{\mathrm{L}}. \tag{6.410}$$

First, the equation of motion for $R(x), R^\dagger(x)$ under time evolution by H_0

$$R^{(\dagger)}(x,t) := \mathrm{e}^{iH_0 t}R^{(\dagger)}(x)\mathrm{e}^{-iH_0 t} = R^{(\dagger)}(x - v_F t) \tag{6.411}$$

produces the commutation relation

$$i[H_0, R^{(\dagger)}(x)] = -v_F\partial_x R^{(\dagger)}(x) \tag{6.412}$$

and hence

$$[H_0, R(x) + R^\dagger(x)] = iv_F[\partial_x R(x) + \partial_x R^\dagger(x)]. \tag{6.413}$$

Thus, we find

$$\begin{aligned}[H_0, \gamma_0] &= iv_F \int_{-\mathrm{L}}^{\mathrm{L}} \mathrm{d}x\; a(x)\,[\partial_x R(x) + \partial_x R^\dagger(x)] \\ &= E_{i\kappa}\mathcal{N}_\kappa \int_{-\mathrm{L}}^{\mathrm{L}} \mathrm{d}x\; s(x)\sinh(\kappa\mathrm{L})\cosh(\kappa[\mathrm{L} - |x|])[R(x) + R^\dagger(x)],\end{aligned} \tag{6.414}$$

where we have integrated by parts and used Eqs. (6.407) on the final line. In performing the integration by parts, we have used the fact that there are no boundary term contributions because $a(\pm\mathrm{L}) = 0$.

Next, we also have

$$\begin{aligned}[H_1, \gamma_0] &= -\frac{i\Delta}{2}\int_{-\mathrm{L}}^{\mathrm{L}} \mathrm{d}x \int_{-\mathrm{L}}^{\mathrm{L}} \mathrm{d}y\, s(x)a(y) \\ &\quad \times \Big\{R^\dagger(x)\delta(x+y) - R^\dagger(-x)\delta(x-y) - R(-x)\delta(x-y) + R(x)\delta(x+y)\Big\} \\ &= -\frac{i\Delta}{2}\int_{-\mathrm{L}}^{\mathrm{L}} \mathrm{d}x\, s(x)a(x)\Big\{R^\dagger(x) - R^\dagger(-x) - R(-x) + R(x)\Big\} \quad \text{because } a(x) \text{ is even} \\ &= -i\Delta\int_{-\mathrm{L}}^{\mathrm{L}} \mathrm{d}x\, s(x)a(x)\Big\{R^\dagger(x) + R(x)\Big\} \quad \text{because } s(x) \text{ is odd.}\end{aligned} \tag{6.415}$$

Then, substituting the sinh expression for $a(x)$ and using Eqs. (6.407) results in

$$\begin{aligned}[H_1, \gamma_0] &= -i\Delta\mathcal{N}_\kappa \int_{-\mathrm{L}}^{\mathrm{L}} \mathrm{d}x\, s(x)\sinh(\kappa[\mathrm{L} - |x|])\,[R^\dagger(x) + R(x)] \\ &= -iE_{i\kappa}\mathcal{N}_\kappa \int_{-\mathrm{L}}^{\mathrm{L}} \mathrm{d}x\, \cosh(\kappa\mathrm{L})\sinh(\kappa[\mathrm{L} - |x|])[R(x) + R^\dagger(x)].\end{aligned} \tag{6.416}$$

Assembling things together finally gives

$$\begin{aligned}[H_0 + H_1, \gamma_0] &= iE_{i\kappa}\mathcal{N}_\kappa \int_{-\mathrm{L}}^{\mathrm{L}} \mathrm{d}x\, s(x)\{\sinh(\kappa\mathrm{L})\cosh(\kappa[\mathrm{L} - |x|]) \\ &\qquad - \cosh(\kappa\mathrm{L})\sinh(\kappa[\mathrm{L} - |x|])\}\,[R(x) + R^\dagger(x)] \\ &= iE_{i\kappa}\int_{-\mathrm{L}}^{\mathrm{L}} \mathrm{d}x\, \mathcal{N}_\kappa s(x)\sinh(\kappa|x|)\,[R(x) + R^\dagger(x)] \\ &= iE_{i\kappa}\gamma_{\mathrm{L}}\end{aligned} \tag{6.417}$$

as claimed because the other Majorana operator is

$$\gamma_{\mathrm{L}} = \int_{-\mathrm{L}}^{\mathrm{L}} \mathrm{d}x\, \mathcal{N}_\kappa \sinh(\kappa x)\, [R(x) + R^\dagger(x)]. \tag{6.418}$$

By similar manipulations as above, one can easily show that

$$[H, \gamma_{\mathrm{L}}] = -iE_{i\kappa}\gamma_0. \tag{6.419}$$

In this case, however, one needs to use the fact that $R(\mathrm{L}) + R(-\mathrm{L}) = 0$ at the boundary.

6.C.2 Extended states operators

We can follow the same strategy as above to verify that

$$[H, \phi_n^\dagger] = E_{k_{n,1}}\phi_n^\dagger, \qquad [H, \varphi_n^\dagger] = E_{k_{n,2}}\varphi_n^\dagger, \tag{6.420}$$

where we have the purported eigensolutions

$$\phi_n = \int_{-\mathrm{L}}^{\mathrm{L}} \mathrm{d}x\, \frac{u_{k_{n,1}}(x)^*}{\sqrt{2}} \left[R(x) + R^\dagger(x)\right], \tag{6.421a}$$

$$u_k(x) = \frac{1}{\sqrt{\mathrm{L}\mathrm{N}_k}} \left(\cos(k|x| + 2\theta_k) + i\sin(kx)\right), \tag{6.421b}$$

$$\varphi_n = \int_{-\mathrm{L}}^{\mathrm{L}} \mathrm{d}x\, \frac{v_{k_{n,2}}(x)^*}{\sqrt{2}} \left[R(x) - R^\dagger(x)\right], \tag{6.422a}$$

$$v_k(x) = \frac{1}{\sqrt{\mathrm{L}\mathrm{N}_k}} \left(\cos(k|x| - 2\theta_k) + i\sin(kx)\right). \tag{6.422b}$$

The momenta $k_{n,1}$ and $k_{n,2}$ above have to satisfy the quantization conditions

$$k_{n,1} = \left(n + \frac{1}{2}\right)\frac{\pi}{\mathrm{L}} - \frac{2\theta_{k_{n,1}}}{\mathrm{L}}, \tag{6.423}$$

$$k_{n,2} = \left(n + \frac{1}{2}\right)\frac{\pi}{\mathrm{L}} + \frac{2\theta_{k_{n,2}}}{\mathrm{L}}, \tag{6.424}$$

with $n \in \mathbb{N}$ and

$$2\theta_k = \tan^{-1}\left(\frac{\Delta}{v_F k}\right). \tag{6.425}$$

Their associated energies are

$$E_{k_{n,i}} := \sqrt{\Delta^2 + v_F^2 k_{n,i}^2}, \qquad i = 1, 2. \tag{6.426}$$

We use the principle branch cut for the inverse tangent function. Firstly, using Eq. (6.412) again yields

$$[H_0, \phi_n^\dagger] = \int_{-\mathrm{L}}^{\mathrm{L}} \frac{-iv_F\partial_x u_{k_{n,1}}(x)}{\sqrt{2}} \left[R(x) + R^\dagger(x)\right], \tag{6.427}$$

$$[H_0, \varphi_n^\dagger] = \int_{-\mathrm{L}}^{\mathrm{L}} \frac{-iv_F\partial_x v_{k_{n,2}}(x)}{\sqrt{2}} \left[R^\dagger(x) - R(x)\right] \tag{6.428}$$

after an integration by parts and by using the fact that

$$u_{k_{n,1}}(-\mathrm{L}) = -u_{k_{n,1}}(\mathrm{L}), \qquad v_{k_{n,2}}(-\mathrm{L}) = -v_{k_{n,2}}(\mathrm{L}) \tag{6.429}$$

and $R(\mathrm{L}) + R(-\mathrm{L}) = 0$ to drop boundary terms.

However, in this case, one has

$$\begin{aligned}[H_1, \phi_n^\dagger] &= -\frac{i\Delta}{2}\int_{-\mathrm{L}}^{\mathrm{L}} \mathrm{d}x \int_{-\mathrm{L}}^{\mathrm{L}} \mathrm{d}y\, s(x) \frac{u_{k_{n,1}}(y)}{\sqrt{2}} [R^\dagger(x)R^\dagger(-x) - R(-x)R(x)\ ,\ R(y) + R^\dagger(y)] \\ &= -i\Delta \int_{-\mathrm{L}}^{\mathrm{L}} \mathrm{d}x\ \frac{s(x)}{\sqrt{2}} u^*_{k_{n,1}}(x)[R(x) + R^\dagger(x)], \end{aligned} \tag{6.430}$$

where we have used the fact that $u_k(-x) = u_k^*(x)$ and that $s(x)$ is an odd function. Likewise, the same type of calculation yields

$$[H_1, \varphi_n^\dagger] = -i\Delta \int_{-\mathrm{L}}^{\mathrm{L}} \mathrm{d}x\ \frac{s(x)}{\sqrt{2}} v^*_{k_{n,2}}(x)[R(x) - R^\dagger(x)]. \tag{6.431}$$

Thus, we have the expressions

$$[H, \phi_n^\dagger] = \int_{-\mathrm{L}}^{\mathrm{L}} \mathrm{d}x \frac{1}{\sqrt{2}} \left\{ -iv_F \partial_x u_{k_{n,1}}(x) - i\Delta s(x) u^*_{k_{n,1}}(x) \right\} [R(x) + R^\dagger(x)], \tag{6.432}$$

$$[H, \varphi_n^\dagger] = \int_{-\mathrm{L}}^{\mathrm{L}} \mathrm{d}x \frac{1}{\sqrt{2}} \left\{ +iv_F \partial_x v_{k_{n,2}}(x) - i\Delta s(x) v^*_{k_{n,2}}(x) \right\} [R(x) - R^\dagger(x)]. \tag{6.433}$$

Then, by direct substitution and making use of the trigonometric identities with

$$v_F k = E_k \cos(2\theta_k), \qquad \Delta = E_k \sin(2\theta_k), \tag{6.434}$$

we have that

$$-iv_F \partial_x u_k(x) - i\Delta s(x) u_k^*(x) = \frac{E_k}{\sqrt{\mathrm{L}}} \left[\cos(k|x| + 2\theta_k) + i\sin(kx)\right], \tag{6.435}$$

$$iv_F \partial_x v_k(x) - i\Delta s(x) v_k^*(x) = -\frac{E_k}{\sqrt{\mathrm{L}}} \left[\cos(k|x| - 2\theta_k) + i\sin(kx)\right]. \tag{6.436}$$

This then gives the desired relations

$$[H, \phi_n^\dagger] = E_{k_{n,1}} \phi_n^\dagger, \qquad [H, \varphi_n^\dagger] = E_{k_{n,2}} \varphi_n^\dagger.$$

Finally, one can also confirm numerically that the set of fermionic modes $\phi_n, \varphi_{n'}, \psi_{E_{i\kappa}}$ mutually anticommute because their mode wavefunctions are orthogonal.

6.D Numerical checks with a lattice model

In this appendix, we present a detailed derivation of a lattice model which yields the continuum Hamiltonian given by Eq. (6.55) at low energies and long wavelengths. By doing so, we can numerically confirm the correctness of the exact continuum solutions of Sec. 6.4.

The task of finding a suitable lattice model is more subtle than it seems at first because the R and L fields are relativistic. Nevertheless, the most direct way to proceed is to express the model purely in terms of Majorana fields (cf. Sec. 6.3.2)

$$\lambda = \frac{1}{2}\begin{pmatrix} R + R^\dagger \\ L + L^\dagger \end{pmatrix}, \qquad \lambda' = \frac{1}{2i}\begin{pmatrix} R - R^\dagger \\ L - L^\dagger \end{pmatrix}. \tag{6.437}$$

These obey the anticommutation relations

$$\{\lambda_\alpha(x), \lambda_\beta(y)\} = \{\lambda'_\alpha(x), \lambda'_\beta(y)\} = \frac{1}{2}\delta_{\alpha\beta}\delta(x-y). \tag{6.438}$$

In this Majorana basis of field operators, the Hamiltonian given in Eq. (6.55) simply decomposes into

$$H = H_+ + H_-, \tag{6.439a}$$

$$H_+ = \int \mathrm{d}x\, \lambda^T(-iv_F\sigma^z\partial_x - \Delta\sigma^y)\lambda, \tag{6.439b}$$

$$H_- = \int \mathrm{d}x\, (\lambda')^T(-iv_F\sigma^z\partial_x + \Delta\sigma^y)\lambda'. \tag{6.439c}$$

The mode Hamiltonians $\mathcal{H}_\pm = -iv_F\sigma^z\partial_x \mp \Delta\sigma^y$ bear striking resemblance to the low-energy effective Hamiltonian of the SSH model [62], but with opposite mass signs. This connection suggests that we consider the single Kitaev chain Hamiltonian [1]

$$H_+ = \sum_{j=1}^{N}\left(\frac{it}{2}\,\gamma_{2j+2}\gamma_{2j+1} - \frac{it'}{2}\,\gamma_{2j}\gamma_{2j+1}\right) \tag{6.440}$$

with $t, t' > 0$ and where the γ_j's are local Majorana operators obeying $\{\gamma_j, \gamma_{j'}\} = 2\delta_{jj'}$.

Next, by taking periodic boundary conditions for the moment, we proceed to transform to momentum space according to

$$\gamma_{k\alpha} := \frac{1}{\sqrt{2N}}\sum_{j=1}^{N} \mathrm{e}^{-ik(ja+r_\alpha)}\,\gamma_{2j+\alpha}, \tag{6.441}$$

where $\alpha = 0, 1$ is an orbital (sublattice) index, $r_0 = -a/4$, $r_1 = +a/4$ are intra-cell site positions, and $a = 2$ is the primitive lattice constant. The momentum k is quantized in units of $2\pi/(Na)$ and we will take N to be even such that $k = \pi/a$ is an allowed momentum. Moreover, these k-space Majorana operators can be shown to obey the Hermitian conjugate and anticommutation relations

$$\gamma_{k\alpha}^\dagger = \gamma_{-k\alpha}, \qquad \{\gamma_{k\alpha}, \gamma_{k'\beta}\} = \delta_{\alpha\beta}\,\delta_{-k,k'}. \tag{6.442}$$

As usually, this implies that the operators $\gamma_{0\alpha}$ and $\mathrm{e}^{i\frac{\pi r_\alpha}{a}}\gamma_{\pi\alpha}$ are Hermitian and hence represent Majorana operators. Now the inverse Fourier transform

$$\gamma_{2j+\alpha} = \sqrt{\frac{2}{N}}\sum_k \mathrm{e}^{+ik(ja+r_\alpha)}\gamma_{k\alpha} \tag{6.443}$$

yields the k-space BdG Hamiltonian

$$H_+ = \frac{1}{2}\sum_k \begin{pmatrix}\gamma_{-k0} & \gamma_{-k1}\end{pmatrix} \mathcal{H}_+(k) \begin{pmatrix}\gamma_{k0}\\ \gamma_{k1}\end{pmatrix}, \tag{6.444a}$$

$$\mathcal{H}_+(k) = (t+t')\sin\left(\tfrac{ka}{2}\right)\sigma^x - (t-t')\cos\left(\tfrac{ka}{2}\right)\sigma^y. \tag{6.444b}$$

The (chiral) topological winding number

$$\nu = -\frac{i}{4\pi a}\int_{-\pi/a}^{\pi/a} \mathrm{d}k\, \mathrm{tr}\left[\mathcal{H}_+(k)^{-1}\sigma^z\nabla_k\mathcal{H}_+(k)\right] \tag{6.445}$$

is $\mathbb{Z}$ quantized whenever $\det\mathcal{H}_+(k) \neq 0$, which is the case when $t \neq t'$. Here the k-space covariant derivative is defined by

$$\nabla_k := \partial_k + i[\hat{r}, \cdot], \qquad \hat{r} := \frac{a}{4}\sigma^z, \tag{6.446}$$

where the operator $\hat{r}$ is the orbital position operator and accounts for the choices of unit cell and boundary surface termination.

From this Bloch Hamiltonian, we specialize to the limit where $t \approx t'$. Since $t, t' > 0$, the band minimum lies at $k = 0$. Performing a gradient expansion about $k = 0$ then yields

$$\mathcal{H}_+(k) \approx \frac{(t+t')a}{2}\, k\, \sigma^x - (t-t')\sigma^y, \tag{6.447}$$

which is a valid approximation whenever $|k|\mathrm{L}\pi/a$ and $|t-t'|\mathrm{L}(t+t')/2$. Going back to real space then produces

$$\mathcal{H}_+ = -i\frac{(t+t')a}{2}\sigma^x\partial_x - (t-t')\sigma^y, \tag{6.448}$$

from which we identify a Fermi velocity and SC gap by

$$v_F = \frac{(t+t')a}{2}, \qquad \Delta = t - t'. \tag{6.449}$$

Note that this gradient expansion is somewhat more faithful to the relativistic continuum model than it might appear at first. This is because the critical theory (when $t = t'$) has a dispersion that possesses no band curvature. In this way, band curvature effects are reduced to a minimum for $\Delta \neq 0$.

Next, it helps to perform an internal $O(2)$ rotation

$$\begin{pmatrix}\gamma_{k0}\\ \gamma_{k1}\end{pmatrix} = \frac{1}{\sqrt{2}}\begin{pmatrix}1 & -1\\ 1 & 1\end{pmatrix}\begin{pmatrix}\lambda_{k1}\\ \lambda_{k2}\end{pmatrix} \tag{6.450}$$

that diagonalizes σ^x and is essentially a rotation into an anti-bonding (λ_{k1}) and bonding (λ_{k2}) basis of k-space Majoranas. This leads to the following form of the Hamiltonian

$$\begin{aligned} H_+ &= \frac{1}{2}\sum_k \begin{pmatrix}\lambda_{-k1} & \lambda_{-k2}\end{pmatrix}\left[(t+t')\sin\left(\tfrac{ka}{2}\right)\sigma^z - (t-t')\cos\left(\tfrac{ka}{2}\right)\sigma^y\right]\begin{pmatrix}\lambda_{k1}\\ \lambda_{k2}\end{pmatrix} \\ &\approx \frac{1}{2}\sum_{|k|<\Lambda} \begin{pmatrix}\lambda_{-k1} & \lambda_{-k2}\end{pmatrix}\left[v_F k\sigma^z - \Delta\sigma^y\right]\begin{pmatrix}\lambda_{k1}\\ \lambda_{k2}\end{pmatrix} \end{aligned} \tag{6.451}$$

with $\Lambda \mathrm{L}\pi/a$ being a short-distance cutoff defining the effective low-energy theory. Now we define real-space continuum Majorana fields by

$$\lambda_\alpha(x) = \frac{1}{\sqrt{2\mathrm{L}}} \sum_{|k|<\Lambda} \mathrm{e}^{ik(x+r_\alpha)} \lambda_{k\alpha}, \tag{6.452}$$

where $\mathrm{L} = Na$ is the length of the system. These fields – in the long wavelength limit – also obey the desired anticommutation relations

$$\{\lambda_\alpha(x), \lambda_\beta(y)\} = \frac{1}{2}\delta_{\alpha\beta}\delta(x-y). \tag{6.453}$$

Finally, transforming back to real space produces the desired low-energy relativistic theory

$$H_+ = \int \mathrm{d}x\, \lambda^T(-iv_F\sigma^z\partial_x - \Delta\sigma^y)\lambda \tag{6.454}$$

valid whenever $|\Delta|\mathrm{L}v_F/a$ and for momenta smaller than $\Lambda\mathrm{L}\pi/a$.

By the same arguments we can construct a lattice realization of H_- by making the change $\Delta \to -\Delta$. In summary, the full form of our desired lattice Hamiltonians is

$$H_+ = \frac{i}{2}\sum_{j=1}^{N}\left(\left[\frac{v_F}{a}+\frac{\Delta}{2}\right]\gamma_{2j+2}\gamma_{2j+1} - \left[\frac{v_F}{a}-\frac{\Delta}{2}\right]\gamma_{2j}\gamma_{2j+1}\right), \tag{6.455a}$$

$$H_- = \frac{i}{2}\sum_{j=1}^{N}\left(\left[\frac{v_F}{a}-\frac{\Delta}{2}\right]\gamma'_{2j+2}\gamma'_{2j+1} - \left[\frac{v_F}{a}+\frac{\Delta}{2}\right]\gamma'_{2j}\gamma'_{2j+1}\right), \tag{6.455b}$$

with γ'_j being another independent set of local lattice Majorana operators.

Before we move on to the issue of boundary conditions in an open system, we have to consider first the symmetries of the lattice models. Although it is manifestly clear that in the limit $\Delta = 0$ the continuum model possesses a global $U(1)$ symmetry, this is obscured in the lattice model. Nevertheless, it is indeed $U(1)$ symmetric. Specializing to the limit $\Delta = 0$ leads to

$$H_+ = \frac{it}{2}\sum_j \left(\gamma_{2j+2}\gamma_{2j+1} - \gamma_{2j}\gamma_{2j+1}\right), \tag{6.456a}$$

$$H_- = \frac{it}{2}\sum_j \left(\gamma'_{2j+2}\gamma'_{2j+1} - \gamma'_{2j}\gamma'_{2j+1}\right). \tag{6.456b}$$

We then relabel the local Majorana operators alternatingly according to even and odd sites

$$a_{2j-1} := \gamma_{2j-1}, \qquad a_{2j} := \gamma'_{2j}, \tag{6.457a}$$

$$b_{2j-1} := -\gamma'_{2j-1}, \qquad b_{2j} := \gamma_{2j}, \tag{6.457b}$$

with a_j and b_j being newly introduced local Majorana operators. Then direct substitution leads to the combined Hamiltonian

$$H_+ + H_- = t\sum_j (-1)^j [c^\dagger_{j+1}c_j + c^\dagger_j c_{j+1}], \tag{6.458}$$

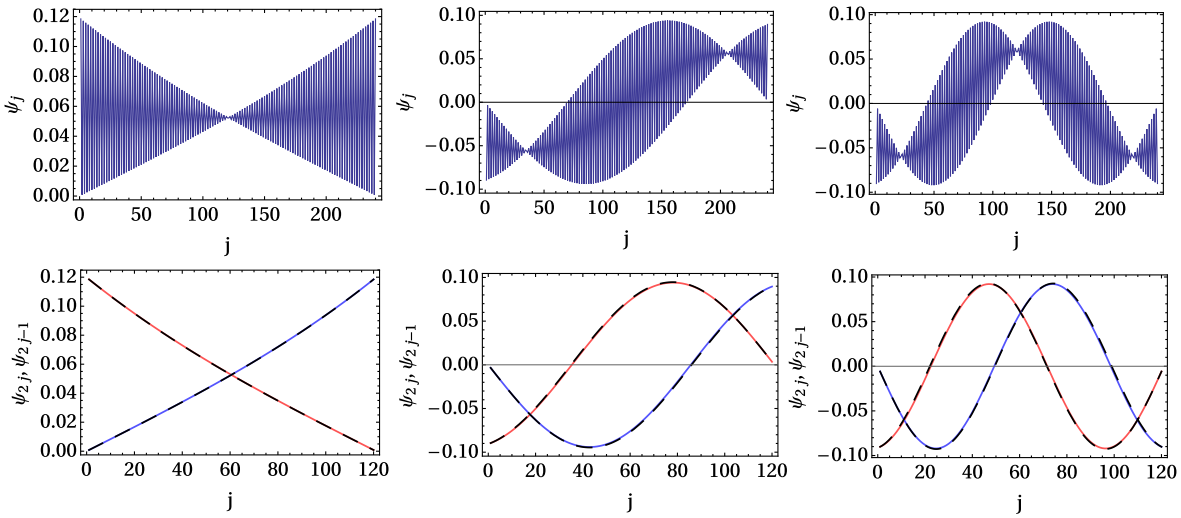

Figure 6.6: Comparison between the numerically determined eigenfunctions of an open Majorana chain [Eq. (6.455a)] and exact solutions to the linearized continuum model [Eq. (6.439b)]. On display are the first three eigenfunctions with positive energy. The state corresponding to the smallest energy (leftmost panel) corresponds to the topological mode. The parameters used here are $\Delta = 0.011$ and $v_F/a = 0.9955$, giving a coherence length of $v_F/\Delta = 90.5$ unit cells or 181 sites. The chain length is L = 120 unit cells. The top panels show the numerically obtained eigenfunctions as a function of site number. The apparent fast oscillations are due to the combined plot of the wavefunction from both sublattices site types. The bottom panels contain the same data but separated into sublattice type, with red curves taken from odd sites and blue curves taken from even sites. Dashed black lines are the analytical expressions Eq. (6.116) [$a(x)$ and $b(x)$] and Eq. (6.82) after resolving the 2-spinor fields into sublattice type (real and imaginary parts), cf. Eq. (6.463).

where $c_j = \frac{a_j + ib_j}{2}$ is a legitimate complex fermion. This lattice Hamiltonian is manifestly $U(1)$ symmetric with conserved particle number $N = \sum_j c_j^\dagger c_j$. Lastly, the fact that

$$\mathcal{T}\lambda\mathcal{T}^{-1} = \sigma^x\lambda, \qquad \mathcal{T}\lambda'\mathcal{T}^{-1} = -\sigma^x\lambda' \tag{6.459}$$

can be shown to lead to a_j and b_j transforming by opposite signs under time reversal.

Moving on, we proceed to determine the appropriate boundary conditions for the low-energy effective fields λ, λ' in an open system. An arbitrary lattice fermionic operator expanded as

$$\psi = \sum_{j=0}^{N+1} \sum_{\alpha=0,1} \psi_{j,\alpha}\gamma_{2j+\alpha} \tag{6.460}$$

will undergo a time evolution according to the Heisenberg equation of motion

$$\partial_t\psi = i[H_+, \psi]. \tag{6.461}$$

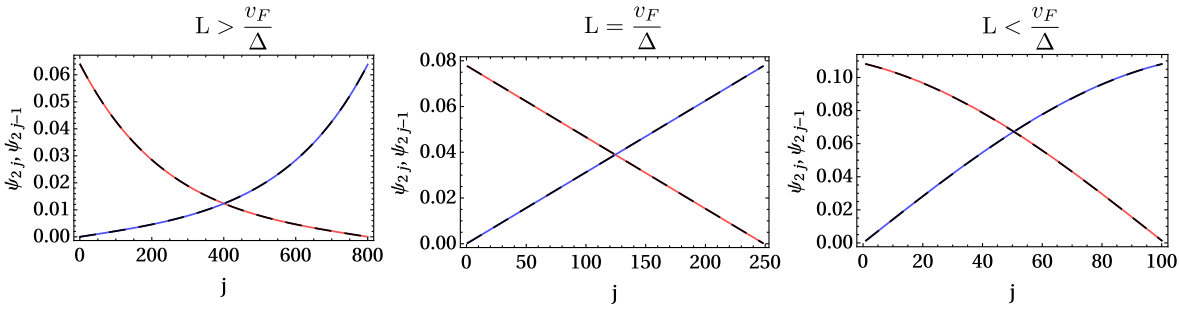

Figure 6.7: Comparison between the numerically computed eigenfunctions (solid lines) and analytical expressions (dashed lines) for the state with the smallest positive energy at different lengths. Like in the bottom panels of Fig. 6.6, the eigenfunctions are plotted according to sublattice type. The parameters $\Delta = 0.004, v_F/a = 0.992$ are chosen such that the coherence length is $v_F/\Delta = 248$ unit cells. (Left) The long wire limit where $\mathrm{L} = 800$ is well described by the in-gap solution $\Phi^{(+)}(x)$ from Eq. (6.116). (Right) The short wire limit with $\mathrm{L} = 100$, where the dashed curve is the eigenfunction $\phi^{(+)}_{k_{0,1}}(x)$ obtained by an $n = 0$ solution of Eq. (6.82). (Middle) The critical case where $\mathrm{L} = 248$ is exactly equal to the coherence length. The eigenfunction now has no curvature and is a piecewise linear function that is described by either $\phi^{(+)}_{k_{0,1}}(x)$ or $\Phi^{(+)}(x)$ in the limit that $k_{0,1}, \kappa \to 0$.

This requires that $\psi_{0,1} = 0$, $\psi_{N+1,0} = 0$ such that the action of H_+ cannot introduce new particles into or out of the finite system. Equivalently this means that the slow fields $\lambda_1(x)$ and $\lambda_2(x)$ should obey

$$\lambda_1(0) + \lambda_2(0) = 0, \qquad \lambda_1(\mathrm{L}) - \lambda_2(\mathrm{L}) = 0, \tag{6.462}$$

because

$$\begin{pmatrix} \gamma_0(x) \\ \gamma_1(x) \end{pmatrix} = \frac{1}{\sqrt{2}} \begin{pmatrix} \lambda_1(x) - \lambda_2(x) \\ \lambda_1(x) + \lambda_2(x) \end{pmatrix}. \tag{6.463}$$

This boundary condition may be identically expressed as

$$\sigma^x \lambda(0) = -\lambda(0), \qquad \sigma^x \lambda(\mathrm{L}) = +\lambda(\mathrm{L}). \tag{6.464}$$

Identical considerations also produce

$$\sigma^x \lambda'(0) = -\lambda'(0), \qquad \sigma^x \lambda'(\mathrm{L}) = +\lambda'(\mathrm{L}). \tag{6.465}$$

Next, the defining relations of λ, λ' in Eqs. (6.437) translate these boundary conditions to

$$R(0) + L(0) = 0, \qquad R(\mathrm{L}) - L(\mathrm{L}) = 0, \tag{6.466}$$

which are our previously stated boundary conditions of Sec. 6.4. Hence we have verified that the open chain boundary conditions will agree with those of our previous exact continuum analysis.

Shown in Fig. 6.1 are exact numerical results from tight-binding model calculations based on Eq. (6.455a). In this instance, the Hamiltonian H_+ is topological with boundary modes

whenever $\Delta > 0$. The other Majorana chain model H_- does not display in-gap states in this parameter regime. The roles of H_+ and H_- are reversed whenever Δ changes sign, such that the total model always contains topological boundary modes. Lastly, one may also compare the form of the eigenfunctions, both localized and extended, as is done in Figs. 6.6 and 6.7. In Fig. 6.7 we observe the transition from a localized (convex-profiled) in-gap mode to an extended (concave-profiled) mode with decreasing L. In the short length regime when $\mathrm{L} < v_F/\Delta$, the analytical eigenmode is described by $\phi^{(+)}_{k_{0,1}}(x)$ from Eq. (6.116), where the quantization condition for $k_{n,1}$ in Eq. (6.87a) now has a valid solution for $n = 0$.

Bibliography

[1] A. Y. Kitaev, Phys. Usp. **44**, 131 (2001).

[2] T. Senthil, Annu. Rev. Condens. Matter Phys. **6**, 299 (2015).

[3] C. Nayak, S. H. Simon, A. Stern, M. Freedman, and S. Das Sarma, Rev. Mod. Phys. **80**, 1083 (2008).

[4] A. M. Turner, F. Pollmann, and E. Berg, Phys. Rev. B **83**, 075102 (2011).

[5] Z.-C. Gu and X.-G. Wen, Phys. Rev. B **90**, 115141 (2014).

[6] L. Fidkowski and A. Kitaev, Phys. Rev. B **83**, 075103 (2011).

[7] C. Beenakker, Annu. Rev. Condens. Matter Phys. **4**, 113 (2013).

[8] R. M. Lutchyn, J. D. Sau, and S. Das Sarma, Phys. Rev. Lett. **105**, 077001 (2010).

[9] Y. Oreg, G. Refael, and F. von Oppen, Phys. Rev. Lett. **105**, 177002 (2010).

[10] V. Mourik, K. Zuo, S. M. Frolov, S. R. Plissard, E. P. A. M. Bakkers, and L. P. Kouwenhoven, Science **336**, 1003 (2012).

[11] A. Das, Y. Ronen, Y. Most, Y. Oreg, M. Heiblum, and H. Shtrikman, Nat. Phys. **8**, 887 (2012).

[12] L. P. Rokhinson, X. Liu, and J. K. Furdyna, Nat. Phys. **8**, 795 (2012).

[13] H. O. H. Churchill, V. Fatemi, K. Grove-Rasmussen, M. T. Deng, P. Caroff, H. Q. Xu, and C. M. Marcus, Phys. Rev. B **87**, 241401(R) (2013).

[14] M. T. Deng, S. Vaitiekenas, E. B. Hansen, J. Danon, M. Leijnse, K. Flensberg, J. Nygård, P. Krogstrup, and C. M. Marcus, Science **354**, 1557 (2016).

[15] E. Prada, P. San-Jose, M. W. A. de Moor, A. Geresdi, E. J. H. Lee, J. Klinovaja, D. Loss, J. Nygård, R. Aguado, and L. P. Kouwenhoven, Nat. Rev. Phys. **2**, 575 (2020).

[16] S. Nadj-Perge, I. K. Drozdov, B. A. Bernevig, and A. Yazdani, Phys. Rev. B **88**, 020407(R) (2013).

[17] J. Klinovaja, P. Stano, A. Yazdani, and D. Loss, Phys. Rev. Lett. **111**, 186805 (2013).

[18] F. Pientka, L. I. Glazman, and F. von Oppen, Phys. Rev. B **88**, 155420 (2013).

[19] M. M. Vazifeh and M. Franz, Phys. Rev. Lett. **111**, 206802 (2013).

[20] B. Braunecker and P. Simon, Phys. Rev. Lett. **111**, 147202 (2013).

[21] K. Pöyhönen, A. Weststrom, J. Röntynen, and T. Ojanen, Phys. Rev. B **89**, 115109 (2014).

[22] S. Nadj-Perge, I. K. Drozdov, J. Li, H. Chen, I. K. Jeon, J. Seo, A. H. MacDonald, B. A. Bernevig, and A. Yazdani, Science **346**, 602 (2014).

[23] M. Ruby, F. Pientka, Y. Peng, F. von Oppen, B. W. Heinrich, and K. J. Franke, Phys. Rev. Lett. **115**, 197204 (2015).

[24] R. Pawlak, M. Kisiel, J. Klinovaja, T. Meier, S. Kawai, T. Glatzel, D. Loss, and E. Meyer, Npj Quantum Inf. **2**, 16035 (2016).

[25] R. Pawlak, S. Hoffman, J. Klinovaja, D. Loss, and E. Meyer, Progress in Particle and Nuclear Physics **107**, 1 (2019).

[26] J. Alicea, Y. Oreg, G. Refael, F. von Oppen, and M. P. A. Fisher, Nat. Phys. **7**, 412 (2011).

[27] D. J. Clarke, J. Alicea, and K. Shtengel, Nat. Commun. **4**, 1348 (2013).

[28] N. H. Lindner, E. Berg, G. Refael, and A. Stern, Phys. Rev. X **2**, 041002 (2012).

[29] A. Vaezi, Phys. Rev. B **87**, 035132 (2013).

[30] Y. Oreg, E. Sela, and A. Stern, Phys. Rev. B **89**, 115402 (2014).

[31] J. Klinovaja and D. Loss, Phys. Rev. B **90**, 045118 (2014a).

[32] J. Klinovaja, A. Yacoby, and D. Loss, Phys. Rev. B **90**, 155447 (2014).

[33] J. Alicea and P. Fendley, Annu. Rev. Condens. Matter Phys. **7**, 119 (2016).

[34] L. H. Santos and T. L. Hughes, Phys. Rev. Lett. **118**, 136801 (2017).

[35] M. Cheng, Phys. Rev. B **86**, 195126 (2012).

[36] R. S. K. Mong, D. J. Clarke, J. Alicea, N. H. Lindner, P. Fendley, C. Nayak, Y. Oreg, A. Stern, E. Berg, K. Shtengel, and M. P. A. Fisher, Phys. Rev. X **4**, 011036 (2014).

[37] J. Klinovaja and D. Loss, Phys. Rev. Lett. **112**, 246403 (2014b).

[38] A. Vaezi, Phys. Rev. X **4**, 031009 (2014).

[39] K. Laubscher, D. Loss, and J. Klinovaja, Phys. Rev. Res. **1**, 032017(R) (2019).

[40] K. Laubscher, D. Loss, and J. Klinovaja, Phys. Rev. Res. **2**, 013330 (2020).

[41] R. Bondesan and T. Quella, J. Stat. Mech. (2013) , P10024.

[42] F. Zhang and C. L. Kane, Phys. Rev. Lett. **113**, 036401 (2014).

[43] C. L. Kane and F. Zhang, Phys. Scr. **2015**, 014011 (2015).

[44] D. Meidan, E. Berg, and A. Stern, Phys. Rev. B **95**, 205104 (2017).

[45] W.-T. Xu and G.-M. Zhang, Phys. Rev. B **97**, 125135 (2018).

[46] S. Eggert and I. Affleck, Phys. Rev. B **46**, 10866 (1992).

[47] M. Fabrizio and A. O. Gogolin, Phys. Rev. B **51**, 17827 (1995).

[48] T. Giamarchi, *Quantum Physics in One Dimension* (Oxford University Press, Oxford, 2004).

[49] D. Rainis, L. Trifunovic, J. Klinovaja, and D. Loss, Phys. Rev. B **87**, 024515 (2013).

[50] L. Fidkowski and A. Kitaev, Phys. Rev. B **81**, 134509 (2010).

[51] M. Stone, *Bosonization* (World Scientific, 1994).

[52] L. Fidkowski, R. M. Lutchyn, C. Nayak, and M. P. A. Fisher, Phys. Rev. B **84**, 195436 (2011).

[53] A. Keselman, L. Fu, A. Stern, and E. Berg, Phys. Rev. Lett. **111**, 116402 (2013).

[54] R. Floreanini and R. Jackiw, Phys. Rev. Lett. **59**, 1873 (1987).

[55] J. Klinovaja, P. Stano, and D. Loss, Phys. Rev. Lett. **109**, 236801 (2012).

[56] J. Klinovaja and D. Loss, Phys. Rev. B **92**, 121410(R) (2015).

[57] S. Gangadharaiah, B. Braunecker, P. Simon, and D. Loss, Phys. Rev. Lett. **107**, 036801 (2011).

[58] J. D. Sau, B. I. Halperin, K. Flensberg, and S. Das Sarma, Phys. Rev. B **84**, 144509 (2011).

[59] A. Keselman and E. Berg, Phys. Rev. B **91**, 235309 (2015).

[60] W. P. Su, J. R. Schrieffer, and A. J. Heeger, Phys. Rev. Lett. **42**, 1698 (1979).

[61] E. Cobanera and G. Ortiz, Phys. Rev. B **92**, 155125 (2015).

[62] V. Chua, J. Klinovaja, and D. Loss, Unpublished (2019).

[63] P. G. Harper, Proc. Phys. Soc. A **68**, 874 (1955).

[64] S. Aubry and A. G., Ann. Israel Phys. Soc. **3**, 133 (1980).

[65] S. Gangadharaiah, L. Trifunovic, and D. Loss, Phys. Rev. Lett. **108**, 136803 (2012).

[66] Y. E. Kraus, Y. Lahini, Z. Ringel, M. Verbin, and O. Zilberberg, Phys. Rev. Lett. **109**, 106402 (2012).

[67] J.-H. Park, G. Yang, J. Klinovaja, P. Stano, and D. Loss, Phys. Rev. B **94**, 075416 (2016).

[68] M. Pletyukhov, D. M. Kennes, K. Piasotski, J. Klinovaja, D. Loss, and H. Schoeller, Phys. Rev. Research **2**, 033345 (2020).

[69] E. Lieb, T. Schultz, and D. Mattis, Annals of Physics **16**, 407 (1961).

[70] P. Heinzner, A. Huckleberry, and M. R. Zirnbauer, Commun. Math. Phys. **257**, 725 (2005).

[71] E. Witten, Rev. Mod. Phys. **88**, 035001 (2016).

[72] D. Loss, Phys. Rev. Lett. **69**, 343 (1992).

[73] P. Lecheminant and E. Orignac, Phys. Rev. B **65**, 174406 (2002).

[74] D. L. Maslov, M. Stone, P. M. Goldbart, and D. Loss, Phys. Rev. B **53**, 1548 (1996).

[75] A. O. Gogolin, A. A. Nersesyan, and A. M. Tsvelik, *Bosonization and Strongly Correlated Systems* (Cambridge University Press, Cambridge, 2004).

[76] J. F. Colombeau, *Elementary Introduction to New Generalized Functions* (Elsevier, Amsterdam, 2011).

[77] J. F. Colombeau, São Paulo Journal of Mathematical Sciences **7**, 201 (2013).

[78] F. D. M. Haldane, J. Phys. C: Solid State Phys. **14**, 2585 (1981).

[79] J. von Delft and H. Schoeller, Annalen der Physik **7**, 225 (1998).

[80] T. R. Klassen and E. Melzer, International Journal of Modern Physics A **8**, 4131 (1993).

[81] E. Fradkin, *Field Theories of Condensed Matter Physics* (Cambridge University Press, Cambridge, 2013).

[82] X.-G. Wen, *Quantum Field Theory of Many-Body Systems: From the Origin of Sound to an Origin of Light and Electrons* (Oxford University Press, Oxford, 2004).

[83] J. Zinn-Justin, *Quantum Field Theory and Critical Phenomena* (Clarendon Press, Oxford, 1996).

[84] M. H. Devoret, A. Wallraff, and J. M. Martinis, arXiv:cond-mat/0411174 (2004).

[85] M. Abramowitz and I. A. Stegun, *Handbook of Mathematical Functions*, Appl. Math. Ser. 55 (U.S. Department of Commerce, National Bureau of Standards, Washington, 1964).

[86] A. E. Mattsson, S. Eggert, and H. Johannesson, Phys. Rev. B **56**, 15615 (1997).

[87] M. Cheng and R. Lutchyn, Phys. Rev. B **92**, 134516 (2015).

[88] L. Mazza, F. Iemini, M. Dalmonte, and C. Mora, Phys. Rev. B **98**, 201109(R) (2018).

[89] V. G. Kac, *Vertex Algebras for Beginners*, University Lecture Series 10 (American Mathematical Society, Providence, RI, 1998).

[90] P. Ginsparg, in *Fields, Strings and Critical Phenomena*, Les Houches Session XLIX, edited by E. Brézin and J. Zinn-Justin (Elsevier, Amsterdam, 1989) pp. 1–168.

[91] A. A. Belavin, A. M. Polyakov, and A. B. Zamolodchikov, Nucl. Phys. B **241**, 333 (1984).

[92] R. Blumenhagen and E. Plauschinn, *Introduction to Conformal Field Theory: With Applications to String Theory*, Lect. Notes Phys. 779 (Springer, Heidelberg Berlin, 2009).

[93] P. Goddard and D. Olive, International Journal of Modern Physics A **1**, 303 (1986).

[94] G. C. Wick, A. S. Wightman, and E. P. Wigner, Phys. Rev. **88**, 101 (1952).

[95] G. Kells, Physical Review B **92**, 155434 (2015).

[96] J. R. Schrieffer and P. A. Wolff, Physical Review **149**, 491 (1966).

[97] S. Bravyi, D. P. DiVincenzo, and D. Loss, Annals of Physics **326**, 2793 (2011).

[98] A. Altland and B. D. Simons, *Condensed Matter Field Theory* (Cambridge University Press, Cambridge, 2010).

[99] U. Graf, *Introduction to Hyperfunctions and their Integral Transforms: An Applied and Computational Approach* (Birkhäuser, Basel, 2010).

[100] M. Stone and P. Goldbart, *Mathematics for Physics: A Guided Tour for Graduate Students* (Cambridge University Press, Cambridge, 2009).

[101] D. Sternheimer, in *Particles, Fields and Gravitation*, edited by J. Rembielinski (AIP, New York, 1998) pp. 107–145.

[102] F. A. Berezin, Sov. Phys. Usp. **23**, 763 (1980).

[103] M. Greiter, Annals of Physics **319**, 217 (2005).

Chapter 7

Fractional boundary charges with quantized slopes in interacting one- and two-dimensional systems

Adapted from:
K. Laubscher, C. S. Weber, D. M. Kennes, M. Pletyukhov, H. Schoeller, D. Loss, and J. Klinovaja,
"Fractional boundary charges with quantized slopes in interacting one- and two-dimensional systems,"
Phys. Rev. B **104**, 035432 (2021)

We study fractional boundary charges (FBCs) for two classes of strongly interacting systems. First, we study strongly interacting nanowires subjected to a periodic potential with a period that is a rational fraction of the Fermi wavelength. For sufficiently strong interactions, the periodic potential leads to the opening of a charge density wave gap at the Fermi level. The FBC then depends linearly on the phase offset of the potential with a quantized slope determined by the period. Furthermore, different possible values for the FBC at a fixed phase offset label different degenerate ground states of the system that cannot be connected adiabatically. Next, we turn to the fractional quantum Hall effect (FQHE) at odd filling factors $\nu = 1/(2l+1)$, where l is an integer. For a Corbino disk threaded by an external flux, we find that the FBC depends linearly on the flux with a quantized slope that is determined by the filling factor. Again, the FBC has $2l+1$ different branches that cannot be connected adiabatically, reflecting the $(2l+1)$-fold degeneracy of the ground state. These results allow for several promising and strikingly simple ways to probe strongly interacting phases via boundary charge measurements.

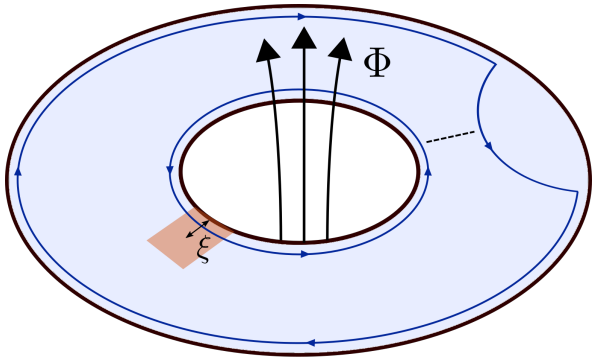

Figure 7.1: Corbino disk in the FQHE regime threaded by an external flux Φ. The FBC is measured in the red region, which extends into the bulk on the order of a few edge state localization lengths ξ. In the presence of a constriction, indicated by the dashed line, tunneling of fractional charges between the chiral edge states (blue lines) is allowed.

7.1 Introduction

The emergence of fractional charges in topologically nontrivial systems is a recurring theme in modern condensed matter physics that has been discussed in several different contexts. In the fractional quantum Hall effect (FQHE), for example, strong electron-electron interactions lead to the emergence of exotic quasiparticles carrying only a fraction of the electronic charge e [1–4]. On the other hand, well-defined fractional charges can also emerge in the ground state of topological insulators. Early examples include the Jackiw-Rebbi [5, 6] and Su-Schrieffer-Heeger [7, 8] models, where domain walls between topologically non-equivalent phases bind fractional charges that are quantized due to symmetry. Generally, fractional boundary charges (FBCs) accumulate at the boundaries of an insulator. Importantly, the possible presence of edge states influences the total boundary charge only by an integer number, while the *fractional* part of the boundary charge contains contributions from all extended states and is directly related to bulk properties via the Zak-Berry phase [9–15]. FBCs of this type have been studied in a large variety of systems, including different types of one-dimensional (1D) models [15–39], topological crystalline insulators [40–44], higher-order topological insulators [45–52], and the integer quantum Hall effect (IQHE) [31]. While the presence of symmetries leads to a quantization of the FBC in rational units, [35] certain *universal* features of the FBC persist even in the absence of symmetries. For generic 1D tight-binding models with periodically modulated on-site potentials, it was shown that the FBC is a sharp quantity[1] that changes linearly with the phase offset of the modulation with a universally quantized slope even in the presence of disorder [15, 28, 31, 34]. Furthermore, this slope can be directly related to the Hall conductance in the 2D IQHE [31].

Motivated by these results on noninteracting systems, the aim of this work is to study the universal properties of the FBC in strongly interacting systems. First, we consider a 1D nanowire with a periodic potential of the form $V_m(x) = 2V_m \cos(2mk_F x + \alpha)$, where k_F is the Fermi momentum, m an integer, and α a phase offset. For $m = 1$, it is well-known that a

[1] Here, 'sharp' refers to the fact that quantum fluctuations are negligibly small compared to the fractional ground state expectation value of the charge [28, 38].

charge density wave (CDW) gap is opened at the Fermi level [53] with an FBC that depends linearly on α with a quantized slope $1/2\pi$ [28, 31]. In the presence of strong interactions, additional gaps can be opened for $m > 1$. We show that in this case the FBC depends again linearly on α with a *fractional* slope $1/2\pi m$. Perhaps even more interestingly, we find that there are now m degenerate ground states labeled by m different branches of the FBC that cannot be connected under adiabatic evolution of α.

Next, we extend our considerations to a two-dimensional electron gas (2DEG) in the FQHE regime at odd filling factors $\nu = 1/(2l+1)$, where l is an integer. For a Corbino disk threaded by an external flux Φ as shown in Fig. 7.1, we find that the FBC depends linearly on Φ with a slope determined by the filling factor. From this the standard Hall conductance follows. Further, the FBC has $2l+1$ distinct branches labeling $2l+1$ degenerate ground states that cannot be adiabatically connected unless fractional charges are allowed to tunnel between the two boundaries due to, e.g., a constriction, see again Fig. 7.1. We outline how these results open up a strikingly simple way to probe strongly interacting systems via boundary charge measurements.

7.2 FBC in one dimension

We first study the FBC in a 1D nanowire of spinless electrons subjected to a spatially modulated potential $V_m(x)$.[2] The single-particle Hamiltonian reads

$$H = \int dx\ \Psi^\dagger(x) \left[-\frac{\hbar^2 \partial_x^2}{2m^*} + V_m(x) \right] \Psi(x), \tag{7.1}$$

where $\Psi^\dagger(x)$ [$\Psi(x)$] creates [annihilates] a spinless electron of mass m^* at the position x. Without interactions, the onsite potential opens a CDW gap at the Fermi level only for $m = 1$ [53]. To study the more general case of an interacting system, we linearize the spectrum around the Fermi points and write $\Psi(x) = R(x)e^{ik_F x} + L(x)e^{-ik_F x}$, where $R(x)$ and $L(x)$ are slowly varying right- and left-moving fields, respectively. Next, we introduce chiral bosonic fields $R(x) \propto e^{i\phi_1(x)}$ and $L(x) \propto e^{i\phi_{\bar{1}}(x)}$ satisfying standard commutation relations [54] $[\phi_r(x), \phi_{r'}(x')] = ir\pi\delta_{rr'}\mathrm{sgn}(x-x')$. This ensures the correct anticommutation relation between fermionic operators of the same species, while the remaining commutation relations can be ensured by Klein factors, which we do not include explicitly. It is also useful to define local conjugate fields $\phi = (\phi_{\bar{1}} - \phi_1)/2$ and $\theta = (\phi_{\bar{1}} + \phi_1)/2$ with $[\phi(x), \theta(x')] = \frac{i\pi}{2}\mathrm{sgn}(x-x')$. Small-momentum interactions are now included via the standard kinetic term $H_0 = \frac{v}{2\pi}\int dx\, \{K[\partial_x\theta(x)]^2 + \frac{1}{K}[\partial_x\phi(x)]^2\}$, where v is the velocity and K the Luttinger liquid parameter [54]. Furthermore, momentum-conserving multi-electron processes involving backscatterings can lead to the opening of gaps when relevant in the renormalization group (RG) sense [54–59]. In our case, to lowest order in the interaction, the corresponding term reads

$$H^m_{CDW} = \tilde{V}_m \int dx\, [(R^\dagger L)^m e^{i\alpha} + \text{H.c.}], \tag{7.2}$$

[2] In an experimental realization, it will be more convenient to tune k_F by varying the filling of the wire rather than adjusting the period of the potential.

where we have neglected rapidly oscillating contributions. Here, $\tilde{V}_m \propto V_m g_B^{m-1}$, where g_B is the strength of the backscattering term induced by interactions and $V_m > 0$. In terms of the bosonic fields, the CDW term takes the form $H^m_{CDW} = \int dx\, \mathcal{H}^m_{CDW}(x)$ with

$$\mathcal{H}^m_{CDW}(x) = \frac{-2|\tilde{V}_m|}{(2\pi a)^m} \cos(2m\phi(x) + \alpha - \alpha_0), \tag{7.3}$$

where a is a short-distance cutoff and α_0 an irrelevant phase shift. The above term is of sine-Gordon form and opens a full gap at the Fermi level whenever relevant in the RG sense. This can be achieved if $K < 2/m^2$ (which generally requires long-range interactions) or if the bare coupling constant is already of order one compared to the Fermi energy. From now on, we therefore focus on the case where H^m_{CDW} is relevant.

We now consider a semi-infinite system with a single boundary at $x = 0$. In the semiclassical limit of infinitely strong pinning, the bosonic field ϕ takes a constant bulk value in order to minimize the cosine term. Explicitly, we find $-\phi(\infty) = (\alpha - \alpha_0)/(2m) + p\pi/m$, where p is an integer. At the edge of the system at $x = 0$, on the other hand, we impose vanishing boundary conditions by demanding $R(0) + L(0) = 0$. This implies $\phi_1(0) - \phi_{\bar{1}}(0) = -2\phi(0) = \pi \mod 2\pi$. We then define the FBC Q_B as the excess charge at the boundary of the system as compared to a constant bulk contribution. Using that the electron density is $\rho(x) = -\partial_x\phi(x)/\pi$, we have $Q_B = -[\phi(\infty) - \phi(0)]/\pi$ in units of the electron charge e. Plugging in the bulk and edge values for ϕ found above, we obtain for $Q^{1D}_B \equiv Q_B$ (up to an irrelevant constant)

$$Q^{1D}_B = \frac{\alpha}{2\pi m} + \frac{p}{m} \mod 1. \tag{7.4}$$

This result has several interesting features: Firstly, we see that the FBC is a linear function of α with a slope $1/2\pi m$. For $m = 1$, this agrees with the result that was previously obtained for noninteracting systems [28, 31], but the derivation presented here also holds in the presence of interactions.[3] Secondly, for fixed α, there are m different values for the FBC, $Q^{1D}_B - \alpha/2\pi m \in \{0, 1/m, ..., (m-1)/m\}$. For $m > 1$, we therefore find that the ground state is m-fold degenerate. Thirdly, these different ground states cannot be connected to one another under adiabatic evolution of α. As such, a given branch of the FBC is $2\pi m$-periodic, while the Hamiltonian is 2π-periodic. Finally, we emphasize that these results are independent of the exact value of K but hold whenever H^m_{CDW} is relevant.

In fact, Eq. (7.4) can also be understood from more general arguments without the use of the bosonization formalism. To see this, let us assume that the bulk is fully gapped by the backscattering mechanism discussed above. If we shift the origin of the system by $\pi/mk_F \equiv \lambda_F/2m$, the FBC cannot change. Furthermore, any shift of the lattice by d can always be compensated by shifting α. Thus, the FBC is a function of both of them and necessarily has the form $Q_B(\alpha, d) \equiv Q_B(\alpha/2\pi + 2md/\lambda_F)$. This is nothing but a form of 'Galilean invariance' in α and d. On the other hand, a shift by d changes Q_B by $d\bar{\rho}_B$, where $\bar{\rho}_B = 2/\lambda_F$ is the average bulk density. Thus, we find that the FBC is a linear function of not only d but also α and has the form $Q_B = (\alpha/2\pi + 2md/\lambda_F)/m + C$, where C is a constant. Again, we find that the slope of the phase dependence is $1/2\pi m$. Simultaneously, there must be m different branches of the FBC [corresponding to m values $C = 0, 1/m, ..., (m-1)/m$] since H is 2π-periodic.

[3] The CDW gap will, however, be renormalized by the interaction, see Ref. [53].

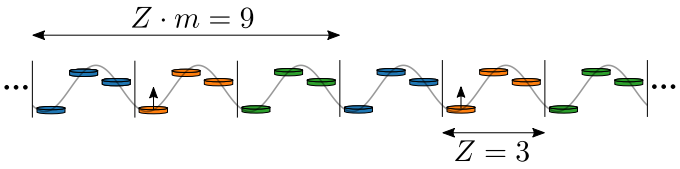

Figure 7.2: Pictorial representation of the ground state for $m = Z = 3$ and a certain phase α in the investigated regime. Every 9th site is occupied by a particle, which is indicated by the small arrows pointing up. The ground state is three-fold degenerate as one can move the particles to the green or blue unit cells.

7.3 Effective model

To illustrate the m-fold degenerate ground state and the phase dependence of the FBC [see Eq. (7.4)], we consider the following tight-binding model with N_s sites

$$H = -t \sum_{n=1}^{N_s-1} (a_n^\dagger a_{n+1} + \text{H.c.}) + \sum_{l=1}^{r} \sum_{n=1}^{N_s-l} U_l \, \hat{\rho}_n \hat{\rho}_{n+l} + \sum_{n=1}^{N_s} v_{ex} \cos\left(\frac{2\pi}{Z} n + \alpha\right) \hat{\rho}_n \,, \tag{7.5}$$

where $\hat{\rho}_n = a_n^\dagger a_n$, t is the hopping amplitude, v_{ex} the amplitude of the potential modulation with period Z and phase α, and U_l the electron-electron interaction with range r, which is required to be sufficiently long-ranged. We choose $U_l = U$ and $r = Z(m-1)$, where $\bar{\rho}_B = \frac{1}{mZ}$ is the average bulk density (corresponding to filling $\nu = \frac{1}{m}$). For sufficiently large v_{ex} or U, this means that every mth minimum is occupied in the thermodynamic limit (see Fig. 7.2). The ground state is then m-fold degenerate because one could shift all particles simultaneously to the next minimum.

Next, we investigate the evolution of the FBC with α, see Fig. 7.3. We calculate Q_B with perturbation theory for $U \gg v_{ex} \gg t$, see Appendix B for details, and compare these results with results obtained from a numerically exact density matrix renormalization group (DMRG) approach. For an open system of finite size one gets a larger degeneracy of the ground state as one can also shift single particles close to the boundaries. Thus, we do not use an integer number of filling unit cells of size $Z \cdot m$ but cut some sites at the boundary. The ground state of the system is then nondegenerate and we can perform a variational ground state search. For more details we refer to Appendix A.

We confirm, in accordance with Eq. (7.4), that Q_B shows a linear slope $1/2\pi m = 1/6\pi$ up to a $2\pi/Z$-periodic function (with $Z = 3$).[4] The inset of Fig. 7.3 shows a false color plot demonstrating for which values of v_{ex} and U this linear slope indicated by $\delta Q_B = Q_B(2\pi) - Q_B\left(\frac{4\pi}{3}\right) = \frac{1}{9}$ (white region) is stabilized. We observe that this is already the case for relatively small v_{ex} and intermediate U. The general phenomenology of fractionally quantized slopes in the FBC of this 1D model is therefore quite general and does not require fine tuning. The additional modulation by a $2\pi/Z$-periodic function that was not present in Eq. (7.4) is a consequence of commensurability between the lattice constant and the Fermi wavelength and vanishes in the continuum limit [28]. In Appendices D and E we show that our results are stable against disorder of the hoppings and the on-site potentials and

[4] For sufficiently long-ranged interactions we expect our result to also hold when including small perturbations in the filling or the modulation period, leading to small deviations of m or Z.

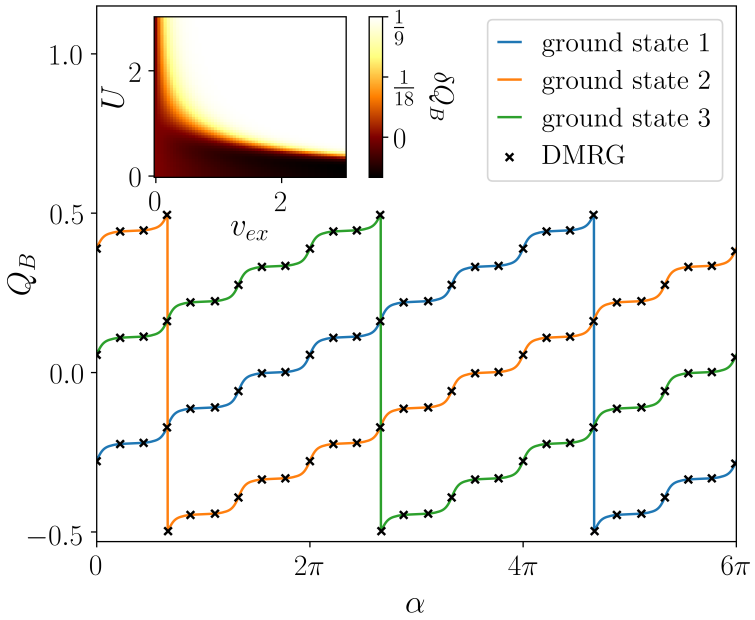

Figure 7.3: FBC Q_B of the effective model with $m = Z = 3$ and $t = 1$. Main panel: Q_B as a function of α at $v_{ex} = 5$ and $U = 10$ calculated with DMRG (crosses) and perturbation theory (solid lines). For details about the calculation see Appendices A–C. The FBC shows a linear slope $1/6\pi$ up to a periodic function and a jump of size unity. Inset: False color plot showing $\delta Q_B = Q_B(2\pi) - Q_B\left(\frac{4\pi}{3}\right)$ for different v_{ex} and U. The expected linear slope (white region) is observed already for relatively small v_{ex} and intermediate U.

that a quantized slope is also present in the case of long ranged interactions $U_l \propto l^{-6}$ or $U_l \propto \exp(-\gamma l)\, l^{-2}$.

7.4 FBC in two dimensions – FQHE

Next, we study the FBC in a 2DEG in the FQHE regime at odd filling factors $\nu = 1/(2l+1)$ for an integer l. To facilitate the analytical treatment of strong interactions, we make use of a coupled-wire construction of the FQHE [58, 59]. We consider an array of N parallel nanowires, where the individual wires are oriented along the x axis and the wires are stacked along the y axis [60, 61]. We assume periodic boundary conditions along the latter, realizing the cylinder geometry shown in Fig. 7.4. The kinetic term is $H_0 = \sum_n H_{0,n}$ with $H_{0,n} = -\frac{\hbar^2}{2m^*}\int dx\ \Psi_n^\dagger(x)\,\partial_x^2\,\Psi_n(x)$, where $\Psi_n^\dagger(x)$ [$\Psi_n(x)$] creates [annihilates] a spinless electron of mass m^* at the position x in the nth wire. A magnetic field $\mathbf{B}$ ($\mathbf{B}'$) is applied perpendicular to the surface (along the axis) of the cylinder and the vector potential is chosen as $\mathbf{A} = Bx\hat{y}$ [$\mathbf{A}' = (B'R/2)\hat{y}$], where $R = Na_y/2\pi$ is the radius of the cylinder and a_y denotes the interwire distance. Finally, the tunneling between neighboring nanowires is described by $H_T = \sum_n H_{T,n+1/2}$ with

$$H_{T,n+1/2} = te^{i\varphi}\int dx\ e^{ik_B x}\Psi_{n+1}^\dagger\Psi_n + \text{H.c.} \tag{7.6}$$

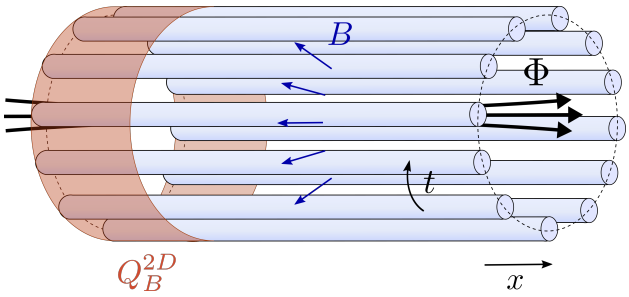

Figure 7.4: An array of nanowires tunnel-coupled by t arranged to a cylinder threaded by an external flux Φ. A magnetic field B perpendicular to the cylinder surface drives the system into an FQHE phase. The FBC Q_B^{2D} is calculated in the red region and shown to vary linearly with Φ, see Eq. (7.9).

Here, $k_B = eBa_y/\hbar$ and $\varphi = \frac{e}{\hbar}\frac{\Phi}{N}$, with the total flux through the cylinder given by $\Phi = \pi R^2 B'$. To treat interactions, we again linearize the spectrum around the Fermi points, $\Psi_n(x) = R_n(x)e^{ik_F x} + L_n(x)e^{-ik_F x}$, and switch to a bosonized language by writing $R_n(x) \propto e^{i\phi_{1n}(x)}$, $L_n(x) \propto e^{i\phi_{\bar{1}n}(x)}$ with $[\phi_{rn}(x), \phi_{r'n'}(x')] = ir\pi\delta_{rr'}\delta_{nn'}\mathrm{sgn}(x-x')$. Small-momentum interactions can then be included in the standard way and lead to a gapless sliding Luttinger liquid phase [59] that we will not characterize here. For our purposes, it suffices to note that if k_F becomes commensurable with k_B such that $2k_F/k_B = \nu$, an additional momentum-conserving multi-electron process can be constructed such that a gap is opened at the Fermi level and the FQHE at filling ν is realized [59]. Explicitly, the term that opens the gap is $H^l_{T,n+1/2} = \int dx\, \mathcal{H}^l_{T,n+1/2}$ with [5]

$$\mathcal{H}^l_{T,n+1/2} = t_l e^{i\varphi} R^\dagger_{n+1} L_n (R^\dagger_{n+1} L_{n+1})^l (R^\dagger_n L_n)^l + \text{H.c.} \tag{7.7}$$

Here, $t_l \propto t g_B^{2l}$. Introducing the fields $\eta_{rn} = (l+1)\phi_{rn} - l\phi_{\bar{r}n}$, Eq. (7.7) becomes

$$\mathcal{H}^l_{T,n+1/2} = \frac{-2|t_l|}{(2\pi a)^{2l+1}} \cos(\eta_{1(n+1)} - \eta_{\bar{1}n} - \varphi + \varphi_0), \tag{7.8}$$

where φ_0 is an irrelevant phase shift. In this representation, it is evident that all fields are pinned pairwise, such that the system is indeed fully gapped given that $\mathcal{H}^l_{T,n+1/2}$ is the leading relevant term. This can always be achieved for a suitable set of interaction parameters [58]. The case $l = 0$ corresponds to the IQHE with $\nu = 1$, where the gap is opened even without interactions.

We now calculate the FBC in dependence on Φ. At low energies, the argument of the cosine term in Eq. (7.8) is pinned. Taking the sum over N, this implies $-\sum_n \phi_n(\infty) = N\nu(\varphi - \varphi_0)/2 + p\nu\pi$ in terms of the local fields $\phi_n = (\phi_{\bar{1}n} - \phi_{1n})/2$. Here, p is an integer. On the other hand, imposing vanishing boundary conditions at $x = 0$ leads to $\sum_n \phi_n(0) = -N\pi/2 \mod \pi$. Writing the 2D FBC as $Q_B^{2D} = \sum_n Q_{B,n}^{1D}$, where $Q_{B,n}^{1D}$ is the FBC in the nth wire, we get (up to an irrelevant constant)

$$Q_B^{2D} = \frac{\Phi\nu}{2\pi}\frac{e}{\hbar} + p\nu \mod 1. \tag{7.9}$$

[5] Here it is crucial that we work with odd filling factors. At even filling factors, the presence of multiple competing momentum-conserving terms can lead to a more complicated behavior that is not captured here.

Thus, the FBC has a linear slope in Φ which is quantized in units of $\nu e/h$. At fractional filling $\nu = 1/(2l+1)$ with $l > 0$, this slope is $(2l+1)$ times smaller than in the IQHE case $l = 0$. Furthermore, there are $2l+1$ different branches of the FBC that cannot be connected under adiabatic evolution of Φ. Finally, the Hall conductance can be obtained from the FBC following Ref. [31], yielding $\sigma_{xy} = e\,\dot{Q}_B^{2D}/\dot{\Phi} = e^2\nu/h$ as expected.[6] Importantly, this result holds for arbitrary changes of Φ and therefore extends the well-known Laughlin argument, where it is assumed that Φ is changed by an integer multiple of h/e.

7.5 Experimental signatures

The sample geometry described above can be realized by a Corbino disk [62–68], see Fig. 7.1. The FBC is then accessible in a rather straightforward way using, e.g., STM techniques [69–73] to measure the charge located at the boundary of the disk. This allows for several interesting ways to probe the FQHE: Firstly, observing the slope of the linear flux dependence allows one to probe the filling factor, see Eq. (7.9). This can further be corroborated by observing the evolution of the FBC as Φ is varied adiabatically. The FBC will then be $(2\pi/\nu)$-periodic in Φ, with a jump of size unity occurring at a particular value of Φ. Secondly, the different branches of the FBC can be connected if fractional charges are allowed to tunnel between opposite boundaries due to, e.g., a constriction, see again Fig. 7.1. By measuring the FBC repeatedly in the presence of a constriction, one finds that it can take $2l+1$ different values, reflecting the $(2l+1)$-fold ground state degeneracy. Similarly, if one now observes the evolution of the FBC with Φ, also jumps of fractional size $s/(2l+1)$, where $s = 1, ..., 2l$ is another integer, can be observed when the system switches from one ground state to another. We note that due to translational invariance it suffices to measure the FBC along a small part of the boundary rather than along the entire circumference, see Fig. 7.1. In this case, instead of measuring the absolute values of the slopes and jumps of the FBCs, one should measure their ratios for different filling factors, which again become universal. Thus, boundary charge measurements open up a direct way to probe the fractionalization of charges in the FQHE and, most importantly, allow for a direct experimental verification of the ground state degeneracy. We note that the FBC could alternatively be studied in cold-atom setups with tunable interactions [74].

7.6 Conclusions

We studied FBCs in strongly interacting CDW-modulated nanowires and in Corbino disks in the FQHE regime at odd filling factors threaded by an external flux. In both cases, the FBC displays universal features that do not depend on microscopic details of the models such as the exact values of the interaction parameters. In the nanowire (FQHE) case, the FBC depends linearly on the phase offset (flux) with a quantized slope that is determined by the filling factor. Furthermore, the different possible values of the FBC at a fixed phase offset (flux) label different degenerate ground states that cannot be adiabatically connected. The observation of these features is well within experimental reach and opens up a promising route to probe strongly interacting phases via FBCs.

[6] While Ref. [31] studied the IQHE, the derivation of the Hall conductance presented there remains valid also in the presence of interactions.

As an outlook, we note that our findings can readily be extended to more general filling factors $\nu = k/(2l+1)$, where k is an integer that is coprime to $2l+1$. A given branch of the FBC will be $2\pi(2l+1)$-periodic under adiabatic evolution of Φ with k jumps of size unity occurring at specific values of Φ.

Acknowledgments. We thank Flavio Ronetti for helpful discussions. This work was supported by the Deutsche Forschungsgemeinschaft via RTG 1995, the Swiss National Science Foundation (SNSF) and NCCR QSIT and by the Deutsche Forschungsgemeinschaft (DFG, German Research Foundation) under Germany's Excellence Strategy - Cluster of Excellence Matter and Light for Quantum Computing (ML4Q) EXC 2004/1 - 390534769. We acknowledge support from the Max Planck-New York City Center for Non-Equilibrium Quantum Phenomena. Simulations were performed with computing resources granted by RWTH Aachen University under project thes0753. Funding was received from the European Union's Horizon 2020 research and innovation program (ERC Starting Grant, Grant Agreement No. 757725).

7.A Ground state for finite and open system

When calculating the ground state of the effective one-dimensional model [see Eq. (7.5)] for an open and finite system with a fixed number of particles N_p, one gets a huge degeneracy due to the missing particles at the system boundaries. To avoid this degeneracy we cut the system and take only $N_s = mZN_p - (m-1)Z = 9N_p - 6$ sites instead of $\bar{N}_s = 9N_p$ sites (for $Z = 3$ and $m = 3$). The degeneracy is then lifted and there is only one possible ground state. This procedure corresponds to forcing the last 6 sites to be empty. The other two possible ground states that would occur in the thermodynamic limit can then be found by putting either 3 or all 6 empty sites to the other boundary of the chain. We will use this procedure for our DMRG calculations as well as for the analytical calculations of the boundary charge.

Using this ground state search, one gets a periodicity of 2π. To get the periodicity of 6π, we calculate all three ground states. We expect these states to evolve into each other when executing an adiabatic time evolution in the grand-canonical ensemble with the chemical potential located in the charge gap. One then gets the periodicity of 6π which we show in the main text. For convenience, we choose the chemical potential in such a way that the jumps of the adiabatic time evolution and the ones of the ground state search occur at the same position. The positions of the jumps in the adiabatic time evolution may change slightly when changing the chemical potential within the gap.

The average of the FBC is given by

$$Q_B = \sum_{n=1}^{\bar{N}_s} f_n(\rho_n - N_p/\bar{N}_s), \tag{7.10}$$

where $\bar{N}_s$ is the number of sites including the 6 empty sites, N_p is the number of particles, and $\rho_n = \langle a_n^\dagger a_n \rangle$. The envelope function is denoted by f_n and needs to decay smoothly from 1 to 0. For our numerical calculations we take a linear slope for the decay of length l_p. The center of this slope has a distance of L_p to the left boundary. For the calculations shown in Fig. 7.3 we use $N_s = 174$ ($\bar{N}_s = 180$) with $L_p = 90$ and $l_p = 90$.

7.B Analytical calculation of the FBC

In this Appendix we calculate the FBC for the effective one-dimensional model in dependence of the phase α analytically. We focus on the case of $Z = 3$ and $m = 3$ (other cases can be treated analogously) and consider the atomic limit with strong electron-electron (Coulomb) interaction $U_l = U \gg v_{ex} \gg t$. We introduce an effective unit cell of $Z_{\text{eff}} = Zm = 9$, so that the average bulk density is $\bar{\rho}_B = \frac{1}{Z_{\text{eff}}} = \frac{1}{9}$.

In the atomic limit the problem of finding the FBC in the given strongly interacting model can be reduced to an effective single-particle model, in which a particle can occupy one of the first Z sites of the effective unit cell with Z_{eff} sites. As shown in Ref. [35] the FBC in this limit is dominantly given by the polarization contribution deep in the bulk, which has the form

$$Q_B \approx Q_P = -\frac{1}{Z_{\text{eff}}} \sum_{j=1}^{Z_{\text{eff}}} j(\rho_j^{\text{bulk}} - \bar{\rho}_B) \tag{7.11}$$

$$= -\frac{1}{Z_{\text{eff}}} \sum_{j=1}^{Z} j\rho_j^{\text{bulk}} + \frac{Z_{\text{eff}}+1}{2Z_{\text{eff}}} \tag{7.12}$$

$$= -\frac{1}{9} \sum_{j=1}^{Z} j\rho_j^{\text{bulk}} + \frac{5}{9}. \tag{7.13}$$

Depending on the minima of the cosine potential (see Fig. 7.5), a particle can sit either on site $j = 1$ (for $0 < \alpha < \frac{2\pi}{3}$), or on $j = 2$ (for $\frac{4\pi}{3} < \alpha < 2\pi$), or on $j = 3$ (for $\frac{2\pi}{3} < \alpha < \frac{4\pi}{3}$). We thus get three plateaus,

$$Q_B\left(0 < \alpha < \frac{2\pi}{3}\right) \approx -\frac{1}{9} + \frac{5}{9} = \frac{4}{9}, \tag{7.14}$$

$$Q_B\left(\frac{4\pi}{3} < \alpha < 2\pi\right) \approx -\frac{2}{9} + \frac{5}{9} = \frac{3}{9}, \tag{7.15}$$

$$Q_B\left(\frac{2\pi}{3} < \alpha < \frac{4\pi}{3}\right) \approx -\frac{3}{9} + \frac{5}{9} = \frac{2}{9}. \tag{7.16}$$

7.B.1 Vicinity of $\alpha = 0, \frac{2\pi}{3}, \frac{4\pi}{3}$

At $\alpha = 0, \frac{2\pi}{3}, \frac{4\pi}{3}$ the minima contain two sites with the same on-site potential. Therefore we consider the first order degenerate perturbation theory in t in the three different intervals around these values.

1) $\underline{\frac{\pi}{3} < \alpha < \pi}$: $|\psi_0\rangle \approx c_1^{(1)}|1\rangle + c_3^{(1)}|3\rangle$. Then we find

$$Q_B\left(\frac{\pi}{3} < \alpha < \pi\right) \approx -\frac{1}{9}\left(|c_1^{(1)}|^2 + 3|c_3^{(1)}|^2\right) + \frac{5}{9} \tag{7.17}$$

$$= -\frac{1}{9}\left(-|c_1^{(1)}|^2 + |c_3^{(1)}|^2\right) + \frac{3}{9}. \tag{7.18}$$

However, this formula is incorrect, because the hybridization between $|1\rangle$ and $|3\rangle$ is in $O(t)$ impossible, and we need to revise the above result.

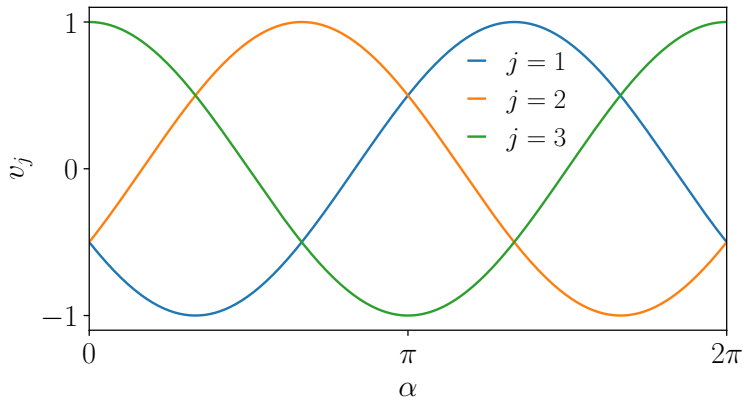

Figure 7.5: On-site potentials $v_j(\alpha) = \cos(\frac{2\pi}{3}j + \alpha)$ for $j = 1, 2, 3$.

Consider the two subintervals 1a) $\frac{\pi}{3} < \alpha < \frac{2\pi}{3}$; 1b) $\frac{2\pi}{3} < \alpha < \pi$:

1a) For $\frac{\pi}{3} < \alpha < \frac{2\pi}{3}$ the density is mostly located on $|1\rangle$, with a small admixture of $|0\rangle$, which replaces $|3\rangle$ in Eq. (7.18). Thus the correct expression reads

$$\begin{aligned} Q_B\left(\frac{\pi}{3} < \alpha < \frac{2\pi}{3}\right) &\approx -\frac{1}{9}\left(|c_1^{(1)}|^2 + 0|c_3^{(1)}|^2\right) + \frac{5}{9} \\ &\approx -\frac{1}{18}\left(|c_1^{(1)}|^2 - |c_3^{(1)}|^2\right) + \frac{1}{2}. \end{aligned} \tag{7.19}$$

1b) For $\frac{2\pi}{3} < \alpha < \pi$ the density is mostly located on $|3\rangle$, with a small admixture of $|4\rangle$, which replaces $|1\rangle$ in Eq. (7.18). Thus the correct expression reads

$$\begin{aligned} Q_B\left(\frac{2\pi}{3} < \alpha < \pi\right) &\approx -\frac{1}{9}\left(4|c_1^{(1)}|^2 + 3|c_3^{(1)}|^2\right) + \frac{5}{9} \\ &\approx -\frac{1}{18}\left(|c_1^{(1)}|^2 - |c_3^{(1)}|^2\right) + \frac{1}{6}. \end{aligned} \tag{7.20}$$

Comparing Eqs. (7.19) and (7.20) and taking into account that $|c_1^{(1)}|^2 - |c_3^{(1)}|^2$ is a continuous function of α (see below) vanishing at $\alpha = \frac{2\pi}{3}$, we observe that at this value of α the boundary charge value jumps from $\frac{1}{2}$ to $\frac{1}{6}$, such that the jump value is $\frac{1}{6} - \frac{1}{2} = -\frac{1}{3}$.

2) $\pi < \alpha < \frac{5\pi}{3}$: $|\psi_0\rangle \approx c_3^{(2)}|3\rangle + c_2^{(2)}|2\rangle$. This gives us

$$\begin{aligned} Q_B\left(\pi < \alpha < \frac{5\pi}{3}\right) &\approx -\frac{1}{9}\left(3|c_3^{(2)}|^2 + 2|c_2^{(2)}|^2\right) + \frac{5}{9} \\ &\approx -\frac{1}{18}\left(|c_3^{(2)}|^2 - |c_2^{(2)}|^2\right) + \frac{5}{18}. \end{aligned} \tag{7.21}$$

3) $-\frac{\pi}{3} < \alpha < \frac{\pi}{3}$: $|\psi_0\rangle \approx c_2^{(3)}|2\rangle + c_1^{(3)}|1\rangle$, leading to

$$\begin{aligned} Q_B\left(-\frac{\pi}{3} < \alpha < \frac{\pi}{3}\right) &\approx -\frac{1}{9}\left(2|c_2^{(3)}|^2 + |c_1^{(3)}|^2\right) + \frac{5}{9} \\ &\approx -\frac{1}{18}\left(|c_2^{(3)}|^2 - |c_1^{(3)}|^2\right) + \frac{7}{18}. \end{aligned} \tag{7.22}$$

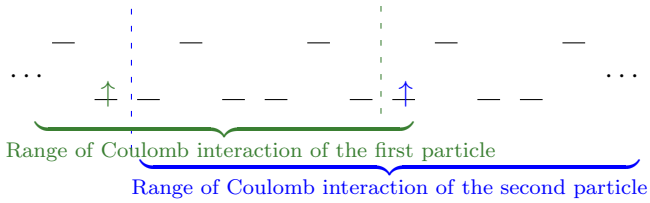

Figure 7.6: States that are ground states at $t = 0$ but can be neglected at $t \neq 0$. Two of the particles have only a distance of $(m-1)$ minima. The energy is higher than for the states where every mth minimum is occupied as the coupling of the green particle to the right and of the blue one to the left is much smaller in these cases.

The coefficients c_a and c_b are found from the eigenvalue problem

$$\begin{pmatrix} \frac{v_a - v_b}{2} & -t \\ -t & -\frac{v_a - v_b}{2} \end{pmatrix} \begin{pmatrix} c_a \\ c_b \end{pmatrix} = -\sqrt{\left(\frac{v_a - v_b}{2}\right)^2 + t^2} \begin{pmatrix} c_a \\ c_b \end{pmatrix} \tag{7.23}$$

and it follows

$$c_b = \left[\frac{v_a - v_b}{2} + \sqrt{\left(\frac{v_a - v_b}{2}\right)^2 + t^2}\right] \frac{c_a}{t}, \tag{7.24}$$

$$c_a^2 = \frac{t^2}{\left[\frac{v_a - v_b}{2} + \sqrt{\left(\frac{v_a - v_b}{2}\right)^2 + t^2}\right]^2 + t^2}, \tag{7.25}$$

$$c_a^2 - c_b^2 = \frac{t^2 - \left[\frac{v_a - v_b}{2} + \sqrt{\left(\frac{v_a - v_b}{2}\right)^2 + t^2}\right]^2}{\left[\frac{v_a - v_b}{2} + \sqrt{\left(\frac{v_a - v_b}{2}\right)^2 + t^2}\right]^2 + t^2} \tag{7.26}$$

$$= -(v_a - v_b) \frac{\frac{v_a - v_b}{2} + \sqrt{\left(\frac{v_a - v_b}{2}\right)^2 + t^2}}{\left[\frac{v_a - v_b}{2} + \sqrt{\left(\frac{v_a - v_b}{2}\right)^2 + t^2}\right]^2 + t^2}. \tag{7.27}$$

The results are shown in Fig. 7.7 for certain parameters, where we also compare them to DMRG data.

When we made the ansatz that we only need one particle in a cell of $Z_{\text{eff}} = 9$ sites, we assumed that there are always two empty minima between the particles due to the repulsive electron-electron interaction. However, it is possible to have configurations where there is only one empty minimum between two particles. Then, both particles need to be located on the outer site of their minimum as shown in Fig. 7.6. In this case they also do not 'see' each other's Coulomb interaction and it would be a ground state for $t = 0$. However, we do not need to consider them for the case with $t \neq 0$. Indeed, the neglected states are not coupled to the used ones in the orders that we look at. So there are no neglected couplings.

Additionally, all states that have a contribution of those new states should have a larger energy than the calculated ground state because the coupling to the adjacent site is much smaller for the configurations shown in Fig. 7.6 due to the Coulomb interaction. Therefore, these states cannot contribute to the ground state for $t \neq 0$.

Using this degenerate perturbation theory, we find some discontinuities at $\alpha = \frac{\pi}{3}, \pi, \frac{5\pi}{3}$ (see Fig. 7.7) because in the vicinity of these points, there are not two sites in the minimum. In the next section we will remove these discontinuities by treating the vicinities of these points in second order in t with a non-degenerate perturbation theory.

7.B.2 Vicinity of $\alpha = \frac{\pi}{3}, \pi, \frac{5\pi}{3}$

In the vicinity of these points we can use non-degenerate perturbation theory where, up to first order in the perturbation, the ground state is given by

$$|\Psi\rangle = |n\rangle + \sum_{m \neq n} \frac{V_{mn}}{E_n - E_m} |m\rangle \ . \tag{7.28}$$

Here, $|n\rangle$ denotes the ground state for $t = 0$, and V_{mn} are the matrix elements between the ground state and the excited states m, which are given by the hopping in our model.

In the given regions there is one site in each minimum of the on-site potential. We will call this site b, while the two adjacent sites will be called a and c. We then get

$$|\Psi_0\rangle = |b\rangle + \frac{t}{v_c - v_b} |c\rangle + \frac{t}{v_a - v_b} |a\rangle \tag{7.29}$$

for the ground state. Taking into account that this state is not normalized, we get

$$|c_b|^2 = 1 - \left(\frac{t}{v_a - v_b}\right)^2 - \left(\frac{t}{v_c - v_b}\right)^2 + \mathcal{O}\left(t^3\right) \ , \tag{7.30}$$

$$|c_a|^2 = \left(\frac{t}{v_a - v_b}\right)^2 + \mathcal{O}\left(t^3\right) , \tag{7.31}$$

$$|c_c|^2 = \left(\frac{t}{v_c - v_b}\right)^2 + \mathcal{O}\left(t^3\right) \ . \tag{7.32}$$

The boundary charge in the three different regions can then be calculated as follows:

$$\begin{aligned} Q_B\left(0 < \alpha < \frac{2\pi}{3}\right) &\approx -\frac{1}{9}\left(0|c_3^{(1)}|^2 + |c_1^{(1)}|^2 + 2|c_2^{(1)}|^2\right) + \frac{5}{9} \\ &\approx \left(-|c_3^{(1)}|^2 + |c_2^{(1)}|^2\right) + \frac{4}{9}, \end{aligned} \tag{7.33}$$

$$\begin{aligned} Q_B\left(\frac{4\pi}{3} < \alpha < 2\pi\right) &\approx -\frac{1}{9}\left(2|c_2^{(2)}|^2 + 3|c_3^{(2)}|^2 + 4|c_1^{(2)}|^2\right) + \frac{5}{9} \\ &\approx \left(-|c_2^{(2)}|^2 + |c_1^{(2)}|^2\right) + \frac{2}{9}, \end{aligned} \tag{7.34}$$

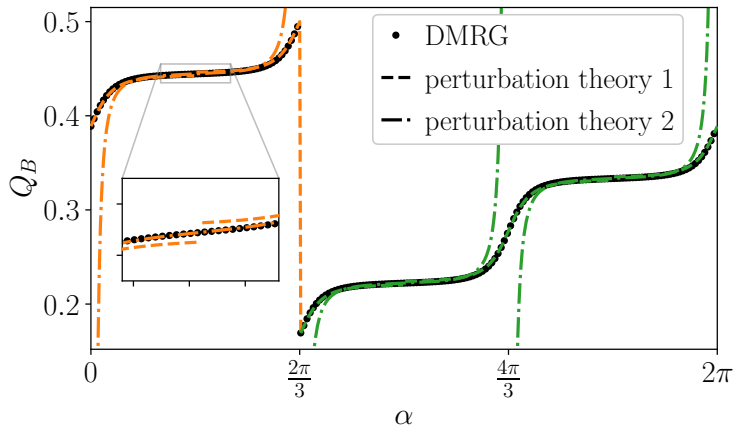

Figure 7.7: Boundary charge as a function of α for the effective model calculated with DMRG and perturbation theory. The other parameters are $m = 3$, $Z = 3$, $t = 1$, $v_{ex} = 5$ and $U_l = U = 10$ for $l = 1, ..., 6$. We used $N_s = 174$ and $L_p = 90$, $l_p = 90$ for the envelope function to get the DMRG results. The dashdotted line shows the results calculated in the vicinity of $\alpha = \frac{\pi}{3}, \pi, \frac{5\pi}{3}$, while the dashed line was calculated in the vicinity of $\alpha = 0, \frac{2\pi}{3}, \frac{4\pi}{3}$.

$$Q_B\left(\frac{2\pi}{3} < \alpha < \frac{4\pi}{3}\right) \approx -\frac{1}{9}\left(|c_1^{(3)}|^2 + 2|c_2^{(3)}|^2 + 3|c_3^{(3)}|^2\right) + \frac{5}{9}$$
$$\approx \left(-|c_1^{(3)}|^2 + |c_3^{(3)}|^2\right) + \frac{3}{9}\,. \tag{7.35}$$

We then insert

$$|c_c|^2 - |c_a|^2 \approx \left(\frac{t}{v_c - v_b}\right)^2 - \left(\frac{t}{v_a - v_b}\right)^2 \tag{7.36}$$

to get the final result that is shown in Fig. 7.7 together with the results of the first order perturbation theory calculated above.

7.B.3 Uniting the results

In the previous sections we calculated the behavior of the boundary charge in different regimes of α. To get a final expected curve, one needs to decide where to change between those regimes. Basically we have two different functions for the boundary charge. One should be valid around $\alpha = \pi/3, \pi, 5\pi/3$ and the other one around $\alpha = 0, 2\pi/3, 4\pi/3$. These two results are plotted in the whole interval of $[0, 2\pi]$ in Fig. 7.7.

As one can see, both results fit a certain part of the numerical curve quite well while there are other parts where they show useless behavior like jumps and divergences. Nevertheless they coincide very well in the intermediate regions between the regimes where they were calculated. To get one final analytical curve the method of calculation was changed at the points where both curves cross each other. The final result can be seen in Fig. 7.8. The numerical and analytical results lie nearly perfectly on top of each other. Fig. 7.8 corresponds to a zoom into Fig. 7.3, where we show all three ground states with their periodicity of 6π. There, we find a jump of unity for each of the ground states because a particle leaves the

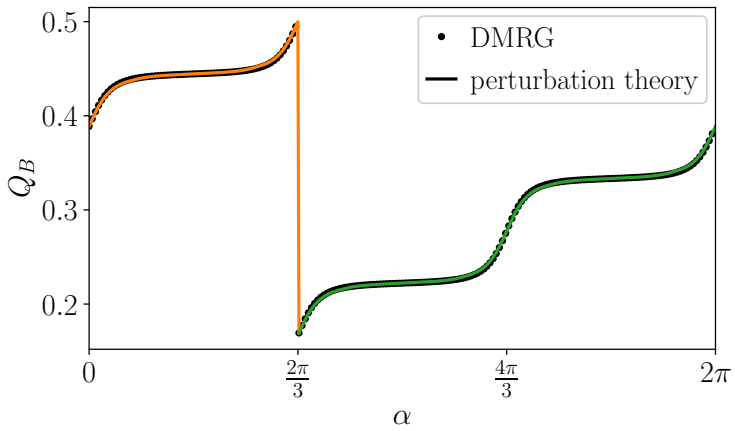

Figure 7.8: Boundary charge as a function of α for the effective model calculated with DMRG and perturbation theory. The other parameters are $m = 3$, $Z = 3$, $t = 1$, $v_{ex} = 5$ and $U_l = U = 10$ for $l = 1, ..., 6$. We used $N_s = 174$ and $L_p = 90$, $l_p = 90$ for the envelope function to get the DMRG results. The two curves of Fig. 7.7 are now combined to one final curve.

system at that point. In Fig. 7.8 we see only a jump by 1/3 because the system changes to another ground state as indicated by the colors. Thereby, all particles are shifted by one minimum to get into the new real ground state of our system. As already mentioned above, the other two ground states can be found by forcing other sites to have zero occupation. For the analytical calculation this means that sites $4, 5, 6$ or $7, 8, 9$ are occupied instead of sites $1, 2, 3$. The boundary charge is then changed by $-1/3$ or $-2/3$.

7.B.4 Limits of our perturbation theory

As we performed the perturbation theory in the regime $U \gg v_{ex} \gg t$, we expect it to fail when U and v_{ex} are not large enough. In Fig. 7.9 we calculate the boundary charge in dependence of α for different U and v_{ex} with constant $U/v_{ex} = 2$. For large values of U and v_{ex} the results coincide very well with our numerical DMRG results. For smaller values of U and v_{ex} the curves start to differ. When U and v_{ex} are of the order of t the perturbation theory does not even give us a smooth curve. For those parameters the results of the different regimes of α do not agree in the intermediate region and cannot be united in a satisfying way.

7.C Dependence on envelope function

In the thermodynamic limit the boundary charge needs to be independent of the details of the envelope function. However, the boundary charge can slightly depend on the envelope function for finite system sizes as shown in Fig. 7.10. To be as close as possible to the thermodynamic limit, we choose the envelope function with $L_p = \bar{N}_s/2$ and $l_p = \bar{N}_s/2$ (orange curve in Fig. 7.10) for our calculations, where $\bar{N}_s = N_s + 6$ denotes the system including the sites that we forced to be empty. With this choice already systems of relatively small size give us a value of $Q_B(2\pi) - Q_B\left(\frac{4\pi}{3}\right)$ that coincides with the one in the thermodynamic limit.

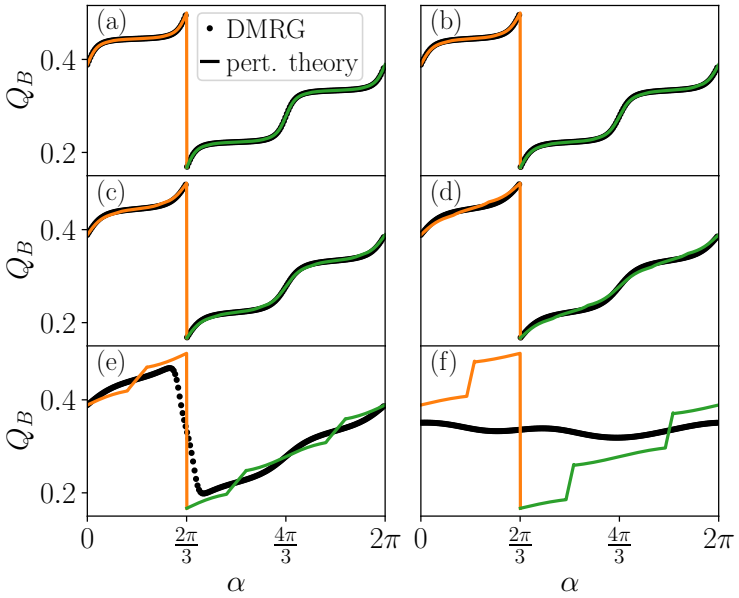

Figure 7.9: Results of DMRG and perturbation theory for $t = 1.0$ and $(v_{ex}, U) =$ (a) $(5.0, 10.0)$, (b) $(4.0, 8.0)$, (c) $(3.0, 6.0)$, (d) $(2.0, 4.0)$, (e) $(1.0, 2.0)$, (f) $(0.5, 1.0)$. The perturbation theory works quite well for large values of v_{ex} and U as expected, while there are clear drawbacks for smaller v_{ex} and U. The DMRG results are obtained with $N_s = 174$, $L_p = 90$, and $l_p = 90$.

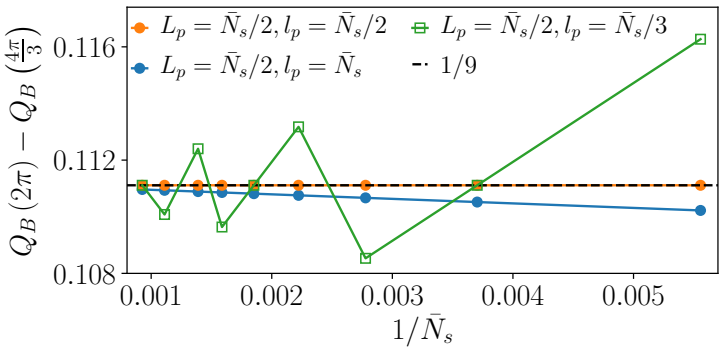

Figure 7.10: $Q_B(2\pi) - Q_B\left(\frac{4\pi}{3}\right)$ for different system sizes and different envelope functions. $\bar{N}_s = N_s + (m-1)Z = N_s + 6$ describes the system size including the blocked sites where the density is forced to be zero. For $\bar{N}_s \to \infty$ all curves tend to $1/9$. The other parameters are $t = 1$, $v_{ex} = 3$, and $U = 3$.

7.D Disorder

To prove that our results are stable against disorder, we investigate small random perturbations of the on-site potential and the hopping terms. Therefore, we study the boundary charge in dependence of the phase α averaged over different disorder configurations. The

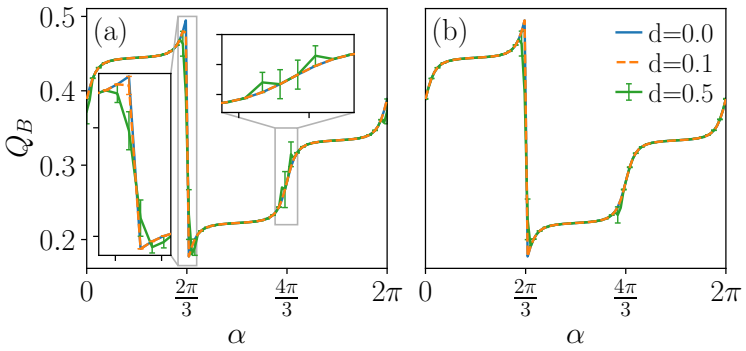

Figure 7.11: Boundary charge in dependence on α with included (a) hopping and (b) on-site disorder averaged over 20 disorder configurations. The error bars show the size of the uncertainty of the mean value for every second data point in the main panels and for all points in the insets. For $d = 0.1$ the error bars are only shown in the left inset as they are smaller than the line width in the other subplots. The other parameters are $m = 3$, $Z = 3$, $t = 1$, $v_{ex} = 5$, $U_l = U = 10$ for $l = 1, ..., 6$, $N_s = 174$, $L_p = 90$, and $l_p = 90$.

added terms are of the form

$$-\sum_{n=1}^{N_s-1} w_n(a_n^\dagger a_{n+1} + \text{H.c.}) \text{ and } \sum_{n=1}^{N_s} z_n \hat{\rho}_n \tag{7.37}$$

for hopping and on-site disorder, respectively. Either the parameter w_n or z_n is uniformly distributed in $[-d/2, d/2)$, while the other ones are set to zero. The results for a certain set of parameters and 20 disorder configurations are shown in Fig. 7.11. For small disorder strengths $d = 0.1$ the curve lies on top of the non-disordered one. The quantized slope is therefore stable against small perturbations. Even for stronger disorder $d = 0.5$ the average still coincides well with the results of the clean system although there are some differences visible. We see that the jump by $-1/3$ gets smoother because its exact position now depends on the disorder configuration. Therefore the standard deviation around the mean value of the disorder average is also larger in that region. At transitions between different plateaus, we also find an enhancement of the standard deviation, while within each plateau the standard deviation is small.

7.E Other long-ranged interactions

In the main text and in the previous sections we always considered a constant interaction $U_l = U$ which drops to zero after $l = (m-1)Z$ sites. Here, we will show that we find the same results for other long ranged interactions. Thereby, we will investigate a power law of the form $U_l = U_0\, l^{-6}$ (as experimentally realized in Ref. [74]) and a Yukawa potential of the form $U_l = U_0 \exp(-\gamma l)\, l^{-2}$. We approximate these long ranged interactions by using a sum of exponential functions ($\sum_{i=1}^{N} \alpha_i \beta_i^l$). The parameters are fitted by minimizing

$$\sum_{l=1}^{l_{\text{cutoff}}} \left(\ln\left(\sum_{i=1}^{N} \alpha_i \beta_i^l \right) - \ln\left(U_l\right) \right)^2 . \tag{7.38}$$

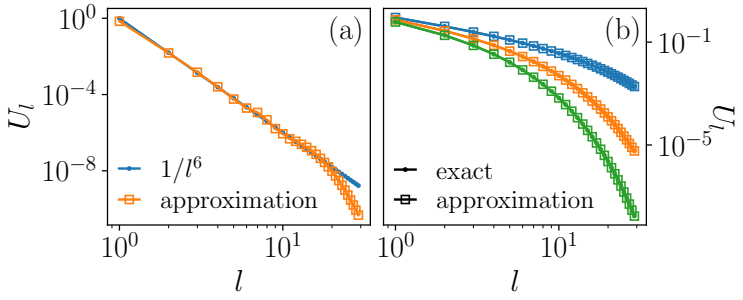

Figure 7.12: Approximated interaction profile compared to the exact functions (a) l^{-6} and (b) $\exp(-\gamma l)\, l^{-2}$ with $\gamma = 0.1$ (blue), 0.3 (orange), and 0.5 (green) on a double logarithmic scale. We use the prefactor (a) $U_0 = 1$ and (b) $U_0 = 2$, $N = 10$ and $l_{\text{cutoff}} = 20$ to determine the parameters of the exponential functions.

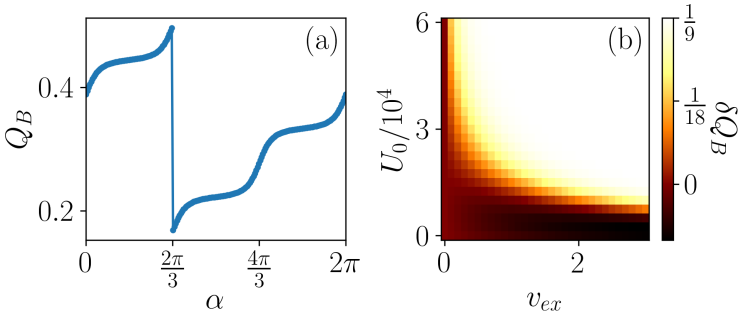

Figure 7.13: Results for an interaction of $U_l = U_0\, l^{-6}$ and $Z = m = 3$. (a) Boundary charge in dependence on the phase α with $U_0 = 60000$ and $v_{ex} = 3$. (b) False color plot of $\delta Q_B = Q_B\,(2\pi) - Q_B\left(\frac{4\pi}{3}\right)$ as a function of v_{ex} and U. The fractional slope is stabilized for large U_0 and intermediate v_{ex} (white region).

Using the logarithm ln corresponds to changing the weights of the different data points in the fitting procedure. This assures that the approximation works well even at larger ranges as we know that an interaction is needed on the first $Z(m-1)$ sites. For all functions we only fit the parameters once and rescale them with the prefactor U_0. We show the approximations compared to the exact functions in Fig. 7.12.

The results of the power law interaction are shown in Fig. 7.13 for $Z = m = 3$. With a sufficiently large U_0 and v_{ex} we find the fractional slope of $1/2\pi m$ up to a $2\pi/Z$-periodic function as shown in Fig. 7.13(a). In Fig. 7.13(b) a false color plot is shown, where the region with $\delta Q_B = 1/9$ (white) is where one finds the quantized fractional slope. We find a similar phase boundary compared to the case discussed in the main text. The phase transition occurs at a large prefactor U_0 due to the rapid decay of the power law function.

In Fig. 7.14 we show false color plots for the Yukawa potential at different values of the screening γ. Again, we see a phase transition similar to the cases discussed so far. For larger γ, the phase boundary is situated at larger U_0 because the Yukawa potential decays faster.

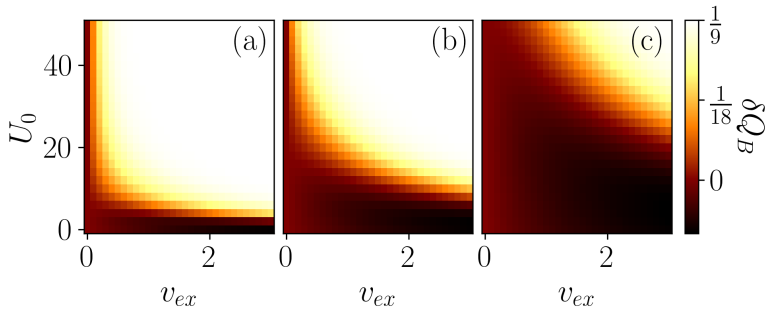

Figure 7.14: False color plots showing $\delta Q_B = Q_B\,(2\pi) - Q_B\left(\frac{4\pi}{3}\right)$ for an interaction of $U_l = U_0\,\exp(-\gamma l)\,l^{-2}$ with (a) $\gamma = 0.1$, (b) $\gamma = 0.3$, and (c) $\gamma = 0.5$. The other parameters are $Z = m = 3$. The phase transition is located at larger U_0 for larger values of γ.

7.F Interface between two CDWs

In this section, we show how the analytical arguments presented in the main text can be extended to describe the charge located at the interface between two CDWs in a 1D nanowire.

We consider an interface between two CDWs described by a spatially modulated potential of the form

$$V_m(x) = \begin{cases} 2V_m \cos(2mk_F x + \alpha_<), & x < 0, \\ 2V_m \cos(2mk_F x + \alpha_>), & x > 0, \end{cases} \tag{7.39}$$

where $\alpha_<$ ($\alpha_>$) describes the phase offset of the CDW in the domain $x < 0$ ($x > 0$). We can now follow the same arguments as in the main text for $x \in (-\infty, 0)$ and $x \in (0, +\infty)$ separately. In terms of the conjugate bosonic fields ϕ and θ, the CDW term then takes the form $H^m_{CDW} = \int dx\, \mathcal{H}^m_{CDW}(x)$ with

$$\mathcal{H}^m_{CDW}(x) = \begin{cases} \frac{-2|\tilde{V}_m|}{(2\pi a)^m} \cos(2m\phi(x) + \alpha_< - \alpha_0), & x < 0, \\ \frac{-2|V_m|}{(2\pi a)^m} \cos(2m\phi(x) + \alpha_> - \alpha_0), & x > 0, \end{cases} \tag{7.40}$$

where α_0 is again an irrelevant overall phase shift. The CDW term is minimized for the pinning values

$$\phi(x) = \begin{cases} -(\alpha_< - \alpha_0)/2m + l\pi/m, & x < 0, \\ -(\alpha_> - \alpha_0)/2m + n\pi/m, & x > 0, \end{cases} \tag{7.41}$$

where l and n are integers. Therefore, the charge located at the interface is given by

$$\begin{aligned} Q_D &= -\int_{-\infty}^{+\infty} dx\, \frac{\partial_x \phi(x)}{\pi} \\ &= -\frac{1}{\pi}[\phi(+\infty) - \phi(-\infty)] \\ &= (l - n)/m + (\alpha_> - \alpha_<)/2\pi m \mod 1. \end{aligned} \tag{7.42}$$

We thus find that the fractional charge changes linearly with the phase difference $\alpha_> - \alpha_<$ with a slope of $1/2\pi m$.

Finally, we note that analogous considerations allow us to recover the fractional charge of the excitations in the 2D case. Indeed, a bulk excitation in the 2D FQHE corresponds to a kink (domain wall) in the pinned combination of the fields $\eta_{1(n+1)} - \eta_{\bar{1}n}$ for a given n, see Eq. (7.8), while the uniform phase φ drops out. By using $\sum_n(\eta_{1(n+1)} - \eta_{\bar{1}n}) = -2(2l + 1)\sum_n \phi_n$ and using that the charge density of a single wire is given by $\rho_n = -\partial_x\phi_n(x)/\pi$ in units of the electron charge e, we find that a kink between two adjacent minima of the cosine carries the charge $e/(2l + 1)$.

Bibliography

[1] F. D. M. Haldane, Phys. Rev. Lett. **51**, 605 (1983).

[2] B. I. Halperin, Phys. Rev. Lett. **52**, 1583 (1984).

[3] R. Willett, J. P. Eisenstein, H. L. Störmer, D. C. Tsui, A. C. Gossard, and J. H. English, Phys. Rev. Lett. **59**, 1776 (1987).

[4] G. Moore and N. Read, Nucl. Phys. B **360**, 362 (1991).

[5] R. Jackiw and C. Rebbi, Phys. Rev. D **13**, 3398 (1976).

[6] R. Jackiw and J. Schrieffer, Nucl. Phys. B **190**, 253 (1981).

[7] W. P. Su, J. R. Schrieffer, and A. J. Heeger, Phys. Rev. Lett. **42**, 1698 (1979).

[8] W. P. Su and J. R. Schrieffer, Phys. Rev. Lett. **46**, 738 (1981).

[9] D. Vanderbilt and R. D. King-Smith, Phys. Rev. B **48**, 4442 (1993).

[10] D. Vanderbilt, *Berry Phases in Electronic Structure Theory: Electric Polarization, Orbital Magnetization and Topological Insulators* (Cambridge University Press, Cambridge, UK, 2018).

[11] R. Resta, Europhys. Lett. **22**, 133 (1993).

[12] R. Resta, Rev. Mod. Phys. **66**, 899 (1994).

[13] G. Ortiz and R. M. Martin, Phys. Rev. B **49**, 14202 (1994).

[14] J.-W. Rhim, J. Behrends, and J. H. Bardarson, Phys. Rev. B **95**, 035421 (2017).

[15] M. Pletyukhov, D. M. Kennes, J. Klinovaja, D. Loss, and H. Schoeller, Phys. Rev. B **101**, 165304 (2020).

[16] M. J. Rice and E. J. Mele, Phys. Rev. Lett. **49**, 1455 (1982).

[17] A. J. Heeger, S. Kivelson, J. R. Schrieffer, and W. P. Su, Rev. Mod. Phys. **60**, 781 (1988).

[18] S. Kivelson, Phys. Rev. B **28**, 2653 (1983).

[19] R. Jackiw and G. Semenoff, Phys. Rev. Lett. **50**, 439 (1983).

[20] X.-L. Qi, T. L. Hughes, and S.-C. Zhang, Nat. Phys. **4**, 273 (2008).

[21] J. I. Väyrynen and T. Ojanen, Phys. Rev. Lett. **107**, 166804 (2011).

[22] J. Klinovaja, P. Stano, and D. Loss, Phys. Rev. Lett. **109**, 236801 (2012).

[23] J. Klinovaja and D. Loss, Phys. Rev. Lett. **110**, 126402 (2013).

[24] D. Rainis, A. Saha, J. Klinovaja, L. Trifunovic, and D. Loss, Phys. Rev. Lett. **112**, 196803 (2014).

[25] D. Sticlet, L. Seabra, F. Pollmann, and J. Cayssol, Phys. Rev. B **89**, 115430 (2014).

[26] R. Wakatsuki, M. Ezawa, Y. Tanaka, and N. Nagaosa, Phys. Rev. B **90**, 014505 (2014).

[27] J. Klinovaja and D. Loss, Phys. Rev. B **92**, 121410(R) (2015).

[28] J.-H. Park, G. Yang, J. Klinovaja, P. Stano, and D. Loss Phys. Rev. B **94**, 075416 (2016).

[29] C. Fleckenstein, N. Traverso Ziani, and B. Trauzettel, Phys. Rev. B **94**, 241406(R) (2016).

[30] A. Camjayi, L. Arrachea, A. Aligia, and F. von Oppen, Phys. Rev. Lett. **119**, 046801 (2017).

[31] M. Thakurathi, J. Klinovaja, and D. Loss, Phys. Rev. B **98**, 245404 (2018).

[32] Y. H. Jeong, S.-R. Eric Yang, and M.-C. Cha, J. Phys.: Condens. Matter **31**, 265601 (2019).

[33] S. Jana, A. Saha, and S. Das, Phys. Rev. B **100**, 085428 (2019).

[34] M. Pletyukhov, D. M. Kennes, J. Klinovaja, D. Loss, and H. Schoeller, Phys. Rev. B **101**, 161106(R) (2020).

[35] M. Pletyukhov, D. M. Kennes, K. Piasotski, J. Klinovaja, D. Loss, and H. Schoeller, Phys. Rev. Research **2**, 033345 (2020).

[36] Y.-T. Lin, D. M. Kennes, M. Pletyukhov, C. S. Weber, H. Schoeller, and V. Meden, Phys. Rev. B **102**, 085122 (2020).

[37] S.-R. Eric Yang, M.-C. Cha, H. J. Lee, and Y. H. Kim, Phys. Rev. Research **2**, 033109 (2020).

[38] C. S. Weber, K. Piasotski, M. Pletyukhov, J. Klinovaja, D. Loss, H. Schoeller, and D. M. Kennes, Phys. Rev. Lett. **126**, 016803 (2021).

[39] Y.-T. Lin, C. S. Weber, D. M. Kennes, M. Pletyukhov, H. Schoeller, and V. Meden, Phys. Rev. B **103**, 195119 (2021).

[40] T. L. Hughes, E. Prodan, and B. A. Bernevig, Phys. Rev. B **83**, 245132 (2011).

[41] A. Lau, J. van den Brink, and C. Ortix, Phys. Rev. B **94**, 165164 (2016).

[42] A. Alexandradinata, Z. Wang, and B. A. Bernevig, Phys. Rev. X **6**, 021008 (2016).

[43] G. van Miert and C. Ortix, Phys. Rev. B **96**, 235130 (2017).

[44] A. Lau and C. Ortix, Eur. Phys. J. Spec. Top. **227**, 1309 (2018).

[45] W. A. Benalcazar, B. A. Bernevig, and T. L. Hughes, Science **357**, 61 (2017).

[46] W. A. Benalcazar, B. A. Bernevig, and T. L. Hughes, Phys. Rev. B **96**, 245115 (2017).

[47] G. van Miert and C. Ortix, Phys. Rev. B **98**, 081110(R) (2018).

[48] W. A. Benalcazar, T. Li, and T. L. Hughes, Phys. Rev. B **99**, 245151 (2019).

[49] C. W. Peterson, T. Li, W. A. Benalcazar, T. L. Hughes, and G. Bahl, Science **368**, 1114 (2020).

[50] H. Watanabe and S. Ono, Phys. Rev. B **102**, 165120 (2020).

[51] T. Hirosawa, S. A. Díaz, J. Klinovaja, and D. Loss, Phys. Rev. Lett. **125**, 207204 (2020).

[52] R. Takahashi, T. Zhang, and S. Murakami, Phys. Rev. B **103**, 205123 (2021).

[53] S. Gangadharaiah, L. Trifunovic, and D. Loss, Phys. Rev. Lett. **108**, 136803 (2012).

[54] T. Giamarchi, *Quantum Physics in One Dimension* (Oxford University Press, Oxford, 2004).

[55] Y. Oreg, E. Sela, and A. Stern, Phys. Rev. B **89**, 115402 (2014).

[56] J. Klinovaja and D. Loss, Phys. Rev. B **90**, 045118 (2014).

[57] J. Klinovaja and D. Loss, Phys. Rev. Lett. **112**, 246403 (2014).

[58] C. L. Kane, R. Mukhopadhyay, and T. C. Lubensky, Phys. Rev. Lett. **88**, 036401 (2002).

[59] J. C. Y. Teo and C. L. Kane, Phys. Rev. B **89**, 085101 (2014).

[60] D. Poilblanc, G. Montambaux, M. Héritier, and P. Lederer, Phys. Rev. Lett. **58**, 270 (1987).

[61] L. P. Gorkov and A. G. Lebed, Phys. Rev. B **51**, 3285 (1995).

[62] J. K. Jain, *Composite Fermions* (Cambridge University Press, Cambridge, 2007).

[63] B. I. Halperin, Phys. Rev. B **25**, 2185 (1982).

[64] D. A. Syphers, K. P. Martin, and R. J. Higgins, Appl. Phys. Lett. **48**, 293 (1986).

[65] P. F. Fontein, J. M. Lagemaat, J. Wolter, and J. P. André, Semicond. Sci. Technol. **3**, 915 (1988).

[66] V. T. Dolgopolov, A. A. Shashkin, N. B. Zhitenev, S. I. Dorozhkin, and K. von Klitzing, Phys. Rev. B **46**, 12560 (1992).

[67] M. J. Zhu, A. V. Kretinin, M. D. Thompson, D. A. Bandurin, S. Hu, G. L. Yu, J. Birkbeck, A. Mishchenko, I. J. Vera-Marun, K. Watanabe, T. Taniguchi, M. Polini, J. R. Prance, K. S. Novoselov, A. K. Geim, and M. Ben Shalom, Nat. Commun. **8**, 14552 (2017).

[68] B. A. Schmidt, K. Bennaceur, S. Gaucher, G. Gervais, L. N. Pfeiffer, and K. W. West, Phys. Rev. B **95**, 201306(R) (2017).

[69] M. J. Yoo, T. A. Fulton, H. F. Hess, R. L. Willett, L. N. Dunkleberger, R. J. Chichester, L. N. Pfeiffer, and K. W. West, Science **276**, 579 (1997).

[70] S. H. Tessmer, P. I. Glicofridis, R. C. Ashoori, L. S. Levitov, and M. R. Melloch, Nature (London) **392**, 51 (1998).

[71] G. Finkelstein, P. I. Glicofridis, R. C. Ashoori, and M. Shayegan, Science **289**, 90 (2000).

[72] G. Ben-Shach, A. Haim, I. Appelbaum, Y. Oreg, A. Yacoby, and B. I. Halperin, Phys. Rev. B **91**, 045403 (2015).

[73] M. Xiao, G. Ma, Z. Yang, P. Sheng, Z. Q. Zhang, and C. T. Chan, Nat. Phys. **11**, 240 (2015).

[74] H. Bernien, S. Schwartz, A. Keesling, H. Levine, A. Omran, H. Pichler, S. Choi, A. S. Zibrov, M. Endres, M. Greiner, V. Vuletić, M. D. Lukin, Nature **551**, 579 (2017).

Chapter 8

RKKY interaction at helical edges of topological superconductors

Adapted from:
K. Laubscher, D. Miserev, V. Kaladzhyan, D. Loss, and J. Klinovaja,
"RKKY interaction at helical edges of topological superconductors,"
arXiv preprint arXiv:2203.08137 (2022)

We study spin configurations of classical magnetic impurities placed close to the edge of a two-dimensional topological superconductor both analytically and numerically. First, we demonstrate that the spin of a single magnetic impurity close to the edge of a topological superconductor tends to align along the edge. The strong easy-axis spin anisotropy behind this effect originates from the interaction between the impurity and the gapless helical Majorana edge states. We then compute the Ruderman-Kittel-Kasuya-Yosida (RKKY) interaction between two magnetic impurities placed close to the edge. We show that, in the limit of large interimpurity distances, the RKKY interaction between the two impurities is mainly mediated by the Majorana edge states and leads to a ferromagnetic alignment of both spins along the edge. This effect can be used to detect helical Majorana edge states.

8.1 Introduction

Two magnetic impurities placed on a host material can effectively interact by coupling to the electron spin density of the host. This so-called Ruderman-Kittel-Kasuya-Yosida (RKKY) interaction [1–3] is crucial in determining the magnetic ordering of the impurities and has recently come into focus due to its key role in designing magnetic-impurity-based *ad hoc* topological superconductors (TSCs) hosting Majorana zero modes [4–43]. The exact form of the RKKY interaction depends on the properties of the underlying host material and has been extensively studied for various bulk systems [44–71]. Generally, the RKKY interaction in metals decays as a power law with an oscillatory prefactor, while it is exponentially suppressed in insulators and superconductors.

More recently, it was realized that the presence of boundaries can lead to interesting modifications to the RKKY interaction. Such boundary effects were studied, for example, in topologically trivial s- and d-wave superconductors [72, 73]. Furthermore, since boundary effects are expected to be particularly interesting in topological materials, several works have studied magnetic impurities coupled to edge or surface states of topological insulators (TIs) [74–87]. For TSCs, on the other hand, only a few studies focusing on quantum spins coupled to 1D Majorana edge states exist [88–90]. So far, these rely on effective 1D models for the edge states without explicitly describing the full 2D TSC and its boundary.

In this work, we extend and deepen the understanding of RKKY effects in topological materials by studying classical magnetic impurities close to the edge of a 2D p-wave TSC with helical Majorana edge states, see Fig. 8.1. Here, we carefully model the full 2D system, allowing us to describe not only the behavior close to the edge but also the crossover to the bulk regime at distances from the edge larger than the edge state localization length. Our main findings for impurities close to the edge can be summarized as follows. First, we find that the spin of a single magnetic impurity tends to align along the edge due to a strong easy-axis anisotropy (EAA) imposed by the symmetries of the TSC Hamiltonian. Second, two magnetic impurities separated by large distances along the edge interact mainly through the Majorana edge states. The corresponding RKKY interaction is of the Ising type, decays inversely proportional to the interimpurity distance, and results in a ferromagnetic alignment of the impurity spins along the edge. All of these results are derived analytically

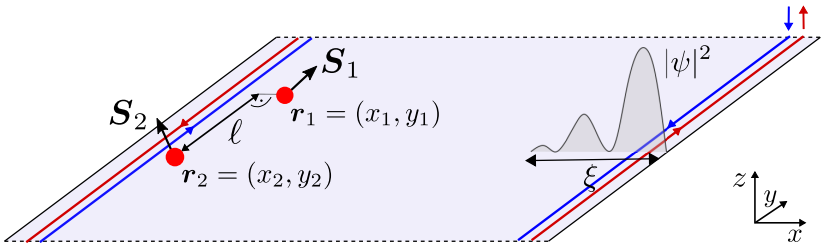

Figure 8.1: A 2D p-wave TSC hosts helical Majorana edge states shown in red (spin up) and blue (spin down). Their wave functions $|\psi|^2$ decay exponentially into the bulk on the scale of the superconducting coherence length ξ. Two magnetic impurities (red dots) with spins $\boldsymbol{S}_1$ and $\boldsymbol{S}_2$ (black arrows) are placed in the vicinity of the edge. Their separation along the direction of the edge is denoted by ℓ.

using a continuum model and independently verified by numerical exact diagonalization of the corresponding tight-binding model.

The above features stand in stark contrast to what is observed in a trivial superconductor without edge states, where the single-impurity EAA term is absent and the RKKY coupling is exponentially suppressed with the interimpurity distance even for impurities close to the edge. Therefore, we believe that spectroscopy of magnetic impurities [36,38,91–101] can serve as a powerful tool to experimentally probe TSCs and systems with topological edge states in general.

8.2 Model

We consider a 2D helical p-wave superconductor [102] described by the mean-field Hamiltonian

$$\mathcal{H} = \frac{k^2 - k_F^2}{2m}\tau_z + \alpha\tau_x\left(\sigma_x k_y - \sigma_y k_x\right) \tag{8.1}$$

written in the Nambu basis $(\psi_{\boldsymbol{k},\uparrow}, \psi_{\boldsymbol{k},\downarrow}, \psi^\dagger_{-\boldsymbol{k},\downarrow}, -\psi^\dagger_{-\boldsymbol{k},\uparrow})$, where $\psi^{(\dagger)}_{\boldsymbol{k},\sigma}$ is the electron annihilation (creation) operator with spin $\sigma \in \{\uparrow,\downarrow\}$ and in-plane momentum $\boldsymbol{k} = (k_x, k_y)$, k_F the Fermi momentum, $k^2 = k_x^2 + k_y^2$, m the effective mass, $\boldsymbol{\sigma}$ ($\boldsymbol{\tau}$) the Pauli matrices acting on the spin (particle-hole) degree of freedom, and $\alpha > 0$ the TSC coupling constant responsible for opening the superconducting gap [1]. We set $\hbar = 1$ throughout this work. The bulk spectrum of $\mathcal{H}$ is fully gapped:

$$\varepsilon_\pm(\boldsymbol{k}) = \pm\sqrt{\left(\frac{k^2 - k_F^2}{2m} + m\alpha^2\right)^2 + \Delta^2}, \tag{8.2}$$

where $\Delta = \alpha\sqrt{k_F^2 - (m\alpha)^2} \approx \alpha k_F$ is the bulk superconducting gap. We work in the regime when $\Delta \ll \varepsilon_F := k_F^2/(2m)$, so $k_F \gg m\alpha$.

As the mean-field Hamiltonian given in Eq. (8.1) is rotationally invariant, all edges are equivalent. In the following, we focus on the straight edge at $x = 0$, such that the TSC occupies the half-space $x > 0$. With the boundary at $x = 0$, the system is still translationally invariant along the y axis, so the momentum k_y is a good quantum number. Moreover, $\mathcal{H}$ commutes with $\sigma_z\tau_z$, which allows for the following choice of eigenstates:

$$\Psi_{\eta,k_y,n}(x,y) = e^{ik_y y}\Psi_{\eta,k_y,n}(x), \tag{8.3}$$

where $\eta = \pm 1$ denotes the eigenvalue of $\sigma_z\tau_z$ [i.e., $\sigma_z\tau_z\Psi_{\eta,k_y,n}(x) = \eta\Psi_{\eta,k_y,n}(x)$], k_y is the momentum along the y axis, and n labels all other quantum numbers in the system. The boundary at $x = 0$ obliges all quantum states to satisfy the boundary condition $\Psi_{\eta,k_y,n}(x = 0) = 0$.

The topologically nontrivial nature of the TSC is reflected in the presence of Majorana edge states, see Fig. 8.1. Their wave functions can be found analytically as

$$\Psi_{\eta,k_y}(x) = \sqrt{\frac{2}{\xi}\left(k_F^2 - k_y^2\right)}\frac{\sin(\kappa x)}{\kappa}e^{-\frac{x}{\xi}}\begin{pmatrix} u_\eta \\ -\eta u_{-\eta}\end{pmatrix}, \tag{8.4}$$

[1] The case $\alpha < 0$ is connected to $\alpha > 0$ through the unitary transformation $H(-\alpha) = \sigma_z H(\alpha)\sigma_z$. This unitary transformation does not affect any of the presented results.

where we have defined $\kappa = \sqrt{k_F^2 - (m\alpha)^2 - k_y^2}$, $u_+^T = (1,0)$, $u_-^T = (0,1)$, and where the localization length $\xi = 1/(m\alpha) \approx v_F/\Delta$ defines the effective width of the edge states. The above edge state wave functions are normalizable for all $k_y \in (-k_F, k_F)$. The corresponding eigenenergies are given by $\varepsilon_{\eta,k_y} = -\eta\alpha k_y$.

In the following, we place magnetic impurities in the vicinity of the TSC edge. The impurity spins interact with the itinerant electrons via the local exchange interaction

$$\mathcal{H}_{\text{imp}} = J \sum_i \boldsymbol{\sigma} \cdot \boldsymbol{S}_i \, \delta(\boldsymbol{r} - \boldsymbol{r}_i), \tag{8.5}$$

where $\boldsymbol{S}_i$ is the spin of the magnetic impurity placed at the position $\boldsymbol{r}_i = (x_i, y_i)$ with $x_i > 0$. The impurity spins are considered large, $S_i \gg 1$, which allows us to treat them as classical vectors. This regime is expected to be relevant, e.g., for transition metal adatoms with spins $S \geq 3/2$ [36–38,94–97,103–108], where quantum effects are expected to be small and theoretical predictions based on classical spins have reasonably explained experimental findings in the past. In particular, the classical approximation allows us to neglect the Kondo effect since the Kondo temperature becomes exponentially small for $S \gg 1$. Additionally, the exchange coupling constant J is assumed to be small compared to the electron bandwidth, $JSm \ll 1$, so we can neglect the renormalization of the superconducting order parameter [109–115] close to the impurity.

8.3 Single magnetic impurity

First, we consider a single magnetic impurity placed at the position $\boldsymbol{r}_0$. Since we work in the limit of weak exchange interaction, the impurity-induced correction to the total energy can be obtained perturbatively. The first-order correction vanishes in time-reversal invariant systems as there is no intrinsic magnetization in the system. The second-order correction comes from the local magnetization induced by the impurity itself:

$$E_{\text{imp}} = \frac{J^2}{2} \int_{-\infty}^{\infty} \frac{d\omega}{2\pi} \text{Tr} \left\{ \left[\boldsymbol{\sigma} \cdot \boldsymbol{S} \, G(\boldsymbol{r}_0, \boldsymbol{r}_0, i\omega) \right]^2 \right\}. \tag{8.6}$$

Here, $G(\boldsymbol{r}, \boldsymbol{r}', i\omega)$ is the Matsubara Green function of the TSC without impurities:

$$G(\boldsymbol{r}, \boldsymbol{r}', i\omega) = \sum_{\eta,k_y,n} \frac{\Psi_{\eta,k_y,n}(x) \Psi^\dagger_{\eta,k_y,n}(x') e^{ik_y(y-y')}}{i\omega - \varepsilon_{\eta,k_y,n}}, \tag{8.7}$$

where $\varepsilon_{\eta,k_y,n}$ is the eigenenergy of the state $\Psi_{\eta,k_y,n}(x)$ [see Eq. (8.3)].

The Hamiltonian $\mathcal{H}$ given in Eq. (8.1) with our choice of boundary conditions is time-reversal symmetric, particle-hole symmetric, and invariant under inversion of the y axis. Using these symmetries, one can show that $G(\boldsymbol{r}_0, \boldsymbol{r}_0, i\omega) \equiv G(x_0, i\omega)$ has the matrix decomposition

$$G(x_0, i\omega) = iA_1(x_0, i\omega) + A_2(x_0, i\omega)\tau_z + iB(x_0, i\omega)\sigma_y\tau_y, \tag{8.8}$$

where $A_1(x, i\omega)$ and $B(x, i\omega)$ [$A_2(x, i\omega)$] are real-valued odd [even] functions of ω. Evaluating the spin trace in Eq. (8.6) using the matrix decomposition Eq. (8.8), we find that $A_{1,2}(x, i\omega)$

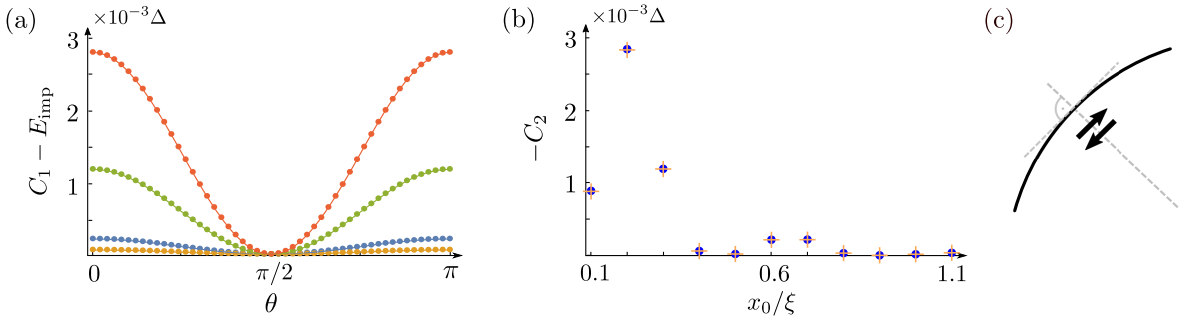

Figure 8.2: (a) The impurity-induced contribution $C_1 - E_{\mathrm{imp}}$ as a function of the polar angle θ for a single magnetic impurity at a distance $x_0 = 0.2\,\xi$ (red), $x_0 = 0.3\,\xi$ (green), $x_0 = 0.4\,\xi$ (orange), and $x_0 = 0.6\,\xi$ (blue) from the edge. The dots represent numerical data obtained via exact numerical diagonalization of a discretized 2D model (see App. 8.A for details) and the solid line is a fit $\propto \cos^2\theta$. We find that the total energy is minimized if the impurity spin is aligned along the edge, i.e., for $\theta = 0$ and $\theta = \pi$. (b) Dependence of C_2 on the distance from the edge obtained via exact numerical diagonalization of a 2D system (blue circles) and via numerical evaluation of Eq. (8.10) in a ribbon geometry (orange crosses). The two curves coincide very well and show that C_2 decays exponentially with the distance from the edge on the scale of the edge state localization length ξ. Furthermore, C_2 exhibits oscillations with a period of π/k_F. (c) While we focused on a straight edge for simplicity, our results can easily be generalized to more complicated edge geometries. In this case, the impurity spin prefers to align tangentially to the edge as is indicated by the black arrows. The parameters used in panels (a) and (b) are $\Delta/\varepsilon_F = 0.28$ and $JSm = 0.1$.

give fully isotropic contributions, while $B(x, i\omega)$ additionally results in an anisotropic term:

$$E_{\mathrm{imp}} = -(2JS_y)^2 \int_{-\infty}^{\infty} \frac{d\omega}{2\pi} B^2(x_0, i\omega) + C_1, \tag{8.9}$$

where $C_1 \propto S^2$ is the isotropic contribution. From the matrix decomposition Eq. (8.8), we further find that $B(x_0, i\omega)$ can be represented as follows:

$$B(x_0, i\omega) = -\frac{\omega}{2} \sum_{\eta,k_y,n}^{\varepsilon>0} \frac{\Psi^\dagger_{\eta,k_y,n}(x_0)\sigma_y\tau_y\Psi_{\eta,k_y,n}(x_0)}{\omega^2 + \varepsilon^2_{\eta,k_y,n}}, \tag{8.10}$$

where the $\Psi_{\eta,k_y,n}(x)$ enlist all eigenstates of $\mathcal{H}$. The upper limit $\varepsilon > 0$ indicates that only the quantum states with positive energies $\varepsilon_{\eta,k_y,n} > 0$ are taken into account.

From the above, we can already infer the most important features of the single-impurity problem. First, from Eq. (8.9), we see that the symmetries of the Hamiltonian allow for an EAA term that is proportional to S_y^2. Second, as $B(x_0, i\omega)$ given in Eq. (8.10) is a real-valued function, this EAA term is always negative and therefore aligns the spin of a single magnetic impurity along the edge of the TSC. Third, it is important to mention that $B(x_0, i\omega)$ decays into the bulk, i.e., $B(x_0 \to +\infty, i\omega) = 0$. This is due to the invariance under inversion of the x axis deep in the bulk, which forces $B(x_0, i\omega)$ to vanish for $x_0 \to +\infty$. As such, the EAA is only significant close to the TSC edge at $x_0 \lesssim \xi$.

We now proceed by studying a discretized version of $\mathcal{H} + \mathcal{H}_{\text{imp}}$ via numerical exact diagonalization, see App. 8.A for details. The (classical) impurity spin is parametrized as $\boldsymbol{S} = S\,(\sin\theta\sin\phi, \cos\theta, \sin\theta\cos\phi)$ with $\theta \in [0, \pi]$ and $\phi \in [0, 2\pi)$ being the polar and azimuthal angles with respect to the y axis, respectively. The ground state energy of the system can be expressed as

$$E_{\text{tot}} = E_0 + E_{\text{imp}}, \tag{8.11}$$

where E_0 is the energy of the clean system (i.e., in the absence of the magnetic impurity) and E_{imp} embodies the impurity-induced contribution. We calculate these energies by exact numerical diagonalization and display our results in Fig. 8.2. In Fig. 8.2(a), we plot the part of E_{imp} that varies as a function of θ for different distances from the edge, while we have verified that E_{imp} is independent of ϕ. We find that the impurity-induced contribution takes the form

$$E_{\text{imp}}(\theta) = C_1 + C_2 \cos^2\theta, \tag{8.12}$$

with an isotropic energy shift C_1 and an anisotropic contribution C_2 depending on the orientation of the impurity spin. Figure 8.2(b) displays $C_2 = E_{\text{imp}}(0) - E_{\text{imp}}(\pi/2)$ in dependence on the distance from the edge. We find that C_2 is always negative, meaning that the impurity spin is favored to align along the edge. Furthermore, C_2 decays exponentially with the distance from the edge on a characteristic length scale ξ and vanishes deep in the bulk of the system. All of these features are fully consistent with the analytical result presented in Eqs. (8.9) and (8.10).

To make an explicit connection to the analytical result, we also evaluate Eq. (8.10) by plugging in the numerically obtained energies and wave functions of a discretized semi-infinite system with a finite width along the x direction and k_y as a good quantum number. By identifying $S_y = S\cos\theta$, the value of C_2 can readily be obtained from Eq. (8.9), see again Fig. 8.2(b). This does indeed perfectly reproduce the result obtained via full exact diagonalization of the finite 2D system. The dependence of C_2 on the exchange coupling constant J is analyzed numerically in App. 8.D, where we confirm $C_2 \propto J^2$ at $J \lesssim 1/(mS)$ as expected from perturbation theory. Contrary to that, in the strong coupling regime $J \gg 1/(mS)$, the dependence on J is no longer quadratic.

Last but not least, we note that our findings can be generalized to more complicated edge geometries. In this case, the single-impurity EAA term takes a more general form such that the energetically preferred configuration has the impurity spin aligned tangentially to the edge, see Fig. 8.2(c).

8.4 RKKY interaction

We now analyze the interaction between two magnetic impurities through the exchange of a particle-hole pair:

$$E_{\text{RKKY}} = J^2 \int_{-\infty}^{\infty} \frac{d\omega}{2\pi} \text{Tr}\{\boldsymbol{\sigma}\cdot\boldsymbol{S}_1 G(\boldsymbol{r}_1, \boldsymbol{r}_2, i\omega)\boldsymbol{\sigma}\cdot\boldsymbol{S}_2 G(\boldsymbol{r}_2, \boldsymbol{r}_1, i\omega)\}, \tag{8.13}$$

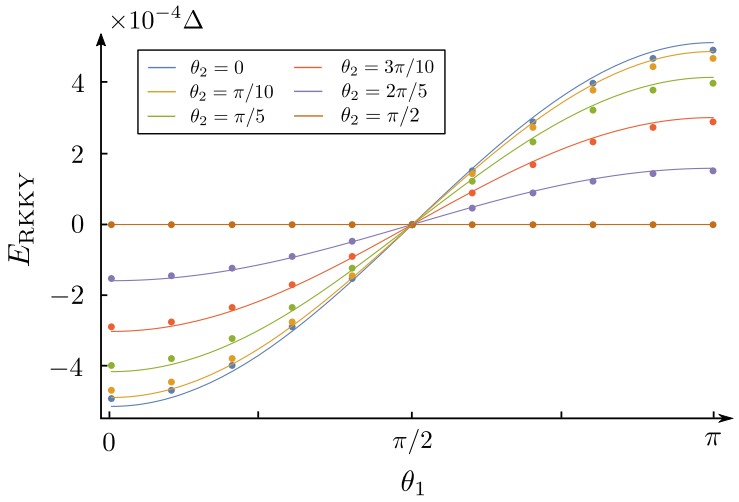

Figure 8.3: E_{RKKY} in dependence on θ_1 calculated numerically via exact diagonalization (dots) for different fixed θ_2 (see inset) and comparison to the analytical Eq. (8.14) (solid lines). The separation between the impurities is $\ell = 3\,\xi$ and both impurities are placed at a distance $x_1 = x_2 = 0.2\,\xi$ from the edge. We see that, for a fixed orientation of the second impurity spin, the first impurity spin is favored to align along the edge. The total energy is minimized if both impurity spins are aligned ferromagnetically along the edge. Here, we have set $\Delta/\varepsilon_F = 0.28$, $JSm = 0.1$, and $\phi_1 = \phi_2 = 0$.

where $\boldsymbol{S}_1$ and $\boldsymbol{S}_2$ are the spins of two magnetic impurities located at $\boldsymbol{r}_1$ and $\boldsymbol{r}_2$, see Fig. 8.1. If the distance between the impurities along the edge $\ell := |y_1 - y_2|$ is much larger than ξ, the contribution of the bulk states is exponentially suppressed and only the gapless Majorana edge states contribute to the RKKY interaction. Evaluating Eq. (8.13) by taking into account only the edge states [see Eq. (8.4)], we find after a straightforward calculation

$$E_{\mathrm{RKKY}} \approx -(Jm)^2 \Delta\, F(\boldsymbol{r}_1, \boldsymbol{r}_2) S_1^y S_2^y, \tag{8.14}$$

$$F(\boldsymbol{r}_1, \boldsymbol{r}_2) = \frac{8}{\pi} \frac{\sin^2(k_F x_1) \sin^2(k_F x_2)}{k_F \ell} e^{-\frac{2}{\xi}(x_1 + x_2)}, \tag{8.15}$$

which is valid in the limit $\ell \gg \xi$. Thus, the RKKY interaction is of Ising type and tends to align the impurity spins ferromagnetically along the edge. Since also the single-impurity term favors to align each individual impurity spin along the edge, the overall ground state will have both impurity spins aligned ferromagnetically along the edge. In accordance with our intuition for 1D systems, we find that E_{RKKY} decays as $1/\ell$. Furthermore, we note that E_{RKKY} oscillates with $x_{1,2}$ due to the spatial profile of the edge state wave functions, while there are no oscillations with ℓ as a direct consequence of particle-hole symmetry.

Again, we verify these results via exact diagonalization of a discretized model. The total ground state energy of the system now consists of three components: the energy of the clean system E_0, the impurity-induced contributions $E_{\mathrm{imp}}^{(1)}$ and $E_{\mathrm{imp}}^{(2)}$ of the individual impurities, and the RKKY exchange energy E_{RKKY}. Thus, we can write

$$E_{\mathrm{tot}} = E_0 + E_{\mathrm{imp}}^{(1)} + E_{\mathrm{imp}}^{(2)} + E_{\mathrm{RKKY}}. \tag{8.16}$$

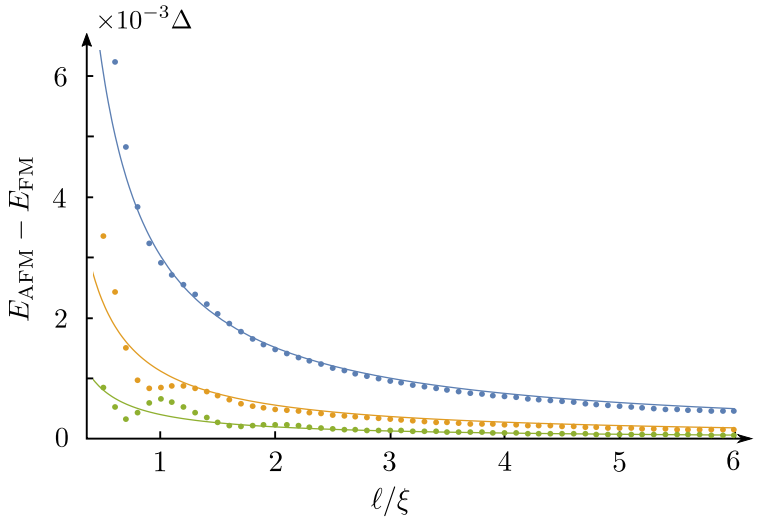

Figure 8.4: Energy difference $E_{\mathrm{AFM}} - E_{\mathrm{FM}}$ for two impurities oriented along the edge in dependence on ℓ calculated numerically via exact diagonalization (dots) and analytically via Eq. (8.14) (solid line). The impurities are placed at a distance $x_1 = x_2 = 0.2\,\xi$ (blue), $x_1 = x_2 = 0.3\,\xi$ (orange), or $x_1 = x_2 = 0.6\,\xi$ (green) from the edge. Generally, we find that $E_{\mathrm{AFM}} - E_{\mathrm{FM}} > 0$, indicating that the FM configuration is energetically favorable over the AFM configuration. Furthermore, the energy difference decays as $1/\ell$ with increasing interimpurity distances, while it vanishes exponentially as the impurities are moved into the bulk. At small ℓ, the exact numerical result shows additional oscillations due to contributions from the bulk states, which were neglected in the analytical treatment. The system parameters are the same as in Fig. 8.3.

Again, the two impurity spins are parametrized as $\boldsymbol{S}_i = S\,(\sin\theta_i \sin\phi_i, \cos\theta_i, \sin\theta_i \cos\phi_i)$ with $\theta_i \in [0, \pi]$ and $\phi_i \in [0, 2\pi)$ for $i \in \{1, 2\}$. In Fig. 8.3, E_{RKKY} is calculated at a large interimpurity distance $\ell = 3\,\xi$ in dependence on θ_1 for different fixed θ_2. Our numerical results show that indeed $E_{\mathrm{RKKY}} \propto \cos(\theta_1)$ with a prefactor that is well approximated by the analytical result given in Eqs. (8.14) and (8.15). We have checked that the same dependence also holds for θ_2 as expected by symmetry. Similarly, we have checked that the numerical curves are antisymmetric around $\theta_{1,2} = \pi/2$ in agreement with the analytical result, which is why we restrict ourselves to $\theta_2 \in [0, \pi/2]$ in Fig. 8.3.

Next, we calculate the energy difference between the antiferromagnetic (AFM) and the ferromagnetic (FM) configuration for two impurities oriented along the edge as a function of ℓ. Figure 8.4 shows the results for several different distances from the edge. As expected, the energy difference is positive—indicating that the FM configuration is energetically favorable over the AFM configuration—and decays as $1/\ell$ with increasing interimpurity distances. In addition to the numerical result, we also display the analytical energy difference obtained from Eqs. (8.14) and (8.15), see Fig. 8.4. Indeed, in the limit of large $\ell \gg \xi$, the analytical expression approximates the numerical result very well. For small impurity separations, however, we see additional oscillations in the energy difference that become more pronounced as $x_{1,2}$ increase. These can be attributed to bulk contributions, which were neglected in the analytical treatment. Finally, as the impurities move away from the edge, the edge-state con-

tribution to the RKKY interaction becomes exponentially suppressed and bulk contributions are no longer negligible.

We have checked numerically that the asymptotic $1/\ell$ decay of the RKKY interaction close to the edge also persists in the presence of potential disorder as long as the bulk gap remains open. Contrary to this, accidental edge states in topologically trivial materials (caused by, e.g., local imperfections of the edge) will not lead to such a stable $1/\ell$ decay nor to the predicted spin anisotropies. Indeed, trivial boundary states will generally be localized along certain parts of the boundary instead of propagating all the way around it in a topologically protected way. As such, they can only give an exponentially decaying contribution to the RKKY interaction.

8.5 Conclusion

We have studied classical magnetic impurities at the edge of a helical TSC both analytically and numerically. For an isolated magnetic impurity, we have found that a strong easy-axis anisotropy tends to align the impurity spin along the edge. Furthermore, we have shown that the RKKY interaction between two magnetic impurities placed close to the edge results in a ferromagnetic alignment of both impurity spins along the edge.

Our results indicate that spectroscopy of dilute magnetic impurities can serve as a powerful tool to experimentally distinguish between topologically trivial and nontrivial materials by probing the magnetic anisotropy induced by the helical edge states. When observed together with additional signatures of bulk superconductivity, these magnetic anisotropies strongly indicate a helical TSC state. As a simple experimental check, one should be able to observe that the magnetic anisotropies—together with the bulk gap and all other features of the helical TSC state—disappear when the temperature is raised above the critical temperature of the superconductor. We also note that while we focused on a simple toy model for a 2D p-wave TSC, our analysis can easily be adapted to more elaborate models of helical TSCs [116–126].

Acknowledgments. We would like to acknowledge fruitful discussions with Flavio Ronetti and Alex Mook. This work was supported by the Georg H. Endress Foundation, the Swiss National Science Foundation and NCCR QSIT. This project received funding from the European Union's Horizon 2020 research and innovation program (ERC Starting Grant, grant agreement No 757725).

8.A Exact numerical diagonalization

In this Appendix, we provide details of the numerical calculations. We describe the TSC by the following tight-binding Hamiltonian defined on a square lattice:

$$\bar{H} = \sum_{n,m} \Big\{ \Psi^\dagger_{n,m} \left(4t - \mu\right) \tau_z \Psi_{n,m} - \big[\Psi^\dagger_{n,m} \left(t\tau_z + i\Delta_0 \sigma_y \tau_x\right) \Psi_{n+1,m} + \Psi^\dagger_{n,m} \left(t\tau_z - i\Delta_0 \sigma_x \tau_x\right) \Psi_{n,m+1} + \text{H.c.} \big] \Big\}, \tag{8.17}$$

written in the Nambu basis $\Psi_{n,m} = (c_{n,m,\uparrow}, c_{n,m,\downarrow}, c^\dagger_{n,m,\downarrow}, -c^\dagger_{n,m,\uparrow})^T$, where $c^{(\dagger)}_{n,m,\sigma}$ annihilates (creates) an electron with spin $\sigma \in \{\uparrow, \downarrow\}$ at the lattice site (n, m). The hopping amplitude, the p-wave superconducting pairing amplitude, and the chemical potential are denoted t, Δ_0,

and μ, respectively. The Pauli matrices $\boldsymbol{\sigma} = (\sigma_x, \sigma_y, \sigma_z)$ and $\boldsymbol{\tau} = (\tau_x, \tau_y, \tau_z)$ act in spin and particle-hole space, respectively. The Hamiltonian $\bar{H}$ describes a helical topological superconductor for $\Delta_0 \neq 0$ and $\mu \in (0,4) \cup (4,8)$ [102]. The continuum limit of this Hamiltonian coincides with Eq. (8.1) upon identifying $\mu = k_F^2/(2m)$, $t = 1/(2ma^2)$, and $\Delta_0 = \alpha/(2a)$, where a denotes the lattice constant.

Next, magnetic impurities are placed at sites (n_i, m_i) close to the edge of the TSC. They are modeled by the Hamiltonian

$$\bar{H}_{\text{imp}} = \bar{J} \sum_i \Psi^\dagger_{n_i,m_i} \boldsymbol{\sigma} \cdot \boldsymbol{s}_i \, \Psi_{n_i,m_i}, \tag{8.18}$$

where $\boldsymbol{s}_i = \boldsymbol{S}_i/S$ is a unit vector pointing along the direction of the impurity spin at site i and the exchange coupling $\bar{J}$ is related to the continuum parameters as $\bar{J} = JS/a^2$. We recall from the main text that the direction of the classical impurity spins is parametrized as $\boldsymbol{s}_i = (\sin\theta_i \sin\phi_i, \cos\theta_i, \sin\theta_i \cos\phi_i)$ with $\theta_i \in [0,\pi]$ and $\phi_i \in [0, 2\pi)$ being the polar and azimuthal angles with respect to the y axis, respectively.

8.B Easy-axis anisotropy

In this Appendix, we derive Eq. (8.9). The Matsubara Green function $G(\boldsymbol{r}, \boldsymbol{r}', i\omega)$ for the Hamiltonian Eq. (8.1) takes the following form:

$$G(\boldsymbol{r}, \boldsymbol{r}', i\omega) = \sum_{\eta,k_y,n} \frac{\Psi_{\eta,k_y,n}(x)\Psi^\dagger_{\eta,k_y,n}(x')e^{ik_y(y-y')}}{i\omega - \varepsilon_{\eta,k_y,n}}, \tag{8.19}$$

where $\varepsilon_{\eta,k_y,n}$ is the eigenenergy of the quantum state $\Psi_{\eta,k_y,n}(x)$ [see Eq. (8.3)] and we define $\boldsymbol{r} = (x,y)$, $\boldsymbol{r}' = (x',y')$ with $x, x' > 0$. The Green function depends only on the difference $y - y'$ due to the translational invariance along the y direction. The block-diagonal symmetry of the Hamiltonian, $[\mathcal{H}, \sigma_z\tau_z] = 0$, results in the corresponding block-diagonal structure of the Green function:

$$\big[G(\boldsymbol{r}, \boldsymbol{r}', i\omega), \sigma_z\tau_z\big] = 0. \tag{8.20}$$

In order to derive Eq. (8.9), we need the Green function taken at the same point $\boldsymbol{r} = \boldsymbol{r}' = \boldsymbol{r}_0 = (x_0, y_0)$, $x_0 > 0$:

$$G(x_0, i\omega) \equiv G(\boldsymbol{r}_0, \boldsymbol{r}_0, i\omega) = \sum_{\eta,k_y,n} \frac{\Psi_{\eta,k_y,n}(x_0)\Psi^\dagger_{\eta,k_y,n}(x_0)}{i\omega - \varepsilon_{\eta,k_y,n}}. \tag{8.21}$$

The new short-hand notation $G(x_0, i\omega)$ shows that $G(\boldsymbol{r}_0, \boldsymbol{r}_0, i\omega)$ depends only on x_0 and not on y_0. Using the symmetries of $\mathcal{H}$, we will now find the matrix decomposition of $G(x_0, i\omega)$, which results in the EAA in Eq. (8.9).

First, the Hamiltonian $\mathcal{H}$ is symmetric under the inversion of the y axis:

$$\sigma_y \mathcal{H}(-k_y)\sigma_y = \mathcal{H}(k_y). \tag{8.22}$$

This symmetry results in the following constraint for the Green function $G(x_0, i\omega)$:

$$[\sigma_y, G(x_0, i\omega)] = 0. \tag{8.23}$$

Second, $\mathcal{H}$ is also time-reversal symmetric:

$$\sigma_y \mathcal{H}^*(-k_y)\sigma_y = \mathcal{H}(k_y), \tag{8.24}$$

Combined with the reflection symmetry Eq. (8.22), this results in the following constraint:

$$\mathcal{H}^*(k_y) = \mathcal{H}(k_y). \tag{8.25}$$

Here * stands for the complex conjugation. Thus, the spinors $\Psi_{\eta,k_y,n}(x)$ can be chosen real-valued:

$$\Psi^*_{\eta,k_y,n}(x) = \Psi_{\eta,k_y,n}(x). \tag{8.26}$$

This results in the following symmetry of the Green function:

$$G^*(x_0, -i\omega) = G(x_0, i\omega). \tag{8.27}$$

In fact the real-valuedness of the spinors, the reflection symmetry Eq. (8.23), and the block-diagonal structure of the Green function Eq. (8.20) result in the following matrix decomposition of $G(x_0, i\omega)$:

$$G(x_0, i\omega) = iA_1(x_0, i\omega) + A_2(x_0, i\omega)\tau_z + iB(x_0, i\omega)\sigma_y\tau_y. \tag{8.28}$$

Here, $A_{1,2}(x, i\omega)$ and $B(x, i\omega)$ are complex functions such that $A_1^*(x, -i\omega) = -A_1(x, i\omega)$, $A_2^*(x, -i\omega) = A_2(x, i\omega)$, and $B^*(x, -i\omega) = -B(x, i\omega)$. We note that the absence of a $\sigma_y\tau_x$ term in $G(x_0, i\omega)$ is somewhat non-trivial here. It becomes clear from the matrix structure of the projectors $\Psi_{\eta,k_y,n}(x_0)\Psi^\dagger_{\eta,k_y,n}(x_0)$, where $\Psi_{\eta,k_y,n}(x_0)$ is real-valued and also an eigenvector of $\sigma_z\tau_z$.

The last symmetry in play is the intrinsic particle-hole symmetry of the superconducting system. In combination with time-reversal symmetry, this gives rise to the chiral symmetry

$$\tau_y \mathcal{H} \tau_y = -\mathcal{H}, \tag{8.29}$$

$$G(x_0, i\omega) = -\tau_y G(x_0, -i\omega)\tau_y. \tag{8.30}$$

Together with Eq. (8.27), Eq. (8.30) obliges the functions $A_{1,2}(x_0, i\omega)$ and $B(x_0, i\omega)$ to be real-valued. Moreover, $A_1(x_0, i\omega)$ and $B(x_0, i\omega)$ are odd functions of ω, whereas $A_2(x_0, i\omega)$ is an even function of ω. At this point the matrix decomposition of $G(x_0, i\omega)$, see Eq. (8.28), becomes especially handy. First of all, it is clear that there is no local spin magnetization because $\mathrm{Tr}\{G(x_0, i\omega)\boldsymbol{\sigma}\} = 0$ in accordance with time-reversal symmetry. As the first two terms in Eq. (8.28) commute with $\boldsymbol{\sigma} \cdot \boldsymbol{S}$, i.e.,

$$[iA_1(x_0, i\omega) + A_2(x_0, i\omega)\tau_z, \boldsymbol{\sigma} \cdot \boldsymbol{S}] = 0, \tag{8.31}$$

we can significantly simplify the spin trace in Eq. (8.6):

$$\mathrm{Tr}\left\{[\boldsymbol{\sigma} \cdot \boldsymbol{S}\, G(x_0, i\omega)]^2\right\} = -B^2(x_0, i\omega)\mathrm{Tr}\left\{(\boldsymbol{\sigma} \cdot \boldsymbol{S}\sigma_y\tau_y)^2\right\} + 4S^2\left(A_2^2(x_0, i\omega) - A_1^2(x_0, i\omega)\right), \tag{8.32}$$

$$(\boldsymbol{\sigma} \cdot \boldsymbol{S}\sigma_y\tau_y)^2 = (S_y + iS_x\sigma_z - iS_z\sigma_x)^2 = S_y^2 - S_x^2 - S_z^2 = 2S_y^2 - S^2. \tag{8.33}$$

This directly leads us to Eq. (8.9).

Following the matrix decomposition Eq. (8.28), we can represent $B(x_0, i\omega)$ in the following form:

$$B(x_0, i\omega) = -\frac{i}{4}\mathrm{Tr}\left\{\sigma_y\tau_y G(x_0, i\omega)\right\}. \tag{8.34}$$

We note that $B(x_0, i\omega)$ is an odd function of ω due to chiral symmetry, see Eq. (8.29). Thus, we can simplify Eq. (8.34) by taking the antisymmetric part of the Green function in Eq. (8.21), which results in the following representation:

$$B(x_0, i\omega) = -\frac{\omega}{4}\sum_{\eta,k_y,n}\frac{\Psi^\dagger_{\eta,k_y,n}(x_0)\sigma_y\tau_y\Psi_{\eta,k_y,n}(x_0)}{\omega^2+\varepsilon^2_{\eta,k_y,n}}. \tag{8.35}$$

From the chiral symmetry, it is also clear that the contribution of the states with negative energies is the same as the contribution coming from the positive energies, which results in Eq. (8.10) in the main text.

8.C Local density of states in the vicinity of an impurity

To begin with, let us calculate the local density of states for the unperturbed TSC. The retarded Green function of the unperturbed system taken at $\boldsymbol{r} = \boldsymbol{r}'$ is the following:

$$G^{(0)}_R(\boldsymbol{r}, \boldsymbol{r}, \omega) = \sum_{\eta,k_y,n}\frac{\Psi_{\eta,k_y,n}(x)\Psi^\dagger_{\eta,k_y,n}(x)}{\omega - \varepsilon_{\eta,k_y,n} + i0^+}, \tag{8.36}$$

where $\eta = \pm 1$ is the eigenvalue of $\sigma_z\tau_z$ operator, k_y is the momentum along y, $x > 0$ is the distance from the edge, and n corresponds to all other quantum numbers in the system. The local density of states is described by the following operator:

$$\rho^{(0)}(\boldsymbol{r}, \boldsymbol{r}, \omega) = -\frac{1}{\pi}\mathrm{Im}\left\{G^{(0)}_R(\boldsymbol{r}, \boldsymbol{r}, \omega)\right\} = \sum_{\eta,k_y,n}\Psi_{\eta,k_y,n}(x)\Psi^\dagger_{\eta,k_y,n}(x)\delta\left(\omega - \varepsilon_{\eta,k_y,n}\right). \tag{8.37}$$

If $|\omega| < \Delta$, then only the in-gap edge states contribute to the local density of states. This allows us to consider only the edge states without the bulk contribution. The edge state wave function is given by Eq. (8.4):

$$\Psi_{\eta,k_y}(x) = \phi(k_y, x)\chi_\eta, \tag{8.38}$$

where χ_η is the Majorana spinor and $\phi(k_y, x)$ is the Majorana wave function normalized by unity:

$$\phi(k_y, x) = 2\sqrt{\frac{k_F^2 - k_y^2}{\xi}}\frac{\sin(\kappa x)}{\kappa}e^{-\frac{x}{\xi}}. \tag{8.39}$$

The spectrum of the edge states is $\varepsilon_{\eta,k_y} = -\eta\alpha k_y$, see the main text. With this, we find the edge state contribution to the unperturbed local density of states:

$$\rho^{(0)}_e(\boldsymbol{r}, \boldsymbol{r}, \omega) = \int\limits_{-k_F}^{k_F}\frac{dk_y}{2\pi}\phi^2(k_y, x)\delta(\omega - \alpha k_y)\mathcal{P} = \frac{\phi^2\left(\frac{\omega}{\alpha}, x\right)}{2\pi\alpha}\mathcal{P} \approx \frac{2m}{\pi}e^{-\frac{2x}{\xi}}\mathcal{P}\sin^2\left(\frac{x}{\alpha}\sqrt{\Delta^2 - \omega^2}\right), \tag{8.40}$$

where $\mathcal{P} = (1 + \sigma_y\tau_y)/2$ is the projector onto the Majorana edge mode subspace $\sigma_y\tau_y = +1$. Here $|\omega| < \Delta \approx \alpha k_F$ and we approximated the ratio $(\alpha^2 k_F^2 - \omega^2)/[\alpha^2 k_F^2 - \omega^2 - (m\alpha^2)^2] \approx 1$ if $\Delta^2 - \omega^2 \gg (m\alpha^2)^2$.

The analyticity of $G_R^{(0)}(\boldsymbol{r}, \boldsymbol{r}, \omega)$ in the upper half-plane $\mathrm{Im}(\omega) > 0$ allows us to restore the edge state contribution to the retarded Green function:

$$G_{R,e}^{(0)}(\boldsymbol{r}, \boldsymbol{r}, \omega) = ime^{-\frac{2x}{\xi}} \left(\exp\left(-\sqrt{(\omega + i0^+)^2 - \Delta^2}\frac{2x}{\alpha} \right) - 1 \right) \mathcal{P}. \tag{8.41}$$

Notice that this function is indeed analytic in the upper half-plane $\mathrm{Im}(\omega) > 0$, satisfies the boundary condition $G_{R,e}^{(0)}(\boldsymbol{r}, \boldsymbol{r}, \omega) = 0$ at $x = 0$, and the imaginary part yields the local density of states given by Eq. (8.40). The bulk contribution, on the other hand, can be estimated by approximating the bulk density of states by the value $\rho_b(\boldsymbol{r}, \boldsymbol{r}, \omega) \approx m/\pi$ for $|\omega| > \Delta$ and zero otherwise:

$$G_b(\boldsymbol{r}, \boldsymbol{r}, \omega) = \int\limits_{-\infty}^{\infty} \frac{\rho_b(\boldsymbol{r}, \boldsymbol{r}, \Omega)\, d\Omega}{\omega - \Omega + i0^+} \approx -\frac{2m\omega}{\pi} \int\limits_{\Delta}^{\infty} \frac{d\Omega}{\Omega^2 - (\omega + i0^+)^2} = -\frac{m}{\pi} \ln\left(\frac{\Delta + \omega + i0^+}{\Delta - \omega - i0^+} \right). \tag{8.42}$$

We are interested in the local density of states at small frequencies $|\omega| \ll \Delta$, where the edge contribution Eq. (8.41) dominates over the bulk state contribution. This corresponds to the condition

$$|\omega| \ll \Delta e^{-\frac{2x}{\xi}}. \tag{8.43}$$

Equation (8.41) can be further simplified at $\omega \ll \Delta$ by using $\sqrt{(\omega + i0^+)^2 - \Delta^2} \approx i\Delta\mathrm{sgn}(\omega)$:

$$G_{R,e}^{(0)}(\boldsymbol{r}, \boldsymbol{r}, \omega) \approx ime^{-\frac{2x}{\xi}} \left(e^{-2ik_F x\, \mathrm{sgn}(\omega)} - 1 \right) \mathcal{P}. \tag{8.44}$$

From Eq. (8.40) we immediately see that there is no magnetization in the unperturbed system:

$$\boldsymbol{\rho}_s^{(0)}(\boldsymbol{r}, \boldsymbol{r}, \omega) \equiv \mathrm{Tr}\left\{ \boldsymbol{\sigma} \rho^{(0)}(\boldsymbol{r}, \boldsymbol{r}, \omega) \right\} = 0, \tag{8.45}$$

where the index s in $\boldsymbol{\rho}_s^{(0)}(\boldsymbol{r}, \boldsymbol{r}, \omega)$ stands for spin. The local charge density of states $\rho_c^{(0)}(\boldsymbol{r}, \boldsymbol{r}, \omega)$ at $|\omega| \ll \Delta$ of the unperturbed system follows from Eq. (8.44):

$$\rho_c^{(0)}(\boldsymbol{r}, \boldsymbol{r}, \omega) \equiv \mathrm{Tr}\left\{ \rho^{(0)}(\boldsymbol{r}, \boldsymbol{r}, \omega) \right\} = \frac{\phi^2\left(\frac{\omega}{\alpha}, x\right)}{\pi\alpha} \approx \frac{4m}{\pi} e^{-\frac{2x}{\xi}} \sin^2(k_F x). \tag{8.46}$$

Now, we calculate the local density of states in the vicinity of a magnetic impurity. Adding the magnetic impurity at $\boldsymbol{r}_0 = (x_0, y_0)$ [see Eq. (8.5)] perturbs the electron Green function in the vicinity of the impurity:

$$G(\boldsymbol{r}, \boldsymbol{r}', i\omega) = G^{(0)}(\boldsymbol{r}, \boldsymbol{r}', i\omega) + JG^{(0)}(\boldsymbol{r}, \boldsymbol{r}_0, i\omega)\boldsymbol{\sigma} \cdot \boldsymbol{S} G(\boldsymbol{r}_0, \boldsymbol{r}', i\omega). \tag{8.47}$$

Here we use the Matsubara formalism. The retarded Green function can be obtained with the help of the analytical continuation $i\omega \to \omega + i0^+$. First, let us plug in $\boldsymbol{r} = \boldsymbol{r}_0$ and solve for $G(\boldsymbol{r}_0, \boldsymbol{r}', i\omega)$:

$$G(\boldsymbol{r}_0, \boldsymbol{r}', i\omega) = \left(1 - JG^{(0)}(\boldsymbol{r}_0, \boldsymbol{r}_0, i\omega)\boldsymbol{\sigma} \cdot \boldsymbol{S} \right)^{-1} G^{(0)}(\boldsymbol{r}_0, \boldsymbol{r}', i\omega). \tag{8.48}$$

Substituting this back into Eq. (8.47) and performing the analytical continuation $i\omega \to \omega + i0^+$, we find the exact retarded Green function of the TSC with a single magnetic impurity:

$$G_R(\boldsymbol{r},\boldsymbol{r}',\omega) = G_R^{(0)}(\boldsymbol{r},\boldsymbol{r}',\omega) + JG_R^{(0)}(\boldsymbol{r},\boldsymbol{r}_0,\omega)\boldsymbol{\sigma}\cdot\boldsymbol{S}\left(1 - JG_R^{(0)}(\boldsymbol{r}_0,\boldsymbol{r}_0,\omega)\boldsymbol{\sigma}\cdot\boldsymbol{S}\right)^{-1} G_R^{(0)}(\boldsymbol{r}_0,\boldsymbol{r}',\omega). \tag{8.49}$$

First, let us check that there are no poles induced by the impurity at $|\omega| \ll \Delta$. For this, we notice that $G_{R,e}^{(0)}(\boldsymbol{r}_0,\boldsymbol{r}_0,\omega) \propto \mathcal{P}$, see Eq. (8.44). Then, we notice that $\mathcal{P}\boldsymbol{\sigma}\cdot\boldsymbol{S}\mathcal{P} = S_y\sigma_y\mathcal{P}$. This is enough to simplify the following operator:

$$(1 - z\mathcal{P}\boldsymbol{\sigma}\cdot\boldsymbol{S})^{-1} = 1 + \frac{1 + zS_y\sigma_y}{1 - z^2S_y^2} z\mathcal{P}\boldsymbol{\sigma}\cdot\boldsymbol{S}, \tag{8.50}$$

where z is a complex number. The pole is possible if $z^2S_y^2 = 1$. In our case z is the following number:

$$z = \frac{J}{2}\mathrm{Tr}\left\{G_{R,e}^{(0)}(\boldsymbol{r}_0,\boldsymbol{r}_0,\omega)\right\} = \mathrm{sgn}(\omega)2Jme^{-\frac{2x_0}{\xi}}\sin(k_Fx_0)\, e^{-i\mathrm{sgn}(\omega)k_Fx_0}. \tag{8.51}$$

Notice that the unperturbed retarded Green function can be conveniently written through z:

$$G_{R,e}^{(0)}(\boldsymbol{r}_0,\boldsymbol{r}_0,\omega) = \frac{z}{J}\mathcal{P}. \tag{8.52}$$

The pole condition can be represented as

$$(2JmS_y)^2 e^{-\frac{4x_0}{\xi}}\sin^2(k_Fx_0) = e^{i\mathrm{sgn}(\omega)k_Fx_0}. \tag{8.53}$$

As before, $|\omega| \ll \Delta e^{-\frac{2x_0}{\xi}}$, see Eq. (8.43). We see that the left-hand side of Eq. (8.53) is a positive real number. The right-hand side is a positive real number only if $k_Fx_0 = \pi n$, n being an integer. However, $\sin(k_Fx_0) = \sin(\pi n) = 0$, which means that Eq. (8.53) does not have any solutions. This confirms our numerical simulations, which did not identify any bound states near the magnetic impurity. Notice that bound states are also impossible at any $|\omega| < \Delta$ because the bulk contribution to $G_R^{(0)}(\boldsymbol{r}_0,\boldsymbol{r}_0,\omega)$ is real-valued at any $|\omega| < \Delta$, while the edge contribution always contains an imaginary part. However, this logic breaks in the bulk where $x_0 \gg \xi$ as the edge contribution vanishes exponentially. Equation (8.49) becomes especially simple if we choose $\boldsymbol{r} = \boldsymbol{r}' = \boldsymbol{r}_0$:

$$G_R(\boldsymbol{r}_0,\boldsymbol{r}_0,\omega) = \left(1 - JG_R^{(0)}(\boldsymbol{r}_0,\boldsymbol{r}_0,\omega)\boldsymbol{\sigma}\cdot\boldsymbol{S}\right)^{-1} G_R^{(0)}(\boldsymbol{r}_0,\boldsymbol{r}_0,\omega). \tag{8.54}$$

Using Eq. (8.50) and the representation given in Eq. (8.52), we can find the correction to the Green function:

$$\delta G_R(\boldsymbol{r}_0,\boldsymbol{r}_0,\omega) \equiv G_R(\boldsymbol{r}_0,\boldsymbol{r}_0,\omega) - G_R^{(0)}(\boldsymbol{r}_0,\boldsymbol{r}_0,\omega) = \frac{1 + zS_y\sigma_y}{1 - z^2S_y^2}\frac{z^2}{J}\mathcal{P}\boldsymbol{\sigma}\cdot\boldsymbol{S}\mathcal{P}. \tag{8.55}$$

Using that $\mathcal{P}\boldsymbol{\sigma}\cdot\boldsymbol{S}\mathcal{P} = S_y\mathcal{P}\sigma_y\mathcal{P}$, we can further simplify this relation:

$$G_R(\boldsymbol{r}_0,\boldsymbol{r}_0,\omega) = \frac{z}{J}\frac{1 + zS_y\sigma_y}{1 - z^2S_y^2}\mathcal{P}. \tag{8.56}$$

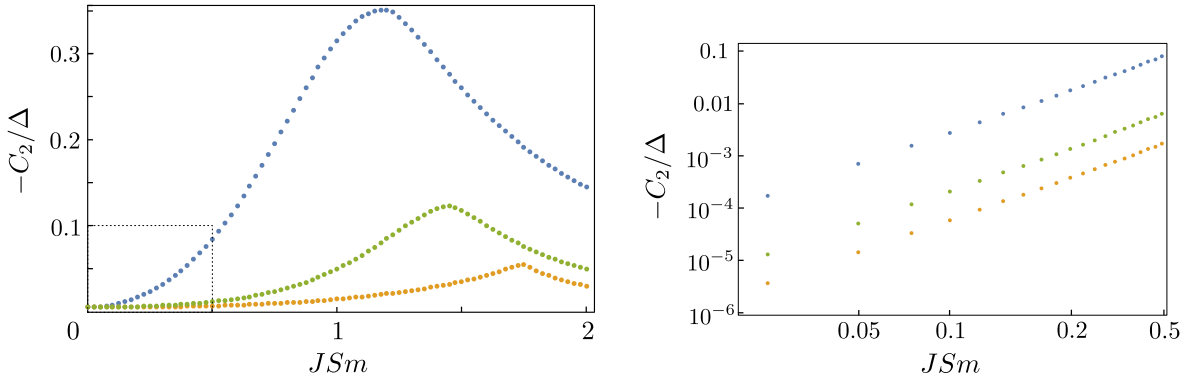

(a) (b)

Figure 8.5: (a) Numerically calculated C_2 as a function of the exchange coupling constant J for three different distances from the edge $x_0 = 0.2\,\xi$ (blue), $x_0 = 0.4\,\xi$ (orange), and $x_0 = 0.6\,\xi$ (green). (b) Dashed rectangle in (a) in the log-log scale. We see that the perturbation theory, which predicts an approximately quadratic dependence $C_2 \propto J^2$, is valid up to $J \lesssim 1/(mS)$. The other parameters are the same as in Fig. 8.2.

The local charge density of states at $|\omega| \ll \Delta e^{-\frac{2x_0}{\xi}}$ is then the following:

$$\rho_c(\boldsymbol{r}_0, \boldsymbol{r}_0, \omega) = \frac{(1+L)\,\rho_c^{(0)}(\boldsymbol{r}_0, \boldsymbol{r}_0, \omega)}{1 - 2L\cos(2k_F x_0) + L^2} \quad \text{with} \quad L \equiv \left(\frac{\pi}{2} JS_y \rho_c^{(0)}(\boldsymbol{r}_0, \boldsymbol{r}_0, \omega)\right)^2, \tag{8.57}$$

where $\rho_c^{(0)}(\boldsymbol{r}_0, \boldsymbol{r}_0, \omega)$ is the unperturbed density of states, see Eq. (8.46). In the perturbative regime $JSm \ll 1$, we have $L \ll 1$. Thus, we see that the density of states is only slightly altered at the impurity site and can be correctly accounted for by perturbation theory. The spin density of states at the impurity site is affected even less, see Eq. (8.56). The same logic can be applied for $G_R(\boldsymbol{r}, \boldsymbol{r}, \omega)$ at other sites $\boldsymbol{r} \neq \boldsymbol{r}_0$ in the vicinity of the impurity. Therefore, we confirm that the perturbation theory yields correct qualitative results for magnetic impurities placed at the edge of a topological superconductor when $JSm \ll 1$.

It is worth noting that there is no pole in Eq. (8.57) even if $L = 1$. Indeed, in order to have a pole we require $\cos(2k_F x_0) = 1$, i.e., $\sin(k_F x_0) = 0$ and therefore $L \propto \sin^4(k_F x_0) = 0$. If the impurity is placed at the maximum of $\rho_c(\boldsymbol{r}_0, \boldsymbol{r}_0, \omega)$, then $\sin^2(k_F x_0) = 1$ and $\cos(2k_F x_0) = -1$. The local charge density of states at the impurity position is therefore scaled down by a factor $\rho_c/\rho_c^{(0)} = 1/(L+1)$, see Eq. (8.57). In general, the ratio $\rho_c/\rho_c^{(0)}$ can be larger or smaller than one depending on the impurity position.

8.D Dependence on the exchange coupling constant J

In this Appendix, we present numerical results for the coefficient C_2 as a function of the exchange coupling constant J for three distances from the edge, see Fig. 8.5. As expected, we find that $C_2 \propto J^2$ for small $J \lesssim 1/(mS)$. Contrary to that, we find a qualitatively different behavior for large $J \gg 1/(mS)$, where C_2 decreases. In this case, the perturbation theory fails together with the mean-field approach to describe the TSC due to a strong local renormalization of the superconducting order parameter close to the magnetic impurity.

8.E RKKY interaction for spin-$\frac{1}{2}$ impurities

In Ref. [90], the RKKY interaction between two spin-1/2 impurities placed at the edge of a 2D TSC was calculated using an effective 1D description of the helical Majorana edge states. It was found that an antiferromagnetic alignment of the impurity spins is preferred. Here, we repeat the corresponding calculations using the model of Ref. [90] and find that the RKKY interaction is ferromagnetic in agreement with our results presented in the main text.

The Majorana edge modes in Ref. [90] are treated within the effective 1D model

$$H_0(\tau) = \frac{1}{2}\sum_\nu v_\nu \int dx\, \Psi_\nu(x,\tau)(-i\partial_x)\Psi_\nu(x,\tau), \tag{8.58}$$

where the index $\nu \in \{L, R\}$ labels left- and right-moving modes, $v_L = -v$ and $v_R = +v > 0$ are the corresponding velocities, and $\Psi_\nu(x,\tau) = \Psi_\nu^\dagger(x,\tau)$ are the Majorana field operators satisfying the following anticommutation relation:

$$\left\{\Psi_\nu(x,\tau), \Psi_{\nu'}(x',\tau)\right\} = \delta_{\nu\nu'}\delta(x-x'). \tag{8.59}$$

The equation of motion for the Majorana field operators in imaginary time is then the following:

$$\frac{\partial\Psi_\nu(x,\tau)}{\partial\tau} = [H_0(\tau), \Psi_\nu(x,\tau)] = iv_\nu\partial_x\Psi_\nu(x,\tau), \tag{8.60}$$

where we used the anticommutation relation Eq. (8.59) to evaluate the commutator.

We define the imaginary time Majorana Green function as follows:

$$\begin{aligned} G_{\nu\nu'}(x,\tau) &= -\left\langle \mathrm{T}\left\{\Psi_\nu(x,\tau)\Psi_{\nu'}(0,0)\right\}\right\rangle \\ &= -\vartheta(\tau)\left\langle\Psi_\nu(x,\tau)\Psi_{\nu'}(0,0)\right\rangle + \vartheta(-\tau)\left\langle\Psi_{\nu'}(0,0)\Psi_\nu(x,\tau)\right\rangle, \end{aligned} \tag{8.61}$$

where T is the time-ordering operator and $\vartheta(\tau)$ is the Heaviside step function. Using Eq. (8.60), we find the differential equation for $G_{\nu\nu'}(x,\tau)$:

$$\partial_\tau G_{\nu\nu'}(x,\tau) = -\delta(\tau)\delta(x)\delta_{\nu\nu'} + iv_\nu\partial_x G_{\nu\nu'}(x,\tau). \tag{8.62}$$

The Green function is especially simple in the frequency-momentum representation:

$$G_{\nu\nu'}(k, i\omega) = \frac{\delta_{\nu\nu'}}{i\omega - v_\nu k}. \tag{8.63}$$

Taking the Fourier transform, we find the Green function in the time-coordinate representation:

$$G_{\nu\nu'}(x,\tau) = -\frac{iT}{2v}\frac{\delta_{\nu\nu'}}{\sinh\left(\pi T\left(\frac{x}{v_\nu} + i\tau\right)\right)}, \tag{8.64}$$

where T is the temperature. The anti-periodic condition is satisfied:

$$G_{\nu\nu'}(x, \tau + 1/T) = -G_{\nu\nu'}(x,\tau). \tag{8.65}$$

We use the effective exchange interaction defined in Ref. [90]:

$$H_J(\tau) = J\left(s\left(-\frac{R}{2},\tau\right)S_{I,1} + s\left(\frac{R}{2},\tau\right)S_{I,2}\right), \tag{8.66}$$

where two spin impurities are located at $x = \pm R/2$, R is the distance between the impurities along the edge, J is the effective exchange coupling, and $S_{I,1}$, $S_{I,2}$ are the projections of the impurity spins onto the so-called Ising direction, see Ref. [90]. In our case, the Ising direction is along the edge. The Majorana spin density operator $s(x,\tau)$ is defined as follows:

$$s(x,\tau) = i\Psi_R(x,\tau)\Psi_L(x,\tau). \tag{8.67}$$

The interaction contribution to the thermodynamic potential $\delta\Omega$ is given by the following statistical average:

$$\delta\Omega = -T\left(\langle\mathfrak{S}\rangle_c - 1\right), \tag{8.68}$$

where the index $_c$ stands for the connected diagrams only and $\mathfrak{S}$ is the statistical S-matrix:

$$\mathfrak{S} = \mathrm{T}\exp\left(-\int\limits_0^{1/T} H_J(\tau)\,d\tau\right), \tag{8.69}$$

where $H_J(\tau)$ is given by Eq. (8.66). The first-order correction vanishes due to the zero net spin density in absence of the magnetic impurities:

$$\langle s(x,\tau)\rangle = 0. \tag{8.70}$$

The second-order correction yields the self-interaction terms proportional to $S_{I,1}^2$ and $S_{I,2}^2$ as well as the RKKY term proportional to $S_{I,1}S_{I,2}$ that we are interested in:

$$\begin{aligned} E_{RKKY} &= -TJ^2 S_{I,1}S_{I,2}\int d\tau_1 d\tau_2 \left\langle \mathrm{T}\left\{ s\left(-\frac{R}{2},\tau_1\right) s\left(\frac{R}{2},\tau_2\right)\right\}\right\rangle \\ &= TJ^2 S_{I,1}S_{I,2}\int d\tau_1 d\tau_2\, G_R(-R,\tau_1-\tau_2)G_L(R,\tau_2-\tau_1), \end{aligned} \tag{8.71}$$

where we used the Wick theorem to evaluate the statistical average. The product of two Green functions in Eq. (8.71) is a periodic function on τ with the period $1/T$. This allows for the following simplification:

$$E_{RKKY} = J^2 S_{I,1}S_{I,2}\int\limits_0^{1/T} d\tau\, G_R(-R,\tau)G_L(R,-\tau). \tag{8.72}$$

Substituting the Green functions Eq. (8.64) into Eq. (8.72), we find:

$$E_{RKKY} = -\frac{J^2T^2}{2v^2}S_{I,1}S_{I,2}\int\limits_0^{1/T}\frac{d\tau}{\cosh\left(2\pi T\frac{R}{v}\right)-\cos\left(2\pi T\tau\right)}. \tag{8.73}$$

The integral over τ can be reduced to the following elementary integral:

$$\int\limits_0^{2\pi}\frac{dt}{\lambda-\cos t} = \frac{2\pi}{\sqrt{\lambda^2-1}},\ \lambda > 1. \tag{8.74}$$

This gives the final result, showing that the RKKY interaction mediated by the helical Majorana edge modes is ferromagnetic:

$$E_{RKKY} = -\frac{J^2 S_{I,1} S_{I,2}}{4\pi v R} \frac{2\pi T R/v}{\sinh(2\pi T R/v)}. \tag{8.75}$$

As such, we find that, for vanishing temperature $T = 0$, the result for quantum impurities is qualitatively similar to the result for classical impurities presented in Eq. (8.14) in the main text.

Bibliography

[1] M. A. Ruderman and C. Kittel, Phys. Rev. **96**, 99 (1954).

[2] T. Kasuya, Prog. Theor. Phys. **16**, 45 (1956).

[3] K. Yosida, Phys. Rev. **106**, 893 (1957).

[4] S. Nadj-Perge, I. K. Drozdov, B. A. Bernevig, and A. Yazdani, Phys. Rev. B **88**, 020407(R) (2013).

[5] F. Pientka, L. I. Glazman, and F. von Oppen, Phys. Rev. B **88**, 155420 (2013).

[6] B. Braunecker and P. Simon, Phys. Rev. Lett. **111**, 147202 (2013).

[7] J. Klinovaja, P. Stano, A. Yazdani, and D. Loss, Phys. Rev. Lett. **111**, 186805 (2013).

[8] M. M. Vazifeh and M. Franz, Phys. Rev. Lett. **111**, 206802 (2013).

[9] F. Pientka, L. I. Glazman, and F. von Oppen, Phys. Rev. B **89**, 180505(R) (2014).

[10] K. Pöyhönen, A. Westström, J. Röntynen, and T. Ojanen, Phys. Rev. B **89**, 115109 (2014).

[11] I. Reis, D. J. J. Marchand, and M. Franz, Phys. Rev. B **90**, 085124 (2014).

[12] Y. Kim, M. Cheng, B. Bauer, R. M. Lutchyn, and S. Das Sarma, Phys. Rev. B **90**, 060401(R) (2014).

[13] J. Li, H. Chen, I. K. Drozdov, A. Yazdani, B. A. Bernevig, and A. H. MacDonald, Phys. Rev. B **90**, 235433 (2014).

[14] A. Heimes, P. Kotetes, and G. Schön, Phys. Rev. B **90**, 060507(R) (2014).

[15] P. M. R. Brydon, S. Das Sarma, H.-Y. Hui, and J. D. Sau, Phys. Rev. B **91**, 064505 (2015).

[16] A. Westström, K. Pöyhönen, and T. Ojanen, Phys. Rev. B **91**, 064502 (2015).

[17] Y. Peng, F. Pientka, L. I. Glazman, and F. von Oppen, Phys. Rev. Lett. **114**, 106801 (2015).

[18] H.-Y. Hui, P. M. R. Brydon, J. D. Sau, S. Tewari, and S. Das Sarma, Sci. Rep. **5** (2015).

[19] J. Röntynen and T. Ojanen, Phys. Rev. Lett. **114**, 236803 (2015).

[20] B. Braunecker and P. Simon, Phys. Rev. B **92**, 241410(R) (2015).

[21] C.-H. Hsu, P. Stano, J. Klinovaja, and D. Loss, Phys. Rev. B **92**, 235435 (2015).

[22] K. Pöyhönen, A. Weststrom, and T. Ojanen, Phys. Rev. B **93**, 014517 (2016).

[23] J. Zhang, Y. Kim, E. Rossi, and R. M. Lutchyn, Phys. Rev. B **93**, 024507 (2016).

[24] J. Li, T. Neupert, B. A. Bernevig, and A. Yazdani, Nat. Commun. **7**, 10395 (2016a).

[25] J. Röntynen and T. Ojanen, Phys. Rev. B **93**, 094521 (2016).

[26] S. Hoffman, J. Klinovaja, and D. Loss, Phys. Rev. B **93**, 165418 (2016).

[27] J. Li, T. Neupert, Z. Wang, A. H. MacDonald, A. Yazdani, and B. A. Bernevig, Nat. Commun. **7**, 12297 (2016b).

[28] M. Schecter, K. Flensberg, M. H. Christensen, B. M. Andersen, and J. Paaske, Phys. Rev. B **93**, 140503(R) (2016).

[29] M. H. Christensen, M. Schecter, K. Flensberg, B. M. Andersen, and J. Paaske, Phys. Rev. B **94**, 144509 (2016).

[30] V. Kaladzhyan, P. Simon, and M. Trif, Phys. Rev. B **96**, 020507(R) (2017).

[31] G. M. Andolina and P. Simon, Phys. Rev. B **96**, 235411 (2017).

[32] A. Kobiałka, P. Piekarz, A. M. Oleś, and A. Ptok, Phys. Rev. B **101**, 205143 (2020).

[33] G. C. Ménard, S. Guissart, C. Brun, R. T. Leriche, M. Trif, F. Debontridder, D. Demaille, D. Roditchev, P. Simon, and T. Cren, Nat. Commun. **8**, 2040 (2017).

[34] G. C. Ménard, C. Brun, R. Leriche, M. Trif, F. Debontridder, D. Demaille, D. Roditchev, P. Simon, and T. Cren, Eur. Phys. J. Spec. Top. **227**, 2303 (2019).

[35] R. Pawlak, M. Kisiel, J. Klinovaja, T. Meier, S. Kawai, T. Glatzel, D. Loss, and E. Meyer, npj Quantum Inf. **2**, 16035 (2016).

[36] S. Nadj-Perge, I. K. Drozdov, J. Li, H. Chen, S. Jeon, J. Seo, A. H. MacDonald, B. A. Bernevig, and A. Yazdani, Science **346**, 602 (2014).

[37] M. Ruby, F. Pientka, Y. Peng, F. von Oppen, B. W. Heinrich, and K. J. Franke, Phys. Rev. Lett. **115**, 197204 (2015a).

[38] M. Ruby, B. W. Heinrich, Y. Peng, F. von Oppen, and K. J. Franke, Nano Lett. **17**, 4473 (2017).

[39] B. E. Feldman, M. T. Randeria, J. Li, S. Jeon, Y. Xie, Z. Wang, I. K. Drozdov, B. A. Bernevig, and A. Yazdani, Nature Phys. **13**, 286 (2016).

[40] H. Kim, A. Palacio-Morales, T. Posske, L. Rózsa, K. Palotás, L. Szunyogh, M. Thorwart, and R. Wiesendanger, Sci. Adv. **4**, eaar5251 (2018).

[41] R. Pawlak, S. Hoffman, J. Klinovaja, D. Loss, and E. Meyer, Progress in Particle and Nuclear Physics **107**, 1 (2019).

[42] H. Ding, Y. Hu, M. T. Randeria, S. Hoffman, O. Deb, J. Klinovaja, D. Loss, and A. Yazdani, Proc. Natl. Acad. Sci. USA **118**, e2024837118 (2021).

[43] K. Laubscher and J. Klinovaja, Journal of Applied Physics **130**, 081101 (2021).

[44] A. Y. Zyuzin and B. Z. Spivak, JETP Lett. **43**, 234 (1986).

[45] A. A. Abrikosov, *Fundamentals of the theory of metals* (Elsevier Science Publishers, 1988).

[46] S. Demokritov, Soviet Physics Uspekhi **35**, 331 (1992).

[47] D. Poilblanc, D. J. Scalapino, and W. Hanke, Phys. Rev. Lett. **72**, 884 (1994).

[48] A. V. Balatsky, M. I. Salkola, and A. Rosengren, Phys. Rev. B **51**, 15547 (1995).

[49] D. N. Aristov, S. V. Maleyev, and A. G. Yashenkin, Zeitschrift für Physik B Condensed Matter **102**, 467 (1997).

[50] V. M. Galitski and A. I. Larkin, Phys. Rev. B **66**, 064526 (2002).

[51] A. T. Hindmarch and B. J. Hickey, Phys. Rev. Lett. **91**, 116601 (2003).

[52] H. Imamura, P. Bruno, and Y. Utsumi, Phys. Rev. B **69**, 121303(R) (2004).

[53] S. Saremi, Phys. Rev. B **76**, 184430 (2007).

[54] E. H. Hwang and S. Das Sarma, Phys. Rev. Lett. **101**, 156802 (2008).

[55] P. Simon, B. Braunecker, and D. Loss, Phys. Rev. B **77**, 045108 (2008).

[56] B. Braunecker, P. Simon, and D. Loss, Phys. Rev. B **80**, 165119 (2009a).

[57] B. Braunecker, P. Simon, and D. Loss, Phys. Rev. Lett. **102**, 116403 (2009b).

[58] A. Schulz, A. De Martino, P. Ingenhoven, and R. Egger, Phys. Rev. B **79**, 205432 (2009).

[59] A. M. Black-Schaffer, Phys. Rev. B **81**, 205416 (2010).

[60] B. Braunecker, G. I. Japaridze, J. Klinovaja, and D. Loss, Phys. Rev. B **82**, 045127 (2010).

[61] S. Chesi and D. Loss, Phys. Rev. B **82**, 165303 (2010).

[62] M. Sherafati and S. Satpathy, Phys. Rev. B **83**, 165425 (2011).

[63] E. Kogan, Phys. Rev. B **84**, 115119 (2011).

[64] J. G. Checkelsky, J. Ye, Y. Onose, Y. Iwasa, and Y. Tokura, Nature Phys. **8**, 729 (2012).

[65] J. Klinovaja and D. Loss, Phys. Rev. B **87**, 045422 (2013).

[66] F. Parhizgar, R. Asgari, S. H. Abedinpour, and M. Zareyan, Phys. Rev. B **87**, 125402 (2013).

[67] N. Y. Yao, L. I. Glazman, E. A. Demler, M. D. Lukin, and J. D. Sau, Phys. Rev. Lett. **113**, 087202 (2014).

[68] S. Hoffman, J. Klinovaja, T. Meng, and D. Loss, Phys. Rev. B **92**, 125422 (2015).

[69] M. Schecter, M. S. Rudner, and K. Flensberg, Phys. Rev. Lett. **114**, 247205 (2015).

[70] A. M. Tsvelik and O. M. Yevtushenko, Phys. Rev. Lett. **119**, 247203 (2017).

[71] O. M. Yevtushenko and V. I. Yudson, Phys. Rev. Lett. **120**, 147201 (2018).

[72] O. Deb, S. Hoffman, D. Loss, and J. Klinovaja, Phys. Rev. B **103**, 165403 (2021).

[73] A. Ghanbari, E. Erlandsen, and J. Linder, Phys. Rev. B **104**, 054502 (2021).

[74] Q. Liu, C.-X. Liu, C. Xu, X.-L. Qi, and S.-C. Zhang, Phys. Rev. Lett. **102**, 156603 (2009).

[75] R. R. Biswas and A. V. Balatsky, Phys. Rev. B **81**, 233405 (2010).

[76] I. Garate and M. Franz, Phys. Rev. B **81**, 172408 (2010).

[77] J.-J. Zhu, D.-X. Yao, S.-C. Zhang, and K. Chang, Phys. Rev. Lett. **106**, 097201 (2011).

[78] D. A. Abanin and D. A. Pesin, Phys. Rev. Lett. **106**, 136802 (2011).

[79] A. A. Zyuzin and D. Loss, Phys. Rev. B **90**, 125443 (2014).

[80] D. K. Efimkin and V. Galitski, Phys. Rev. B **89**, 115431 (2014).

[81] J. Gao, W. Chen, X. C. Xie, and F.-c. Zhang, Phys. Rev. B **80**, 241302(R) (2009).

[82] T. Meng, P. Stano, J. Klinovaja, and D. Loss, Eur. Phys. J. B **87**, 203 (2014).

[83] Y.-W. Lee and Y.-L. Lee, Phys. Rev. B **91**, 214431 (2015).

[84] G. Yang, C.-H. Hsu, P. Stano, J. Klinovaja, and D. Loss, Phys. Rev. B **93**, 075301 (2016).

[85] V. D. Kurilovich, P. D. Kurilovich, and I. S. Burmistrov, Phys. Rev. B **95**, 115430 (2017).

[86] C.-H. Hsu, P. Stano, J. Klinovaja, and D. Loss, Phys. Rev. B **96**, 081405(R) (2017).

[87] C.-H. Hsu, P. Stano, J. Klinovaja, and D. Loss, Phys. Rev. B **97**, 125432 (2018).

[88] R. Shindou, A. Furusaki, and N. Nagaosa, Phys. Rev. B **82**, 180505(R) (2010).

[89] R. Žitko and P. Simon, Phys. Rev. B **84**, 195310 (2011).

[90] E. Eriksson, A. Zazunov, P. Sodano, and R. Egger, Phys. Rev. B **91**, 064501 (2015).

[91] P. Stano, J. Klinovaja, A. Yacoby, and D. Loss, Phys. Rev. B **88**, 045441 (2013).

[92] K. von Bergmann, M. Ternes, S. Loth, C. P. Lutz, and A. J. Heinrich, Phys. Rev. Lett. **114**, 076601 (2015).

[93] J.-P. Xu, M.-X. Wang, Z. L. Liu, J.-F. Ge, X. Yang, C. Liu, Z. A. Xu, D. Guan, C. L. Gao, D. Qian, Y. Liu, Q.-H. Wang, F.-C. Zhang, Q.-K. Xue, and J.-F. Jia, Phys. Rev. Lett. **114**, 017001 (2015).

[94] L. Cornils, A. Kamlapure, L. Zhou, S. Pradhan, A. A. Khajetoorians, J. Fransson, J. Wiebe, and R. Wiesendanger, Phys. Rev. Lett. **119**, 197002 (2017).

[95] S. Jeon, Y. Xie, J. Li, Z. Wang, B. A. Bernevig, and A. Yazdani, Science **358**, 772 (2017).

[96] J. Li, S. Jeon, Y. Xie, A. Yazdani, and B. A. Bernevig, Phys. Rev. B **97**, 125119 (2018).

[97] L. Schneider, M. Steinbrecher, L. Rózsa, J. Bouaziz, K. Palotás, M. dos Santos Dias, S. Lounis, J. Wiebe, and R. Wiesendanger, npj Quantum Materials **4**, 42 (2019).

[98] D.-J. Choi, N. Lorente, J. Wiebe, K. von Bergmann, A. F. Otte, and A. J. Heinrich, Rev. Mod. Phys. **91**, 041001 (2019).

[99] B. Jäck, Y. Xie, J. Li, S. Jeon, B. A. Bernevig, and A. Yazdani, Science **364**, 1255 (2019).

[100] B. Jäck, Y. Xie, and A. Yazdani, Nature Reviews Physics **3**, 541 (2021).

[101] D. Wang, J. Wiebe, R. Zhong, G. Gu, and R. Wiesendanger, Phys. Rev. Lett. **126**, 076802 (2021).

[102] B. A. Bernevig and T. L. Hughes, *Topological Insulators and Topological Superconductors* (Princeton University Press, 2013).

[103] S.-H. Ji, T. Zhang, Y.-S. Fu, X. Chen, X.-C. Ma, J. Li, W.-H. Duan, J.-F. Jia, and Q.-K. Xue, Phys. Rev. Lett. **100**, 226801 (2008).

[104] M. Ruby, F. Pientka, Y. Peng, F. von Oppen, B. W. Heinrich, and K. J. Franke, Phys. Rev. Lett. **115**, 087001 (2015b).

[105] M. Ruby, Y. Peng, F. von Oppen, B. W. Heinrich, and K. J. Franke, Phys. Rev. Lett. **117**, 186801 (2016).

[106] M. Ruby, B. W. Heinrich, Y. Peng, F. von Oppen, and K. J. Franke, Phys. Rev. Lett. **120**, 156803 (2018).

[107] D.-J. Choi, C. G. Fernández, E. Herrera, C. Rubio-Verdú, M. M. Ugeda, I. Guillamón, H. Suderow, J. I. Pascual, and N. Lorente, Phys. Rev. Lett. **120**, 167001 (2018).

[108] D.-J. Choi, C. Rubio-Verdú, J. de Bruijckere, M. M. Ugeda, N. Lorente, and J. I. Pascual, Nat. Commun. **8**, 15175 (2017).

[109] M. E. Flatté and J. M. Byers, Phys. Rev. Lett. **78**, 3761 (1997).

[110] M. I. Salkola, A. V. Balatsky, and J. R. Schrieffer, Phys. Rev. B **55**, 12648 (1997).

[111] M. E. Flatté and D. E. Reynolds, Phys. Rev. B **61**, 14810 (2000).

[112] A. V. Balatsky, I. Vekhter, and J.-X. Zhu, Rev. Mod. Phys. **78**, 373 (2006).

[113] D. K. Morr and J. Yoon, Phys. Rev. B **73**, 224511 (2006).

[114] T. Meng, J. Klinovaja, S. Hoffman, P. Simon, and D. Loss, Phys. Rev. B **92**, 064503 (2015).

[115] K. Björnson, A. V. Balatsky, and A. M. Black-Schaffer, Phys. Rev. B **95**, 104521 (2017).

[116] L. Fu and C. L. Kane, Phys. Rev. Lett. **100**, 096407 (2008).

[117] M. Sato and S. Fujimoto, Phys. Rev. B **79**, 094504 (2009).

[118] C.-X. Liu and B. Trauzettel, Phys. Rev. B **83**, 220510(R) (2011).

[119] S. Deng, L. Viola, and G. Ortiz, Phys. Rev. Lett. **108**, 036803 (2012).

[120] S. Nakosai, Y. Tanaka, and N. Nagaosa, Phys. Rev. Lett. **108**, 147003 (2012).

[121] F. Zhang, C. L. Kane, and E. J. Mele, Phys. Rev. Lett. **111**, 056402 (2013).

[122] J. Wang, Y. Xu, and S.-C. Zhang, Phys. Rev. B **90**, 054503 (2014).

[123] F. Parhizgar and A. M. Black-Schaffer, Sci. Rep. **7**, 9817 (2017).

[124] S. Kashiwaya, K. Saitoh, H. Kashiwaya, M. Koyanagi, M. Sato, K. Yada, Y. Tanaka, and Y. Maeno, Phys. Rev. B **100**, 094530 (2019).

[125] Y. Volpez, D. Loss, and J. Klinovaja, Phys. Rev. B **97**, 195421 (2018).

[126] R.-X. Zhang and S. Das Sarma, Phys. Rev. Lett. **126**, 137001 (2021).

Chapter 9

RKKY interaction in one-dimensional flat band lattices

Adapted from:
K. Laubscher, C. S. Weber, M. Hünenberger, H. Schoeller, D. M. Kennes, D. Loss, and J. Klinovaja,
"RKKY interaction in one-dimensional flat band lattices,"
arXiv preprint arXiv:2210.10025 (2022)

We study the Ruderman-Kittel-Kasuya-Yosida (RKKY) interaction between two classical magnetic impurities in one-dimensional lattice models with flat bands. As two representative examples, we pick the stub lattice and the diamond lattice at half filling. We first calculate the exact RKKY interaction numerically and then compare our data to results obtained via different analytical techniques. In both our examples, we find that the RKKY interaction exhibits peculiar features that can directly be traced back to the presence of a flat band. Importantly, these features are not captured by the conventional RKKY approximation based on non-degenerate perturbation theory. Instead, we find that degenerate perturbation theory correctly reproduces our exact results if there is an energy gap between the flat and the dispersive bands, while a non-perturbative approach becomes necessary in the absence of a gap.

9.1 Introduction

Magnetic impurities embedded in a host material can interact indirectly by coupling to the electron spin density of the host. This so-called Ruderman-Kittel-Kasuya-Yosida (RKKY) interaction [1–3] can result in a magnetic ordering of the impurity spins, leading to a wide range of interesting phenomena with potential applications in the fields of spintronics [4, 5], spin-based quantum computation [6–10], or engineered topological superconductivity [11–21]. The exact form of the RKKY interaction depends on the properties—in particular, the band structure—of the underlying host material and has been extensively studied for various types of systems [22–53].

Conventionally, the RKKY interaction is calculated in second-order perturbation theory assuming that the exchange coupling between the impurity spins and the itinerant electrons is small compared to the typical energy scale of the latter. Recently, however, systems with so-called *flat bands* have attracted significant attention [54, 55]. The energy of these bands is completely independent of momentum or, in a weaker sense, at least approximately constant over a large range of allowed momenta. While the recent interest in flat-band systems has mainly been fueled by significant theoretical and experimental progress on Moiré materials such as twisted bilayer graphene [56–61], flat bands can also emerge as Landau levels in two-dimensional electron gases subjected to a strong magnetic field or in a variety of artificial lattice models [62, 63], some of which have successfully been realized in experiments using photonic lattices or cold-atom setups [64–69].

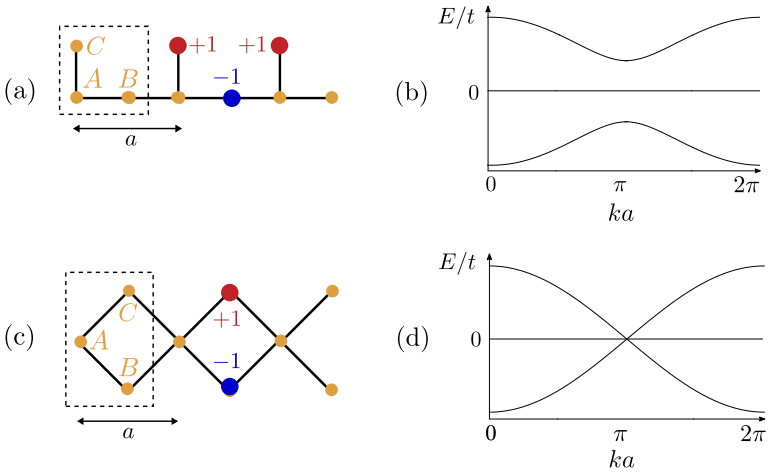

Figure 9.1: (a) Stub lattice. The unit cell (dashed rectangle) consist of three sites (orange dots) labeled A, B, and C. Nearest-neighbor sites are connected by a hopping term of strength t (black lines). The flat band is spanned by a set of CLSs that has support on only three lattice sites each (red and blue dots). The amplitudes of the unnormalized CLSs are $+1$ (-1) for the red (blue) sites. (b) Bulk spectrum of the stub lattice. The dispersive bands are separated from the flat band by an energy gap. (c) Diamond lattice. The graphical elements have the same meaning as in panel (a). Here, the CLSs spanning the flat band have support on only two lattice sites each. (d) Bulk spectrum of the diamond lattice. The dispersive bands touch the flat band in a linear band touching point.

In this case, the vanishing band width and the large degeneracy of the flat band make it questionable whether the conventional perturbative approach to the RKKY interaction is still applicable. This issue was first touched upon in the context of zigzag graphene nanoribbons, where exact numerical studies of edge impurities revealed unconventional features of the RKKY interaction that had not been captured by preceding analytical studies [33, 70]. Later, Ref. [71] studied the RKKY interaction in partially filled graphene Landau levels using *degererate* perturbation theory. On the other hand, a few more recent studies calculate the RKKY interaction in flat-band lattice models via standard non-degenerate perturbation theory [72, 73]. As such, it becomes evident that a general understanding of RKKY effects in flat-band systems—including, in particular, insights regarding the applicability and limitations of perturbation theory—is still lacking. With this motivation, we carefully study the RKKY interaction in two simple one-dimensional (1D) flat-band systems at half filling, see Fig. 9.1. We first calculate the exact RKKY interaction numerically and then compare our data to results obtained via different analytical techniques. In both our examples, we find that the RKKY interaction exhibits peculiar features that are not captured by the conventional RKKY approximation based on non-degenerate perturbation theory. Instead, we find that degenerate perturbation theory correctly reproduces our exact results if there is an energy gap between the flat and the dispersive bands, while a non-perturbative approach becomes necessary in the absence of a gap.

9.2 Models

Let us start by introducing the stub lattice, see Fig. 9.1(a). A unit cell consists of three sites labeled A, B, and C. Neighboring sites are coupled by a hopping element of strength t, such that

$$H_{\text{stub}} = t \sum_n \left(c^\dagger_{n,A} c_{n,B} + c^\dagger_{n,C} c_{n,B} + c^\dagger_{n+1,B} c_{n,A} \right) + \text{H.c.} \tag{9.1}$$

Here, $c^\dagger_{n,l}$ ($c_{n,l}$) creates (destroys) a spinless electron on sublattice $l \in \{A, B, C\}$ in the nth unit cell. Imposing periodic boundary conditions on a chain with a finite number of unit cells N, the Hamiltonian can be rewritten in momentum space as $H_{\text{stub}} = \sum_k \Psi^\dagger_k \mathcal{H}(k) \Psi_k$ with $\Psi_k = (c_{k,A}, c_{k,B}, c_{k,C})^T$ and

$$\mathcal{H}(k) = t \begin{pmatrix} 0 & 1 + e^{ika} & 1 \\ 1 + e^{-ika} & 0 & 0 \\ 1 & 0 & 0 \end{pmatrix}, \tag{9.2}$$

where a denotes the lattice spacing. The corresponding bulk spectrum consists of two dispersive bands $E_\pm(k) = \pm t\sqrt{3 + 2\cos(ak)}$ as well as one completely flat band $E_0(k) = 0$ that is separated from the dispersive bands by an energy gap, see Fig. 9.1(b). The flat band is macroscopically degenerate and is spanned by a set of N linearly independent states. These can be chosen to have support on only three lattice sites each: $|v_n\rangle = (|n, C\rangle - |n, B\rangle + |n+1, C\rangle)/\sqrt{3}$ for $n \in \{1, ..., N\}$. One of these so-called compact localized states (CLSs) [55] is visualized in Fig. 9.1(a). While the CLSs are chosen such that they are strictly localized, they are not mutually orthogonal. In order to construct a set of mutually orthogonal basis states for the flat band, the strict localization has to be traded in for exponential localization, e.g., by changing to a basis of maximally localized Wannier states.

As a second example, we introduce the diamond lattice depicted in Fig. 9.1(c). Again, the unit cell consists of three atoms labeled A, B, and C, and neighboring lattice sites are coupled by a hopping element of strength t. The Hamiltonian then reads

$$H_{\text{dia}} = t\sum_n (c^\dagger_{n,A}c_{n,B} + c^\dagger_{n,A}c_{n,C} + c^\dagger_{n+1,A}c_{n,B} + c^\dagger_{n+1,A}c_{n,C}) + \text{H.c.} \tag{9.3}$$

In momentum space, this leads to $H_{\text{dia}} = \sum_k \Psi^\dagger_k \mathcal{H}(k)\Psi_k$ with

$$\mathcal{H}(k) = t\begin{pmatrix} 0 & 1+e^{ika} & 1+e^{ika} \\ 1+e^{-ika} & 0 & 0 \\ 1+e^{-ika} & 0 & 0 \end{pmatrix}. \tag{9.4}$$

Again, the bulk spectrum consists of two dispersive bands $E_\pm(k) = \pm 2\sqrt{2}t\cos(ka/2)$ and a flat band $E_0(k) = 0$, see Fig. 9.1(d). Importantly, however, there is now no energy gap separating the flat band from the dispersive bands. Rather, the two dispersive bands intersect the flat band in a linear band touching point. Nevertheless, the flat band can again be described in terms of a set of CLSs having support on two lattice sites each, see Fig. 9.1(c). Explicitly, their wave functions are given by $|v_n\rangle = (|n,C\rangle - |n,B\rangle)/\sqrt{2}$.

9.3 RKKY interaction

We now calculate the RKKY interaction between two classical magnetic impurities on the stub and diamond lattice. For this, we consider a system of spinful electrons with both spin species independently described by H_{stub} or H_{dia}, respectively. Additionally, two magnetic impurities are placed in the unit cells n_1 and n_2 at the sublattice positions α and β, respectively. The local exchange coupling to the impurities can then be described as $H^{(1)}_{imp} + H^{(2)}_{imp}$ with

$$H^{(i)}_{imp} = \frac{J_i}{2}\sum_{\sigma,\sigma'} c^\dagger_{n_i,l_i,\sigma}\left[\mathbf{S}_i\cdot\boldsymbol{\sigma}\right]^{\sigma\sigma'} c_{n_i,l_i,\sigma'}, \tag{9.5}$$

where we have defined $l_1 = \alpha$ and $l_2 = \beta$. Compared to Eqs. (9.1) and (9.3), the electronic creation (annihilation) operators $c^\dagger_{n,l,\sigma}$ ($c_{n,l,\sigma}$) now carry an additional spin label $\sigma \in \{\uparrow,\downarrow\}$. Furthermore, $\boldsymbol{\sigma}$ is the vector of Pauli matrices, $\mathbf{S}_i$ are classical impurity spins with $S_i = |\mathbf{S}_i| \gg 1$, and J_i denotes the exchange coupling between the impurity spin and the electron spin density. We assume $\mathbf{S}_i = (0,0,\pm S_i)$ without loss of generality.

The standard expression for the RKKY interaction in second-order perturbation theory is then

$$J^{\alpha\beta}_{RKKY} = -\frac{J_1J_2}{2\pi}\int_{-\infty}^{0} dE\,\text{Im}[G^{(0)}_{\alpha\beta}(R,E)G^{(0)}_{\beta\alpha}(-R,E)], \tag{9.6}$$

where $G^{(0)}_{\alpha\beta}$ is the retarded single-particle Green function of the unperturbed system and $R = r_2 - r_1 = (n_2 - n_1)a > 0$. However, in our case, we would like to avoid the usual perturbative approach as its validity for flat-band systems is not clear *a priori*. Instead, we calculate $J^{\alpha\beta}_{RKKY}$ exactly by numerically computing the exact ground state energies $E^{\alpha\beta}_{FM}$ and $E^{\alpha\beta}_{AFM}$ for the ferromagnetic (FM) and the antiferromagnetic (AFM) configuration of the impurities, respectively. This gives us

$$J^{\alpha\beta}_{RKKY} = (E^{\alpha\beta}_{FM} - E^{\alpha\beta}_{AFM})/2. \tag{9.7}$$

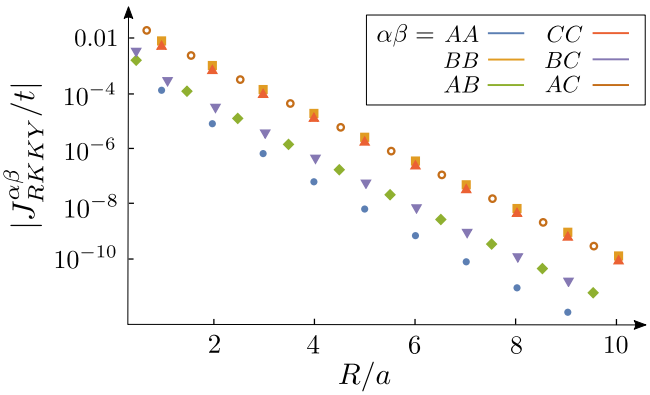

Figure 9.2: Absolute value of the RKKY coupling $|J^{\alpha\beta}_{RKKY}|$ in the stub lattice in dependence on the inter-impurity distance R, calculated via ED and displayed in a logarithmic scale. For all sublattice configurations, $|J^{\alpha\beta}_{RKKY}|$ decays exponentially exponentially with R. Here, we set $J_1 = J_2 = 0.2t$.

The energies $E^{\alpha\beta}_{FM}$ and $E^{\alpha\beta}_{AFM}$ can be computed via exact diagonalization (ED) [33]. Alternatively, we can also calculate the ground state energies in terms of the exact lattice Green functions using the optimized algorithm presented in the SM. This allows us to study significantly larger system sizes while at the same time improving the numerical accuracy of our results.

We start by discussing the stub lattice. First, we look at the dependence of $J^{\alpha\beta}_{RKKY}$ on the inter-impurity distance R. By ED, we find that $J^{\alpha\beta}_{RKKY}$ decays exponentially with R for all sublattice configurations, see Fig. 9.2. For the AA configuration, this is obvious since the eigenstates spanning the flat band do not have support on the A sublattice. As such, J^{AA}_{RKKY} is exponentially suppressed with the energy gap between the two dispersive bands like for a conventional insulator [74]. For the other sublattice configurations, the flat band participates in mediating the RKKY interaction. However, the flat-band states are spatially localized (e.g., they can be constructed as exponentially localized Wannier states), such that their contribution is exponentially suppressed with R as well. Furthermore, in accordance with the general result for bipartite lattices at half filling [27], we find that the ground state is FM (AFM) if the two impurities are located on the same (on different) sublattices of the bipartition [1].

Next, in order to gain further insight into the nature of the RKKY interaction, we study $J^{\alpha\beta}_{RKKY}$ in dependence on one of the exchange coupling constants—say, J_1—for $J_{1,2}/t \ll 1$. For the AA configuration [Fig. 9.3(a)] we find that $J^{AA}_{RKKY} \propto J_1$ as expected from Eq. (9.6). Indeed, since the flat-band states do not have support on the A sublattice, the standard RKKY approximation can be applied without any caveats. For the BB configuration [Fig. 9.3(b)], however, we find a more complicated dependence that cannot be described by Eq. (9.6). This is because Eq. (9.6) does not take into account the large degeneracy of the flat band. Instead, *degenerate* perturbation theory—controlled by the ratio between $J_{1,2}$ and the energy gap that separates the flat from the dispersive band—should be used to accurately

[1] We note, however, that the results in Ref. [27] were obtained from a perturbative approach rather than an exact one.

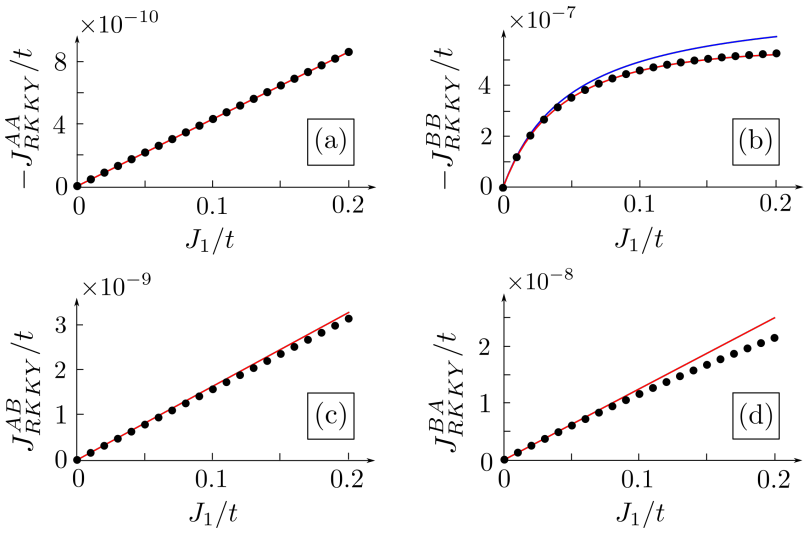

Figure 9.3: RKKY coupling $J^{\alpha\beta}_{RKKY}$ in the stub lattice in dependence on the exchange coupling J_1 calculated via ED (dots) and perturbation theory (lines). (a) AA configuration. Here, $J^{AA}_{RKKY} \propto J_1$ as expected from Eq. (9.6) (red line). (b) BB configuration. Here, J^{BB}_{RKKY} shows an unconventional behavior due to a first-order contribution (blue line) originating from the degenerate flat band. The red line additionally includes the second-order contribution. (c) AB configuration. Here, $J^{AB}_{RKKY} \propto J_1$ with a slope that is well approximated by Eq. (9.6) (red line). (d) BA configuration. Here, $J^{BA}_{RKKY} \propto J_1$ to lowest order (red line). As J_1 increases, an unconventional third-order term $\propto J_1^2 J_2$ originating from the flat band becomes important. In all panels, we set $J_2/t = 0.05$ and $R/a = 5$.

capture the effect of the flat band. This gives a non-vanishing first-order contribution to $J^{\alpha\beta}_{RKKY}$ that is responsible for the unusual J_1-dependence shown in Fig. 9.3(b). To calculate this contribution, we construct a set of flat-band basis states by applying the Gram-Schmidt orthogonalization method to the set of CLSs illustrated in Fig. 9.1(a). It is straightforward to see that we can always construct $N-2$ basis states that do not have support on the impurity sites, such that the entire first-order contribution is contained in an effective 2×2 Hamiltonian that results from projecting $H^{(1)}_{imp} + H^{(2)}_{imp}$ onto the remaining two basis states. Assuming $J_{1,2} \geq 0$, we then find that the RKKY coupling is, to first order, given by

$$J_{RKKY} = aJ_1 + bJ_2 - \sqrt{a^2 J_1^2 + b^2 J_2^2 + cJ_1 J_2} \tag{9.8}$$

for real coefficients a, b, c that correspond to overlap integrals of the participating flat-band basis states. We calculate these coefficients numerically and display the result in Fig. 9.3(b). We see that for small enough J_1, we get a good agreement with the exact result. As J_1 gets larger also the second-order contribution can be taken into account to get a better match. Lastly, we study the AB [BA] configuration, see Fig. 9.3(c) [Fig. 9.3(d)]. Here, Eq. (9.6) gives the correct lowest-order approximation. As J_1 gets larger, an unconventional third-order contribution $\propto J_1 J_2^2$ [$\propto J_1^2 J_2$] originating from the flat band gets important.

Next, we turn to the diamond lattice. Our numerical results for the RKKY interaction in dependence on the inter-impurity distance R are shown in Fig. 9.4. We display only the AA, BB, AB, and BC configurations since, by symmetry, the CC (AC) configuration is equivalent

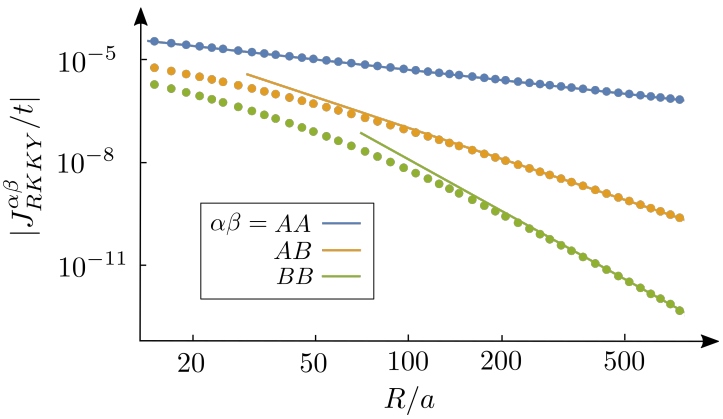

Figure 9.4: Absolute value of the RKKY coupling $|J^{\alpha\beta}_{RKKY}|$ in the diamond lattice in dependence on the inter-impurity distance R displayed in a log-log scale. The dots correspond to numerically calculated data using the algorithm described in App. 9.D, while the solid lines are the asymptotic analytical expressions given in Eqs. (9.11)–(9.13). For the AA configuration, we find the usual $1/R$ decay that is expected in 1D metals. For the other sublattice configurations, the flat band leads to an unusual asymptotic $1/R^3$ ($1/R^5$) decay for the AB (BB) case. Here, we set $J_1 = J_2 = 0.2t$.

to the BB (AB) configuration. Again, we find that the ground state is FM (AFM) if the two impurities are located on the same (on different) sublattices of the bipartition. Furthermore, $J^{\alpha\beta}_{RKKY}$ decays as a power law in R with a leading exponent that depends on the sublattice configuration. For the AA configuration, we find that J^{AA}_{RKKY} decays as $1/R$. Again, this is not surprising since the flat-band states do not have support on the A sublattice. As such, we expect to find the same qualitative behavior as in a conventional 1D metal. However, when one (both) impurities are placed on the B or C sublattices, the flat band leads to an unusual $1/R^3$ ($1/R^5$) decay. We will show later that this unusual behavior is non-perturbative in origin.

Next, we can again study the dependence on J_1 for small $J_{1,2}/t$. For the AA configuration [Fig. 9.5(a)], we again find that $J^{AA}_{RKKY} \propto J_1$ as expected from Eq. (9.6). For the AB configuration [Fig. 9.5(c)], we find $J^{AB}_{RKKY} \propto J_1$ as well, but Eq. (9.6) cannot reasonably approximate the corresponding slope. The BB and BA configurations [Figs. 9.5(b) and (d)] show an even more peculiar behavior: Here, the RKKY interaction first grows rapidly for very small J_1 but then decreases. This observation makes it highly questionable whether perturbation theory is applicable at all, and the following paragraphs will show that it is indeed not. To see this, we use the T-matrix formalism to obtain an exact expression for the impurity-induced shift to the ground state energy in the FM/AFM configuration. Since spin is conserved, we focus on the two spin sectors individually in the following. In App. 9.B, we show that the impurity-induced change in the density of states in a given spin sector and for a given impurity configuration can be written as

$$\Delta\rho(E) = -\frac{1}{\pi}\mathrm{Im}\,\mathrm{tr}\sum_{i,j}\int\frac{dk}{2\pi}[G^{(0)}(k,E)]^2 e^{ik(r_j-r_i)}T_{ij}(E), \tag{9.9}$$

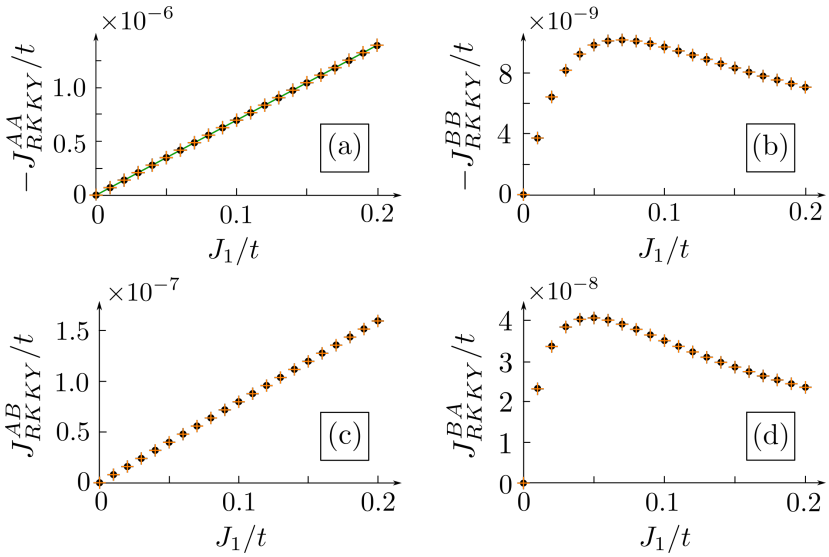

Figure 9.5: RKKY coupling $J^{\alpha\beta}_{RKKY}$ in the diamond lattice in dependence on J_1 calculated via ED (black dots) and via Eq. (9.10) (orange crosses). (a) AA configuration. Here, $J^{AA}_{RKKY} \propto J_1$ as expected from Eq. (9.6) (green line). (b) BB configuration. Here we find that J^{BB}_{RKKY} increases only for very small J_1/t before it starts to decrease. (c) AB configuration. Here, we again have $J^{AB}_{RKKY} \propto J_1$. (d) BA configuration. Here, J^{BA}_{RKKY} shows an unconventional behavior that is qualitatively similar to panel (b). In all panels, we set $J_2/t = 0.05$ and $R/a = 100$.

where $G^{(0)}(k, E)$ is the momentum-space Green function of the unperturbed system and $T_{ij}(E)$ for $i, j \in \{1, 2\}$ are the components of the standard two-impurity T-matrix [75]. This can be used to express $J^{\alpha\beta}_{RKKY}$ as

$$J^{\alpha\beta}_{RKKY} = \frac{1}{2}\sum_{\sigma}\int_{-\infty}^{0} dE\, E\,[\Delta\rho_{FM,\sigma}(E) - \Delta\rho_{AFM,\sigma}(E)]. \tag{9.10}$$

In Fig. 9.5, we present our results for $J^{\alpha\beta}_{RKKY}$ obtained from numerically performing the integration over energy in Eq. (9.10) and find that this reproduces the results from ED very well. Even more interestingly, Eq. (9.10) can be approximated analytically in the limit of large R and small $J_{1,2}/t$. Following the steps outlined in App. 9.C, this leads us to

$$J^{AA}_{RKKY} \approx -\frac{J_1 J_2}{16\sqrt{2}t\pi(R/a)}, \tag{9.11}$$

$$J^{AB}_{RKKY} \approx \frac{J_1 t}{2\sqrt{2}\pi J_2 (R/a)^3}, \tag{9.12}$$

$$J^{BB}_{RKKY} \approx -\frac{12\sqrt{2}\,t^3}{\pi J_1 J_2 (R/a)^5}. \tag{9.13}$$

We plot these approximations in Fig. 9.4 and find that they nicely approach the numerical curves for large enough R, thereby confirming the power laws we previously read off from our numerical data. Importantly, for sufficiently large R, Eqs. (9.11)-(9.13) hold down to

arbitrarily small but finite $J_{1,2}$. As such, the results for the AB and BB configuration show a highly non-perturbative behavior. The above relations further confirm our findings from Fig. 9.5, where we observed qualitatively that the RKKY interaction grows linearly with J_1 if the first impurity is on the A sublattice, while it decreases with J_1 if the impurity is on the B sublattice. However, in this case, the asymptotic $1/J_1$ behavior was not yet clearly visible since the impurity separation was not large enough.

9.4 Conclusions

We have studied the RKKY interaction in two 1D flat-band models at half filling. In our first example—the stub lattice—we have found an unconventional first-order contribution to the RKKY interaction due to the degeneracy of the isolated flat band. In our second example—the diamond lattice—the absence of an energy gap between the flat and the dispersive bands leads to a breakdown of perturbation theory altogether, and non-perturbative contributions cause the RKKY interaction to decay more rapidly with the inter-impurity distance than naïvely expected. Our results illustrate that the RKKY interaction in flat-band systems can exhibit unexpected features and has to be treated with care. We expect this to be relevant in particular for Moiré materials such as, e.g., twisted bilayer or trilayer graphene, which can host isolated flat bands [56–61] or intersecting flat and Dirac-like bands [76–81], respectively.

Of course, it is now interesting to ask how our results are modified by, e.g., electron-electron interactions or disorder. We leave these questions to future work. Furthermore, we have focused on the case of a perfectly flat band at half-filling, where we expect flat-band effects to be the most pronounced. Nevertheless, it would also be interesting to study more general fillings and small deviations from perfect flatness. In general, as long as the exchange coupling constants are larger than any additional energy scale resulting, e.g., from a small but finite bandwidth, we expect the unconventional effects reported here to persist.

Acknowledgments. We thank Henry F. Legg for helpful discussions. This work was supported by the Deutsche Forschungsgemeinschaft via RTG 1995, the Swiss National Science Foundation (SNSF) and NCCR QSIT and by the Deutsche Forschungsgemeinschaft (DFG, German Research Foundation) under Germany's Excellence Strategy - Cluster of Excellence Matter and Light for Quantum Computing (ML4Q) EXC 2004/1 - 390534769. We acknowledge support from the Max Planck-New York City Center for Non-Equilibrium Quantum Phenomena. This project received funding from the European Union's Horizon 2020 research and innovation program (ERC Starting Grant, grant agreement No 757725). Simulations were performed with computing resources granted by RWTH Aachen University under projects rwth0752 and rwth0841.

9.A Matsubara Green functions for the diamond lattice

In this Appendix, we list the Matsubara Green functions for the diamond lattice. To simplify the notation, we set $a = t = 1$ throughout this and all following Appendices. For $r \geq 0$ and $\omega \neq 0$, we then find:

$$G^{(0)}_{AA}(r, i\omega) = \frac{-i\left[-1 + \frac{\omega}{4}(-\omega + \gamma)\right]^r}{\gamma}, \tag{9.14}$$

$$G^{(0)}_{AB}(r, i\omega) = \frac{4^{-1-r}(\omega - \gamma)\left[-4 + \omega(-\omega + \gamma)\right]^r}{\gamma}, \tag{9.15}$$

$$G^{(0)}_{BB}(r, i\omega) = -i\left(\frac{\left[-1 + \frac{\omega}{4}(-\omega + \gamma)\right]^r}{2\gamma} + \frac{\delta_{r,0}}{2\omega}\right), \tag{9.16}$$

$$G^{(0)}_{BC}(r, i\omega) = -i\left(\frac{\left[-1 + \frac{\omega}{4}(-\omega + \gamma)\right]^r}{2\gamma} - \frac{\delta_{r,0}}{2\omega}\right), \tag{9.17}$$

$$G^{(0)}_{BA}(r, i\omega) = \frac{4^{-1-r}(\omega + \gamma)\left[-4 + \omega(-\omega + \gamma)\right]^r}{\gamma} - \frac{\delta_{r,0}}{2}, \tag{9.18}$$

where we have defined $\gamma = \mathrm{sgn}(\omega)\sqrt{8 + \omega^2}$. The other components can be obtained from the above as $G^{(0)}_{AC} = G^{(0)}_{AB}$, $G^{(0)}_{CA} = G^{(0)}_{BA}$, $G^{(0)}_{CB} = G^{(0)}_{BC}$, and $G^{(0)}_{CC} = G^{(0)}_{BB}$, where we omitted the frequency argument for brevity. The Green functions for $r < 0$ can be found from the relation $G^{(0)}_{\alpha\beta}(r, i\omega) = [G^{(0)}_{\beta\alpha}(-r, -i\omega)]^*$.

9.B Impurity-induced change in the density of states

In this Appendix, we derive Eq. (9.9). Using the two-impurity T-matrix, the full Green function of the perturbed system can be expressed as

$$G(r, r', E) = G^{(0)}(r - r', E) + \sum_{i,j} G^{(0)}(r - r_i, E) T_{ij}(E) G^{(0)}(r_j - r', E), \tag{9.19}$$

where $i, j \in \{1, 2\}$. The four components of the two-impurity T-matrix are given by [75]:

$$T_{11}(E) = \left[\mathbb{1} - V_1 G^{(0)}(0, E) - V_1 G^{(0)}(-R, E) T^{(0)}_2(E) G^{(0)}(R, E)\right]^{-1} V_1, \tag{9.20}$$

$$T_{12}(E) = T^{(0)}_1(E) G^{(0)}(-R, E) T_{22}(E), \tag{9.21}$$

$$T_{21}(E) = T^{(0)}_2(E) G^{(0)}(R, E) T_{11}(E), \tag{9.22}$$

$$T_{22}(E) = \left[\mathbb{1} - V_2 G^{(0)}(0, E) - V_2 G^{(0)}(R, E) T^{(0)}_1(E) G^{(0)}(-R, E)\right]^{-1} V_2, \tag{9.23}$$

where we have defined $V_1 = \pm\frac{J_1}{2}|\alpha\rangle\langle\alpha|$ and $V_2 = \pm\frac{J_2}{2}|\beta\rangle\langle\beta|$, where each of the four different sign combinations corresponds to a choice of spin sector and relative orientation (FM/AFM) of the two impurities. Moreover, we have defined the single-impurity T-matrices as

$$T^{(0)}_i = \left[\mathbb{1} - V_i G^{(0)}(0, E)\right]^{-1} V_i. \tag{9.24}$$

The unperturbed Green functions for the diamond lattice that enter the above expressions are given in Sec. 9.A.

The exact Green function can then be used to obtain the impurity-induced change in the local density of states (DoS) of the system:

$$\Delta\rho(r,E) = -\frac{1}{\pi}\mathrm{Im\,tr}[G(r,r,E) - G^{(0)}(0,E)] \tag{9.25}$$

$$= -\frac{1}{\pi}\mathrm{Im\,tr}\Big[\sum_{ij} G^{(0)}(r-r_i,E)T_{ij}(E)G^{(0)}(r_j-r,E)\Big]. \tag{9.26}$$

From this, we obtain the total change of the DoS due to a given impurity configuration as

$$\begin{aligned}
\Delta\rho(E) &= \int dr\,\Delta\rho(r,E) \\
&= -\frac{1}{\pi}\mathrm{Im\,tr}\sum_{ij}\int dr\,G^{(0)}(r-r_i,E)T_{ij}(E)G^{(0)}(r_j-r,E) \\
&= -\frac{1}{\pi}\mathrm{Im\,tr}\sum_{ij}\int\frac{dk}{2\pi}\int\frac{dk'}{2\pi}\int dr\,e^{i(k'-k)r}G^{(0)}(k,E)G^{(0)}(k',E)e^{ikr_j}e^{-ik'r_i}T_{ij}(E) \\
&= -\frac{1}{\pi}\mathrm{Im\,tr}\sum_{ij}\int\frac{dk}{2\pi}[G^{(0)}(k,E)]^2e^{ik(r_j-r_i)}T_{ij}(E).
\end{aligned} \tag{9.27}$$

This is Eq. (9.9) of the main text.

9.C Asymptotic expressions for the RKKY coupling

In this Appendix, we extract the asymptotic behavior of Eq. (9.10) in the limit of large R. For convenience, we write $J^{\alpha\beta}_{RKKY} = \sum_{i,j} J^{\alpha\beta,ij}_{RKKY}$ with

$$J^{\alpha\beta,ij}_{RKKY} = \frac{1}{2}\sum_\sigma\int_{-\infty}^{0} dE\,E\,[\Delta\rho^{ij}_{FM,\sigma}(E) - \Delta\rho^{ij}_{AFM,\sigma}(E)], \tag{9.28}$$

$$\Delta\rho^{ij}(E) = -\frac{1}{\pi}\mathrm{Im\,tr}\int\frac{dk}{2\pi}[G^{(0)}(k,E)]^2e^{ik(r_j-r_i)}T_{ij}(E). \tag{9.29}$$

We start by discussing the AA configuration. In this case, the flat band is not affected by the impurities and we can safely expand the full T-matrix in orders of $J_{1,2}$. Since the unperturbed system is time-reversal symmetric, first-order contributions to the RKKY coupling cancel when the two spin sectors are added up. As such, to lowest order, the RKKY coupling is given by second-order terms $\propto J_1J_2$. These terms are contained within the off-diagonal contributions to the RKKY coupling:

$$J^{AA,12}_{RKKY} = J^{AA,21}_{RKKY} = -\frac{J_1J_2}{\pi}\int_0^\infty d\omega\,(-i\omega)\,G^{(0)}_{AA}(R,i\omega)P^{(0)}_{AA}(-R,i\omega), \tag{9.30}$$

where we have introduced the short-hand notation $P^{(0)}(r,i\omega) = \int\frac{dk}{2\pi}[G^{(0)}(k,i\omega)]^2e^{ikr}$ and where we have already used that $G^{(0)}_{AA}$ ($P^{(0)}_{AA}$) is purely imaginary (real). Note that we find it

convenient to evaluate the above integral in the Matsubara representation. Plugging in the Green functions given in Sec. 9.A, we find that Eq. (9.30) gives us

$$J^{AA}_{RKKY} = -\frac{J_1 J_2}{\pi}\int_0^\infty d\omega\,\omega\left[\frac{16^{-R}(4+\omega^2-\omega\gamma)^{2R}(\omega+2\gamma R)}{\gamma^4}\right] \tag{9.31}$$

with $\gamma = \sqrt{8+\omega^2}$. The integral converges on a scale $\propto 1/R$, which is why we can change the integration variable to $\omega' = \omega R$ and then cut the upper integration limit at some finite constant C that does not depend on R. This allows us to expand the integrand for small ω'/R in order to obtain the asymptotic behavior at large R. In particular, we can approximate

$$16^{-R}\left[4+\left(\frac{\omega'}{R}\right)^2-\frac{\omega'}{R}\sqrt{8+\left(\frac{\omega'}{R}\right)^2}\right]^{2R} \approx 16^{-R}\left(4-\frac{\sqrt{8}\omega'}{R}\right)^{2R} = \left(1-\frac{\omega'}{\sqrt{2}R}\right)^{2R} \approx e^{-\sqrt{2}\omega'}. \tag{9.32}$$

Keeping only the leading contributions also in the rest of the integral, we obtain

$$J^{AA}_{RKKY} \approx -\frac{J_1 J_2}{8\sqrt{2}\pi R}\int_0^\infty d\omega'\,\omega' e^{-\sqrt{2}\omega'} = -\frac{J_1 J_2}{16\sqrt{2}\pi R}. \tag{9.33}$$

After reinstating a and t, this leads us to Eq. (11) in the main text.

In a similar fashion, we can also obtain an asymptotic expression for the AB configuration. Since the second impurity is now sitting on the B sublattice, this impurity will also affect the flat band. In this case, the vanishing band width of the flat band makes it questionable whether we can expand our expression for the RKKY coupling in orders of J_2. We therefore keep the full T-matrix for the second impurity while still expanding in orders of J_1. To lowest order in J_1, we then find two different non-vanishing contributions to the RKKY coupling:

$$J^{AB,12}_{RKKY} = J^{AB,21}_{RKKY} = -\frac{4J_1 J_2}{\pi}\int_0^\infty d\omega\,(-i\omega)\,\frac{G^{(0)}_{BA}(R,i\omega)P^{(0)}_{AB}(-R,i\omega)}{4-J_2^2[G^{(0)}_{BB}(0,i\omega)]^2}, \tag{9.34}$$

$$J^{AB,22}_{RKKY} = -\frac{4J_1 J_2^3}{\pi}\int_0^\infty d\omega\,(-i\omega)\,\frac{G^{(0)}_{BA}(R,i\omega)G^{(0)}_{AB}(-R,i\omega)G^{(0)}_{BB}(0,i\omega)P^{(0)}_{BB}(0,i\omega)}{\left(4-J_2^2[G^{(0)}_{BB}(0,i\omega)]^2\right)^2}. \tag{9.35}$$

Plugging in the Green functions, we get

$$J^{AB,12}_{RKKY} = -\frac{8J_1 J_2}{\pi}\int_0^\infty d\omega\,\omega\left[\frac{16^{-R}\omega^2(\omega-\gamma)(4+\omega^2-\omega\gamma)^{2R-2}[4+(\omega^2-\omega\gamma)(1-R)-8R]}{\gamma^2[8\omega^2\gamma^2+(4+\omega^2)J_2^2+\omega\gamma J_2^2]}\right], \tag{9.36}$$

$$J^{AB,22}_{RKKY} = -\frac{4J_1 J_2^3}{\pi}\int_0^\infty d\omega\,\omega\left[\frac{16^{-R}\omega(4+\omega^2-\omega\gamma)^{2R}[-8\gamma+\omega(8+\omega^2-2\omega\gamma)]}{\gamma^5[\omega^2\gamma^2(4+\omega^2-\omega\gamma)+2J_2^2]^2}\right]. \tag{9.37}$$

These integrals can be approximated following the same steps as above, and, in particular, using again Eq. (9.32). We obtain

$$J^{AB}_{RKKY} = 2J^{AB,12}_{RKKY} + J^{AB,22}_{RKKY} \approx \frac{J_1}{\pi J_2 R^3}\int_0^\infty d\omega'\left(\frac{\omega'^3}{\sqrt{2}}-\omega'^2\right)e^{-\sqrt{2}\omega'} = \frac{J_1}{2\sqrt{2}\pi J_2 R^3}, \tag{9.38}$$

which leads us to Eq. (9.12) in the main text. Finally, for the BB configuration, we now keep the full T-matrices for both impurities. We now get three different non-vanishing contributions to the RKKY coupling:

$$J^{BB,12}_{RKKY} = J^{BB,21}_{RKKY} = -\frac{8J_1J_2}{\pi}\int_0^\infty d\omega\,(-i\omega)\Bigg[\frac{G^{(0)}_{BB}(R,i\omega)P^{(0)}_{BB}(-R,i\omega)}{F_1(R,i\omega)F_2(R,i\omega)} \times\{16-4G^{(0)}_{BB}(0,i\omega)^2(J_1^2+J_2^2)+[G^{(0)}_{BB}(0,i\omega)^4-G^{(0)}_{BB}(R,i\omega)^4]J_1^2J_2^2\}\Bigg], \quad (9.39)$$

$$J^{BB,11}_{RKKY} = \frac{16J_1^3J_2}{\pi}\int_0^\infty d\omega\,(i\omega)\Bigg[\frac{G^{(0)}_{BB}(0,i\omega)P^{(0)}_{BB}(0,i\omega)}{F_1(R,i\omega)F_2(R,i\omega)} \times G^{(0)}_{BB}(R,i\omega)^2\{4-[G^{(0)}_{BB}(0,i\omega)^2-G^{(0)}_{BB}(R,i\omega)^2]J_2^2\}\Bigg], \quad (9.40)$$

$$J^{BB,22}_{RKKY} = \frac{16J_1J_2^3}{\pi}\int_0^\infty d\omega\,(i\omega)\Bigg[\frac{G^{(0)}_{BB}(0,i\omega)P^{(0)}_{BB}(0,i\omega)}{F_1(R,i\omega)F_2(R,i\omega)} \times G^{(0)}_{BB}(R,i\omega)^2\{4-[G^{(0)}_{BB}(0,i\omega)^2-G^{(0)}_{BB}(R,i\omega)^2]J_1^2\}\Bigg], \quad (9.41)$$

with

$$F_{1,2}(R,i\omega) = 16-4G^{(0)}_{BB}(0,i\omega)^2(J_1^2+J_2^2)\pm 8G^{(0)}_{BB}(R,i\omega)^2J_1J_2 - [G^{(0)}_{BB}(R,i\omega)^2-G^{(0)}_{BB}(0,i\omega)^2]^2J_1^2J_2^2 \quad (9.42)$$

and where we have used that $G^{(0)}_{BB}(R,i\omega)=[G^{(0)}_{BB}(R,-i\omega)]^*=G^{(0)}_{BB}(-R,i\omega)$. After plugging in the Green functions, the full expressions become too involved to be displayed here. Nevertheless, the integrals can be approximated in the same way as before, which leads us to Eq. (9.13) in the main text:

$$J^{BB}_{RKKY} = 2J^{BB,12}_{RKKY}+J^{BB,11}_{RKKY}+J^{BB,22}_{RKKY} \approx \frac{1}{J_1J_2\pi R^5}\int_0^\infty d\omega'\left(-4\sqrt{2}\omega'^5+16\omega'^4\right)e^{-\sqrt{2}\omega'} = -\frac{12\sqrt{2}}{J_1J_2\pi R^5}. \quad (9.43)$$

9.D Exact results using Green functions

In this Appendix, we present an efficient algorithm that computes the RKKY coupling numerically using the exact lattice Green functions of the full system. For this, we start by noting that the Hamiltonians studied in the main text have a block-tridiagonal structure. The calculation of Green functions for such Hamiltonians, or in general the calculation of inverse matrices of this kind, has been vastly optimized using several methods [82, 84–89]. In this work, we use an algorithm that can efficiently invert block-tridiagonal matrices as described in Ref. [82]. This algorithm is especially efficient if only a few diagonals, rows, or columns of the matrix are needed since it scales linearly with the system size in these cases. In contrast to Ref. [82] we do not study translationally invariant systems due to the presence of impurities. Therefore, we modify the algorithm of Ref. [82] by adding the needed position dependency as shown in Ref. [83] for tridiagonal matrices. For convenience we recapitulate the algorithm here and present its modified version.

Since the Hamiltonian is Hermitian, the matrix that needs to be inverted has the following structure:

$$A = \begin{pmatrix} a_1 & b_1 & & & & \\ b_1^\dagger & a_2 & b_2 & & & \\ & b_2^\dagger & a_3 & b_3 & & \\ & & b_3^\dagger & a_4 & \ddots & \\ & & & \ddots & \ddots & b_{N-1} \\ & & & & b_{N-1}^\dagger & a_N \end{pmatrix}. \tag{9.44}$$

Here, the a_n and b_n are the blocks that the matrix consists of and N is the number of diagonal blocks. Using a UDL-decomposition this matrix can be decomposed into $A = UDL$ with matrices of the form

$$U = \begin{pmatrix} 1 & U_1 & & & \\ & 1 & U_2 & & \\ & & \ddots & \ddots & \\ & & & \ddots & U_{N-1} \\ & & & & 1 \end{pmatrix}, \tag{9.45}$$

$$L = \begin{pmatrix} 1 & & & & \\ L_1 & 1 & & & \\ & L_2 & \ddots & & \\ & & \ddots & \ddots & \\ & & & L_{N-1} & 1 \end{pmatrix}, \tag{9.46}$$

and a block-diagonal matrix D with blocks D_n for $n \in \{1, \ldots, N\}$. The matrix elements can be calculated using the recursion relations

$$D_L = a_L, \tag{9.47}$$
$$U_n = b_n D_{n+1}^{-1}, \tag{9.48}$$
$$L_n = D_{n+1}^{-1} b_n^\dagger, \tag{9.49}$$
$$D_n = a_n - U_n b_n^\dagger = a_n - b_n D_{n+1}^{-1} b_n^\dagger. \tag{9.50}$$

The inverse of the matrix A can then be decomposed as well and we find $B = A^{-1} = L^{-1}D^{-1}U^{-1}$ with

$$D^{-1} = \begin{pmatrix} D_1^{-1} & & & \\ & D_2^{-1} & & \\ & & \ddots & \\ & & & D_N^{-1} \end{pmatrix}, \tag{9.51}$$

$$U^{-1} = \begin{pmatrix} 1 & -U_1 & U_1U_2 & \cdots & (-1)^{N-1}U_1\cdots U_{N-1} \\ & 1 & -U_2 & \ddots & \vdots \\ & & \ddots & \ddots & U_{N-2}U_{N-1} \\ & & & \ddots & -U_{N-1} \\ & & & & 1 \end{pmatrix}, \tag{9.52}$$

$$L^{-1} = \begin{pmatrix} 1 & & & & \\ -L_1 & \ddots & & & \\ L_2L_1 & \ddots & \ddots & & \\ \vdots & \ddots & -L_{N-2} & 1 & \\ (-1)^{N-1}L_{N-1}\cdots L_1 & \cdots & L_{N-1}L_{N-2} & -L_{N-1} & 1 \end{pmatrix}. \tag{9.53}$$

The diagonal elements of B can be calculated recursively by exploiting the relations

$$B_{1,1} = D_1^{-1}, \tag{9.54}$$

$$\begin{aligned} B_{n+1,n+1} &= D_{n+1}^{-1} + L_n B_{n,n} U_n \\ &= D_{n+1}^{-1} + D_{n+1}^{-1} b_n^\dagger B_{n,n} b_n D_{n+1}^{-1}\,. \end{aligned} \tag{9.55}$$

The off-diagonal matrix elements can then be computed as well. With $m \geq n$, we find the recursive formulas

$$B_{n,m+1} = -B_{n,m}U_m, \tag{9.56}$$

$$B_{m+1,n} = -L_m B_{m,n}, \tag{9.57}$$

such that we are able to calculate all matrix elements. We want to stress that the $B_{i,j}$ are blocks of the inverse matrix B concerning the different unit cells with elements $B^{\alpha,\beta}_{m,n}$ that can be identified with the Green function $G_{\alpha,\beta}(m,n)$.

With these recursion relations we are able to calculate the energy difference, and therefore also the RKKY coupling, by rewriting it as

$$\Delta E = \langle H^{FM}\rangle - \langle H^{AFM}\rangle \tag{9.58}$$

$$= \sum_{n,m,\alpha,\beta} H^{FM}_{n\alpha,m\beta} \langle c^\dagger_{n,\alpha} c_{m,\beta}\rangle_{FM} - \sum_{n,m,\alpha,\beta} H^{AFM}_{n\alpha,m\beta} \langle c^\dagger_{n,\alpha} c_{m,\beta}\rangle_{AFM} \tag{9.59}$$

$$= \frac{1}{2\pi}\int d\omega e^{i\omega 0^+} \left[\left(\sum_{n,m} H^{FM}_{n\alpha,m\beta} G^{FM}_{\beta\alpha}(m,n;i\omega)\right) - \left(\sum_{n,m} H^{AFM}_{n\alpha,m\beta} G^{AFM}_{\beta\alpha}(m,n;i\omega)\right)\right] \tag{9.60}$$

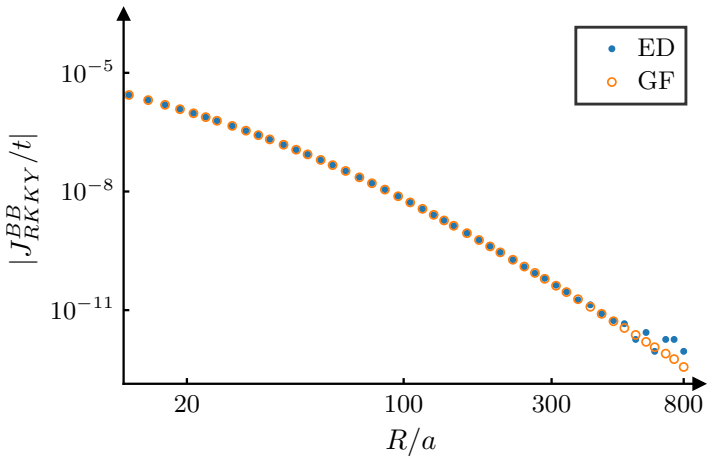

Figure 9.6: Comparison of the results obtained by exact diagonalization (ED) and the described Green function approach (GF). We show the absolute value of the RKKY coupling $|J^{BB}_{RKKY}|$ in dependence of the distance R with $J_1 = J_2 = 0.2t$. The results are calculated with a system size of 4000 unit cells but they are converged up to numerical errors. For moderate R we find perfect agreement between the two methods. For very large R we start to see some differences due to the numerical error of the ED. The GF algorithm therefore enables us to calculate the RKKY interaction for larger distances.

Here we used that the needed expectation values are given by

$$\langle c^\dagger_{n,\alpha} c_{m,\beta} \rangle = \frac{1}{i} G^<_{\beta\alpha}(m,n;t=0,t'=0) \tag{9.61}$$

$$= \frac{1}{2\pi} \int d\omega \, G^<_{\beta\alpha}(m,n;\omega) \tag{9.62}$$

$$= -\int d\omega \, n_F(\omega) \left(\frac{1}{\omega - H + i\eta} - \frac{1}{\omega - H - i\eta} \right)_{m\beta,n\alpha} \tag{9.63}$$

$$= \lim_{T\to 0} \frac{1}{\beta} \sum_{i\omega_n} G_{\beta\alpha}(m,n;i\omega_n) \, e^{i\omega_n 0^+} \tag{9.64}$$

$$= \frac{1}{2\pi} \int d\omega \, G_{\beta\alpha}(m,n;i\omega) \, e^{i\omega 0^+} \, . \tag{9.65}$$

For each spin sector this calculation can be done separately. The total energy difference is then given by

$$\Delta E_{tot} = \Delta E_\uparrow + \Delta E_\downarrow = 2\,\Delta E_\uparrow - J \, . \tag{9.66}$$

Since we only need the first few diagonals of the Green functions to evaluate the formula, the inversion scales only linear with the number of unit cells [$\mathcal{O}(N)$]. Therefore, the usage of this method allowed us to simulate much larger systems (with up to $8 \cdot 10^5$ unit cells). Additionally, it was possible to calculate the RKKY coupling for larger distances with smaller J_{RKKY} since the numerical error could be reduced. In Fig. 9.6 we compare the results obtained with this algorithm with those calculated with ED. We can see that the results for moderate distances perfectly agree. For very large distances we find that the Green functions

approach shows even better results than the ED since the numerical error of the ED starts influencing the results.

Bibliography

[1] M. A. Rudermann and C. Kittel, Phys. Rev. **96**, 99 (1954).

[2] T. Kasuya, Prog. Theor. Phys. **16**, 45 (1956).

[3] K. Yosida, Phys. Rev. **106**, 893 (1957).

[4] P. Bruno and C. Chappert, Phys. Rev. Lett. **67**, 1602 (1991).

[5] P. Bruno and C. Chappert, Phys. Rev. B **46**, 261 (1992).

[6] N. J. Craig, J. M. Taylor, E. A. Lester, C. M. Marcus, M. P. Hanson, and A. C. Gossard, Science **304**, 565 (2004).

[7] L. I. Glazman and R. C. Ashoori, Science **304**, 524 (2004).

[8] G. Usaj, P. Lustemberg, and C. A. Balseiro, Phys. Rev. Lett. **94**, 036803 (2005).

[9] P. Simon, R. López, and Y. Oreg, Phys. Rev. Lett. **94**, 086602 (2005).

[10] G. Yang, C.-H. Hsu, P. Stano, J. Klinovaja, and D. Loss, Phys. Rev. B **93**, 075301 (2016).

[11] F. Pientka, L. I. Glazman, and F. von Oppen, Phys. Rev. B **88**, 155420 (2013).

[12] B. Braunecker and P. Simon, Phys. Rev. Lett. **111**, 147202 (2013).

[13] J. Klinovaja, P. Stano, A. Yazdani, and D. Loss, Phys. Rev. Lett. **111**, 186805 (2013).

[14] M. M. Vazifeh and M. Franz, Phys. Rev. Lett. **111**, 206802 (2013).

[15] F. Pientka, L. I. Glazman, and F. von Oppen, Phys. Rev. B **89**, 180505(R) (2014).

[16] Y. Kim, M. Cheng, B. Bauer, R. M. Lutchyn, and S. Das Sarma, Phys. Rev. B **90**, 060401(R) (2014).

[17] B. Braunecker and P. Simon, Phys. Rev. B **92**, 241410(R) (2015).

[18] C.-H. Hsu, P. Stano, J. Klinovaja, and D. Loss, Phys. Rev. B **92**, 235435 (2015).

[19] M. Schecter, K. Flensberg, M. H. Christensen, B. M. Andersen, and J. Paaske, Phys. Rev. B **93**, 140503(R) (2016).

[20] R. Pawlak, M. Kisiel, J. Klinovaja, T. Meier, S. Kawai, T. Glatzel, D. Loss, and E. Meyer, npj Quantum Inf. **2**, 16035 (2016).

[21] R. Pawlak, S. Hoffman, J. Klinovaja, D. Loss, and E. Meyer, Progress in Particle and Nuclear Physics **107**, 1 (2019).

[22] A. Y. Zyuzin and B. Z. Spivak, JETP Lett. **43**, 234 (1986).

[23] D. Poilblanc, D. J. Scalapino, and W. Hanke, Phys. Rev. Lett. **72**, 884 (1994).

[24] A. V. Balatsky, M. I. Salkola, and A. Rosengren, Phys. Rev. B **51**, 15547 (1995).

[25] V. M. Galitski and A. I. Larkin, Phys. Rev. B **66**, 064526 (2002).

[26] H. Imamura, P. Bruno, and Y. Utsumi, Phys. Rev. B **69**, 121303(R) (2004).

[27] S. Saremi, Phys. Rev. B **76**, 184430 (2007).

[28] E. H. Hwang and S. Das Sarma, Phys. Rev. Lett. **101**, 156802 (2008).

[29] B. Braunecker, P. Simon, and D. Loss, Phys. Rev. Lett. **102**, 116403 (2009).

[30] J. Gao, W. Chen, X. C. Xie, and F.-c. Zhang, Phys. Rev. B **80**, 241302(R) (2009).

[31] Q. Liu, C.-X. Liu, C. Xu, X.-L. Qi, and S.-C. Zhang, Phys. Rev. Lett. **102**, 156603 (2009).

[32] I. Garate and M. Franz, Phys. Rev. B **81**, 172408 (2010).

[33] A. M. Black-Schaffer, Phys. Rev. B **81**, 205416 (2010).

[34] A. M. Black-Schaffer, Phys. Rev. B **82**, 073409 (2010).

[35] B. Braunecker, G. I. Japaridze, J. Klinovaja, and D. Loss, Phys. Rev. B **82**, 045127 (2010).

[36] S. Chesi and D. Loss, Phys. Rev. B **82**, 165303 (2010).

[37] J.-J. Zhu, D.-X. Yao, S.-C. Zhang, and K. Chang, Phys. Rev. Lett. **106**, 097201 (2011).

[38] D. A. Abanin and D. A. Pesin, Phys. Rev. Lett. **106**, 136802 (2011).

[39] M. Sherafati and S. Satpathy, Phys. Rev. B **83**, 165425 (2011).

[40] E. Kogan, Phys. Rev. B **84**, 115119 (2011).

[41] J. Klinovaja and D. Loss, Phys. Rev. B **87**, 045422 (2013).

[42] S. R. Power and M. S. Ferreira, Crystals **3**, 49 (2013).

[43] N. Y. Yao, L. I. Glazman, E. A. Demler, M. D. Lukin, and J. D. Sau, Phys. Rev. Lett. **113**, 087202 (2014).

[44] A. A. Zyuzin and D. Loss, Phys. Rev. B **90**, 125443 (2014).

[45] D. K. Efimkin and V. Galitski, Phys. Rev. B **89**, 115431 (2014).

[46] M. Schecter, M. S. Rudner, and K. Flensberg, Phys. Rev. Lett. **114**, 247205 (2015).

[47] A. M. Tsvelik and O. M. Yevtushenko, Phys. Rev. Lett. **119**, 247203 (2017).

[48] V. D. Kurilovich, P. D. Kurilovich, and I. S. Burmistrov, Phys. Rev. B **95**, 115430 (2017).

[49] C.-H. Hsu, P. Stano, J. Klinovaja, and D. Loss, Phys. Rev. B **96**, 081405(R) (2017).

[50] C.-H. Hsu, P. Stano, J. Klinovaja, and D. Loss, Phys. Rev. B **97**, 125432 (2018).

[51] H. F. Legg and B. Braunecker, Sci. Rep. **9**, 17697 (2019).

[52] O. Deb, S. Hoffman, D. Loss, and J. Klinovaja, Phys. Rev. B **103**, 165403 (2021).

[53] K. Laubscher, D. Miserev, V. Kaladzhyan, D. Loss, and J. Klinovaja, arXiv:2203.08137.

[54] Z. Liu, F. Liu, and Y.-S. Wu, Chinese Phys. B **23**, 077308 (2014).

[55] D. Leykam, A. Andreanov, and S. Flach, Adv. Phys. **3**, 1473052 (2018).

[56] R. Bistritzer and A. H. MacDonald, Proc. Natl. Acad. Sci. USA **108**, 12233 (2011).

[57] Y. Cao, V. Fatemi, A. Demir, S. Fang, S. L. Tomarken, J. Y. Luo, J. D. Sanchez-Yamagishi, K. Watanabe, T. Taniguchi, E. Kaxiras, R. C. Ashoori, and P. Jarillo-Herrero, Nature **556**, 80 (2018).

[58] Y. Cao, V. Fatemi, S. Fang, K. Watanabe, T. Taniguchi, E. Kaxiras, P. Jarillo-Herrero, Nature **556**, 43 (2018).

[59] A. H. MacDonald, Physics **12**, 12 (2019).

[60] E. Y. Andrei and A. H. MacDonald, Nat. Mater. **19**, 1265 (2020).

[61] L. Balents, C. R. Dean, D. K. Efetov, and A. F. Young, Nat. Phys. **16**, 725 (2020).

[62] E. H. Lieb, Phys. Rev. Lett. **62**, 1201 (1989).

[63] B. Sutherland, Phys. Rev. B **34**, 5208 (1986).

[64] R. Shen, L. B. Shao, B. Wang, and D. Y. Xing, Phys. Rev. B **81**, 041410 (2010).

[65] V. Apaja, M. Hyrkäs, and M. Manninen, Phys. Rev. A **82**, 041402 (2010).

[66] T. Zhang and G.-B. Jo, Sci. Rep. **5**, 16044 (2015).

[67] M. R. Slot, T. S. Gardenier, P. H. Jacobse, G. C. P. van Miert, S. N. Kempkes, S. J. M. Zevenhuizen, C. Morais Smith, D. Vanmaekelbergh, and I. Swart, Nature Phys. **13**, 672 (2017).

[68] S. Xia, A. Ramachandran, S. Xia, D. Li, X. Liu, L. Tang, Y. Hu, D. Song, J. Xu, D. Leykam, S. Flach, and Z. Chen, Phys. Rev. Lett. **121**, 263902 (2018).

[69] M. N. Huda, S. Kezilebieke, and P. Liljeroth, Phys. Rev. Research **2**, 043426 (2020).

[70] J. E. Bunder and H.-H. Lin, Phys. Rev. B **80**, 153414 (2009).

[71] J. Cao, H. A. Fertig, and S. Zhang, Phys. Rev. B **99**, 205430 (2019).

[72] D. O. Oriekhov and V. P. Gusynin, Phys. Rev. B **101**, 235162 (2020).

[73] G. Bouzerar, arXiv:2106.10117.

[74] N. Bloembergen and T. J. Rowland, Phys. Rev. **97**, 1679 (1955).

[75] E. N. Economou, *Green's Functions in Quantum Physics*, third edition (Springer, Berlin, 2006).

[76] E. Khalaf, A. J. Kruchkov, G. Tarnopolsky, and A. Vishwanath, Phys. Rev. B **100**, 085109 (2019).

[77] S. Carr, C. Li, Z. Zhu, E. Kaxiras, S. Sachdev, and A. Kruchkov, Nano Lett. **20**, 3030 (2020).

[78] C. Lei, L. Linhart, W. Qin, F. Libisch, and A. H. MacDonald, Phys. Rev. B **104**, 035139 (2021).

[79] H. Kim, Y. Choi, C. Lewandowski, A. Thomson, Y. Zhang, R. Polski, K. Watanabe, T. Taniguchi, J. Alicea, S. Nadj-Perge, arXiv:2109.12127.

[80] C. Shen, P. J. Ledwith, K. Watanabe, T. Taniguchi, E. Khalaf, A. Vishwanath, D. K. Efetov, arXiv:2204.07244.

[81] Y. Li, S. Zhang, F. Chen, L. Wei, Z. Zhang, H. Xiao, H. Gao, M. Chen, S. Liang, D. Pei, L. Xu, K. Watanabe, T. Taniguchi, L. Yang, F. Miao, J. Liu, B. Cheng, M. Wang, Y. Chen, Z. Liu, arXiv:2209.02199.

[82] N. Müller, D. M. Kennes, J. Klinovaja, D. Loss, and H. Schoeller, Phys. Rev. B **101**, 155417 (2020).

[83] S. Andergassen, T. Enss, V. Meden, W. Metzner, U. Schollwöck, and K. Schönhammer, Phys. Rev. B **70**, 075102 (2004).

[84] F. Guinea, C. Tejedor, F. Flores, and E. Louis, Phys. Rev. B **28**, 4397 (1983).

[85] M. P. Lopez Sancho, J. M. Lopez Sancho, and J. Rubio, J. Phys. F: Met. Phys. **15**, 851 (1985).

[86] C. H. Lewenkopf and E. R. Mucciolo, Journal of Computational Electronics **12**, 203 (2013).

[87] M. M. Odashima, B. G. Prado, and E. Vernek, Rev. Bras. Ens. Fis. **39**, e1303 (2017).

[88] K. S. Dy, Shi-Yu Wu, and T. Spratlin, Phys. Rev. B **20**, 4237 (1979).

[89] G. Meurant, SIAM J. Matrix Anal. Appl. **13**, 707 (1992).

Acknowledgments

First and foremost, I would like to thank my supervisor Prof. Jelena Klinovaja for accepting me as a PhD student, for guiding me through all aspects of these last $4+\epsilon$ years, for teaching me so much more than I could ever list here, and for always pushing me to make the most of my own abilities.

Next, I would also like to thank my second supervisor Prof. Daniel Loss for his infinite experience both when it comes to physics as well as to academia in general, for always knowing exactly what to do no matter what's the situation, and for sharing all of this knowledge so generously with me whenever I would ask for advice.

The fact that I have enjoyed these four years as a PhD student so much is also to a large extent due to my wonderful (current and former) colleagues in the Condensed Matter Theory and Quantum Computing Group at the University of Basel: Christoph Adelsberger, Pavel Aseev, Mónica Benito González, Stefano Bosco, Denis Chevallier, Victor Kooi Ming Chua, Renato Dantas, Oindrila Deb, Olesia Dmytruk, Sebastian Diaz, Pierre Fromholz, Tamás Haidekker Galambos, Richard Hess, Bence Hetényi, Tomoki Hirosawa, Silas Hoffman, Zhe Hou, Joel Hutchinson, Vardan Kaladzhyan, Christoph Klöffel, Aksel Kobiałka, Valerii Kozin, Henry Legg, Melina Lüthi, Dmitry Miserev, Alex Mook, Kirill Plekhanov, Christina Psaroudaki, Marko Rančić, Christopher Reeg, Flavio Ronetti, Ferdinand Schulz, Marcel Serina, Maria Spethmann, Aleksandr Svetogorov, Pawel Szumniak, Manisha Thakurathi, Even Thingstad, Yanick Volpez, James Wootton, Xianpeng Zhang, and Yuhao Zhao.

Additionally, I would also like to thank my collaborators from outside of Basel: Dante M. Kennes, Mikhail Pletyukhov, Herbert Schoeller, and, most of all, Clara S. Weber. Working with all of you has been—and still is—an immense pleasure.

Moreover, I would also like to express my gratitude to all the Master students I have had the joy to co-supervise: Danial Chughtai, Maximilian Hünenberger, and Pim Keizer.

Finally, I am very thankful to Prof. Yuval Oreg for accepting to co-referee this Thesis and for being part of my examination committee.